Fakultät für Physik
Technische Universität München

TУΠ

Generalisation of track extrapolation, reconstruction and parametrised simulation for the ACTS project in the context of experiment-comprehensive, future tracking challenges using the example of the ATLAS detector

Fabian Klimpel

Abstract

To study the universe at the microscopic level, the particles created in the collisions of high-energy hadrons at accelerators such as LHC are registered by dedicated detector facilities. The obtained data are utilised to reconstruct the structure of the underlying collision event. As the rate of collisions and the amount of simultaneously occurring interactions will be increased in the future experiments in order to observe rare events, the computational efficiency of the current event reconstruction algorithms will become a limiting factor for the research. In this thesis the requirements for particle track reconstruction and simulation algorithms in the High Luminosity-LHC era are investigated using the ATLAS detector as an example. As an outcome of the dedicated studies and implementation of an advanced track reconstruction workflow, a speed-up factor of up to approximately 8 was achieved in the track reconstruction procedure of the ATLAS experiment, while the physics performance experienced only minor losses. In the future, to reach even greater performance, these improvements can be combined with other approaches such as exploitation of more performant hardware not available today.

This thesis focuses on developments for the ACTS software project, which is a detector-independent framework for track reconstruction and simulation. The development of a generalised track reconstruction software requires a deep understanding of the underlying problem and a well-developed mathematical and physical model. Within the context of this thesis, a theoretical model for track reconstruction based on Bayes' theorem was derived. The description of the developed model in this thesis provides an insight in commonly applied approximations in this field and discusses the resulting limitations and constraints for algorithmic developments.

Furthermore, this thesis presents the development and implementation of a detector independent extrapolation of particle trajectories. Namely, it was demonstrated how a single algorithm is capable to incorporate a large variety of different effects affecting particle trajectories with a minor amount of changes. Additionally, for the first time, the tracking formalism was extended to include time as a parameter of the particle trajectory. This formalism allows for a generalisation of the Kalman filter track reconstruction algorithm to utilise data from e.g. gas detectors without further constraints. The corresponding adaptions of the algorithm are discussed and the track reconstruction performance in a test setup is compared to the classical Kalman filter approach.

Finally, a fast simulation utilising the ACTS software is presented. An overview of the major physical effects and their implementation is shown. A focus is set on a parametrisation of nuclear interactions, derived within the context of this thesis. This parametrisation relies on histogram sampling and is designed to allow for improving the simulation accuracy without the re-parametrizing former histograms. The later property is important for an efficient tuning of the simulation parameters.

Zusammenfassung

Die in den Kollisionen von hochenergetischen Hadronen an Beschleunigern wie dem LHC erzeugten Teilchen benötigen spezielle Detektoren, welche die Teilchenkollisionen aufgezeichnet, damit diese ausgewertet werden können. Ziel dieser Experimente ist die Untersuchung der Wirkungsweise von fundamentalen Kräften und physikalischen Prozessen des Universums. Die aufgezeichneten Daten dienen der Rekonstruktion der zugrundeliegenden Ereignisstruktur. Da die Kollisionsrate und die Anzahl gleichzeitig stattfindender Ereignisse in der Zukunft steigen wird, um auch sehr seltene Ereignisse aufzeichnen zu können, wird die rechnerische Effizienz der heutigen Rekonstruktionsalgorithmen zu einem limitierenden Faktor. In dieser Dissertation wurden die Anforderungen für die Algorithmen der Teilchenspurrekonstruktion und -simulation in der High Luminosity-LHC Ära am Beispiel des ATLAS Detektors untersucht. Als Ergebnis der Studien und Implementierung des fortgeschrittenen Spurrekonstruktionsablaufs wurde ein bis zu 8-facher Geschwindigkeitsanstieg im Spurrekonstruktionsablauf des AT-LAS Experiments erreicht, während die physikalischen Ergebnisse nur kleinere Einbußen verzeichneten. Um einen weiteren Leistungsanstieg zu erzielen können diese Verbesserungen in der Zukunft mit anderen Ansätzen wie der Nutzung von performanterer Hardware kombiniert werden, welche heutzutage nicht verfügbar ist.

Diese Dissertation ist fokussiert auf Entwicklungen für das ACTS Softwareprojekt, welches ein detektorunabhängiges Framework zur Spurrekonstruktion und -simulation ist. Die Entwicklung einer verallgemeinerten Spurrekonstruktionssoftware benötigt ein tiefes Verständnis des zugrundeliegenden Problems und ein gut entwickeltes mathematisches und physikalisches Modell. Im Rahmen dieser Dissertation wurde ein theoretisches Modell für die Spurrekonstruktion, basierend auf dem Satz von Bayes hergeleitet. Die Beschreibung des in dieser Dissertation hergeleiteten Modells bietet einen Einblick in gewöhnlich angewandte Näherungen und diskutiert die daraus resultierenden Grenzen und Einschränkungen für algorithmische Entwicklungen.

Zudem präsentiert diese Dissertation die Entwicklung und Implementierung eines Algorithmus zur detektorunabhängigen Extrapolation von Teilchentrajektorien. Es wurde demonstriert wie ein einziger Algorithmus in der Lage ist, eine große Vielfalt an unterschiedlichen Effekten zu berücksichtigen, welche die Teilchentrajektorie beeinflussen, während nur geringe Änderungen notwendig sind. Zusätzlich wurde zum ersten Mal der Spurrekonstruktionsformalismus erweitert um die Zeit als Parameter der Teilchentrajektorie hinzuzufügen. Dieser Formalismus erlaubt es den Kalman-Filter Spurrekonstruktionsalgorithmus zu verallgemeinern um Daten aus beispielweise Gasdetektoren ohne weitere Bedingungen zu verwenden. Die zugehörigen Anpassungen des Algorithmus werden diskutiert und das Spurrekonstruktionsergebnis innerhalb eines Testaufbaus mit dem klassischen Kalman-Filter Ansatz verglichen.

Zusammenfassung

Im letzten Teil wird eine schnelle Simulation unter Verwendung von ACTS präsentiert. Eine Übersicht über die wichtigsten physikalischen Effekte und deren Implementierung wird dargestellt. Ein Fokus liegt dabei auf der Parametrisierung der hadronischen Wechselwirkung, welche im Rahmen dieser Dissertation konstruiert wurde. Diese Parametrisierung basiert auf dem Nehmen von Stichproben aus Histogrammen und ist konzipiert um die Simulationsgenauigkeit zu verbessern ohne die Parametrisierung früherer Histogramme erneut auszuführen.

Contents

Contents

Contents

1 Introduction

A philosophical question in the era of ancient Greece was around what happens if one takes e.g. a piece of wood and cuts it in halves, takes one half, cuts it again into halves and so on. If this procedure is repeated often enough then does one still have wood or is there an elementary, indestructible component out of which the wood is composed? The Greek philosopher Democritus favoured the latter one and called this elementary component ἄτομος (engl. uncuttable, indivisible) [1].

In ancient Greece this remained a purely philosophical discussion without any possibility to prove or falsify this concept. The idea of Democritus was revived in the modern age and during the 20th century evidence for the existence of *atoms* were provided [2]. The term is thereby derived from Democritus term. Afterwards, it was observed that the atom itself is not an elementary particle but consists of smaller particles: electrons [3], protons [4] and neutrons [5]. Although the atom itself is not an elementary particle, the name was kept.

During the 21st century more and more particles were discovered. In the 1960s, the huge amount of particles was then called a *particle zoo* [6] which raised the question of whether these particles consist themselves of particles. The solution became the *Standard Model of particle physics* (SM) [7]. It is aimed to describe a set of elementary particles, including their possible interactions and transformations.

During the early 20th century the role of theoretical physics grew [8]. Originally, the theoretical physics had little to no impact upon the physics society. This changed due to the prediction possibilities in quantum mechanics with key figures like A. Sommerfeld [9]. As the provided predictions could be proven later on by experiments, the benefit of theoretical physics became obvious. The SM has a similar history. After a first theoretical framework was built, experimental results either confirmed the theory or required an extension of the model. On the other hand, the model was able to predict possible observations. An overview over the SM and remaining open question are given in Chapter 2.

Since the SM enables the prediction of the existence of elementary particles and possible interactions, experimental setups are required for testing the hypotheses. In order to test a given hypothesis from the SM, it is necessary to provide an observable. According to the relation between energy E and a particles mass m at rest [10]

$$E = mc^2$$

it is thus possible to produce a particle with mass m. The energy is thereby not the only condition that needs to be fulfilled but it allows to derive a first concept for investigating the correctness of the SM: If particles have a sufficient high energy then it is possible to

test a hypothesis. Obtaining particles with a certain energy(-regime) is done by *particle accelerators*. They can be divided into two different kinds: cosmic and earth-bound accelerators. The former is the result of processes outside earth (e.g. supernovae) and can provide the highest observable particle energies. On the other hand, these processes are not repeatable. The earth-bound accelerators, on the contrary, reach lower energies but provide repeatable interactions with similar energies. Therefore, the earth-bound accelerators provide more control over the investigation. Additionally, for fulfilling the conditions to obtain an observable, the process under investigation is a stochastic process. Hence, it is beneficial if experiments are repeatable.

Alongside the possibility to produce a particle, a process etc. predicted by a theoretical model, it is mandatory to observe it. Since every observation relies on interaction, a setup is required that registers certain interactions. Furthermore, processes in particle physics occur on a very short timescale, so that it is almost impossible to observe a certain process of interest itself but rather measure result of the process. In Chapter 3 an overview of the earth-bound accelerator *Large Hadron Collider* (LHC) is provided together with a description of the *ATLAS* detector, one of the four major detectors located at the LHC. Within that chapter, the current state of these two are presented and future updates and experimental challenges are shown.

Since a hypothesis is usually tested by observing products of a particle collision rather than the process itself, it is mandatory to utilise the data obtained from the detector and reconstruct the processes that occurred. A part of this procedure that deals with the charged particles is called *track reconstruction* or *tracking*. As the data are the only hint to the underlying processes, the statistical treatment is crucial for further analysis and therefore hypothesis testing. A derivation of the usage of data for utilising the measurements and reconstruct the trajectories of particles alongside their properties is presented in Chapter 4.

In order to perform tracking, dedicated hardware or software based implementations are required. In Chapter 5 the tracking software *ACTS* (A Common Tracking Software) is presented as an example for a software based solution. Within this chapter the initial state for the tracking workflow from Chapter 4 and the utilisation of the results from the tracks are presented.

In the future, tracking has to encounter multiple challenges. While Chapter 3 shows that more data per time will be provided and hence increases the complexity, the computational requirements of the software needs to be lowered without the loss of precision of the stated results. A dedicated study for addressing this issue is presented in Chapter 6.

In Chapter 7 the extrapolation of particle properties along its trajectory and its required components is presented. Starting from modern concepts in the first part of this chapter, the second part is focused upon generalising the concept to allow tracking in future detector setups involving additional information of the particle properties. As the software is intended to be kept detector independent a general scheme for dynamic extrapolation is presented.

While the reconstruction theory in Chapter 4 is centred around discrete and static points at which data can be provided. Chapter 8 generalises this concept. Within this

chapter the location of measurements are considered everywhere leading to generalised formalism of track reconstruction in the context of Chapter 7. The underlying theory from Chapter 4 is thereby considered as a special case.

Besides the reconstruction of tracks, track extrapolation can be utilised for simulating tracks. This allows for investigate detector responses upon certain particles and its properties or to study the sensitivity of an observable with respect to its definition and the detector. The simulation of tracks can be performed with high granularity. This level of granularity is not mandatory for some studies. An implementation for a simplified simulation is presented in Chapter 9.

A summary is presented in Chapter 10.

2 Theory

The description of the smallest constituents of matter and their interactions on the smallest scale are combined in the *Standard Model of particle physics* (SM). This model was developed during 20th century [11]. It is the result of the combined effort of theorists and experimentalists who questioned and predicted many individual components of the model over time. This development process led to a deeper understanding of the nature of elementary particles. An overview over this model is given in Sec. 2.1. Since this is a model, it depends on several model parameters which cannot be derived from first principles. Hence, the theory of the SM has still open question that remain unanswered up to now and rely on further data and experiments. Beside open questions within the SM, there exist concepts of expanding the model motivated by various observations that are not covered by the SM. A selection over some prominent theoretical challenges of the SM are given in Sec. 2.2.

2.1 Standard Model of Particle Physics

The theory of the SM describes the elementary particles and their interactions. Since the completion of the theory the agreement between theoretical predictions and experiments was very successful. With the discovery of the Higgs boson[1], announced in a seminar on July 4th 2012 [12], the existence of all mandatory components was confirmed.

In order to overcome difficulties in the explanation of a growing number of particles discovered in the first half of the 20th century, in 1964 Gell-Mann and Zweig [13, 14] suggested a substructure, the so-called *quark model* for several particles, the hadrons. Hence, these hadrons itself would not be considered as elementary particles but would rather consist out of elementary particles. Establishing this new theory provided a consistent explanation of the Bjorken Scaling [15, 16]. Similar to this example, the SM has many free parameters, like particle masses that cannot be derived from the theory itself but need to be measured. This motivates an ongoing research for a more general model that provides constraints upon these parameters while providing the same results as the SM. The SM is in this context considered as a special case. Up to now, no particle predicted by extensions of the SM has been directly detected in experiments.

The SM can be divided into particles as constituents of matter and interaction-mediating gauge bosons. The latter ones allow interactions between the former but also between the mediators itself. A summary of the SM particles is shown in Tab. 2.1. The fermions[2], quarks and leptons, are grouped into generations. Ordinary matter,

---

[1]The term *boson* denotes in general particles with an integer spin.
[2]The term *fermion* denotes in general particles with a half odd integer spin.

Type	Name	Spin	Electric charge $[e]$
Quark	u, c, t	1/2	+2/3
	d, s, b	1/2	−1/3
Lepton	e^-, μ^-, τ^-	1/2	−1
	ν_e, ν_μ, ν_τ	1/2	0
Mediator	g_i, $i = 1, 2, \ldots, 8$	1	0
	γ	1	0
	W^+, W^-, Z^0	1	+1, −1, 0
Higgs	H	0	0

Table 2.1: Summary of particles contained in the SM [17].

i.e. matter that is observable in everyday life, consists out of u, d and e^-. Expanding this set by the ν_e then forms the first generation. The second and third generation consists of (c, s, μ^-, ν_μ) and (t, b, τ^-, ν_τ) respectively. The masses of the charged fermions of each generation is higher compared to the fermions of the previous generation.

Additionally to the fermions shown in Tab. 2.1, each particle has a corresponding anti-particle. These anti-particle have the same mass as the particle but opposite sign in the quantum numbers.

The SM is a theory that describes the electromagnetic, weak and strong interaction between point-like fermions and bosons. It is a quantum field theory with gauge invariant operators with four dimensions. The corresponding gauge group of the SM is a $SU(3)_C \times SU(2)_L \times U(1)_Y$ symmetry group [18].

The $SU(3)_C$ is the symmetry group of the strong interaction. Strong interacting particles, quarks and gluons carry a degree of freedom called colour charge (indicated by the C). Colours are named red, blue and green, anti-particles carry an anti-colour (e.g. anti-red). Gluons carry a colour and an anti-colour. Since the underlying symmetry group has eight generators, there exist eight different colour-anti-colour combinations and therewith eight different gluons.

The unified symmetry group $SU(2)_L \times U(1)_Y$ represents the weak and electromagnetic interaction. These interactions are the result of the combined theory of electroweak interactions. The subscript L and Y refer to left-handed chirality and the weak hypercharge respectively. In order to provide a relation between these terms, the chirality is required. From the Dirac-equation one obtains the spinor

$$\begin{pmatrix} \psi_L \\ \psi_R \end{pmatrix}$$

with the left-handed spinor ψ_L and the right-handed spinor ψ_R. Both spinors are independent of each other and represent the left and right chirality of a fermion. Within each generation of particles in the SM the left-handed leptons form an $SU(2)_L$ doublet whereas the right-handed leptons form a singlet. The weak isospin can be calculated and be put in relation to the weak hypercharge via

$$Q = T_3 + \frac{1}{2} Y_W \tag{2.1}$$

Type	Chirality	Name	Weak isospin T_3	Weak hypercharge Y_W
Lepton	Left-handed	e^-, μ^-, τ^-	-1/2	-1
		ν_e, ν_μ, ν_τ	1/2	-1
	Right-handed	e^-, μ^-, τ^-	0	-2
		No neutrinos observed		0
Quark	Left-handed	u, c, t	1/2	1/3
		d, s, b	-1/2	1/3
	Right-handed	u, c, t	0	4/3
		d, s, b	0	-2/3

Table 2.2: Summary of weak isospin and weak hypercharge of particles in the SM [17].

with the electric charge of a particle Q, the weak isospin T_3 and the weak hypercharge Y_W. This leads to the values summarised in Tab. 2.2. The doublets are thereby linked to the charged weak interaction, the $W^\pm$ bosons with $T_3 = \pm 1$ and $Y_W = 0$. These bosons allow the transitions within the doublets. In nature this transition is covert by the observation that quark mass eigenstates are different from the weak eigenstates. This phenomenon is described by the Cabibbo-Kobayashi-Maskawa (CKM) matrix. This matrix is a unitary 3×3 matrix V with

$$\begin{pmatrix} d' \\ s' \\ b' \end{pmatrix} = V \begin{pmatrix} d \\ s \\ b \end{pmatrix} = \begin{pmatrix} V_{ud} & V_{us} & V_{ub} \\ V_{cd} & V_{cs} & V_{cb} \\ V_{td} & V_{ts} & V_{tb} \end{pmatrix} \begin{pmatrix} d \\ s \\ b \end{pmatrix}.$$

The vector (d', s', b') represents the weak eigenstates, (d, s, b) the mass eigenstates. If both eigenstates would be identical, V would be diagonal. However it was observed that there are nonzero off-diagonal entries.

A similar observation was done for neutrinos. The corresponding transition matrix is called Pontecorvo–Maki–Nakagawa–Sakata (PMNS) matrix. Since this matrix is not diagonal [19], it implies nonzero neutrino masses [20].

2.1.1 Lagrangian of the Standard Model

An isolated, mechanical system in classical mechanics can be described by a Lagrange function $L(q, \dot{q}, t)$ with the generalised coordinates q, $\dot{q} = dq/dt$ and time t [21]. An

evolution of a physical system is then given by the minimisation of the action S:

$$\delta S = \delta \int_{t_1}^{t_2} dt L(q(t), \dot{q}(t)) = 0$$
$$= \int_{t_1}^{t_2} dt \left[\frac{\partial L}{\partial q} \delta q + \frac{\partial L}{\partial \dot{q}} \delta(\dot{q}) \right]$$
$$= \int_{t_1}^{t_2} dt \left[\frac{\partial L}{\partial q} \delta q + \frac{\partial L}{\partial \dot{q}} \left(\frac{d}{dt} \delta q \right) \right]$$
$$= \int_{t_1}^{t_2} dt \left[\frac{\partial L}{\partial q} - \frac{d}{dt} \frac{\partial L}{\partial \dot{q}} \right] \delta q$$

A consequence of this principle is that the physical system, i.e. the system with respect to small variations by δq has to satisfy the Euler-Lagrange equation

$$\frac{\partial L}{\partial q} = \frac{d}{dt} \left(\frac{\partial L}{\partial \dot{q}} \right).$$

In quantum field theory the generalised coordinates are replaced by fields $\phi(x, y, z, t)$ depending on the space-time coordinates (t, x, y, z). The Lagrange function thereby becomes a Lagrange density or *Lagrangian* with the relation

$$L = \int d^3 r dt \mathcal{L} = \iiiint dx dy dz dt \mathcal{L} \left(\phi, \frac{\partial \phi}{\partial x}, \frac{\partial \phi}{\partial y}, \frac{\partial \phi}{\partial z}, \frac{\partial \phi}{\partial t} \right).$$

With $\mu \in [0, 3]$ the derivatives can be written as $d\phi/dx^\mu = \partial_\mu \phi$. The equation of motion in terms of the Lagrangian then becomes

$$\frac{d\mathcal{L}}{d\phi} = \partial_\mu \frac{d\mathcal{L}}{(\partial_\mu \phi)}$$

following the Einstein notation.

In the SM the electroweak Lagrangian consists out of several parts:

$$\mathcal{L}_{\text{EW}} = \mathcal{L}_{\text{Matter}} + \mathcal{L}_{\text{Gauge}} + \mathcal{L}_{\text{Higgs}} + \mathcal{L}_{\text{Yukawa}} \tag{2.2}$$

The matter Lagrangian $\mathcal{L}_{\text{Matter}}$ describes the evolution with time as well as the interaction between the fermions of the SM and the electroweak gauge bosons:

$$\mathcal{L}_{\text{Matter}} = i \sum_{j=1}^{3} \bar{\psi}^j \gamma^\mu D_\mu \psi_j$$

The index j represents thereby the three generations, ψ^j is the spinor field, γ^μ the Dirac gamma-matrix and D_μ the covariant derivative

$$D_\mu = \partial_\mu - i g W_\mu^a \frac{T^a}{2} - i g' B_\mu \frac{Y}{2}.$$

For $a = 1, 2, 3$ the generators of the $SU(2)_L$ are denoted as W^a, the generator of the $U(1)_Y$ as B. The parameters g and g' denote the coupling strength of the weak and electromagnetic interaction respectively. Y is the weak hypercharge and T^a the components of the weak isospin. The relation between g and g' is given by

$$\tan(\theta_W) = g'/g \qquad (2.3)$$

with the Weinberg-angle θ_W.

The second term $\mathcal{L}_{\mathrm{Gauge}}$ in the electroweak Lagrangian $\mathcal{L}_{\mathrm{EW}}$ describes the kinetic components of gauge bosons and the interaction between the generators of the $SU(2)_L \times U(1)_Y$, W^a_μ and B_μ itself:

$$\mathcal{L}_{\mathrm{Gauge}} = -\frac{1}{4} W^a_{\mu\nu} W^{a\mu\nu} - \frac{1}{4} B_{\mu\nu} B^{\mu\nu}$$

where the tensors $W^a_{\mu\nu}$ and $B_{\mu\nu}$ are thereby given as

$$W^a_{\mu\nu} = \partial_\mu W^a_\nu - \partial_\nu W^a_\mu + g\epsilon^{abc} W^b_\mu W^c_\nu$$
$$B_{\mu\nu} = \partial_\mu B_\nu - \partial_\nu B_\mu$$

with $a, b, c = 1, 2, 3$ and the $SU(2)_L$ structure constant ϵ^{abc}.

The third term of the Lagrangian, $\mathcal{L}_{\mathrm{Higgs}}$ is related to the Higgs mechanism. This mechanism is the result of the requirement that the SM has to be gauge invariant. The explicit introduction of Dirac mass terms, of the form $m\bar{\psi}\psi$, would break the gauge invariance. In order to overcome this issue and to preserve the gauge invariance of the theory an additional complex field of the form

$$\Phi = \begin{pmatrix} \phi^+ \\ \phi^0 \end{pmatrix} = \frac{1}{\sqrt{2}} \begin{pmatrix} \phi_1 + i\phi_2 \\ \phi_3 + i\phi_4 \end{pmatrix}$$

was introduced [22]. This ansatz is known as Englert–Brout–Higgs–Guralnik–Hagen–Kibble mechanism [23] or Higgs mechanism in short. The corresponding Lagrangian is given by

$$\mathcal{L}_{\mathrm{Higgs}} = (D^\mu \Phi)^\dagger (D_\mu \Phi) - V(\Phi) \qquad (2.4)$$

with the potential

$$V(\Phi) = -\mu^2 \Phi^\dagger \Phi + \lambda (\Phi^\dagger \Phi)^2.$$

With $\lambda \geq 0$ the potential $V(\Phi)$ has a minimum. For $-\mu^2 < 0$ the minimum will be displaced from 0. This is necessary in order to provide the spontaneous breaking of the symmetry. Since only contributions of the type $\Phi^\dagger \Phi$ are present in the potential, the minimum is located on the surface of a sphere with radius

$$\langle \Phi \rangle = \sqrt{\frac{\mu^2}{2\lambda}}.$$

A consequence of the Higgs mechanism is that after the symmetry breaking the generators from $\text{SU}(2)_L$ and $\text{U}(1)_Y$, W^a and B will become

$$W^{\pm} = \frac{1}{\sqrt{2}} \left(W^1 \mp iW^2 \right)$$

$$\begin{bmatrix} \gamma \\ Z^0 \end{bmatrix} = \begin{bmatrix} \cos\left(\theta_W\right) & \sin\left(\theta_W\right) \\ -\sin\left(\theta_W\right) & \cos\left(\theta_W\right) \end{bmatrix} \begin{bmatrix} B^0 \\ W^0 \end{bmatrix}$$

with the three massive bosons, $W^{\pm}$ and Z^0 and one massless boson γ. Similar to Eq. (2.3) the mixing angles are thereby directly linked to the coupling parameters g and g' via

$$\cos\left(\theta_W\right) = \frac{g}{\sqrt{g^2 + g'^2}} \quad \sin\left(\theta_W\right) = \frac{g'}{\sqrt{g^2 + g'^2}}.$$

The last term in Eq. (2.2) is the Yukawa interaction. This term describes analogously to $\mathcal{L}_{\text{Higgs}}$ the interaction between the Higgs field and the SM fermions. The Lagrangian is given by

$$\mathcal{L}_{\text{Yukawa}} = \sum_{i=1}^{3} \left(f_i^l \bar{l}_{iL} \Phi e_{iR} + f_i^u \bar{q}_{iL} \tilde{\Phi} u_{iR} + f_i^d \bar{q}_{iL} \Phi d_{iR} \right)$$

with the coupling strengths f_i^l, f_i^u and f_i^d for leptons, positively charged quarks and negatively charged quarks respectively. The left-handed doublets are given by l_{iL} for leptons and q_{iL} for quarks. Right-handed particles are denoted as singlets e_{iR}, u_{iR} and d_{iR} for leptons and quarks. The index i represents the generation. The field $\tilde{\Phi}$ is defined as $\tilde{\Phi}_i = \epsilon_{ij} \Phi_j^*$.

Compared to the electroweak interactions the strong interaction has no additional Higgs terms since the mediators are assumed to be massless [24]. Noteworthy is a different aspect in strong interaction compared to the electroweak interactions: The coupling parameter in the latter interaction depends on and increases with the energy regime. The value of the strong coupling parameter α_s on the other hand strongly depends on the energy regime Q as shown in Fig. 2.1. Known by the term *confinement* [26] quarks cannot be observed as free particles in contrary to leptons but only bound by gluons to a colour neutral object. These combinations are the hadrons that are observable by particle detectors. This plot on the other hand reveals that for higher energies the coupling gets weaker. This phenomenon is called *asymptotic freedom* [27]. A consequence of this effect is that high energy quarks and gluons will asymptotically behave like free particles. The particle radiates bosonic particles and its energy is reduced in this way. Consequently, the coupling becomes stronger and at some point hadrons are formed. This process is called hadronisation.

2.2 Theoretical Challenges of the Standard Model

An ideal theoretical model describes all elementary particles, their interactions and all corresponding properties and parameters such that all measured physical observables
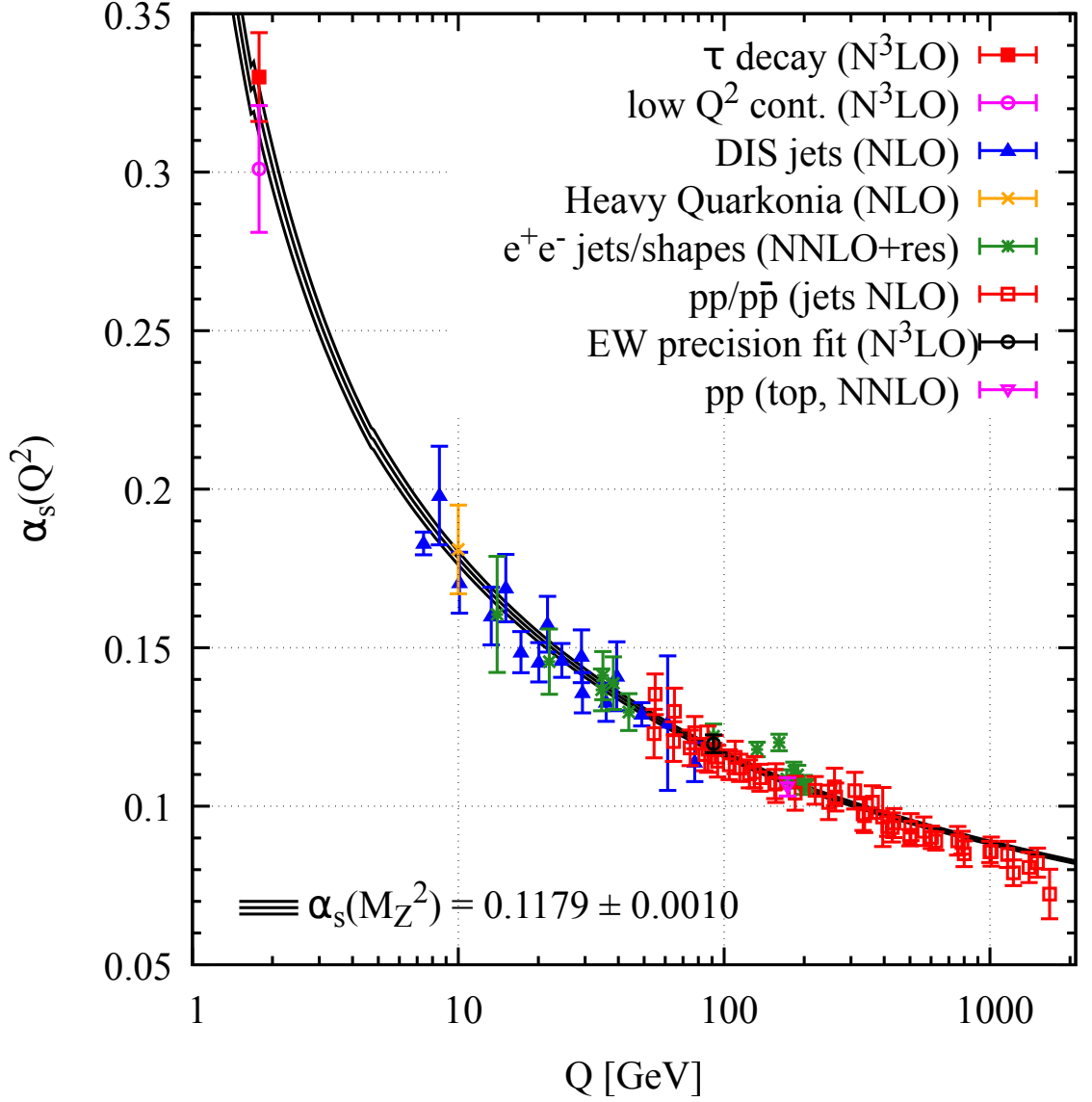
Figure 2.1: Summary of measurements of α_s as a function of the energy scale Q. The respective degree of QCD perturbation theory used in the extraction of α_s is indicated in brackets (NLO: next-to-leading order; NNLO: next-to-next-to-leading order; NNLO+res.: NNLO matched to a resummed calculation; N3LO: next-to-NNLO) [25].

agree with predictions from the model. The SM parameters like the coupling strengths are free parameters. Their values rely on experimental measurements.

Beside the missing model intrinsic constraints on such model parameters, the SM describes the electroweak and strong interaction but not the gravity. The absence of this fundamental force in the model is the most obvious limitation but not the only one.

The phenomenological prediction power of the SM is tested by HEP experiments but also by other fields in physics such as cosmological experiments. Many different aspects of the SM are under ongoing investigation. Since most rely on explanations that are beyond the scope of this thesis, two recent measurements are presented that motivate future research. Afterwards, a short overview of current theoretical modelling efforts are shown.

Lepton Flavour Universality

In March 2021, the LHCb collaboration published results of the branching ratio in B-decays [28]. One of the processes investigated is shown in Fig. 2.2 (left).
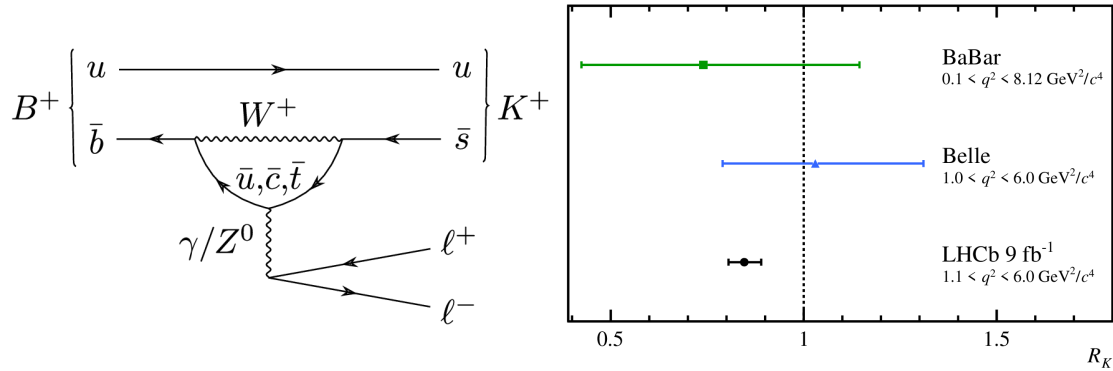
Figure 2.2: Left: Feynman diagram displaying the decay $B^+ \to K^+ l^+ l^-$ with the leptons $l = e, \mu$. Right: Comparison of R_k from BaBar, Belle and LHCb. The dotted line represents the SM prediction. Both figures are taken from Reference [28].

The final state leptons produced in the decay of a B-meson into a kaon can be either an e^+e^- or a $\mu^+\mu^-$ pair. The quantity of interest within the analysis is the ratio

$$R_K = \frac{\mathcal{B}(B \to K\mu^+\mu^-)}{\mathcal{B}(B \to Ke^+e^-)}$$

with $B = B^+, B^0, B_s^0, \Lambda_b^0$ and $K = K^+, K^{*0}$. The function $\mathcal{B}$ describes the transition probability of its argument, according to Fermi's golden rule [29]. The SM assumes implicitly that the couplings of leptons to gauge bosons is independent of the lepton flavour (lepton flavour universality). For sufficiently large momenta, the SM predicts that $R_H \simeq 1$. Fig. 2.2 (right) shows the latest result from the LHCb collaboration together with the previous results from BaBar and Belle. In comparison of the obtained result to the prediction of the SM, the data show that the SM does not describe the observation properly. Considering the uncertainty of R_K, the result is currently interpreted as a hint

for new physics. The collaboration stated in this context a 3.1σ [28] deviation from the SM prediction[3].

Anomalous Magnetic Moment of Muons

The magnetic moment $\vec{\mu}$ of muons is given by

$$\vec{\mu}_\mu = g_\mu \left(\frac{q}{2m_\mu} \right) \vec{s} = (1 + a_\mu) \frac{q}{m_\mu} \vec{s}$$

with the charge q, the muon mass m_μ, the spin $\vec{s}$ and the anomalous magnetic moment of the muon a_μ [30]. The parameter $g_\mu = 2(1 + a_\mu)$ describes the strength of the magnetic moment. his factor can be derived simply from the Dirac equation and is predicted to be equal to 2 at leading order. Quantum corrections to the muon interaction vertex with an external magnetic field lead to a small deviation from this value. The current best theoretical prediction from the SM, which includes QED, EW, hadronic vacuum polarisation and hadronic light-by-light loop corrections, yields a value of $a_\mu(SM) = 116591810(43) \cdot 10^{-11}$ [31].

The anomalous magnetic moment describes the variety of effects and their impact on the magnetic moment. A schematic overview of the different effects considered by the Muon g-2 collaboration is shown in Fig. 2.3 (left). In 2006, the Brookhaven National
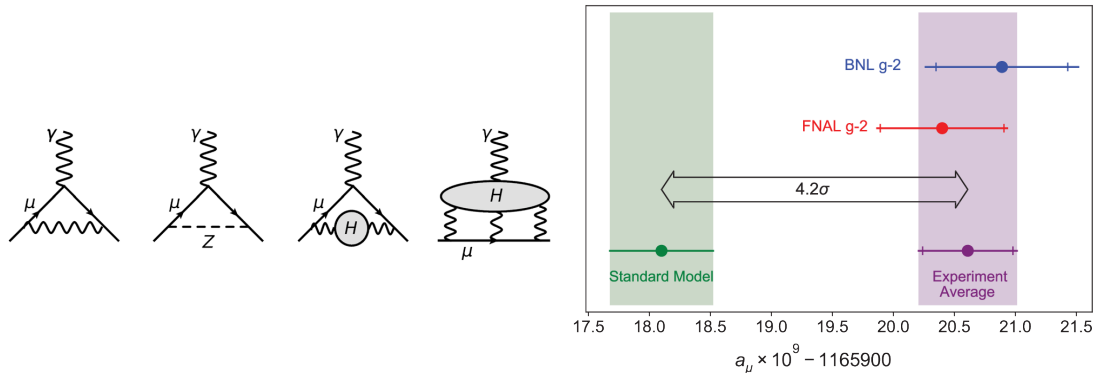
Figure 2.3: Left: Feynman diagrams displaying the SM corrections to the magnetic moment of the muon. From left to right: QED and weak processes, hadronic vacuum polarisation and light-by-light contributions. Right: Comparison between the measured anomalous magnetic moment and the SM prediction. Both figures are taken from Reference [30].

---

[3]A common definition for a hint or a discovery is given in terms of standard deviations σ. For a multiple n of σ, the probability $1 - \int_{\mu-n\sigma}^{\mu+n\sigma} \mathcal{G}(x|\mu,\sigma)dx$ with the normal distribution $\mathcal{G}$ and the mean of the distribution μ, a probability for a null hypothesis can be stated. A common choice for a null hypothesis is the absence of an observation. A hint or a discovery are then stated if this probability becomes smaller than a certain threshold or equivalently a sufficient large n. It is obvious that the threshold for a hint is at a larger probability than the actual observation. One choice is thereby 3σ and 5σ respectively.

Laboratory (BNL) published a measurement of a_μ [32]. The obtained value showed deviation from the SM prediction by 3.7σ. In order to obtain an independent measurement of this quantity, the Muon g-2 collaboration, located at the Fermilab National Accelerator Laboratory (FNAL) repeated the experiment. In April 2021, the collaboration published the results of their measurement [30]. As shown in Fig. 2.3 (right), the FNAL result confirms the prior observation. The combination of the BNL and FNAL measurements shows a 4.2σ deviation between the experimental data and the SM predictions.

Beyond the Standard Model

Certain phenomena such as gravity are not described by the SM, others such as the measured Higgs mass lead to questions concerning naturalness and the fine-tuning of the SM parameters. While e.g. on a cosmological scale dark matter and energy play a significant role in certain observations, the SM is incapable of describing their origin. Utilising this as an example, although the SM is considered completed since the discovery of the Higgs boson, physics beyond the SM (BSM) is researched. The prediction power of the SM for a large variety of physical effects as well as the experimental validations provide tight constraints on a BSM model succeeding the SM. Additionally, the new model has to be compatible with data and constraints from observations that are not part of the SM.

In the past century, many BSMs like the string theory were developed. One particular field currently under investigation, both theoretically and at the LHC, is the so-called *Supersymmetry* (SUSY). SUSY is an extension of the SM which introduces a symmetry operator relating bosons and fermions. This in turn implies the existence of corresponding mirror particles, called superpartners, to the existing SM particles [33]. The superpartners of SM fermions are scalar bosons, of SM bosons are fermions. The additional symmetry in SUSY models introduce further a conversion mechanism between fermions and bosons. While this is a very simplified representation of SUSY, the general message intended is that BSMs treat the SM as a special case of a more general theory. SUSY is in the field of BSMs a, compared to other theories, small modification of the SM, appearing more natural. Among the variety of SM extensions, the minimal supersymmetric SM (MSSM) is of special interest since it represents the smallest set of supersymmetric particles necessary to obtain a SUSY theory.

Although a large variety of different theories exist with the intention of describing observations and phenomena, their validation relies on unique observations predicted by a particular model, i.e. an experimental validation due to observables that are not part of the SM. Up to the time of writing this thesis, no experimental evidence has been found for any BSM theory.

3 Experiment

The quantum mechanical nature of elementary particles as shown in Chapter 2 means that the deterministic predictions for microscopic processes are impossible. Hence, in order to investigate probabilistic processes repetitions of an experiment are mandatory. This involves the chance for the observation itself as well as the statistical confidence in the observation. Beside this requirement for an experimental setup it is necessary to consider conditions and boundaries given by nature. The most obvious is thereby the energy. If a process involves a particle of a certain mass then there exists a lower threshold for the energy of a particle.

Within this chapter two aspects will be considered. In the first half of this chapter the particle accelerator LHC will be presented. This machine is responsible for both, the energy of the particles and the generation of interactions. Furthermore, a preview for the future of the machine is given. In the second part of this chapter the principle of measuring the products of interactions with the LHC detector ATLAS are presented. Since this detector is a general purpose detector, it provides many aspects that are common among detectors in particle physics. Corresponding to the future of the LHC, an overview of the future of the ATLAS detector is explained.

3.1 CERN Accelerator Complex

The Large Hadron Collider (LHC) [34] is a hadron accelerator and collider located in the area of Geneva. Fig. 3.1 shows that different accelerators are needed for different experiments and additionally that the LHC is not the only accelerator in this complex. The reason for the existence of multiple accelerators is historically motivated. The CERN was established in 1954 and hence before the SM was formulated. Beside the missing components in the theory many constituents of the SM were neither measured nor constrained. Over the years more and more predictions from the SM were confirmed, starting from the lightest particles and most probable processes to heavier and rarer ones. Along this historical development the accelerator complex grew as higher energies or more precise and frequent measurements became necessary. The older ones often became pre-accelerators of their successor.

3.1.1 Pre-accelerators

For the usage of the LHC only a subset of pre-accelerators are used. Those underwent multiple modifications and upgrades over the years. In the following an overview restricted to the current specifications and to the acceleration of protons is presented:
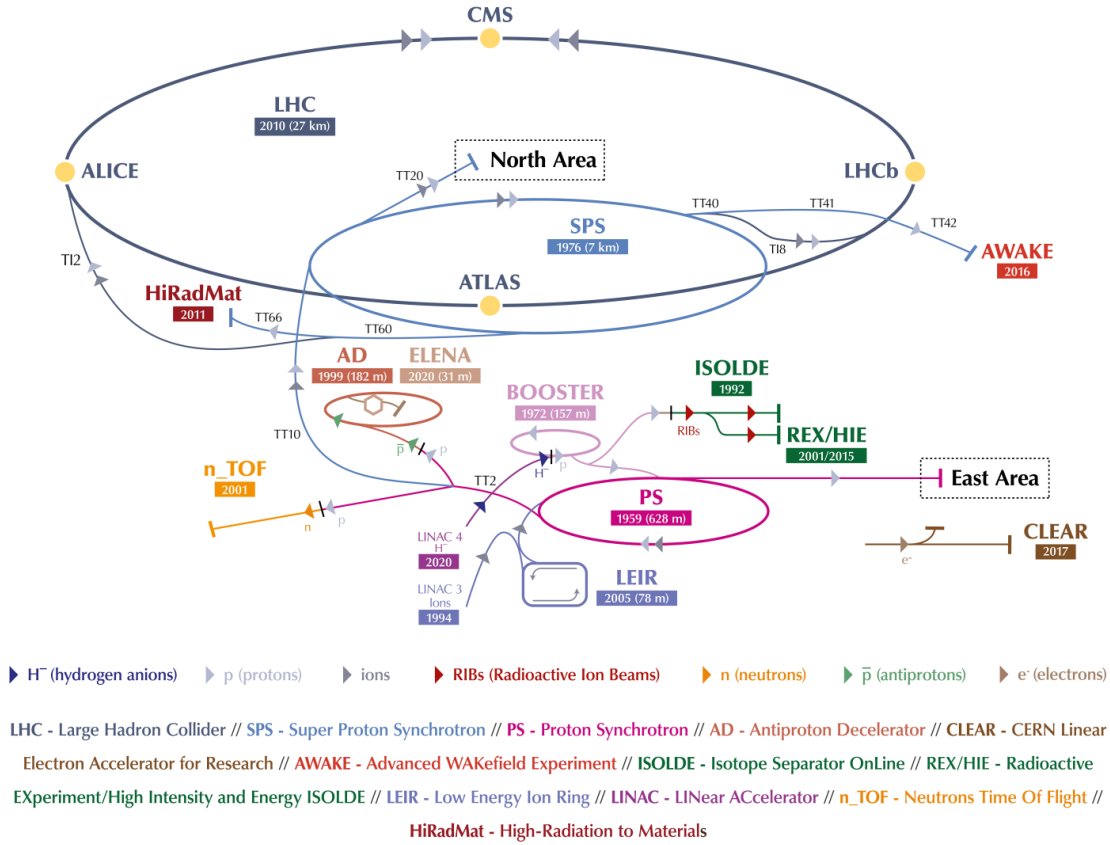
Figure 3.1: Schematic visualisation of the CERN accelerator and experiment complex [35].

Linac4

The Linear Accelerator 4 (Linac4) [36] is the first acceleration stage for the LHC. An overview of the individual components of the Linac4 is shown in Fig. 3.2. Starting from
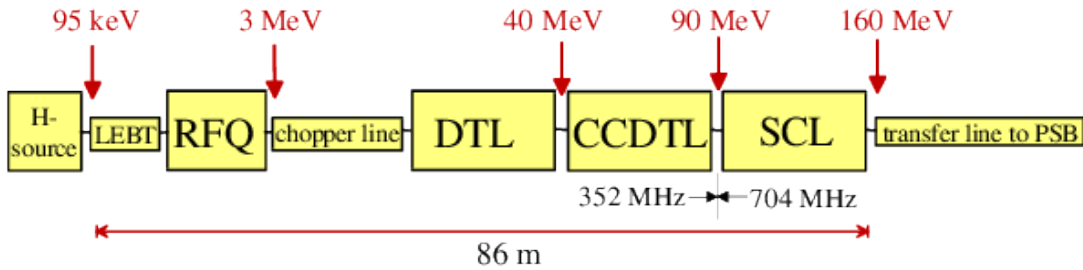
Figure 3.2: Schematic overview of the individual modules of the Linac4. Starting from the H$^-$ source on the the left, the individual acceleration steps are shown with the corresponding exit energies of the ion bunches [36].

a H$^-$ source delivering 100 μs pulses of 40 mA with a frequency of 5 Hz, the hydrogen

ions leave this source with 95 keV[1] and are transported through the Low-Energy Beam Transport (LEBT) to the Radio-Frequency Quadrupole (RFQ). The RFQ groups the ions into bunches and accelerates the bunches to 3 MeV over a length of approximately 6 m. These bunches are then guided to the Medium Energy Beam Transport (MEBT) or "chopper line". By using an electrostatic beam deflector this device is capable of stopping and dumping selected sequences of bunches. A bunch thereby receives a kick using a ± 400 V field that performs a deflection of the bunch by 5.7 mrad. This dumping system allows to remove low-quality bunches already in an early stage of the acceleration process that otherwise would be dumped in a later stage of the acceleration. An estimation for the dropping rate of bunches in the current scheme is about 37.5%. After the chopping and rejecting the bunches enter the Drift Tube Linac (DTL). This component consists out of three tanks with voltage gradients of 3.3 MV/m, 3.5 MV/m and 3.5 MV/m respectively. The bunches leave the tanks with the energies 9.8 MeV, 25.0 MeV and finally 39.9 MeV. During the acceleration the beam is under the influence of a magnetic field provided by Permanent Magnet Quadrupoles (PMQ) instead of electromagnetic ones. This decision is due to the radiation hardness of the PMQ, the smaller size of the magnets and higher shunt impedance.

Since the bunch energy inside the DTL is rather small, the alignment of the components of the DTL are very demanding. With an exit energy of 40 MeV from the module a less strict drift tube linac system can be used: the Cell-coupled DTL (CCDTL). Compared to the DTL the CCDTL is an alternating setup of drift tubes and quadrupoles as shown in Fig. 3.3. Compared to the DTL the magnets in the CCDTL are electro-
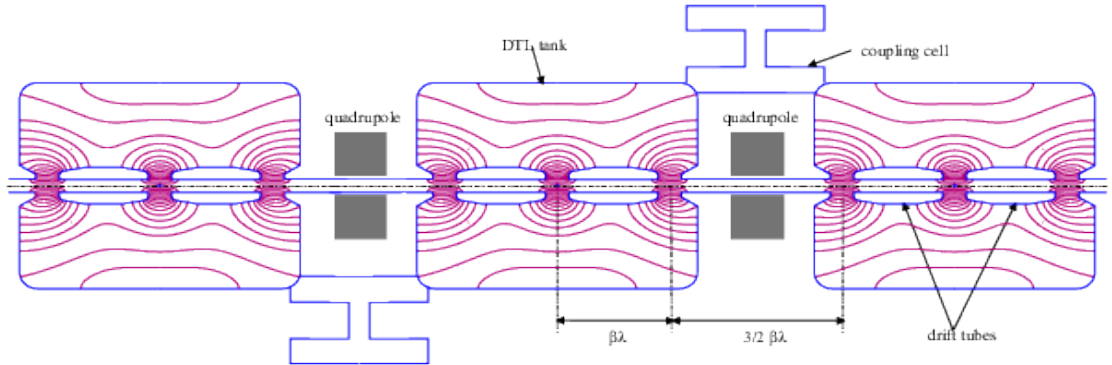
Figure 3.3: Overview over the components in a CCDTL module [36].

magnetic quadrupoles. The entire CCDTL setup consists of 24 tanks grouped into eight modules. Each tank consists out of three gaps with a field gradient of up to 3.9 MV/m. Over the length of the CCDTL of 25.2 m the bunches are accelerated from 40 MeV up to 91.7 MeV. This output is the entrance energy to the last module of the Linac4, the Side-coupled linac (SCL). Compared to previous parts that operate at 352 MHz,

---

[1]The exit energy of the ions is actually 35 keV. In order to match the requirements of the RFQ a post-acceleration is performed.

the SCL operates with 70.4 MHz. The alternation between acceleration and focusing is similar to the CCDTL layout. The SCL consists of four modules with five tanks each. Each tank has thereby eleven gaps that operate with a gradient of 4 MV/m. Therewith the bunches are accelerated over a distance of 28 m up to 160.1 MeV.

After the bunches exit the Linac4, the H^- ions pass a stripping foil that removes all electrons from the atoms. If an atom is afterwards neutral or negatively charged the individual atom will be dumped by magnetic deflection.

Proton Synchrotron Booster

Before the year 1972 the former linear accelerator Linac1 fed the Proton Synchrotron (PS) with 50 MeV protons directly. The therewith maximum number of protons per pulse (ppp) was limited to 10^{10} [37]. This value was insufficient when plans for a new accelerator, the Super Proton Synchrotron were in development. In order to solve this issue a new synchrotron was proposed between the linear accelerator and the PS: The Proton Synchrotron Booster (PSB).

The PSB is a synchrotron with a radius of 25 m that accelerates the originally 50 MeV protons from the Linac1 up to 800 MeV. It consists of 16 groups of components, each containing two dipole and three quadrupole magnets. Furthermore it contains five regions without magnetic deflection. These straight subsections allow for beam diagnostics and corrections.

Although the radius of the PSB is just a quarter of the PS, the intensity limitations due to space-charge could be solved by splitting the incoming beam into four rings as shown in Fig. 3.4. By utilising several dipole magnets, the bunches are kicked vertically
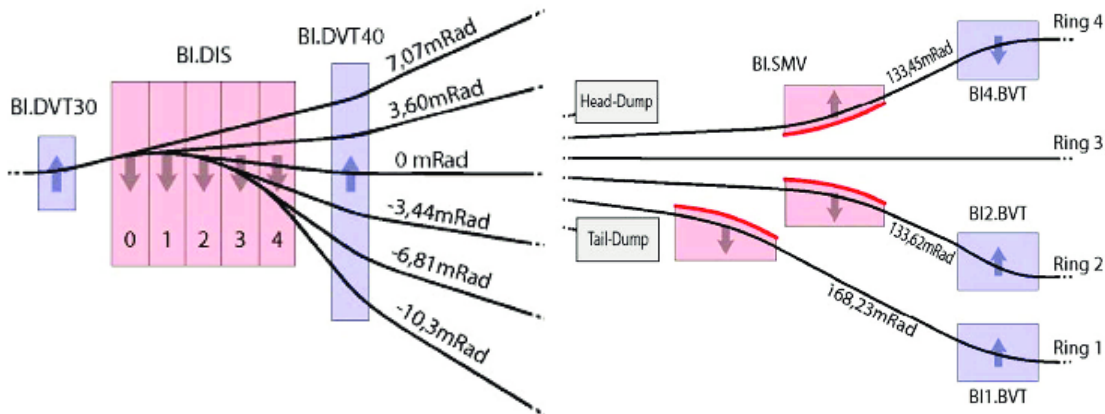
Figure 3.4: Schematic visualisation of the beam splitting (left) and guidance (right) during the Proton Synchrotron Booster injection from the linear accelerator. Left: The incoming beam is split into six different beams using five dipole magnets with different polar angles with respect to the beam axis. Right: The vertically arranged four rings of the synchrotron are filled top to bottom, i.e. starting with Ring 4, finishing with Ring 1. The head and tail of the beam is dumped above Ring 4 and below Ring 1 respectively. The figures were taken from Reference [37].

and guided into the rings starting from top to bottom. In order to guarantee a sufficient beam quality the head and tail of the beam pulse provided by the linear accelerator are dumped.

As the beam is accelerated in each ring individually, the phases between the bunches of the rings are arbitrary. In order to provide an optimal filling for the PS, a synchronisation is required. Shown as red dots at t_0 in Fig. 3.5, after the synchronisation all bunches in the rings have the same phase immediately before the beam extraction. The bunches
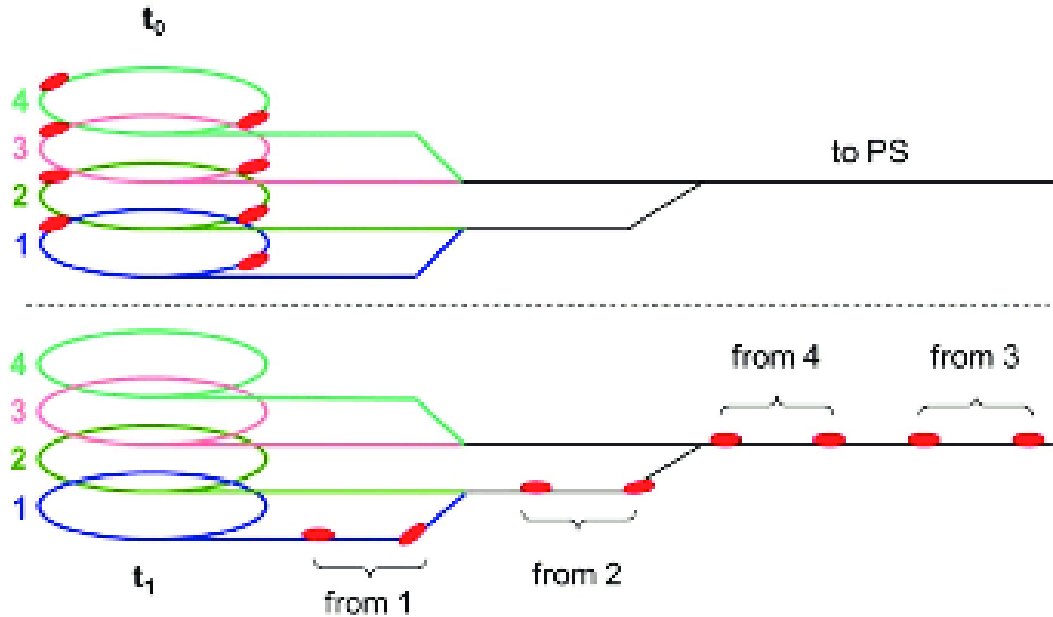
Figure 3.5: Beam extraction scheme from Proton Synchrotron Booster. The phases of individual bunches from the four rings are synchronised until the time t_0. Afterwards one ring after another is emptied starting with Ring 3, then 4, 2 and 1. This figure is taken from Reference [37]

from each ring are then emptied one after another and transported to the PS.

The PSB as intermediate stage between the Linac1 and the PS allowed to lift the ppp up to 10^{13} by 1974. Up to today this value was increased by a factor of four. Additionally, the initial output energy of the PSB was lifted up to 1.4 GeV. For the Linac4 it is planned to stretch it further to 2 GeV.

Proton Synchrotron

The Proton Synchrotron [38] (PS) or CERN Proton Synchrotron (CPS) was commissioned in 1959 [39] and is therewith one of the oldest accelerators at the CERN accelerator complex. The PS is a synchrotron located at ground level. By using 101 dipole magnets with up to 1.26 T, the particles are forced on a circular path with a circumfer-

ence of 628 m. During the circulations the particles are accelerated up to 26 GeV in 24 accelerating cavities.

Along the acceleration process the PS splits the bunches. The first splittings occurs at 2.5 GeV [40] and splits two bunches into three as shown in Fig. 3.6. After reaching
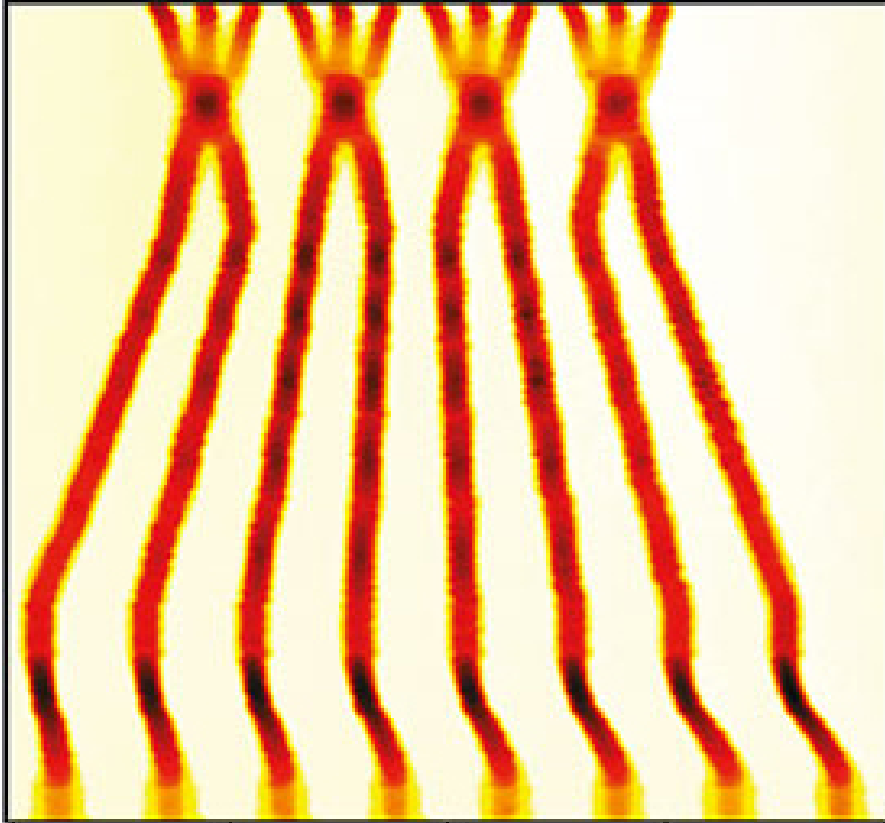
Figure 3.6: Beam splitting in the Proton Synchrotron using the Batch Compression Merging and Splitting (BCMS). The abscissa allows the identification of individual bunches while the time evolution is is shown on the ordinate axis [41].

the output energy two subsequent splitting occur. This time each bunch is split into two bunches. Hence the PS is capable to deliver a range of bunches ranging from 12 to 72. Also a variable spacing of 25, 50, 75 and 150 ns between the bunches can be obtained from the machine. In the beginning of the LHC era the PS provided 36 bunches with a spacing of 50 ns. Since mid-July 2015 the spacing was reduced to 25 ns and the number of bunches was increased to 72 with $1.15 \cdot 10^{11}$ protons per bunch. With the implementation of the Batch Compression Merging and Splitting (BCMS) in mid 2016 the number of bunches was reduced to 48 with $1.3 \cdot 10^{11}$ protons per bunch.

Super Proton Synchrotron

The last pre-accelerator for the LHC is the Super Proton Synchrotron (SPS). This synchrotron was commissioned in July 1976 [42] to the CERN accelerator complex and led to the discovery of the weak bosons (Nobelprize 1984 [43]). With up to 2 T magnetic fields provided by 744 dipole magnets, the particles are deflected to move along the ring with a circumference of around 6.9 km. The 26 GeV particles from the PS are accelerated inside the SPS up to 450 GeV in four cavities. Together with the last acceleration process before the injection into the LHC, the SPS builds the bunch train consisting of 288 bunches [44] which is four times the number of bunches provided by the PS.

3.1.2 Large Electron-Positron Collider

As these accelerator complex grew historically due to new challenges and based upon the knowledge obtained about the SM from earlier experiments the LHC itself is no exception to its pre-accelerators. In fact, the approximately 27 km long tunnel used for the LHC was built initially for the Large Electron-Positron Collider (LEP) [45]. This accelerator was operating from 1989-2000. The LEP was running on a range of centre-of-mass energies $\sqrt{s}$ from approximately 91 GeV from 1989-1995 and afterwards with 130-209 GeV [46]. The results obtained from this accelerator can be seen as motivation for the construction of the LHC and to constrain the required parameters for the accelerator.

Although the SM has a variety of model parameters that would benefit from more precise measurements, the probably most famous motivation for a new generation of particle accelerators at the end of the last century was the missing Higgs boson. As it was shown in Sec. 2.1.1 the Higgs mechanism itself is crucial for preserving the gauge invariance of the SM. Since the former searches for particles and processes predicted by the SM were successful, a dedicated search for this missing particle was reasonable. Although its discovery happened in the LHC era [12] LEP provided already some constraints to its mass as shown in Fig. 3.7 (left). As the plot already indicates it was possible to cover higher regions with LEP at the higher centre-of-mass energies. Considering on the other hand the cross-section σ for a Higgs boson production channel as shown in Fig. 3.7 (right), the process is very rare. Although the centre-of-mass energy grew over time, it was limited. Due to synchrotron radiation [50] the leptons radiate the power

$$P \propto \frac{E^4}{r^2 m^4}.$$

Hence, the acceleration of $e^{\pm}$ compared to hadrons is due their small mass m stronger affected from this energy loss. The loss is even enhanced for higher energies E. In order to compensate this energy loss, the particles need to be accelerated, though the possible acceleration is limited. Given a technical limitation, the possible particle energies are limited. Additionally, due to to the power law, the fraction of power consumption for compensating the synchrotron radiation becomes a major economical factor.

Since the LEP ring is considered to be static and cannot be changed, the magnetic field B needs to be adapted when varying the particle's energy. Higher particle energies are going along with stronger magnetic fields. Also the magnetic field strength is limited.
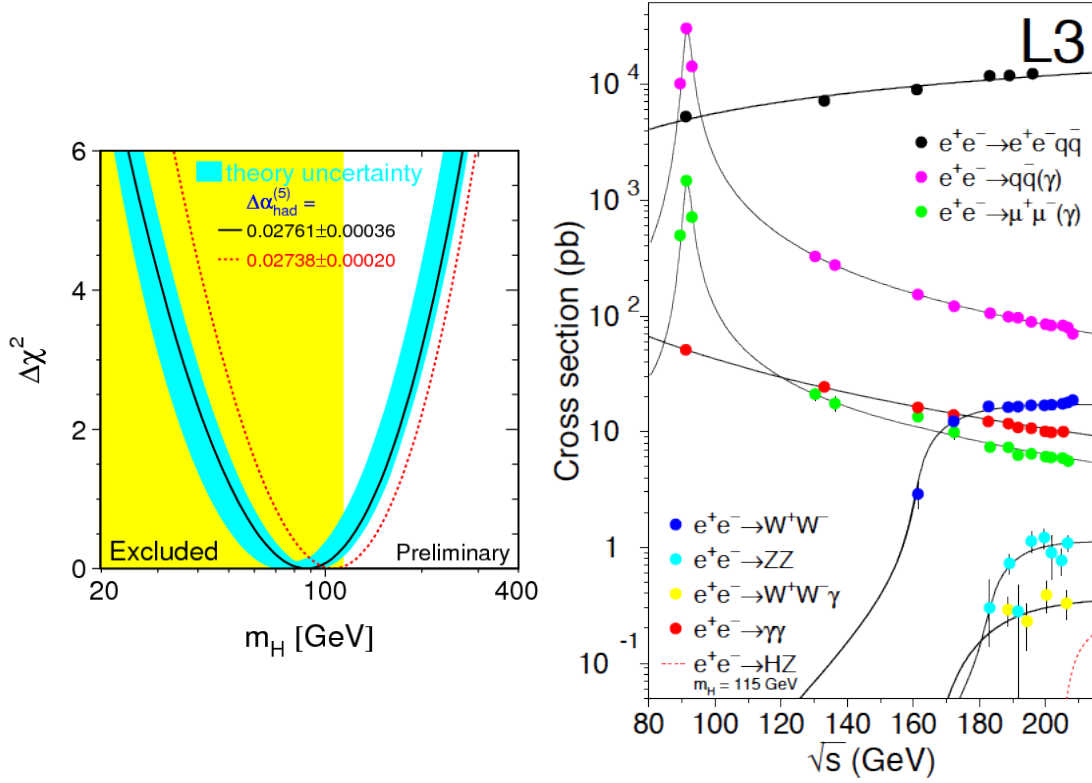
Figure 3.7: Left: $\Delta\chi^2 = \chi^2 - \chi^2_{\min}$ versus the mass of the Higgs boson m_H from the year 2000 [47]. The black line is the fit using all data including the LEP data. The cyan band represents the theoretical uncertainty due to missing corrections. The yellow area is the 95% CL exclusions limit for the m_H as a result from direct search. The red line is the result using $\Delta\alpha^{(5)}_{\mathrm{had}}(m_Z^2)$ from Reference [48]. Right: Cross-sections of electroweak SM processes versus centre-of-mass energy $\sqrt{s}$ from the year 2013. The black curves show the theoretical predictions of the SM. The dots and its error bars show the measurements. The red dashed line shows the HZ production cross-section under the assumption of a Higgs boson mass $m_H = 115$ GeV. This plot is taken from Reference [49].

The low production probability of the Higgs boson made it difficult for the LEP experiments to proof its existence and measure the Higgs boson properties. With a continuously rising interaction rate dN/dt and thus luminosity [51]

$$L = \frac{1}{\sigma}\frac{dN}{dt} \tag{3.1}$$

as shown in Fig. 3.8 the data recording rate as well as the amount of available date grew over time.

Furthermore, the Higgs boson production cross-section grew as a function of the centre-of-mass energy. Though, despite a higher data rate and $\sqrt{s}$, a certain amount of data is required in order to claim a hint to or even a discovery of the Higgs boson.
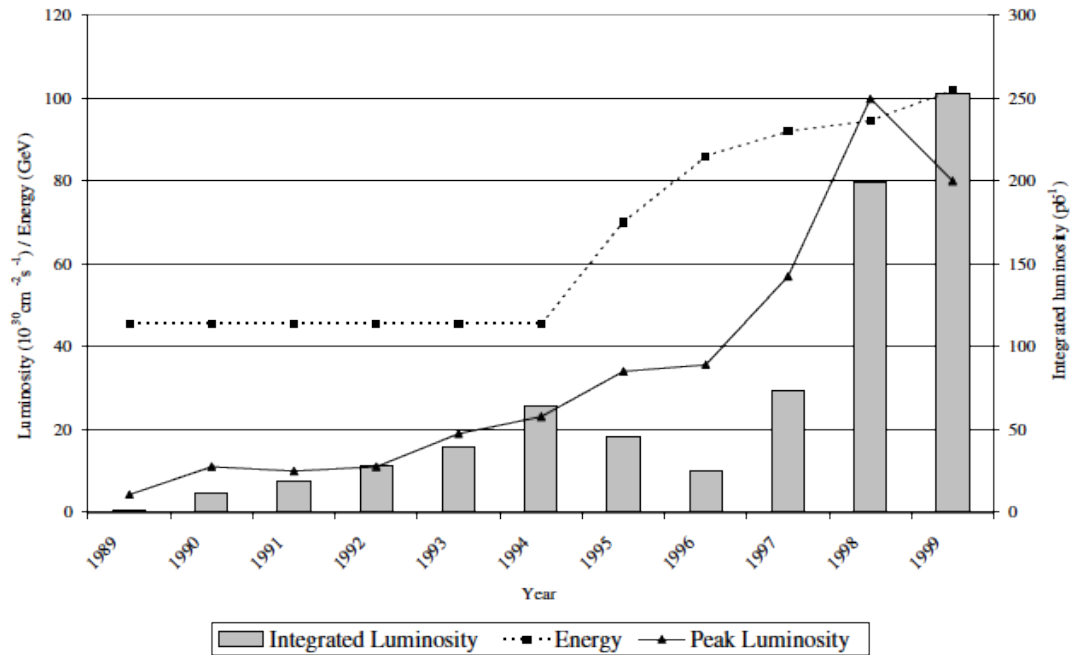
Figure 3.8: centre-of-mass energy and luminosity provided by LEP per year. This plot is taken
from Reference [52].

As this was insufficient for LEP, the existence of the boson was not resolved by this
accelerator.

In the context of the search for the Higgs boson, the result of the issues mentioned
above was to replace the LEP by the LHC.

3.1.3 The Large Hadron Collider

The LHC is a hadron collider that reuses the tunnels from LEP. It is designed for the
acceleration and collision of protons and various heavy ions. As the latter is more specific,
the following description is focused upon the proton acceleration. While the LHC started
with $\sqrt{s} = 7$ TeV, it is designed to be capable of delivering centre-of-mass energies of
14 TeV. Before the acceleration of the particles from the 450 GeV particles provided by
the SPS up to its collision energy, the ring is filled with 2808 bunches with $1.15 \cdot 10^{11}$
protons per bunch. Similar to the filling of the SPS from the PS, multiple injections into
the LHC are performed. The bunches are stored in the ring using 1232 dipole magnets.
In order to provide the highest possible energies, the magnetic fields need to provide
the corresponding bending power. Therefore, these magnets are superconducting Nb-Ti
magnets cooled by superfluid helium below 2 K. The temperature allows to increase the
magnetic field strength further, i.e. for 1.9 K this corresponds to a beam energy increase
of $\approx 20\%$ compared to temperatures above 2 K [34].

Once the ring is filled the particles are accelerated by an RF system that provides an energy gain of 485 keV per turn. Hence it takes around 20 min to reach the lowest design values of $\sqrt{s}$.

After the acceleration the beams will be focused in the four interaction points, shown as yellow dots in Fig. 3.1. These are the locations of the four experiments ALICE, ATLAS, CMS, and LHCb. The main driving parameter for data acquisition is the luminosity L. Under the assumption of normal distributed bunches, Eq. (3.1) can be written as

$$L = \frac{N_1 N_2 f N_b}{4\pi\sigma_x\sigma_y} \tag{3.2}$$

with the number of particles N_1, N_2 in each bunch, their standard deviations σ_x and σ_y in both transverse axes, the revolution frequency f and the number of bunches in the ring N_b. Parameters that can be modified in order to provide a higher luminosity are the standard deviations. Hence the bunches need to be as small as possible. In these overlap regions, the around 8 cm long bunches [34] cross each other at an angle of around 300 μrad. By utilising quadrupole magnets the beam is focused in that region.

As shown in Fig. 3.9(left) the centre-of-mass energy rose over time up to 13 TeV. Furthermore, the annually delivered luminosity was increased over the years. This pa-
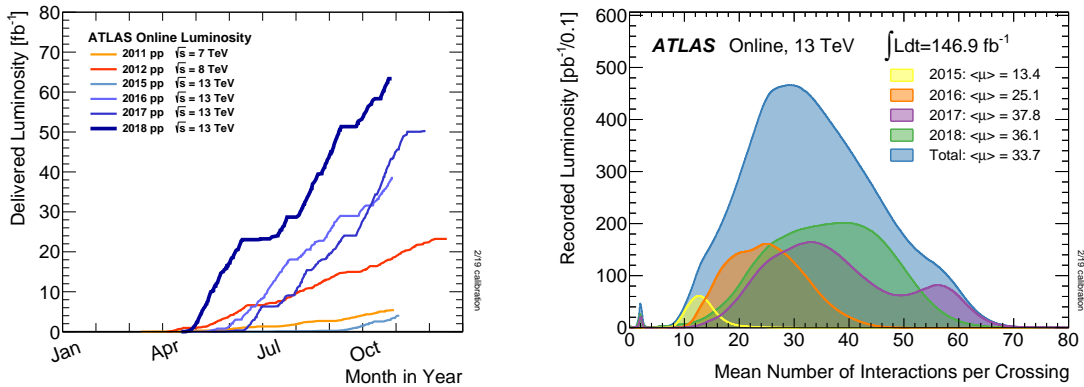
Figure 3.9: Left: Delivered luminosity versus the time of a year. This plot shows the luminosity for Run-1 and Run-2 measured by the ATLAS detector [53]. Right: Recorded luminosity versus the number of interaction per bunch crossing. This plot show the data for the period 2015-2018 recorded by the ATLAS detector [54].

rameter is shown here as the integrated luminosity

$$L_{\mathrm{int}} = \int_0^{t'} L\,dt$$

for the abscissa value t'. Thus, the instantaneous luminosity L is the slope of each graph. The data was collected more rapidly over the years. A clear improvement is observable after the second half of 2015. As mentioned in the previous section the spacing between the bunches then was reduced from 50 ns to 25 ns. From Eq. (3.2) this would correspond to a doubled luminosity.

A larger luminosity means not just a higher probability for an interaction as Eq. (3.1) suggests but can also increase the number of interactions that occur in a bunch crossing. The recorded luminosity per number of interactions is shown in Fig. 3.9 (right). The interaction multiplicity is called *pile-up μ*.

3.1.4 High luminosity LHC

In the previous section and in Reference [34] a long term upgrade plan for the LHC was designed together with the accelerator itself. An overview of this schedule is shown in Fig. 3.10. The periods between the long shutdowns (LS) are referred to as *Run*. During
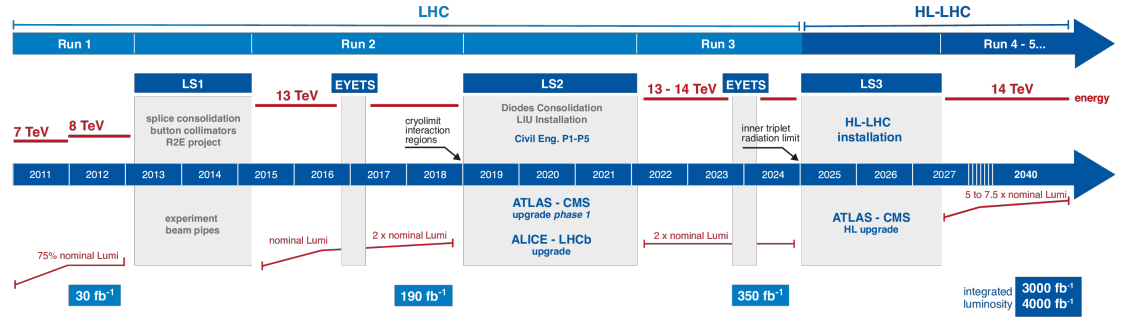
Figure 3.10: Timeline of the LHC including the centre-of-mass energy and a schematic visualisation of the delivered luminosity. Also the shutdown schedule is presented. This plot is taken from Reference [55].

the LSs the upgrades of the LHC and the experiments can be installed and the hardware be maintained.

Despite the increasing luminosity shown in Fig. 3.9 (left), in 2010 plans were made for a future upgrade of the LHC: The High-Luminosity LHC (HL-LHC) [56]. The idea of this project is to maximise the knowledge gain through data per time. It can be understood as improvement of the statistical accuracy per time and thus as acceleration of scientific progress.

While the concept of the HL-LHC is keeping the spacing between the bunches and the centre-of-mass energy at a constant level, the luminosity is planned to be increased by a factor of five, the integrated luminosity by ten compared to the initial design goals, i.e. the HL-LHC is thought of delivering an integrated luminosity of 250 fb^{-1} per year and 3000 fb^{-1} in a decade. This requires some changes in the beam parameters in order to achieve this goal.

Eq. (3.2) states an increasing luminosity for smaller transverse beam sizes. This is achieved by a stronger beam focus β^*. The parameter is related to the envelope of the oscillating beam $\beta(s)$ via

$$\beta(s) = \beta^* + \frac{s^2}{\beta^*}$$

for the distance parameter s along the beam direction [57]. For the HL-LHC β^* is planned to be reduced from 0.55 to 0.15. Thus, the beam diameter at the focal plane

gets smaller but grows more rapidly afterwards. The consequences for the magnets involve that the interaction angle between both beams in the interaction point gets larger. At the same time so-called *crab cavities* are required to ensure a sufficient high level of overlap between both bunches in the context of luminosity. These cavities cause a torque upon the bunches for a heads-on overlap during the bunch crossing as shown in Fig. 3.11. The net result is a larger overlap in the interaction region, therewith a higher
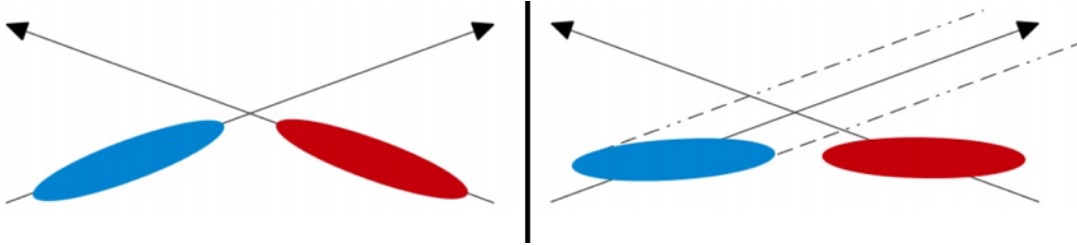
Figure 3.11: Illustration of a bunch crossing under an interaction angle. The bunches are shown as red and blue ellipses, the black arrows indicate their direction. Left: Unmodified bunch crossing. Right: Bunch crossing with crab cavities rotating the ellipses. This figure is taken from Reference [58].

interaction probability and thus luminosity.

Furthermore the number of protons per bunch shall be increased to $2.2 \cdot 10^{11}$ while the number of bunches in the HL-LHC shall be slightly reduced. Hence, the bunch crossing rate get slightly reduced while the pile-up shall rise. For the LHC the pile-up is operating above the original design goal of $\langle \mu \rangle = 19$ as shown in Fig. 3.9(right). Considering all required modifications to the beam guidance for the HL-LHC the expected pile-up is between 140 and 200 [56].

The installation of the alterations are planned for the LS3 period.

3.2 The ATLAS Detector

Processes that occur in a particle collision, the thereby involved particles and their properties are not directly measurable. As mentioned in Sec. 2.1.1 quarks appear always in a bound state due to confinement. Furthermore, some particles can decay. The top-quark for example has a mean lifetime of $\approx 0.5 \cdot 10^{-24}$ s [17] which corresponds to a travel distance of $\approx 1.4 \cdot 10^{-16}$ m from the creation to its decay. Hence, only the products of the these processes are measurable, i.e. leptons and hadrons that are stable[2] (final state). These observable particles are studied since a long time and therefore their properties are usually well known. This means that these particles need to be measured in order to obtain knowledge about the underlying event structure.

Beside the fact that particles and processes of interest, i.e. the ones that are not directly observable are only measurable indirectly, the principle of measuring needs special

---

[2]Stable in the sense that they do either not decay at all or with a lifetime that is long enough in order to not decay inside detector.

considerations. A particle detector is a device that measures particle properties with the purpose to reconstruct from the given data the processes that occurred since the beam particles collided. The detector consists of several, different components. Each component measures some properties of the final state particles as precisely as possible. This allows to determine and to distinguish the processes that happened since the beam particles collided together with conservation laws and the underlying theory of the SM.

As a description of the general working principle of a particle detector, the ATLAS detector [59], shown in Fig. 3.12 will be presented in the following. This detector is
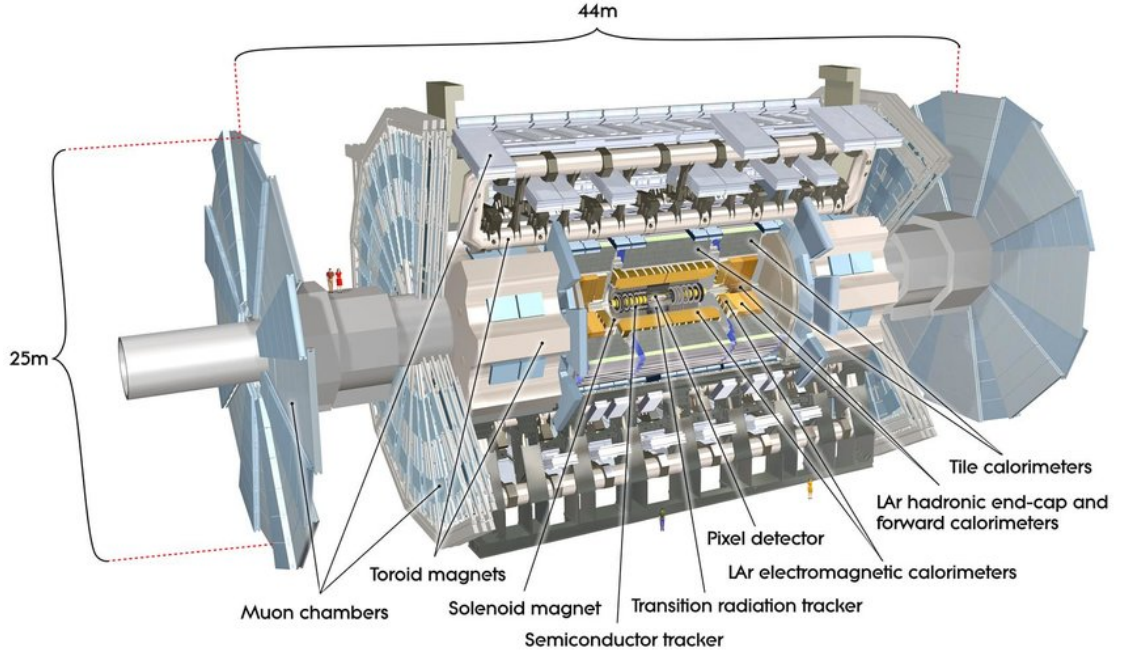
Figure 3.12: Cutaway overview of the ATLAS detector and the individual components [60].

located in one of the four interaction points of the LHC. It is a general purpose detector, i.e. a detector capable of measuring a broad variety of physics processes designed for the LHC parameters of about $\sqrt{s} = 14$ TeV centre-of-mass energy, a luminosity of 10^{34} cm^{-1}s^{-1} with 25 ns between collisions and a pile-up of up to 23 [59]. A brief overview over the particle types measurable by the individual components in the ATLAS barrel is shown in Fig. 3.13. The Tracking Detector or Inner Detector is the part closest to the beam collision and provides information primary about electrically charged particles. It is surrounded by a solenoid magnetic field. The Electromagnetic Calorimeter provides detailed information about the energy of electrons, positrons and photons, the Hadronic Calorimeter about hadrons. Both calorimeters have the purpose to stop the particle inside the respective component. Muons traverse all these components and can be measured outside in the Muon Spectrometer. Neutrinos will exit the detector without being measured at all. These particles can be reconstructed by utilising conservation
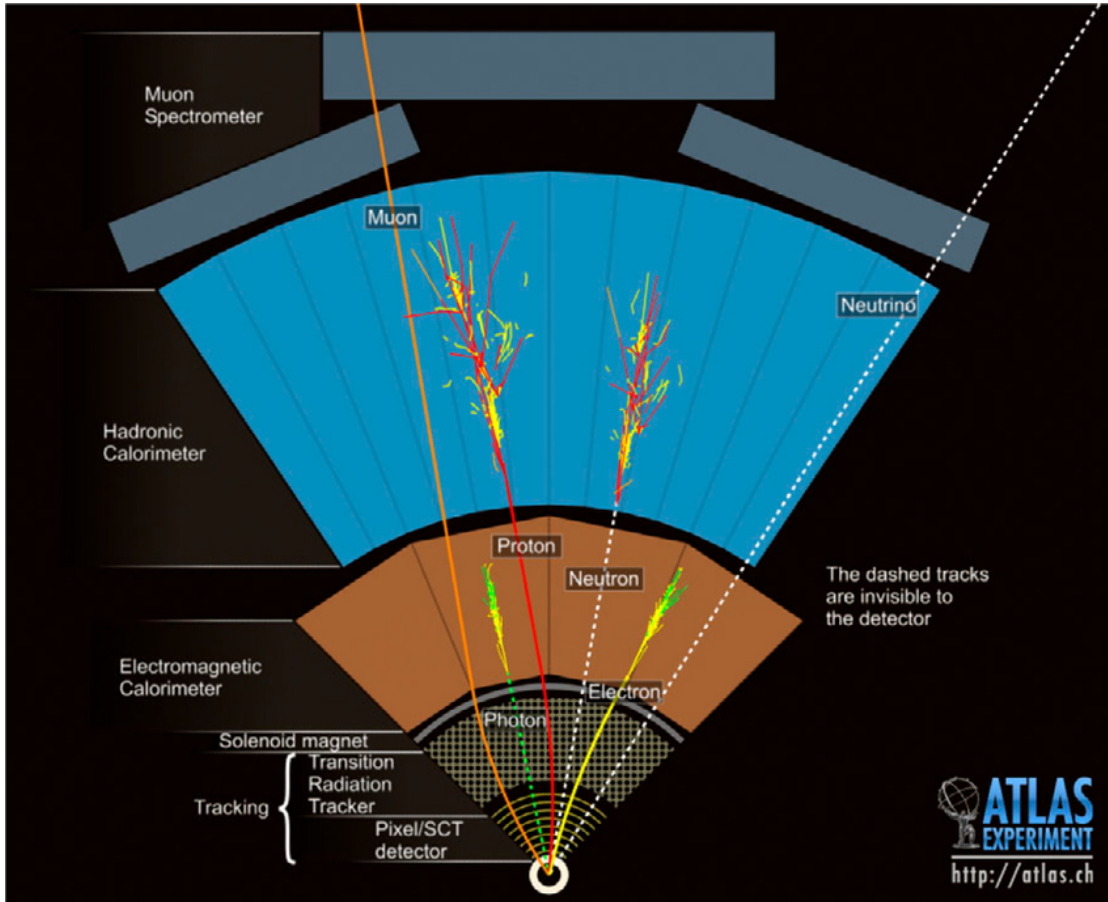
Figure 3.13: Cutaway overview of different particles traversing the barrel of the ATLAS detector in radial direction. The beam pipe is shown as white circle at the bottom [61].

laws, leading to missing momentum or energy. The density of particles in a detector component and the stopping of particles in the detector pre-define an order of the detector components. In the following these components of the detector, the trigger and the data acquisition are presented in more detail. For a better understanding the thereby used coordinate system is explained first.

3.2.1 Coordinate System and Conventions

The coordinate system used for the description is a right-handed Cartesian coordinate system with the origin located at the nominal centre of the detector. The counterclockwise centre of the beam pipe defines the $+z$-axis, the horizontal axis is the $+x$-axis, pointing towards the centre of the LHC ring and the $+y$-axis upwards. The origin of the coordinate system is the nominal centre of the particle collision. Additionally, two angles θ and ϕ are used. θ is the polar angle of a spherical coordinate system measured from the positive z-axis in an interval $\theta \in [0, \pi)$. ϕ is the azimuthal angle defined in the

x-y-plane. This angle is defined such that $\phi = 0$ rad corresponds to the x-axis. The range of this parameter is in the interval $\phi \in [-\pi, \pi)$. Both angles are related to the underlying Cartesian coordinate system by

$$\tan(\theta) = r/z \qquad \tan(\phi) = y/x \tag{3.3}$$

with the radius $r = \sqrt{x^2 + y^2}$. An equivalent description is obtained for a momentum vector $p = (p_x, p_y, p_z)$. The equivalent parameter to the radius for the momentum is given by by transverse momentum $p_T = \sqrt{p_x^2 + p_y^2}$. Thus, the direction along the z-axis is defined as the longitudinal direction. The same accounts for the longitudinal component of the momentum $p_L = p_z$.

The produced particles per θ interval is not constant and the polar angle is not invariant under Lorentz boost. That is why another quantity is preferred: The rapidity

$$y = \frac{1}{2}\ln\left(\frac{E + p_L}{E - p_L}\right)$$

is shifted by a constant factor under Lorentz transformations and therefore better suited for descriptions in particle physics. Considering high energy particles with negligible masses compared to their momenta, i.e. $|p| \gg m$, then the energy E can be approximated as $E = \sqrt{p^2 + m^2} \approx |p|$. Within this limit the rapidity is equivalent to the pseudorapidity

$$\eta = \frac{1}{2}\ln\left(\frac{|p| + p_L}{|p| - p_L}\right) = -\ln\left(\tan\left(\frac{\theta}{2}\right)\right).$$

Since η is a function of θ and therefore directly connected to the underlying coordinate system of the detector, it is a handier parameter than the rapidity and often the favoured parameter over the rapidity.

3.2.2 Inner Detector

The Inner Detector (ID) [62] is the part of the ATLAS detector closest to the beam-pipe. This part is designed to allow precise measurements in a covered region in pseudorapidity of ± 2.5. The goal is to achieve the reconstruction of vertices including the association of corresponding particles for heavy-flavour and τ-tagging. For secondary vertices it is necessary to detect outgoing particles as close as possible to the primary interaction from the beam particles. This requires a minimisation of the radii of the detector components.

The surrounding solenoid constraints the outer radius of the ID in the radial direction. Due to the end-cap of the Electromagnetic Calorimeter the length of the ID is about 7 m long. The solenoid magnet has a length of 5.3 m. This leads to a non-constant magnetic field inside the ID as shown in Fig. 3.14. As consequence of these deviations from a uniform magnetic field of 2 T is a distortion from a helical trajectory of charged particles raising more difficulties in the event reconstruction and resolution. Furthermore, the Lorentz angle (see Sec. 3.2.2.1) especially in the end-caps becomes position dependent.
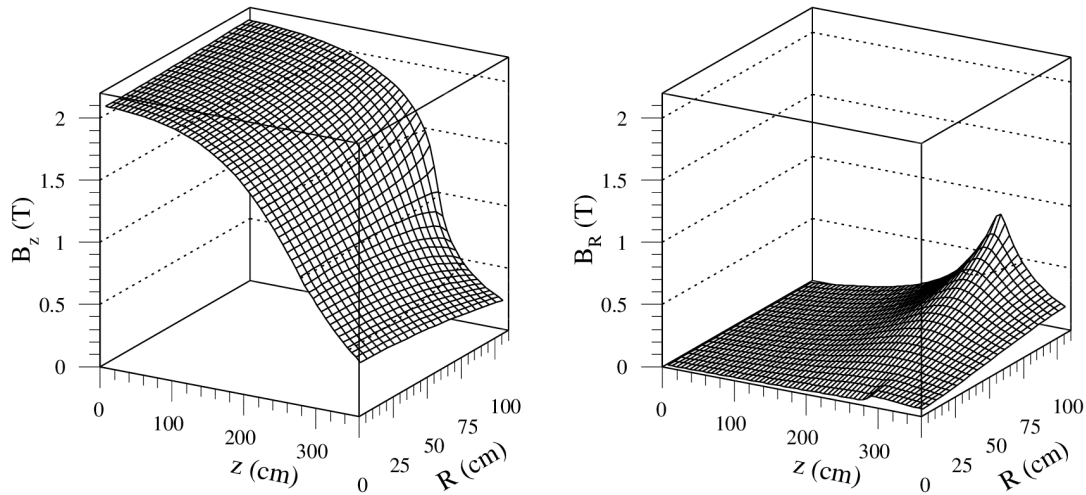
Figure 3.14: Solenoidal magnetic field strength in longitudinal direction (left) and radial direction (right) as a function of the position in the *r*-*z*-plane [62].

The ID itself consists of three different units: A barrel that covers a region of ±80 cm and two identical end-caps. An overview over the units in the barrel is shown in Fig. 3.15. This detector utilises two different techniques. One is based on silicon semiconductors,
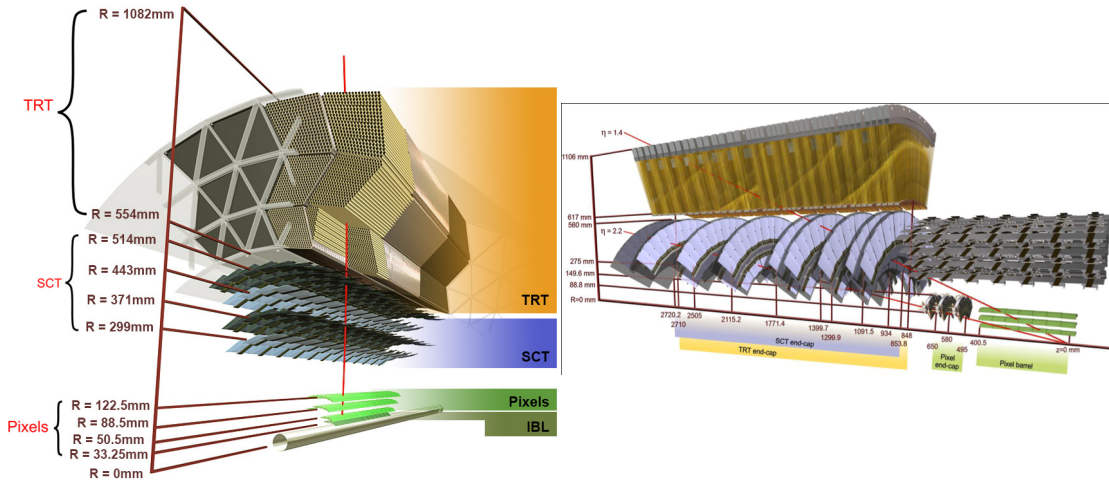
Figure 3.15: Schematic overview of the ID components in the barrel (left) and the end-caps (right) and their nominal distance to the centre of the beam-pipe [63, 64].

the other one is based on transition radiation.

Starting with the semiconductors, two different layouts are used: Pixels and Strips. The innermost part of the Silicon Detectors and also the ID is the Pixel Detector. This part will be described in the next section. The surrounding parts are presented afterwards.

Item	Radial Extension [mm]	Length [mm]	Modules	Megapixels	Pixel Size [μm^2]
IBL	$\langle R \rangle = 33.25$	$|z| < 332$	224	6.02	50×250
B-Layer	$\langle R \rangle = 50.5$	$|z| < 400.5$	286	13.2	50×400
Layer 1	$\langle R \rangle = 88.5$	$|z| < 400.5$	494	22.8	50×400
Layer 2	$\langle R \rangle = 122.5$	$|z| < 400.5$	676	31.2	50×400
Disc 1	$88.8 < R < 149.6$	$\langle z \rangle = 495$	48×2	4.4	50×400
Disc 2	$88.8 < R < 149.6$	$\langle z \rangle = 580$	48×2	4.4	50×400
Disc 3	$88.8 < R < 149.6$	$\langle z \rangle = 650$	48×2	4.4	50×400

Table 3.1: Parameters of the Pixel Detector layers in the barrel and end-caps [59, 65].

3.2.2.1 Pixel Detector

The pixel detector consists of originally three layers in the barrel. In 2014 the Insertable B-Layer (IBL) [65] was added as the new innermost layer. Along the beam-pipe four end-cap discs are placed perpendicular to the z-axis symmetrically placed at both ends of the Pixel Detector. An overview of the nominal positions and the number of pixels is given in Tab. 3.1. In total approximately 1500 modules are placed in the barrel and 700 in the discs. The modules itself are identical in both parts. A module is 60.8 mm long, 16.4 mm wide and approximately 250 μm thick [66]. Each module contains 47232 pixels arranged in a 18×164 array per readout chip. The readout chips are arranged such that a module consists of 144 columns and 328 rows. In 16 columns the size is 50×600 μm^2. Additionally eight pairs of pixels per column near the centre lines are *ganged*, i.e. read-out together. This leads to an ambiguous read-out of the pixels. Overall around 80 million readout channels are therewith given by the pixel detector. For the IBL smaller modules are used with an area of 20.2×18.8 mm^2 [67]. A module has a thickness of 150 μm. The pixels on the IBL are arranged in a 80×336 matrix. Since the pixels in the pixel system do not cover the entire area of the module, the modules are rotated to each other and placed with an overlap to ensure a hermetic layer of sensitive material.

A single pixel is thereby a semiconductor diode with a bias voltage applied which leads to a depletion zone. Traversing charged particles with sufficient energy can interact with the atoms in the depletion zone. The interaction itself can lead to ionisation of an atom as shown in Fig. 3.16 (left). In other terms, a pair of an electron and a so-called *hole* was created. A hole is in first approximation the positively charged atom. Due to the electric field inside the diode the charges move towards the borders of the diode. Due to induction the moving charges can be measured and read-out. For the pixel cells an analogue readout allows the estimation of the signal amplitude by using the Time-over-Threshold method. With this method, the time is measured for which a signal is above a given threshold. The measured time is related to the shape of the signal and hence, a charge sensitive signal is measurable. Compared to a digital readout a better spatial resolution can therewith be obtained in cases of incidence angles larger than 0° [66].

Since the electrons and holes drift inside the semiconductor, the magnetic field from the solenoid will deflect them as shown in Fig. 3.16 (right). The deflection angle is called Lorentz angle and leads to displaced signals in the pixel modules. If the material and
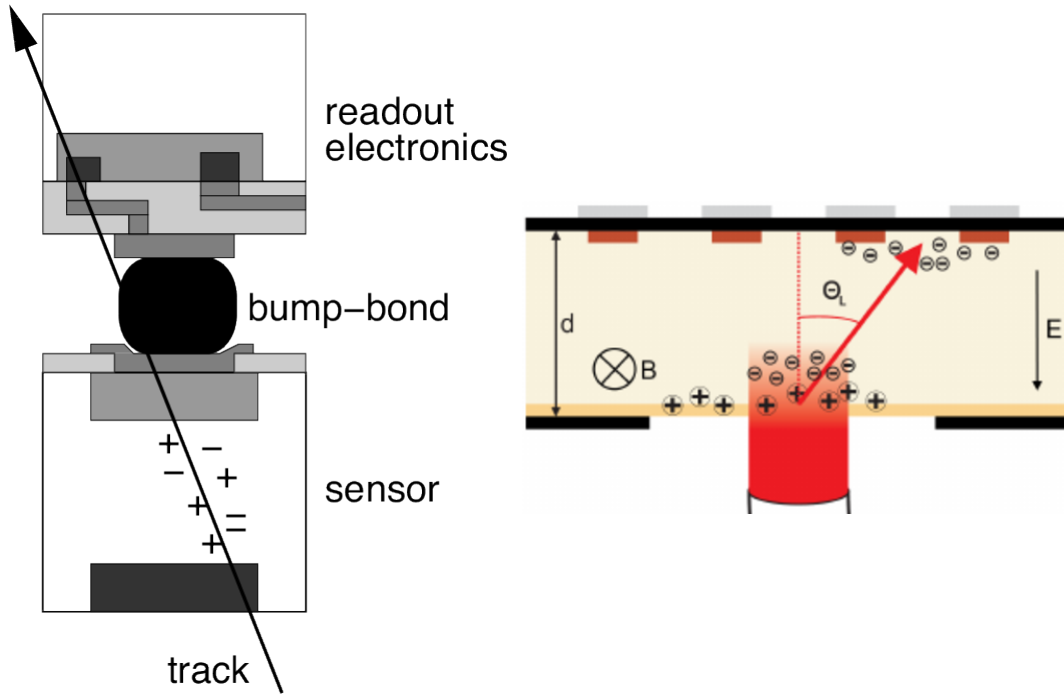
Figure 3.16: Left: Sketch of a hybrid pixel detector. A particle track ionises atoms in the sensor volume [66]. Right: Sketch of the deflection of electrons by the Lorentz angle Θ_L in a semiconductor due to the magnetic field B [68].

magnetic field are known the Lorentz angle can be calculated and the position of the electron-hole-pair creation can be corrected.

A measurement obtained from the pixel detector allows to estimate the position of a particle along its trajectory. Such a statement is linked to an uncertainty of the estimate. As an individual pixel provides only the information whether the collected charge is above a threshold or not means that no preferences for the actual position of the track can be stated. Hence, the probability distribution for the track position is a uniform distribution and therewith the standard deviation or resolution in x- or y direction for a single pixel is given by

$$\sigma_{x/y} = \frac{L_{x/y}}{\sqrt{12}} \tag{3.4}$$

with the length $L_{x/y}$. If multiple, neighbouring pixels send a signal from either a single or multiple collinear particles then all pixels are combined to a cluster. The corresponding uncertainty is then smaller than the actual size of the cluster due to the analogue readout and charge interpolation between pixels.

3.2.2.2 Semiconductor Tracker

The Semiconductor Tracker (SCT) surrounds the pixel detector. In the 1492 mm long barrel it consists of eight cylindrical layers located pairwise on the four different radii of 29.9, 37.1, 44.3 and 51.4 cm [69]. The end-cap modules are mounted on nine discs containing three rings with various sizes at both ends of the barrel [70]. These discs are located in the range 847.5 mm$< |z| < 2727$ mm covering up to $|\eta| < 2.5$.

Since the distances of the SCT modules to the nominal centre of the interaction is larger compared to the pixel detector, the particle density is lower. Thus the required granularity of the SCT is lower than for the pixel detector. This requirement allows to use a different concept which comes along with less passive material and therefore less disturbance of the particle trajectory.

The SCT consists of 2112 modules in the barrel. The modules are pairwise glued back-to-back to each other under a stereo angle of 40 mrad. While the modules in the barrel region have the same properties, the ring arrangement in the end-caps require a trapezoidal module shape resulting in different sensor properties. A module consists of 768 semiconductor strips with a resolution of 17 μm in the $r\phi$-direction, 580 μm in the z-direction (r-direction for the end-caps) for a module pair and a 80 μm pitch.

Compared to the pixel detector, the underlying semiconductor physics and therefore the measurement creation process is similar. The same accounts for the uncertainty of the measurement. However, the readout in the SCT provides a digital binary signal [69]. Hence, the information content of a strip is either *hit* or *no hit*.

The applied pairing of strip modules under an angle allows to calculate three-dimensional space-points from the measurements. This is of special importance for the initial estimation of a particle trajectory, the so-called *seeding*.

3.2.2.3 Transition Radiation Tracker

The outermost part of the ID is the Transition Radiation Tracker (TRT). Compared to the semiconductors in the Pixel Detector and the SCT, the working principle of the TRT is based upon a different technique: Transition radiation. This phenomenon affects charged particles traversing boundaries between materials of different dielectric or magnetic properties [71]. In these cases photons are emitted in the forward direction of the particles trajectory. For ultra-relativistic particles, the opening angle of the emitted photons becomes close to zero. In this case the emitted photons are in the x-ray regime [71]. The emission of a charged particle with energy E and mass m is thereby dependent upon the Lorentz factor $\gamma = E/m$. Given that the energy or momentum is known, the transition radiation allows to identify the particle type.

It consists out of 298304 kapton straws, reinforced with carbon fibre [72]. Each straw has a diameter of 4 mm and 70 μm thick walls that are held at a potential of -1530 V in comparison to the gold-plated tungsten wire at the centre of the straw on ground level. These wires have a diameter of 31 μm. The straws are filled with a gas mixture. During Run-1 it was a mixture of Xe, CO_2 and O_2. For Run-2 straws with gas leaks were filled with Ar instead of Xe. Compared to the surrounding polypropylene or polyethylene,

a charged particle emits transition radiation when it enters a straw. Ionisation of the gas mixture in the straw from the charged particle leads, due to the inhomogeneous electric field inside the straw to an acceleration of the ionisation-electrons. This leads to an avalanche effect which is measurable. The transition radiation provides thereby additional primary ionisations and enhances the signal. A typical energy deposit is around 2.5 keV in the gas producing 5-6 primary ionisations per mm. The surrounding material supports thereby the electron identification.

In the barrel 52544 straws are aligned with the beam axis and cover a region of 560 mm$< r < 1080$ mm and $|z| < 712$ mm [73]. In each end-cap region 122880 straws are aligned perpendicular to the beam axis, pointing in radial direction. The straws sectioned into two identical, independent wheels cover a region of 644 mm$< r <$1004 mm and 827 mm$< |z| < 2744$ mm [74]. The overall coverage of the TRT is $|\eta| < 2.0$.

The straws in the barrel are, except for the innermost layers 142.4 cm long. The innermost straws are 34 cm long. In the end-caps 36 cm long straws are used. Based upon the drift time of the electrons the distance of the track to the wire can be estimated. This leads to a spatial resolution of about 110 μm for a mean pile-up of $\langle \mu \rangle = 5 - 10$. The barrel straws are arranged in 73 layers, in each end-cap in 160 layers. Therewith many measurements can be produced by a single charged particle allowing a precise reconstruction of the trajectory. However, the TRT was designed for the LHC pile-up of $\langle \mu \rangle \lesssim 23$. For higher pile-up the straws are not suitable anymore as too many particles produce signals per straw and in too many straws. As too many straws produce a signal, the complexity in associating measurements and particles becomes larger. At a certain occupation level in the TRT, the association can not be performed anymore and hence, the data can not be utilised anymore. The most extreme case is when all straws produce a signal.

3.2.3 Calorimeters

After particles exit the TRT and the solenoid magnet they enter the calorimeters. In the ATLAS experiment this component covers a range of $|\eta| < 4.9$ [59]. The calorimeters can be separated into two different types: *Electromagnetic Calorimeter* (ECAL) and *Hadronic Calorimeter* (HCAL). An ECAL is used to measure the energy of leptons and photons, a HCAL measures the energy of hadrons. The general principle for measuring a particle's energy in a calorimeter is given by particle interactions. Due to interaction a particle transfers a portion of its energy until it stops. The thereby transferred energy is measured. The measured energy E is linked to the calorimeter specific energy resolution σ which is parametrised [75] as

$$\frac{\sigma}{E} = \frac{s}{\sqrt{E}} \oplus \frac{b}{E} \oplus c.$$

with the $\oplus$ operator denoting the quadratic sum. The parameter s denotes a stochastic contribution to the measurement, b denotes a noise term related to e.g. electronic noise and c denotes a constant contribution from e.g. calibration uncertainties, dead cells or

non-uniformities. By correcting for the noise, the dependency of the resolution upon the b can be removed from the equation above.

An overview over the ATLAS calorimeters is shown in Fig. 3.17. In the barrel, the
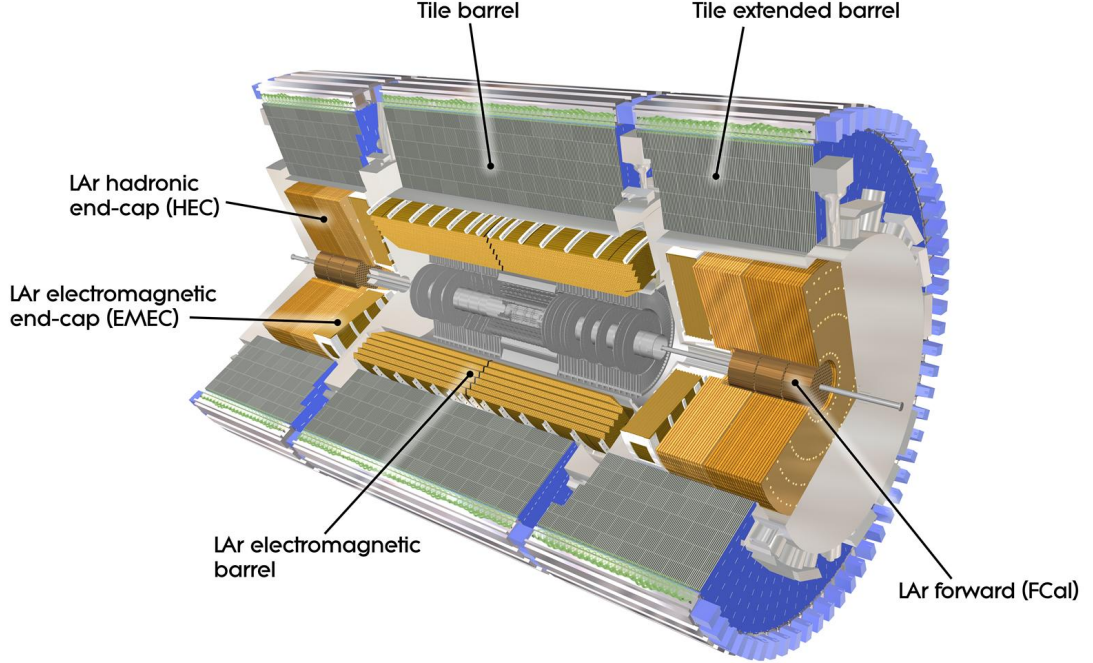
Figure 3.17: Cutaway overview over the ATLAS LAr and Tile Calorimeter [76].

inner calorimeter is the LAr Electromagnetic Calorimeter, the outer the Tile Hadronic Calorimeter. Additionally calorimeters denoted as forward calorimeters are added for additional coverage of $|\eta|$. In the following the components are described.

3.2.3.1 LAr Electromagnetic Calorimeter

The ECAL is split into a barrel that covers $|\eta| < 1.475$ and end-cap regions located at $1.375 < |\eta| < 3.2$. The barrel is separated into two half-barrels with a 4 mm gap at $z = 0$. The end-caps consists out of two coaxial wheels. The outer wheel covers $1.375 < |\eta| < 2.5$, the inner one covers $2.5 < |\eta| < 3.2$. In the region $|\eta| < 1.8$ an active LAr presampler is located to correct for energy losses.

A design goal of the ATLAS ECAL is a high granularity for precision measurements of electron and photons [59]. As detector material a lead-liquid argon (LAr) combination is used with accordion-shaped kapton electrodes and lead absorbers.

The used material defines thereby the required thickness of the calorimeter itself. High-energy electrons lose their energy mostly via bremsstrahlung. This energy loss per

path length x can be described with the material dependent *radiation length* X_0 as

$$E(x) = E_0 e^{-\frac{x}{X_0}} \tag{3.5}$$

for electrons with initial energy E_0. For high-energy photons the main interaction process is pair-production. Due to a different cross-section, the intensity I of a photon beam after the path length x is given by

$$I(x) = I_0 e^{-\frac{7}{9}\frac{x}{X_0}} \tag{3.6}$$

with the initial intensity I_0. As bremsstrahlung and pair-production produces secondary particles with less energy, a sufficiently thick detector in terms of X_0 is required in order to stop the shower evolution. Hence, the ATLAS ECAL thickness is $> 22X_0$ in the barrel and $> 24X_0$ in the end-caps.

The achieved spatial resolution ranges in the barrel for pseudorapidity intervals η from $0.025/8$ up to 0.025 and for the azimuthal intervals $\Delta\phi$ from 0.025 to 0.1. In the end-caps the resolution in η is between $0.025/8$ and 0.050, the resolution in $\Delta\phi$ is between 0.025 and 0.1. The achieved energy resolution is $\sigma/E = 10\%/\sqrt{E} \oplus 170$ MeV$/E \oplus 0.7\%$ [77].

3.2.3.2 Tile Calorimeter

The HCAL in the ATLAS experiment is divided into a barrel and an extended barrel part. The former covers a region of $|\eta| < 1.0$, the latter $0.8 < |\eta| < 1.7$ [59]. It is a sampling calorimeter[3] consisting of a steel absorber and scintillator tiles with photomultiplier tubes used as readout.

The dimensions of a HCAL is defined by the utilised materials. This is characterised by the nuclear interaction length λ which is usually longer in HCALs than X_0 in an ECAL. It can be shown that a similar description for a hadron beam can be derived as for photons. In comparison to the purely material dependent parameter X_0, the nuclear interaction length is also dependent upon the hadron type [75]. As hadron interactions are more complicated, the shower becomes wider and longer than for electrons or photons. Hence, HCALs are usually thicker compared to ECALs.

The ATLAS HCAL is designed to have a thickness of 9.7λ in the barrel region whereas the end-caps have a thickness of 10λ. As shown in Fig. 3.13 the ideal goal is to capture all hadrons (also electrons and photons) inside the calorimeter such that only muons and neutrions can pass these detector parts. The HCAL is enclosed by an outer support structure that adds further 1.3λ to the stopping power of the HCAL.

Compared to the demanded precision in the LAr ECAL the Tile Calorimeter has a coarser granularity which is sufficient for physics requirements in jet reconstruction and E_T^{miss} measurements. Per interval in $\Delta\eta$ the HCAL has a resolution of 0.1 in all parts except the outermost layer ($\Delta\eta = 0.2$). The angular resolution $\Delta\phi$ is everywhere 0.1. The achieved energy resolution is $\sigma/E \approx 50\%/\sqrt{E} \oplus 6\%$ for pions [77].

---

[3]A sampling calorimeter consists of two components: passive and active. The passive component is responsible for creation of the particle shower. The active component measures the constituents of the shower. A typical arrangement is an alternating order of both components.

3.2.3.3 LAr End-Cap and Forward Calorimeter

In the higher $|\eta|$-regions behind the ECAL two additional calorimeters are placed: the LAr hadronic end-cap calorimeter (HEC) and the LAr Forward Calorimeters (FCal). The HEC covers thereby a region of $1.5 < |\eta| < 3.2$, the FCal covers $3.1 < |\eta| < 4.9$ [59].

The HEC consists of two independent wheels per end-cap. Considering the pseudorapidity interval, an overlap with the Tile Calorimeter and the FCal is given in the most centrally covered and most forward covered region respectively. Therewith, the material density is kept steady in the transition region. The HEC itself consists of copper plates (25 mm for the innermost, 50 mm for all others) that are interleaved with 8.5 mm LAr gaps representing the active area of the sampling calorimeter.

The HEC has a spatial resolution $\Delta\eta \times \Delta\phi$ of 0.1×0.1 for $1.5 < |\eta| < 2.5$ and 0.2×0.2 for $2.5 < |\eta| < 3.2$. The energy resolution for pions is thereby around $\sigma/E = 70\%/\sqrt{E} \oplus 6\%$ [59]. The FCal is located close to the beam-pipe and reduces with a length of approximately $10X_0$ the radiation background in the muon spectrometer. The length is thereby limited in order to reduce the neutron albedo that would otherwise travel from the FCal back into the inner detector. In order to reduce it, the FCal is recessed by about 1.2 m away from the centre of the interaction point. The detector consists out three layers: In the first layer a copper matrix is installed, the other two have a tungsten matrix. Thereby the first layer is mainly for electromagnetic calorimetry, the other two for hadronic. Inside the layers concentric rods and tubes as electrodes are placed regularly spaced. LAr between the rods and tubes is thereby the sensitive medium.

The spatial resolution of the FCal varies a lot depending on the pseudorapidity interval and the considered layer. The energy resolution is thereby for electrons around $\sigma/E = 29\%/\sqrt{E} \oplus 4\%$. For pions a resolution of around $\sigma/E = 70\%/\sqrt{E} \oplus 3\%$ can be achieved [59].

3.2.4 Muon System

The outermost part of the ATLAS detector is the Muon System. Since particles are either stopped in the calorimeters (electrons, photons and hadrons) or traverse the detector without interacting often enough for their reconstruction (neutrinos) the only remaining particles are muons. The Muon System serves thereby as a long lever in combination with the data obtained from the ID improving the estimation of the muon properties in the track reconstruction. Compared to the strict conditions in the ID, the track density in the Muon System is by far lower allowing for a larger system with coarser granularity.

The Muons System itself consists of a Muon Spectrometer and a magnetic field. The magnetic field is independent of the solenoidal field from Sec. 3.2.2. In this configuration the magnets are superconducting toroid magnets with an air-core. It is divided into three different parts: A barrel part in the region $|\eta| < 1.4$ which is given by the barrel toroids, two smaller end-cap magnets are located in the region $1.6 < |\eta| < 2.7$ and the transition region $1.4 < |\eta| < 1.6$ where the magnetic field is given by a superposition of the barrel and end-cap magnets. The spectrometer can also be divided into three parts following the regions defined by the magnets. An overview of the entire system is

shown in Fig. 3.19. The components shown in this figure are described in the following,
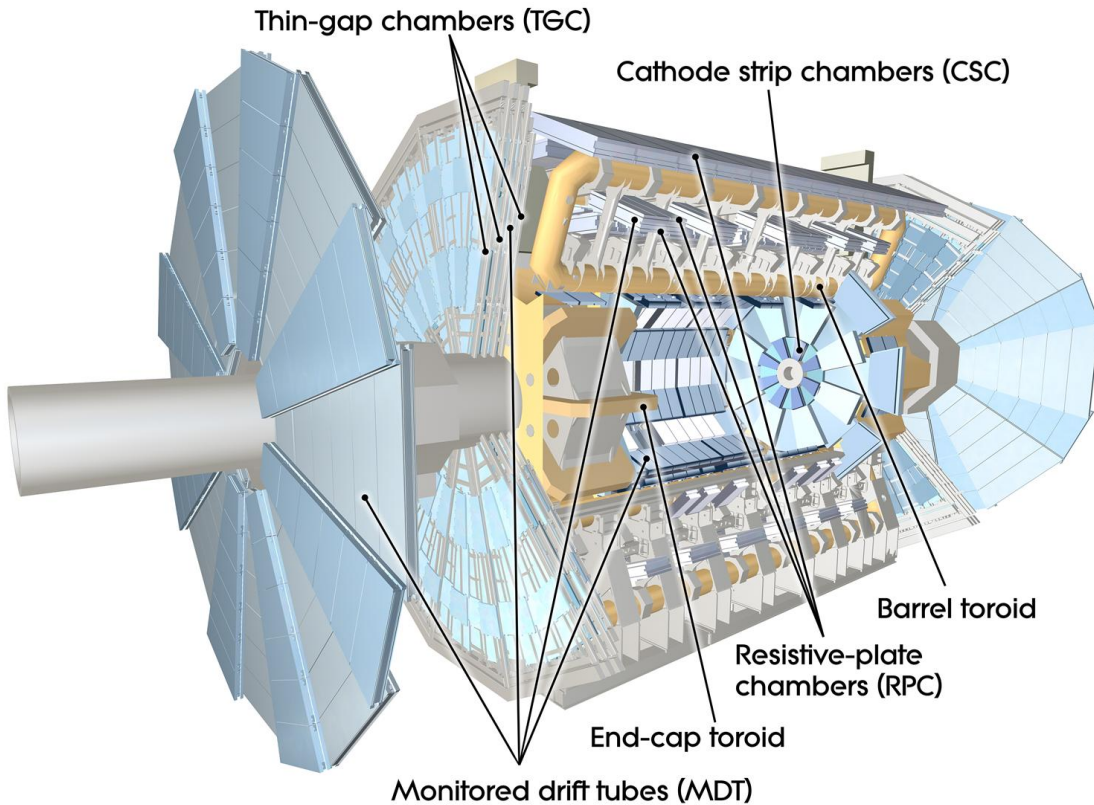
Figure 3.18: Cutaway overview of the ATLAS Muon Spectrometer [78].

starting with the magnetic field.

3.2.4.1 Toroid Magnets

The magnetic field is designed such that it is orthogonal to the trajectories of a muon. Additionally, the material is intended to minimise the impact upon the particle trajectory and therefore preserve the best resolution in the muon spectrometer.

The barrel and both end-cap magnetic fields are provided by eight, radially and symmetrically assembled coils around the beam axis. Both end-caps are lined up with the barrel coils. Additionally, the end-cap coils are rotated by 22.5° with respect to the barrel toroid. Therewith, the overlap of the magnetic fields is improved. The magnetic field in this configuration is shown in Fig. 3.19. As these plots already show the magnetic field produced by the coils is not constant in the muon system but strongly depends upon the position.

A parameter for summarising the magnetic field strength is the *bending power*. This parameter is defined as $\int B dl$ with the magnetic field component B defined as orthogonal to the muon direction. The integral is evaluated along the path l of a muon with infinite
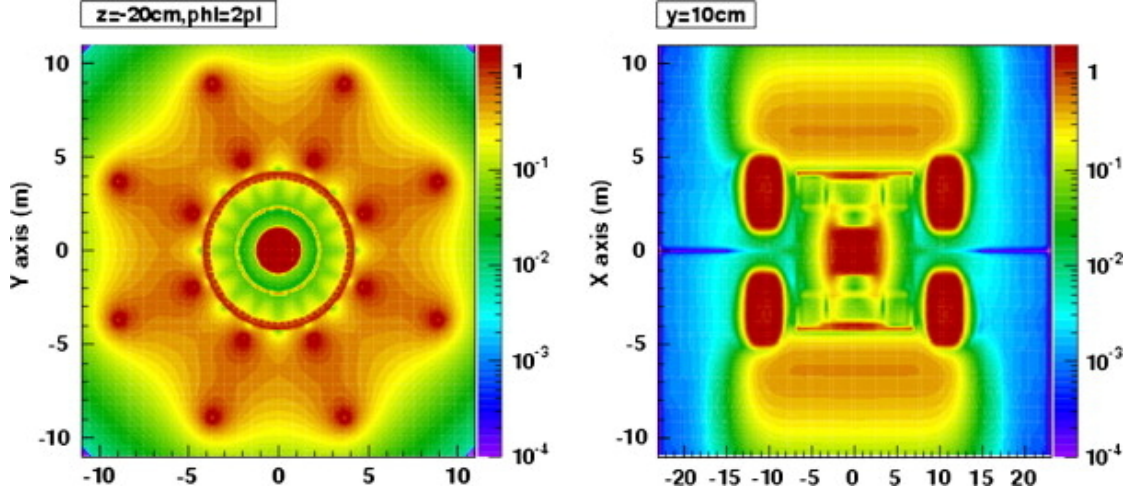
Figure 3.19: Magnetic field map of the ATLAS experiment in x-y-direction (left) and z-x-direction (right) [79].

momentum. For the barrel region values between 1.5 Tm and 5.5 Tm are achieved, in the end-caps the values vary between 1 Tm and 7.5 Tm [59]. In the transition area $1.4 < |\eta| < 1.6$ the magnetic field is only provided by the superposition of the barrel and the end-cap toroid. The bending power in this region is shown in Fig. 3.20. Although the barrel and end-cap magnetic fields are not constant, in the transition region large bending power gradients are observable demanding a very careful treatment of muon positions inside the magnetic field.

3.2.4.2 Muon Spectrometer

The muon spectrometer fulfils two different tasks: it serves as a separate trigger and allows for high-precision tracking measurements of muons. The tracking elements in the barrel region are chambers which are arranged in three cylindrical layers around the beam axis. In the transition and end-cap region the chambers are also arranged in three layers but perpendicular to the beam axis which gives the ATLAS detector the characteristic wheels in the forward direction.

One of the main technologies used in this part of the detector are Monitored Drift Tubes (MDT). While in the innermost layer they cover a region of $|\eta| < 2.0$, they are used in the other layers in a region of $|\eta| < 2.7$. In order to handle the rate and background in the large $|\eta|$ range, the innermost layer in the region $2.0 < |\eta| < 2.7$ is built with Cathode Strip Chambers (CSC). The wires of these segmented multiwire proportional chambers are placed orthogonal to the MDT tubes.

Over 1000 MDTs are used in total with a hit position resolution in z-direction of about 35 μm. In the large pseudorapidity region beside the MDT measurements 32 CSCs provide measurements with a resolution of 40 μm in r-direction and 5 mm in ϕ-direction each [59]. These resolutions are neglecting alignment uncertainties, though.
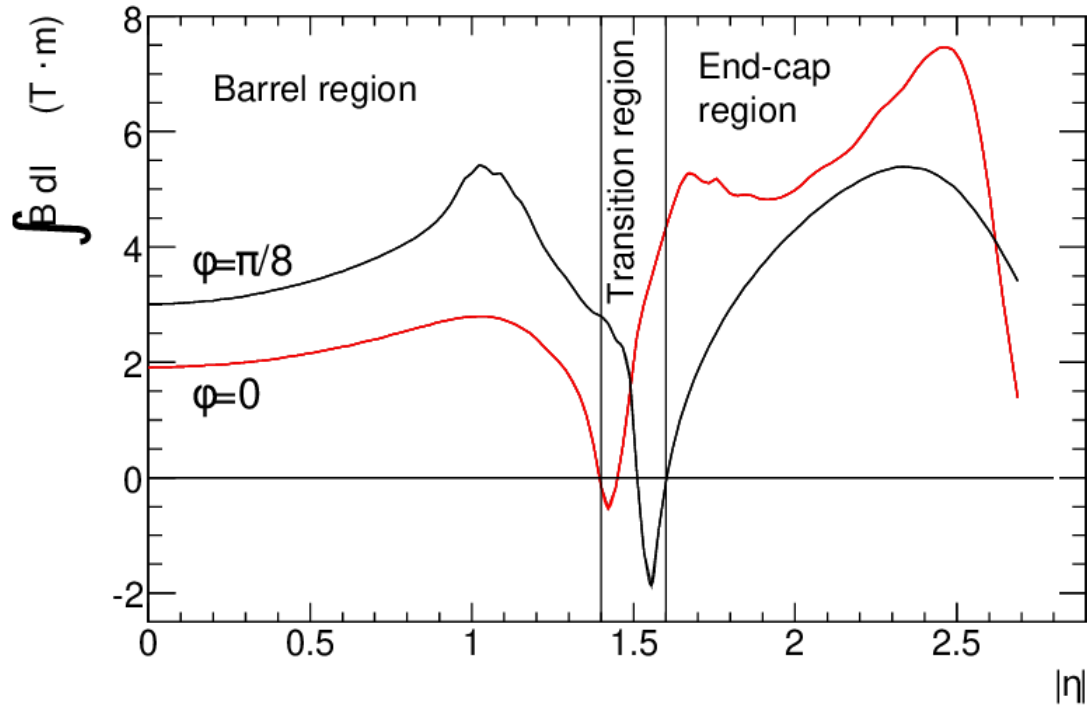
Figure 3.20: Bending power in the toroidal magnetic field versus $|\eta|$ [59].

In total about 20 MDT measurements and (where present) four CSC measurements enhance the reconstruction accuracy of muons similarly to the concept of the TRT.

The trigger system in the spectrometer covers the range $|\eta| < 2.4$ and consists of Resistive Plate Chambers (RPC) in the region $|\eta| < 1.05$ and Thin Gap Chambers (TGC) in the region $1.05 < |\eta| < 2.7$. Though only the region $|\eta| < 2.4$ is used. The purpose of this system is first of all a bunch-crossing identification. Furthermore, the installed components provide a well-defined p_T threshold for the spectrometer. Also the chambers measure the spatial muon coordinate in the orthogonal direction with respect to the MDTs and CSCs. Under neglect of alignment uncertainties the RPCs measure with a resolution of 10 mm in z- and ϕ-direction, the TGCs with 2-6 mm in r- and 3-7 mm in ϕ-direction.

3.2.5 Trigger and Data Acquisition

An event measured by the ATLAS detector requires approximately 1.3 MByte. The bunch-crossing in the LHC occurs in 25 ns intervals. This corresponds to an event rate of 40 MHz. Recording the provided data without any pre-selection would lead to approximately 520 TByte per second. As this would involve expensive data storage hardware while a large fraction of events are not of interest, a veto and conditional

data storage system for physically interesting events is required: The Trigger and Data Acquisition (TDAQ).

The TDAQ systems consist of logical components and building blocks that are partitioned into sub-systems. These sub-systems are usually associated with specific parts of the detector. For the trigger system three different levels are used in ATLAS. These levels are called *L1*, *L2* and *event filter* and operate in this order. While the Data Acquisition system receives the data from the detector and buffers them, the trigger system decides whether to store the event or not. Considering the data taking rate predefined by the LHC bunch-crossing rate and the pile-up per bunch crossing, the time window for the decision is very short. For the L1 trigger, a time window of 2.5 μs is available for the response. The adherence of this time window is achieved by utilising only a subset of the total data provided by the detector, implying a loose argument for the data acquisition. For the decision process data from the Muon System trigger chambers and from the calorimeters with reduced granularity are used.

The L1 decision is given in a trigger *menu*. This is a set of individual conditions defined on a low level. In ATLAS the menu includes searches for high p_T leptons and jets, hadrons from τ-lepton decays and large missing E_T. Therewith, the initial 40 MHz data rate is reduced to 75 kHz.

The L2 trigger then operates on the result of the L1 trigger, i.e. the fulfilled conditions from the menu and the corresponding Regions-of-Interest (ROI's) in η and ϕ. The L2 menu is designed for utilising the full granularity and precision from the full detector data within the ROI's. This corresponds to approximately 2% of the total event data. The processing takes thereby on average 40 ms with an output rate of approximately 3.5 kHz.

The event filter afterwards acts on the results of both predecessors. At each step additional data from the detector is incorporated leading to stricter and more detailed selection based on additional selection criteria where applicable. In the event filter offline analysis procedures are used. Hereby the event processing time is on average four seconds. The final output rate is about 200 Hz.

During the decision process the data is moved. After the L1 trigger accepted the event, data from the pipe-line is transferred off from the detector to the Readout Drivers (ROD's). These drivers are detector-specific functional elements for the front-end systems. Compared to the sub-detector front-end systems, the ROD's are standardised. This standard involves interfaces to the DAQ system as well as data formatting rules.

The digitised signals are formatted as raw data and transferred to the DAQ system. In the first DAQ stage, the readout system buffers the data and provides parts to the L2 trigger as required for the L2 menu in the given ROI's. The L2 trigger transfers the data to the event-building system and from there to the event filter. Events that passed the event filter are permanently stored.

Additionally, the DAQ enables to control and correct the detector hardware via the Detector Control System (DCS). This communication is bi-directional allowing synchronisation between data taking and detector state. The DCS is also capable to communicate with other systems like LHC or the ATLAS magnets.

For the software based data processing the ATLAS experiment [80] uses the framework *Athena*. This framework is based on the LHCb framework *Gaudi*. Athena is designed to allow to perform a broad spectrum of tasks from online event reconstruction as for triggering to event reconstruction and physics analysis. For the purpose as a long time application, the possibility to replace individual algorithms is provided in the design of the software itself. The data accepted by the TDAQ system is distributed through multiple levels of computing facilities named Tier-0 to Tier-3. While the Tier-0 is located on-site, the other facilities are distributed around the globe. Hence, the data processing performed within the Athena framework has to be capable of handling distributed data. Furthermore, as the luminosity grew since the start of operation of the LHC, the software framework is under continuous maintenance to optimise the data handling during the detector operation and for offline processing. Although the upcoming computing situation was already published in 2005, the software and thus the computing landscape is up to today not frozen but is in permanent change.

3.3 ATLAS Detector Upgrades for the HL-LHC

The ATLAS detector is operating since 2011. Due to the traversing of high energy particles through the detector and their interaction with the detector material, radiation damage affects its sensitivity. As shown in Fig. 3.21 the damage depends on the distance to the interaction point and hence to the particle trajectory density. As this indicates, radiation damage affects the innermost part the most. Although measures can be taken in order to regulate the effects, the lifetime of the detector components is limited.

Additionally the expected pile-up in the HL-LHC era is expected to be in the range of 140 to 200. Such a high particle flux would imply a high occupancy in the TRT. The high track density will also lead to a more complex reconstruction of the trajectories. The ROD's, especially in the tracking detector operate already in Run-2 pile-up at its bandwidth limit. Hence, HL-LHC pile-up would exceed the bandwidth and would lead to data losses.

In order to provide an optimal performance in the HL-LHC era the issues from radiation damage and the high pile-up must be considered. Therefore the ATLAS detector will receive several upgrades and replacements. Some major changes in the scope of this thesis are described in the following.

3.3.1 Inner Tracker

The innermost part of the detector, the ID will be replaced entirely by the Inner Tracker (ITk) [82, 83]. Compared to the ID, the ITk will only utilise silicon semiconductors as sensitive devices. Hence, the concept of the gas-detector TRT wont be a part of this detector.

The ITk is comprised of two parts: Pixel and Strip detector. An overview of the layout of the ITk is shown in Fig. 3.22 (left). Compared to the ID that covers a range of $|\eta| < 2.5$, the ITk coverage is extended up to $|\eta| < 4.0$, allowing high tracking performance over the entire pseudorapidity range. An indication of tracking performance
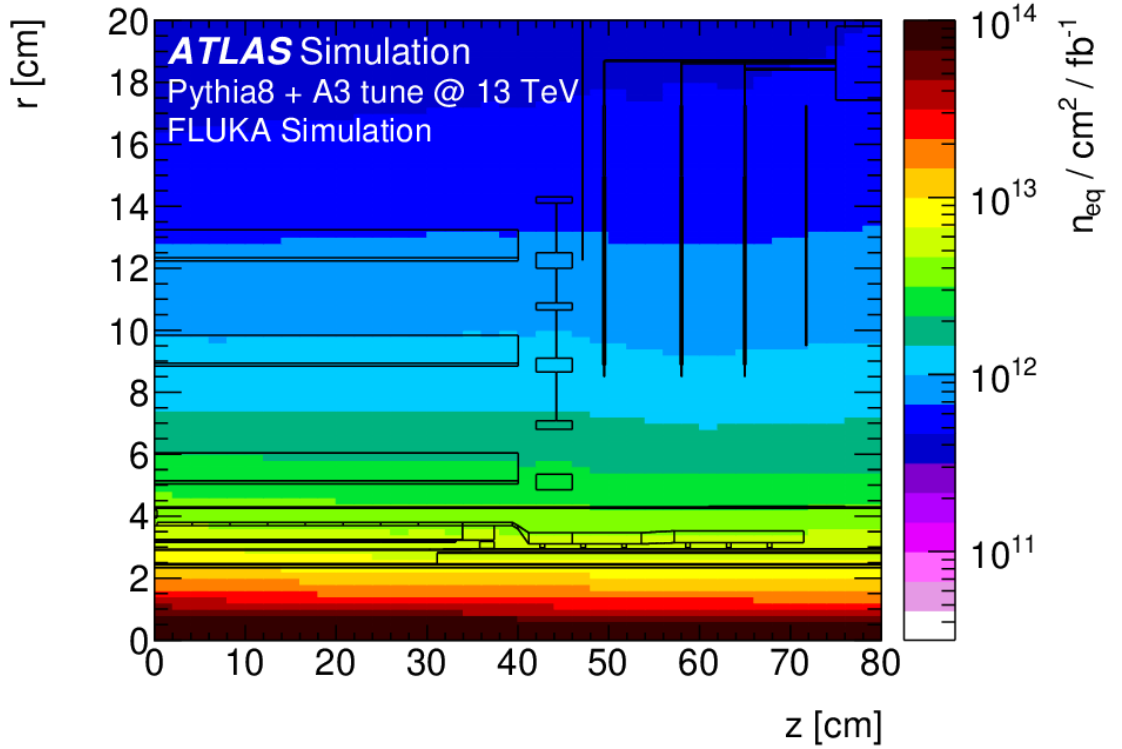
Figure 3.21: Simulated prediction of a 1 MeV neutron-equivalent flux per fb^{-1} in the silicon detectors of the ATLAS ID. The plot shows a one-quarter slice ($z > 0$ cm and above the beam) of the radial distance from the geometrical centre of the detector [81].

can be stated in the number of measurements (hits) along the trajectory. For the ITk this is shown in Fig. 3.22 (right). Due to the increased number of hits per track compared to the ID, it allows for stricter requirements for tracks. Furthermore it takes into account the technological progress in the meantime in order to maximise the performance while minimising the costs for detector material. The design parameters were chosen such that the required offline performance for track reconstruction gets maximised. A more detailed description of the individual parts is given in the following.

3.3.1.1 Inner Tracker Pixel Detector

The Pixel Detector [82] of the ITk consists of a barrel and an end-cap region that covers altogether a region of $|\eta| < 4$. This detector is enclosed by the Pixel Support Tube (PST). In the barrel part five layers of pixel detector modules are arranged. Due to radiation damage it is expected to replace the innermost layers. Hence, the inner two pixel layers are separated from the other layers by an Inner Support Tube (IST). The
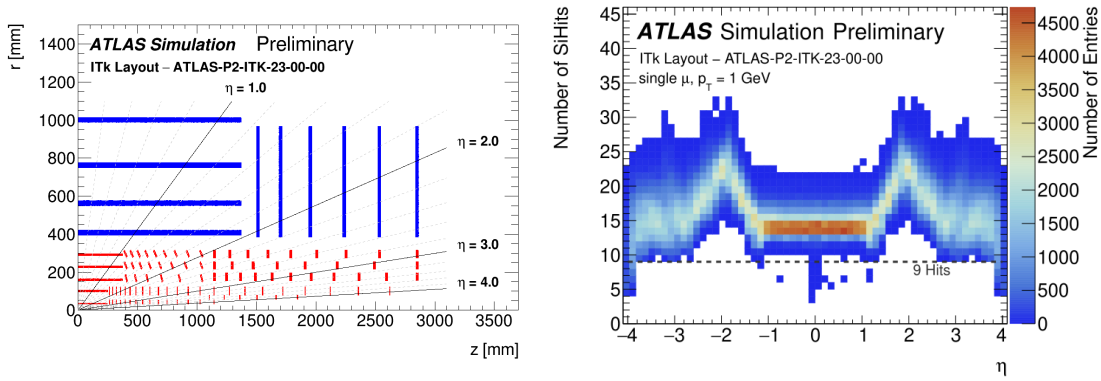
Figure 3.22: Left: Layout of the ITk. The location and radial distance of sensitive modules are shown versus z. Only the half $z > 0$ mm is shown. The red elements belong to the pixel detector, the blue elements to the strip detector. Right: Number of hits obtained from the ITk versus pseudorapidity η. Both plots are taken from Reference [84].

Barrel Layer	Radius [mm]	Rows of sensors	Flat sensors per row	Inclined sensors per row
0	34	12	12	-
1	99	20	6	-
2	160	32	9	6
3	228	44	9	8
4	291	56	9	9

Table 3.2: Nominal parameters of the ITk barrel. The number of sensors per row refer to the half $z > 0$ mm. The term *flat* refers to sensor modules arranged parallel to the beam axis whereas *inclined* refers to angles differing from the flat sensors [84].

IST allows an easy replacement of the inner two layers. An overview of the current[4] barrel design is given in Tab. 3.2. Due to a novel staving concept modules in the outer region of the barrel are inclined allowing a better coverage while reducing the required material. Therewith the number of hits per interval in η can be regularised.

The ITk utilises read-out chips with an active area of 19.2 mm $\times$ 20 mm. A module in the barrel consists of two (duals) chips in the innermost layer and four (quads) in the other four. A single chip consists of 384×400 pixels. The size of a single pixel will be either 50×50 μm^2 or 25×100 μm^2. Up to the time of writing this thesis, the final decision of the size is not made. The read-out chip is planned to be the RD53B [85]. This chip allows to read-out multiple pixels simultaneously and strongly compress the data. This allows to read clusters of pixels. For particles originating from $z = +15$ cm it is thereby expected that one hit is created per layer.

---

[4]The ITk is not installed yet. Therefore the stated parameters are based upon the current design and simulation. The final version may vary from these numbers.

Ring Layer	Radius [mm]	$|z|$ [mm]	Rings	Sensors per Ring	Hits
Barrel	33.20	263-1142	15	18	2-4
End-cap	58.70	1103-1846	6	30	3-4
End-cap	80.00	1272-2621	23	20	2-4
End-cap	154.50	1145.5-2850	11	32	1-2
End-cap	214.55	1145.5-2850	8	44	1
End-cap	274.60	1145.5-2850	9	52	1

Table 3.3: Nominal parameters of the ITk end-caps. The radii refer to the innermost point of the sensors of a ring. The stated number of hits refer to the number of hits that are created per layer for a particle originating from $z = +15$ cm [84].

Barrel Layer	Number of Staves	Radius [mm]	$|z|$ [mm]	Tilt Angle [degree]
0	27	399	0-1372	13
1	40	562	0-1372	12
2	56	762	0-1372	12
3	72	1000	0-1372	11

Table 3.4: Nominal parameters of the ITk Strip Detector barrel layers [86].

Compared to a common end-cap design for a tracking detector that utilises sensitive discs, the ITk end-cap modules are attached to a ring system. Each ring can thereby be placed individually. This allows for an optimisation of the coverage but also to provide enough and stable hits per pseudorapidity. Thus a high tracking performance can be achieved over the full range of the ITk. Additionally the flexible ring design allows to reduce material in the detector and therefore disturbances of the particle trajectory which affects the tracking resolution.

The Pixel Detector end-cap rings are grouped into six layers. Their current design parameters are summarised in Tab. 3.3. While the barrel layer and the innermost end-cap layer use a single chip (singles) per module, all other modules utilise quads.

3.3.1.2 Inner Tracker Strip Detector

The ITk Strip Detector encloses the PST. It consists of four barrel layers and six end-cap discs in both directions. The entire Strip Detector covers a range of $|\eta| < 2.7$. Comparable to the ID SCT the strip modules are paired with a small stereo angle in order to provide z- or r-resolution for the barrel or end-cap region respectively.

The barrel utilises two different strip lengths. The strips in the inner two layers are about 24.1 mm long (short-strips). The other two layers use 48.2 mm long strips (long-strips). All strips have thereby a pitch of 75.5 μm. The arrangement of the strips is summarised in Tab. 3.4. The number of staves allows the installation of the strip modules and serve for alignment purposes in order to preserve hermeticity [86]. On each stave 28 modules are attached with 1280 channels each [83]. In the short-strips a sensor

Disc	Radius [mm]	$|z|$ [mm]
0	385	1512
1	385	1702
2	385	1952
3	385	2237
4	385	2532
5	385	2850

Table 3.5: Nominal parameters of the ITk Strip Detector end-cap discs [86].

is connected to four modules, in the long-strips to two. The denoted angles are per module, a pair has consequently a stereo angle of about 22-26 degree.

In the end-cap petal-design discs the modules are radially arranged, pointing to the centre of the beam axis. Driven by demanding a strip occupancy of below 1%, the strip sizes are, different to the barrel layers not of uniform size per disc. In addition, the placement of the strips needs to be taken into account. A summary is given in Tab. 3.5. As the particle track density is larger near the beam axis, the inner strips are shorter compared to the outer ones. The same accounts for the pitch of the strips. The strip lengths vary from 19.0 mm to 60.1 mm with pitches from 69.9 μm to 80.7 μm [83]. The explicit dimension of each module thereby depends on the disc and the radius. For each disc 32 petals are used with nine modules each.

3.3.2 High Granularity Timing Detector

The HL-LHC will provide an expected pile-up of up to $\langle \mu \rangle = 200$. It is estimated that the interactions will occur with a Gaussian spread of 30 to 60 mm. The underlying probabilistic nature of the interactions lead to a primary vertex density distribution as shown in Fig. 3.23 (left). This distribution shows the expected fluctuation in pile-up density compared to earlier LHC pile-up.

In order to preserve a high tracking and vertex reconstruction performance, the High-Granularity Timing Detector (HGTD) [87] will be installed for the ATLAS Phase-II upgrade. This detector component will complement the ITk in the forward direction. As Fig. 3.23 (right) shows, the vertex density in longitudinal z-direction can be reduced by extending the measurements from the ITk by a time component t. While pure spatial measurements would lead to a projection of all vertices on the abscissa, the time component provides additional information about the vertices. Thus, the local vertex density in the z-t-plane is lower than in the marginalised case from Fig. 3.23 (left). A reduced complexity of the track-to-vertex association by using timing information allows in addition a more precise measurement of the bunch-by-bunch pile-up and the beam-spot characteristics. This knowledge is also beneficial for the estimation of the online luminosity as well as the offline integrated luminosity. For the HL-LHC era it is expected that the interaction region spreads in time from 175 ps to 260 ps.

The HGTD will be located at ± 3.5 m from the nominal centre of the detector and covers a region of $2.4 < |\eta| < 4.0$. This detector will be located just outside the ITk and
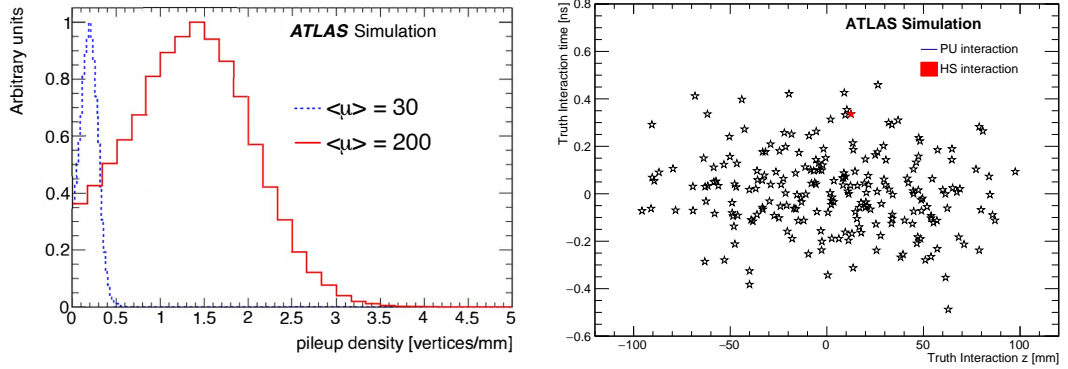
Figure 3.23: Left: Distribution of the vertex density for a pile-up of $\langle \mu \rangle = 30$ (blue) and 200 (red). Right: Distribution of z-coordinates versus time of primary vertices in an event with $\langle \mu \rangle = 200$. The red marker indicates the hard scattering event and the black markers the pile-up interactions. The vertices are sampled from random samples with a standard deviation of 50 mm and 175 ps in z-direction and time respectively to mimic the ATLAS interaction point. Both plots are taken from Reference [87].

with an envelope of a radial extend from 110 mm to 1000 mm, the detector reaches up to the gap between the barrel and the end-cap of the LAr calorimeter. The envelope in z-direction is about 125 mm including a 50 mm-thick neutron moderator at the front and rear end for reducing neutron back-scattering from the LAr calorimeter.

As the HGTD will be located in the forward direction, the timing information of the particle trajectory is only provided in this direction, supporting hereby the ITk in the large pseudorapidity regime. This allows to restore the reconstruction performance in the forward direction to levels similar to the central direction of the detector. As shown in Fig. 3.24 the vertex parameters of the ITk is worse compared to the regions of small psuedorapidity. Within this forward region the HGTD is intended to support the ITk
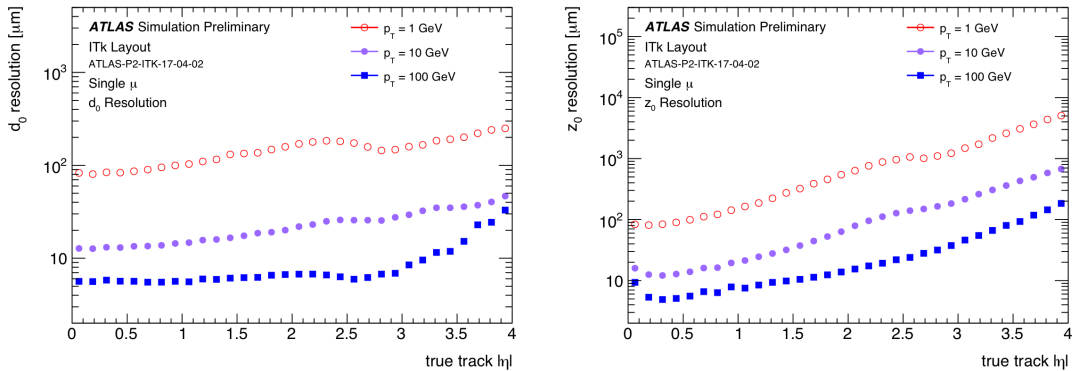
Figure 3.24: Transverse d_0 (left) and longitudinal z_0 (right) parameter resolution as a function of $|\eta|$ single muons with $p_T = 1, 10, 100$ GeV [88].

in the track reconstruction and track-to-vertex association.

The HGTD working principle itself is centred around measuring minimum-ionising charged particles (MIP's) with a time resolution from 30 ps (beginning of the HL-LHC operation) to 50 ps (end of HL-LHC operation). It is intended to achieve the resolution by utilising Low Gain Avalanche Detector (LGAD) pads. A single pad is planned to have an area of 1.3×1.3 mm^2 and an active thickness of 50 μm. In total about 3.6 million pads are arranged in two rotated, double-sided layers per end-cap such that each end-cap forms a hermitic vessel. Therewith it is foreseen to record in the region 120 mm$< r <$230 mm, 230 mm$< r <$470 mm and 470 mm$< r <$640 mm per track 2.6, 2.4 and 2.0 hits respectively.

Since the timing information was not handled in the ATLAS experiment before, a special consideration of this parameter is required. For the HGTD, it is planned to associate the hits in the individual pads via extrapolation from the outermost layer of the ITk using a progressive Kalman filter (see Chapters 4 and 7). Compatible measurements from the HGTD pads allow therewith the assignment of timing information upon the particle's trajectory. The measurement of the additional time parameter allows to reduce the complexity of the track reconstruction and to suppress the rate of reconstruction errors.

3.3.3 Trigger and Data Acquisition

The HL-LHC is expected to provide seven times the original LHC design peak instantaneous luminosity. With up to $\langle \mu \rangle = 200$ inelastic proton-proton collisions every 25 ns, the data volume provided by the detector gets drastically increased. Hence, the TDAQ [89] system needs to be adapted for the upcoming scenario in order to fully exploit the physics potential offered by the HL-LHC. The physics menu covers thereby a broad range of studies including the electroweak symmetry breaking, rare processes and searches for new particles. In order to achieve a proper triggering and data acquisition for the ambitious physics program it is expected that a ten times higher rate is needed.

The workflow compared to Phase-I will be modified. Beside the pure requirements due to the luminosity during Phase-II, the TDAQ system needs to be adapted for the modified ATLAS detector. An overview of the Phase-II workflow is shown in Fig. 3.25. The system will be grouped into three stages: Level-0, DAQ and EF System. For the Level-0 triggering only data from the calorimeters (*L0Calo*) and the muon system (*L0Muon*) are used. Both sub-systems operate on a subset of the corresponding detector data. For the calorimeters this is divided into different Feature EXtraction (FEX) schemes, either electron (e), jet (j), global (g) or forward (f). For the L0Muon the different parts of the muon system are the relevant sections: Barrel, Endcap, New Small Wheel (NSW) or MDT. The result is then further processed in the *Global Trigger*. At that stage the full granularity of the calorimeters are utilised and event-level quantities are evaluated. The Global Trigger applies thereby offline-like algorithms. As final trigger stage in the Level-0 system, the Central Trigger Processor (CTP) decides upon the results from the Global Trigger and the provided detector data. Furthermore the CTP is capable of introducing dead times in order to avoid a saturation in the front-end systems of the

detector or the readout systems. This dead time is given by an algorithm that depends on the current trigger rate, the estimated data that would be read-out and the status of subsequent components in the TDAQ workflow. If the event is accepted by the CTP and therewith by the Level-0 in total, the processor steers the Trigger, Timing and Control system (TTC) to start with the readout process of the ATLAS detector systems. This entire decision chain operates with a maximal latency of 10 μs.

Triggered by the TTC, the decision is transmitted to all detectors and the data is read-out with a rate of 1 MHz. The Front-End LInk EXchange (FELIX) and Data Handlers drive the readout. The Dataflow subsystem builds and aggregates therewith the events and manages the storage.

The last storage decision in the ATLAS Phase-II TDAQ is done by the Event Filter (EF). This system consists of a CPU farm with custom designed Hardware-based Tracking for the Trigger (HTT) as co-processor. The purpose of the EF is to reduce the final event output rate by refining the trigger objects. Once the EF accepts an event, the Dataflow writes it to the permanent storage with up to 10 kHz.

As the HL-LHC challenges for the TDAQ have been encountered before, the expected data rates can vary. It is therefore foreseen to evolve the TDAQ system into a dual-level hardware trigger with a 2-4 MHz Level-0 and a 600-800 kHz Level-1. While the Level-0 latency would be unchanged, the Level-1 latency is estimated with up to 35 μs. The Level-1 would thereby already perform hardware-based track reconstruction and thus the HTT would need to be reconfigured.

3.3.4 Phase-II Computing

The initial design report for the required computing in order to operate the ATLAS experiment was published in 2005 [80]. This plan considered that raw data is processed in the lower levels whereas Tier-2 starts utilising derived data. This kind of data is meant to contain data for physics analyses and hence computing processes in between. The initial schedule foresaw that the luminosity would grow during the lifetime of the LHC and thus the data rate.

Beside the ongoing challenge for the computing facilities hardware due to the growing data rate, the software itself requires a certain flexibility in order to be adaptable for upcoming task and to improve the current tasks. The menu of tasks reaches thereby from high-level trigger tasks to physics analyses. For the purpose of continuous performance, the ATLAS software framework *Athena* is designed around the demanded tasks and the underlying computing landscape.

However, the expected requirements for computing software and hardware changed when the HL-LHC was commissioned in 2010 [56].

While the HL-LHC is planned to provide a large amount of data and the TDAQ for the ATLAS Phase-II is intended to store as much data as possible related to the ambitious physics program of the ATLAS Collaboration, the amount of data is closely linked with computational requirements. Therefore it is mandatory to closely monitor the required computing and to point out open questions before the start of Run-4. For

that purpose a summary of the current requirements and an extrapolation based upon different assumptions for the future was performed [90].

The requirements can be categorised into computing hardware such as CPUs and GPUs and storage media like disks or tapes. While the ATLAS software is mainly built and optimised for CPU application, an ongoing effort is taken in order to investigate application possibilities for GPUs. Up to now, the computing in ATLAS is dominated by utilising CPUs. An overview of the expected requirements for CPU and disk storage is shown in Fig. 3.26. While the blue markers consider a scenario with a maximal pile-up of 140 during Run-4 and afterwards 200, the red markers consider the case of reaching the upper limit already in 2028. In both predictions three different scenarios are considered. The Baseline scenario assumes a modified analysis model planned for Run-3, a multi-threaded execution of the ATLAS software and updates of the tracking code. Beside these changes it is assumed to be mostly similar to the Run-2 software.

The Conservative R&D scenario instead assumes that additional developments for Run-3 are successful. This involves a per-request data transfer from tape to disk (*data carousel*), the application of a fast track reconstruction, lossy compression of data and a broader usage of a simplified simulation (fast simulation).

As third scenario the Aggressive R&D is shown in Fig. 3.26. Within this scenario it is assumed that further and significant improvements in data compression and speed compared to the Conservative R&D are achieved. This involves e.g. a wide execution on GPUs and a high-precision fast simulation that is capable of replacing a detailed full simulation in almost all cases.

The sustained budget model from Fig. 3.26 (black line) indicates for CPU and disk usage an over-consumption of resources around the start of Phase-II. Given that the Aggressive R&D scenario is the achievable, the expected resources are sufficient if the +20% annual capacity model is fulfilled for a certain period of time. For the CPU capacity the requirements are a bit lower. However, this is still an extrapolation based on the present estimations and require therefore constant monitoring and updates.

The extrapolation summarises all CPU and disk contributions in a single marker. In Fig. 3.27 the CPU contributions are itemised by category. During 2018 the main contribution for the CPU consumption was given by the simulation of events (*Monte Carlo* or MC) and their reconstruction. The largest contribution in MC related consumption was given by the event simulation (38%), followed by the reconstruction (18%) and the event generation (11%). Already this branch of consumers emphasises the investment in simulation and reconstruction R&D, as given by the prediction scenarios. The MC event generation on the other hand is usually driven by small teams that are primary concerned about precise predictions rather than an optimised utilisation of computing hardware [90].

Currently half of the events are generated using the full simulation provided by Geant4[5] [92, 93]. As this contributes around 40% to the total consumption, ongoing efforts are taken in order to replace wherever possible the full by a fast simulation. As-

---

[5]Geant4 is a framework for the detailed simulation of particle trajectories and the interaction of particles with materials.

suming the replacement of full simulations by a certain percentage with fast simulations leads to the split in MC contributions in the pie chart shown in Fig. 3.27 (right). An according separation of the reconstruction can be done, too.

In both cases, the 2018 summary and the Baseline prediction for 2030 MC is the main contributor. This would be even the case when the objects specified in the Aggressive R&D scenario are achieved. For that purpose a more detailed investigation for a fast track reconstruction is given within this thesis in Chapter 6. A fast simulation implementation is discussed in Chapter 9.
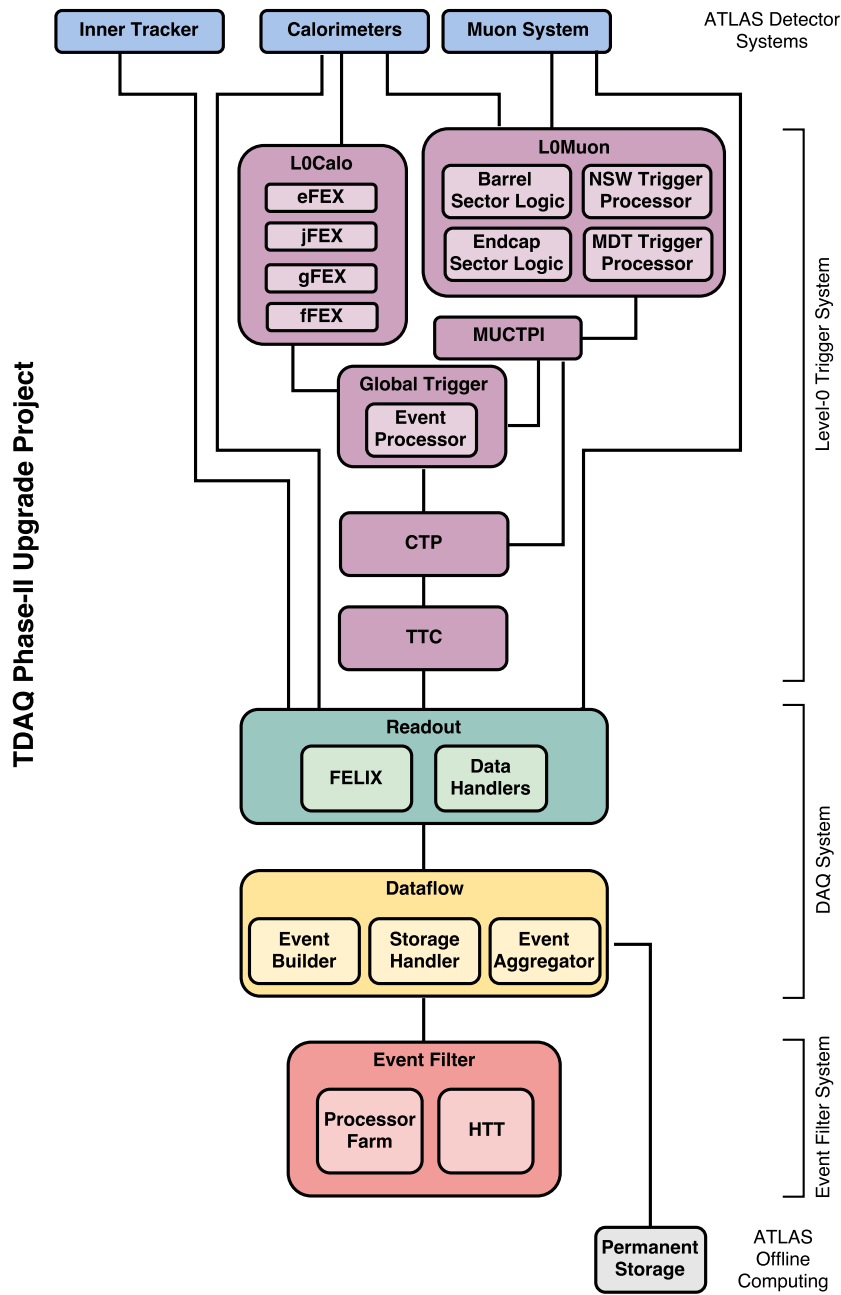
Figure 3.25: ATLAS Phase-II TDAQ design showing the sub-systems involved and their connection among each other as well as the connection to the detector systems. For simplicity the connection between components of a system are not drawn [89].
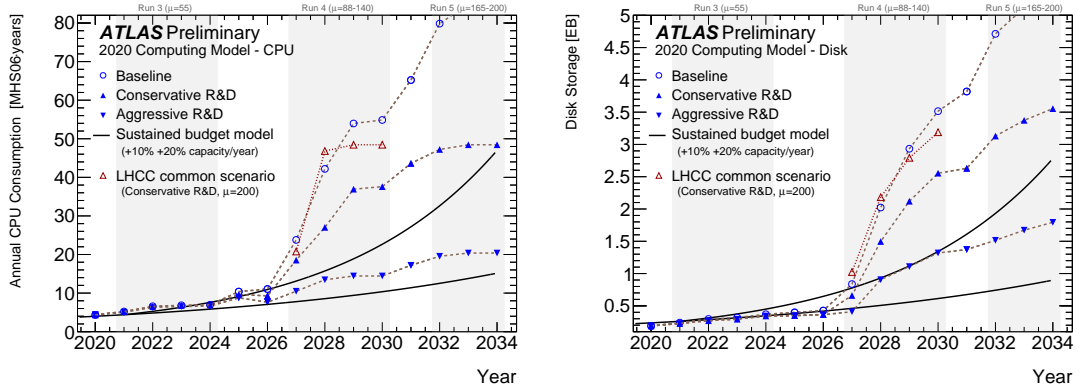
Figure 3.26: Estimated CPU and disk resources consumption needed for the ATLAS experiment for the years 2020 to 2034 in MHS06·years [91] and EB respectively. The black solid line represents the estimated available resources under the assumption of an annual improvement of 10% and 20%. The blue markers with brown lines indicate different scenarios for future computing requirements (see text). The red markers indicate the conservative R&D scenario assuming $\langle \mu \rangle = 200$ by 2028 [90].
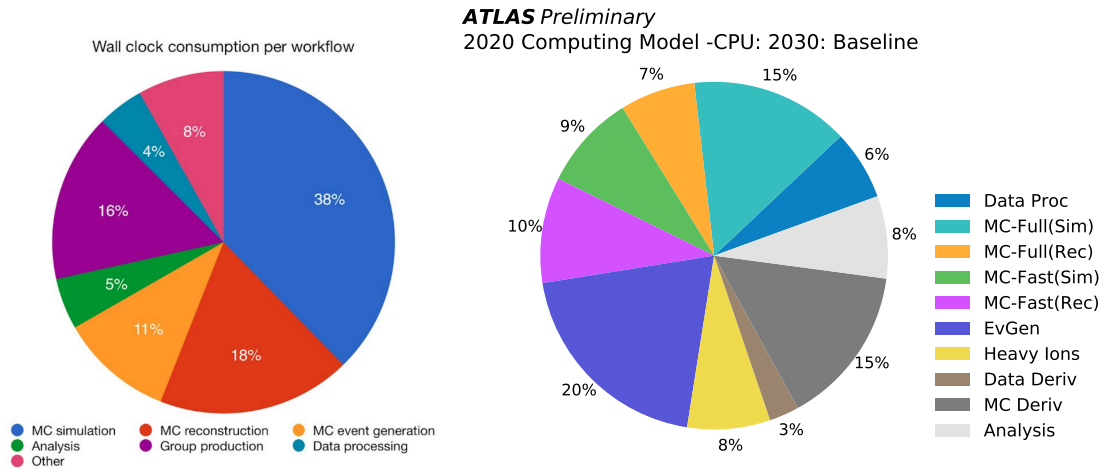
Figure 3.27: ATLAS CPU hours used by various activities in 2018 (left) and predicted for 2030 (right) based on the Baseline model [90].

4 Theory of Model Based Track Reconstruction

Any detector in particle physics has to provide data from particle collisions (events), such that the properties of produced particles can be reconstructed. In the very beginning of nuclear and particle physics, these data were provided by producing pictures in bubble and cloud chambers as exemplary shown in Fig. 4.1. Although this allowed to vi-
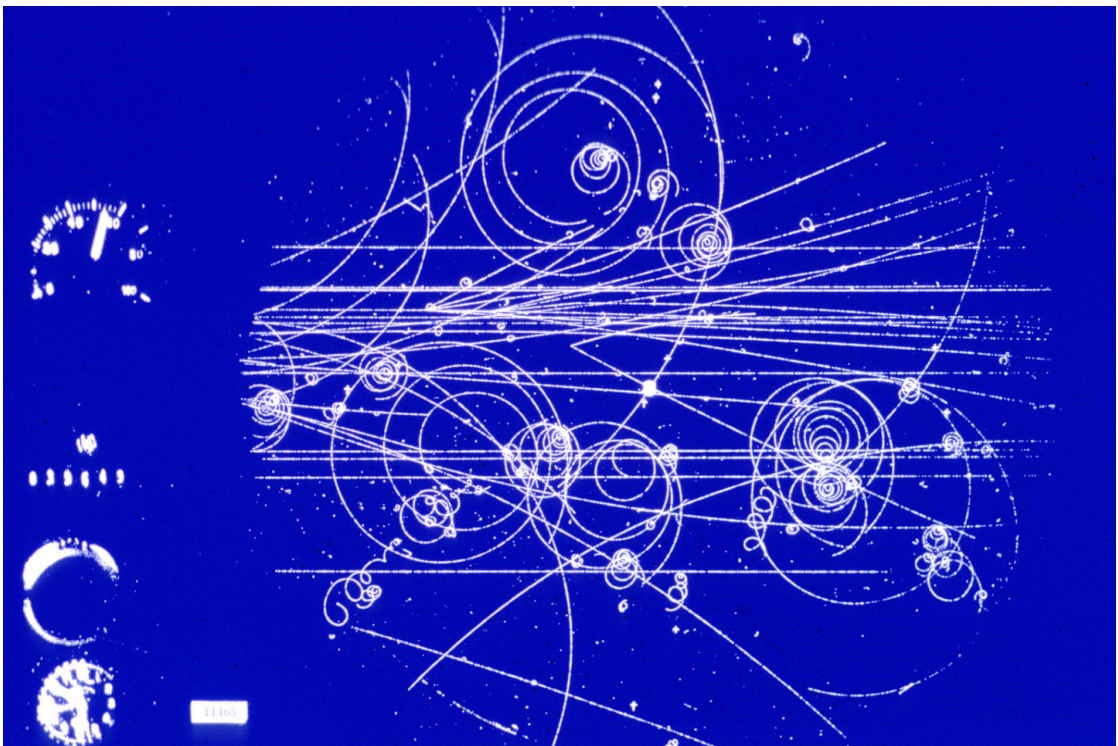
Figure 4.1: Photography of 16 GeV charged pions entering CERN's first liquid hydrogen bubble chamber in 1960 [94].

sualise particle physics, the analysis of the obtained measurements had to be performed manually. Beside being error-prone, the achievable data rate was limited.

Nowadays the data for the reconstruction provided by the detector is given by electrical signals, either digital or analogue. In both ways, the picture and the electronic based read-out, any data refers to interactions of the particles with sensitive components of the detector. Therewith, the data give hints to the structure of the event. Of special

interest in the event structure is thereby the hard interaction process, i.e. the primary particle interaction (primary vertex). The data is thereby utilised to reconstruct the outgoing particles from this vertex as well as the location of the vertex itself. Thus, the underlying processes can be studied.

While the trajectory of the outgoing particles could be estimated in the bubble chamber visually, a modern particle detector requires further processing. In comparison with Fig. 4.1, the ID and ITk as shown in Sec. 3.2.2 and 3.3.1 respectively provide data only at discrete points along the particle's trajectory. Thereby, the workflow from electronic signals to an estimation of particle properties at the vertex consists of multiple steps. Starting from interpreting the signals source and the contained information, triggers can estimate whether the underlying event structure could be of interest and therefore further processed or rejected. In case of further processing the individual signals are combined to clusters and space-points. Latter ones are used to produce a first estimate of potential trajectories in the detector, the so-called *seeds*.

The particle properties or parameters after the seeding step are constrained by the triggers and the seeds. In order to obtain the best estimation of the parameters at the vertex position, the information contained in the measured clusters (measurements) need to be combined with the initial parameter estimation, the seeds, and evaluated at the vertex position.

As the reconstruction consists of several steps relying on the interpretation of data, a statistically consistent formulation of the problem is crucial. Especially a further usage of the results, e.g. for SM analyses rely thereby on the statistical correctness and the corresponding uncertainty. Up to today the track reconstruction workflow is treated as a sequence of consecutive steps. This is partially grown step-wise by new technological advance, e.g. in computing or mathematical discoveries and became a "fixed workflow" due to its successful application in the first place and due to historical reasons afterwards.

In the context of Sec. 3.3.4, any improvement which is not related to plain code-optimisation requires a fundamental understanding of the problem. Up to today, the track reconstruction steps were never considered as parts of a statistical reasoning. As part of this this thesis, a theoretical ansatz to track reconstruction is formulated within this chapter. A theoretical formulation provides a total picture of the field. A formal description of this workflow can be derived from Bayes' theorem [95]. Starting from a general introduction of the theorem and corresponding properties, the modelling of individual properties is discussed and applied. This is done in ascending complexity of the problem. In Sec. 4.2 Bayes' theorem is applied for a single measurement and the influence of a measurement upon the particle parameter estimation is shown. In Sec. 4.3 the derived expressions are generalised for a general track and event reconstruction.

4.1 Bayes' Theorem

In this section a derivation of Bayes' theorem is presented alongside an introduction of the nomenclature that will be used afterwards. Both parts are based on Reference [96].

In the second part of the section some statistical properties related to the theorem but also to the subsequent discussion are presented.

This theorem of Bayes can be derived from axioms of probability theory proposed by Andrei Kolmogorow [97]. The axioms allow the description of the conditional probability $P(B|A)$ for an event B to happen under the circumstance that an event A occurred:

$$P(B|A) = \frac{P(A \cap B)}{P(A)}$$

with the probability $P(A \cap B)$ that A and B occurred and the probability $P(A)$ that event A occurs. This equation can be transformed under the assumption that $P(A \cap B) = P(B \cap A)$ to the Bayes' theorem:

$$P(A|B) = \frac{P(B|A)P(A)}{P(B)}.$$

Since the description of events A and B is very abstract, these will be replaced in the following by model parameters λ and data m respectively:

$$P(\lambda|m) = \frac{P(m|\lambda)P(\lambda)}{P(m)} \tag{4.1}$$

For discrete distributions the individual terms are probability functions, in the continuous case they represent probability density functions (pdfs). For simplicity, the focus will be on treating pdfs. Furthermore, each term is labelled differently. A description of them is given in the following:

- **Prior** $P(\lambda)$
  The prior is an initial distribution reflecting the belief in the values of λ before any data is considered, i.e. this distribution may not rely on any data at all. It can also reflect knowledge gained from former measurements of parameters. The priors can be classified as *hard* and *soft* ones. The former describes a distribution that excludes certain parameter values. For example that would refer to negative values of the particles energy. The soft prior disfavours certain values but does not exclude these.

- **Likelihood** $P(m|\lambda)$
  The likelihood represents how likely it is to obtain the measured data with respect to fixed model parameters. It is not mandatory to restrict the data to a single measurement. For two measurements m_1, m_2, the likelihood can be written as

$$P(m|\lambda) = P(m_1, m_2|\lambda) = P(m_2|m_1, \lambda)P(m_1|\lambda)$$
$$\underset{m_1, m_2 \text{ independent}}{=} P(m_2|\lambda)P(m_1|\lambda). \tag{4.2}$$

The pdf $P(m_2|m_1, \lambda)$ denotes hereby the correlation between m_1 and m_2. Additionally, both measurements are interchangeable without affecting the result.

- **Evidence** $P(m)$

  The evidence denotes the probability of the measurements itself. As the underlying model for the data is usually unknown, the law of total probability

  $$P(m) = \int P(m|\lambda)P(\lambda)d\lambda. \tag{4.3}$$

  is utilised. Thus, the underlying distribution can be expressed in terms of the given model that refers to λ. By integrating over all possible values of λ, the evidence itself is a number, such that a proper normalisation of the pdfs is preserved.

- **Posterior** $P(\lambda|m)$

  Compared to the likelihood, the posterior is a function of the model parameters itself. As it depends upon the prior assumption and the measurements, the posterior represents a learning procedure, achieved by the data.

The properties and the role of the four terms allow to consider general properties of the Bayes' theorem and the introduction of further terminology. A selection of those is presented in the following:

- **Iterative learning**

  Eq. (4.2) suggests that the posterior does not have to be calculated using all measurements in the likelihood. A progressive learning with a posterior considering only m_1 and serving afterwards as prior for an iteration that only considers m_2 provides the same final posterior. Furthermore, this iterative learning demonstrates that precise data as well as a large amount of data allow to suppress the impact of the prior. However, parameter values excluded by a hard prior are not affected by this property.

- **Posterior likelihood**

  The numerator is referred to as posterior likelihood

  $$\mathcal{L}(\lambda|m) = P(m|\lambda)P(\lambda) \propto P(\lambda|m). \tag{4.4}$$

  The proportionality is given by the fact that the evidence is a number that just scales the posterior. Hence, quantiles of the underlying model remain unchanged. For simplicity reasons, the posterior likelihood is often favoured. This invokes on the other hand the condition that a proper normalisation is granted.

- **Identity likelihood**

  For a given finite volume V a special likelihood with $m \in V$ is given by the uniform distribution

  $$P(m|\lambda) = \frac{1}{\int dV}. \tag{4.5}$$

  As this likelihood is a constant number and independent of λ, it scales the posterior likelihood without changing any quantiles. For the posterior, the relation

$P(\lambda|m) = P(\lambda)$ shows the identity property, i.e. the prior and the posterior pdf are identical. Hence, this identity refers to the absence of any information about the model parameters. This construction is helpful in the following to express a conditional inclusion of data.

- **Conjugate prior**
  The prior reflects a prior belief in certain values of the model parameters. This belief is reflected in the moments characterising the pdf. If the shapes of the prior and likelihood pdf are provided then the distribution of the posterior pdf can be evaluated. As the likelihood pdf is predefined by the experimental setup, the shape of the posterior pdf depends on the chosen prior. If applicable, the prior can be chosen such that the posterior has the same shape as the prior. Hence, the posterior pdf consists of the moments of the prior, modified by the likelihood. If the parameters are updated multiple times with likelihoods of the same shape and if such a conjugate prior can be found and is applicable for the underlying problem, then the shapes of the posterior pdf are foreseeable. This consequently simplifies the problem.

4.2 Kalman Filter

In this section a description of measurements and therefore of the likelihood is discussed. Based on the results of this description, a discussion about the corresponding prior is presented. For both factors of the posterior likelihood from Eq. (4.4), approximations are derived and applied. In the last part of this section, the simplest case of a single measurement produced by a single particle is considered and the posterior likelihood evaluated with respect to the applied approximations.

4.2.1 Measurement Description

In Sec. 3.2 multiple different measurement principles are presented. Considering the silicon based detectors[1] in Sec. 3.2.2.1, 3.2.2.2 and 3.3.1, the measurements are created based on the same physical property of semiconductors. Although all three differ in detail, the common procedure of producing electron-hole-pairs that are registered on one end is identical. The exact position inside the semiconductor where the pair was created and therefore the trajectory of the particle through the material is unknown. Since these detectors are arranged hermetic, the particle has to penetrate the read-out layer. The data obtained from these detectors can therefore be interpreted as a position of the particle along its trajectory. Also, just the read-out plane needs to be considered in describing the measurement.

Since a pixel or a strip has a finite pitch and width, the measurement has an uncertainty. Correcting for the Lorentz angle narrows the uncertainty. Depending upon the

---

[1]A similar concept for the measurement description can be applied for other working principles. Though, the description is less intuitive and therefore neglected.

corrected cluster size[2], the simplest pdf describing the measurement is a flat distribution in the measurement plane $A \subseteq \mathbb{R}^2$ given by

$$p(x, y) = \begin{cases} 1/|C|, (x,y) \in C \\ 0, \text{else} \end{cases}$$

for a cluster $C \subseteq A$ and the vector $(x, y) \in A$. This expression corresponds to the least amount of information that can be provided. Due to analogue read-out as in the ID pixel detector, the collected charge allows to weight the individual pixels that are interpolated afterwards. After invoking this information, the resulting pdf is not demanded to be flat anymore. For the used strip modules the distributions are flat. Additionally, for the long-strip modules the relation $y \notin C \Rightarrow y \notin A$ holds.

Central Limit Theorem

In order to simplify the measurement description and to avoid the handling of multiple different likelihoods, the *central limit theorem* (CLT) can be considered. For understanding the applicability of this theorem, the conditions and the limitations, a derivation based on Reference [98] is given in the following.

For the derivation of the CLT, the *characteristic function* $\phi(k)$ is required. This function is related to the pdf $p(x)$ via the Fourier transform

$$\phi(k) = \int_{-\infty}^{\infty} e^{ikx} p(x) dx, \tag{4.6}$$

the inverse transformation is given by

$$p(x) = \frac{1}{2\pi} \int_{-\pi}^{\pi} e^{-ikx} \phi(k) dk. \tag{4.7}$$

This function is introduced due to its properties. Considering a variable $z = x + y$, defined as the sum of two variables x and y. The pdf of x is given by $p_x(x)$, the pdf of y by $p_y(y)$. Under the assumption that x and y are sampled independently leads to the combined pdf $p_z(z) = p(x, y) = p_x(x)p_y(y)$. The characteristic function of z, $\phi_z(k)$ is then given by

$$\phi_z(k) = \int e^{ikz} p_z(z) dz \tag{4.8}$$

$$= \int e^{ikz} \left[\int \delta(z - x - y) p(x, y) dx dy \right] dz$$

$$= \int \left[\int e^{ikz} \delta(z - x - y) dz \right] p_x(x) p_y(y) dx dy$$

$$= \int e^{ikx} p_x(x) dx \int e^{iky} p_y(y) dy$$

$$= \phi_x(k) \phi_y(k) \tag{4.9}$$

---

[2]The size is defined by neighbouring pixels or strips that produced a signal.

with the characteristic functions $\phi_x(k)$ and $\phi_y(k)$ of $p_x(x)$ and $p_y(y)$ respectively. In the context of the definition z, the characteristic function of $p_z(z)$ is given by the product of the characteristic functions given by the pdfs of the corresponding addends of z.

This result can be expanded to $n \in \mathbb{N}$ independent variables x_i with $i = 1, ..., n$. It is assumed that each x_i is a variable from the pdf $p_{x_i}(x_i) = p(x_i) = p(x)$, i.e. each variable is sampled from the same pdf. It is assumed that for the pdf a finite mean $\overline{x} = \frac{1}{n}\sum_{i=1}^{n} x_i$ exists. The corresponding expectation value $E[\overline{x}]$ of $\overline{x}$ is then given by

$$E[\overline{x}] = \int \overline{x}p(x)dx = \int \frac{1}{n}\sum_{i=1}^{n} xp(x)dx = \frac{1}{n}n\mu = \mu$$

with the mean μ of $p(x)$. This parameter is assumed to be also finite. Furthermore, the corresponding variance $\sigma^2 = E[(x - E[x])^2]$ of $p(x)$ is assumed to exist and to be finite.

Considering the difference $\xi = \sqrt{n}(\overline{x} - \mu) = \sum_{i=1}^{n}\frac{x_i - \mu}{\sqrt{n}}$ with the corresponding pdf $p_\xi(\xi)$ leads under utilisation of the Eqs. (4.8), (4.6) and (4.9) to

$$\phi_\xi(k) = \prod_{i=1}^{n} \phi_{\frac{x_i - \mu}{\sqrt{n}}}(k) = \prod_{i=1}^{n} \int e^{ik\frac{x-\mu}{\sqrt{n}}} p(x)\, dx. \tag{4.10}$$

By expanding the exponential function in the last expression in a Taylor series around $x_0 = \mu$ leads to

$$\phi_\xi(k) = \prod_{i=1}^{n} \int \left(e^{\frac{ik}{\sqrt{n}}(x-\mu)} \right)\Big|_{x_0=\mu} p(x)dx$$

$$= \prod_{i=1}^{n} \int \left(1 + \frac{ik}{\sqrt{n}}(x - \mu) - \frac{k^2}{2n}(x - \mu)^2 + \mathcal{O}\left(\frac{(x - \mu)^3}{n^{\frac{3}{2}}} \right) + ... \right) p(x)dx.$$

Considering the last expression in the limit $n \to \infty$ with the assumption that terms of third and higher order can be neglected leads to

$$\lim_{n\to\infty} \phi_\xi(k) = \lim_{n\to\infty} \prod_{i=1}^{n} \left(1 + \frac{ik}{\sqrt{n}}E[x - \mu] - \frac{k^2}{2n}E[(x - \mu)^2] \right) \tag{4.11}$$

$$= \lim_{n\to\infty} \prod_{i=1}^{n} \left(1 - \frac{k^2}{2n}\sigma^2 \right) = \lim_{n\to\infty} \left(1 - \frac{k^2}{2n}\sigma^2 \right)^n$$

$$= e^{-\frac{k^2}{2}\sigma^2}.$$

Hereby the properties $E[x] = \mu$ and $\sigma^2 = E[(x - E[x])^2]$ were used. Thus, the pdf

$$p_\xi(\xi) = \frac{1}{\sqrt{2\pi}\sigma_\xi} e^{-\frac{1}{2}\frac{\xi^2}{\sigma_\xi^2}} \tag{4.12}$$

can be calculated using Eq. (4.7). The standard deviation $\sigma_\xi = \sqrt{\sigma_\xi^2}$ is thereby related to σ via $\sigma_\xi = \sqrt{n}\sigma$.

The approximations applied for the mean of a sample $\{x_i\}$ to be normal distributed around the mean of the underlying distribution $p(x)$ is the CLT. The strength of the theorem is due to the loose conditions it depends on, which is for the pdf the existence of a finite mean and variance.

Statistical Model of Measurements

In the context of a silicon detector, a particle penetrating the read-out layer and producing electron-hole-pairs is equivalent to the production of a sample $\{(x_i, y_i)\}^3$ from an underlying pdf. After correcting for the Lorentz angle, the cluster mean is thereby given by the true position $\mu_{\text{true}}^{\text{particle}}$ of the particle. The covariance matrix Σ_{det} on the other hand is dominated by the sizes of the pixels/strips. An additional contribution is given by the semiconductor material and the read-out electronics. Therewith additional noise contributions are added while thresholds cut the signal. Further techniques such as charge collection and interpolation between channels re-weights the impact of individual tuples wherever applicable. Invoking these additional information can be interpreted as a modification of the underlying sampling pdf. Hence, under the assumption that the sample size n is sufficiently large and each sample is independent of each other, the probability density of the cluster position can be summarised as $m = (\overline{x}, \overline{y})^T = \frac{1}{n} \sum_{i=1}^{n} (x_i, y_i)^T$ by the multivariate normal distribution

$$\mathcal{G}\left(m | \mu_{\text{true}}^{\text{particle}}, \Sigma_{\text{det}}\right) = \frac{1}{\sqrt{(2\pi)^{\dim(m)} \det(\Sigma_{\text{det}})}} e^{-\frac{1}{2}\left(m - \mu_{\text{true}}^{\text{particle}}\right)^T \Sigma_{\text{det}}^{-1} \left(m - \mu_{\text{true}}^{\text{particle}}\right)} \quad (4.13)$$

with the dimension $\dim(m)$. This generalisation of the CLT to higher dimensions relies on the requirement that Σ_{det} is a regular matrix.

Under the assumption that the clusters fulfil the required conditions, the approximation for the pdf for the cluster mean allows the same functional shape for each measurement while encapsulating the detector properties in the covariance matrix. The mean on the other hand relies on the knowledge of the particle and is therefore unknown. On the other hand the application of Eq. (4.13) as likelihood as given in Eq. (4.1) leads to

$$P\left(m | \lambda\right) = \mathcal{G}\left(m | \lambda, \Sigma_{\text{det}}\right) \quad (4.14)$$

with the given mean λ. The given covariance matrix is thereby only depending on the detector and may vary for different modules but also inside the module, e.g. due to damaged individual pixels/strips. Consequently, for a module *mod*, the covariance matrix is itself given by $\Sigma_{\text{det}}(\lambda, mod)$.

Another aspect worthy of mention in the context of this likelihood is that the parameters λ can be different from $\mu_{\text{true}}^{\text{particle}}$. The CLT on the other hand relies on the usage

---

[3]In general, a restriction to spatial information is not mandatory and can be extended to further or replaced by other parameters. Since stating only spatial information is more intuitive and other dimensions can be considered analogously, the generalisation is not treated here for simplicity.

of the mean λ as implied by Eq. (4.14) while m is distributed around to $\mu_{\text{true}}^{\text{particle}}$. Thus, the term on the right hand side of Eq. (4.11) becomes

$$
\lim_{n\to\infty} \prod_{i=1}^{n} \left(1 + \frac{ik}{\sqrt{n}} E[x - \lambda] - \frac{k^2}{2n} E[(x - \lambda)^2] \right)
$$
$$
= \lim_{n\to\infty} \prod_{i=1}^{n} \left(1 - \frac{ik}{\sqrt{n}} \Delta\mu - \frac{k^2}{2n} \left(\sigma^2 + 2E[2\mu\Delta\mu - x\Delta\mu + \Delta\mu^2]) \right) \right)
$$
$$
= \lim_{n\to\infty} \prod_{i=1}^{n} \left(1 - \frac{ik}{\sqrt{n}} \Delta\mu - \frac{k^2}{2n} (\sigma^2 + \Delta\mu^2) \right) \tag{4.15}
$$

with $\Delta\mu = \lambda - \mu_{\text{true}}^{\text{particle}}$. If $\Delta\mu$ cannot be neglected the resulting pdf, if it exists, deviates from the form in Eq. (4.12). The resulting pdf remains unchanged in the special case of $\Delta\mu = 0$. Starting from the latter scenario and Eq. (4.12), the occurrence of likelihoods with $\Delta\mu \neq 0$ can be excluded or their impact suppressed by using a proper prior. This will be the item of discussion in the next section.

4.2.2 Prior Description

In the Bayes' theorem, the prior is a subjective distribution that can be modelled under constraints. The model parameters λ reflect particle properties. It is intended to learn about these parameters by utilising the data from the detector. Hence, the parameters are (partially) physical quantities that are measurable. Consequently, the prior distribution of some parameters is restricted to certain values, e.g. the energy of a particle cannot be negative. Depending on the considered properties, a hard prior is therefore given by nature without any modelling.

Beside the exclusion of certain values, the most conservative choice of priors would be flat. However, up to the stage of reconstructing tracks, additional stages provide information. By considering the applied detection principles, particles such as neutrino may exit the detector without producing measurements. This can be considered as exclusion of the property *particle type*. Furthermore, particles traverse a magnetic field. Charged particles with a momentum under a certain threshold will not reach any sensitive material. Such quantities are therefore further restricted.

Beside the pure detector properties, the TDAQ utilises (parts) of the detector data in order to deduce ROI's, therewith kinematic constraints and due to the utilisation of calorimeters and the muon system estimations about the particle type. Further processing of the data provides even more information about possible particle parameters. As last stage before the actual track reconstruction starts, seeds are formed for charged particles from the space-points in the tracking detector (see Sec. 5.3.1). Although taking the detector data already into account, it emphasises or suppresses the track reconstruction in certain model parameter regions, similar to a soft prior.

Considering the entire list of detector properties and pre-processing steps that provide actual prior information is mandatory for optimal treatment of the data but out scope

of the current consideration. On the other hand, the incorporation of any information into the prior distribution is not crucial but simplifies the upcoming problem.

Eq. (4.14) showed that the likelihood for the measurements can be described as (multivariate) normal distributed under the assumption of fulfilled requirements in and the approximations applied for the CLT. However, it was shown in Eq. (4.15), that this requires that λ is sufficient close to $\mu_{\text{true}}^{\text{particle}}$. This motivates the incorporation of as much information as possible from the detector and the pre-processing. In the context of the numerator of Eq. (4.1), the prior is intended to favour values of $\lambda \approx \mu_{\text{true}}^{\text{particle}}$ while suppressing large deviations. It should be considered that this is only the case for the CLT based modelling of the likelihood. Hence, the prior can be soft in λ. The learning procedure can also be formulated and summarised in a bayesian learning process as

$$P(\lambda|\mathcal{S},\mathcal{T},\mathcal{P}) = P(\mathcal{S}|\lambda,\mathcal{T},\mathcal{P})P(\mathcal{T}|\lambda,\mathcal{P})P(\mathcal{P}|\lambda)P(\lambda) \tag{4.16}$$

with the information from physics $\mathcal{P}$, from TDAQ $\mathcal{T}$ and the seeding $\mathcal{S}$. For simplicity reasons, the contributions will not be mentioned in the following. The prior will be denoted hereinafter as $P(\lambda)$.

The distribution of the prior itself is partially driven by the mathematical and thus, the computational complexity. For that purpose, a conjugate prior is a common choice. For the (multivariate) normal distribution likelihood, the conjugate prior is also a (multivariate) normal distribution

$$\mathcal{G}\left(\lambda|\mu_\lambda,\Sigma_\lambda\right) = \frac{1}{\sqrt{(2\pi)^{\dim(\lambda)}\det(\Sigma_\lambda)}}e^{-\frac{1}{2}(\lambda-\mu_\lambda)^T\Sigma_\lambda^{-1}(\lambda-\mu_\lambda)} \tag{4.17}$$

for the considered parameters λ with the mean μ_λ and the covariance matrix Σ_λ. The mean and covariance matrix reflect the knowledge gained from the trigger and the seeding. Although the model parameters can be chosen freely, a bijective mapping has to exist between λ and the measurement coordinate system (see Sec. 5.2) in order to be the conjugate prior.

As the application of a (multivariate) normal distribution is a soft prior, the constraints are not rejected, i.e. negative energies are possible. The rejected values correspond to a region $R \subseteq P$ in the parameter space P. Although hard cuts can be applied upon the distribution, it affects the distribution itself. Under the assumption that $\int_R P(\lambda)d\lambda$ is small, the effect can be neglected.

4.2.3 Posterior Likelihood

Within this section, the normal distributed approximation from Eq. (4.14) is used for the likelihood, the prior is used as given in Eq. (4.17). For the reason of simplicity, it is assumed in the following that only a single measurement exists on a read-out surface that was created by a single particle.

The particle properties are described in an $n \in \mathbb{N}$ dimensional vector $\lambda \in \Lambda^n \subseteq \mathbb{R}^n$. The subset Λ^n denotes the constraints applied from Eq. (4.16). Furthermore, a d-dimensional geometrical object $O \subseteq \mathbb{R}^d$ with $d \leq n$ is considered, with a unique

description of each point p_O of the object via a base $\{o_1, ..., o_d\} \in \mathbb{R}^d$, i.e. a unique solution of

$$\sum_{i=1}^{d} \alpha_i o_i = p_O$$

exists for $\alpha_1, ..., \alpha_d \in \mathbb{R}$. It is assumed that $\forall \lambda$ a unique solution for a projection matrix $H_O \in \mathbb{R}^{d \times n}$ with

$$\sum_{i=1}^{d} \alpha_i o_i = h(\lambda) = H_O \lambda \tag{4.18}$$

as the linear formulation of a projection function $h : \Lambda^n \to O$ exists. Therewith the particle properties are described in the context of the object and thus the coordinate vectors $\{o_i\}$ by the vector $\lambda_O = \{\alpha_i\} \in O$. The corresponding mean and covariance matrix in this coordinate system are denoted as $\mu_{\lambda,O}$ and $\Sigma_{\lambda,O}$ respectively.

For the measurements a surface is considered in which the measurement is represented. Since it is considered to be a read-out plane, it corresponds to the recording of spatial data. This concept could be generalised to a set of additional dimensions but would just add further complexity to following descriptions. Hence, this possibility is neglected in the following. Additionally, the recorded information is not restricted to only spatial data. The corresponding surface is denoted as $A \subseteq \mathbb{R}^{s+e}$ with the spatial dimension $0 < s \leq 2$ [4] and the additional, non-spatial dimension $0 \leq e \leq n - s$. As the surface provides a constraint only in spatial parameters, the additional information can be considered as an unconstrained sample except for physical reasons. Since the data contained in the measurement can be separated into spatial and other dimensions, the corresponding subspace A with base $\{a_1, ..., a_{s+e}\}$ can be split into two spaces A_s and A_e with bases $\{a_1^s, ..., a_s^s\}$ and $\{a_1^e, ..., a_e^e\}$ respectively. Due to the property

$$(\forall p_s \in A_s \Rightarrow p_s \notin A_e) \wedge (\forall p_e \in A_e \Rightarrow p_e \notin A_s) \tag{4.19}$$

a point $p_A \in A$ can be described as linear combination

$$p_A = \sum_{i=1}^{s+e} \alpha_i a_i = \sum_{i=1}^{s} \beta_i a_i^s + \sum_{i=1}^{e} \gamma_i a_i^e = p_s + p_e = H_s p_A + H_e p_A \tag{4.20}$$

with the projection matrices $H_s \in \mathbb{R}^{s \times n} : \Lambda^n \to A_s$, $H_e \in \mathbb{R}^{e \times n} : \Lambda^n \to A_e$ and a unique solution for $\alpha_1, ..., \alpha_{s+e} \in \mathbb{R}$ or $\beta_1, ..., \beta_s, \gamma_1, ..., \gamma_e \in \mathbb{R}$. The therewith projected vectors are denoted as p_s and p_e for the sub-spaces A_s and A_e respectively. As these two vectors do not interfere with each other, they can be treated individually. Since p_e is considered as unconstrained sample, no further treatment is required and Eq. (4.14) can be utilised for the description of the likelihood in the context of A_e. p_s on the other hand requires additional considerations due to the underlying surface constraint.

With the particle properties described in the context of a geometrical object O as in Eq. (4.18), two cases for $s \leq d$ can be distinguished: $A_s \subseteq O$ and $A_s \nsubseteq O$ [5]. The

---

[4] In theory a surface with $s = 0$ could be considered but due to the location of the surface, a signal from the surface indirectly delivers spatial data.

[5] For example: A_s is a pixel module in a tracking detector. If O is the pixel detector system then $A_s \subset O$. If O is the calorimeter then $A_s \nsubseteq O$.

latter case describes a surface that can not be described by parametrisation. With Eqs. (4.4), (4.14) and (4.19) this leads to a scenario with $\lambda_O \notin A_s$ and hence to a contradiction of the normal distributed modelling of the likelihood $P(m|\lambda)$. In such a case, the information contained in the measurement $m \in A$ is not taken into account and the likelihood becomes an identity as in Eq. (4.5).

For the case of $A_s \subseteq O$ one finds that $\exists \lambda_s \in O, \{\beta_i\} \in \mathbb{R} : \sum_{i=1}^{s} \beta_i H_O \widetilde{H_s} a_i^s = \lambda_s$ with the projection matrix $\widetilde{H_s} \in \mathbb{R}^{n \times s} : A_s \to \Lambda^n$. Hence, the set $\{\lambda_s\}$ is a subset of $\{\lambda_O\}$. The disjoint set $\{\lambda_O\}\backslash\{\lambda_s\}$ leads thereby to the same ill-definition of the normal distributed likelihood[6] and is treated as identity.

The prior in Eq. (4.17) allows the expression of a λ as $\mu_\lambda + \lambda_v = \lambda$ with a finite variation λ_v from the mean μ_λ. The expectation of both sides of the equation yields $E[\mu_\lambda] + E[\lambda_v] = E[\lambda] \Leftrightarrow \mu_\lambda + 0 = \mu_\lambda$. Since only $\{\lambda_s\}$ is considered in the context of the surface-related likelihood, the mean $E[\lambda_s] = \mu_\lambda + \Delta\mu_\lambda$ is on the surface. Hence, if $\mu_\lambda \notin \{\lambda_s\}$, the expectation value of λ_s would be biased by $\Delta\mu_\lambda$. Additionally, the covariance matrix $\Sigma_\lambda = E[(\lambda_s - \mu_\lambda)(\lambda_s - \mu_\lambda)^T]$ is allowed to spread λ_s only across A_s in order to be unbiased[7].

In summary, the prior parametrisation is required to be the same as the measurements object. Hence, the corresponding mean $H_s \mu_{\lambda,O} = \mu_{\lambda,A_s} \in A_s$ and covariance $H_s \Sigma_{\lambda,O} H_s^T = \Sigma_{\lambda,A_s}$ can be expressed as normal distribution analogously to Eq. (4.17) with $\lambda_{A_s} \in A_s$. These considerations can be formulated for the s-dimensional measurement in terms of the likelihoods as

$$P(m|\lambda) = \begin{cases} \frac{1}{\int_A dv} = \frac{1}{V_A} & H_O\lambda \notin \{\lambda_s\} \vee H_O E[P(\lambda_O)] \notin \{\lambda_s\} \\ \mathcal{G}(m|H_A\lambda, \Sigma_{\det}) & \text{else} \end{cases} \tag{4.21}$$

with the prior from Eq. (4.17) and the identity from Eq. (4.5). This expression can also be formulated as a single function

$$\begin{aligned} P(m|\lambda) = &\frac{1}{V_A} + \int_{A_s} \delta(H_O \widetilde{H_s} v - H_0 \lambda) \left[\mathcal{G}(m|H_A\lambda, \Sigma_{\det}) - \frac{1}{V_A} \right] dv \\ &\cdot \int_{A_s} \delta\left(\int_O \lambda_O P(\lambda_O) d\lambda_O - H_O \widetilde{H_s} v \right) dv \end{aligned} \tag{4.22}$$

with the Dirac-delta δ and the prior $P(\lambda_O)$ restricted to the subspace $O \subseteq \Lambda^n$. This summary shows that the constraint provided by the surface is thereby the only limitation that steers whether the measurement leads to a parameter update or not. Hence, parameters from A_e can be neglected in the steering but are treated in the posterior evaluation.

---

[6]In this case the data is normal distributed exclusively in A_s but it would be required that the mean of the distribution is not in A_s.

[7]Bayes' theorem can be interpreted as an iterative learning about the parameter distributions in the posterior pdf. Under the assumption of a correct model and an infinite amount of measurements, the only non-zero value should then become the value of the underlying truth. This limit is described by the term *unbiased*.

Evaluation of the Posterior Likelihood

In order to evaluate the posterior likelihood, Eq. (4.22) indicates two scenarios as given in Eq. (4.5) and (4.14). While the former is a trivial solution $P(\lambda|m) = P(\lambda)$, it is assumed in the following that the integrals in Eq. (4.22) evaluate to non-zero. Therewith, the posterior likelihood with Eq. (4.17) is given by

$$
\begin{aligned}
P(\lambda|m) &= \mathcal{G}(m|H_A\lambda, \Sigma_{\det})\mathcal{G}(\lambda|\mu_\lambda, \Sigma_\lambda) \\
&\propto \exp\left(-\frac{1}{2}(m - H_A\lambda)^T \Sigma_{\det}^{-1}(m - H_A\lambda)\right) \cdot \exp\left(-\frac{1}{2}(\lambda - \mu_\lambda)^T \Sigma_\lambda^{-1}(\lambda - \mu_\lambda)\right)
\end{aligned}
\tag{4.23}
$$

under the assumption that $d|\Sigma_{\det}|/d\lambda = 0$ and $d|\Sigma_\lambda|/d\lambda = 0$. As the likelihood is measured in $s + e \leq n$ dimensions, the parameters in the remaining $n - s - e$ dimensions will be treated like an identity likelihood. In order to consider this behaviour, the prior can be modified by introducing the disjoint projection matrix $\overline{H_A} \in \mathbb{R}^{n \times (n-s-e)} : \Lambda^n \to \Lambda^n \backslash A$. Therewith the parameters can be written as

$$
\lambda = H_A^T H_A \lambda + \overline{H_A}^T \overline{H_A} \lambda.
\tag{4.24}
$$

The application $H^T H$ projects the components from the subspace into Λ^n. The same accounts for the μ_λ and Σ_λ.

As mentioned in Sec. 4.2.2, the utilisation of the conjugate prior allows the prediction of the function of the posterior. In this case it is given by a multivariate normal distribution. Hence, the posterior pdf is known if its mean μ_λ' and covariance matrix Σ_λ' are known. Hence, the mean of Eq. (4.23) expressed with Eq. (4.24) becomes

$$
\begin{aligned}
\mu_\lambda' &= E[\lambda] = \int_{\Lambda^n} \lambda P(\lambda|m)d\lambda \\
&\propto \int_{\Lambda^n} \lambda \exp\left(-\frac{1}{2}(m - H_A\lambda)^T \Sigma_{\det}^{-1}(m - H_A\lambda)\right) \\
&\quad \cdot \exp\left(-\frac{1}{2}(\lambda - \mu_\lambda)^T \Sigma_\lambda^{-1}(\lambda - \mu_\lambda)\right) d\lambda \\
&= \int_{\Lambda^n} (H_A^T H_A \lambda + \overline{H_A}^T \overline{H_A} \lambda)\exp\left(-\frac{1}{2}(m - H_A\lambda)^T \Sigma_{\det}^{-1}(m - H_A\lambda)\right) \\
&\quad \cdot \exp\left(-\frac{1}{2}\left[(H_A + \overline{H_A})(\lambda - \mu_\lambda)\right]^T (H_A + \overline{H_A})\Sigma_\lambda^{-1}(H_A + \overline{H_A})^T \left[(H_A + \overline{H_A})(\lambda - \mu_\lambda)\right]\right) d\lambda.
\end{aligned}
\tag{4.25}
$$

Since the spaces $A = \Lambda^n \cap A$ and $\Lambda^n \backslash A$ are disjoint, there is no mixing between elements of the spaces. Thus, Eq. (4.25) can be rephrased:

$$
\int_{\Lambda^n} (H_A^T H_A \lambda + \overline{H_A}^T \overline{H_A} \lambda) \exp\left(-\frac{1}{2}(m - H_A\lambda)^T \Sigma_{\text{det}}^{-1}(m - H_A\lambda)\right)
$$

$$
\cdot \exp\left(-\frac{1}{2}(\lambda - \mu_\lambda)^T H_A^T H_A \Sigma_\lambda^{-1} H_A^T H_A(\lambda - \mu_\lambda)\right)
$$

$$
\cdot \exp\left(-\frac{1}{2}(\lambda - \mu_\lambda)^T \overline{H_A}^T \overline{H_A} \Sigma_\lambda^{-1} \overline{H_A}^T \overline{H_A}(\lambda - \mu_\lambda)\right) d\lambda
$$

$$
= \int_A H_A^T H_A \lambda \exp\left(-\frac{1}{2}(m - H_A\lambda)^T \Sigma_{\text{det}}^{-1}(m - H_A\lambda)\right)
$$

$$
\cdot \exp\left(-\frac{1}{2}(\lambda - \mu_\lambda)^T H_A^T H_A \Sigma_\lambda^{-1} H_A^T H_A(\lambda - \mu_\lambda)\right) d(H_A\lambda)
$$

$$
+ \int_{\Lambda^n \backslash A} \overline{H_A}^T \overline{H_A} \lambda \exp\left(-\frac{1}{2}(\lambda - \mu_\lambda)^T \overline{H_A}^T \overline{H_A} \Sigma_\lambda^{-1} \overline{H_A}^T \overline{H_A}(\lambda - \mu_\lambda)\right) d(\overline{H_A}\lambda)
$$

$$
\tag{4.26}
$$

$$
= H_A^T E[H_A \lambda] + \overline{H_A}^T E[\overline{H_A}\lambda]
$$

For Eq. (4.26) the properties of the linear operation of the expectation value were exploited and the by-definition disjoint spaces. The first addend leads to updated parameters due to the measurement, the second to the unaffected parameters. Thus, it is obvious that $E[\overline{H_A}\lambda] = \overline{H_A}\mu_\lambda$. For the first one a product of two multivariate normal distributions can be identified, which leads to [99]

$$
H_A \Sigma'_\lambda H_A^T = \left((H_A \Sigma_\lambda^{-1} H_A^T) + \Sigma_{\text{det}}^{-1}\right)^{-1} \tag{4.27}
$$

$$
H_A \mu'_\lambda = \Sigma'_\lambda \left((H_A \Sigma_\lambda^{-1} H_A^T) H_A \mu_\lambda + \Sigma_{\text{det}}^{-1} m\right). \tag{4.28}
$$

In summary, the posterior mean and covariance matrix are then given by

$$
\begin{aligned}
\mu'_\lambda &= E[\lambda] = H_A^T E[H_A\lambda] + \overline{H_A}^T E[\overline{H_A}\lambda] \\
&= H_A^T \Sigma'_\lambda \left((H_A \Sigma_\lambda^{-1} H_A^T) H_A \mu_\lambda + \Sigma_{\text{det}}^{-1} m\right) + \overline{H_A}^T \overline{H_A} \mu_\lambda \\
\Sigma'_\lambda &= E[(\lambda - \mu'_\lambda)(\lambda - \mu'_\lambda)^T] \\
&= H_A^T E[H_A(\lambda - \mu'_\lambda)(\lambda - \mu'_\lambda)^T H_A^T] H_A + \overline{H_A}^T E[\overline{H_A}(\lambda - \mu'_\lambda)(\lambda - \mu'_\lambda)^T \overline{H_A}^T] \overline{H_A} \\
&= H_A^T \left((H_A \Sigma_\lambda^{-1} H_A^T) + \Sigma_{\text{det}}^{-1}\right)^{-1} H_A + \overline{H_A}^T \overline{H_A} \Sigma_\lambda \overline{H_A}^T \overline{H_A}.
\end{aligned} \tag{4.29}
$$
$$
\tag{4.30}
$$

The matrix H_A and $\overline{H_A}$ were not considered any further yet. If it can be assumed that a base $B_1 = \{\hat{e}_i\}$ exists that describes $\lambda = \sum_i \lambda_i \hat{e}_i$ and a base $B_2 = \{\hat{e}_j\}$ that describes $m = \sum_j m_j \hat{e}_j$ with $\forall \hat{e}_j \in B_2 : \exists \hat{e}_i \in B_1$ with $\hat{e}_j = \hat{e}_i$ then both projection matrices

become sparse matrices with

$$(H_A)_{i,j} = \begin{cases} 1, \hat{e}_i \in B_2, \hat{e}_j \in B_1 : \hat{e}_i = \hat{e}_j \\ 0, \text{else} \end{cases} \tag{4.31}$$

$$1 = \overline{H_A}^T \overline{H_A} + H_A^T H_A.$$

Thus the addends of Eqs. (4.29) and (4.30) do not interfere with each other.

In the non-interfering case of H_A and $\overline{H_A}$, it becomes obvious that the term $\overline{H_A}^T \overline{H_A} \mu_\lambda$ from Eq. (4.29) and $\overline{H_A}^T \overline{H_A} \Sigma_\lambda \overline{H_A}^T \overline{H_A}$ from Eq. (4.30) describe a status quo, i.e. the corresponding components of λ remain unchanged. The other contributions to the expectation value and the covariance matrix of the posterior are given by Eqs. (4.28) and (4.27). This allows to re-write μ'_λ and Σ'_λ as

$$\begin{aligned} \Sigma'_\lambda &= \left(\Sigma_\lambda^{-1} + H_A^T \Sigma_{\text{det}}^{-1} H_A \right)^{-1} \\ \mu'_\lambda &= \Sigma'_\lambda \left(\Sigma_\lambda^{-1} \mu_\lambda + (H_A^T \Sigma_{\text{det}}^{-1} H_A) H_A^T m \right) \end{aligned} \tag{4.32}$$

which encapsulates both contributions.

Since the calculation of μ'_λ and Σ'_λ rely on inverted matrices which are computationally expensive, an alternative but equivalent formulation can be used:

$$\Sigma'_\lambda \left(\Sigma_\lambda^{-1} \mu_\lambda + (H_A^T \Sigma_{\text{det}}^{-1} H_A) H_A^T m \right) = \mu_\lambda + \Sigma_\lambda H_A^T \left(H_A \Sigma_\lambda H_A^T + \Sigma_{\text{det}} \right)^{-1} (m - H_A \mu_\lambda) \tag{4.33}$$

A similar transformation of the expression of Σ'_λ is possible:

$$(\Sigma_\lambda^{-1} + H_A^T \Sigma_{\text{det}}^{-1} H_A)^{-1} = (1 - \Sigma_\lambda H_A^T (H_A \Sigma_\lambda H_A^T + \Sigma_{\text{det}})^{-1} H_A) \Sigma_\lambda \tag{4.34}$$

The equality of both statements is shown in Sec. A.

Beside the fact that the right side of Eq. (A.1) and the right side of Eq. (A.2) require less inversions, another detail can be found: Substituting $K = \Sigma_\lambda H_A^T (H_A \Sigma_\lambda H_A^T + \Sigma_{\text{det}})^{-1}$ gives

$$\mu'_\lambda = \mu_\lambda + K(m - H_A \mu_\lambda) \tag{4.35}$$

$$\Sigma'_\lambda = (1 - KH_A)\Sigma_\lambda \tag{4.36}$$

which is commonly known as the Kalman filter formalism[8].

---

[8]The original derivation of filtering algorithm developed by R.E. Kalman [100] was performed by minimising a quadratic loss function. As an opposite to that, in this thesis, the derivation is based on the bayesian, distribution-oriented approach. The original derivation from by R.E. Kalman assumed the measured vectors of states were sums of the true states and randomly distributed noise terms. The derivation in this thesis makes no assumptions on the relation between the measurements and the true states, considering the most general case via the usage of pdfs.

4.3 Track and Event Reconstruction

In Sec. 4.2 the normal distributed approximation of measurements and the application of a conjugate prior for a single measurement was discussed. This approximation with the same prior will be extended in this section to multiple measurements in three stages with increasing complexity. Starting with a given order of measurements from a single particle, then an arbitrary order is considered and finally an arbitrary ordered set of measurements produced by multiple particles.

4.3.1 Track Reconstruction

In this section a set of k independent measurements m_i with $i = 1, ..., k$ is considered. As described in Sec. 4.2.3, each measurement is assigned to a surface $A_i \subseteq \mathbb{R}^{s_i + e_i}$. In the normal distributed approximation scenario, the likelihood of each measurement $P(m_i | \lambda, \Sigma_{\text{det}}^i)$ is then given according to Eq. (4.22). As the covariance matrix Σ_{det} can vary for each surface, it also depends on it. The simplest case is then $A_i = A_j \forall i, j = 1, ..., k$, i.e. all surfaces are identical, with the posterior likelihood

$$P(\lambda | m_1, ..., m_k) \propto \prod_{i=1}^{k} P(m_i | \lambda, \Sigma_{\text{det}}) P(\lambda) \tag{4.37}$$

as the direct formulation of the iterative learning of Bayes theorem from Sec. 4.1. Due to combination of each measurement on the surface to a single measurement, the problem can be reduced to Eq. (4.23) and is therewith solved by Eqs. (4.35) and (4.36).

In the following it is assumed that $i \neq j \Rightarrow A_i \neq A_j \forall i, j$, i.e. different measurements are present and each measurement is associated to a different surface. From a given prior $P(\lambda)$ expressed in the context of an object O, Eq. (4.22) allows up to one parameter update. In order to consider multiple measurements, the likelihoods needs to be extended by a parameter extrapolation. The necessary condition for the likelihood to become non-trivial is that μ_λ is given on the surface itself. From a given point, an extrapolation over a length $s \in \mathbb{R}$ is required. Along the extrapolation physical effects upon the particle trajectory need to be considered in order to preserve the unbiased requirement of the parameter update. The extrapolation will be denoted as $S(s|\lambda)$. As the parameter ordering indicates, this can be considered as likelihood-like. Compared to the likelihood described in Eq. (4.1), the extrapolation does not depend on a static, external input as for the measurement and the detector response but on the inclusion of effects on the prior parametrisation, steered by s. Furthermore, the extrapolation relies on the knowledge of the posterior in order to be evaluated. Hence, the general formulation for the extrapolation is given by

$$S(s|\lambda) = \frac{P(\lambda|s)}{P(\lambda)} \tag{4.38}$$

and thus modifies the prior. In this form, it is w.l.o.g assumed that $P(\lambda|0) = P(\lambda)$. Furthermore, the chain of two successive extrapolations can be considered

$$
\begin{aligned}
P(\lambda|s_1, s_2) &= S(s_2|\lambda, s_1)S(s_1|\lambda)P(\lambda) \\
&= \frac{P(\lambda|s_2, s_1)}{P(\lambda|s_1)} \frac{P(\lambda|s_1)}{P(\lambda)} P(\lambda) \\
&= \frac{P(\lambda|s_2, s_1)}{P(\lambda)} P(\lambda) \\
&= S(s_2, s_1|\lambda)P(\lambda) = S(s_2 + s_1|\lambda)P(\lambda)
\end{aligned}
\tag{4.39}
$$

which corresponds to the independence from Eq. (4.2). Also a unification of multiple extrapolations to a single is demanded, especially for $s_1 = -s_2$ one obtains the prior itself. The extrapolation is therefore invertible. A discussion about the extrapolation under a continuous parameter is given in Chapter 7.

In order to update the prior with the data from a measurement m on the surface $A \subseteq O$, the likelihood $P(m|\lambda, \Sigma_{\text{det}})$ from Eq. (4.22) gets extended by two extrapolations:

$$
\begin{aligned}
P(m|\lambda) =& \frac{1}{V_A} + \int_{-\infty}^{\infty} S(s'|\lambda, s) \int_{A_s} \delta(H_O \widetilde{H}_s v - H_O \lambda) \left[\mathcal{G}(m|H_A \lambda, \Sigma_{\text{det}}) - \frac{1}{V_A} \right] dv \\
& \cdot \int_{A_s} \delta \left(\int_O \lambda_O S(s|\lambda_O) P(\lambda_O) d\lambda_O - H_O \widetilde{H}_s v \right) dv S(s|\lambda) ds
\end{aligned}
\tag{4.40}
$$

While in theory s is unrestricted, the assumption that the particle is at least in a detector restricts the integral to finite limits. Furthermore, the second extrapolation $S(s'|\lambda, s)$ allows to describe the posterior pdf independent of any extrapolation, e.g. for a fixed starting surface $A_0 \subseteq O$ as constraint, the parametrisation would be at the same object afterwards with at most updated parameters. This could be the innermost sensitive layer for example, since the combined information at that point can be utilised to estimate the corresponding vertex. Due to the update of the parameters, it is not mandatory that $s' = -s$. In this case an additional evaluation of s' is necessary. For simplicity it is assumed in the following that the approximation $s' \simeq -s$ is sufficient. As the posterior is independent on the extrapolation of a previously considered likelihood, their combination using Eq. (4.40) can be written as given in Eq. (4.37).

Given that the measurements are ordered, i.e. for the required extrapolation lengths s_i and s_j for two measurements m_i and m_j in order to become a non-identity likelihood, $s_i \leq s_j$ for $\forall i, j = 1, ..., k : i \leq j$, then Eq. (4.37) applies them in the same ordering. It is further observable from Eq. (4.39) for subsequent non-trivial treated likelihoods, that the backwards extrapolation over $s_i \leq 0$ from A_i and the forward extrapolation over $s_{i+1} \geq 0$ to A_{i+1} leads to a net extrapolation distance of $s_{i+1} - s_i \geq 0$. Hence, the ordered formalism provides the minimal extrapolation distance in order to perform all parameter updates while ending at a given (constrained) object.

4.3.1.1 Discrete Extrapolation Effects

Within the formulation of the likelihood in Eq. (4.40), an extrapolation is performed based on the existence of a measurement. Beside the continuous effects like deflection

due to magnetic fields, discrete effects from e.g. detector material may affect the prior pdf under extrapolation. Such effects can be treated by describing discrete effects in Eq. (4.38) explicitly. Since a discrete manipulation of the prior is identical to Eq. (4.1) and moreover independent as denoted in Eq. (4.2), the natural formulation of discrete effects is given by formulating the contributions as a likelihood. In order to preserve the conjugate prior of the measurements, the individual effects require either a normal distributed approximation similar to Eq. (4.14) or to just modify the model parameters μ_λ and Σ_λ as in Eq. (4.38). In both cases, the contribution is, similar to the extrapolation, not a measurement and therefore expressed by evaluation of previous posterior pdfs. In contrast to the extrapolation, the effect does not depend on a scalar but is associated with an object $A^M \subseteq \mathbb{R}^{s+e}$. A^M can thereby be decomposed as in Eq. (4.19) and (4.20) for A_s^M and A_e^M. In order to preserve an analogy to a likelihood expression, discrete effects may trigger an extrapolation as in Eq. (4.40). On the other hand discrete effects may be treated like an additive extrapolation from Eq. (4.39). Hence, the second case can be expressed as

$$
\begin{aligned}
M_f(s_f|\lambda) = & \frac{1}{V_{A_s^M}} + \int_0^{s_f} \int_{A_s^M} \delta(H_O \widetilde{H_s^M} v - H_0\lambda) \left[\frac{P(\lambda|\widetilde{\mu_\lambda}, \widetilde{\Sigma_\lambda})}{P(\lambda|\mu_\lambda, \Sigma_\lambda)} - \frac{1}{V_{A^M}} \right] dv \\
& \cdot \int_{A_s^M} \delta \left(\int_O \lambda_O S(s|\lambda_O) P(\lambda_O) d\lambda_O - H_O \widetilde{H_s^M} v \right) dv S(s|\lambda) ds
\end{aligned}
\tag{4.41}
$$

with the modified mean $\widetilde{\mu_\lambda}$ and covariance matrix $\widetilde{\Sigma_\mu}$ due to the material interaction. Furthermore, the triggered extrapolation is not reverted in comparison to (4.40) since $M_f(s_f|\lambda)$ can be considered as the extrapolation itself. The subscript f denotes thereby a forward extrapolation and thus restricts $s_f \geq 0$. A corresponding reverse discrete effect $M_b(s_b|\lambda)$ is restricted to $s_b \leq 0$ with the property $M_b(s_b|\lambda)M_f(s_f|\lambda)P(\lambda) = P(\lambda)$, i.e. the pdf parameter manipulation is undone in the backward direction with an additional extrapolation over $s_b \leq 0$. Eq. (4.41) can be utilised in order to describe e.g. energy loss of charged particles in material. In Fig. 4.2 the per unit path length mean energy loss $\mu_\lambda - \widetilde{\mu_\lambda}$ is shown. Thereby the mean energy loss depends on the current mean energy. Therefore the knowledge about the posterior allows to express $M_f(s_f|\lambda)$.

Beside the preservation of the conjugate prior by utilising $P(\lambda|\widetilde{\mu_\lambda}, \widetilde{\Sigma_\lambda})/P(\lambda|\mu_\lambda, \Sigma_\lambda)$ from Eq. (4.41), for a normal distributed effect, a more explicit formulation can be found. Starting from the Eqs. (4.35) and (4.36), it is assumed that the posterior mean and covariance matrix can be expressed as $\mu_\lambda' = \mu_\lambda + \mu_q$ and $\Sigma_\lambda' = \Sigma_\lambda + \Sigma_q$ respectively. The parameters μ_q and Σ_q denote the manipulation of μ_λ and Σ_λ respectively due to interactions. Furthermore, both need to be known prior and may depend on μ_λ and Σ_λ as well. Hence, it is necessary to evaluate these parameters when the parameter modification occurs, while the measurements are independent of the prior parametrisation.
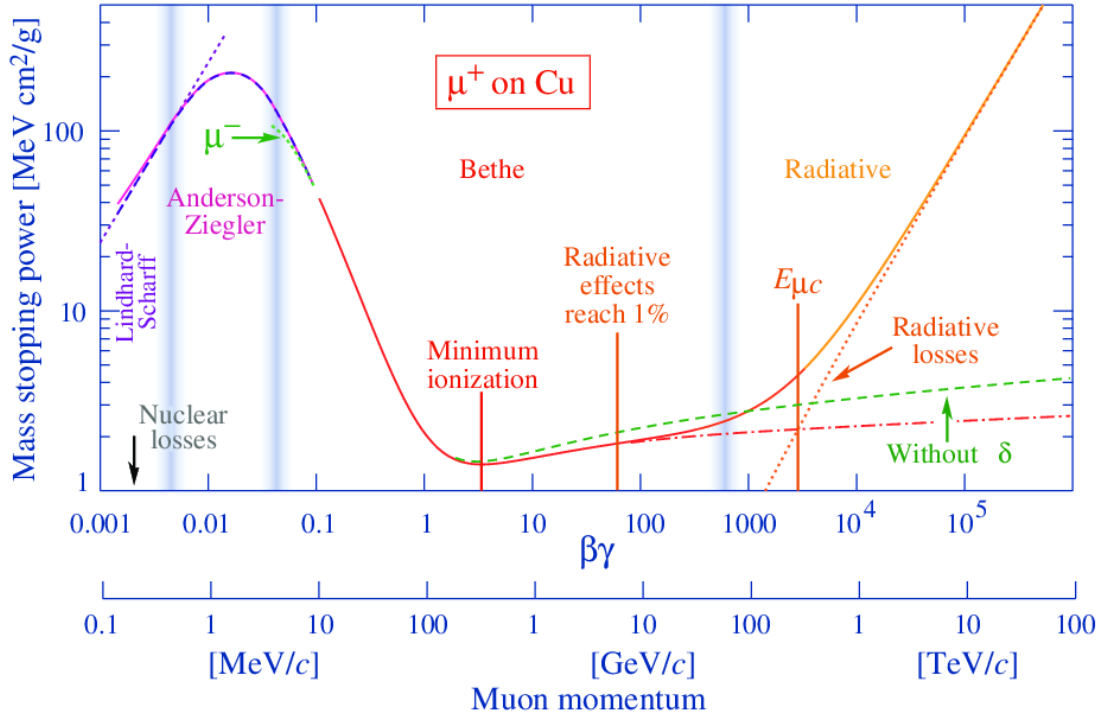
Figure 4.2: Dependency of the mean energy loss per path length of a μ^+ in copper on the Lorentz factor $\beta\gamma$ [17].

One obtains thereby for a given Σ_q

$$
\begin{aligned}
&\Sigma_\lambda + \Sigma_q = (1 - KH^M)\Sigma_\lambda \\
\Leftrightarrow\,&\Sigma_q = KH^M\Sigma_\lambda \\
\Leftrightarrow\,&H^M\Sigma_q H^{MT} = H^M\Sigma_\lambda H^{MT}(H^M\Sigma_\lambda H^{MT} + \Sigma_m)^{-1}H^M\Sigma_\lambda H^{MT} \\
\Leftrightarrow\,&H^M\Sigma_q H^{MT}(H^M\Sigma_\lambda H^{MT})^{-1}(H^M\Sigma_\lambda H^{MT} + \Sigma_m) = H^M\Sigma_\lambda H^{MT} \\
\Leftrightarrow\,&H^M\Sigma_q H^{MT}(H^M\Sigma_\lambda H^{MT})^{-1}\Sigma_m = H^M\Sigma_\lambda H^{MT} - H^M\Sigma_q H^{MT} \\
\Leftrightarrow\,&\Sigma_m = H^M\Sigma_\lambda H^{MT}\left[(H^M\Sigma_q H^{MT})^{-1}H^M\Sigma_\lambda H^{MT} - 1\right]
\end{aligned}
\tag{4.42}
$$

that there exists a covariance matrix Σ_m which can be understood as the covariance matrix of a measurement but with the same effect as the addition of Σ_q. The utilised gain matrix K is used as defined for a regular measurement with Σ_m. The matrix Σ_m exists under the assumption that $\mathrm{rg}(H^M\Sigma_\lambda H^{MT}) = \mathrm{rg}(H^M\Sigma_q H^{MT}) = s + e$. While a measurement is associated with the learning in the context of the Bayes' theorem this matrix represents a *forgetting* due to material interaction.

For the mean one obtains from a given μ_q

$$
\begin{aligned}
&\mu_\lambda + \mu_q = \mu_\lambda + K(m - H^M \mu_\lambda) \\
\Leftrightarrow &\mu_q = \Sigma_\lambda H^{MT}(H^M \Sigma_\lambda H^{MT})^{-1} H^M \Sigma_q H^{MT}(H^M \Sigma_\lambda H^{MT})^{-1}(m - H^M \mu_\lambda) \\
\Leftrightarrow &H^M \Sigma_\lambda H^{MT}(H^M \Sigma_q H^{MT})^{-1} H^M \mu_q + H^M \mu_\lambda = m
\end{aligned}
\tag{4.43}
$$

utilising the result from Eq. (4.42). Therewith, a discrete, linear manipulation of the prior parameterisation can be expressed as likelihood from Eq. (4.40) with Σ_m and m as given in Eq. (4.42) and (4.43).

As the discrete contributions can be modelled analogously to the likelihood of a measurement, the extrapolation $S(s|\lambda)$ in Eq. (4.40) can also be expressed in terms of those interactions. Given $n \in \mathbb{N}$ discrete interactions along the extrapolation for $0 \le s < \infty$ and an ordering of the individual lengths with $\sum_{j=1}^{i} s_j \le \sum_{j=1}^{i+1} s_j$ for $i = 1, ..., n-1$ for each interaction in order to provide a non-trivial solution, the following expression can be utilised:

$$
S_f\left(s = \sum_{i=1}^{n} s_i + \tilde{s}|\lambda\right) = S\left(\tilde{s} = s - \sum_{i=1}^{n} s_i|\lambda\right) \cdot \prod_{i=1}^{n} M_{f,i}(s_i|\lambda)
\tag{4.44}
$$

While s_i contributes with discrete lengths, the remainder is covered by a plain propagation. Since $\widetilde{\mu_\lambda} = \mu_\lambda$ and $\widetilde{\Sigma_\lambda} = \Sigma_\lambda$ are possible, the expression can be considered generic and provides the extrapolation including discrete effects up to the surface A. The corresponding backward extrapolation then becomes

$$
S_b\left(s' = \sum_{i=1}^{n} s_i + \tilde{s}|\lambda\right) = \prod_{i=1}^{n} M_{b,i}(s_i|\lambda) \cdot S\left(\tilde{s} = s' - \sum_{i=1}^{n} s_i|\lambda\right).
\tag{4.45}
$$

Due to the formulation of the extrapolation in terms of subsequent interactions, a natural loop through interactions originates.

4.3.1.2 Smoothing

The likelihood of measurements from Eq. (4.40) with Eq. (4.37) leads to a posterior pdf that encapsulates the information of all measurements produced by the particle represented at a (conditional) starting position. After the outermost measurement was utilised for updating the parameters the parameterisation at the surface A_k carries the information of all measurements. Therefore the best knowledge about the particle properties is given at that point so far. As the parametrisation at starting position is usually the point of interest for further processing, e.g. for vertexing, the knowledge of other measurements is required at that point instead. Hence, the information needs to be propagated to that point. Although this is carried out by the backward propagation, a better performance can be achieved. While the inversion property in Eq. (4.38) is demanded, due to subsequent parameter updates, the information from previously utilised measurements provide less impact on even closer ones to the starting point. Considering

the mean update (u) of the ith measurement m_i, a forward extrapolation to the $(i+1)$th measurement t_i^{i+1}, update there and extrapolate back

$$
\begin{aligned}
\mu_\lambda^i &= u(\mu_\lambda, m_i) \\
\mu_\lambda^{i+1} &= u(t_i^{i+1}(u(\mu_\lambda, m_i)), m_{i+1}) \\
\mu_\lambda^i &= t_{i+1}^i(u(t_i^{i+1}(u(\mu_\lambda, m_i)), m_{i+1})).
\end{aligned}
$$

Comparing this with the direct update order

$$
\mu_\lambda^i = u(t_{i+1}^i(u(\mu_\lambda, m_{i+1})), m_i)
$$

the information contained in the measurement m_i of the first case is "burried" deeper in the filter process. Therefore, the impact of m_i on m_{i-1} is therefore suppressed, similar to a larger distance between both. Thus, the extrapolation distance of each information should be kept to a minimum given the underlying extrapolation effects. Considering furthermore errors from numerical evaluations may enhance this argument.

Eq. (4.37) additionally implies a single long-distance backward extrapolation from the last measurement to the starting point. Since all measurements are already used for filtering the parametrisation, those can not be used anymore. Otherwise the double-counting would bias the parametrisation. This is the same issue for the seeding. A more precise and stable solution is obtained if all measurements are taken into account at each measurement or surface during the finalising extrapolation. The problem is a linear sequence of measurements, therefore the optimal utilisation of measurements while fulfilling both conditions is given by the combination of two independent extrapolations as shown in Fig. 4.3 (top). The combination of all information at each measurement is called *smoothing* and allows the optimal estimation at the starting position [102] as shown in Fig. 4.3 (bottom). As the last forward filtered point indicates, it is identical to the smoothed result. However, the consequent smoothing leads to an improvement at $s = 0$. The suppressed error in the forward filtering is thereby driven by the measurements while the backward extrapolation error gets smaller as closer as the parametrisation is to $s = 0$ due to the backward extrapolation and therewith the removal of physical effects on the trajectory and due to repetitive combination with a forward filter.

The combination scheme leads to the conclusion that the final posterior pdf is obtained once the backward filter reached the starting position. However this leads to two problems: What is the prior of the backward filter and how to minimise the computational complexity for the forward filter evaluation. In order to resolve both issue, the simplest case considerable is a prior $P(\lambda)$ for a forward extrapolation located at A_0 and single measurement located at a surface A_1. The posterior pdf $P(\lambda|m)$ from Eq. (4.37) after applying Eq. (4.40) is independent of the prior due to the additional information obtained from the measurement and given at A_0. Hence, the combination of both pdfs would resolve in the best posterior pdf at A_0. This workflow is visualised in Fig. 4.4. Although a measurement can not be treated as a particle state λ and can therefore not be extrapolated, this utilisation of a second, independent prior allows a "transport" of the measurement to another object. Thus, the problem becomes identical to Eq. (4.1)
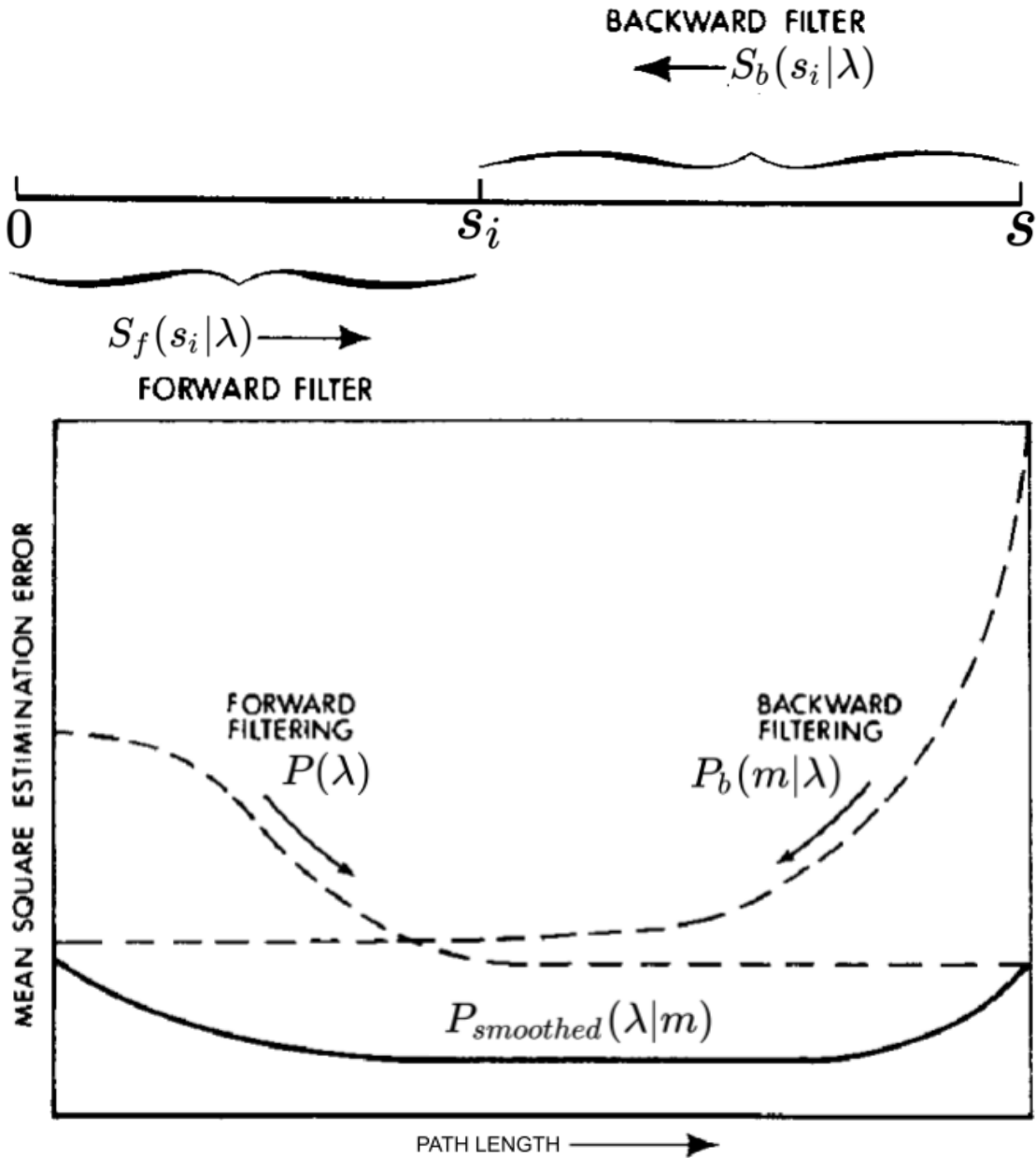
Figure 4.3: Top: Schematic illustration of two independent extrapolations starting at $s = 0$ in forward and from $s = \sum_{i=1}^{k} s_i$ in backward direction. The information is combined in a point in between. Bottom: Schematic illustration of the uncertainties of each extrapolation as a function of the distance to $s = 0$. Also the combination, called *smoothing* is shown. Both figures are taken from Reference [101] and modified to match the this chapters notation.

with a non-trivial measurement expressed at the same object as the prior

$$P_{\text{smoothed}}(\lambda|m) \propto [S(-s|\lambda)P(m|\lambda, \Sigma_{\text{det}})S(s|\lambda)P(\lambda)] \cdot P(\lambda) = P_b(m|\lambda)P(\lambda). \quad (4.46)$$
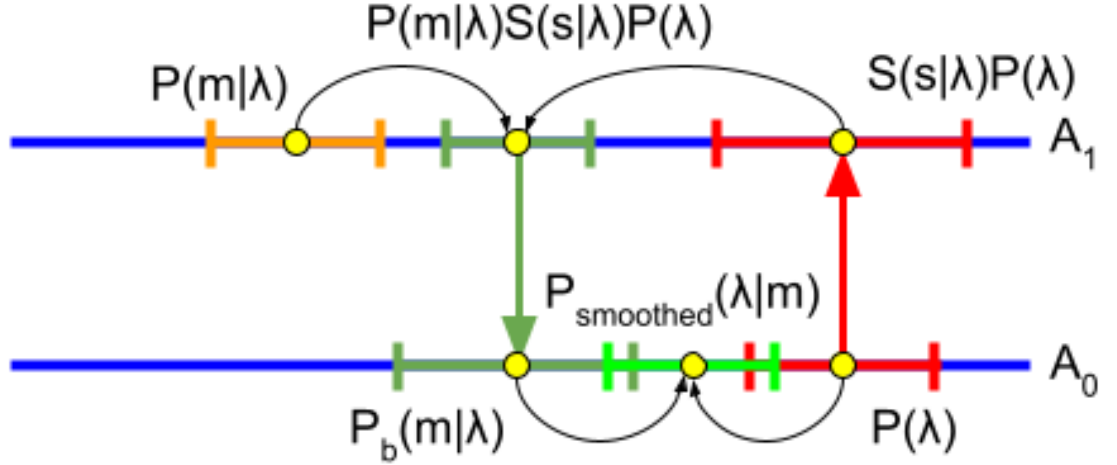
Figure 4.4: Filtering and smoothing for a single measurement m with two surfaces A_0 and A_1 (blue lines). The mean of the distributions is shown as yellow dots, the width of the distributions is indicated in different colours around the points. The initial parametrisation (red) is extrapolated from A_0 to A_1, filtered using the data (orange). The resulting distribution (green) is extrapolated backwards to A_0 and combined with the initial parameters (lime).

Consequently, the parameter update is again following the Kalman filter formalism from Eq. (4.35) and (4.36). Compared to the regular filter, in this case an entire state given by the additional prior is available. Therefore the projections in the Kalman filter becomes an identity matrix and thus, the entire state is updated in the smoothing. So, the smoothing can be considered as a measurement of λ itself.

In order to generalise this procedure to n measurements m_i for $i = 1, ..., n$, a recursive formulation can be found:

$$
\begin{aligned}
P_{\text{smoothed}}(\lambda|m_1, ..., m_n) &\propto \left[S_b(s'|\lambda) P_b(m_2, ..., m_n|\lambda) \mathcal{G}(m_1, \lambda, \Sigma^1_{\text{det}}) S_f(s|\lambda) P(\lambda) \right] \cdot P(\lambda) \\
&= \left[S_b(s'|\lambda) P_{\text{smoothed}}(m_2, ..., m_n|\lambda) \right] \cdot P(\lambda) \\
&= P_b(m_1, ..., m_n|\lambda) P(\lambda).
\end{aligned}
\tag{4.47}
$$

with the smoothed result $P_b(m_1, ..., m_n|\lambda)$ according to Eq. (4.46) at the surface A_0. The term $P_{\text{smoothed}}(m_i, ..., m_n|\lambda)$ for $1 \leq i \leq n$ describes the posterior pdf obtained at A_{i-1} used as likelihood. In order to evaluate the posterior pdf $P_{\text{smoothed}}(\lambda|m_2, ..., m_n)$, a recursive calculation is required. The termination condition of this recursion is given at the outermost surface. Unrolling leads to a forward filtering up to the $(n-1)$th surface. Starting with Eq. (4.46) for obtaining the smoothed result at the $(n-1)$th surface, a backward loop from surface to surface occurs until A_0 is reached. Eq. (4.47) then delivers the final result. In summary, at least one entire forward and one entire backward extrapolation and filtering is required.

4.3.2 Combinatorial Kalman Filter

In Sec. 4.3.1 the posterior pdf evaluation is discussed under the assumption of a distance ordering. The presented concept will be extended in the following by allowing an arbitrary ordering, leading to a more general formulation. This affects the extrapolation and the filtering. Since the smoothing is an unrolling of a linear sequence of utilised measurements, the formalism remain unchanged. While the first part of this section still considers a single particle, in the second part the formulation is generalised to many particles.

4.3.2.1 Extrapolation

A general description of an extrapolation is given in Eq. (4.38) with the main property in Eq. (4.39). The considerations in Sec. 4.3.1.1 allow to formulate extrapolation in terms of an object loop in order to reach a destination.

In the following it is assumed that a starting surface A_0 and a single target surface A_1 with a measurement exists. Due to Eq. (4.40), the likelihood demands an extrapolation in forward and backward direction. Assuming $n \in \mathbb{N}$ discrete effects on the trajectory due to the detector associated to surface A_i^M with $i = 1, ..., n$. The entire extrapolation can be described following the concept of Eqs. (4.44) and (4.45). Unlike in this case, the order of the discrete interactions $M_{f,i}$ and $M_{b,i}$ are not given but must be derived based on the demanding measurement. Furthermore, the prior may restrict due to the mean the contribution of surfaces as shown in Eq. (4.41), only a subset will be considered. Therefore, the prior is the second selection criteria.

A path for the surface loop is necessary and the natural approach is thereby given by starting from the prior parametrisation rather than from the target surface. As the plain extrapolation $S(s|\lambda)$ in the absence of additional discrete effects is considered to be deterministic and therefore identical for each $M_{f,i}$ or $M_{b,i}$, the shortest distance needs to be selected. Using the interpretation from Eqs. (4.43) and (4.42), the requirement of the shortest information transport distance as considered in Sec. 4.3.1.2 becomes mandatory.

The function

$$\alpha_f(s_l|\lambda) = \int_0^{s_l} \sum_{i=1}^{n} M_{f,i}(s_f|\lambda) ds_f \tag{4.48}$$

has up to $k \leq n$ extrema over the domain of the function $s_l \in [0, \infty)$. These extrema, denoted as $\alpha_f(s_l^j|\lambda)$ form a finite set of parameters s_l^j. The minimum

$$s_l^{\min} = \min\left(\{s_l^1, ..., s_l^k\}\right) \tag{4.49}$$

provides the minimal extrapolation distance in order to reach a discrete interaction. Since the trajectory can be translated to a sequence of extrapolations in the surface loop, the extrapolation of Eq. (4.44) becomes

$$S_{f,\alpha}\left(s = \sum_{i=1}^{k} s_l^i + \tilde{s}|\lambda\right) = S\left(\tilde{s} = s - \sum_{i=1}^{k} s_l^i|\lambda\right) \cdot \prod_{i=1}^{k} \alpha_f(s_l^i = s_l^{\min,i}|\lambda) \tag{4.50}$$

in the unordered case. An analogous solution $S_{b,\alpha}$ can be found for Eq. (4.45).

4.3.2.2 Single Track Reconstruction

The utilisation of the generalised extrapolation from Eq. (4.50) for the likelihood (4.40) allows to apply the best extrapolation to the surface associated to a measurement. For $p \in \mathbb{N}$ measurements associated to surfaces $A_1, ..., A_p$ with $A_i \subseteq \mathbb{R}^{s_i+e_i}$, up to $q \leq p$ filter steps are required in order to fit the track parametrisation provided by the prior to the obtained measurements. In the simplification of a single particle which produced the measurements, it can be assumed that each measurement demands an extrapolation since it was produced by that particle.

The extrapolation due to the likelihood is thereby conceptually identical to the discrete interactions. Hence, a similar formalism can be utilised for the likelihood constrained to forward extrapolated

$$P(m_i, s_r|\lambda) = \frac{1}{V_{A_i}} + \int_0^{s_r} S_{b,\alpha}(s'|\lambda, s) \int_{A_{i,s}} \delta(H_O\widetilde{H_{i,s}}v - H_0\lambda) \left[\mathcal{G}(m_i|H_{A_i}\lambda, \Sigma_{\text{det}}^i) - \frac{1}{V_{A_i}} \right] dv$$

$$\cdot \int_{A_{i,s}} \delta \left(\int_O \lambda_O S(s|\lambda_O) P(\lambda_O) d\lambda_O - H_O\widetilde{H_{i,s}}v \right) dv S_{f,\alpha}(s|\lambda) ds \qquad (4.51)$$

with the extrema function β and minimum distance $s_r^{\min}$

$$\beta(s_r|\lambda) = \int_0^{s_r} \sum_{i=1}^{p} P(m_i, s_r|\lambda) ds_r \qquad (4.52)$$

$$s_r^{\min} = \min_{>0} \left(\{s_r^1, ..., s_r^q\} \right) \qquad (4.53)$$

based on Eqs. (4.48) and (4.49). For convenience reasons $s_r^{\min} = 0$ is excluded. This prevents multi-counting of measurements, when defining the track fitting as

$$P_{\text{smoothed}}(\lambda|m_1, ..., m_q) \propto \left[S_{b,\alpha}(s'|\lambda) P_b(m_1, ..., m_n|\lambda) \left(\prod_{i=1}^{p} P(m_i, 0|\lambda) \right) \right.$$

$$\left. \cdot S_{f,\alpha}(s_r^{\min}|\lambda) P(\lambda) \right] \cdot P(\lambda)$$

$$= \left[S_{b,\alpha}(s'|\lambda) P_{\text{smoothed}}(m_1, ..., m_q|\lambda) \right] \cdot P(\lambda)$$

$$= P_b(m_1, ..., m_q|\lambda) P(\lambda). \qquad (4.54)$$

as generalised workflow of Eq. (4.47). While p measurements are available, due to the parameter manipulations from Eqs. (4.35), (4.36), (4.43), (4.42) and (4.46), a surface may become unreachable and is therefore not part of the smoothed parametrisation.

4.3.2.3 Multi Track Reconstruction

The last stage of generalisation is to consider an entire event consisting of $n \in \mathbb{N}$ particles. From those particles $n' \leq n$ particles produce measurements in the detector that

allow the reconstruction of their tracks. Furthermore, the ith particle produces k_i measurements. The jth measurements m_j^i of the ith particle is thereby associated to the surfaces A_j^i. In difference to Sec. 4.3.2.2, the association of a particle to its produced measurements is not assumed. Hence, it is assumed that $A_j^i = A_{j'}^{i'}$ is even possible for $i \neq i' \vee j \neq j'$. It is therefore convenient to utilise the p surfaces that contain $q \geq 1$ measurements.

A further difference is the amount of particles considered. After forming the prior as given in Eq. (4.16), each particle r can be considered to be modelled in a multivariate normal distribution $P_r(\lambda)$. The full (unnormalised) prior then becomes

$$P(\lambda) = \mathcal{G}(\lambda | \mu_\lambda, \Sigma_\lambda) \propto \sum_{r=1}^{n} \mathcal{G}(\lambda | \mu_\lambda^r, \Sigma_\lambda^r) = \sum_{r=1}^{n} P_r(\lambda). \tag{4.55}$$

The rightmost expression is thereby given under the assumption that particles in the processing of trigger and seeding are distinguishable. Following the decomposition of the prior into a sum of priors allows to express Eq. (4.4) as

$$\mathcal{L}(\lambda | \{m_j^i\}) = P(\{m_j^i\} | \lambda) P(\lambda) = \sum_{r=1}^{n} P(\{m_j^i\} | \lambda) P_r(\lambda) = \sum_{r=1}^{n} \mathcal{L}_r(\lambda | \{m_j^i\}) \tag{4.56}$$

with the short notation $\{m_j^i\} = \{m_1^1, ..., m_{k_1}^1, ..., m_1^n, ..., m_{k_n}^n\}$. Thus, although multiple particles are considered, the prior separation allows for the reconstruction of single tracks.

Compared to Eq. (4.51), the likelihood in this scenario is for convenience grouped by surfaces and therefore indirectly to the associated measurements

$$\begin{aligned}
P(A_i, s_r | \lambda) =& \frac{1}{V_{A_i}} + \int_0^{s_r} S_{b,\alpha}(s' | \lambda, s) \int_{A_{i,s}} \delta(H_O \widetilde{H_{i,s}} v - H_0 \lambda) \\
&\cdot \left[\frac{1}{c} \sum_j \mathcal{G}(m_j^{A_i} | H_{A_i} \lambda, \Sigma_{\det}^i) - \frac{1}{V_{A_i}} \right] dv \\
&\cdot \int_{A_{i,s}} \delta \left(\int_O \lambda_O S(s | \lambda_O) P(\lambda_O) d\lambda_O - H_O \widetilde{H_{i,s}} v \right) dv S_{f,\alpha}(s | \lambda) ds \tag{4.57}
\end{aligned}$$

with the normalisation factor $c = \sum_j \int_{-\infty}^{\infty} \mathcal{G}(m_j^{A_i} | H_{A_i} \lambda, \Sigma_{\det}^i) dm_j^{A_i}$ and the measurements $m_j^{A_i}$ that are associated to the surface A_i. The covariance matrix $\Sigma_{\det}^i$ describes thereby a function of λ as the covariance matrix may depend upon the considered mean an hence may differ for the individual measurements $m_j^{A_i}$. The grouping of measurements associated to the same surfaces leads in this formalism consequently to a Kalman filter update of a single prior $P_r(\lambda)$ with multiple measurements. Although it can be assumed that a particle produced at most a single measurement, since the association of measurements to particles is not given, each measurement is a theoretical candidate[9]. Before this issue is discussed, the reconstruction of the entire tracks is considered.

---

[9]The validity of the CLT is assumed to be granted in the following.

Eq. (4.54) describes the track fit using Kalman filtering and smoothing. Equivalent to the likelihood in the general case, the surfaces containing measurements are favoured in the formalism rather than the measurements itself. Thus, the extrema function β from Eq. (4.52) becomes

$$\beta'(s_r|\lambda) = \int_0^{s_r} \sum_{i=1}^p P(A_i, s_r|\lambda) ds_r$$

and finally, the final track parameters for a single prior $P_r(\lambda)$ are given by

$$
\begin{aligned}
P_{\text{smoothed}}^r(\lambda|\{m_i^j\}) &\propto \left[S_{b,\alpha}(s'|\lambda) P_b(\{m_i^j\}|\lambda) \left(\prod_{i=1}^p P(A_i, 0|\lambda) \right) \right.\\
&\quad \left. \cdot\, S_{f,\alpha}(s_r^{\min}|\lambda) P_r(\lambda) \right] \cdot P_r(\lambda)\\
&= P_b(\{m_i^j\}|\lambda) P_r(\lambda).
\end{aligned}
$$

The combination from Eq. (4.56) then delivers the global posterior likelihood. Although this expression is very compact, it encapsulates many details and thus requires further discussion.

After a filter step utilising the expression $\frac{1}{c} \sum_j \mathcal{G}(m_j^{A_i}|H_{A_i}\lambda, \Sigma_{\det}^i)$ from Eq. (4.57), the prior becomes a sum of normal distributions. Therefore, the posterior pdf can be handled as a sum, equivalent to Eq. (4.55). Considering each addend independently is equivalent to a measurement-particle association performed at each surface. Therewith, each addend can be extrapolated independently afterwards. Repeating this procedure for multiple surfaces leads to an iterative branching of the prior. Furthermore this implies that multiple branches may be filtered using the same measurements. This leads to a combinatorial problem as the correct assignment for all surfaces are required. On a higher level, this needs to be fulfilled for all addends in Eq. (4.56). From a computational point of view, this problem needs to be handled using a suppression of the branch production at each surface. A per surface suppression, e.g. by a weighted distance between extrapolated mean and the measurement can be utilised in order to enhance the chance to pick the correct measurement. Given multiple candidates, the decision of the correct must be postponed. Given that a addend has picked the correct measurement for the filtering then subsequent surfaces are likely to provide further measurements that fulfil a suppression expression. A filter using the wrong measurement will lead to a deflection of the particle trajectory away from the underlying true trajectory. Hence, it becomes less likely to find subsequent measurements and finally the posterior pdf will disperse. This feature allows for a second suppression of branch production at a later stage. A third level is given by the combination of the posterior pdf of individual seeds. As multiple seeds could be produced by the same particle, the redundancy in the posterior pdfs can reduce the complexity. Additionally, if a measurement was produced by a single particle then it can be assigned to at most one addend in the posterior pdf.

This procedure of parameter estimation allows due to the step-wise update of the parameters an early rejection of measurement candidates. Accepted measurements on

the other hand enhance the rejection possibilities for further measurements. Therewith the total complexity of the event reconstruction can minimised. Beside this approach, other concepts exist, e.g. based on a global χ^2-minimisation. The expressions derived above will thereby remain valid but tend to consider the entire event[10] simultaneously rather than utilising a sequence of measurements.

---

[10]For a single particle, the measurements reachable by extrapolation are sufficient. By considering the entire event, all seeds can be treated simultaneously.

5 ACTS - A Common Tracking Software

To obtain a meaningful physical information from a detector in particle collisions the data have to be processed. The processing involves the reconstruction of the particles and their tracks, produced within the event. Since electronic detector read-outs are used, the data can be provided digitally and can be easily processed with a dedicated software.

Throughout the years different particle detectors were designed and built in order to answer different questions. Although the underlying problem of reconstruction remains the same, the software based track reconstruction had to be performed for these detectors. As the hardware architectures and programming languages evolved constantly during this period, the best fitting software for a detector was in a permanent change. The limitation of computing resources demanded optimisations for a particular detector layout. As a result of this progress, similar or even the same problems were solved multiple times by different collaborations. This was even enhanced due to the fact that track reconstruction is rather considered as a black box, necessary to answer the physical questions rather than a field in particle physics. Hence, it is a branch of science with a small community.

Out of the given limitations in person power, the repetitive (similar) implementation of the same problem solutions and the future challenges in particle physics (e.g. see Sec. 3.3.4), the project A Common Tracking Software (ACTS) [103, 104] was born. The general goal is to build an open source software framework that is capable of operating independent of the detector layout by finding a description that is valid in general. As multi-threaded executions of software are the standard modus operandi, the software is designed as explicit thread-local data handling (currently[1]) using the C++17 standard [105].

The project is planned to be a long term maintainable and portable framework. Hence, the set of dependencies is kept at a minimum. The baseline of the project is provided by the ATLAS common tracking. Since the required components necessary for a tracking software and their interplay are known, the design of a detector independent framework gets simpler. Therewith, an entirely modular design was constructed with a computation workflow using template classes which are resolved at compile time. As a specific collaboration may rely on certain optimisations and specifications that can not be implemented in general, the design allows replacements and extensions wherever necessary.

Within this chapter several key components of ACTS as a specific solution to the track reconstruction problem are presented. The description is restricted to parts that are discussed in the context of this thesis. In the first part of this chapter, the detector geometry and the material are described. Afterwards, the parametrisation of the

---

[1]This standard is used at the time of writing this thesis and may change in the future.

trajectory are mentioned alongside the parametrisation of measurements and the storage concept. As part of this thesis, various contributions were added to the first two parts. In the last part of this chapter the pre- and post-processing of the reconstructed tracks, the seeding and vertexing procedures are briefly described. Thereby, the data pre-processing for the seeding, the space point formation was implemented into ACTS as part of this thesis.

5.1 Detector Description

In Chapter 4 it was implied that the extrapolation describes the trajectory of a particle with a given parametrisation by modifying the parameters under influence of the external environment. Furthermore, the extrapolation of the parametrisation occurs between detector components. Hence, a digital representation of the detector and its environmental conditions is necessary. Within this section the detector geometry, the magnetic field and material description in ACTS is presented.

5.1.1 Detector Geometry

As shown in Sec. 3.2 and 3.3 a particle detector contains a large variety of different components. Besides the sensitive components like pixel modules, the detector requires staves, cables, pipes etc. for the arrangement, powering and cooling of the components. Hence, a detailed description of the detector is rather complex. In the context of Sec. 3.3.4, it is obvious that reasonable simplifications are necessary in order to provide a sufficient large throughput.

A common structure as simplification and also the structure within ACTS is based on the geometry concepts surface, layer and volume. Those concepts are arranged hierarchically. The concept is also intended to simplify the sorting problem of detector components from Sec. 4.3. This will be further discussed in Sec. 7.7.

As these three geometrical concepts are entangled, a first overview of all components is shown in Fig. 5.1. In the following the surface, layer and volume are presented in more detail.

Surfaces

The core component of the detector geometry is the concept of a surface. A surface is in general a two-dimensional area of various shapes. As a large variety of surfaces is possible, the description in the following will be centred around the most common and simplest surfaces as shown in Fig. 5.2.

The defining parameters describing their dimensions are treated independently of the placement of the surface in space. For the placement an additional transformation is required for translation and rotation of the object by defining an affine transformation.

Furthermore, a surface can be declared as active or passive surface. The former denotes a surface that represents a detector module and hence is capable of producing a measurement. For e.g. a pixel module, this would be represented as the green plane
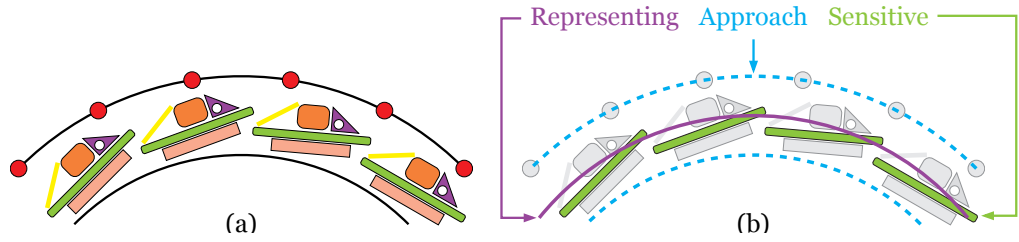
Figure 5.1: Illustration of a layer geometry in a common tracking detector. The shown part represents a cut-out segment of e.g. a pixel detector. (a) shows the schematically the composition of the different elements in the detector, involving both sensitive and passive ones. (b) shows the simplified version, where all passive elements are discarded (grayed out). The detector components is represented by a set of objects from the geometry concepts with different specifications (see text). The figure is based on Reference [103].
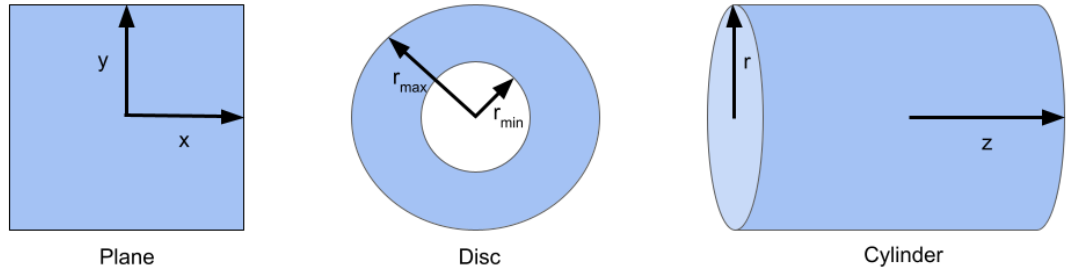

Figure 5.2: Overview of the most common surface shapes and the defining parameters.

surface in Fig. 5.1. A passive surface is e.g. given by a cylinder surface that represents the beam pipe. These kind of surfaces measure nothing but either disturb the trajectory (see Sec. 5.1.3) or represent a logical component (e.g. for layer and volumes). Finally, a disc surface can be utilised to describe end-caps as in Secs. 3.2.2.1, 3.2.2.2, 3.2.4.2, 3.3.1 or 3.3.2.

Layers

While the general formulation of the track reconsutruction in Sec. 4.3 required an ordering on a surface to surface level, the complexity can be reduced by adding higher level sorting concepts. The first concept is the layer. By considering the arrangement of the detector components e.g. in Figs. 3.15 and 3.22, it is a natural approach to group the surfaces in terms of r- and z-direction. Consequently, a range for those parameters has to be defined.

A layer in ACTS can be considered as three dimensional body. It follows the shape definitions from the surfaces but has an additional thickness parameter. This leads to the construction shown in Fig. 5.1 (b). The representing surface at the centre can be understood as a cylindrical surface. The thickness then defines the approach surfaces.

The approach surfaces define the boundaries of the layer. As the name already suggests, the layer itself is built by a set of surfaces.

Inside the layer surfaces may be stored. If the layer contains sensitive surfaces, the layer is labelled as sensitive layer, if passive surfaces are stored as passive layer and without any surfaces as navigation-layer[2]. The storage itself is organised in an array. A sorting of the array allows to estimate possible subsequent surfaces that the particle trajectory may intersect. Hence, for a given particle position, surfaces on the opposite side of the detector are not taken into account. By requiring that the particle trajectory intersects the approach surface, the surface content is considered only after the particle entered the volume defined by the layer and ignored as soon as the particle leaves it. The representing surface on the other hand allows a fast navigation to find possible layers along the trajectory. Surfaces contained in a layer are only considered when the trajectory intersects the layer. This simplifies the surface finding complexity drastically but requires a search for suitable layers.

Volumes

The volumes represent the highest level in the geometry hierarchy. The definition of the volume shape and dimensions is equivalent to the layer. The main idea behind this geometry object is to further reduce the complexity. Similar to the idea of grouping pixel or SCT modules within a certain range into a layer, the entire pixel detector or the SCT can be grouped into a volume. Hence, a volume is meant to contain a set of layers. In comparison to the surface array for the layers, the layers contained in a volume have a non-zero thickness. Thus, it is possible to fill the entire volume with different types of layers. While the sensitive and passive layers are provided by the detector geometry, the space in between can be filled up with navigation-layers. Consequently, the volume manages an ordered navigation from layer to layer. Hence, the naming of the navigation-layer is given by the concept to navigate from one layer to another through this empty layer.

The composition of a volume is slightly different from a layer. Compared to the latter, a volume does not contain a representative surface. Although it can also be considered as set of volumes, the approach surfaces of the layer are called boundary surfaces for the volume. While the approach surface indicates whether the contained surfaces should be resolved or not, the order is pre-defined by the sorting of the layers inside the volume. For the volume as the top level geometry concept, this requires a different logic. This logic is encapsulated in the boundary surface itself. In addition to the general information about the surface (shape, dimension, position, orientation), these surfaces store the next volume. Hence, whenever the trajectory intersects a boundary surface, the next volume can be resolved and thus all subordinate objects in the geometry hierarchy.

Following the boundary surface logic, the possibility to store volumes inside the volume was added. As this just provides boundary surface in addition inside the volume, a cut-out volume can be constructed. The additional surfaces are then treated the same way

---

[2]The naming of this type of layer will be described together with the volume concept.

as the original boundaries of the volume. By expanding the concept even further and allowing to store surfaces in a volume and sorting them in an array, the similarity to the layer gets larger. Finally, since the layers are arranged such that the volume is filled, the same approach is possible using volumes. Thereby the top level navigation can be replaced by the boundary surface portals. Hence, the layer concept is about to become deprecated. Since at the time of writing of this thesis this concept is still in use, it was presented for completeness.

The last property of a volume noteworthy is the possibility to attach material. This feature allows to describe components such as calorimeters. The material will be introduced in Sec. 5.1.3 and further discussed in Chapter 7.

Detector composition

In order to construct a detector, the geometry hierarchy is utilised. Starting from *world volume*, a volume is constructed such that the entire detector is inside the volume. Inside this volume, the different volumes of the detector components and the corresponding contents are produced. Finally, the world volume has the possibility to find a certain geometry object from a given position due to a hierarchical search. This allows e.g. an initialisation of the start volume, layer and surface for an extrapolation. Each component is thereby associated with a unique geometry identification (geoID). Hence, the next objects can be resolved automatically. Once the geometry construction is finished, the detector becomes immutable.

As the alignment of the detector components may change over time, the positioning and orientation of the components need to be adjusted accordingly. While the nominal detector is immutable, a special interface allows to handle the alignment with respect to the nominal transformation. The so-called *geometry context* is an object that is moved through the hierarchy and accessed whenever accesses to the position and orientation of an object[3] is requested. The nominal detector geometry is shared among multiple threads. As the context itself may change between events, it has to be stored thread-locally.

A detector consists of many different objects and relies consequently on an appropriate way to write, store and read the geometry data as well as the relation between the constituents. For ACTS different tools such as DD4hep [106] or TGeo [107] are supported on top a ACTS-standalone implementation. Thus, as the chosen modelling tool is experiment specific, the access of the ACTS framework gets simplified.

5.1.2 Magnetic Fields

A detector utilises a magnetic field to provide momentum and charge information about the particle from the curvature of the trajectory. Although, this is a property provided by the detector, the field is for the software application decoupled from the underlying

---

[3]The objects are restricted to the representation of detector components, since logical structures can be defined such that the detector components have to remain inside for all reasonable alignment conditions.

detector geometry and is treated independently from the detector. This design allows to define an arbitrary field setup.

Within ACTS two different major types of magnetic field models are implemented: Constant and interpolated. The former represents a field with the property $B(r) = $ const, i.e. it is independent of the position r. Although this is a strong simplification of the true description with respect to Figs. 3.14 and 3.19, this configuration offers an opportunity for debugging. Furthermore, the absence of a magnetic field, $B(r) = 0$ T can be easily described by this model.

The other magnetic field type represents a more realistic description. This representation is based on a three dimensional grid as shown in Fig. 5.3. For each grid point,
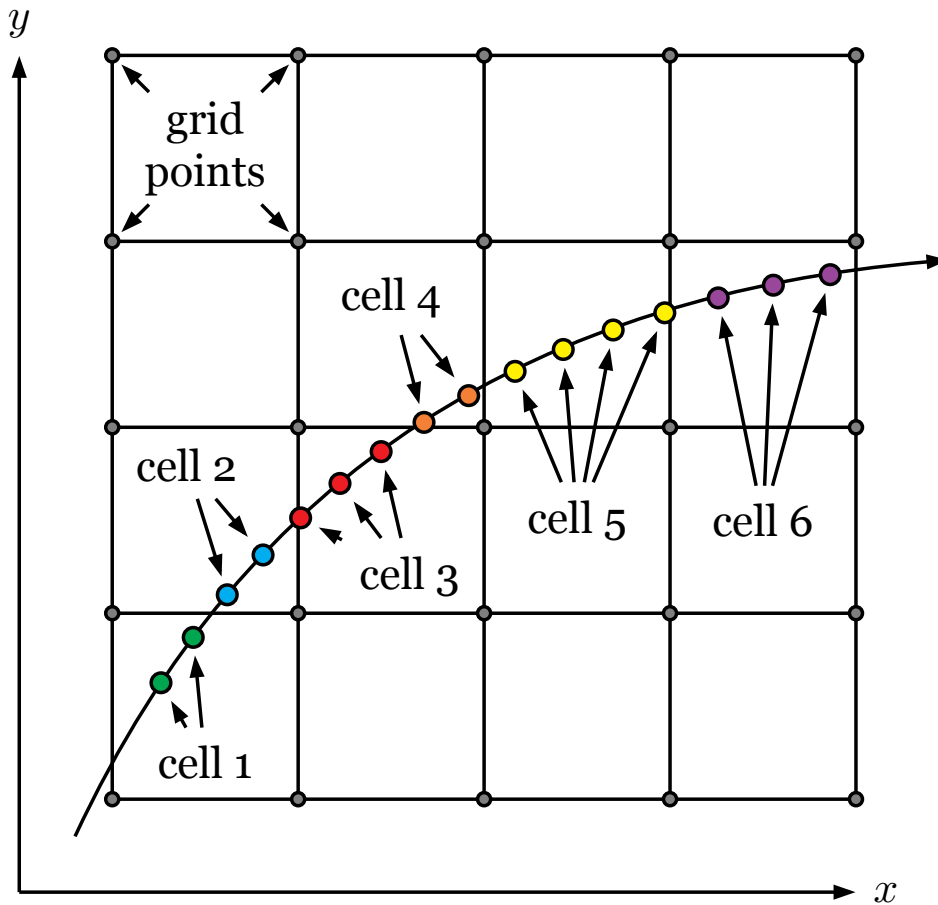

Figure 5.3: Overview of a two dimensional grid structure providing discrete values of the magnetic field and defining the area of a cell. The black arrow indicates a trajectory in the x-y-plane. The coloured dots represent individual magnetic field accesses for the trajectory estimation. The colour code refers to the cell that provides the field values [103].

the magnetic field is measured and provided by a map. The continuity of this field is built with a polynomial interpolation between grid points. As the search for a polynomial function describing the entire magnetic field is computationally too complex, the description is reduced to a smaller, local volume, the so-called *cells*. This volume is defined by the surrounding grid points as shown as black lines in Fig. 5.3. Hence, for a map in dim(Map) dimensions, only the $2^{\text{dim(Map)}}$ points are utilised for the construction of the polynomial of first order. The polynomial is evaluated for all points inside a cell and thus calculated once per cell.

Similar to the detector geometry, the magnetic field may change over time. For that purpose, a second context object is required and passed around to all components accessing the field. This allows for utilising per event the corresponding description of the magnetic field.

5.1.3 Detector Materials

The detector geometry in ACTS applies the simplification of surfaces, layers and volumes as representation of the detector geometry. While the detailed geometry allows for interactions in air and passive components of the detector, a similar description has to be utilised in the simplified approach. By considering the layer as a pure logical concept, the surfaces and volumes have to provide a material description that is comparable to a detailed description.

However, before the attachment of material to the geometrical objects can be discussed, the question about how material can be described needs to be considered first. As shown in Fig. 5.1, the detector components can be thought of as squashed. Furthermore, the material interaction at a single point along the particles trajectory has to be similar to the sum of interactions that occur in the detailed description. By attaching material to these components, it is obvious that the material properties in ACTS do not refer to real materials but have to be a meaningful combination. The materials attached to the components, do not reproduce all the macroscopic properties of the detector, however should resemble the properties of the real materials that are relevant for the tracking.

In Chapter 7 and 9 the material interaction of a particle are discussed from the perspective of reconstruction and simulation respectively. The considered properties are the radiation length X_0, the nuclear interaction length L_0, the atomic mass A, the nuclear charge number Z and the molar density ρ. Those numbers can be utilised to describe the material effects of a particles trajectory.

The construction of effective material numbers for the particle interactions will be considered initially for surfaces such as shown in Fig. 5.1. The underlying principle relies on side-by-side comparison between the two geometry representations. While the right hand side is used in ACTS, the left one can be modelled in Geant4. Since the latter relies on the detailed description, it is capable of providing the individual materials. Furthermore, the Geant4 simulation extrapolates a particle in steps through the detector. Hence, it delivers the material at many positions along the trajectory. Alongside the material properties, the length of a step in the material is recorded.

The Geant4 framework performs usually a detailed simulation of particles and their interaction. In order to avoid any kind of interactions, the concept of the geantino is used. This special Geant4 uncharged particle does not interact with any material. Thus, the straight line trajectory is comparable with the ACTS pendant.

For a single track in Geant4, for each step the ACTS surface next to its position is searched and assigned to a matrix of bins. This matrix allows for a non-homogeneous description of the squashed detector elements. Since the trajectory is a straight line, a Geant4 track will populate at most a single bin on a surface. This particular bin may obtain multiple steps assigned. Hence, the average of all assigned steps has to be calculated. The individual material properties are weighted depending on the step length through a particular material.

As for the magnetic field, the matrix defines a grid attached to the surface. Hence, the same interpolation strategy can be applied as before. Analogously, a homogeneous material can be defined.

The other type of material map necessary is for volumes. Thus, the description of e.g. calorimeters becomes possible. This variant of a material map was added in the context of this thesis as a consequence of the implementation the corresponding extrapolation procedure (see Sec. 7.4). By drawing parallels to magnetic field constructions, it becomes obvious that the volume material follows the same concept. The grid, cell and interpolation concept can be also utilised for a volume oriented material. In comparison to the surface material, the projection does not occur to individual surfaces and hence to different two dimensional grids but to a three dimensional grid as in the case of magnetic fields. While the latter can be expressed everywhere, the volume material is restricted to positions inside the volume. Hence, the grid is resolved only if the position is within the volume.

Again, the collection of tracks and the averaging of material properties as in the surface material mapping has to be performed. While the straight line intersects the surface at a single bin, the same trajectory may intersect multiple bins inside the volume. Hence, the plain collection of material and the corresponding thickness, denoted by the step length, in a certain interval around the surface is insufficient. For a given grid, the simplest approach is a selection of (random) positions in the volume, evaluating the material and accumulating it on the grid points. However, in order to be compatible with the surface material mapping, the straight line concept is favoured in this scenario. For a volume, a step in the same volume is divided into multiple steps. Although this remains an approximation, it allows the association of individual positions to different grid points.

5.2 Event Data Model

In Chapter 4 the parametrisation of particle properties and measurements were introduced. While this concept was kept general with the only restriction to continuous parameters, in the following the set of parameters used in ACTS will be introduced together with the main properties and required calculations. In Chapter 7 a derivation of the parametrisations will be presented, providing an additional reasoning for the used

parameters. In the second part of this section, additional requirements for measurements are presented.

5.2.1 Track Parametrisation

Throughout the Chapter 4 the parametrisation was projected between different coordinate systems using the projection matrices H. Since the detector geometry in ACTS is simplified to volumes and surfaces, the logical consequence is that two different representations are required. Furthermore, as Eq. (4.31) shows, the chosen parametrisation benefits from being the same as for the measurements. As both are defined to be identical, only the particle parametrisation will be considered in the following.

Starting with the volumes, a particle is located inside the three dimensional space and may move through this volume. Therefore, the position and the direction vector are required. Furthermore, the curvature, denoted by the momentum p and the charge q, is required. The vector describing a particles trajectory is given by

$$\lambda_{\text{global}} = \begin{pmatrix} x \\ y \\ z \\ [t] \\ T^x \\ T^y \\ T^z \\ \frac{q}{p} \end{pmatrix} \tag{5.1}$$

with the Cartesian coordinates x, y, z of the particles position as defined in Sec. 3.2.1. The directions T^x, T^y, T^z are used in Cartesian coordinates with the property

$$\frac{\frac{d(x\ y\ z)}{ds}}{\left| \frac{d(x\ y\ z)}{ds} \right|} = (T^x\ T^y\ T^z).$$

Due to the combination q/p a continuous parameter is constructed. For a neutral particle the parameter is replaced by $1/p$. The last parameter in this vector is the time t. The square brackets denote that this parameter is not mandatory to describe the trajectory but beneficial for the complexity of track reconstruction. This parameter is extrapolated among the others and hence mentioned here. In addition to the extrapolated parameters there are parameters such as the particle type and its mass that manipulate the trajectory. However, those parameters are discrete and hence not a part of the manipulation due to extrapolation but fixed initially. Since the parameterisation is given in the coordinate system of the entire detector, it is called a *global* parametrisation.

Another common term is *free* parametrisation. The latter one refers to the property that the parametrisation is expressed free from surface constraints. Consequently, a parametrisation expressed in the coordinate system of a surface is called *bound* or *local* parametrisation. Since the parameters are defined in the context of a surface, the set of

required parameters can be smaller compared to the global parametrisations. In ACTS the parameter vector

$$\lambda_{\text{local}} = \begin{pmatrix} l0 \\ l1 \\ \phi \\ \theta \\ \frac{q}{p} \\ [t] \end{pmatrix} \tag{5.2}$$

is used. The angles ϕ and θ are used as defined in Eq. (3.3) and thus replace the Cartesian direction vector. For q/p and t the same statements as for the global parametrisation are used. The position is denoted in the parameter $l0$ and $l1$. These two parameters are not defined in general but depend on the underlying surface type or convention. As Fig. 5.2 implies, for a plane surface a Cartesian coordinate system is used and for discs polar coordinates. For a cylinder surface, a point on the surface is identified by $r\phi$- and z-coordinates.

In addition to the different surface shapes, a special surface type has to be mentioned. The curvilinear surface is defined as an unbound, plane surface with the normal vector parallel to the direction vector of the global parametrisation. The local position is set to the origin of the coordinate system. Thus, it is possible to define a local parametrisation at any point along the trajectory.

5.2.2 Coordinate Transformations

Between the global and local representation of the parametrisation, the transformation is required. While time and q/p are treated independent of the underlying parametrisation, the other parameters have to be transformed. Since the surface shapes can be arbitrary and the utilised coordinate system per shape is not unique, only the three types from Fig. 5.2 as the most important ones in the context of this thesis are considered. The required transformations are restricted to a local to global transformation and vice versa. A local to local transformation can be considered as a combination with global parameters as intermediate state.

For any surface, the direction vector from Eq. (5.1) is transformed to an angular representation as given in Eq. (5.2). The relation between those representations is given by the spherical coordinates on a unit sphere

$$\begin{aligned} T_x &= \cos(\phi)\sin(\theta) \\ T_y &= \sin(\phi)\sin(\theta) \\ T_z &= \cos(\theta). \end{aligned} \tag{5.3}$$

Consequently, the inverse transformation is given by

$$\theta = \arccos\left(\frac{T_z}{\sqrt{T_x^2 + T_y^2 + T_z^2}} \right)$$

$$\phi = \text{atan2}\left(T_y, T_x\right).$$

with *atan*2, the piece-wise defined extension of the inverse of the tangent.

The spatial components on the other hand depend on the surface type. Hence, additional considerations are required. The position and orientation of each surface is defined by an affine transformation of the geometrical centre. For a plane surface, the geometrical centre is on the surface. From the orientation, the normalised normal vector T can be obtained. The Cartesian coordinate axes U and V are then defined as

$$U = \begin{cases} X \times T, \text{ for } T \parallel Z \\ Z \times T, \text{ else} \end{cases}$$

$$V = T \times U$$

with the unit vectors X and Z along the x- and z-axis respectively. Thus, any global point on the surface can be expressed as linear combination of the vector to the centre and the base vectors U and V.

For a disc surface, a similar procedure is performed with an additional transformation from the local Cartesian to polar coordinates given by

$$x = r\cos(\phi)$$
$$y = r\sin(\phi)$$

and the inverse

$$r = \sqrt{x^2 + y^2}$$
$$\phi = \text{atan2}(y, x)$$

with the coordinates x and y expressed in the local coordinate system of the disc. The $l1$ on a cylinder surface is given by the z-components of the global parameters. The $l0$ is given by the predefined radius of the cylinder multiplied with the azimuthal angle from the polar coordinates equivalent of the global $(x \ y)$ vector. The inverse transformation for all surface types is given by the transformation in reverse order.

A surface that represents e.g. a detector module has a limited size. This size is defined by the parameters shown in Fig. 5.2. Although the vectors defining a point on a surface would lead to a reasonable result, the point is not within the bounds. Hence, an additional step is required for the transformation to local coordinates by testing whether a global point is within the bounds of the surface or not. For an unbound surface that is not representing a real object like the curvilinear surface, this test is not performed. The inverse transformation does not rely on such constraints.

5.2.3 Measurement Description

A particle trajectory relies on the parameter vectors from Eq. (5.1) and (5.2) in order to perform the extrapolation. A sensitive surface on the other hand may measure a subset of those parameters. Hence, the vector representing the measured parameters is not just usually smaller but may also vary between different detector principles. For that purpose, the ACTS measurements store in addition to the value of the parameters the

information which parameter the value represents. Since the surface coordinate systems are defined prior and the measured indices are known from the detector architecture, the projection matrices H can be expressed as sparse matrices from Eq. (4.31).

As mentioned in Sec. 4.2.1, the parameters describing a measurement are given by the mean and covariance matrix. In order to obtain those values, the data pre-processing step *clusterisation* is required. Due to the finite pitch of e.g. a semiconductor, multiple bins (pixels or strips) may produce a signal. After correcting for the Lorentz-angle, Eq. (3.4) shows the uncertainty obtained from a single bin. The combination of multiple bins then provides the required parameters. For the combination itself, a weighted geometrical mean is used on the surface with the weights being either uniform distributed among the bins (digital readout) or utilise additional information about the particles trajectory (analogue readout).

As the measurement parameters do not necessarily constitute a full parameters vector, a global transformation is not applicable in general. As it relies on the information about the measuring surface, the corresponding geoID is stored withing the measurement object. This also allows to trigger the extrapolation to the corresponding surface. Another purpose of the storage of the corresponding surface is the *calibration*. After the extrapolation of the particles parameters to the surface and before the Kalman filter update is performed, the position on the surface allows to correct the measurement. Since the measuring components e.g. the wires in the TRT or MS are sagging at the centre, the measurement position can be corrected.

Since ACTS can be used in different experiments, the interface between the measurements and the experiment specific implementation may differ. In order to overcome this issue, the linkage of the parameters to the corresponding surface and the related methods is templated with the requirement of a certain API.

5.3 Prior Generation and Posterior Utilisation

In Sec. 4.2.2 the model of a prior was introduced. As the only software related part of its construction is the seeding, the general idea is shown in Sec. 5.3.1. In Sec. 5.3.2 the reconstruction of the vertices using the found tracks is presented.

5.3.1 Seeding

The seeding in ACTS is based on algorithms from the ATLAS software [108]. By combining measurements, an initial guess for the prior is produced. Compared to the Kalman filter in Chapter 4, the seeding does not rely on an accurate treatment of the data. Thus, the calculation can become faster and a double counting of measurements due to the filter is prevented. Furthermore, the seeding combines space points (SPs) instead of measurements. In the context of this thesis, the calculation of SPs were translated from the ATLAS software into ACTS. A derivation can be found in Appendix B. The SPs are three dimensional points (four dimensional if the time is also measured) in global coordinates. Hence, the obtained representations of the measurements are expressed spatially independent from the measuring surface. Since SPs are usually formed from

pixel and strip detector data, the transformed spatial information describes the entire measured parameter space.

Starting with the initial assumption that a track originates from a point near the z-axis, multiple SPs have to be combined in order to obtain a prior estimate. From parameters in Eq. (5.1) or (5.2) at least three points are required: a single provides the spatial information, a second the direction additionally, the third the curvature and hence q/p. Due to this minimum requirement, the number of layers in a tracking detector are fixed.

The seeding algorithm in ACTS is independent of the extrapolation function from Eq. (4.38). This is achieved due to the assumption of an almost homogeneous magnetic field, directed in z-direction. Hence, the trajectory becomes a helix. Within this model SPs from three layers are used and combined to a helix. In order to obtain reasonable seeds afterwards, the combinations have to fulfil angular conditions in order to be valid. This combination occurs using multiple iterators. The middle layer is iterated once. For each middle layer SP, a fitting inner layer SP and an outer layer SP is searched independently.

Thus, two sets of doublets are obtained per middle layer SP as the common point. In a second iteration, the doublets are combined under weights depending on the direction of the curvature and the minimum distance to the z-axis. Additionally, experiment specific cuts can be performed in order to increase the purity of the seeds. The purity in terms of seeding is given by requiring that per particle that traversed the detector a seed exists whereas seeds from different particles or noise have to be suppressed. The number of seeds from the same particle should be reduced to ideally one.

5.3.2 Vertexing

The particles traversing the detector have their origin in so-called *vertices*. After the tracks and their parameters are obtained from the reconstruction, the data are utilised to find the vertices. For this search all reconstructed particles are utilised, independent of their charge. The vertices are categorised as primary and secondary vertices. Primaries are directly related to the *pp*-collisions in the beam pipe whereas secondaries consider e.g. particle decays. The former vertices are usually close to the z-axis, the latter spread over a large radial region. Depending on the process, secondary vertices may be found inside the detector and between the sensitive surfaces. While the beam pipe can be considered as constraint for primary vertex locations, for the secondary vertices additional degrees of freedom are present. Hence, the secondary vertexing is more complex and thus out of scope of this thesis. In the following, just primary vertices are considered.

To simplify the presentation of the physics processes that take place during the particle collision event a concept of vertex is introduced. The vertex can be seen as a space point at which one or several particles were produced. During the event reconstruction the vertices are located as the most probable origin point of selected particles assuming these came from the same point. This is usually at smaller radii than the first pixel layer. As a representation helper of the track parameters at the vertex, the concept of perigee surfaces are utilised. This special kind of surface serves as standalone expression

of the parametrisation, i.e. the reduction of necessary parameters is not obtained by the additional storage of surface information. In order to achieve this reduction, the perigee surface is defined as a line pointing in the z-direction. Furthermore, the trajectory has to be expressed at the so-called *point of closest approach* (PCA). This point along the trajectory is defined as the point minimising the distance between the trajectory and the z-axis. The parameters $l0$ and $l1$ are called d_0 and z_0 respectively. While the latter parameter is the z-coordinate in global coordinates, the radial position is encrypted in d_0. At the PCA, the relation

$$\begin{pmatrix} x \\ y \\ 0 \end{pmatrix} \perp \begin{pmatrix} T^x \\ T^y \\ T^z \end{pmatrix} \wedge \begin{pmatrix} x \\ y \\ 0 \end{pmatrix} \perp \begin{pmatrix} 0 \\ 0 \\ z_0 \end{pmatrix}$$

allows the construction of the vector c with

$$c \equiv \begin{pmatrix} 0 \\ 0 \\ z_0 \end{pmatrix} \times \begin{pmatrix} T^x \\ T^y \\ T^z \end{pmatrix} \parallel \begin{pmatrix} x \\ y \\ 0 \end{pmatrix}$$

which by construction points at the same direction as the radial distance to the PCA with respect to the z-axis. Hence, d_0 is defined as $\sqrt{x^2 + y^2}$. The orientation of the local position vector is obtained from a dot product of c and $(x, y, 0)$, leading to a sign flip of d_0 if its smaller than zero. The construction allows to uniquely reconstruct the global position using the provided information.

The location of the perigee surface, i.e. the location of the line itself is related to the position of the vertex. Hence, re-calculations of the track parameters may occur. With the track parameters expressed in perigee parameters, the goal of vertexing is to find the position and if available the time of the vertex. By combining the means and covariance matrices of the tracks with respect to an estimated SP of the vertex allows an iterative adaption [109] of the vertex parameters based on a χ^2-minimisation. For interactions with pile-up, more advanced methods like the Adaptive Multi-Vertex Fitting [110] are necessary as it is not prior known which track belongs to which vertex. The particles are then assigned with a certain weight to a vertex and the final assignment is performed iteratively on the entire set of vertices. In the context of the bayesian smoothing from Chapter 4, the combination of multiple tracks in the context of vertexing is linked to the utilisation of data encapsulated in the track parametrisation for the parametrisation of another.

6 Fast Track Reconstruction

The ATLAS detector recorded during Run-2 data from up to $\langle\mu\rangle \approx 70$ pp-collisions per bunch-crossing as shown in Fig. 3.9. With the beginning of HL-LHC era it is expected to obtain a pile-up of 140 to 200. In order to estimate the computational requirements for the high pile-up track reconstruction, a high-μ run was performed in 2017. The dependency of the reconstruction time on the pile-up is shown in Fig. 6.1. It is observable
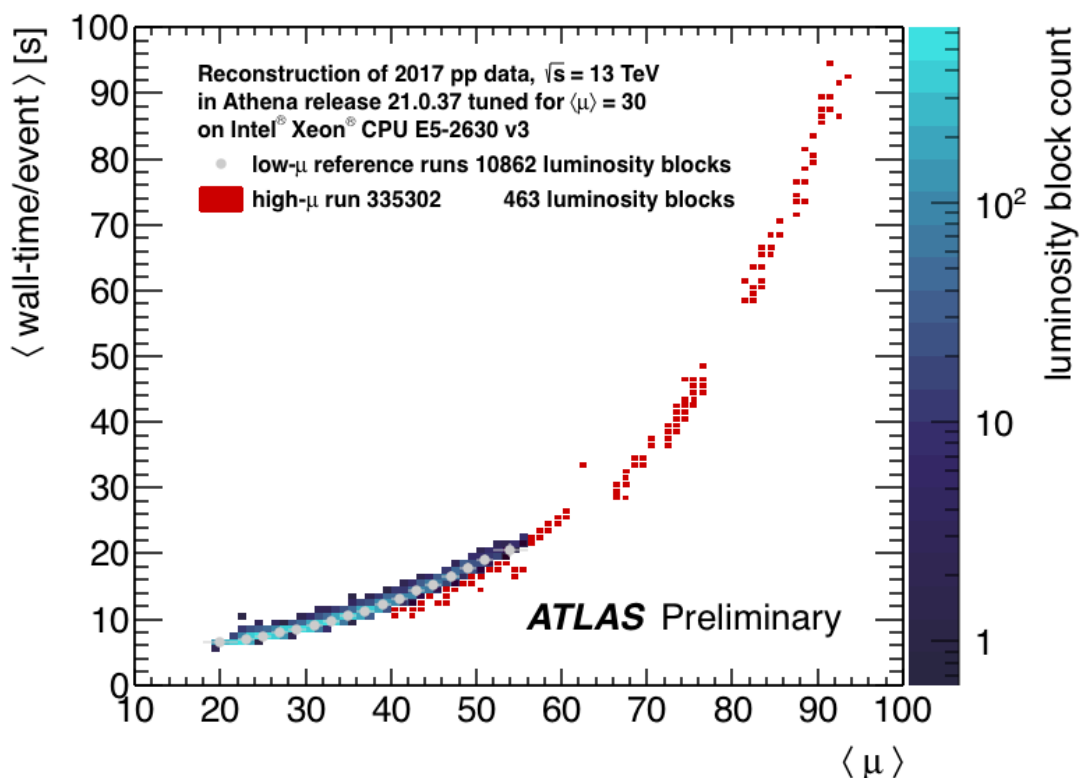

Figure 6.1: Reconstruction time as a function of the mean pile-up of the ATLAS Run-2 detector [111].

that the reconstruction time grows exponentially with the pile-up. While this pile-up is still below the expected HL-LHC pile-up, it can be concluded that tracking will become a challenge in Phase-II. The fraction of track reconstruction contributing to the total CPU requirements of the ATLAS experiment is shown in Fig. 3.27. As it is one of the major components in the total consumption, any computational improvement in this category would provide a large benefit to the overall consumption. Furthermore, the

predictions for the future demands of CPU resources of the ATLAS experiment, shown in Fig. 3.26, imply that the CPU consumption has to be reduced drastically[1].

The high pile-up run from 2017 was performed with the Run-2 ATLAS detector. This detector was designed for a pile-up scenario of $\langle \mu \rangle \lesssim 23$ and hence, this run was performed at up to ≈ 4 times this design value. Furthermore, the software used for the track reconstruction was applied unchanged in this environment. For the HL-LHC, the detector will receive several hardware upgrades. Additionally, the tracking software also needs to be optimised for those conditions. While the high pile-up run provides a baseline of the required tracking CPU consumption, R&D has to be performed in order to optimise the software. For that purpose, several initiatives dedicated to achieve this goal were taken. An overview of the optimisation of the current tracking software is shown in the following together with the resulting CPU requirements. Afterwards, the fast track reconstruction [112, 113], a study for further CPU utilisation reduction that was created in the context of this thesis, is presented and compared to the initial optimisation.

6.1 ATLAS Phase-II Tracking

The ATLAS Inner Detector will be replaced by the Inner Tracker for Phase-II. Its replacement is motivated by several aspects. One aspect is that the Inner Detector will reach the end of its lifetime due to radiation damage. On the other hand, the ID operates already above the design pile-up conditions and thus at its bandwidth limit. The high pile-up is especially problematic for the TRT. At a pile-up of $\langle \mu \rangle = 70$, the occupancy in this detector part is up to 50% [113]. In order to provide the optimal tracking performance in the HL-LHC era, the ITk is designed to handle the upcoming conditions and to assist the tracking CPU requirements. Furthermore, the range in pseudorapidity becomes larger compared to the ID and the amount of sensitive layers gets increased as shown in Fig. 3.22 (left). The material in the detector and the required bandwidth is designed to be kept at a minimum in order to provide ideal tracking conditions. At the same time the average amount of hits per track is increased to at least nine hits as shown in Fig. 3.22 (right). As a consequence of the optimised detector hardware, the cuts applied to the track reconstruction for the ITk can become tighter compared to the ID [114]. An overview of the applied cuts is shown in Tab. 6.1.

The track selection together with the expected number of hits per track results in high and stable tracking efficiency for the entire range of $|\eta| < 4$ while the reconstruction of fake tracks gets reduced. A comparison is shown in Fig. 6.2. These plots imply the potential benefit of the ITk in comparison to the ID detector layout for Phase-II.

---

[1]Although this motivation for this chapter remains valid, it has to be noted that the study presented within this chapter was performed before the latest computing requirements extrapolations from [90] were created. Consequently, the considerations in that report already incorporate the results of this chapter.

Requirement	Pseudorapidity interval		
	$|\eta| < 2.0$	$2.0 < |\eta| < 2.6$	$2.6 < |\eta| < 4.0$
Pixel+Strip hits	≥ 9	≥ 8	≥ 7
Pixel hits	≥ 1	≥ 1	≥ 1
Holes	≤ 2	≤ 2	≤ 2
p_T [MeV]	> 900	> 400	> 400
$|d_0|$ [mm]	≤ 2	≤ 2	≤ 10
$|z_0|$ [cm]	≤ 20	≤ 20	≤ 20

Table 6.1: Set of cuts applied for the ITk default track reconstruction from Reference [86]. Holes are counted as missing hits on active sensors for track candidates. d_0 and z_0 are defined with respect to the mean position of the beam spot.
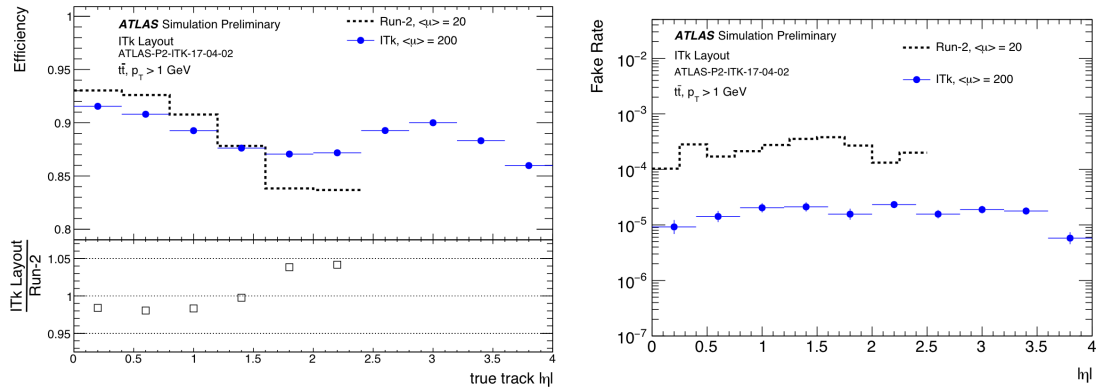

Figure 6.2: Comparison of the efficiencies (left) and fake rate (right) between the ID at $\langle \mu \rangle = 20$ and the ITk at $\langle \mu \rangle = 200$ as a function of $|\eta|$ [88].

6.1.1 Computing Requirements

The ITk will be installed in the ATLAS detector for Run-4 and thus, all considerations are related to simulations. While the detector is currently designed and constructed, the same holds for the tracking software. The track reconstruction simulations of the ITk are performed utilising the Run-2 software. Within this environment, the major contributors to the event reconstruction time are given by the (Silicon) Track Finding and the Ambiguity Resolution as shown in Tab. 6.2 in units of HS06s[2]. The former refers to the combinatorial measurement-track association. The latter term refers to the association of multiple tracks to a single measurement and the reconstruction of the same track from multiple seeds. In addition, a major contribution to the CPU consumption just present in the ID is given by the TRT and Back Tracking[3].

Track reconstruction aims to provide the most accurate results of the tracks produced in an event under the circumstances of the data provided by the detector. The same

---

[2]This unit represents a CPU independent measure of the required computing [91].

[3]This terms refers to the extension of track segments in the TRT into the silicon detectors of the ID.

Detector	$\langle\mu\rangle$	Cluster Finding	Space Points	Si Track Finding	Ambiguity Resolution	TRT+Back Tracking	Primary Vertex	Total ITk/ID
ITk Layout	200	22	6.5	78	97	-	6	219
Run-2	20	1.5	0.7	23	15	19	0.5	64

Table 6.2: Averaged CPU requirements per event for the individual stages of track reconstruction together with the total requirements. The table displays the requirements of the ITk at $\langle\mu\rangle = 200$ and the ID at $\langle\mu\rangle = 20$. Both setups use the Run-2 software. The numbers are given in units of HS06s. The table is taken from Reference [82].

holds for the configuration of the software. Here, additionally the computing budget has to be taken into account. The CPU requirements shown in Fig. 6.3 shows the Run-2 software applied for different pile-up values using the ID and ITk. The latter utilised
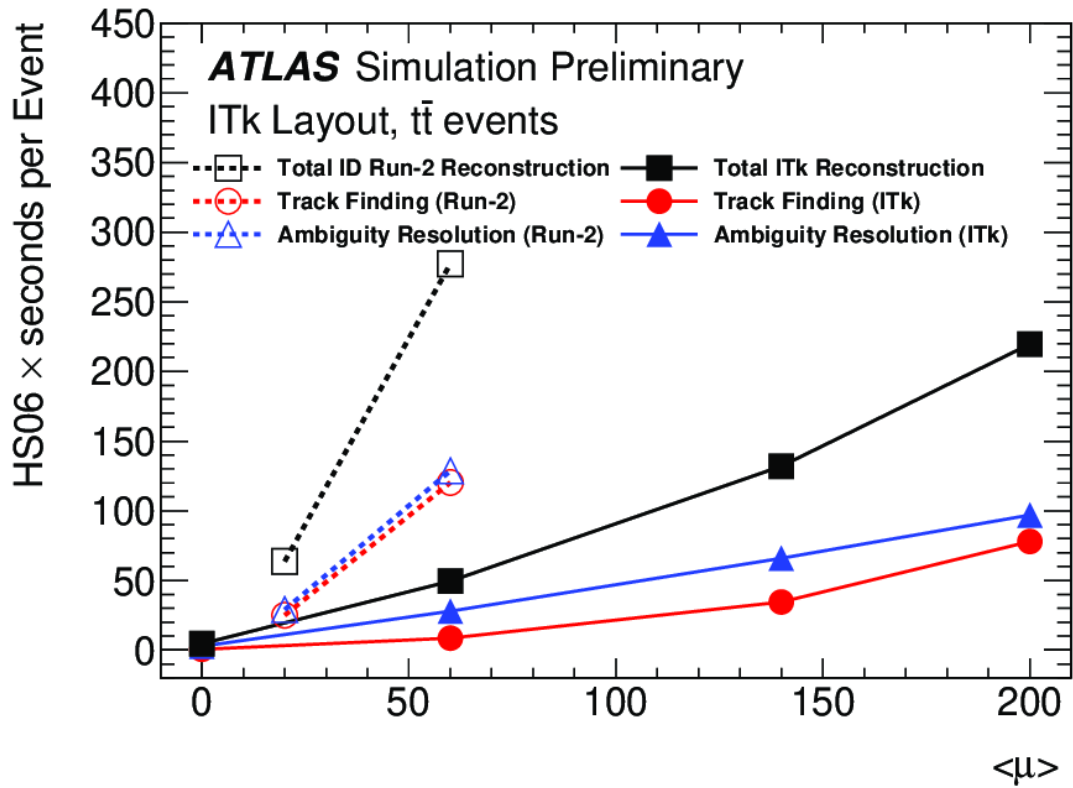

Figure 6.3: Comparison of the CPU requirements for track reconstruction of $t\bar{t}$ events between the ID and ITk as a function of $\langle\mu\rangle$. The contributions of the Track Finding and Ambiguity Resolution are drawn separately [114].

the adapted set of track selection cuts from Tab. 6.1. This plot shows that the ITk tracking CPU performance at $\langle\mu\rangle = 200$ is better than the Run-2 ID at $\langle\mu\rangle = 60$. This improvement is obtained from replacing the detector architecture and adapting the

current software accordingly. This setup at a more recent stage is used to extrapolate the CPU requirements for the future of the ATLAS experiment [90]. This setup, labelled as *Baseline* is shown in Fig. 3.26 (left) and consumes $\approx 45\%$ of the total CPU resources. Although the new detector will reduce the tracking time drastically, it is still far above the estimated amount of available CPU resources[4].

The tracking speed has to be improved with respect to the expected HL-LHC conditions. This can be achieved in two ways: improving hardware and software performance. The former is given by the detector layout and already covered in the design of the ITk. Also the utilised computing hardware is a variable that can be considered. Beside improvements in the CPU performance, other hardware architecture such as FPGAs and GPUs can be considered. The ATLAS software framework Athena is optimised for the usage of CPUs. The reconstruction time from a hardware point of view is mostly limited by the number of available CPUs, and thus essentially by the financial budget. This situation is different for other hardware architectures. As FPGA or GPU architectures rely rather on a dedicated software design, Athena has to be adapted. This leads to the second possibility to speed-up the Phase-II tracking. The required R&D in this category can be split again into two different fields. On the one hand dedicated exploration of new architectures and new algorithms can be performed. As an example, the TrackML challenge [115], a public competition in tracking speed and accuracy is mentioned here. Another example is this thesis itself. The other possibility to speed-up tracking is optimising the existing code. The second one is the item of the following discussion.

6.2 Fast Track Reconstruction Strategy

In the process of designing the Phase-II TDAQ system for the ATLAS experiment, the question came up whether a high level software based trigger would be viable. Within this progress the fast track reconstruction was motivated. Object of study is the modification of the ATLAS track reconstruction workflow and tuning its parameters in order to achieve a throughput sufficient for the expected HL-LHC conditions. The study was performed using the ITk detector geometry with the expected lower and upper bound of the HL-LHC mean pile-up, 140 and 200. This study was focused upon decreasing the CPU requirements for the reconstruction. Compared to a common tuning of tracking, a loss in physics performance was acceptable in this study but should be kept at a minimum.

The starting point is the unmodified workflow of the default ITk track reconstruction as shown in Fig. 6.4. This workflow can be considered as three subsequent stages, pre-processing, combinatorial track finder and ambiguity resolution. In the context of the study the workflow was successively modified and the event processing time was monitored.

The largest contribution to the event reconstruction time in Tab. 6.3 is the ambiguity resolution. The tasks performed within this stage grew historically. As a first

---

[4]The extrapolation is a snapshot in time and hence may change in the future.

Figure 6.4: Default track reconstruction workflow used with ITk geometry [113].

modification, this stage was disabled. Within the ambiguity resolution a precise track fit is performed that was disabled alongside. Additionally, it is expected to reduce the b-tagging efficiency due to the missing neural network cluster splitting in jets performed in this stage.

Since the ambiguity resolution is the last stage in the track reconstruction, built tracks that are rejected at that point can be considered as a waste of time. On the other hand, the resolving the ambiguities is mandatory. In order to preserve the track quality without the ambiguity resolution, the workload is partially moved from this stage to the combinatorial track finder. The moving is manifested in the track finding as a suppression of the creation of ambiguities. It is achieved by tightening the track cuts in the Silicon Track Finder. That way, tracks are built with a higher purity and earlier in the workflow. It is expected that the reduction of number of track candidates and the tightening of their constrains would decrease the reconstruction time. Furthermore, the disabling of the ambiguity resolution implies that the combinatorial track finder estimates the final track parameters. An overview of the applied track finder cuts is given in Tab. 6.3. The number of required hits within this stage is identical to the final

Requirement	Pseudorapidity interval		
	$|\eta| < 2.0$	$2.0 < |\eta| < 2.6$	$2.6 < |\eta| < 4.0$
Pixel+Strip hits	≥ 9 (7)	≥ 8 (7)	≥ 7 (7)
unique hits	≥ 7 (1)	≥ 6 (1)	≥ 5 (1)
shared hits	≤ 2 (no cut)	≤ 2 (no cut)	≤ 2 (no cut)
p_T [MeV]	> 1000 (900)	> 400 (400)	> 400 (400)
$|z_0|$ [cm]	≤ 15 (20)	≤ 15 (20)	≤ 15 (20)

Table 6.3: Applied tracking cuts in the track finder of the fast track reconstruction [112]. The default values are given in brackets. z_0 is defined with respect to the mean position of the beam spot.

selection from Tab. 6.1. Due to the number of unique hits is drastically increased while the number of shared hits gets an upper limit, the creation of ambiguities is expected to be suppressed. In addition to the cuts, an approximated material model and cluster correction was applied. The cluster calibration on the other hand was not changed. As these approximations reduce the description accuracy of measurements and disturbance

contributions, the lower threshold for p_T in the central region was increased while the vertex position in z_0 became tighter.

The second step in modifying the reconstruction workflow considers the seeding. During Run-2 this consumed approximately 20% of the CPU time. It is expected that this increases up to 50% under HL-LHC conditions [112]. The seeds are built from space points that are located either in the pixel layers or the strip layers. Their individual contribution to the overall set of seeds per interval of pseudorapidity is shown in Fig. 6.5. The five pixel layers in the ITk provide the major amount of seeds. Compared
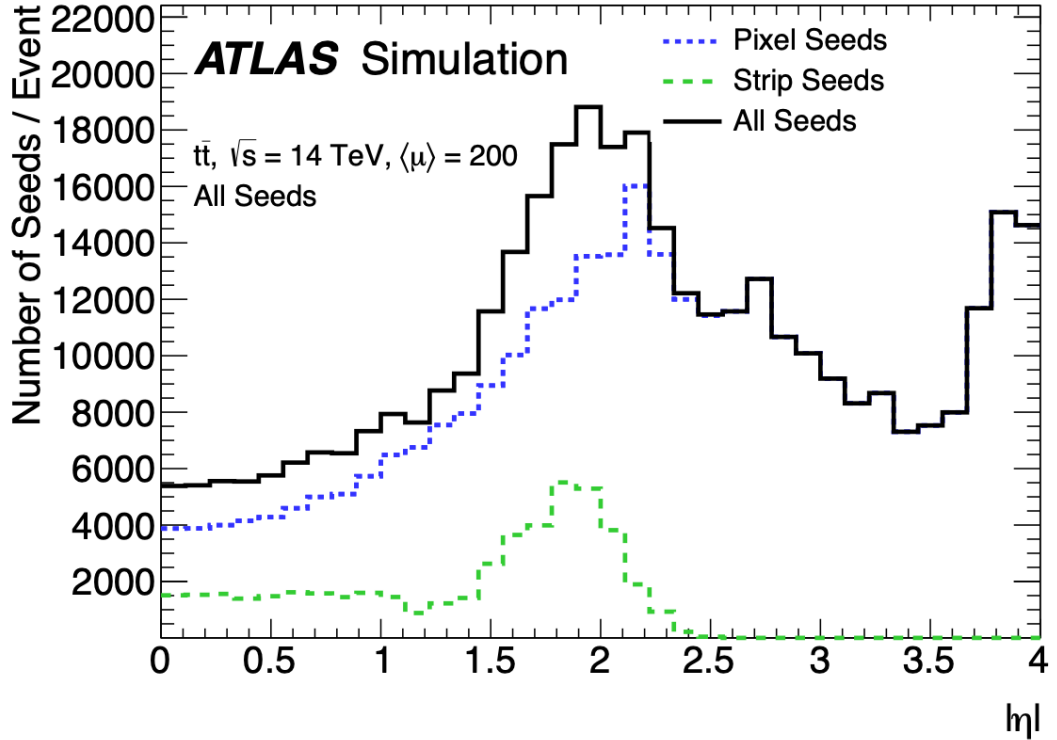

Figure 6.5: Mean number of accepted seeds in the ITk pixel and strip detector together with the sum of both as a function of $|\eta|$ [82].

to the coverage of the strip detector of $|\eta| < 2.7$, the pixel detector covers the full range of $|\eta| < 4$. Consequently, a goal was to increase the pixel seed purity, covered by the cuts in Tab. 6.3, such that the strip seeds can be disabled from the workflow. As a side effect of an increased purity, the combinatorial complexity due to selecting measurement candidates is further reduced, speeding up the subsequent components of the workflow. The last modification in the combinatorial track finder is a temporary disabling of the recovery strategy from bremsstrahlung (c.f. [116]) within this study.

The last stage to modify is the pre-processing. In order to speed this stage up, several code optimisations of the pixel and strip detector clusterisation were performed.

Additionally, the strip space point formation is a very CPU consuming fraction of the pre-processing while pixel space points are obtained from a plain deep-copy. As the space points are only required for the seeding but the seeds in the fast track reconstruction are obtained only from the pixel detector, the strip space point formation is disabled. While the strip detector read-out provides already clusters, the 2D pixel clustering is computationally more complex. The pixel detector front-end chip RD53B allows to read-out multiple pixels simultaneously in a tree-like and strongly compressed byte-coding. This feature allows to read pixel clusters directly from the detector. Additionally, the data compression leads to comparable event sizes in the pixel and strip detector. At the time of the study, no software existed for decoding the byte-stream. The behaviour of the RD53B was emulated in this study by measuring the Run-2 raw data decoding time and scaling to the expected ITk event size. For events generated by Monte Carlo simulations, the decoding of simulated hits from ROOT files was utilised.

6.3 CPU and Physics Performance

Due to the modification of the tracking workflow for the fast track reconstruction, two performance fields are affected: the event reconstruction time and the physics performance.

6.3.1 CPU Performance

In order to measure the CPU performance of the fast track reconstruction, MC generated samples with $t\bar{t}$ events with a pile-up of 140 and 200 were used. The time measurements were performed using a dedicated machine with two Intel Xeon E5-2620v2 CPUs with approximately 17.8 HS06 per physical core and single threaded execution [112]. The performance is compared to the default ITk track reconstruction workflow from Reference [86]. The obtained timings for both workflows and pile-up conditions are shown in Tab. 6.4. The fast track reconstruction achieves in the Silicon Track Finding a speed-up

$\langle\mu\rangle$	Tracking	Byte Stream Decoding	Cluster Finding	Space Points	Si Track Finding	Ambiguity Resolution	Total ITk
140	default	$1.2^{(*)}$	17.1	6.0	41.1	58.2	123.6
	fast		4.5	0.9	12.4	-	19.0
200	default	$1.6^{(*)}$	26.3	8.6	85.8	92.0	214.3
	fast		6.3	1.2	22.6	-	31.7

$(*)$Scaled from Run-2, see text.

Table 6.4: Comparison of CPU requirements in HS06s between default and fast track reconstruction for $\langle\mu\rangle$ of 140 and 200 split into individual parts of the workflow [112].

of approximately a factor eight compared to the default configuration with the additional ambiguity resolution. The additional modifications in the workflow for the cluster

finding and space point formation lead to a total speed-up of approximately a factor six with $\langle\mu\rangle = 140$ and approximately eight for $\langle\mu\rangle = 200$. The obtained results are summarised graphically in Fig. 6.6. The stated CPU requirements are evaluated on the
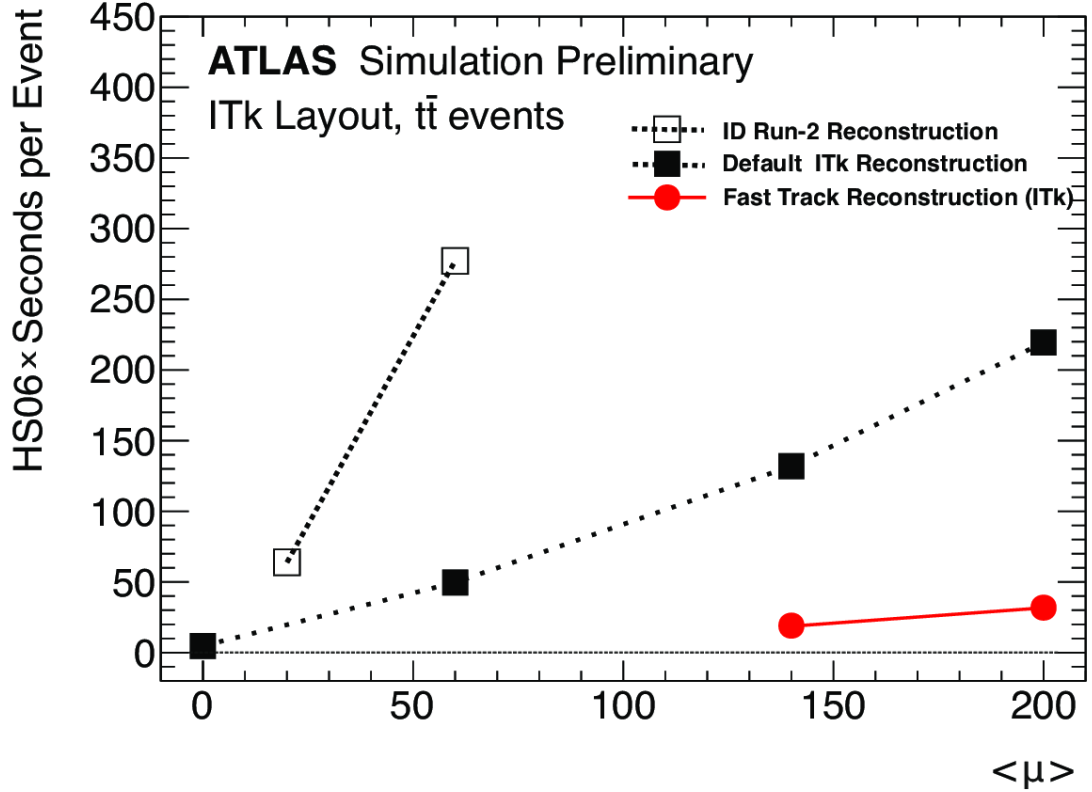

Figure 6.6: Reconstruction time for ID Run-2, default and fast ITk track reconstruction [112].

dedicated machine after the publication of Reference [86]. Hence, the numbers slightly vary compare to Tab. 6.2.

6.3.2 Physics Performance

The default ITk track reconstruction is optimised for CPU and physics performance. This balance is shifted for the fast track reconstruction to favour the former. Within this section the physics performance is compared between both workflows. For that purpose, reconstructed tracks over the full range of $|\eta| < 4$ are considered for particles with $p_T > 2$ GeV. The minimum p_T was increased in order to avoid turn-on effects.

The first observable which will be considered is the reconstruction efficiency. The obtained results for MC generated single muons and $t\bar{t}$ events are shown in Fig. 6.7. Within all pseudorapidity bins a slight degradation of the reconstruction efficiency is observable for the muons as well as for the $t\bar{t}$ events. This observation is smaller for 100 GeV muons and the $t\bar{t}$ events with $\langle\mu\rangle = 140$ compared to the 2 GeV muons and the
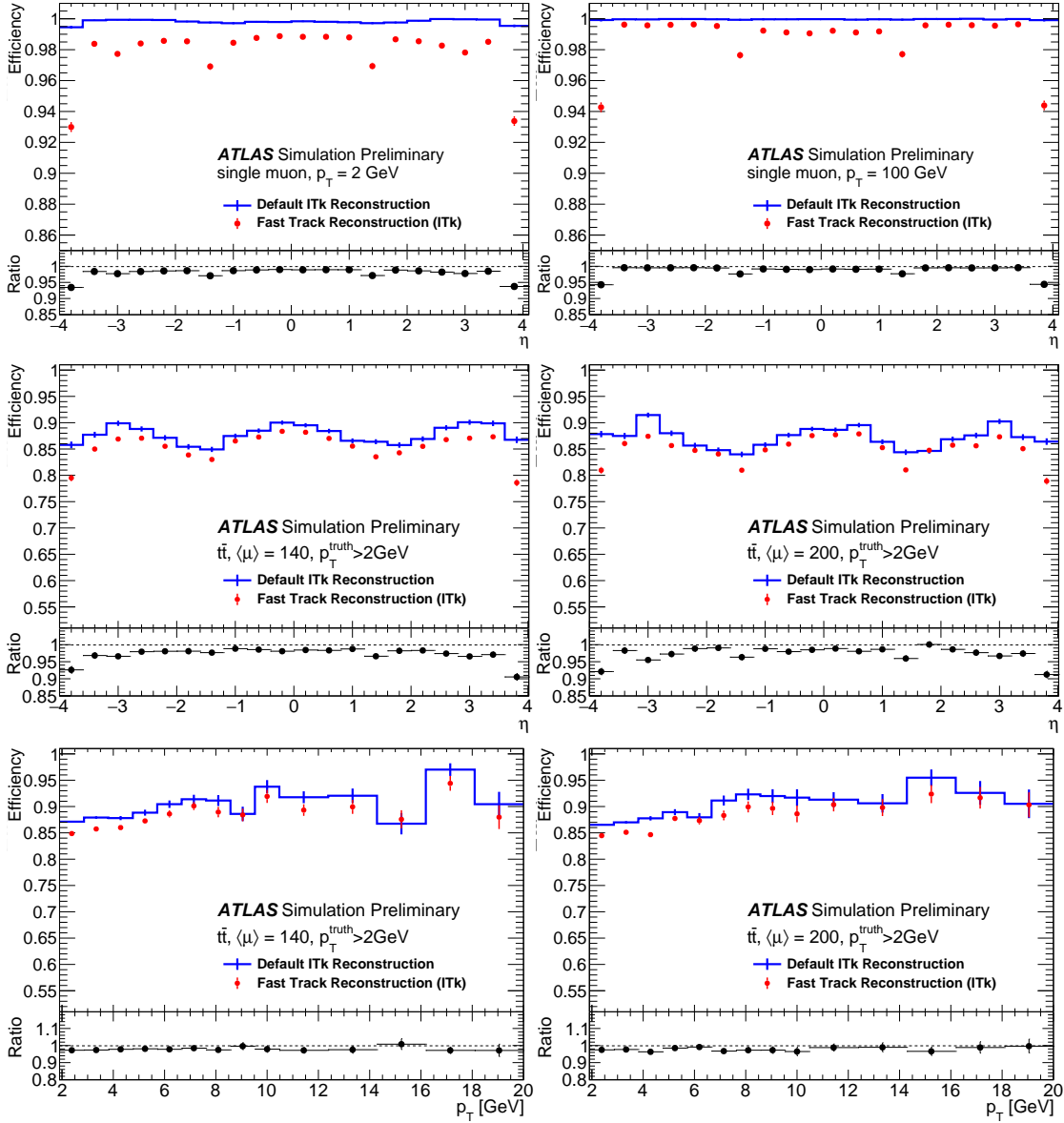
Figure 6.7: Track reconstruction efficiency for single μ (top row) with a p_T of 2 GeV (left) and 100 GeV (right) versus η and for $t\bar{t}$ events versus η (middle row) and p_T (bottom row) with $\langle\mu\rangle$ of 140 (left column) and 200 (right column). The figures are taken from Reference [112].

$t\bar{t}$ events with $\langle\mu\rangle = 200$. The deviation for low-p_T muons is an expected result due to the momentum dependency of multiple scattering upon the trajectory and the applied approximations in the material model. Additionally, in all four distributions versus η a more significant deviation from the fast track reconstruction to the default settings is observable in the transition region between barrel and end-cap and at the very forward
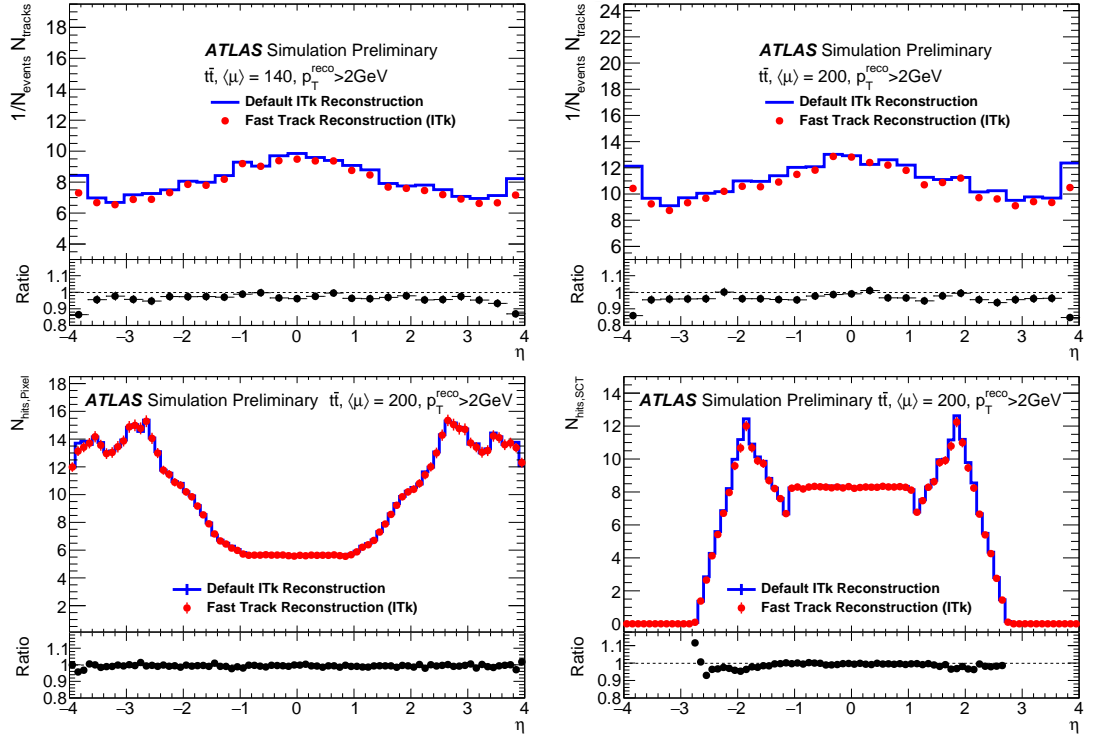
Figure 6.8: Mean number of reconstructed tracks (top row) in $t\bar{t}$ events with $\langle\mu\rangle$ of 140 (left) and 200 (right). The bottom row shows the associated hits in the pixel (left) and strip detector (right) versus η. The figures are taken from Reference [112].

region. These artefacts may be the result of the preliminary tuning imperfections within this study and remain tasks for future studies. Considering the p_T dependency, the track reconstruction efficiency is lower for low-p_T particles in the fast track reconstruction but becomes more similar to the default setup for higher p_T. Furthermore, no strong pile-up dependency is observable.

A reduced track reconstruction efficiency leads to a smaller set of final tracks. This is shown for the $t\bar{t}$ events in Fig. 6.8 (top row). Although the number of tracks is lower in the fast track reconstruction due to the reduced efficiency, it also shows that workflow modifications do not result in a significantly enhanced fake-rate. Despite the disabled ambiguity resolution and track re-fitting, the selected tracks have an almost identical amount of hits in the pixel and strip detector as shown in Fig. 6.8.

Beside the obtained tracks, the track parameters at the perigee surface are of interest. The parameter resolutions for single muons are shown in Fig. 8.16. For most of the distributions the fast track reconstruction is in good agreement with the default track reconstruction. However, the momentum resolution for low momentum particles shows a more significant loss of approximately 20% for 2 GeV muons. This deviation is a consequence of the approximations in the material model. As the energy loss fraction is larger for low momentum particles, the 100 GeV muons do not show this deviation. On
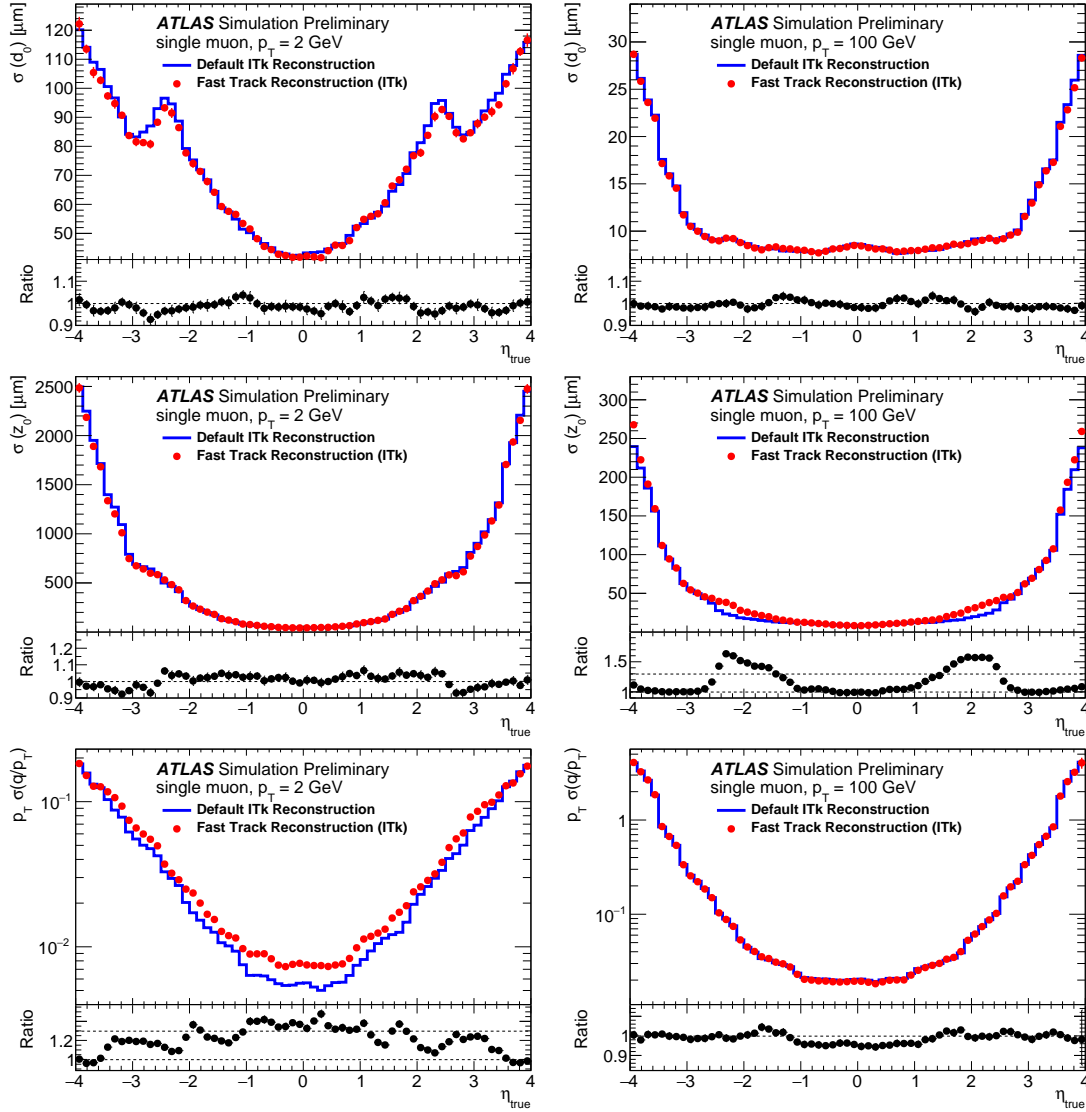
Figure 6.9: Resolution of d_0 (top row), z_0 (middle row) and the relative p_T (bottom row) for single muons with 2 (left column) and 100 GeV (right column) versus η. The figures are taken from Reference [112].

the other hand, the 100 GeV muons show a loss of approximately 50% in z_0 in the region of $|\eta|$ around 2. This is a result of the approximations applied in the cluster correction.

These observables for $t\bar{t}$ events are shown in Fig. 6.10. While the spatial parameters d_0 and z_0 remain overall in good agreement between both setup, the momentum resolution shows an approximately 30% worse resolution for the fast track reconstruction. This is again a result originating from low momentum particles as shown for 2 GeV muons.

In total, the deviations resulting from the fast track reconstruction are well understood and remain objects for future study. As the goal of this study was to obtain a speed-up
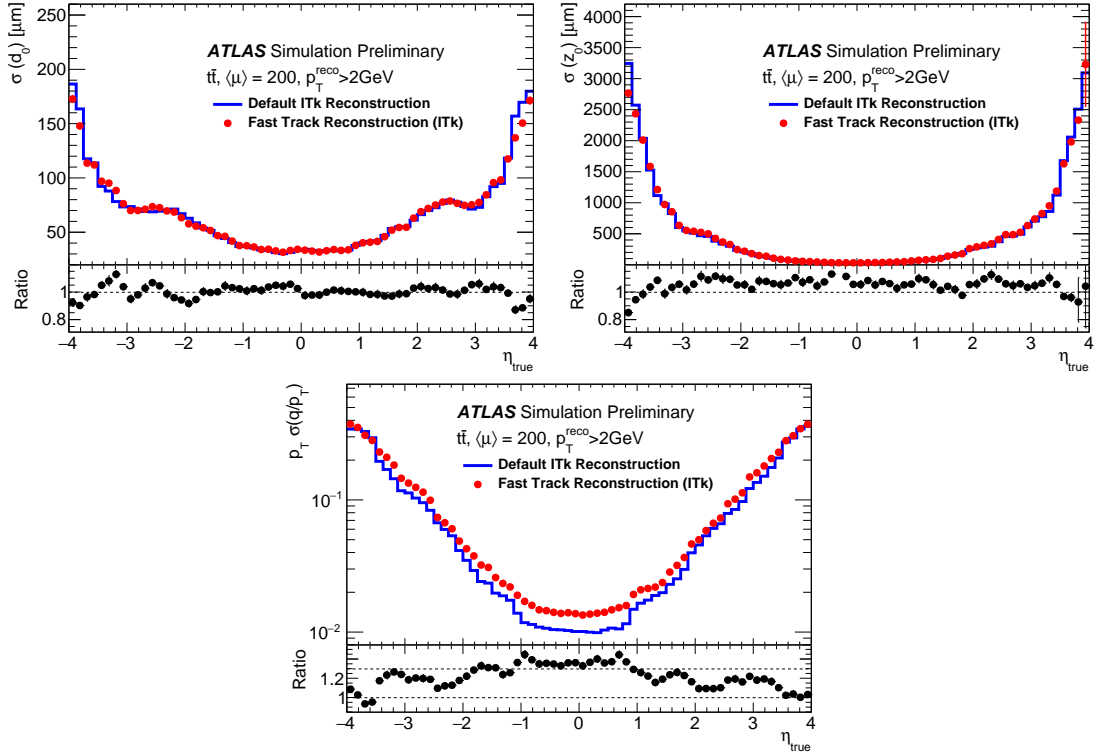
Figure 6.10: Resolution of d_0 (left), z_0 (right) and the relative p_T (bottom) for $t\bar{t}$ events with $\langle\mu\rangle = 200$. The figures are taken from Reference [112].

of the tracking code, which was measured to be up to a factor of approximately eight, a significant reduction was achieved. With respect to the physics performance, the trigger requirements are reachable as the demanded accuracy of the reconstruction is lower. For offline tracking the situation is more strict. Within this study certain approximations were applied and algorithms disabled to reduce the execution time. In order to obtain a comparable physics performance in the fast track reconstruction compared to the default configuration, the deviations coming from the modifications have to vanish. This encourages the need for a fast tracking software or a software that provides an improved physics performance in order to meet the expected HL-LHC requirements. The time measurements presented in Sec. 6.3.1 are preliminary and may change due to future code optimisations. Beside this optimisation branch, R&D is performed for different hardware architectures and algorithms. This provides an additional motivation for the ACTS project and for this thesis in particular as detailed modelling of the underlying problem.

7 Track Parameter Propagation

The data recorded by the detector consist of clusters that measure particle properties at a point or region. In order to measure the underlying physics quantities, track reconstruction is required. In terms of track reconstruction, each measurement needs to be assigned to the particle which produced it. A denser measurement environment increases the complexity of reconstruction and demands more precise solutions to perform the correct measurement-particle assignment. That issue becomes more important in the HL-LHC environment and its expected pile-up of up to 200.

This chapter describes the baseline components of the track reconstruction, the extrapolation, by using an initial parametrisation of the final state, given at a surface and extrapolating the estimation along the trajectory. The focus of this chapter is a derivation of an explicit expression of the extrapolation from Eq. (4.38) with respect to Eq. (4.39).

In order to make the underlying ideas for the estimation of the trajectory understandable, this chapter starts with simplest case, the so-called straight line approximation. Within this model the trajectory is assumed to be a straight line as given for neutral particles or in the absence of a magnetic field. Afterwards the deflection by a magnetic field is handled. Both scenarios are thereby considered in vacuum. Alongside both scenarios the parameters from Sec. 5.2.1 are reasoned as explicit formulation of λ from Chapter 4.

In Sec. 7.3 the behaviour of the covariance matrix under the extrapolation is investigated. Afterwards the influence of material upon the track parametrisation is considered. Those parts are a combination of previous works, mainly based on References [117–120] but the individual parts are streamlined into a consistent notation and reasoning and were implemented in ACTS as part of this thesis. The concepts are extended in the second part of this chapter. Firstly, within this thesis the lab time is introduced as additional parameter. With the main components presented, a broader perspective upon the extrapolation is considered. Thereby, a detector independent formulation of the different scenarios is formulated as part of this thesis and a top level management environment, the so-called *Propagator* is introduced. By combining both parts, a general implementation of Sec. 4.3 can be achieved. In the last part of this chapter, the found concepts and expressions for the extrapolation are compared with Geant4 [92, 93] simulations.

7.1 Straight Line Extrapolation

The extrapolation of a particles trajectory over a distance s can be understood as the modification of the model parameters λ. The chosen parameters of λ are thereby not uniquely defined. Hence, in HEP communities and collaborations there exist multiple

interchangeable parametrisations. For the purpose of consistency, only the parametrisation of the ATLAS collaboration is considered in the following.

The choice of parameters have to cover initially the parameters that can be measured by the detector, either with or without a coordinate transformation. Also, parameters may exist that influence the trajectory but are not measured. Those parameters can be linked to the measured parameters indirectly. Hence, the accuracy of these parameters may profit from the information in measurements. Also, parameters may be required that remain constant during the extrapolation, i.e. parameters that are not linked to measured parameters but affect the parametrisations behaviour during the extrapolation. Finally, the chosen parametrisation is not required to consist of the minimal set of parameters that achieve the objectives mentioned above and depend on the extrapolation model.

The simplest case for track parametrisation is the simplified model of a particle that moves in a straight line through the detector, without deflections by magnetic fields or material interactions. Such a track can be parametrised by

$$r \equiv \begin{pmatrix} x \\ y \\ z \end{pmatrix} \qquad T \equiv \begin{pmatrix} T^x \\ T^y \\ T^z \end{pmatrix} \qquad \lambda \equiv \begin{pmatrix} r \\ T \end{pmatrix} \tag{7.1}$$

with the Cartesian coordinates x, y, z and the directions T^x, T^y, T^z in the corresponding dimensions. The vector r represents the position of the particle and T is the (normalised) direction vector in which the particle moves. λ represents the entire parametrisation. r and T are thereby related with each other by

$$\frac{dr}{ds} = T = \text{const} \tag{7.2}$$

along a path length s. A classical silicon detector measures spatial coordinates. Thus, r is measured directly in those cases whereas T is connected indirectly to the measured parameters via the derivative in Eq. (7.2). Since the underlying model assumes a straight line, an extrapolation over the distance h can be expressed as

$$r(h) = r_0 + h \cdot T_0 \tag{7.3}$$

from the initial parametrisation r_0 and T_0. Splitting the total distance s into n extrapolation steps with length h_i for $i = \{1, ..., n\}$, then the parametrisation under extrapolation can be expressed as

$$\lambda(s) = \begin{pmatrix} r(s) \\ T(s) \end{pmatrix} = \begin{pmatrix} r_0 + \sum_{i=1}^{n} h_i \cdot T_0 \\ T_0 \end{pmatrix}$$

using the property from Eq. (7.2) and the iterative expression implied by Eq. (7.3). Hence, the property from Eq. (4.39) is fulfilled and the total distance s can be treated as tuple of multiple distances h_i. These parameters are able to describe the entire straight line trajectory in a global frame and the absence of magnetic and material effects.

Since it was found in Sec. 4.2.3 that the parametrisation is needed in the same coordinate system as the measurement, the corresponding local parameters in the measurement

frame need to be expressed. If the particle is represented at the surface, the (fixed) location of the surface in space provides geometrical data which can be used to reduce the amount of dimensions. In the straight line scenario the vectors become

$$r_\text{local} \equiv \begin{pmatrix} l_0 \\ l_1 \end{pmatrix} \qquad T_\text{local} \equiv \begin{pmatrix} \phi \\ \theta \end{pmatrix} \qquad \lambda_\text{local} \equiv \begin{pmatrix} r_\text{local} \\ T_\text{local} \end{pmatrix} \qquad (7.4)$$

with the azimuthal angle ϕ, the polar angle θ and the spatial coordinates l_0 and l_1 which are constrained to the surface. The angles are connected to the global parameters via Eq. (5.3). The spatial coordinates on the other hand depend on the underlying surface geometry as shown in Sec. 5.2.2.

With the appropriate transformation between the two track representations λ and λ_local an extrapolation of local parameters between surfaces and therefore from measurement to measurement is possible. Since the global parameters are not constrained by the requirement of a surface, it serves as an intermediate parametrisation. Consequently, the mean of the stepper function $S(s|\lambda)$ from Eq. (4.38) can be expressed as

$$\mu_\lambda^\text{local}(s) = H\mu_\lambda(s) = H\left(\mu_\lambda(0) + s\frac{d\mu_\lambda(0)}{ds}\right) = H\left(H^T\mu_{\lambda,0}^\text{local} + s\frac{d\left(H^T\mu_{\lambda,0}^\text{local}\right)}{ds}\right) \quad (7.5)$$

with the projection matrix $H \in \mathcal{R}^{4\times6}$ that performs the coordinate transformations. In comparison to H_A from Chapter 4, this matrix is not considered to be restricted to the measured parameters, though the projection into the measurement frame is possible afterwards. Thus, the entire parametrisation is transformed at surfaces allowing a consistent description from local parameters on one surface to local parameters on another surface. In addition, this expression demonstrates that only the global parametrisation needs to be considered during the extrapolation while the constraints due to the surfaces can be neglected. Those constraints are treated at both end points by an appropriate coordinate transformation. This observation will also be utilised in the following section.

7.2 Propagation of Charged Particle

The next step in the derivation of a general parameter extrapolation formalism can be obtained by considering an electrically charged particle in a magnetic field. The general expression of the trajectory of a particle is given by the Lorentz force [117]

$$F = m\frac{d^2r}{dt^2} = q\left(v \times B(r)\right)$$
$$\Leftrightarrow m|v|^2\frac{d^2r}{ds^2} = q|v|\left(\frac{v}{|v|} \times B(r)\right)$$
$$\Leftrightarrow \frac{d^2r}{ds^2} = \frac{q}{p}\left(T \times B(r)\right) \qquad (7.6)$$

with the magnetic field vector $B(r)$, the electric charge q and the absolute value of the particles momentum p. Thereby, the relation between the path length and the time

$ds = vdt$ and the expression for the direction vector $T = v/|v|$ were utilised. q/p can be understood as a curvature parameter since the value of q defines the direction of the deflection and the inverse momentum represents the radius of the trajectory. In the case of $p \to \infty$ eV, $q = 0$ C or $B(r) = 0$ T, the second derivative becomes $d^2r/ds^2 = 0$ which reproduces the straight line case[1]. Hence, the straight line can be understood as a special case of deflection under the Lorentz force.

Eq. (7.6) implies that the parameter q/p is important for the shape of the trajectory. Even if this parameter is never measured in the detector, its relation to r and T via the differential equation suggests an indirect learning about this parameter and thus an indirect affection of r and T on the other hand. Noteworthy are also the values of q. For the simplicity of notation it is presumed that $q \in \{-1, 0, 1\}$. Otherwise q/p has to be separated into two variables. In order to preserve the momentum information for neutral particles the parameter is stored as $1/p$. This is convenient to express both parameters in the units of an inverse energy. In summary, the parametrisation becomes in this case

$$\lambda^{\text{charged}} \equiv \begin{pmatrix} r \\ T \\ q/p \end{pmatrix} \qquad \lambda^{\text{neutral}} \equiv \begin{pmatrix} r \\ T \\ 1/p \end{pmatrix} \tag{7.7}$$

for charged and neutral particles respectively.

In simplified detector setups (e.g. for constant magnetic fields), the differential equation (7.6) has an analytical solution leading to a helical trajectory but has no analytical solution in a general case. As Fig. 3.14 shows for the ATLAS solenoid magnet and Sec. 3.2.4.1 for the toroid magnets, the magnetic field is inhomogeneous in the detector. In order to solve this problem, a numerical integration of the differential equation has to be performed.

7.2.1 Runge-Kutta-Nyström Integration of Fourth Order

The trajectory of charged particles in a magnetic field and in vacuum can be expressed by the differential equation from Eq. (7.6). As this is the physical description of the underlying behaviour, the solving of the differential equation is inevitable. If $B(r)$ is considered non-constant then the solution must be obtained from numerical integration.

For solving a differential equation many different algorithms exist that are specialised on aspects such as computational speed or accuracy. Since track reconstruction relies on both, an optimal mixture of both aspects needs to be found. While the form of Eq. (7.6) is given by nature, the choice of the integration method is eligible. A common choice to achieve both criteria and also the choice for ACTS is the Runge-Kutta-Nyström integration of fourth order [121] (RKN4).

The RKN4 method is a numerical integration method which allows the step-wise integration of a differential equation, i.e. the solution of the nth step is used to evaluate the $(n + 1)$th parameters which are the distance h along the trajectory away from the

---

[1]The straight line would be also given in principle in the case of $T \parallel B(r)$ but a common magnetic field in a HEP detector geometry is designed to avoid this case since in this case the q/p information cannot be obtained.

nth point. Based on the parametrisation of Eq. (7.1), the Eq. (7.6) can be formulated as

$$\frac{d}{ds}\begin{pmatrix} r \\ T \end{pmatrix} = \begin{pmatrix} \frac{dr}{ds} \\ \frac{d^2r}{ds^2} \end{pmatrix} = \begin{pmatrix} r' \\ \frac{q}{p}\left(T \times B(r)\right) \end{pmatrix} \equiv \begin{pmatrix} f_1(s, r, T) \\ f_2(s, r, T) \end{pmatrix} \tag{7.8}$$

and therewith as twice as many differential equations of first order[2]. The parameter q/p is considered to remain constant in the vacuum case and can therefore be neglected in the expression above. While in the continuous case the identity $r' = dr/ds = T$ is valid, in the discrete case the separation becomes important.

The RKN4 formalism requires the evaluation of four sub-steps or stages, which allow the evaluation of the the next. These sub-steps are given by [117]

$$\begin{aligned}
k_1^j &= f_j(s_n, r_n, T_n) \\
k_2^j &= f_j(s_n + \frac{h}{2}, r_n + \frac{h}{2}T_n + \frac{h^2}{8}k_1^2, T_n + \frac{h}{2}k_1^2) \\
k_3^j &= f_j(s_n + \frac{h}{2}, r_n + \frac{h}{2}T_n + \frac{h^2}{8}k_1^2, T_n + \frac{h}{2}k_2^2) \\
k_4^j &= f_j(s_n + h, r_n + hT_n + \frac{h^2}{2}k_3^2, T_n + hk_3^2)
\end{aligned} \tag{7.9}$$

and provide therewith an iterative evaluation process since each component depends on the previous one. Since in general the functions f_1 and f_2 are coupled, the solutions for r_{n+1} and T_{n+1} would depend on each other. By expressing the positions in k_2^j, k_3^j and k_4^j using the second order Taylor expansion around r_n and identifying the second derivative d^2r_n/ds^2 as the corresponding k_i^2 a decoupling of the two functions is achieved. As all k_i^j therewith depend on f_2, the order of evaluation is predefined.

The four expressions in Eq. (7.9) can be visualised as shown in Fig. 7.1. Based on the previous knowledge, the estimation of the underlying trajectory becomes more precise with each sub-step. In other terms, the method can be understood as an iterative application of corrections of the trajectory estimate. In order to obtain the parameters at the $(n+1)$th step, the equations

$$\begin{aligned}
T_{n+1} &= T_n + \frac{h}{6}\left(k_1^2 + 2k_2^2 + 2k_3^2 + k_4^2\right) \\
r_{n+1} &= r_n + hT_n + \frac{h^2}{6}\left(k_1^2 + k_2^2 + k_3^2\right)
\end{aligned} \tag{7.10}$$

need to be evaluated. Considering only the calculations of f_1 and therewith the solution for r_{n+1} the individual sub-steps of that extrapolation can be formulated in terms of the same k_i calculated for the extrapolation of T_{n+1}. This can be understood as an indirect modification of r_{n+1} based on the deflection affecting the direction. Moreover, the solution shows that for $k_i^2 = 0$ for $i = 1, 2, 3, 4$, the solution is identical to Eqs. (7.2)

---

[2]Although this might look like a bad trade, this can be compared to the solving of differential equations in classical mechanics using either Newton- or Lagrange-formalism. Hence, the problem becomes easier to solve.
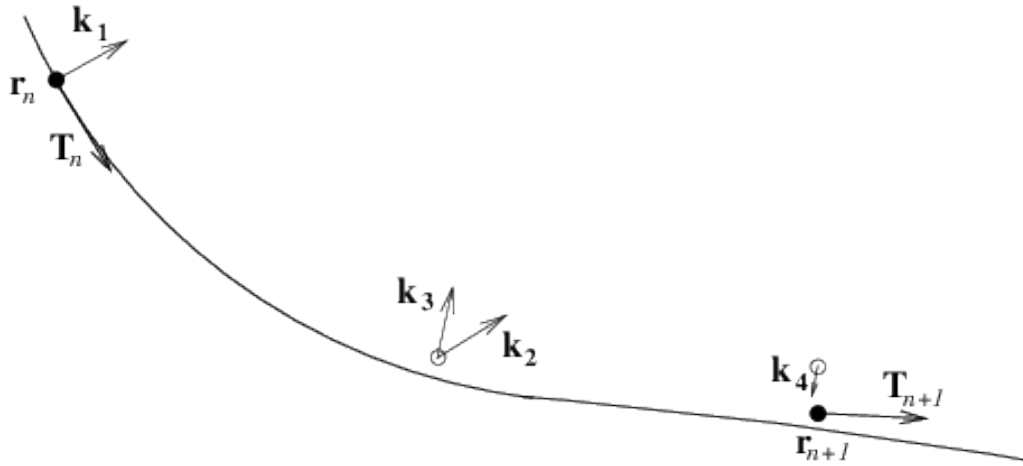
Figure 7.1: Step evaluation in the RKN4 formalism from the given nth point, parametrised by r_n and T_n, to the approximated $(n+1)th$ result via the evaluation of each component k_i at three different positions in parameter space. The black line shows the *true* trajectory for comparison [117].

and (7.3). This empathises the argument of a generalised solution of the straight line extrapolation for the case of absence of the Lorentz force in vacuum. On the other hand, the straight line would be also obtained using a Runge-Kutta-Nyström integration of first order. While the former case is linked to the underlying physical deflection, the latter case would enforce a straight line extrapolation for any trajectory by construction. As mentioned in the beginning of this section, the physical problem is fixed but the numerical integration method is chosen. Hence, the deciding criteria for choosing the method or as in this case the order of the integration is driven by the corresponding error related to the numerical integration. This will be discussed in the following.

7.2.2 Integration Error

Since the presented RKN4 method is a step-wise solution of the Eq. (7.6) by applying a numerical approach, there exists an intrinsic error on the results of each step. A common local error description is given by [117]

$$\epsilon \equiv \lambda_{n+1} - \hat{\lambda}_{n+1} \tag{7.11}$$

with the obtained parameter vector $\lambda = (r, T, q/p)^T$ and the vector $\hat{\lambda}$ obtained from third order calculations. While the goal would be a comparison to the true result, this idealised description is not applicable in real conditions since the true parameters are

unknown[3] and thus need to be approximated. Based on the Runge-Kutta-Fehlberg method [122], the step error can be approximated by comparison with a higher order solution. Although the estimated error is skewed to larger values, it has become the standard to utilise the lower order error estimation as error estimation of the higher order integration [117]. Furthermore, the lower order is fixed to three.

A common approach for the estimation is given by considering the Taylor expansions

$$\lambda_{n+1} = \lambda\left(s_n + h\right) = \lambda_n + h\lambda'(s_n) + \frac{h^2}{2}\lambda''(s_n) + \frac{h^3}{6}\lambda^{(3)}(s_n) + \frac{h^4}{24}\lambda^{(4)}(s_n) + \mathcal{O}(h^5)$$

around $\lambda_n = \lambda(s_n)$. This series is truncated in the RKN4 formalism at fourth order. All higher order terms consequently contribute to the error of the integration.

The Taylor expansion relies on the numerical evaluation of derivatives with the central difference quotient

$$\lambda'(s_n) \approx \frac{\lambda(s_n + \tilde{h}) - \lambda(s_n - \tilde{h})}{2\tilde{h}} \tag{7.12}$$

is used with the distance $\tilde{h}$[4]. Higher order derivatives can be calculated recursively. The usage of the central derivative allows the statement of a symmetric error around the evaluated point. Since the difference quotient delivers the correct derivative in the case

$$\lambda'(s_n) = \lim_{\tilde{h} \to 0} \frac{\lambda(s_n + \tilde{h}) - \lambda(s_n - \tilde{h})}{2\tilde{h}}$$

the used finite derivative from Eq. (7.12) is again associated with an error. Therefore the integration error of the RKN4 based on the Taylor expansion will be just an estimation of the true numerical error.

Assuming that the contributing terms can be treated in a descending order, i.e. higher order terms can be neglected, the fourth order term is treated as the error estimation term [117]

$$\epsilon \approx \frac{h^4}{24}\lambda^{(4)}(s_n + \frac{h}{2})$$

with the error estimation at the centre of the step due to the symmetric error of the derivatives in Eq. (7.12). Its evaluation [117] provides the error estimation

$$\epsilon \approx h^2(k_1^2 - k_2^2 - k_3^2 + k_4^2). \tag{7.13}$$

A remarkable feature of this estimation for the RKN4 is that the local error only depends on the step-size h (which is also the only free parameter of the k_i^j). In other terms, changing h reduces or increases the numerical integration error. While $\epsilon \neq 0$ can be expected for charged particles with finite momentum in magnetic fields, a certain error

---

[3]This is also valid if measurements are taken into account. The measurements give a hint to a set of true parameters but the underlying uncertainties make this inapplicable for a reliable estimation of ϵ.

[4]The notation was chosen to indicate that $\tilde{h}$ may be different from h, which is used as the extrapolation step-size.

tolerance τ has to be applied above which an adjustment is necessary. If the step size is modified, except for k_1^j all sub-steps need to be re-evaluated. In order to minimise the computational requirement, the adjustment has to be performed with the least amount of trials. On the other hand, the largest possible step-size below the error tolerance has to be taken to reduce the number of steps. A common solution for the adjustment from the step-size h_n to h_{n+1} is given by [117]

$$h_{n+1} = h_n \left(\frac{\tau}{[2]\,|\epsilon|} \right)^{\frac{1}{\xi+1}} \tag{7.14}$$

with the order ξ of the $\hat{\lambda}$ integration. The factor two in square brackets was added in order to reduce the error within less trials. For a fixed ξ, the error estimation from Eq. (7.11) is fixed. Thus, τ is the main parameter steering the step-size adjustment. As the fraction $\tau/|\epsilon|$ can lead to strong modifications step-wise while the external conditions usually change rather smoothly, an additional restriction is applied. A trimming for $\xi = 3$ provides as the next step-size a value in

$$\frac{1}{\xi+1} h_n = \frac{1}{4} h_n \leq h_{n+1} \leq (\xi+1)h_n = 4h_n. \tag{7.15}$$

This iterative adjustment ends as soon as the error estimation is below the tolerance. While the adjustment is performed as given in Eq. (7.14) and hence gets reduced steeper due to the additional scaling by the factor of two. Once the error is below the threshold, it can be assumed that there is a certain stretching of h possible without crossing the threshold as additionally, the accepted step size would be smaller or equal to the previously accepted step size, the steps get shorter while extrapolating. For that purpose, the step size is scaled one more time after the step is evaluated. This step size adjustment is then performed without the additional scaling factor and serves as initial guess for the next step. Thus, longer steps are possible and following the assumption that the environmental conditions change sufficiently slowly, the error estimate can be assumed to be valid for the next step.

The error calculations above assume fixed order calculations for the step evaluation as well as for the comparison step $\hat{\lambda}$. Additionally to the mentioned degrees of freedom for the step evaluation and error estimation, the distances for the k_i^j in Eq. (7.9) and the coefficients in Eqs. (7.10) and (7.13) are not fixed for a given order. Also the amount of k_i^j necessary for the step evaluation is flexible. These coefficients are described by a Butcher tableau [123]. The chosen coefficients allow due to the same position at k_2^j and k_3^j less accesses to the magnetic field $B(r)$. It is noteworthy that other conventions are possible, including different orders as mentioned in the previous section. This is however linked to the error estimation. Hence, beside the adjustment of h, the order of integration could be considered as additional adjustment parameter. With a convenient Butcher tableau, the required calculations in case of $|\epsilon| > \tau$ can be performed using a higher order integration. Therewith, two parameters can be theoretically adapted in order to obtain the optimal results. However, this is a more complex system as different computational complexities and error contributions have to be considered.

7.3 Covariance Transport

Beside the mean extrapolation as described in Secs. 7.1 and 7.2.1, the covariance matrix needs to be extrapolated. This will be considered within this section.

The extrapolation of the pdf is performed in general by Eq. (4.38). The modifications of the parameters under extrapolation will be denoted as $S'(\lambda|s)$ with $\dim(S'(\lambda|s)) = \dim(\lambda(\text{s}))$. For a given s the extrapolation of a parametrisation λ can be expressed in a Taylor series around the mean μ_λ:

$$S'(\lambda|s) = \lambda(s) = S'(\lambda|s)|_{\lambda=\mu_\lambda} + \left.\frac{\partial S'(\lambda|s)}{\partial \lambda}\right|_{\lambda=\mu_\lambda} (\lambda - \mu_\lambda) + \mathcal{O}(\lambda^2)$$

$$\approx \mu_\lambda(s) + J\,(\lambda - \mu_\lambda) \tag{7.16}$$

Thereby the short notation $J_{ij} = \partial S'(\lambda|s)_i / \partial \lambda_j|_{\lambda=\mu_\lambda}$ was used. By multiplying this equation with its transpose one obtains

$$(\lambda(s) - \mu_\lambda(s))\,(\lambda(s) - \mu_\lambda(s))^T = J\,(\lambda - \mu_\lambda)\,(\lambda - \mu_\lambda)^T\,J^T$$

$$\Rightarrow \Sigma_{\text{final}} = J\Sigma_{\text{initial}}J^T \tag{7.17}$$

with the covariance matrices Σ_{initial} and Σ_{final} before and after the extrapolation respectively. The matrix J can be identified as the Jacobian matrix. Thus, the extrapolation of the covariance matrix relies only on the calculation of said matrix. Furthermore, the transport via Jacobian matrices shows that the individual uncertainties can be related with each other. This relationship in terms of the Kalman filter allows to learn about parameters, even though they are not measured, indirectly through others parameters.

In order to obtain the Jacobian different concepts can be used. For ACTS two different concepts were implemented: Ridders algorithm and transport matrix formalism. While the former provides by design more robust results and relies on less assumptions than the transport matrix formalism it serves as verification algorithm for the latter one. The transport matrix formalism on the other hand is intended to be the main algorithm in the track reconstruction. Those two algorithms are described in the following.

7.3.1 Transport Matrix Formalism

Within this section the covariance matrix under extrapolation is described by the transport matrix formalism. The underlying concept is thereby based on Ref. [118].

The goal of the covariance transport is to obtain the final covariance matrix Σ_{final} at a given surface. It is related to the initial covariance matrix Σ_{initial} via Eq. (7.17). Since the covariance matrix is expressed in the same coordinate system as the mean and the extrapolation occurs from surface to surface, the initial and final parametrisation is, based on Eq. (7.4) given by

$$\lambda^{\text{local}} \equiv \begin{pmatrix} l_0 \\ l_1 \\ \phi \\ \theta \\ \frac{q}{p} \text{ or } \frac{1}{p} \end{pmatrix} \tag{7.18}$$

with the last entry depending on the particles charge. For simplicity q/p will be used in the following. The formalism is analogous for neutral particles. Additionally, since the extrapolation is considered to occur in vacuum, q/p is a constant.

The Jacobian is the matrix that needs to be calculated. Expressing the Jacobian by its definition from Eq. (7.16) with the parametrisation from Eq. (7.18) leads to

$$
J = \begin{pmatrix} \frac{\partial l_0^{\text{final}}}{\partial l_0^{\text{initial}}} & \cdots & \frac{\partial l_0^{\text{final}}}{\partial \frac{q}{p}^{\text{initial}}} \\ \vdots & \ddots & \vdots \\ \frac{\partial \frac{q}{p}^{\text{final}}}{\partial l_0^{\text{initial}}} & \cdots & \frac{\partial \frac{q}{p}^{\text{final}}}{\partial \frac{q}{p}^{\text{initial}}} \end{pmatrix} \Bigg|_{\lambda = \mu_\lambda} = \frac{\partial \lambda_{\text{final}}^{\text{local}}}{\partial \lambda_{\text{initial}}^{\text{local}}} \Bigg|_{\lambda = \mu_\lambda} . \tag{7.19}
$$

Here the short notation for the point of evaluation $\lambda = \lambda_{\text{initial}}^{\text{local}}$ and $\mu_\lambda = \mu_{\lambda,\text{initial}}^{\text{local}}$ was used. The parameters $\lambda_{\text{final}}^{\text{global}}$ are linked to the initial parameters through the extrapolation function.

This formalism is just based on the local parametrisation while the RKN4 track parameter extrapolation is formulated in global parameters. Since the extrapolation of the covariance matrix in a coordinate system different from the extrapolation of the mean provides additional complexity, the Jacobian needs to be treated in global parameters. A global treatment allows a direct application in the RKN4 formalism. Therefore, the local 5×5 Jacobian needs to be projected into the global 7×7 frame given by Eq. (7.7). This frame can treat the variation of the covariance matrix in a global parametrisation. This implies the application of coordinate transformations between the parametrisations similar to Eq. (7.5).

The transformation from local to global parameters can be considered by defining $S'(\lambda^{\text{local}}|0) = \lambda^{\text{global}}$. From Eq. (7.16) and the definition of the Jacobian in Eq. (7.19) one obtains the local to global Jacobian

$$
J_{g \leftarrow l} = \frac{\partial \lambda^{\text{global}}}{\partial \lambda^{\text{local}}} \Bigg|_{\lambda = \mu_\lambda} . \tag{7.20}
$$

Using this expression allows to define a Jacobian as

$$
J' = \frac{\partial \lambda_{\text{final}}^{\text{global}}}{\partial \lambda_{\text{initial}}^{\text{local}}} \Bigg|_{\lambda = \mu_\lambda} = \left(\frac{\partial \lambda_{\text{final}}^{\text{global}}}{\partial \lambda_{\text{initial}}^{\text{global}}} \cdot \frac{\partial \lambda_{\text{initial}}^{\text{global}}}{\partial \lambda_{\text{initial}}^{\text{local}}} \right) \Bigg|_{\lambda = \mu_\lambda}
$$

that expresses the dependency of the final, global parameter on the initial, local parameters. Before describing the second coordinate transformation for obtaining the final, local parameters dependency on the initial, local parameters, this matrix allows for a further discussion.

The form of the matrix $\partial \lambda_{\text{initial}}^{\text{global}} / \partial \lambda_{\text{initial}}^{\text{local}}$ depends only on the surface type. This dictates the required coordinate transformations in order to obtain the global parameters. Finally, the derivations of the transformations lead to this Jacobian.

The other matrix, $\partial\lambda_{\text{final}}^{\text{global}}/\partial\lambda_{\text{initial}}^{\text{global}}$ is entirely given in global parameters. As the RKN4 method leads to a step-wise extrapolation of the parameters, the same separation can be done here. Therewith one obtains

$$J' = \left(\frac{\partial\lambda_{\text{final}=n}^{\text{global}}}{\partial\lambda_{n-1}^{\text{global}}} \cdot ... \cdot \frac{\partial\lambda_1^{\text{global}}}{\partial\lambda_{\text{initial}}^{\text{global}}} \cdot \frac{\partial\lambda_{\text{initial}}^{\text{global}}}{\partial\lambda_{\text{initial}}^{\text{local}}}\right)\Bigg|_{\lambda=\mu_\lambda} \equiv J_n \cdot ... \cdot J_1 \cdot J_{g\leftarrow l} \tag{7.21}$$

The step-wise transport of the Jacobian follows therewith the steps evaluated for the mean. For the $(n+1)$th step the matrix J_{n+1} has to be calculated. An additional matrix-matrix multiplication then delivers the updated Jacobian J'. The evaluation of J_{n+1} will be considered in the following. For its calculation, the step evaluations from Eq. (7.10) are used. By direct calculation one obtains the derivatives

$$F_n \equiv \frac{\partial r_{n+1}}{\partial r_n} = \frac{\partial}{\partial r_n}\left(r_n + hT_n + \frac{h^2}{6}\left(k_1^2 + k_2^2 + k_3^2\right)\right)$$

$$= 1 + \frac{h^2}{6}\left(\frac{\partial k_1^2}{\partial r_n} + \frac{\partial k_2^2}{\partial r_n} + \frac{\partial k_3^2}{\partial r_n}\right)$$

$$F_n' \equiv \frac{\partial r_{n+1}}{\partial T_n} = \frac{\partial}{\partial T_n}\left(r_n + hT_n + \frac{h^2}{6}\left(k_1^2 + k_2^2 + k_3^2\right)\right)$$

$$= h1 + \frac{h^2}{6}\left(\frac{\partial k_1^2}{\partial T_n} + \frac{\partial k_2^2}{\partial T_n} + \frac{\partial k_3^2}{\partial T_n}\right)$$

$$G_n \equiv \frac{\partial T_{n+1}}{\partial r_n} = \frac{\partial}{\partial r_n}\left(T_n + \frac{h}{6}\left(k_1^2 + 2k_2^2 + 2k_3^2 + k_4^2\right)\right)$$

$$= \frac{h}{6}\left(\frac{\partial k_1^2}{\partial r_n} + 2\frac{\partial k_2^2}{\partial r_n} + 2\frac{\partial k_3^2}{\partial r_n} + \frac{\partial k_4^2}{\partial r_n}\right)$$

$$G_n' \equiv \frac{\partial T_{n+1}}{\partial T_n} = \frac{\partial}{\partial T_n}\left(T_n + \frac{h}{6}\left(k_1^2 + 2k_2^2 + 2k_3^2 + k_4^2\right)\right)$$

$$= 1 + \frac{h}{6}\left(\frac{\partial k_1^2}{\partial T_n} + 2\frac{\partial k_2^2}{\partial T_n} + 2\frac{\partial k_3^2}{\partial T_n} + \frac{\partial k_4^2}{\partial T_n}\right)$$

with the k_i^j as defined in Eq. (7.9). Those matrices form the Jacobian

$$J_{n+1} = \begin{pmatrix} F_n & F_n' & 0 \\ G_n & G_n' & 0 \\ 0 & 0 & 1 \end{pmatrix}. \tag{7.22}$$

The last row and last column are thereby defined by the constant q/p. Therewith the necessary calculations can be combined in the matrices

$$A_i \equiv \frac{\partial k_i^2}{\partial T_n} \qquad C_i \equiv \frac{\partial k_i^2}{\partial r_n} \tag{7.23}$$

As shown in Sec. 7.2.1, the vectors k_i^2 can be expressed by the second derivatives of r_n or by the first derivatives of $T_n = dr_n/ds$. Using Eq. (7.8), the system that needs to be

evaluated is therefore

$$
k_i^2\big|_{i\in[1,4]} = \begin{pmatrix} x_i'' \\ y_i'' \\ z_i'' \end{pmatrix}\Bigg|_{i\in[1,4]} = \begin{pmatrix} T_i^{x\prime} \\ T_i^{y\prime} \\ T_i^{z\prime} \end{pmatrix}\Bigg|_{i\in[1,4]} = \begin{pmatrix} \frac{q}{p}\left(T_i^y B_z\left(r_i\right) - T_i^z B_y\left(r_i\right)\right) \\ \frac{q}{p}\left(T_i^z B_x\left(r_i\right) - T_i^x B_z\left(r_i\right)\right) \\ \frac{q}{p}\left(T_i^x B_y\left(r_i\right) - T_i^y B_x\left(r_i\right)\right) \end{pmatrix}\Bigg|_{i\in[1,4]}
$$

with the subscription i for the parameters denoting the evaluation according to the right hand side of Eq. (7.9) at the points

$$
r_i = r_n + h_i T_n + \frac{h_i^2}{2} k_{i-1}^2 \tag{7.24}
$$

$$
T_i = T_n + h_i k_{i-1}^2. \tag{7.25}
$$

The coefficients are thereby defined through the utilised Butcher tableau as $h_i \in \{0, h/2, h/2, h\}$. The vector k_0^2 is considered arbitrary. The derivative of the resulting vectors provide the matrices

$$
A_i = \begin{pmatrix} \frac{\partial x_i''}{\partial T_n^x} & \frac{\partial x_i''}{\partial T_n^y} & \frac{\partial x_i''}{\partial T_n^z} \\ \frac{\partial y_i''}{\partial T_n^x} & \frac{\partial y_i''}{\partial T_n^y} & \frac{\partial y_i''}{\partial T_n^z} \\ \frac{\partial z_i''}{\partial T_n^x} & \frac{\partial z_i''}{\partial T_n^y} & \frac{\partial z_i''}{\partial T_n^z} \end{pmatrix}
$$

$$
= \begin{pmatrix} 0 & \frac{q}{p}\frac{\partial T_i^y}{\partial T_n^y}B_z\left(r_i\right) & -\frac{q}{p}\frac{\partial T_i^z}{\partial T_n^z}B_y\left(r_i\right) \\ -\frac{q}{p}\frac{\partial T_i^x}{\partial T_n^x}B_z\left(r_i\right) & 0 & \frac{q}{p}\frac{\partial T_i^z}{\partial T_n^z}B_x\left(r_i\right) \\ \frac{q}{p}\frac{\partial T_i^x}{\partial T_n^x}B_y\left(r_i\right) & -\frac{q}{p}\frac{\partial T_i^y}{\partial T_n^y}B_x\left(r_i\right) & 0 \end{pmatrix}
$$

and

$$
C_i = \begin{pmatrix} \frac{\partial x_i''}{\partial x_n} & \frac{\partial x_i''}{\partial y_n} & \frac{\partial x_i''}{\partial z_n} \\ \frac{\partial y_i''}{\partial x_n} & \frac{\partial y_i''}{\partial y_n} & \frac{\partial y_i''}{\partial z_n} \\ \frac{\partial z_i''}{\partial x_n} & \frac{\partial z_i''}{\partial y_n} & \frac{\partial z_i''}{\partial z_n} \end{pmatrix}
$$

$$
= \begin{pmatrix} \frac{q}{p}\left(\frac{\partial B_z(r_i)}{\partial x_n}T_i^y - \frac{\partial B_y(r_i)}{\partial x_n}T_i^z\right) & \frac{q}{p}\left(\frac{\partial B_z(r_i)}{\partial y_n}T_i^y - \frac{\partial B_y(r_i)}{\partial y_n}T_i^z\right) & \frac{q}{p}\left(\frac{\partial B_z(r_i)}{\partial z_n}T_i^y - \frac{\partial B_y(r_i)}{\partial z_n}T_i^z\right) \\ \frac{q}{p}\left(\frac{\partial B_x(r_i)}{\partial x_n}T_i^z - \frac{\partial B_z(r_i)}{\partial x_n}T_i^x\right) & \frac{q}{p}\left(\frac{\partial B_x(r_i)}{\partial y_n}T_i^z - \frac{\partial B_z(r_i)}{\partial y_n}T_i^x\right) & \frac{q}{p}\left(\frac{\partial B_x(r_i)}{\partial z_n}T_i^z - \frac{\partial B_z(r_i)}{\partial z_n}T_i^x\right) \\ \frac{q}{p}\left(\frac{\partial B_y(r_i)}{\partial x_n}T_i^x - \frac{\partial B_x(r_i)}{\partial x_n}T_i^y\right) & \frac{q}{p}\left(\frac{\partial B_y(r_i)}{\partial y_n}T_i^x - \frac{\partial B_x(r_i)}{\partial y_n}T_i^y\right) & \frac{q}{p}\left(\frac{\partial B_y(r_i)}{\partial z_n}T_i^x - \frac{\partial B_x(r_i)}{\partial z_n}T_i^y\right) \end{pmatrix}
$$

without the explicit evaluations of the derivatives of some components whose terms are very oblong and therefore skipped at this point to keep it readable.

One can see that many calculations reoccur in the evaluation of A_i and C_i. Therefore, the overview indicates performance optimisation possibilities. Especially if one considers that these components need to be calculated iteratively for each i and combined for the transport Jacobian J_{n+1}. Additionally, the matrix C_i contains several components of the gradient $\nabla_{r_n}B\left(r_i\right)$ which appear multiple times. Under the assumption that the magnetic field does not change too rapidly within a single step, it can be approximated that $C_i \approx 0$ for $i \in [1,4]$.

Beside the consideration of the charged particle covariance transport, the straight line can be considered. As mentioned in Sec. 7.2.1, the straight line extrapolation is obtained from the charged particle RKN4 integration for $q = 0$. This leads to $k_i^j = 0$ and consequently to a simpler Jacobian J_{n+1} compared to Eq. (7.22) but based on the same calculations:

$$J_{n+1} = \begin{pmatrix} 1 & 0 & 0 & h & 0 & 0 & 0 \\ 0 & 1 & 0 & 0 & h & 0 & 0 \\ 0 & 0 & 1 & 0 & 0 & h & 0 \\ 0 & 0 & 0 & 1 & 0 & 0 & 0 \\ 0 & 0 & 0 & 0 & 1 & 0 & 0 \\ 0 & 0 & 0 & 0 & 0 & 1 & 0 \\ 0 & 0 & 0 & 0 & 0 & 0 & 1 \end{pmatrix}$$

While the $J_{g \leftarrow l}$ are identical to the charged particle case, the same formalism is applicable for the straight line scenario. If applicable, the computational complexity can be drastically reduced. Consequently, the strict separation between the charged particle and straight line extrapolation is motivated through this complexity argument despite both calculations would lead to the same result for a straight line trajectory.

The result of the considerations above are that the necessary calculations required for the modification of the covariance matrix under extrapolation can be transformed into smaller problems denoted by Eq. (7.23). The components of the Jacobian within this section are given by Eq. (7.21).

7.3.1.1 Jacobian to Curvilinear and Bound Parameters

In the last section the transport of the covariance matrix in the extrapolation of the track parameters was introduced. It was shown that an initial, local covariance matrix is transported by calculating the Jacobian from Eq. (7.19). While the last section described the separation of the Jacobian into multiple matrices as shown in Eq. (7.21), the therewith obtained result would be given in global parameters. Within this section the Jacobian for the dependency of the final, local parameters on the final, global parameters is considered. By thinking of the covariance matrix as a cone around the mean during the extrapolation, the last missing connection between J and J' becomes a projection of the cone on the surface.

Two major projection types have to be considered. Both can be understood as a cut of the target surface through this cone in order to obtain the result. The first type is given by the curvilinear surface, the second by other surfaces. While the former is a plane surface which is by definition orthogonal to the particle direction at any point along the trajectory and therewith definable for any value of s, the latter one refers to a surface that is fixed in space and shape. Since both projections are a onto a surface, the requirements for the Jacobian are fulfilled for both. Those two types are presented in the following.

Curvilinear surfaces

This section will consider the transport Jacobian of a local track parametrisation to a point in parameter space which then will be expressed in curvilinear parameters. Given that J' is already calculated, the final, global mean $\mu_\lambda^{\text{global}}$ is considered as a point on the curvilinear surface. The connection between parameter vectors λ^{global} and λ^{local} is given by a coordinate transformation, if λ^{global} is at the surface corresponding to the transformation. Additionally, as just the mean is considered to be at the surface, this is not guaranteed for $\lambda^{\text{global}} \neq \mu_\lambda^{\text{global}}$. This means that for a given s that fulfils the requirements set for $\mu_\lambda^{\text{global}}$ an additional extrapolation for other parameter vectors are required. From Eq. (7.10) with the corresponding coordinate transformations to obtain λ^{local}, the local, final parameter vector can be expressed as Taylor series expansion around s. This leads to

$$
\lambda^{\text{local}}(\tilde{s} = s + ds) = \lambda^{\text{local}}(s')\Big|_{s'=s} + \frac{\partial \lambda^{\text{local}}(s')}{\partial s'}\Big|_{s'=s}(\tilde{s} - s) + \mathcal{O}\left(s^2\right)
$$
$$
\approx \lambda^{\text{local}}(s) + \frac{\partial \lambda^{\text{local}}(s')}{\partial s'}\Big|_{s'=s} ds. \tag{7.26}
$$

Noteworthy is for this expression the definition of the curvilinear surface itself. Although it is not assumed that $\lambda^{\text{global}}(s)$ is at the target surface, an equivalent surface can be defined for all values of s. Therewith it allows the expression of the first addend. Another justification of this addend is given by following the application in the Jacobian as it involves the evaluation at $\lambda = \mu_\lambda$ which is a point at the target surface by definition.

Compared to the considerations required for $J_{g\leftarrow l}$ in Eq. (7.20), Eq. (7.26) has an additional path length dependency. Putting this together with Eq. (7.19) and Eq. (7.21) leads to

$$
J = \frac{\partial \lambda_{\text{final}}^{\text{local}}}{\partial \lambda_{\text{initial}}^{\text{local}}}\Big|_{\lambda=\mu_\lambda} = \left(\frac{\partial \lambda^{\text{local}}(s)}{\partial \lambda_{\text{initial}}^{\text{local}}} + \frac{\partial \lambda^{\text{local}}(s')}{\partial s'}\Big|_{s'=s} \frac{\partial s}{\partial \lambda_{\text{initial}}^{\text{local}}}\right)\Big|_{\lambda=\mu_\lambda}
$$
$$
= \left(\frac{\partial \lambda^{\text{local}}(s)}{\partial \lambda_n^{\text{global}}}\right)\Big|_{\lambda=\mu_\lambda} \cdot J_n \cdot \ldots \cdot J_1 \cdot J_{g\leftarrow l} + \left(\frac{\partial \lambda^{\text{local}}(s')}{\partial s'}\Big|_{s'=s} \frac{\partial s}{\partial \lambda_{\text{initial}}^{\text{local}}}\right)\Big|_{\lambda=\mu_\lambda}
$$
$$
= J_{l\leftarrow g} J' + J_{\text{projection}} \tag{7.27}
$$

with the required number of steps n to reach the target surface and the Jacobians $J_{l\leftarrow g} \equiv \left(\partial \lambda^{\text{local}}(s)/\partial \lambda_n^{\text{global}}\right)\Big|_{\lambda=\mu_\lambda}$, $J' = J_n \cdot \ldots \cdot J_1 \cdot J_{g\leftarrow l}$ and $J_{\text{projection}} \equiv \left(\left(\partial \lambda^{\text{local}}(s')/\partial s'\right)\Big|_{s'=s} \partial s/\partial \lambda_{\text{initial}}^{\text{local}}\right)\Big|_{\lambda=\mu_\lambda}$. Analogous to $J_{g\leftarrow l}$, the matrix $J_{l\leftarrow g}$ is defined by the coordinate transformations from the specific surface.

The matrix J' is discussed in the previous section but the matrix $J_{\text{projection}}$ on the other hand requires further explanations.

The expression can be transformed by taking the corresponding global parameters into account:

$$\left(\left. \frac{\partial \lambda^{\text{local}}(s')}{\partial s'} \right|_{s'=s} \frac{\partial s}{\partial \lambda^{\text{local}}_{\text{initial}}} \right) \Bigg|_{\lambda=\mu_\lambda} = \left(\left. \frac{\partial \lambda^{\text{local}}(s)}{\partial \lambda^{\text{global}}(s)} \frac{\partial \lambda^{\text{global}}(s')}{\partial s'} \right|_{s'=s} \frac{\partial s}{\partial \lambda^{\text{local}}_{\text{initial}}} \right) \Bigg|_{\lambda=\mu_\lambda}$$

$$= J_{l\leftarrow g} \left(\begin{array}{c} r'_n \\ T'_n \\ \frac{q'}{p} \end{array} \right) \Bigg|_{\lambda=\mu_\lambda} \frac{\partial s}{\partial \lambda_{\text{localinitial}}}$$

$$= J_{l\leftarrow g} \left(\begin{array}{c} T_n \\ k^2_{4,n-1} \\ 0 \end{array} \right) \Bigg|_{\lambda=\mu_\lambda} \frac{\partial s}{\partial \lambda_{\text{localinitial}}} \tag{7.28}$$

with the derivatives r'_n and T'_n of the global parameters after n steps. By definition $r'_n = T_n$ and with the fourth sub-step of the $(n-1)$th step $k^2_{4,n-1}$, T'_n can be calculated through the definition. This sub-step can be evaluated directly from the constructions of the RKN4 step. Since q/p is assumed to be constant, its derivative is zero.

The last factor that is missing here is an expression for the remaining path length ds onto the surface. In order to derive an expression, the total differential of the global, final position mean $r(s)$, can be considered based on [120]

$$dr(s) = \frac{\partial r(s)}{\partial \lambda^{\text{local}}_{\text{initial}}} d\lambda^{\text{local}}_{\text{initial}} + \frac{\partial r(s)}{\partial s} ds = \frac{\partial r(s)}{\partial \lambda^{\text{local}}_{\text{initial}}} d\lambda^{\text{local}}_{\text{initial}} + T(s) ds \tag{7.29}$$

$$\Leftrightarrow T^T(s) dr(s) = T^T(s) \frac{\partial r(s)}{\partial \lambda^{\text{local}}_{\text{initial}}} d\lambda^{\text{local}}_{\text{initial}} + T^T(s) T(s) ds$$

$$\Leftrightarrow 0 = T^T(s) \frac{\partial r(s)}{\partial \lambda^{\text{local}}_{\text{initial}}} d\lambda^{\text{local}}_{\text{initial}} + ds \tag{7.30}$$

$$\Leftrightarrow \frac{\partial s}{\partial \lambda^{\text{local}}_{\text{initial}}} = -T^T(s) \frac{\partial r(s)}{\partial \lambda^{\text{local}}_{\text{initial}}} \tag{7.31}$$

with the global, final direction mean $T(s)$. Due to the definition of the curvilinear surface to be orthogonal to the direction vector and since every position variation of the mean $dr(s)$ has to be on the surface by definition, the dot product $T^T(s) dr(s)$ becomes zero. Due to the normalisation of the direction vector, the dot product $T^T(s) T(s)$ is one.

The right hand side of Eq. (7.31) becomes under this transformation an expression of the path length dependency on the initial, local parameters. By combining this result with Eq. (7.28) the second addend of Eq. (7.27) becomes

$$J_{\text{projection}} = J_{l\leftarrow g} \cdot \left(\begin{array}{ccc} \frac{\partial x_{\text{global}}(s)}{\partial s} T(s) \frac{\partial r(s)}{\partial x^{\text{local}}_{\text{initial}}} & \cdots & \frac{\partial x_{\text{global}}(s)}{\partial s} T(s) \frac{\partial r(s)}{\partial \lambda^{\text{local}}_{\text{initial}}} \\ \vdots & \ddots & \vdots \\ \frac{\partial \frac{q}{p}_{\text{global}}(s)}{\partial s} T(s) \frac{\partial r(s)}{\partial x^{\text{local}}_{\text{initial}}} & \cdots & \frac{\partial \frac{q}{p}_{\text{global}}(s)}{\partial s} T(s) \frac{\partial r(s)}{\partial \lambda^{\text{local}}_{\text{initial}}} \end{array} \right).$$

Therewith, all components required for the Jacobian are present and the covariance matrix modifications under extrapolation can be calculated using the initial formalism from Eq. (7.17).

Bound surfaces

For bound surfaces the approach is similar to curvilinear surfaces. Since the Jacobians $J_{l \leftarrow g} J'$ from Eq. (7.27) only depends on the coordinate transformations related to the underlying surface, no further considerations are required. For $J_{\text{projection}}$ the conceptual differences between the curvilinear and the bound surface have to be considered. While the former is definable for any s and is by definition orthogonal to the direction vector mean, the bound surface is considered fixed in shape, position and orientation. This has on the one hand the effect that $\lambda^{\text{local}}(s)$ from Eq. (7.26) is theoretically just valid for $\lambda^{\text{global}}(s) = \mu_\lambda^{\text{global}}$. However, a surface similar to the target surface can be defined for the sole purpose of a coordinate transformation. Again as in the curvilinear case, the justification for this approach is given posterior by the evaluation parameters of the matrix $J_{l \leftarrow g}$.

The other difference to the former scenario is given by the derivation of $\partial s / \partial \lambda_{\text{initial}}^{\text{local}}$. While the orthogonality criterion of the curvilinear surface simplified the problem and led to the final expression in Eq. (7.31), the handling of a bound surface is more complicated. In order to obtain the left hand side of Eq. (7.30), the vector orthogonal to $dr(s)$ has to be utilised. This vector is given by the normal vector on the surface at $r(s)$. Denoting this vector as I, leads to the modified equation

$$\Leftrightarrow I^T dr(s) = I^T \frac{\partial r(s)}{\partial \lambda_{\text{initial}}^{\text{local}}} d\lambda_{\text{initial}}^{\text{local}} + I^T T(s) ds$$

$$\Leftrightarrow 0 = I^T \frac{\partial r(s)}{\partial \lambda_{\text{initial}}^{\text{local}}} d\lambda_{\text{initial}}^{\text{local}} + I^T T(s) ds$$

$$\Leftrightarrow \frac{\partial s}{\partial \lambda_{\text{initial}}^{\text{local}}} = - \frac{I^T}{I^T T(s)} \frac{\partial r(s)}{\partial \lambda_{\text{initial}}^{\text{local}}}$$

and hence to a generalised formulation of the curvilinear case with $I = T(s)$.

Noteworthy is thereby that the transport of the covariance matrix as defined in Eq. (7.17) is a first order solution of the problem. Since a bound surface is, other than the curvilinear surface not restricted to a certain shape the conic section performed by the projection does not have to provide a symmetric uncertainty interval. Also a surface boundary could be considered which leads to a partial intersection of the uncertainty cone and the target surface. Within ACTS the surfaces are assumed to be sufficiently planar at the intersection region, such that they can be approximated by a plane. By neglecting the boundaries during the projection, the normal distributed feature of the track parametrisation can be conserved. This approximation is not taken into account for the intersection of the mean. In addition, the coordinate system related to a certain surface type remains applicable despite the approximations.

7.3.2 Ridders Algorithm

The covariance matrix gets modified during extrapolation according to Eq. (7.17). This requires the calculations of the Jacobian as shown in Eq. (7.19). While Sec. 7.3.1 demonstrated a computational efficient way for the calculation of the Jacobian, its correctness

requires validation. For that purpose an alternative has been implemented in ACTS. Based on a concept [124] named within ACTS after the author C.F.J. Ridders, the entries of the Jacobian can be evaluated by multiple extrapolations.

The general idea on Eq. (7.16) for $\lambda = \mu_\lambda + \Delta\lambda$ is leading to

$$\left. \frac{\partial S'(\lambda|s)}{\partial \lambda} \right|_{\lambda=\mu_\lambda} \approx \frac{S'(\mu_\lambda + \Delta\lambda|s) - S'(\mu_\lambda|s)}{\Delta\lambda}. \tag{7.32}$$

The approximative nature of the solutions is given by neglecting the higher order terms of the series. While the left hand side corresponds to the required Jacobian matrix, the right hand side depends only on the extrapolation of the mean. Hence, multiple extrapolations with different initial parameters lead to an approximation of the correct result. While the problem addressed by Ridders for calculating the derivative of a function with increasing accuracy, the implementation for ACTS is centred around a lower accuracy. The goal remains thereby to obtain a reference value for the transport matrix formalism. Hence, although the name for the procedure is kept, the actual workflow is simplified compared to [124].

As λ is a vector and the Jacobian entries are defined as component-wise derivatives, additional structure is required. The structure of the Jacobian is such that the jth column is given by

$$J_j = \frac{\partial S'(\lambda|s)}{\partial \lambda_j}.$$

As the extrapolated result is derived by a single component, $\Delta\lambda$ has to be restricted to a single non-zero entry. This also involves that a variation of the initial parameters will provide derivatives of a single column in the Jacobian. Hence, the variation has to be performed for all parameters in λ independently.

The dimensionality of the parametrisation leads to a higher computational complexity. Rather than aiming for a single high precision evaluation of the Jacobian, multiple finite differences are calculated, symmetrically and component-wise spread around μ_λ. This leads to a set of derivatives according to Eq. (7.32). As this is a first order derivative of an unknown and hence arbitrary complicated distribution, a mixture between variations and numerical stability have to be found. It was found that variations for numerical values of $\pm 4 \cdot 10^{-4}$ and $\pm 2 \cdot 10^{-4}$ around μ_λ provide, independent of the considered parameter, suitable results. This generalisation of variations for all parameters in λ is possible due to the underlying system of units. Thus, the order of magnitude of parameters is equalised.

As the extrapolation distance and end-point surfaces are not fixed, the Ridders extrapolation provides a flexible tool for comparing and validating the covariance matrix extrapolation. The extrapolation of the mean as underlying mechanism shows to be, despite the underlying approximations, a robust algorithm that can be applied using existing features in ACTS.

7.4 Extrapolation in Magnetic Fields with Material Interactions

In the previous sections, the track parameter extrapolation for the mean and the co-variance matrix were introduced. The required modifications of the parameters were considered in the context of a straight line trajectory as well as a trajectory under the influence of magnetic field deflections. It was furthermore shown that the former case can be considered a special scenario of the latter one for $k_i^j = 0$ with $j = 1, 2$ and $i = 1, 2, 3, 4$. For the underlying equation of motion in Eq. (7.6) the parameter q/p was introduced. This parameter was treated as a constant along the extrapolation, i.e. the extrapolations were assumed to occur in vacuum. Although this is true for q, the absolute value of the momentum p is usually not constant along the propagation due to interactions with the detector material, e.g. for the production of measurements. In this section a changeable momentum will be treated. For this purpose the extrapolation of the particle parameters will be considered in the following for two different cases:

1. In an environment with discrete detector material

2. In a continuous material

7.4.1 Discrete Material Interaction

In a tracking detector, the dominant fraction of material is located at discrete locations described by surfaces. Due to the material mapping the effect of the air in the detector is mapped onto the surfaces. Therewith it is assumed that between the surfaces just vacuum is present. This simplification allows the application of the previously derived formalism between the surfaces. Furthermore this chapter considers the extrapolation of track parameters while the particle is not effected by inelastic interactions and decay. As the occurrence of such effects are not deterministically predictable, a data driven handling is required, including potential re-processing of the measurements. Additionally, minor effects upon the track parameters are neglected.

The first effect considered on the particles momentum is given by the energy loss due to excitation and ionisation of lattice atoms. A charged particle in matter loses energy along the propagation through it. Although it is a discrete procedure, it can be approximated as a continuous interaction. Additionally, the individual energy loss is a statistical quantity. Consequently the interaction is described by the mean of the energy losses, denoted by the mean operator $\langle \cdot \rangle$. The stopping power is thereby described in multiple regions as shown in Fig. 4.2. In an intermediate momentum region the mean energy loss $\langle dE/ds \rangle$ per path length s is described by the Bethe-Bloch formula [17]. In natural units it is given by

$$\langle \frac{dE}{ds} \rangle_{\mathrm{BB}} = -Kq^2 \frac{Z\rho}{A\beta^2} \left(\frac{1}{2} \ln \left(\frac{2m_e\beta^2\gamma^2 T_{\max}}{I^2} \right) - \beta^2 - \frac{\delta}{2} \right). \qquad (7.33)$$

An explanation of the used variables can be found in Tab. C.1.

Based on [119] additional terms have to be considered, starting with the energy loss due to bremsstrahlung. The Bethe-Heitler equation [125] provides an expression for the

mean energy loss of charged, relativistic particles due to bremsstrahlung in matter

$$\langle\frac{dE}{ds}\rangle_{\mathrm{BH}} = -\frac{E}{X_0}\left(\frac{m_e}{m}\right)^2 \tag{7.34}$$

with the radiation length X_0 and the particles mass m. Additionally, energy loss effects for muons are considered. As described in [119], a $\mu^{\pm}$ may lose energy due to direct e^+e^- pair production (PP) and photonuclear interaction (PI). This is parametrised for two different intervals of energy, $E \in (8\mathrm{GeV}, 1\mathrm{TeV})$ and $E \geq 1\mathrm{TeV}$ by the functions

$$\langle\frac{dE}{ds}\rangle_{\mathrm{PP+PI}}^{E\in(8\mathrm{GeV},1\mathrm{TeV})} = 0.5345\frac{1}{X_0}\mathrm{MeV} - 6.803\cdot 10^{-5}\frac{E}{X_0}$$
$$- 2.2278\cdot 10^{-11}\frac{E^2}{X_0}\mathrm{MeV}^{-1}$$
$$+ 9.899\cdot 10^{-18}\frac{E^3}{X_0}\mathrm{MeV}^{-2} \tag{7.35}$$
$$\langle\frac{dE}{ds}\rangle_{\mathrm{PP+PI}}^{E\geq 1\mathrm{TeV}} = 2.986\frac{1}{X_0}\mathrm{MeV} - 9.253\cdot 10^{-5}\frac{E}{X_0}$$

An illustration of the individual impact of the radiative contributions to the total energy loss are shown in Fig. 7.2.

As all these effects may occur concurrently and continuously in material, they are combined as

$$g \equiv \langle\frac{dE}{ds}\rangle_{\mathrm{BB}} + \langle\frac{dE}{ds}\rangle_{\mathrm{BH}} + \langle\frac{dE}{ds}\rangle_{\mathrm{PP+PI}} \tag{7.36}$$

denoting the case sensitive[5] total differential energy loss per unit path length. Hence, the overall energy loss in matter is described by the sum of all effects. Although each component has a certain distribution, it is usually a sufficient good approximation to just consider their combined mean in order to take the effects into account. For that reason only g will be considered in the following.

As this energy loss is a statistical process, beside the modification of the q/p mean via the energy loss, a contribution to the covariance matrix has to be considered.

The energy loss and thus the momentum loss in material is not normal distributed. In the context of the Kalman filter, especially in Sec. 4.3.1.1 measurements are modelled using multivariate normal distributions. As the material can be mapped onto surfaces like in a common tracking detector, the impact of the detector material on the particle properties can be considered as small. This includes that a detector element is as thin as possible in terms of interaction lengths which the particle has to traverse in order to minimise the energy loss. Therewith the disturbance of the trajectory is minimised. On the other hand the detector element requires a certain thickness in order to produce a measurement. The mixture between both issues is a commonly thin detector element with a small radiation length X_0. In the case of the ATLAS pixel detector, a planar module is 300 μm thick [126]. As shown in Fig. 7.3, the energy loss can be approximated by a Landau-Vavilov function. By utilising the full width at half maximum (fwhm) in

---

[5]This refers to the differences in the energy loss depending on the particle type and the energy regime.
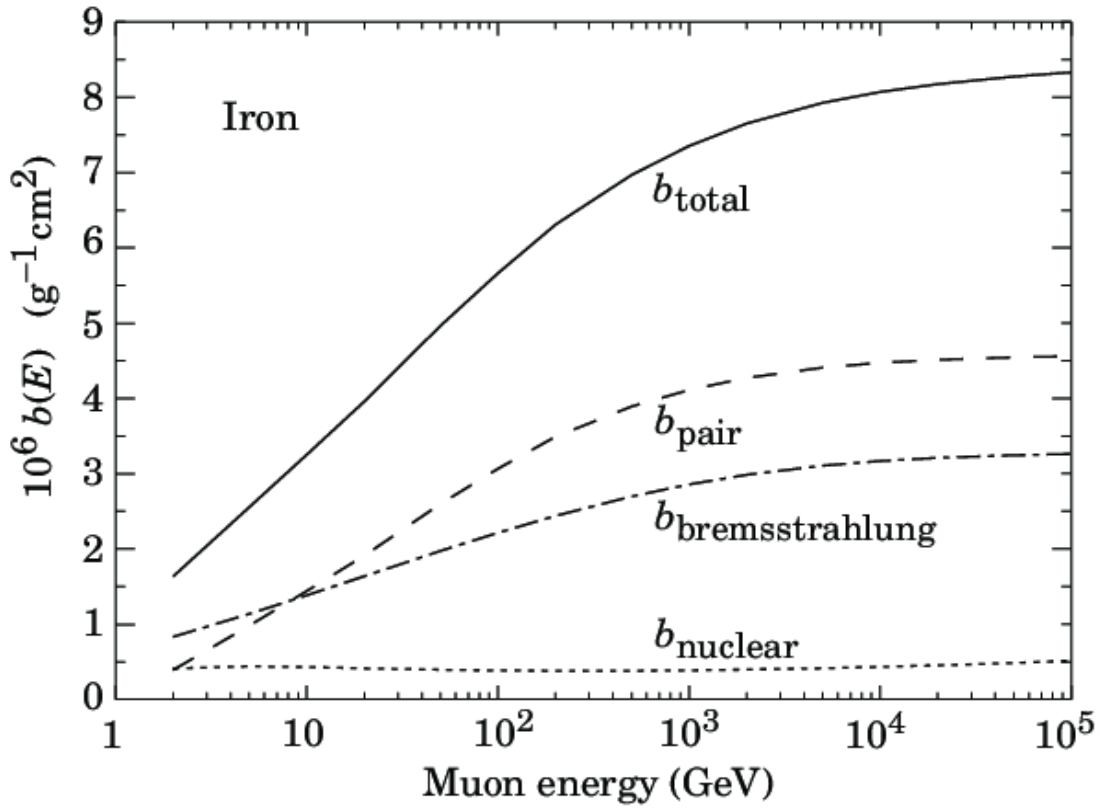
Figure 7.2: Composition of the radiative mechanisms of muons in iron as a function of the muon energy. The function $b(E)$ denotes the mean energy loss per path length [17].

order to approximate the standard deviation σ of a normal distribution as

$$\mathrm{fwhm} = 2\sqrt{2\ln(2)}\sigma_E$$

$$\Leftrightarrow \sigma_E = \frac{4(K/2)(Z/A)\rho\Delta s(q^2/\beta^2)}{2\sqrt{2\ln(2)}}$$

using the physical description of the fwhm from [17]. The term Δs describes the thickness of the material. As the parameter vector from Eq. (7.7) describes q/p, the found standard deviation has to be transformed:

$$\sigma_{q/p}^2 = \left(\frac{d\frac{q}{p}}{dE}\right)^2 \sigma_E^2 = \left(\frac{d}{dE}\frac{q}{\sqrt{E^2 - m^2}}\right)^2 \sigma_E^2 = \frac{q^2}{\beta^2 p^4}\sigma_E^2. \tag{7.37}$$

In addition to the energy loss, the particle scattering within the material has to be considered. It is assumed that those interactions are fully elastic and hence only change the particles direction. As this (multiple) scattering is again a statistical quantity, the mean and covariance matrix have to be considered. While the mean of the energy
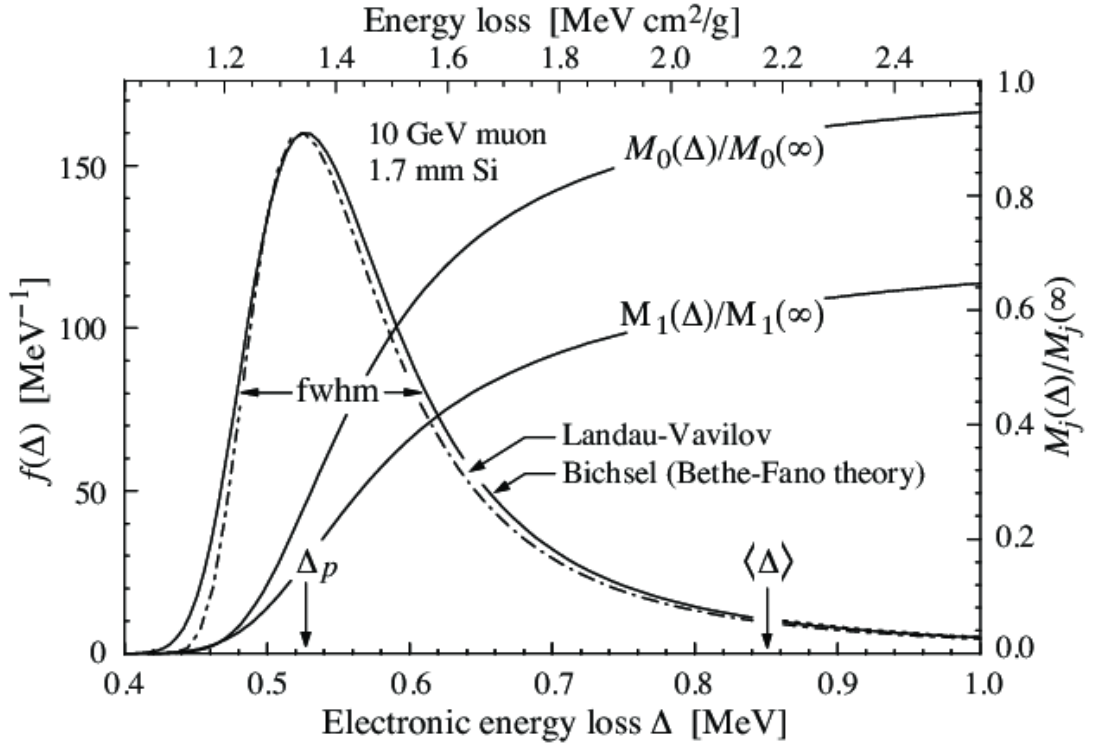
Figure 7.3: Distribution of electronic energy deposit for a 10 GeV muon traversing 1.7 mm
of silicon. The dot-dashed line shows the Landau-Vavilov function using an ap-
proximated Rutherford cross-section. The solid curve was calculated using the
Bethe-Fano theory. $M_0(\Delta)$ and $M_1(\Delta)$ are the corresponding cumulative 0th mo-
ment (mean number of collisions) and first moment (mean energy loss) respectively.
Δp shows the mode of the energy loss pdf and $\langle\Delta\rangle$ shows $\langle\frac{dE}{ds}\rangle_{\text{BB}} \cdot s$ [17].

loss provides a value of ≤ 0 eV, for the scattering no special direction can be stated.
Therewith the mean of the scattering angle pdfs is identical to the track angle means.
The per-layer covariance matrix for the local parameters $\lambda^{\text{local}} = (l_0, l_1, \phi, \theta, q/p)$ on the
other hand is given by [119]

$$\Sigma_{\text{Scattering}} = \sigma_\theta^2 \begin{pmatrix} \frac{\Delta s^2}{3} + \Delta sd + d^2 & 0 & \frac{\Delta s}{2\sin(\theta)} + \frac{d}{\sin(\theta)} & 0 & 0 \\ 0 & \frac{\Delta s^2}{3} + \Delta sd + d^2 & 0 & -\frac{\Delta s}{2} - d & 0 \\ \frac{\Delta s}{2\sin(\theta)} + \frac{d}{\sin(\theta)} & 0 & \frac{1}{\sin^2(\theta)} & 0 & 0 \\ 0 & -\frac{\Delta s}{2} - d & 0 & 1 & 0 \\ 0 & 0 & 0 & 0 & 3\Delta s^2 \left(\frac{d\frac{q}{p}}{ds}\right)^2 \sigma_\theta^2 \end{pmatrix}$$

$$(7.38)$$

with the distance d between the end of the layer and the target surface. Due to the
material mapping, the entire material contribution is approximately performed at a

single point. Hence the length Δs can be considered as zero and the interaction becomes point-like at the surface. Furthermore the d dependency describes the effect upon the final covariance matrix at the target surface. Due to the measurement-like description of the interaction from Sec. 4.3.1.1 and the therewith linked implicit transport through the extrapolation, the contributions from d are encapsulated in ACTS within the transport matrix formalism. After removing both contributions $\Sigma_{\text{Scattering}}$ is simplified to the only non-zero entries for σ_ϕ^2 and σ_θ^2.

Both entries depend on σ_θ^2. This term is evaluated for electrons using the Rossi-Greisen scattering formula [127]

$$\sigma_\theta^{\text{RGS}} = 17.5\text{MeV}\frac{\sqrt{\frac{\Delta s}{X_0}\frac{q^2}{\beta^2}}}{p}\left(1 + \frac{\log_{10}\left(10\frac{\Delta s}{X_0}\right)}{8}\right) \tag{7.39}$$

and for other particles by using the Highland scattering formula [128]

$$\sigma_\theta^{\text{HS}} = 13.6\text{MeV}\frac{\sqrt{\frac{\Delta s}{X_0}\frac{q^2}{\beta^2}}}{p}\left(1 + 0.074\ln\left(\sqrt{\frac{\Delta s}{X_0}\frac{q^2}{\beta^2}}\right)\right) \tag{7.40}$$

Following the notation from Sec. 4.3.1.1, the discrete material interaction is given by

$$\mu_q = \begin{pmatrix} 0 \\ 0 \\ 0 \\ 0 \\ \frac{q}{\min\left(\sqrt{\langle\frac{dE}{ds}\rangle^2_{\text{BB}}-m^2},p\right)} \end{pmatrix}$$

$$\Sigma_q = \begin{pmatrix} 0 & 0 & 0 & 0 & 0 \\ 0 & 0 & 0 & 0 & 0 \\ 0 & 0 & \frac{\sigma_\theta^2}{\sin^2(\theta)} & 0 & 0 \\ 0 & 0 & 0 & \sigma_\theta^2 & 0 \\ 0 & 0 & 0 & 0 & \sigma_{q/p}^2 \end{pmatrix}$$

with the mean of the parametrised trajectory q, p, θ. The min-function for the mean picks the smaller of both arguments and restricts the parameters values to physical values.

Within this section the mass appeared. This parameter plays a special role in the track parameter extrapolation. While all other parameters are continuous parameters, the particle rest masses are discrete values dictated by nature and can not be described by a normal distribution as presumed by the underlying conceptions from Sec. 5.2.1. Since the particle type may be assigned with certain probabilities, the corresponding masses can be considered as a multinomial distribution. Furthermore, for a given particle type this value is a constant that is independent of the extrapolation. Hence, this parameter can be neglected in the RKN4 integration of λ_{total}. This scenario is similar to the role of q/p in vacuum. Considering in addition that a particle detector does not measure

the particles mass, the underlying pdf will remain unchanged under extrapolation. The absence of knowledge gathering for this parameter from the detector data and the discrete nature of the particle masses result in an extrapolation performed for each particle mass independently. As this parameter depends on the particle identification technique of the detector or is deducible from scanning through various particle types, it is for the reason of simplicity assumed within the ACTS framework that this parameter is fixed prior to the extrapolation.

In summary, the approximation of discrete interactions within a step-wise extrapolation does not interfere with the found expressions of the previous sections of this chapter but rely on the particle type identification.

7.4.2 Continuous Material

In the previous section the material interaction of a particle was introduced and was approximated for the special case of discrete, thin material which is traversed. Also it was shown that in this case another parameter, the momentum, beside the parameters r and T are not constant along the propagation. Within this section it will be assumed that the surface material mapping is an insufficient approximation. This is equivalent to a thick material layer or volume. The environment is denoted as *dense*, i.e. it is assumed that the material is everywhere inside the volume. This section considers the consequences for the extrapolation of parameters under these conditions.

The function g from Eq. (7.36) is a differential function depending on the step size h. As in a dense environment the energy loss occurs continuously, the position r and the direction T are affected by this energy loss, leading to a step size dependent bias. Consequently, the modifications for q/p have to be treated equivalently.

Starting with the formulation of the equation of motion, analogous to Eq. (7.8) leads to

$$\frac{d\frac{q}{p}}{ds} = -\frac{q}{p^2}\frac{dp}{dE}\frac{dE}{ds} = -\frac{q}{p^2}\frac{E}{p}g = -\frac{\left(\frac{q}{p}\right)^3 Eg}{q^2} \tag{7.41}$$

As the integration of this expression also affects the k_i^j, a simultaneous integration of all components is required. This can be achieved by the STEP (Simultaneous Track and Error Propagation) algorithm [118]. This formalism introduces the additional variable Λ defined as $d\Lambda/ds = q/p$. This allows the definition of

$$\tilde{r} \equiv \begin{pmatrix} x \\ y \\ z \\ \Lambda \end{pmatrix} \qquad \tilde{T} \equiv \begin{pmatrix} T^x \\ T^y \\ T^z \\ \frac{q}{p} \end{pmatrix} \tag{7.42}$$

and hence preserve the feature $dr/ds = T$. Due to this formulation Eq. (7.8) becomes

$$\frac{d}{ds}\begin{pmatrix} \tilde{r} \\ \tilde{T} \end{pmatrix} = \begin{pmatrix} \begin{pmatrix} r' \\ \Lambda' \end{pmatrix} \\ \begin{pmatrix} \frac{q}{p}\,(T \times B(\tilde{r})) \\ -\frac{\left(\frac{q}{p}\right)^3 Eg}{q^2} \end{pmatrix} \end{pmatrix} \equiv \begin{pmatrix} \tilde{f}_1(s,\tilde{r},\tilde{T}) \\ \tilde{f}_2(s,\tilde{r},\tilde{T}) \end{pmatrix}.$$

While the entire usage of Λ is restricted to the symmetry of the vacuum extrapolation, only the single integrations of q/p have to be evaluated. This is equivalent to the direction step in Eq. (7.10). From the symmetry to the function f_1 and f_2, the RKN4 integration by evaluation of Eq. (7.9) is directly applicable for $\tilde{f}_1$ and $\tilde{f}_2$. In order to denote the difference between f_i and $\tilde{f}_i$, the sub-steps for the latter will be named $\tilde{k}_i^j$.

The sub-steps for q/p are given by

$$\tilde{k}_{1,q/p}^2 = -\frac{\left(\frac{q}{p}_n\right)^3 E\left(\frac{q}{p}_n\right) g_1}{q^2}$$

$$\tilde{k}_{2,q/p}^2 = -\frac{\left(\frac{q}{p}_n + \frac{h}{2}\tilde{k}_{1,q/p}\right)^3 E\left(\frac{q}{p}_n + \frac{h}{2}\tilde{k}_{1,q/p}\right) g_2}{q^2}$$

$$\tilde{k}_{3,q/p}^2 = -\frac{\left(\frac{q}{p}_n + \frac{h}{2}\tilde{k}_{2,q/p}\right)^3 E\left(\frac{q}{p}_n + \frac{h}{2}\tilde{k}_{2,q/p}\right) g_3}{q^2}$$

$$\tilde{k}_{4,q/p}^2 = -\frac{\left(\frac{q}{p}_n + h\tilde{k}_{3,q/p}\right)^3 E\left(\frac{q}{p}_n + h\tilde{k}_{3,q/p}\right) g_4}{q^2}$$

with the energy evaluated with the q/p value at the sub-step $E(q/p_n)$. The terms g_1 to g_4 are thereby the evaluations of g for the momenta at the sub-steps and the material at r_i. The evaluation of each g_i is computationally expensive and if the step size is adjusted a re-evaluation of g_2 to g_4 becomes necessary. As the momentum also contributes to the integration error ϵ, another degree of freedom is present and hence it may become more likely that the adjustment is necessary. Since therewith the step size tends to become smaller than in vacuum it can be assumed that all g_i have values close to each other. Since the material is an interpolated function mapped from a highly granular detector simulation, the individual values will be similar. As a consequence, only the first element g_1 is evaluated and used for all other sub-steps. Thus, it is not affected by the step-size adjustment.

With this adaption, the mean of q/p can be extrapolated. Additionally the covariance matrix entries have to be treated under extrapolation. Due to the symmetry from Eq. (7.42), the concept of Sec. 7.3 remains valid. Hence only the entries of the Jacobian provided by A_i and C_i from Eq. (7.23) have to consider the correct q/p_i. Those are defined equivalent to T_i in Eq. (7.25). Furthermore the last row and the last column from Eq. (7.22) will be modified. This involves from the definition of F'_n, G_n and G'_n

while using r and $\tilde{T}$ the additional terms

$$
\begin{aligned}
\frac{\partial r_{n+1}}{\partial \frac{q}{p}_n} &= \frac{\partial}{\partial \frac{q}{p}_n}\left(r_n + hT_n + \frac{h^2}{6}\left(\tilde{k}_{1,T}^2 + \tilde{k}_{2,T}^2 + \tilde{k}_{3,T}^2\right)\right) \\
&= \frac{h^2}{6}\left(\frac{\partial \tilde{k}_{1,T}^2}{\partial \frac{q}{p}_n} + \frac{\partial \tilde{k}_{2,T}^2}{\partial \frac{q}{p}_n} + \frac{\partial \tilde{k}_{3,T}^2}{\partial \frac{q}{p}_n}\right) \\
\frac{\partial \frac{q}{p}_{n+1}}{\partial r_n} &= \frac{\partial}{\partial r_n}\left(\frac{q}{p}_n + \frac{h}{6}\left(\tilde{k}_{1,q/p}^2 + 2\tilde{k}_{2,q/p}^2 + 2\tilde{k}_{3,q/p}^2 + \tilde{k}_{4,q/p}^2\right)\right) \\
&= \frac{h}{6}\left(\frac{\partial \tilde{k}_{1,q/p}^2}{\partial r_n} + 2\frac{\partial \tilde{k}_{2,q/p}^2}{\partial r_n} + 2\frac{\partial \tilde{k}_{3,q/p}^2}{\partial r_n} + \frac{\partial \tilde{k}_{4,q/p}^2}{\partial r_n}\right) \\
\frac{\partial \frac{q}{p}_{n+1}}{\partial \tilde{T}_n} &= \frac{\partial}{\partial \tilde{T}_n}\left(\frac{q}{p}_n + \frac{h}{6}\left(\tilde{k}_{1,q/p}^2 + 2\tilde{k}_{2,q/p}^2 + 2\tilde{k}_{3,q/p}^2 + \tilde{k}_{4,q/p}^2\right)\right) \\
&= (0\ 0\ 0\ 1) + \frac{h}{6}\left(\frac{\partial \tilde{k}_{1,q/p}^2}{\partial \tilde{T}_n} + 2\frac{\partial \tilde{k}_{2,q/p}^2}{\partial \tilde{T}_n} + 2\frac{\partial \tilde{k}_{3,q/p}^2}{\partial \tilde{T}_n} + \frac{\partial \tilde{k}_{4,q/p}^2}{\partial \tilde{T}_n}\right).
\end{aligned}
$$

The first equation thereby defines the last column except for the element in the last row from Eq. (7.22). The second equation defines the left part, the third the right part of the last row. This leads to the modified A_i and C_i matrices, denoted by $\tilde{A}_i$ and $\tilde{C}_i$ respectively. Those are then defined as

$$
\tilde{A}_i =
\begin{pmatrix}
\frac{\partial x_i''}{\partial T_n^x} & \frac{\partial x_i''}{\partial T_n^y} & \frac{\partial x_i''}{\partial T_n^z} & \frac{\partial x_i''}{\partial \frac{q}{p}_n} \\
\frac{\partial y_i''}{\partial T_n^x} & \frac{\partial y_i''}{\partial T_n^y} & \frac{\partial y_i''}{\partial T_n^z} & \frac{\partial y_i''}{\partial \frac{q}{p}_n} \\
\frac{\partial z_i''}{\partial T_n^x} & \frac{\partial z_i''}{\partial T_n^y} & \frac{\partial z_i''}{\partial T_n^z} & \frac{\partial z_i''}{\partial \frac{q}{p}_n} \\
\frac{\partial \frac{q}{p}_i'}{\partial T_n^x} & \frac{\partial \frac{q}{p}_i'}{\partial T_n^y} & \frac{\partial \frac{q}{p}_i'}{\partial T_n^z} & \frac{\partial \frac{q}{p}_i'}{\partial \frac{q}{p}_n}
\end{pmatrix}
$$

$$
=
\begin{pmatrix}
0 & \frac{q}{p}_i \frac{\partial T_i^y}{\partial T_n^y} B_z(r_i) & -\frac{q}{p}_i \frac{\partial T_i^z}{\partial T_n^z} B_y(r_i) & \frac{\partial \frac{q}{p}_i T_i^y}{\partial \frac{q}{p}_n} B_z(r_i) - \frac{\partial \frac{q}{p}_i T_i^z}{\partial \frac{q}{p}_n} B_y(r_i) \\
-\frac{q}{p}_i \frac{\partial T_i^x}{\partial T_n^x} B_z(r_i) & 0 & \frac{q}{p}_i \frac{\partial T_i^z}{\partial T_n^z} B_x(r_i) & \frac{\partial \frac{q}{p}_i T_i^z}{\partial \frac{q}{p}_n} B_x(r_i) - \frac{\partial \frac{q}{p}_i T_i^x}{\partial \frac{q}{p}_n} B_z(r_i) \\
\frac{q}{p}_i \frac{\partial T_i^x}{\partial T_n^x} B_y(r_i) & -\frac{q}{p}_i \frac{\partial T_i^y}{\partial T_n^y} B_x(r_i) & 0 & \frac{\partial \frac{q}{p}_i T_i^x}{\partial \frac{q}{p}_n} B_y(r_i) - \frac{\partial \frac{q}{p}_i T_i^y}{\partial \frac{q}{p}_n} B_x(r_i) \\
0 & 0 & 0 & \left(\frac{1}{\frac{q}{p}_i} \frac{\partial \frac{q}{p}_i}{\partial \frac{q}{p}_n}\left(3 - \frac{p_i^2}{E^2\left(\frac{q}{p}_i\right)}\right) + \frac{1}{g}\frac{\partial g}{\partial \frac{q}{p}_i}\right)\frac{q}{p}_i'
\end{pmatrix}
$$

and

$$
\tilde{C}_i =
\begin{pmatrix}
\frac{\partial x_i''}{\partial x_n} & \frac{\partial x_i''}{\partial y_n} & \frac{\partial x_i''}{\partial z_n} \\
\frac{\partial y_i''}{\partial x_n} & \frac{\partial y_i''}{\partial y_n} & \frac{\partial y_i''}{\partial z_n} \\
\frac{\partial z_i''}{\partial x_n} & \frac{\partial z_i''}{\partial y_n} & \frac{\partial z_i''}{\partial z_n} \\
\frac{\partial \frac{q'}{p_i}}{\partial x_n} & \frac{\partial \frac{q'}{p_i}}{\partial y_n} & \frac{\partial \frac{q'}{p_i}}{\partial z_n}
\end{pmatrix}
$$

$$
=
\begin{pmatrix}
\left(\frac{\partial \frac{q}{p_i} B_z(r_i)}{\partial x_n} T_i^y - \frac{\partial \frac{q}{p_i} B_y(r_i)}{\partial x_n} T_i^z \right) & \left(\frac{\partial \frac{q}{p_i} B_z(r_i)}{\partial y_n} T_i^y - \frac{\partial \frac{q}{p_i} B_y(r_i)}{\partial y_n} T_i^z \right) & \left(\frac{\partial \frac{q}{p_i} B_z(r_i)}{\partial z_n} T_i^y - \frac{\partial \frac{q}{p_i} B_y(r_i)}{\partial z_n} T_i^z \right) \\
\left(\frac{\partial \frac{q}{p_i} B_x(r_i)}{\partial x_n} T_i^z - \frac{\partial \frac{q}{p_i} B_z(r_i)}{\partial x_n} T_i^x \right) & \left(\frac{\partial \frac{q}{p_i} B_x(r_i)}{\partial y_n} T_i^z - \frac{\partial \frac{q}{p_i} B_z(r_i)}{\partial y_n} T_i^x \right) & \left(\frac{\partial \frac{q}{p_i} B_x(r_i)}{\partial z_n} T_i^z - \frac{\partial \frac{q}{p_i} B_z(r_i)}{\partial z_n} T_i^x \right) \\
\left(\frac{\partial \frac{q}{p_i} B_y(r_i)}{\partial x_n} T_i^x - \frac{\partial \frac{q}{p_i} B_x(r_i)}{\partial x_n} T_i^y \right) & \left(\frac{\partial \frac{q}{p_i} B_y(r_i)}{\partial y_n} T_i^x - \frac{\partial \frac{q}{p_i} B_x(r_i)}{\partial y_n} T_i^y \right) & \left(\frac{\partial \frac{q}{p_i} B_y(r_i)}{\partial z_n} T_i^x - \frac{\partial \frac{q}{p_i} B_x(r_i)}{\partial z_n} T_i^y \right) \\
-\frac{1}{q^2} \frac{q}{p_i}^3 E\left(\frac{q}{p_i} \right) \frac{\partial g}{\partial x_n} & -\frac{1}{q^2} \frac{q}{p_i}^3 E\left(\frac{q}{p_i} \right) \frac{\partial g}{\partial y_n} & -\frac{1}{q^2} \frac{q}{p_i}^3 E\left(\frac{q}{p_i} \right) \frac{\partial g}{\partial z_n}
\end{pmatrix}.
$$

The matrix C contains non-zero contributions if the gradient of the magnetic field of the material is non-zero. Thus, environmental requirements have to be fulfilled. Hence, for constant magnetic fields and/or materials, the evaluation is skipped. On the other hand, the evaluation of this matrix provides additional computational costs. That is another reason to skip the evaluation. Although this matrix affects the precision of the covariance matrix transport, the benefit is negligible in some cases[6].

Beside the energy loss, the scattering has to be considered that occurs continuously within the material. While the discrete material case allowed for a simplification of Eq. (7.38), the finite distance does not allow this form anymore. The general description relies on the given thickness of the material Δs that has to be utilised. The distance to target d implies that the matrix is added after the extrapolation to the target occurred. Since the matrix can be applied at the boundary surface of a layer, this implementation for ACTS leads to $d = 0$ mm. The consequence of this approach is that the scattering will be transported afterwards as part of the covariance matrix. As a dense volume can be treated as a set of layers of variable sizes, the definition of a layer thickness and thus, Δs is variable. For ACTS, the path length in the material is monitored and the matrix is applied whenever the volume changes or a covariance matrix transport is required (e.g. due to the inclusion of a measurement). Since the material composition can be arbitrary along Δs, a finite difference $\Delta q/p$ between the momentum at the entrance of the layer or the point of the previous evaluation and the point of current evaluation is used instead of a derivative. Thus, the used scattering matrix from Eq. (7.38) becomes

$$
\Sigma_q^{\text{Volumescattering}} = \sigma_\theta^2
\begin{pmatrix}
\frac{\Delta s^2}{3} & 0 & \frac{\Delta s}{2\sin(\theta)} & 0 & 0 \\
0 & \frac{\Delta s^2}{3} & 0 & -\frac{\Delta s}{2} & 0 \\
\frac{\Delta s}{2\sin(\theta)} & 0 & \frac{1}{\sin^2(\theta)} & 0 & 0 \\
0 & -\frac{\Delta s}{2} & 0 & 1 & 0 \\
0 & 0 & 0 & 0 & 3\Delta\frac{q}{p}^2 \sigma_\theta^2
\end{pmatrix}
\tag{7.43}
$$

---

[6]This matrix is not used within ACTS but expressed here for completeness and expanded in the following sections.

By comparison with the previous sections of this chapter the modular construction of this formalism becomes obvious. For $g = 0$ the presented calculations become identical to the extrapolation in Sec. 7.2.1 and 7.3, without deflection the same as in Sec. 7.1. The case sensitivity is thereby provided for all scenarios within the contribution of environmental variables such as $B(r)$ and g. Consequently, the found expressions from this section can be considered as another generalisation of the previous sections.

7.5 Time Propagation

It is planned that for the HL-LHC the mean of the pile-up grows by a factor 2-3 compared to the current state. As discussed in Chapter 4, the corresponding number of measurements lead to an additional complexity for the track reconstruction. In order to regulate the reconstruction complexity, all available data have to be utilised. For that purpose, in the last years the measurement of timestamps in addition to the other parameters became technically precise enough to allow a sufficient suppression of the pile-up induced complexity (see Sec. 3.3.2). For the ATLAS detector, the HGTD [87] represents an application of the time measurement. Since the measurements are thereby concentrated in a spatial region, the major benefit of this detector part is given for the vertexing (see Fig. 3.23). As it can be assumed that similar technological applications will be present in future particle detectors, the time parameter has to become a part of the ACTS track parametrisation. This issue will be discussed within this section.

In Sec. 7.4 the expansion of the extrapolated parameters by an additional degree of freedom was discussed. Following the same thoughts allows the inclusion of the time. As Eq. (7.6) presented the relation between the lab time t and the path length s, the equation of motion can be expressed as

$$\frac{dt}{ds} = \frac{1}{v} = \frac{1}{\beta} = \frac{E}{p} = \frac{\sqrt{m^2 + p^2}}{p} = \sqrt{\frac{m^2}{p^2} + 1}. \tag{7.44}$$

As this equation shows, the time only depends on the momentum p and the particles rest mass m. While in the Secs. 7.2.1 and 7.4 the parameter q/p is extrapolated under external influences, its value is a part of the track parametrisation. However, since $\Lambda \neq t$, i.e. $dt/ds \neq q/p$ the time has to be treated as additional parameter under the assumption that the time is measured explicitly. On the other hand, a replacement of q/p by $\sqrt{m^2/p^2 + 1}$ is computationally not reasonable due to Eq. (7.6).

Another aspect is the appearance of the mass term in the equation of motion. By considering the time window of a bunch crossing in a particle collider, the time differences between the first and last collisions are very small. The additional finite time resolution of the detector components demand a very precise handling of this parameter. While the mass dependency in Eq. (7.34) provides a minor contribution to the overall track parametrisation after a certain extrapolation distance s in dense environment, the impact of the mass on the time evolution under extrapolation is a major factor upon the result. Hence, beside the time as additional parameter, the mass becomes a parameter, too. So,

the overall track parametrisation vector gets extended to

$$\lambda_{\text{total}} \equiv \begin{pmatrix} r \\ \tilde{T} \\ t \\ [m] \end{pmatrix} = \begin{pmatrix} r \\ \tilde{\tilde{T}} \\ [m] \end{pmatrix}. \tag{7.45}$$

The square brackets around the mass is meant to denote the special role of the mass in the track parametrisation.

Following the thoughts from Sec. 7.4 for extending the parametrisation by an additional parameter, the analogous considerations for the mean extrapolation of the time are given by the sub-steps

$$\tilde{\tilde{k}}_{1,t}^2 = \sqrt{\frac{m^2}{q^2}\left(\frac{q}{p}\bigg|_n\right)^2 + 1}$$

$$\tilde{\tilde{k}}_{2,t}^2 = \sqrt{\frac{m^2}{q^2}\left(\frac{q}{p}\bigg|_n + \frac{h}{2}\tilde{\tilde{k}}_{1,q/p}\right)^2 + 1}$$

$$\tilde{\tilde{k}}_{3,t}^2 = \sqrt{\frac{m^2}{q^2}\left(\frac{q}{p}\bigg|_n + \frac{h}{2}\tilde{\tilde{k}}_{2,q/p}\right)^2 + 1}$$

$$\tilde{\tilde{k}}_{4,t}^2 = \sqrt{\frac{m^2}{q^2}\left(\frac{q}{p}\bigg|_n + h\tilde{\tilde{k}}_{3,q/p}\right)^2 + 1}.$$

The double-tilde is used to denote the utilisation of λ_{total}. The time is, like $\tilde{T}$ a parameter that is integrated once. Hence, the time step is evaluated as in Eq. (7.10). Given that the extrapolation occurs in vacuum, $\tilde{k}_{i,q/p}^2$ becomes zero and the step evaluation is simplified to

$$t_{n+1} = t_n + h\sqrt{\frac{m^2}{p^2} + 1}.$$

As the time evolution only depends on q/p, the modifications for the Jacobian in terms of $\tilde{\tilde{A}}_i$ and $\tilde{\tilde{C}}_i$, the analogous expressions of $\tilde{A}_i$ and $\tilde{C}_i$ but for λ_{total} are rather simple. The only non-zero contributions are given by the derivatives

$$\frac{\partial t'_i}{\partial \frac{q}{p}\big|_n} = \frac{m^2}{q^2}\frac{q}{p_i}\frac{\partial \frac{q}{p_i}}{\partial \frac{q}{p}\big|_n}\left(\sqrt{\frac{m^2}{q^2}\left(\frac{q}{p_i}\right)^2 + 1}\right)^{-1}$$

$$\frac{\partial t'_i}{\partial r_n} = \frac{m^2}{q^2}\frac{q}{p_i}\frac{\partial \frac{q}{p_i}}{\partial r_n}\left(\sqrt{\frac{m^2}{q^2}\left(\frac{q}{p_i}\right)^2 + 1}\right)^{-1}$$

with the definition of t_i analogous to T_i in Eq. (7.25). For the Jacobian the additional term $\partial t_{n+1}/\partial t_n = 1$ has to be used.

Similar to the momentum in the previous section, the scattering in a dense environment affects the variance of the time parameter. From the derivation of the contribution from Eq. (7.43) for $\sigma_{q/p}$ which can be found in [119], an analogous expression can be found for the time. The derivation is based on the additional momentum loss due to an extended path length from scattering in the material. For the time this leads to adding $3\Delta t^2 \sigma_\theta^4$ to the covariance matrix entry σ_t^2. Δt is thereby defined as the difference in time between the entrance of the layer and the point of evaluation of the scattering matrix.

The dependency of the time parameter on the other parameters and vice versa shows that measuring the time affects the other parameters indirectly. Due to the only explicit coupling between time and momentum, the latter parameter is affected by these measurements. The thereby obtained information about the particles trajectory are then, represented in Eq. (7.17) forwarded through matrix multiplications to the direction and the position parameters. The same accounts in the opposite direction. Thus, the measurement of the time under the assumption of the parameter resolution achievable nowadays has a minor effect on other parameter resolutions. The main impact provided by this parameter though is given by the suppression possibilities of track reconstruction complexity induced by pile-up events and the therewith linked reduction of computational complexity and computing resource consumption.

7.6 Auctioneer Formalism

The formulations for extrapolating the mean and the covariance matrix of a track parametrisation from Sec. 7.2.1 can be considered as a general expression. Secs. 7.4 and 7.5 added more functionality to the extrapolation by including special conditions. The former expansion of the formalism is thereby driven by environmental conditions of the detector. Moreover, the existence of volume material depends on the current step during the extrapolation. Extrapolating the time parameter on the other hand either has to be considered throughout the entire detector if time measurements are present or not. A similar consideration can be performed for the straight line extrapolation from Sec. 7.1. While it is known prior to an extrapolation whether the detector measures time, it is also known from the seed whether a particle is charged or has a sufficiently high momentum to be treated as particle with a straight line trajectory. If the straight line case is applicable then the RKN4 formalism is not required, i.e. Eq. (7.13) becomes zero. Furthermore, the RKN4 step evaluation is computationally more expensive. Hence the existence of the straight line and RKN4 based extrapolations are implemented both for ACTS and have to be utilised based on the initial conditions.

While the time and dense environment extrapolation are either present depending on the detector architecture and the current state of the extrapolation, a user definable interface is required. Therewith the design goal of the detector independence of ACTS can be preserved. Additionally, the dense environment step extrapolation adds further computational complexity. Hence these calculations should be performed only when volume material is present. The combination of the requirements and the implementation for ACTS is shown in Fig. 7.4. Given a state, denoted by $\lambda_n = \lambda(s)$, the RKN4
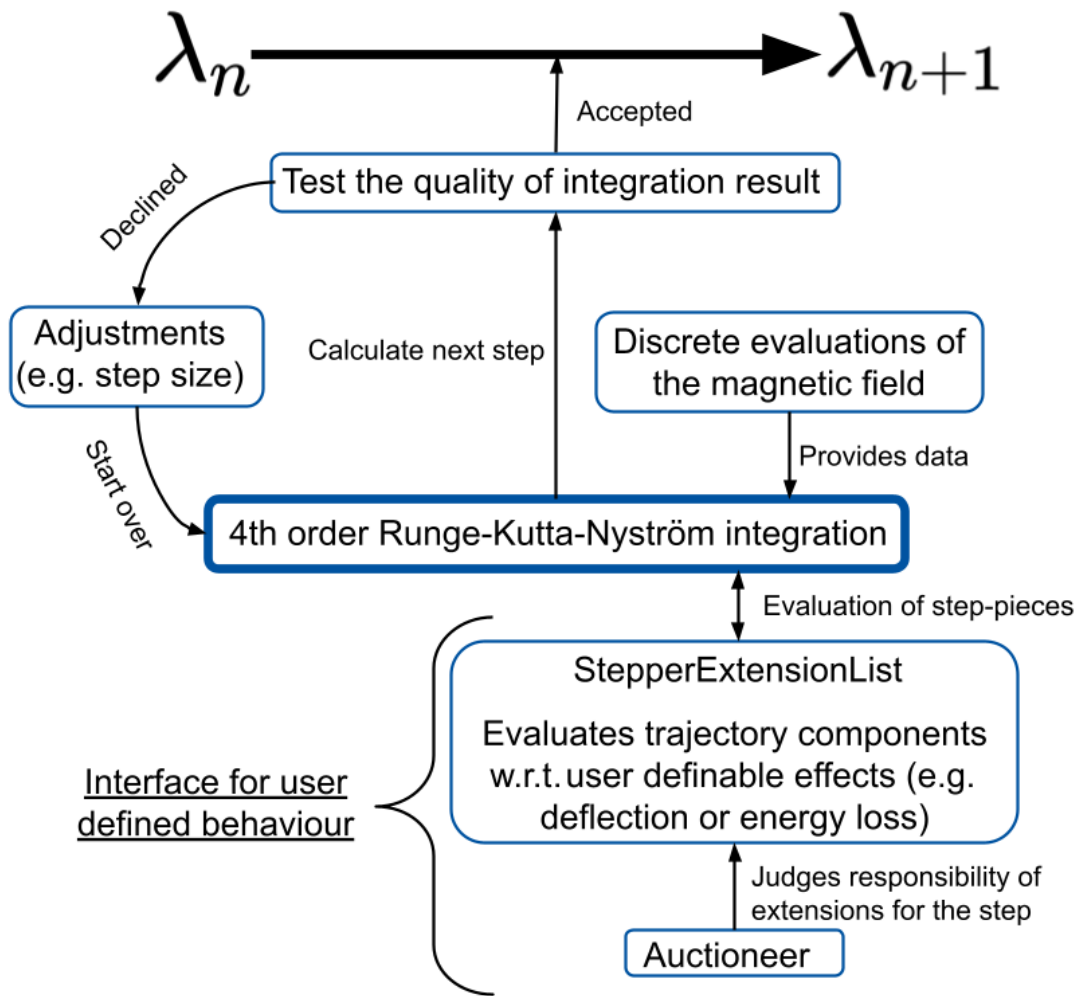
Figure 7.4: Flow chart showing the individual components of an extrapolation step from λ_n to λ_{n+1} using the RKN4 integration [129].

integration performs the required calculations with a given step size h_i. Thereby the formalism evaluates the magnetic field at the positions r_i from Eq. (7.10). By evaluating the numerical error as given in Eq. (7.13) and comparing it to a given tolerance, the performed calculations are either accepted or require an adjustment. In the former case the $(n + 1)$th state gets evaluated, in the latter case the step size is modified according to Eqs. (7.14) and (7.15).

As the RKN4 integration is just the method applied to solve a differential equation, the set of differential equations for the parameters in λ_n can be arbitrary. For ACTS a grouping mechanism was developed. Based on the underlying environment, the considerable effects and parameters, the differential equations may change. As the RKN4 step evaluation relies on the calculation of the sub-steps k_1 to k_4, a set of differential

equations just has to provide those results. In ACTS a set of differential equations is called an *extension*. In order to cover a range of different cases, multiple extensions can be handed over. Those are stored in the *StepperExtensionsList*. As the extensions may be dependent on the environmental conditions and are thus not applicable in general, a selection mechanism is required. This mechanism is called *Auctioneer*. Before a step is evaluated, all extensions obtain the environmental data. Based on the provided information each extension calculates a so-called *bid*. The auctioneer mechanism then evaluates all bids and declares which extension(s) will calculate the next step. As the StepperExtensionList is user defined, the implemented physical effects can be considered arbitrary. Additionally, the amount of required extensions for a certain step are unpredictable for an ACTS implementation. The auctioneer itself is user defined. Since the production of the bids as well as the overseeing auctioneer are user defined, the actual implementation flexibility is granted.

For the ACTS software the extrapolation following Sec. 7.2.1 and 7.4 are implemented as two separated lists. Both include the time parameter extrapolation per default. In addition, an auctioneer is implemented that prefers the latter expressions whenever volume material is present. Otherwise the vacuum extrapolation is considered.

Beside the argument of flexibility for custom user applications and the therewith linked utilisation for future experiments, the auctioneer formalism provides another benefit: This architecture allows to address an arbitrary number of different physical scenarios. Thereby unnecessary calculations are skipped on a step-by-step evaluation. This provides a reduction of the necessary computational complexity to a minimum in the context of the RKN4 integration. Furthermore additional effects can be included when necessary. This leads to the possibility to perform an entire track extrapolation through the detector within a single class. As this involves that a single state object is required in order to store all necessary data defining the state, there is no necessity to move data between extrapolation classes or to convert the data structures.

In summary, this formalism allows a flexible and detector independent solution of an extrapolation problem within a single class. The design of the auctioneer was created and implemented into ACTS within the context of this thesis.

7.7 Propagator

The previous sections within this chapter discussed the requirements in order to extrapolate a track parametrisation. Various conditions affecting the trajectory and consequently the parametrisation itself were considered. Thereby, the extrapolation itself is calculated step-wise. This section utilises the found expressions and discusses the extrapolation on a global scope. The top-level manager concept is called *Propagator*, in ACTS this is represented as a class. The propagator starts and ends an extrapolation, provides the environmental data and allows state accesses and manipulations between individual steps. In order to perform these tasks, three more concepts, a *Navigator*, *Actionlist* and *Abortlist* are required. As the extrapolation occurs step-wise, the Propagator demands certain tasks from all these components iteratively. The conditions are

provided to the stepper and the evaluated step can be further processed in the other components. These components, their tasks and interplay with the Propagator are explained in the following. At first the Navigator will be described, afterwards the Action- and Abortlist.

Navigator

The Navigator is a concept responsible for handling the detector geometry. It is capable of accessing the individual components and provide information about the volume, layer and surface that corresponds to the current position of the trajectory. Due to the hierarchical architecture of the detector geometry, the lookup is performed at the lowest possible level. After an initial lookup, the Navigator knows all three components. The other task the Navigator fulfils is targeting the next geometry object along the trajectory. As this task requires knowledge about the trajectory beyond the current position, the track parametrisation itself has to be extrapolated. Since this would involve many additional extrapolations and thus computational resources, the trajectory is approximated by a straight line. Beside the justification of the separation between straight line and charged particle extrapolation within the previous sections, the (potentially) simplified extrapolation is applied here. Since the trajectory diverges for charged particles in magnetic fields between the RKN4 extrapolation and the straight line approximation, the Navigator tests for the next geometrical objects before each step. Thus, a different object can be targeted if the curvature of the trajectory disfavours the initial target reachability. Furthermore, the extrapolation distance from the straight line allows to estimate the step size h. In addition to the integration error driven step size adjustment from Sec. 7.2.2, the detector geometry provides an additional constraint. In order to resolve the concurrent assignment, the smallest step size is chosen.

As the current position inside the geometry and the target are resolved, the extrapolation will modify the current position of the particle. Thus, the current surface, layer and volume might need to be updated. This is performed in the Navigator by utilising the hierarchy of the detector geometry. It also allows to access the current geometry objects at any time and to obtain environmental variables such as material parameters.

As this approach aims to reduce the set of candidates and perform status modifications on the lowest level of the hierarchy, the complexity can be reduced. The Propagator requires the Navigator to evaluate the current status in the hierarchy before each step and before the target can be evaluated. On the other hand the volumes are encapsulated in a world volume to allow an initial evaluation of the volume, layer and surface.

Action- and AbortList

The Action- and AbortList are two sets which can be defined and extended by the user. The underlying concept is comparable to the Auctioneer formalism from Sec. 7.6. The major difference is that the lists in this case are not moderated by an Auctioneer instance, i.e. each element of the Action- and AbortList, called *actor* and *aborter* is evaluated when called. The call itself occurs before each step.

The aborter allows to terminate the extrapolation. This occurs as soon as one aborter in the list requests it. The judgment itself is only based on the current state of the Propagator, the Navigator and the extrapolation stepper. This concept is kept generally to cover a large range of conditions. The standard conditions cover the exiting of the world volume, a maximum total path length s and a reached predefined surface.

While the aborters utilise the state, the actors are capable of manipulating the state. Compared to the Auctioneer formalism, the manipulation does not occur during the step evaluation within the extrapolation but between the steps. This allows to perform material interactions or to manipulate the state in general. As the track parameter modification due to the Kalman filter can be treated similar to discrete material effects, a design of the actors is the implementation of this formalism. Beside the plain update of the mean and the covariance matrix, the state manipulation also allows for the smoothing.

Both lists can require a certain step size for their purpose. Since the step sizes may differ, each list controls an independent step size. The applied step size is the minimum of four different values along the extrapolation direction.

7.8 Results

Within this section the calculations and concepts are investigated for their correctness. Since the straight line extrapolation is a special case that is not affected by most of the concepts introduced here for the track extrapolation, it will be ignored in this section. The material interaction though affecting the straight line is considered in the following. The analogous validity is given by definition. All other concepts are based on the numerical transport of a track parametrisation through the parameter space under the influence of different effects by using the RKN4 integration. Thus, the items of investigation are the extrapolation through vacuum and material. The material is considered in both categories: surface and volume material. As for all extrapolation steps the mean and the covariance matrix of a parametrisation are the only quantities that have to be considered, the focus relies on those two. While this section is focused upon the accuracy of the extrapolation, a timing study can be found in [103].

In order to cover the different aspects, a setup for a proper comparison is required. This will be described in Sec. 7.8.1. Afterwards, the different extrapolation scenarios will be presented. In a last step the Ridders algorithm is used for further investigation of the covariance matrix transport.

7.8.1 Simulation Setup

In order to test the extrapolation quality, a reliable algorithm is mandatory. This is achieved by utilising the Geant4 framework as a reference. As it provides detailed models of interactions, it is the most trustworthy software for the purpose. The level of detail is hereby centred on accuracy. Hence, the material effects from Sec. 7.4 represent just a fraction of possible interactions but the major effects affecting the particle trajectory. Furthermore, Geant4 simulates individual particles instead of statistical quantities. As

the extrapolation from the previous sections are extrapolating means and covariance matrices, a corresponding adaption has to be performed in order to reflect the stochastic nature of interactions. If the extrapolated mean and covariance matrix are correct then the mean and covariance matrix of multiple Geant4 extrapolation should lead to the same result. Under this premise, a sampling setup is required.

The initial parameter means for the stepper extrapolation are sampling from the uniform distributions. Those are defined as $\mu_\phi \in [0, 2\pi)$, $\mu_\eta \in [-2.5, 2.5]$[7], $\mu_z \in [-10, 10]$ mm and $\mu_p \in [1, 100]$ GeV. The starting time and the two other spatial parameters are without loss of generality set to zero. With the sampled parameters a curvilinear surface can be defined. The initial parameters are given in this coordinate system. Additionally, uncertainties are defined as $\sigma_{l0} = \sigma_{l1} = 100 \ \mu m$, $\sigma_\theta = \sigma_\phi = 1°$, $\sigma_p = 100$ MeV and $\sigma_t = 100$ ps. As the sampled parameters define the centre of the surface and the uncertainties the 1σ region of the multivariate normal distribution, the Geant4 start parameters are sampled from this pdf.

In order to compare the different aspects of the extrapolation, a detector geometry is required. The described components can be found in the ATLAS ID together with the Calorimeters. While the pixel detector and the SCT represent an extrapolation region mostly filled with air, it can be approximated to have a comparable effect as vacuum. Approximating the sensitive components as a set of surfaces with a corresponding material map provides a scenario with discrete material interactions. The architecture of the TRT, the LAr calorimeter and the tile calorimeter allow for testing the application in a dense environment. Therefore, the volume of those components is mapped into material volumes[8].

The particles that are simulated within this detector setup are muons. This shows the influence of different charges on the particles trajectory. Furthermore, muons are affected by the entire set of interaction processes that are treated and are capable of traversing the entire detector. For each configuration of initial parameters, 1000 Geant4 particles are simulated. In total 800 different configurations are used. The Geant4 simulation is restricted to the simulation of the initial particle, i.e. secondaries are ignored within the simulation.

During the extrapolation of the ACTS stepper and the Geant4 simulation, the free parameters are recorded after each step. By setting the Geant4 initial parameters in one iteration on the mean values from the sample, the step-wise positions and parameters define the target surface for the ACTS extrapolation. The obtained data are used to investigate the behaviour. Since the Geant4 steps do not necessarily correspond to the ACTS steps, an approximation is required. By constructing a curvilinear surface for each step of the extrapolation, a bound parametrisation can be provided. For each Geant4 simulation, the parameters closest to the surface are searched. This is performed by a straight line intersection.

---

[7]For the extrapolation, the sampled pseudorapidity is converted into θ.

[8]As this is a simplified representation of the detector geometry, the detector components require a proper translation. Up to today the MS is missing and hence can not be included in the setup.

7.8.2 Vacuum Extrapolation with Discrete Material

As a first step the behaviour of the particles during extrapolation in vacuum with discrete material effects between the steps is investigated up to a radial distance of 550 mm. This covers the pixel detector and the SCT. The distribution of differences between the initial parameters obtained from a sample in ACTS and the calculated mean from the sampled initial parameters for Geant4 is shown as black dots in Fig. 7.5. As the initial parameters
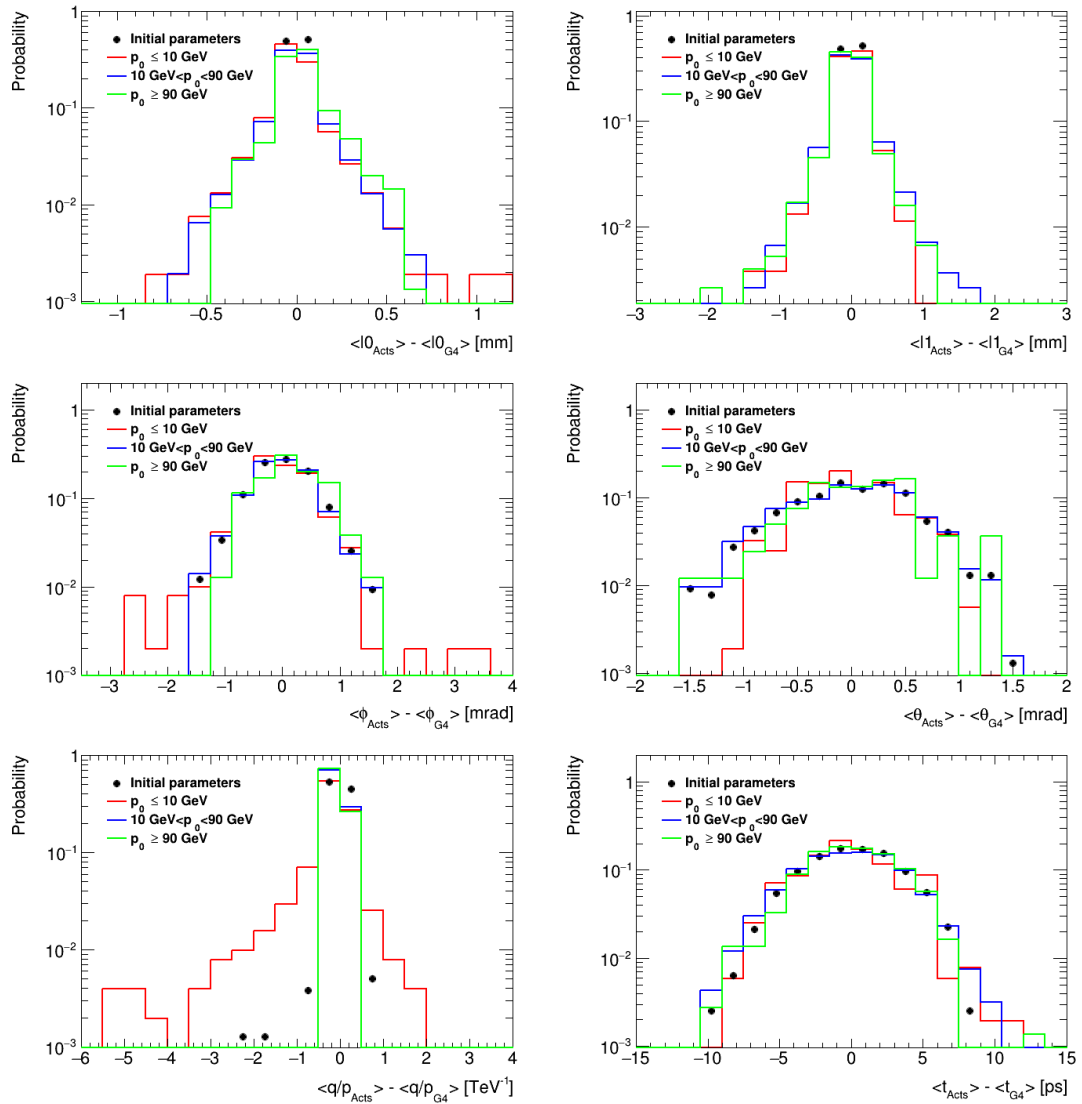

Figure 7.5: Difference between the mean values of parameters obtained from ACTS and from Geant4. The initial distribution of parameters is shown as dots. The lines represent the distribution of parameters obtained at each surface, split into momentum intervals.

are distributed around zero, the construction of the initial sample works properly. The width of these distribution is given due to the limited sample size in Geant4. Due to a sample in terms of momenta instead of q/p, the corresponding distribution is centred around zero but has a skew slightly different from a normal distribution.

The three lines represent a superposition of all 800 muons used for the extrapolation, evaluated parameter-wise at each surface. Hence, in each distribution a correlation between the individual points is present. As the means of the initial parameters for Geant4 vary around the mean used for ACTS, the kinematics vary, too. This leads to a progressive deviation during the extrapolation between the two models. This deviation can be seen in spatial parameters in the top row of Fig. 7.5. However, the deviation is enhanced due to the underlying projection of the Geant4 particles onto the curvilinear surface. The further the bin is away from the initial parameters the longer it takes to be filled with values as the deviation occurs step-wise.

Noteworthy is in this set of plots the q/p distribution. It can be seen that the distribution is skewed towards negative values for the low momentum particles. This corresponds to smaller momenta in the Geant4 simulations compared to the ACTS extrapolation. As the material interaction is simulated only at certain surface in the latter case, the cumulative effect applied at these points has to be same as for the Geant4 simulation. The step-wise momentum change is shown in Fig. 7.6 (left). This plot shows the mo-
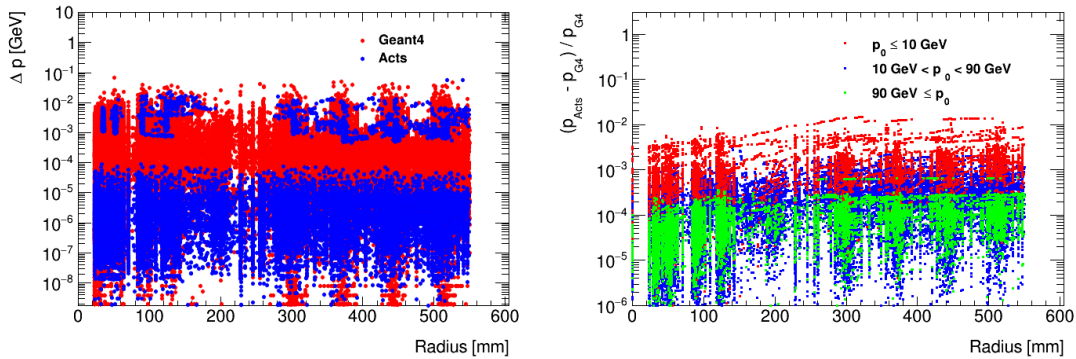
Figure 7.6: Left: Step-wise momentum difference for the Geant4 and ACTS extrapolation. Right: Relative momentum difference between the Geant4 and ACTS extrapolation.

mentum difference for each simulated Geant4 particle and each ACTS extrapolation. While during the Geant4 simulation the particles momentum gets reduced at each step due to the full simulation of the detector geometry and thus a distributed material, the momentum loss for ACTS is restricted to the pixel and strip surfaces. These contributions are visible for radii below 200 mm (pixel detector) and above 300 mm (SCT) with value between $10^{-3} - 10^{-2}$ GeV. The momentum differences for ACTS below 10^{-4} GeV are numerical noise.

In addition to the discrete interaction, the underlying energy loss mechanisms, denoted in g from Eq.(7.36), are naturally Landau distributed as shown in Fig. 7.3. As

explained in the corresponding section and in Chapter 4, the applied statistical models are restricted to (multivariate) normal distributions. Hence, the approximation does not describe the tail of the Landau distribution well. Consequently, the Geant4 simulations that perform the proper sampling have a higher probability for larger energy losses compared to the models used for the track reconstruction. As a result of this enhanced momentum loss, the q/p distribution in Fig. 7.5 tend towards smaller values. Additionally, the impact of the energy loss mechanism depends on the momentum of the particle as shown in Fig. 7.6 (right). This plot shows the step-wise relative deviation between Geant4 and ACTS. Although the values spread over four orders of magnitude (blue), a clearly stronger deviation is obtained for low momentum particles (red) compared to higher momenta (green). This plot also shows a small slope for each category that displays the impact of the approximation of the underlying pdf. Furthermore, this gets visible in the ϕ values as shown in Fig. 7.5. As the magnetic field is directed perpendicular to the radial vector, the azimuthal angle is mostly affected, again mostly for low momentum particles. The probability difference in the tail region between the Landau distribution and a normal distribution can be seen at the small probability for larger absolute ϕ values. Considering additionally the correlation of the histogram entries shows that even in the absence of measurements and hence parameter regulation mechanisms, the impact is small but not negligible.

Beside the mean the uncertainty of the parameters are of interest. The corresponding distributions are shown in Fig. 7.7. These distributions utilise the same conventions as in Fig. 7.5. As for the means, the difference of the uncertainties are centred around zero except for q/p due to the sampling procedure. Again as in the former set of plots, the spatial parameters show the step-wise growing deviation for the spatial parameters in the top row. Also the normal distributed approximation of the underlying energy loss mechanism leads to a skew in the q/p distribution. Here, the dependency on the particles momentum and the energy loss modelling gets visible. While a low momentum particle may lose a larger fraction of its momentum due to the underlying model, the higher momentum particles are less affected. As the individual uncertainties for the Geant4 simulation parameters are affected by the individual outliers of the low momentum particles, the uncertainties in ϕ tend towards larger values. This produces an enhanced region for negative values in the azimuthal angle plot in Fig. 7.7. As the momentum may reach smaller values than a normal distributed energy loss would predict, the material interaction described by Eqs. (7.40) and (7.39) leads to larger variations. As a consequence, the σ_{l0} parameter for Geant4 becomes larger than in ACTS, hence the corresponding plot tends to negative values.

The presented distributions for the mean and the covariance matrix difference between ACTS and Geant4 show that the extrapolation methods for vacuum extrapolation with discrete material interaction in the comparison with projected Geant4 simulation delivers reasonable results but reveals limitations for low momentum particles in the applied energy loss approximations. However, as the extrapolation in the context of track reconstruction occurs along with measurements that provide additional information about the particle properties along the extrapolation, the application of this implementation
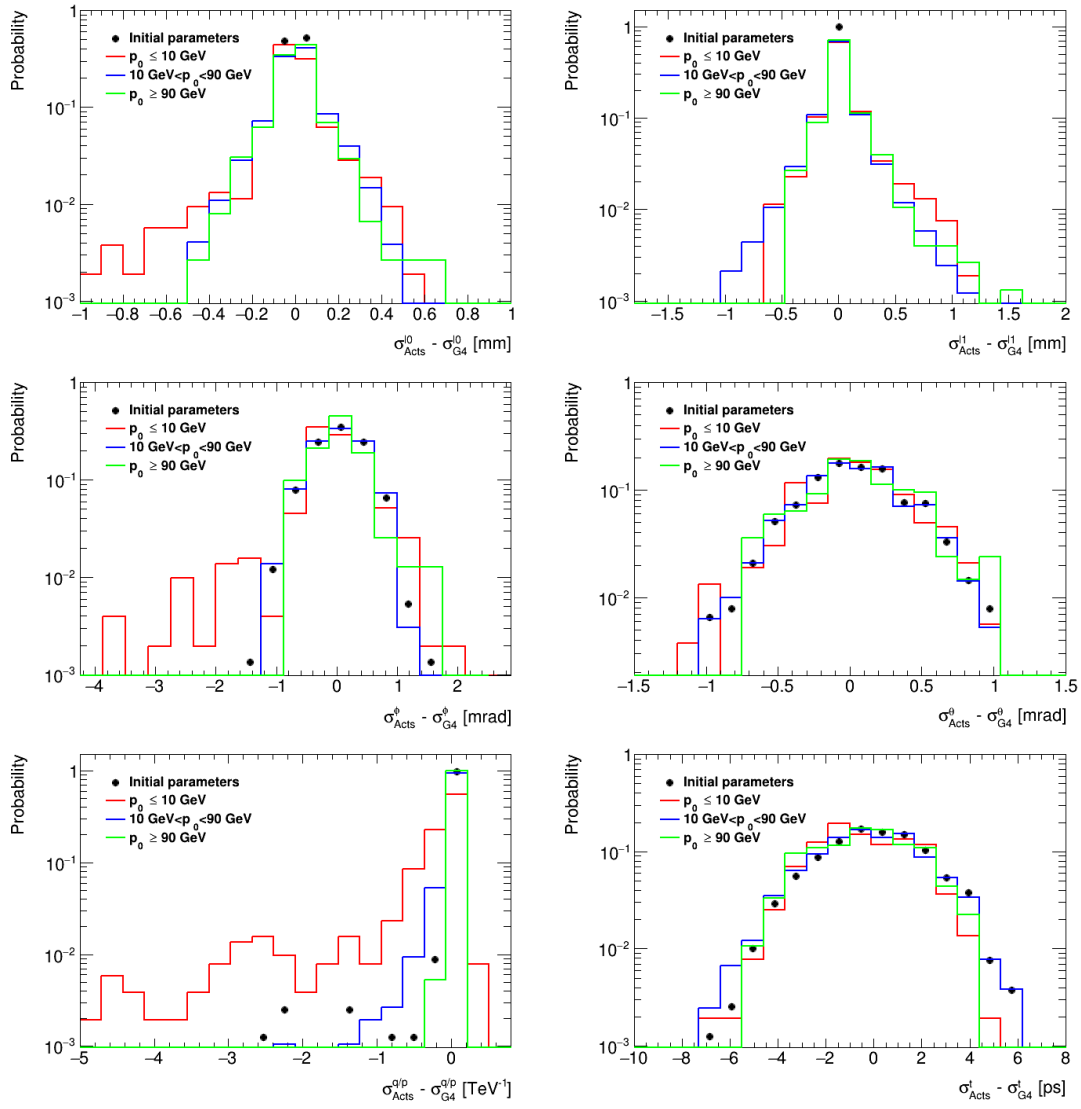
Figure 7.7: Difference between the uncertainty values of parameters obtained from ACTS and from Geant4. The initial distribution of parameters is shown as dots. The lines represent the distribution of parameters obtained at each surface, split into momentum intervals.

will provide more accurate results for the required task. This includes the recovery from the energy loss pdf and the material model.

7.8.3 Extrapolation in Dense Environment

After the particles traversed the silicon detectors, they enter the TRT and the calorimeters. The material in these detector parts is described by volume materials, resulting in a continuous energy loss of traversing charged particles. Thus, the situation is different compared to the pixel detector and SCT detector and requires further treatments.

The mean and covariance matrix of the Geant4 simulations are derived by a projection of nearby points onto the curvilinear surface defined by the ACTS extrapolation. While the previous section considered only surface material, the projection of individual points next to the surface in vacuum is close to the actual value in space, momentum and hence the entire phase space of the parametrisation. Since the ACTS implementation requires an actor call for handling the material at the surface in between the vacuum regions, a step has to end at the surface. A similar treatment occurs by Geant4. Hence, both implementations deliver parameters at the same phase space region by design.

When dealing with volume material, more complicated situations may occur. As the individual detector parts have a certain spacing between them, those regions cause less (in case of Geant4) to no (in case of ACTS) energy loss compared to the TRT and calorimeters. Hence, the evaluation of the mean and covariance matrix at those points lead to values that are close in space but not close in momentum. The latter parameter can be understood as the mixing of Geant4 steps inside and outside the detector material. While the first ones are rather constant in terms of momentum, the second ones are decreasing as a function of the distance in the material. Similar situations exist in various places within the detector components, enhancing the conceptual projection error from the comparison. For that purpose different projections are utilised in the following. For the momentum and time parameters estimation, a straight line distance of less than 1 mm from the Geant4 step to the curvilinear surface is required per particle. For the other components the tight constraint is not necessary, especially outside the solenoid magnet. Since the deflection by the magnetic field is small compared to the ID, a projection of spatial components over a longer distance with straight lines is possible without causing too large errors. Due to the reduced deflection, the direction vector is assumed to change less rapidly as in the ID, too.

Compared to the previous section, the frequent occurrence of transition regions along the extrapolation leading to artefacts in the parameter distributions arising just from the underlying concept, in the following the final parameters are presented rather than the parameters at each step. From the particles simulated in the previous section, the mean parameter distributions at the entrance of the radial region are shown as dots in Fig. 7.8. These correspond to the parameters at the end of the silicon region. The final spatial parameters in the top and middle row are affected by the same effects as in the previous section during the extrapolation, projection and statistical limitation. This leads to a broadening in those parameters. Again, the effect is larger for low momentum particles. As the magnetic field is mainly directed in z-direction, the distributions of $\langle \theta_{\mathrm{ACTS}} \rangle$ are less affected by these effects compared to $\langle \phi_{\mathrm{ACTS}} \rangle$.

The bottom row plots require further investigation. The momentum distribution is again affected by the modelling of the energy loss. The time distribution is a result of
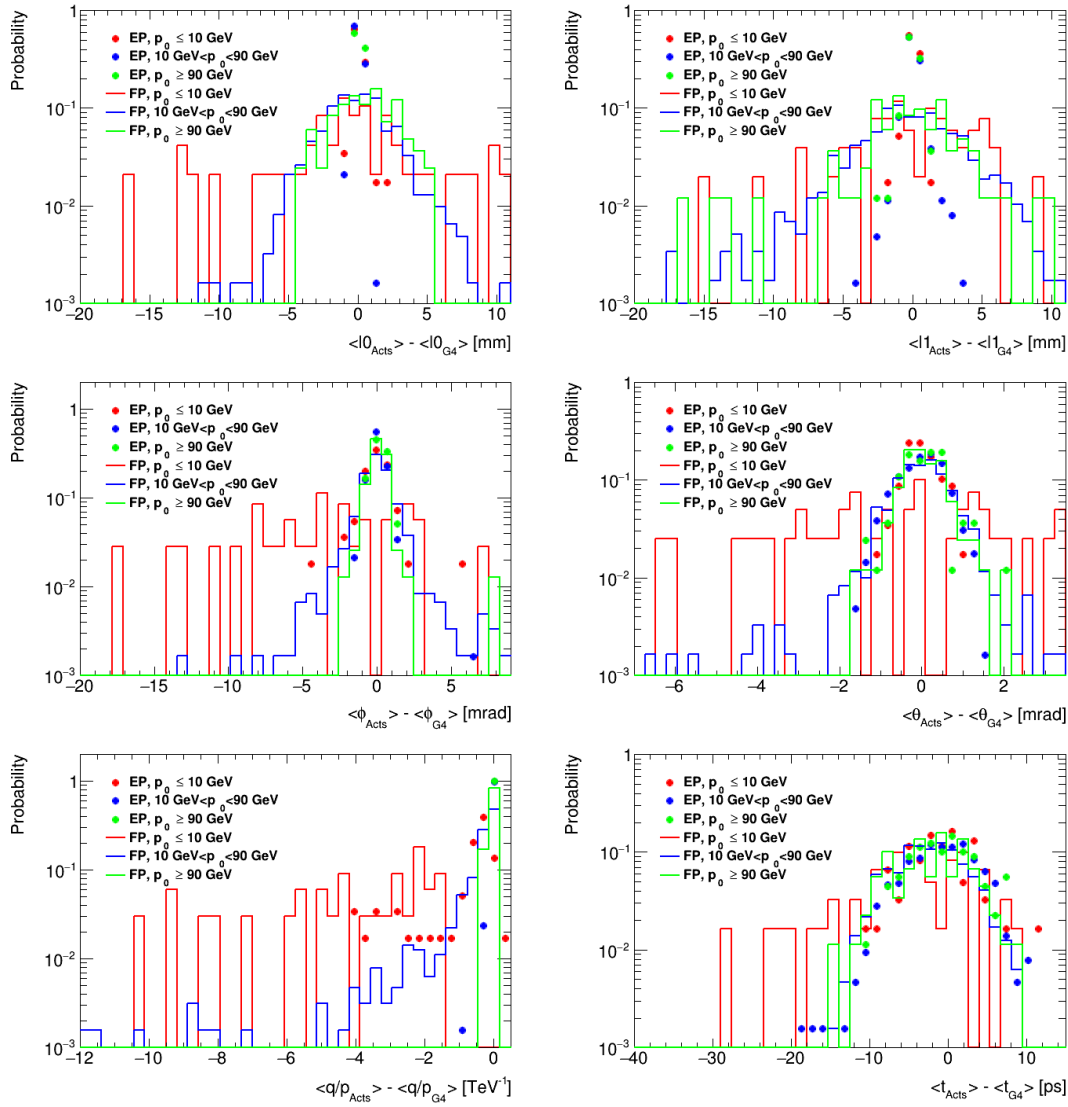
Figure 7.8: Difference between the mean values of parameters obtained from ACTS and from Geant4. The initial distribution of parameters (IP) is shown as dots. The lines represent the distribution of parameters obtained after traversing the TRT and calorimeters (FP), split into momentum intervals.

the momentum distribution. Compared to Fig. 7.6, the material interaction occurs here at almost all steps. Hence, the previous presentation of the energy loss in Fig. 7.6 is not suitable here. The relative, step-wise momentum loss due to material interaction is shown in Fig. 7.9. For this plot the steps for both, ACTS and Geant4, in which the ACTS particle had no energy loss, were removed as these steps correspond to the spacing region between the detector components. As this plot shows, the probability of the momentum loss due to material interaction tends towards larger values in Geant4
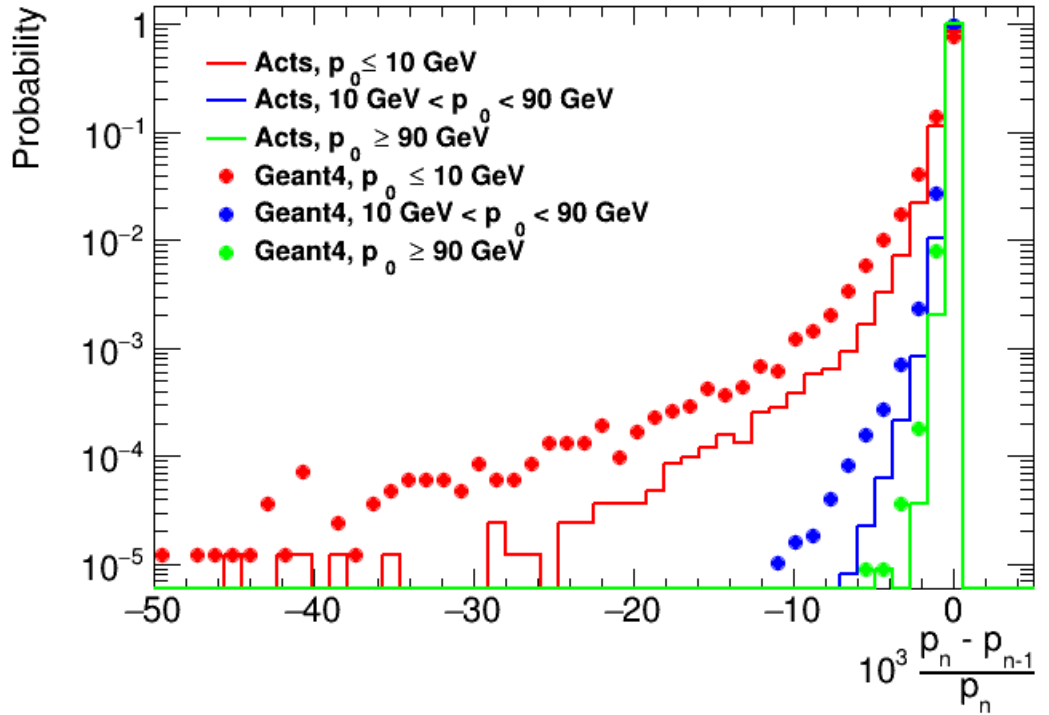
Figure 7.9: Momentum loss per step between the nth and $(n-1)$th step for Geant4 and ACTS. Steps with $p_n = p_{n-1}$ are removed. Sorted in the momentum regimes, the dots represent the Geant4 momentum loss, the lines the ACTS momentum loss.

compared to ACTS in all considered momentum regimes. This is again a direct consequence of modelling of parametrisation modification using normal distributions instead of Landau distributions. Since it occurs on many steps, the deviation between $\langle q/p_{\mathrm{ACTS}} \rangle$ and $\langle q/p_{\mathrm{G4}} \rangle$ gets larger over the entire distance in this case, as shown in Fig. 7.8 (bottom left), compared to the surface material case shown in Fig. 7.5 (bottom left). Due to the tendentious lower momentum of particles in Geant4, the mean lab time of the particles becomes larger than for Geant4. While the general shape of the differences of the means in Fig. 7.8 (bottom right) for the entrance and final parameters remains similar, a slight shift towards negative values of the entire distribution can be observed.

The distributions of the uncertainties corresponding to the dense environment extrapolation is shown in Fig. 7.10. The plots rely on the same conventions as the means. It is observable that partially the same energy loss fluctuation behaviour is present as in the discrete material case. The momentum range of the Geant4 particles remains stable for the low momenta. For higher momenta, the situation is different. Due to the more frequent material interaction, the material modelling effects become visible. However, in comparison to the former case, the interaction occurs continuously and hence has a larger impact on the distributions of q/p. On the other hand, the impact of the broadening of the q/p standard deviation has a negligible impact on the standard deviation
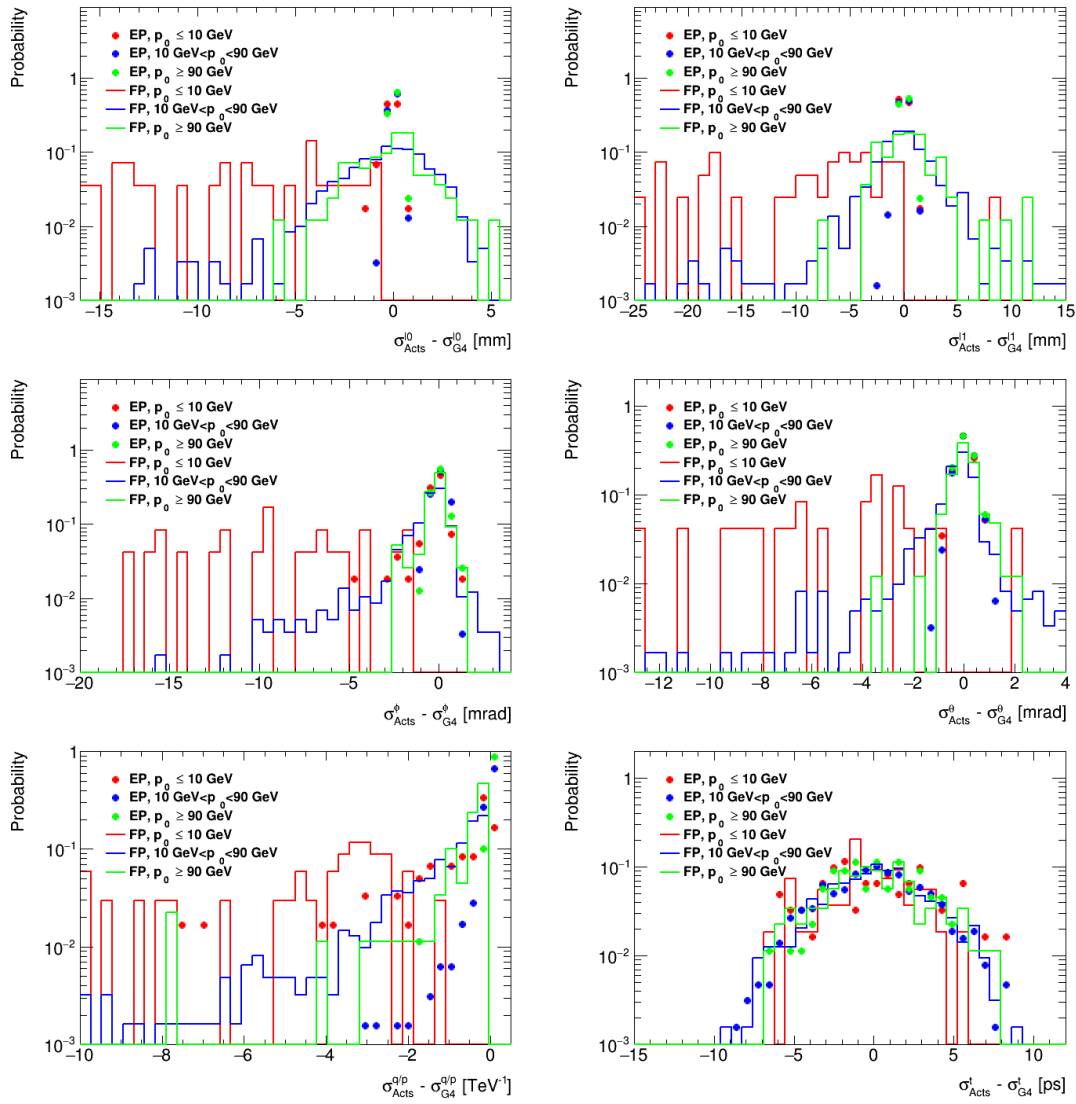
Figure 7.10: Difference between the uncertainty values of parameters obtained from ACTS and from Geant4. The initial distribution of parameters (IP) is shown as dots. The lines represent the distribution of parameters obtained after traversing the TRT and calorimeters (FP), split into momentum intervals.

of the time, showing that the impact of the momentum change on the time evolution is low compared to the intrinsic evolution from the Jacobian term $\partial t_{\text{final}}/\partial t_{\text{entrance}}$.

The azimuthal angle and the polar angle are more skewed towards negative values the lower the particles momentum is. As the momentum of the particles in Geant4 is rather smaller than in ACTS and the scattering contribution θ depends reciprocal on p and β, the variance of the polar angle gets larger. Since according to Eq. (7.43) the scattering

contribution is proportional to this variance, a systematic underestimation is observable mainly for the angular distributions in Fig. 7.10.

In summary, the comparison of ACTS with Geant4 shows that the implementation of the extrapolation as it was done for ACTS shows in most cases a good agreement for a sufficiently large momentum with respect to projection and statistical errors. The major deviation between both algorithms is driven by momentum loss due to material interaction. This is a consequence of the used model of the interaction impact. While the silicon detector provided just issues related to the material interaction at a few points along the trajectory, in the dense environment the problem is more complicated. In addition to the energy loss, the scattering requires a careful treatment. This emphasises a careful construction and application of a material map.

Although the formalism allows a flexible application for various scenarios, the plots show that the environment provided for the Propagator defines the similarity of the extrapolation and the Geant4 simulation and thus the reliability of the reconstructed tracks. By considering the absence of any measurements that would reduce the uncertainty and regulate the mean parameters, the results shown in this chapter are worse than in the track reconstruction. Since a common particle detector consists of several sensitive layers, the momentum drift gets damped after a certain extrapolation distance. Hence, it can concluded that the extrapolation of the track parametrisation is applicable for track reconstruction.

7.8.4 Ridders Algorithm

The Geant4 simulation provides the results that are intended to be reproducible by other software. As shown in the previous sections, a comparison between ACTS and Geant4 is rather complicated while certain error sources remain due to the different approach to things such as material. Since the covariance matrix is error prone with the applied approximations, the Ridders algorithm is used in the following. As this was implemented for the ACTS, the entire application is executable without the external dependency on Geant4. Furthermore, the material and magnetic field description as well as the detector geometry is identical. Hence, a direct comparison between algorithms is possible. However, considering the Geant4 extrapolation as the true trajectory in simulation, the following section focuses on the comparison of algorithms while the truth connection relies on Geant4.

As in the previous sections, the covariance transport will be considered in two different scenarios: Vacuum and dense environment. For both scenarios, the covariance transport using different, random initial parameters is considered. The spatial parameters are sampled from normal distributions with a mean of zero. For x and y a standard deviation of 50 mm, for z of 100 mm was used. The angles ϕ and θ are sampled uniformly from their entire domain. For the particles momentum uniform values between 50 MeV and 100 GeV are used. The charge is set randomly to -1, 0 or 1 and the extrapolation distance is drawn randomly between zero and 5 m. For both cases a constant magnetic field of 2 T in z-direction is applied, for the dense environment constant volume material consisting of Beryllium is used. While the extrapolation from a surface to another surface

through vacuum is by definition performed without scattering, for the volume material case it had to be disabled explicitly. Since the Ridders algorithm extrapolates multiple times, the algorithm is incapable of treating these effects. Although they could be added afterwards, the effect would be identical as for the covariance matrix transport and thus negligible. The mean of the start parameters and from the end parameters define the curvilinear surface at which the covariance matrices are associated to.

While the different initial parameters are also considered in the comparison to Geant4, the distance was given by the detector geometry. The component-wise entries of the uncertainties and the determinants versus the extrapolation distance as obtained from the Ridders algorithm and the covariance transport are shown in Fig. 7.11 for vacuum and in Fig. 7.12 for volume material. For both scenarios, both algorithms provide almost identical results over the entire range. The observable small, bin-wise deviation is thereby a result of the performed linear regression in the Ridders algorithm with the given finite precision and variations.

The results emphasise the point from the previous section: The description of the underlying detector geometry and its components is a crucial part for a precise extrapolation. As the only difference between the two methods are the evaluation of the covariance matrix, it shows that the Ridders algorithm will produce the same deviations as the covariance transport formalism. Furthermore, there is no improvement visible compared to the covariance transport. This can be interpreted as a correct extrapolation of the covariance under the given circumstances of environmental information and the material interaction model.

Although the Ridders algorithm strengthens the confidence in the covariance transport method, the underlying physical effects and environmental conditions are identical for both scenarios. Hence, the comparison between the two algorithms rely on a correct extrapolation of the mean. Though, under this assumption, the algorithm serves for ACTS as a possibility of continuously testing[9] the correctness of the extrapolation without additional external dependencies. As this part is one of the major components in the track reconstruction, it is crucial to provide a continuous integration (CI)[10] of these elements.

The shown distributions are a projection of the sampled parameters on a single parameter. For completeness, the projections on the other parameters are shown in Sec. C.1.

---

[9]Any code development is tested for correctness before it becomes a part of the code base. In this case a comparison between the algorithms is performed and it is required that the results are sufficiently similar.

[10]This term describes the continuous combination of software parts for compilation, testing etc. to ensure and improve the software quality.
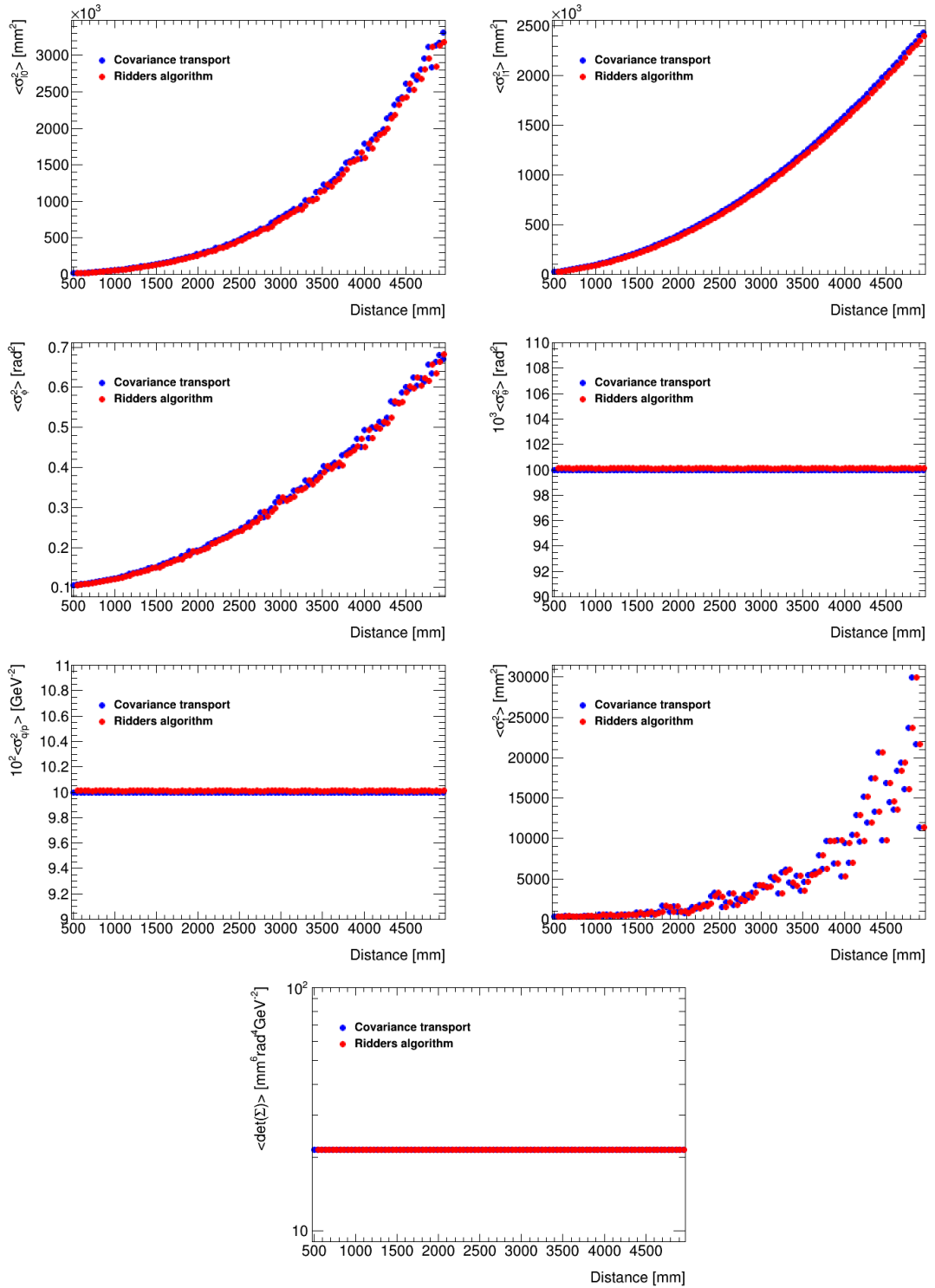
Figure 7.11: Comparison of the diagonal terms of the covariance matrix and the determinant for an extrapolation from curvilinear to curvilinear parameters in vacuum between the Ridders algorithm and the covariance transport as function of the distance. The bin centres are shifted for readability.
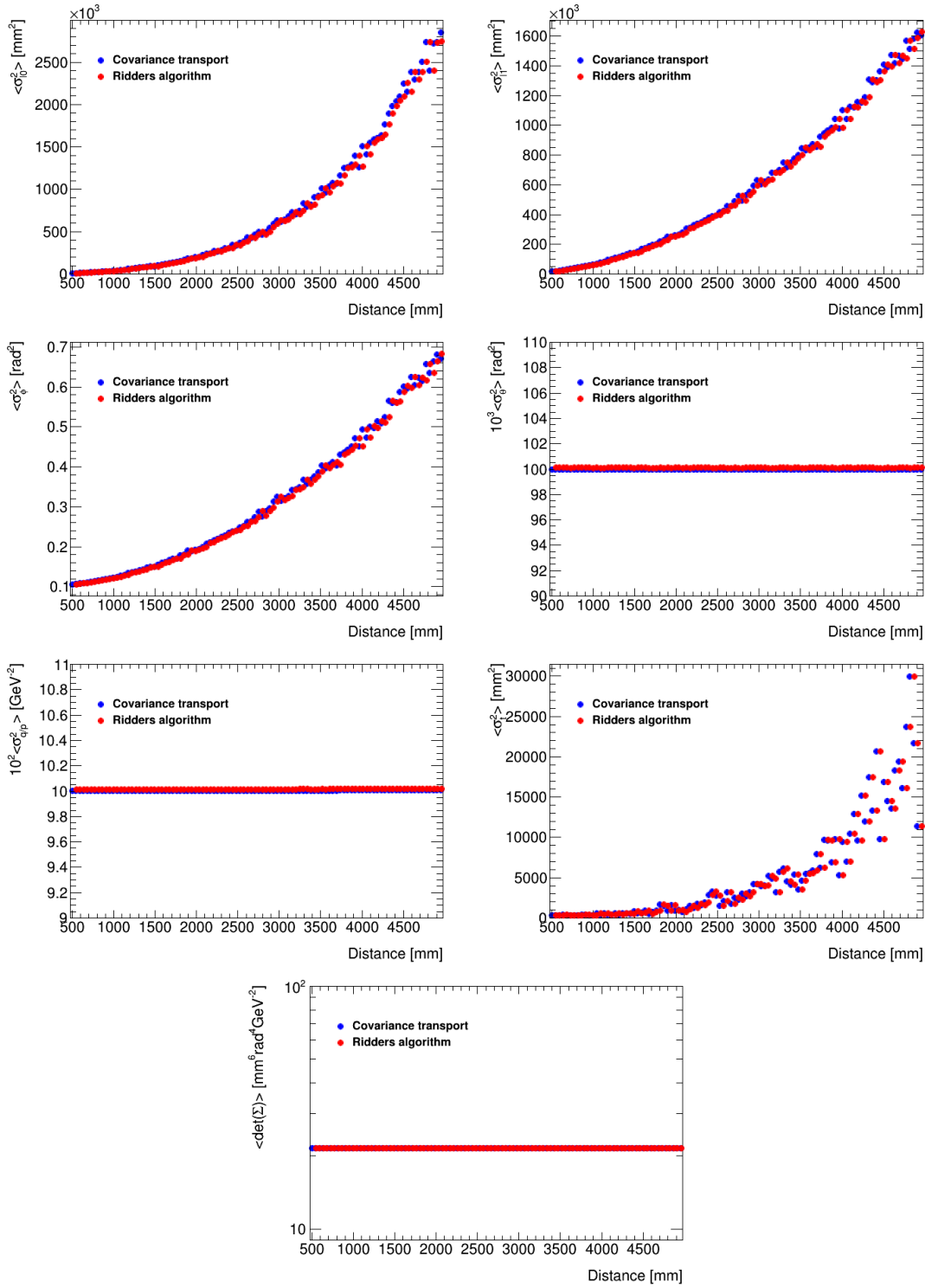
Figure 7.12: Comparison of the diagonal terms of the covariance matrix and the determinant for an extrapolation from curvilinear to curvilinear parameters in matter between the Ridders algorithm and the covariance transport as function of the distance. The bin centres are shifted for readability.

8 Track Reconstruction with Volume Bound Measurements

In Sec. 3.2.2.1, 3.2.2.2 and 3.3.1 different semiconductor tracking detectors are introduced that follow the working principle shown in Fig. 3.16. Due to the modules arrangement, a charged particle will traverse a well-defined plane at the centre of a module, in the following referred to as *read-out plane*. Although the electron-hole pairs, created during the particles transition, produce the actual measurement that is read-out, it can be considered as a sample of the true trajectory. At the read-out plane itself, the sample can be expressed as given in Eq. (4.13). Thereby, the mean $\mu_{\text{truth}}^{\text{particle}}$ and the sample parameters are given at the read-out plane, projected into the subspace of measured parameters. In tracking detectors, those parameters are usually spatial parameters.

In contrast to the semiconducting detectors, the TRT and also the MDTs are gas detectors. In both detector components, the electron-ion pairs created by the incident particle in the gas volume are registered by the wire at the centre of the drift tube. Hence, the particle trajectory does not need to traverse the read-out wire. This corresponds to a displacement of the actual measurement origin in the gas and registration of the measurement at the wire. Thus, for such measurements the mean $\mu_{\text{truth}}^{\text{particle}}$ of the sample at the wire does not exist. Due to information about the distance travelled by the ionisation electrons, the origin of the ionisation can be reconstructed. For those reconstructed measurement origins, Eq. (4.13) can be utilised. Here, Σ_{det} also needs to take the uncertainty due to the reconstruction into account.

Within this chapter detectors with a displacement between the origin and the registration of a measurement are considered. In Sec. 8.1 a typical type of gas detectors is presented. This type provides the same displacement by principle but is easier to grasp from the underlying geometry in comparison to the tube design of the TRT and MDT. In Sec. 8.2 the description of the measurement and in Sec. 8.3 the description of the extrapolation is considered. Both parts will be used in Sec. 8.4 in order to reconstruct the particles trajectory. The last section then compares the found result with the different approximations. While the first two sections describe the scenario, the other sections were developed and applied as part of this thesis.

8.1 Time Projection Chamber

In 1978 the so-called *Time Projection Chamber* [130] (TPC), a gas detector principle was proposed. An overview of the TPC concept is shown in Fig. 8.1. The entire volume is filled with a gas mixture consisting of a noble gas and a quenching gas. The atoms of the noble gas X are thereby the ones intended to be ionised by the incident particle. Hence,
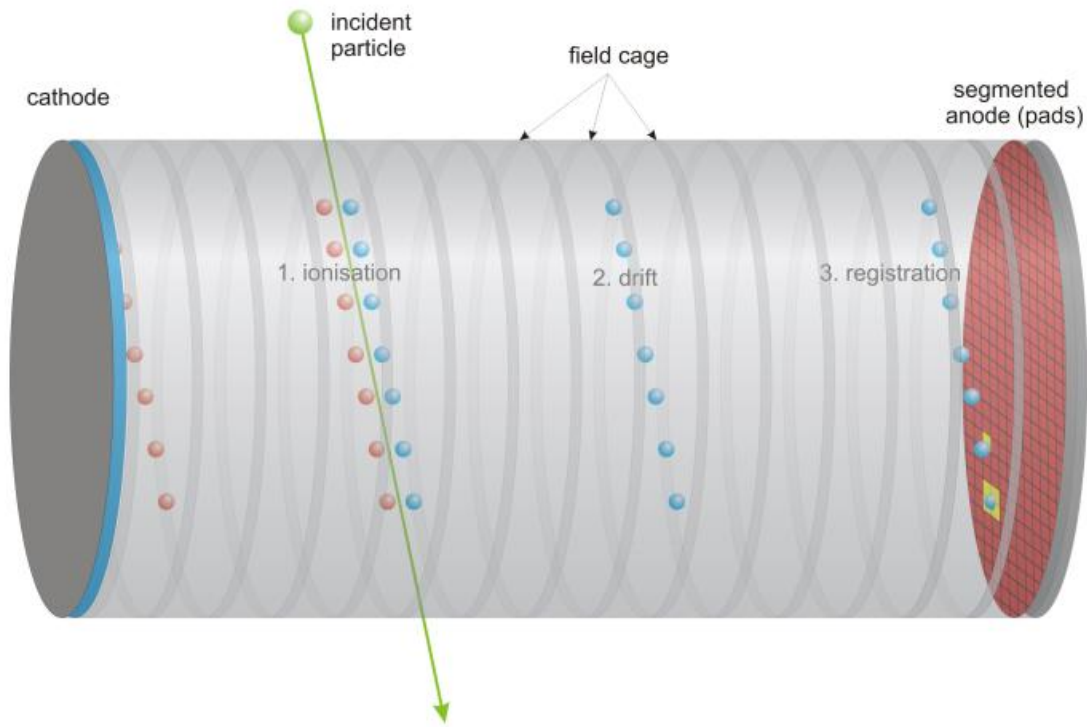
Figure 8.1: Schematic illustration of the TPC detection principle [131].

the choice of gas is thereby driven by the required ionisation energy and the ionisation cross-section as shown in Fig. 8.2 (left). As the atom can be in an excited state X^* after the interaction, a photon would be emitted. Due to photoelectric effect, this can lead to sparks in the sensitive components of the detector [134]. In order to prevent this from happening, the quenching gas is utilised. Due to the Penning effect [135], the photon is transferred to quenching gas which emits an electron instead. The charged ions then drift in an electric field to the cathode and get neutralised. As shown in Fig. 8.2, the quenching gas can thereby be just a small fraction in the mixture.

The measurement is created by the ionisation electrons. Under the influence of an electric field, those drift towards the anode. In order to optimise the measurement precision, the electric field is built such that it is parallel to the magnetic field inside the TPC. This leads to an acceleration of the electrons parallel to the direction of the magnetic field and thus to a vanishing of the Lorentz force. While cathode and anode provide a plate capacitor, the field is supported by the field cage. Therewith the homogeneity is enhanced. This field leads to an even acceleration of the electron. As the electron drifts through the gas towards the anode, diffusion and other interactions like distortions of the particles trajectory due to the presence of space charge in the gas mixture occur. These effects affect the overall resolution and the enhancing of the signal production. In order to suppress the effect from diffusion, high electrical fields are required. The choice of gas mixture influences thereby the applicable field strength
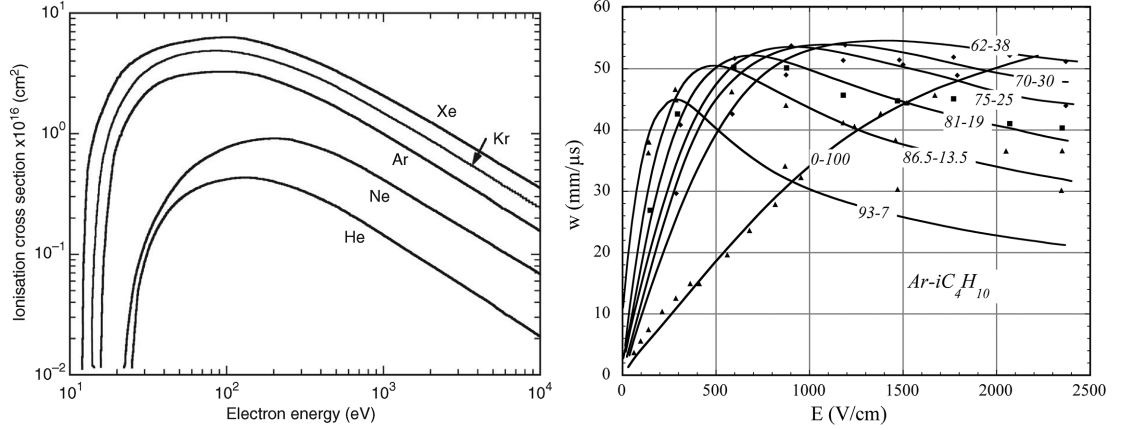
Figure 8.2: Left: Ionisation cross-section of the five lightest noble gases versus the energy of an incident electron. Heavier atoms have a larger cross section for a given electron energy [132]. Right: Electron drift velocity in argon-isobutane for different concentrations versus the external electric field. Even a small fraction of quenching gas modifies the shape of the graph significantly leading to higher drift velocities for smaller electric field [133].

regime. While the operation in proportional mode is intended, the transition point to Geiger mode can be pushed towards stronger field strengths by the mixture.

The pads at the anode measure the incoming electrons. For the layout of the detector multiple different concepts are used. Common designs utilise gas detectors such as Multi-Wire Proportional Chambers (MWPC's), Gas Electron Multipliers (GEM's) and Micro-MEsh Gaseous Structures (MicroMegas) or silicon detectors. Therewith a position measurement in r-ϕ-direction can be provided. For the reconstruction of the measurements origin, the z-position needs to be determined. This requires an external input from other detector components such as additional tracking detectors. The therewith provided information about the third spatial coordinate then allows the extrapolate the measurements back to its hypothetical origin. Although the measurement is not restricted to only spatial information, without loss of generality the focus in the following relies on reconstructed measurements with only three spatial coordinates.

8.2 Measurement Description

A measurement obtained in the TPC can be stored using the same container concept as described in Sec. 5.2.3. While the concept itself is centred around surface bound measurements, some modifications are required. Both, the concept and the implementation are discussed in the following. Classes related to the implementation from Chapter 5 are printed in small caps within this section.

The measurement of a particles trajectory is registered at the anode of the TPC. Since the data storage is closely linked to the track reconstruction and fitting workflow, the concept of the SOURCE LINK is required which provides a linkage between the mea-

surement and the measuring GEOMETRY OBJECT. Eq. (4.40) can be understood as the sensitive SURFACE that triggers the extrapolation. Inside the TPC, the sensitive SUR-FACE is given by the pads. However, a trigger to extrapolate to this SURFACE assumes that the trajectory intersects with the anode. In this case, the VOLUME of the TPC is the only considerable object for the source of the measurement and the trigger of an extrapolation, since the particle traversed the TPC. Furthermore, the pads can be considered as part of the BOUNDARY SURFACE of the TPC and hence are a part of the associated GEOMETRY OBJECT. Since the data storage in ACTS is centred around the storage of SURFACES as source of measurements, this concept needs to be extended to include VOLUMES, too. Both have in common that they are GEOMETRICAL OBJECTS identified via a GEOMETRY IDENTIFICATION NUMBER (geoID). Therewith, the underlying object type gets generalised, as an arbitrary GEOMETRY OBJECT can be stored but requires a type deduction in order to be applicable.

Besides the association of a measurement to a GEOMETRICAL OBJECT, the SOURCE LINK also provides the parameters of the measurement itself. The pads register two dimensional measurements. By utilising the external provided z-position information, the three dimensional position information can be obtained. Although the source is just the two dimensional measurement at the anode, the Kalman filter relies on updating the parameters at a certain point along the trajectory and thus requires an UNCALIBRATED output along the trajectory. Therefore, the reconstruction of the two dimensional measurement is required in order to obtain the origin of the measurement. As this procedure is related to the underlying detector, including the electrical field and the external z-position information, a back propagation of the measured electrons to the location of the ionisation needs to be performed. Thus, this will be considered as an experiment specific detail that is not treated in ACTS. Consequently, it is assumed in the following that the SOURCE LINK produces internally and provides the access to a reconstructed, CALIBRATED MEASUREMENT at its origin.

In the context of a SURFACE bound measurement, the required parameters are reduced due to the knowledge of the SURFACE parameters. This allows to store at maximum two instead of three spatial parameters while the information contained in the measurement is preserved. As shown in Sec. 5.2.1 the maximum of stored parameters in this case is five parameters, if time information is present six. As the measurements of the TPC are bound to a VOLUME, the data reduction is not applicable in this case. Since three spatial parameters are required and Chapter 7 already considered a parametrisation free from a SURFACE constraint, the exact same parametrisation allows the storage of the TPC measurements. As the data storage requires more memory for VOLUME bound measurements than for SURFACE bound ones, a careful treatment is mandatory in this case. This is even more important since a TPC can produce more measurements per particle than a tracking detector. Another difference is given by the indices of the coordinates. Comparing the parameters in Eq. (7.18) with the free parameters in Eq. (7.45) shows that the spatial, direction, q/p and time indices differ between both vectors. Differing between the access patterns allows thereby the identification of the underlying parametrisation and thus also the identification of the stored GEOMETRY OBJECT type.

8.3 Free Parameter Propagation

The extrapolation shown in Chapter 7 is conceptionally designed to start and end at a surface. Between both points an arbitrary amount of steps can occur, driven by external conditions and constraints such as the integration error, described in Sec. 7.2.2. While the start and end point are described in the coordinate system bound to the surface, the steps in between use the global coordinate from Eq. (7.45). Hence, the mean of the extrapolation is already provided in global coordinates by construction. As the measurement is provided inside the volume without any surface constraint, the simplest choice of its parametrisation is given by the one used for the extrapolation. In comparison to the bound measurements, this parametrisation, as it is also used for the global representation of the extrapolation, would then be in a global frame, i.e. the provided parameters are not mandatory inside the volume itself.

Given that both, the mean and the measurement use the same parametrisation, the required extrapolation distance s can be derived without any parameter conversions. Furthermore, since the mean is extrapolated in global parameters, the extrapolation end point can be chosen arbitrarily along the trajectory, i.e. it does not depend on a surface intersection or requires the creation of a (curvilinear) surface.

Considering the extrapolation itself, the formalism in Chapter 7 is driven by the differential Eq. (7.6). This equation describes the influence of a magnetic field on the particles trajectory. As described in Sec. 8.1, due to ionisation electrons and charged ions in the TPC drift towards the end-caps under the influence of an applied electrical field. Hence, the differential equation needs to be extended by this in general position dependent field $E(r) \in \mathbb{R}^3$. Therewith the general equation of the Lorentz force

$$\frac{d^2r}{ds^2} = \frac{q}{p}\left(\frac{dr}{ds} \times B(r)\right) + \frac{qm}{p^2}E(r) = \lambda\left(T \times B(r)\right) + \lambda^2\frac{m}{q}E(r) \tag{8.1}$$

prescribe the trajectory of a particle with momentum p, charge q and relativistic mass $m = \gamma m_0$ through the geometry. The last equality assumes thereby $q \neq 0$. The addition of the electric field will consequently modify Eq. (7.8) such that the direction vector T is now given by

$$\frac{d}{ds}T = \lambda\left(T \times B(r)\right) + \lambda^2\frac{m}{q}E(r).$$

The position is thereby indirectly affected by the modification of the direction vector. Also momentum and time are just indirectly affected. Consequently, modifying the differential equation for the direction vector will automatically lead to the corrected step evaluation in the RKN4 integration. Under the assumption that the electric field is constant inside the TPC, i.e. $E(r) = E_0$ the contribution of the electric field to a step through vacuum following Eq. (7.10) is given by

$$T_{n+1} = T_n + \frac{h}{6}\left(k_1 + 2k_2 + 2k_3 + k_4\right) + h\lambda^2\frac{m}{q}E_0$$

$$r_{n+1} = r_n + hT_n + \frac{h^2}{6}\left(k_1 + k_2 + k_3\right) + \frac{h^2}{2}\lambda^2\frac{m}{q}E_0$$

with k_1, k_2, k_3 and k_4 as defined in Eq. (7.9). Due to the magnetic field the considerable momenta need to be sufficiently large. As electric fields for such setups are of $\mathcal{O}(100)$ V/m, the contribution of this addend to the particles trajectory will be a small correction, especially due to the lower momentum threshold and hence usually negligible. In addition, the interaction of the particle and the gas and hence the momentum loss as described in Sec. 7.4 has to be considered. The form of the integration error remains due to the additional addend unchanged.

Beside the mean, the covariance matrix needs to be represented at the end point of the extrapolation. This will be considered in the following Section, starting with the modifications of the Ridders algorithm. Afterwards the modifications of the numerical covariance transport are described.

8.3.1 Ridders Propagator

While the extrapolation of the mean between a start and an end point is always performed in global coordinates, the target coordinate system requires at most a single coordinate transformation. This transformation is just necessary if the target coordinate system is bound to a surface. The transformation of the initial coordinates to the global frame is thereby mandatory in order to initiate the extrapolation itself. While this is a rather simple problem for the mean, the covariance matrix requires more considerations.

The Ridders algorithm provides a semi-analytical solution for the covariance transport by repetitive extrapolation of the mean and a component-wise wiggling of the start parameters. As in this case the start and end parameters can be either bound to a surface or free from such constraint, four different scenarios exist. The wiggling is thereby defined by the start parameters. The bound parametrisation is covered in Sec. 7.3.2. For the global start parameters as defined in Eq. (7.45), the spatial, momentum and time parameters can be modified independently as in the bound case. The direction $T \in \mathbb{R}^3$ on the other hand with $|T| = 1$ is a Cartesian representation of a point on a unit sphere with three parameters. Hence, a component T^i of the vector has to satisfy the condition

$$T^i = \sqrt{T^{j2} + T^{k2} - 1}$$

with $i, j, k \in \{1, 2, 3\}$ and $i \neq j$, $j \neq k$ and $k \neq i$. An independent variation of any of those parameters is consequently impossible. Although this is a more complicated situation for the Ridders algorithm, the utilisation of the direction vector itself in the parametrisation is beneficial due to the Lorentz force. In order to vary the direction components, a coordinate transformation is required to decouple the interdependencies of T using Eq. (5.3). The parameters vector used inside the Ridders algorithm is then

given by

$$
y^R = \begin{pmatrix} x \\ y \\ z \\ t \\ \phi \\ \theta \\ q/p \end{pmatrix}
\tag{8.2}
$$

and thus component-wise independent. The obtained variation can afterwards be transformed back into the global parametrisation and used for the extrapolation.

The Ridders algorithm itself just needs to calculate the Jacobian J in order to obtain the final covariance matrix. The general workflow compared to the scenario described in Sec. 7.3.2 remains unchanged. Noteworthy is thereby that the covariance matrices Σ_{initial} and Σ_{final} can be six or eight dimensional, depending on the start and end parametrisation. The variation of the start parameters have to provide the corresponding dimensions in the Jacobian. For the case from and to bound parametrisation the Jacobians are obtained by the formalism in Sec. 7.3.2. A similar complexity is required for the bound to free parametrisation case. However, both scenarios starting in free parameters, free to bound and free to free parametrisation, utilise the parametrisation from Eq. (8.2). As this leads to a 6×7 or 8×7 Jacobian, an additional transformation is required:

$$
J = \frac{\partial y_{\text{final}}}{\partial y_{\text{initial}}} = \frac{\partial y_{\text{final}}}{\partial y^R} \frac{\partial y^R}{\partial y_{\text{initial}}}
\tag{8.3}
$$

While $\partial y_{\text{final}}/\partial y^R$ is the output of the Ridders algorithm, the second term is not calculated by default. Since this additional transformation $\partial y^R/\partial y_{\text{initial}}$ is just required for extrapolations starting in free parameters, y_{initial} is given in free parameters. Therewith, the matrix can be calculated directly as

$$
\frac{\partial y^R}{\partial y_{\text{initial}}} = \frac{\partial(x, y, z, \phi, \theta, q/p)}{\partial(x, y, z, T^x, T^y, T^z, q/p)}
$$

$$
= \begin{pmatrix}
1 & 0 & 0 & 0 & 0 & 0 & 0 & 0 \\
0 & 1 & 0 & 0 & 0 & 0 & 0 & 0 \\
0 & 0 & 1 & 0 & 0 & 0 & 0 & 0 \\
0 & 0 & 0 & 1 & 0 & 0 & 0 & 0 \\
0 & 0 & 0 & 0 & \frac{-T^y}{T^{x2}+T^{y2}} & \frac{-T^x}{T^{x2}+T^{y2}} & 0 & 0 \\
0 & 0 & 0 & 0 & \frac{T^x T^z}{\sqrt{T^{x2}+T^{y2}}} & \frac{T^y T^z}{\sqrt{T^{x2}+T^{y2}}} & \sqrt{T^{x2}+T^{y2}} & 0 \\
0 & 0 & 0 & 0 & 0 & 0 & 0 & 1
\end{pmatrix}
$$

using the relations between spherical and Cartesian coordinates

$$
\theta = \arccos\left(\frac{T^z}{\sqrt{T^{x2}+T^{y2}+T^{z2}}}\right) \qquad \phi = \text{atan2}(T^y, T^x).
$$

Although the Ridders algorithm allows the transport of the covariance matrix, due to the required calculations the algorithm itself only delivers results for comparisons. Therefore, the additional matrix calculation is unproblematic. While the application of the

parametrisation in ACTS optimises the step evaluation of the Lorentz force, a drawback can be found in the generalisation of start parametrisations.

8.3.2 Covariance Transport

The covariance transport formalism has to handle all four cases of bound and free start and end parametrisations, too. Furthermore, the required end parametrisation is known as soon as the covariance transport is initiated. While the extrapolation of the mean only requires at most one single coordinate transformation at the end point, the situation for the covariance transport is more complex since a combination of Jacobians is required. Within this section the three missing cases that involve free parameters are discussed.

As discussed in Sec. 7.3 the Jacobian consists of

$$
\begin{aligned}
J &= J_{q \leftarrow g} J_{\text{transport}} J_{g \leftarrow p} + J_{\text{projection}} \\
&= \frac{\partial y_f^q}{\partial y_i^q} + \frac{\partial y_f^q}{\partial s} \frac{\partial s}{\partial y_i^p} \\
&= \frac{\partial y_f^q}{\partial y_f^g} \frac{\partial y_f^g}{\partial y_i^g} \frac{\partial y_i^g}{\partial y_i^p} + \frac{\partial y_f^q}{\partial y_f^g} \frac{\partial y_f^g}{\partial s} \frac{\partial s}{\partial y_i^p} \\
&= \frac{\partial y_f^q}{\partial y_f^g} \left(\frac{\partial y_f^g}{\partial y_i^g} \frac{\partial y_i^g}{\partial y_i^p} + \frac{\partial y_f^g}{\partial s} \frac{\partial s}{\partial y_i^p} \right)
\end{aligned}
$$

with the global parametrisation g and the start and end parametrisations p and q. The indices i and f denote the initial and final position of the extrapolation respectively. Within this form $J_{\text{transport}}$ is independent from the outer conditions of the used parametrisations p and q. Hence, this part is remain unchanged in all scenarios. The coordinate transformation Jacobians for bound parameters of p and q are already discussed in Sec. 7.3. It is therefore assumed in the following that at least one of these parametrisations is given in free parameters.

Starting with the case of free to bound parameters, i.e. $p = g$. This scenario leads to $J_{g \leftarrow p} = \partial y_i^g / \partial y_i^p = 1$. The derivative $\partial s / \partial y_i^p$ can be derived using the same idea as in Eq. (7.31). One obtains therewith for the curvilinear case

$$
dr_f = \frac{\partial r_f}{\partial y_i^p} dy_i^p + \frac{\partial r_f}{\partial s} ds \Rightarrow \frac{\partial s}{\partial y_i^p} = -T_f \frac{\partial r_f}{\partial y_i^p}.
$$

As described in Sec. 7.3.1.1 the first factor on the right hand side will change for the non-curvilinear case. Since the start parameters are assumed to be given in the global frame, the dimension of the matrix $\partial r_f / \partial y_i^p$ will be larger in comparison to the local parametrisation considered in Chapter 7.

Beside the changes in the two matrices mentioned above, as the propagation start in free parameters, the same consideration as in Sec. 8.3.1 regarding the direction T need to be performed. In the pure bound case, any variation of the start parameters is performed using the bound parameters and therewith the angular representation of the direction. Thus, all Jacobians obtain the correlation between the individual direction

vector components due to the $\partial y_i^g / \partial y_i^p$ Jacobian. Since this component is missing in the free parametrisation, the correlation terms $\partial T^i / \partial T^j$ for $i, j = 1, 2, 3$ and $i \neq j$ vanish. While the calculations above remain valid for an independent parametrisation, the utilised direction vector demands an additional transformation analogue to Eq. (8.3).

The Ridders algorithm allows the direct construction of the Jacobian using an arbitrary initial parametrisation. Since the covariance transport formalism is closely linked to the used parametrisations of the mean in the construction of the transport Jacobian, the Jacobian $\partial y_{\mathrm{final}} / \partial y^R$ in the Ridders algorithm is not constructible. However, by introducing an additional Jacobian of the form

$$
\frac{\partial y_i^g}{\partial y_i^R} = \frac{\partial(x, y, z, T^x, T^y, T^z, q/p)}{\partial(x, y, z, \phi, \theta, q/p)}
$$

$$
= \begin{pmatrix}
1 & 0 & 0 & 0 & 0 & 0 & 0 \\
0 & 1 & 0 & 0 & 0 & 0 & 0 \\
0 & 0 & 1 & 0 & 0 & 0 & 0 \\
0 & 0 & 0 & 1 & 0 & 0 & 0 \\
0 & 0 & 0 & 0 & -\sin(\theta)\sin(\phi) & \cos(\theta)\cos(\phi) & 0 \\
0 & 0 & 0 & 0 & \sin(\theta)\cos(\phi) & \cos(\theta)\sin(\phi) & 0 \\
0 & 0 & 0 & 0 & 0 & -\sin(\theta) & 0 \\
0 & 0 & 0 & 0 & 0 & 0 & 1
\end{pmatrix}
$$

the required transport Jacobian can be obtained afterwards. The derivatives are thereby obtained from the coordinate transformations in Eq. (5.3) from Cartesian to spherical coordinates. Applying the back transformation as in Eq. (8.3) leads to the Jacobian from a free to a bound representation

$$
\begin{aligned}
J_{b \leftarrow f} &= \frac{\partial y_f^q}{\partial y_f^g} \left(\frac{\partial y_f^g}{\partial y_i^R} \frac{\partial y_i^R}{\partial y_i^g} + \frac{\partial y_f^g}{\partial s} \frac{\partial s}{\partial y_i^g} \right) \\
&= \frac{\partial y_f^q}{\partial y_f^g} \left(\frac{\partial y_f^g}{\partial y_i^g} \frac{\partial y_i^g}{\partial y_i^R} \frac{\partial y_i^R}{\partial y_i^g} + \frac{\partial y_f^g}{\partial s} T_f^T \frac{\partial r_f}{\partial y_i^g} \right) \\
&= \frac{\partial y_f^q}{\partial y_f^g} \left(\frac{\partial y_f^g}{\partial y_i^g} \frac{\partial y_i^g}{\partial y_i^R} + \frac{\partial y_f^g}{\partial s} T_f^T \frac{\partial r_f}{\partial y_i^g} \frac{\partial y_i^g}{\partial y_i^R} \right) \frac{\partial y_i^R}{\partial y_i^g}
\end{aligned}
$$

in the used free parametrisation. The last transformation is given by identifying $\partial r_f / \partial y_i^g$ as part of the transport Jacobians. The factor $\partial y_i^R / \partial y_i^g$ is added in order to preserve the correct denominator in the Jacobian. Noteworthy is here that within this coordinate transformation the product $\partial y_i^g / \partial y_i^R \cdot \partial y_i^R / \partial y_i^g$ is not an identity matrix.

The second scenario that will be considered is the Jacobian from a bound to a free representation. In this case the final coordinate transformation by $\partial y_f^q / \partial y_f^g$ becomes an identity matrix due to $q = g$. Furthermore, as the extrapolation ends in free parameters, a projection onto a surface is not required in this case. Thus, the cone defined by the covariance matrix around the mean remains unchanged as soon as the propagation

terminates, i.e. no path length variations occur. In the context of Eq. (7.26), any variation ds would then correspond to an additional step in the extrapolation but not to an in-place modification around the current position. Therewith, $\partial y_f^g / \partial s$ becomes a zero vector and finally the projection Jacobian $J_{\mathrm{projection}}$ becomes a zero matrix. The leads to the total Jacobian

$$J_{f \leftarrow b} = \frac{\partial y_f^g}{\partial y_i^g} \frac{\partial y_i^g}{\partial y_i^p}.$$

The last case is the transport from and to free parameters, i.e. $p = q = g$. Within this setup a mixture of the previous considerations has to be applied. Firstly, $\partial y_f^q / \partial y_f^g$ is again an identity matrix and using the same argument as before, the projection Jacobian vanishes. Since the extrapolation starts in free parameters, the correlation between the direction components need to be treated. As also in this case the transport Jacobian is provided alongside the parametrisation of the mean, the same additional Jacobians need the applied. This leads to the total Jacobian

$$J_{f \leftarrow f} = \frac{\partial y_f^g}{\partial y_i^g} \frac{\partial y_i^g}{\partial y_i^R} \frac{\partial y_i^R}{\partial y_i^g}.$$

While the Jacobians of all four scenarios are different, the explicit application cannot be foreseen. Given the knowledge that the start of the extrapolation is given in a certain parametrisation allows to deduce several components required in the following such as $J_{g \leftarrow l}$, $\partial y_i^g / \partial y_i^R$ or $\partial y_i^R / \partial y_i^g$.

8.3.3 Comparison between Covariance Transport Formalism and Ridders Algorithm

In Sec. 7.8 the extrapolation starts and ends at a surface. From that point the mean of the extrapolation with the three other combinations can be compared. This is done by starting an extrapolation at the origin using curvilinear or free parameters. The end parametrisation is then given in either curvilinear of free parameters. Thereby the curvilinear to curvilinear case serves as reference for the assumable correct solution.

Over the entire extrapolation distance a constant magnetic field of 2 T in z-direction is present. In the presence of magnetic deflection a comparison of the final positions mean is sufficient, since any difference in direction or momentum would lead to a different position.

For each extrapolation the initial parameters and the extrapolation distance are drawn from uniform distributions. An overview of the obtained differences is shown in Fig. 8.3. Considering the difference for the curvilinear to free parameters, the results are in all projected variations zero. For the other two cases one can see in all projections a certain deviation from the curvilinear to curvilinear case. As the underlying difference is given here by the different initial parametrisation, a coordinate transformation is missing in the extrapolations starting in free parameters. In comparison to the former case, the impact of a coordinate transformation before the extrapolation occurs is a larger impact than the transformation when finalising the extrapolation. This argument is supported
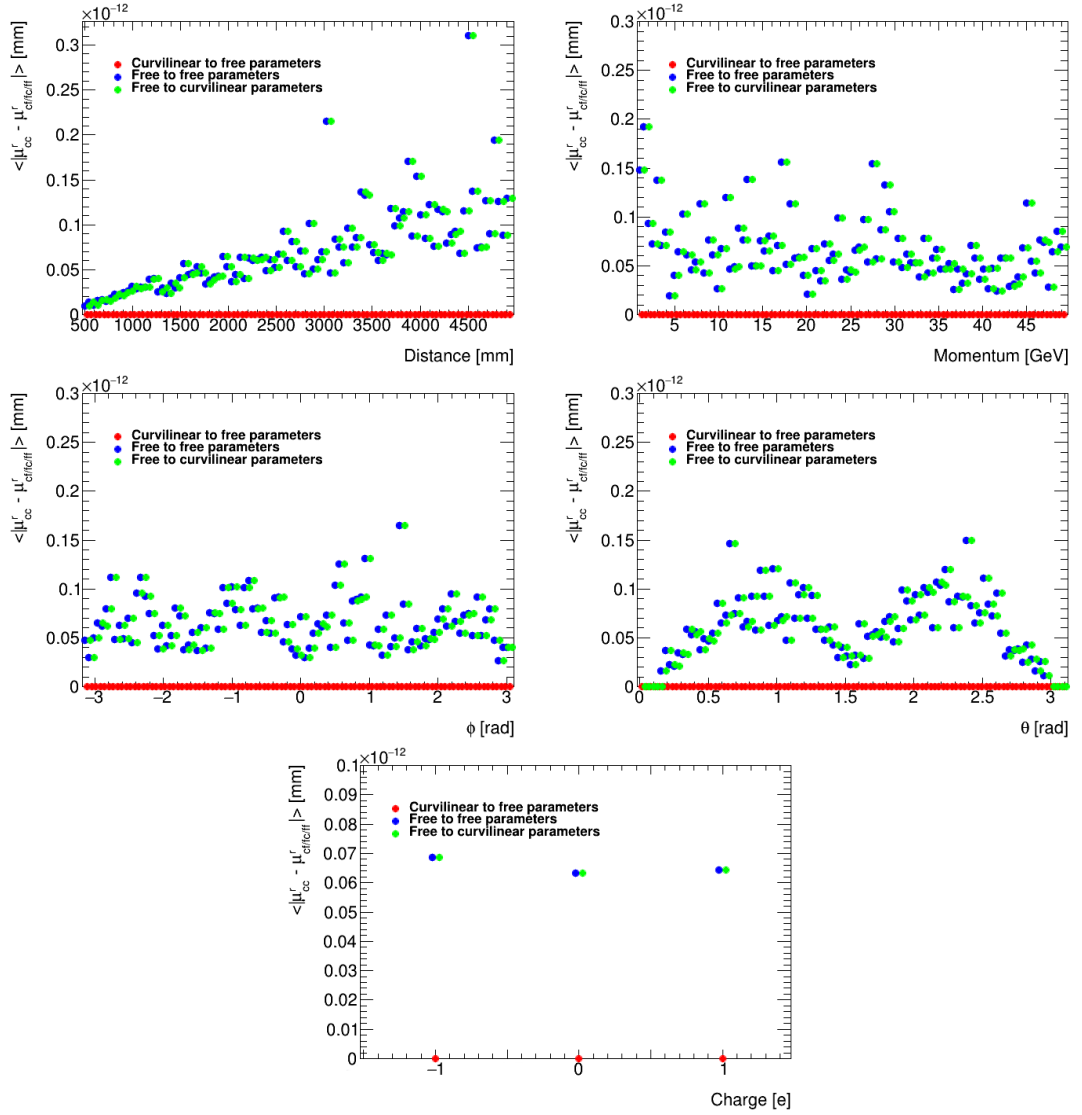
Figure 8.3: Comparison of the mean of the spatial distance between an extrapolation from and to curvilinear parameters (cc) and free to curvilinear (fc), curvilinear to free (cf) and free to free (ff) parameters. The plots show the deviation versus a variation of the total extrapolation distance (top left), initial momentum (top right), azimuthal angle (middle left), polar angle (middle right) and the electric charge (bottom). The bin centres are shifted for visibility.

by the observation that in all cases the deviation is almost identical in these two cases. Noteworthy are also the obtained ordinate values. As all of them are very small, the difference reaches the order of machine precision. This leads to the conclusion that the difference has its origin in the numerical accuracy of the applied transformation. Especially the distance dependency of the deviation supports the argument as the deviation

gets larger for longer extrapolations. Furthermore, a dependency of the initial angles on the final deviations can be found. As trigonometric functions are required for the coordinate transformations, the precision of their evaluation affects the final parametrisation. In total, the mean obtained from the three modifications are in good agreement with the former case. Stating a proper extrapolation in all scenarios by considering the difference in the final position leads to the conclusion that the path length of the trajectory is equivalent. Hence, the contribution of material is identical in all cases and thus can be neglected.

Beside the mean, the covariance matrix needs to be investigated, too. The same extrapolation setup is used as for the mean. Assuming that the extrapolation of the mean works properly, the Ridders algorithm allows to calculate the final covariance matrix from extrapolations of the mean. A validation of the correctness of the mean values relied on the similarity of the surface bound and unbound parametrisation. The Ridders algorithm on the other hand allows for a direct comparison to the covariance matrix transport technique by using the same parametrisation for start and end parameters in both cases. The covariance matrix has more entries that need to be compared. As a summary parameter the determinant of the covariance matrices are used. That way, the volume of the base vectors spanning up the space of the covariance matrix can be compared in a single number. The obtained results for the curvilinear to free parameters are shown Fig. 8.4, for free to free in Fig. 8.5 and for free to curvilinear in Fig. 8.6. The first two sets show very similar shapes in all parameters. For both distributions a very good agreement with the results obtained from the Ridders algorithm can be observed. A similar observation can be done for the third set for the extrapolation from free to curvilinear parameters. In this case the additional Jacobian for the projection of the covariance matrix onto the target surface is utilised. As the eight dimensional matrix is projected to the lower dimension, the distribution shapes become different. Except for the polar angle the distributions are flat. For this angle the projected ellipsoid of the determinant of the covariance matrix forms a parabola. This is the result of the uncertainties in the initial spatial components. Again, the transported covariance matrix is in all distributions in a very good agreement with the result from the Ridders algorithm.

Although the determinants do not exclude situations of unlucky compositions of matrix entries such that the determinant appear in good agreement while e.g. matrix elements are swapped. In order to strengthen the confidence in the shown results, in Sec. D.1 the distributions for the diagonal terms of each covariance matrix is shown. In summary, it can be considered that the extrapolation including free parameters as start or end point provides reliable results for the mean and the covariance matrix.

8.4 Free Kalman Formalism

In case of a surface bound measurement, the Kalman filter updates the parameters according to Eq. (4.35) and (4.36). As denoted in Eq. (4.21) an unbiased update required the mean of the extrapolation to be represented at the same surface. In order to achieve
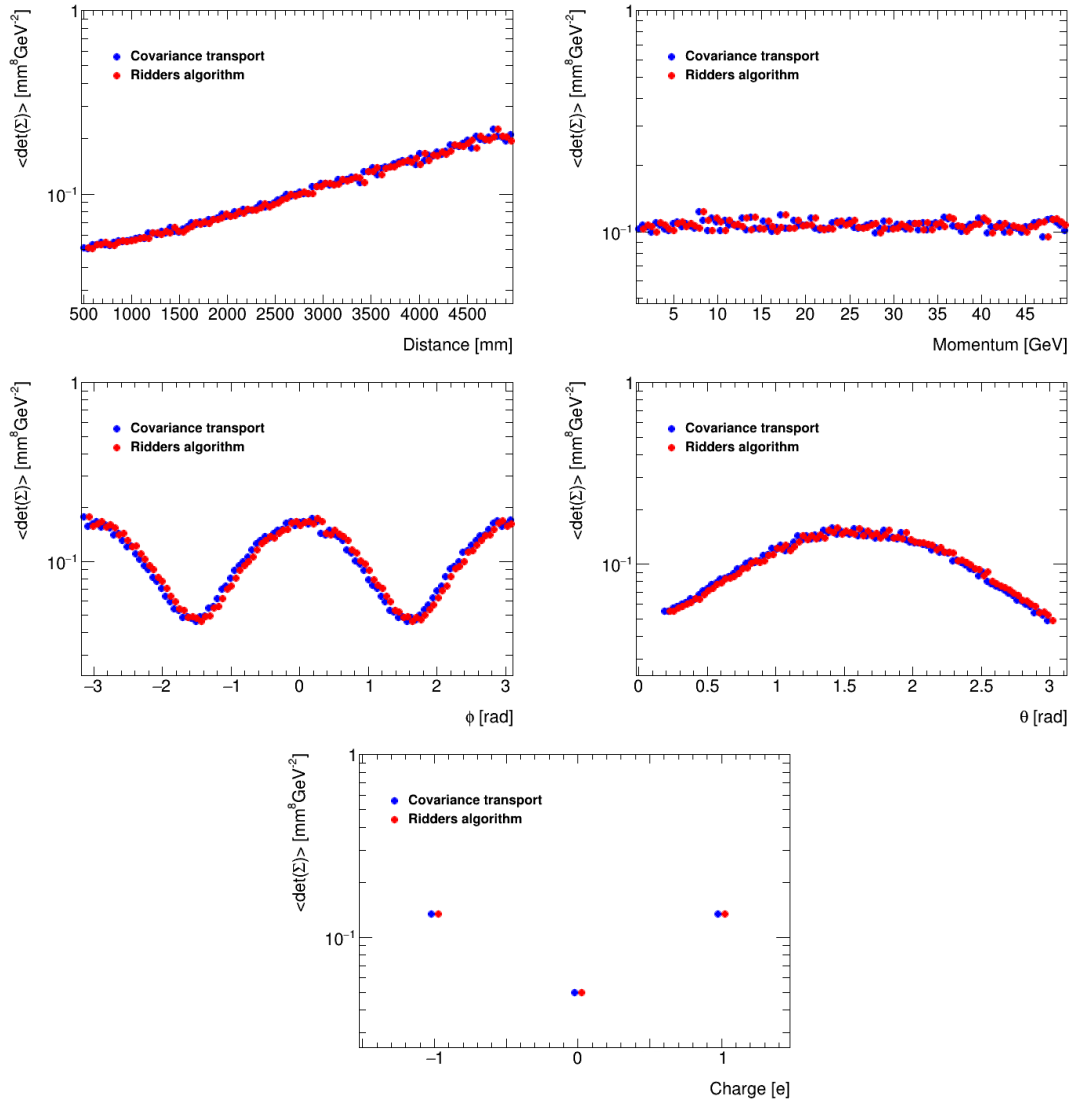
Figure 8.4: Determinant of the covariance matrix obtained from covariance transport and the Ridders algorithms in an extrapolation from curvilinear to free parameters versus the extrapolation distance (top left), initial momentum (top right), azimuthal angle (middle left), polar angle (middle right) and particle charge (bottom). The bin centres are shifted for visibility.

this update, the measurement itself triggers an extrapolation over the distance s as shown in Eq. (4.40).

While the surface bound measurement case has a single solution for s, a certain interval of extrapolation parameters lead to representations of the parametrisation inside the volume. Furthermore, the surface bound measurement case allows a workflow that separates the extrapolation to the surface and the measurement lookup. For volume
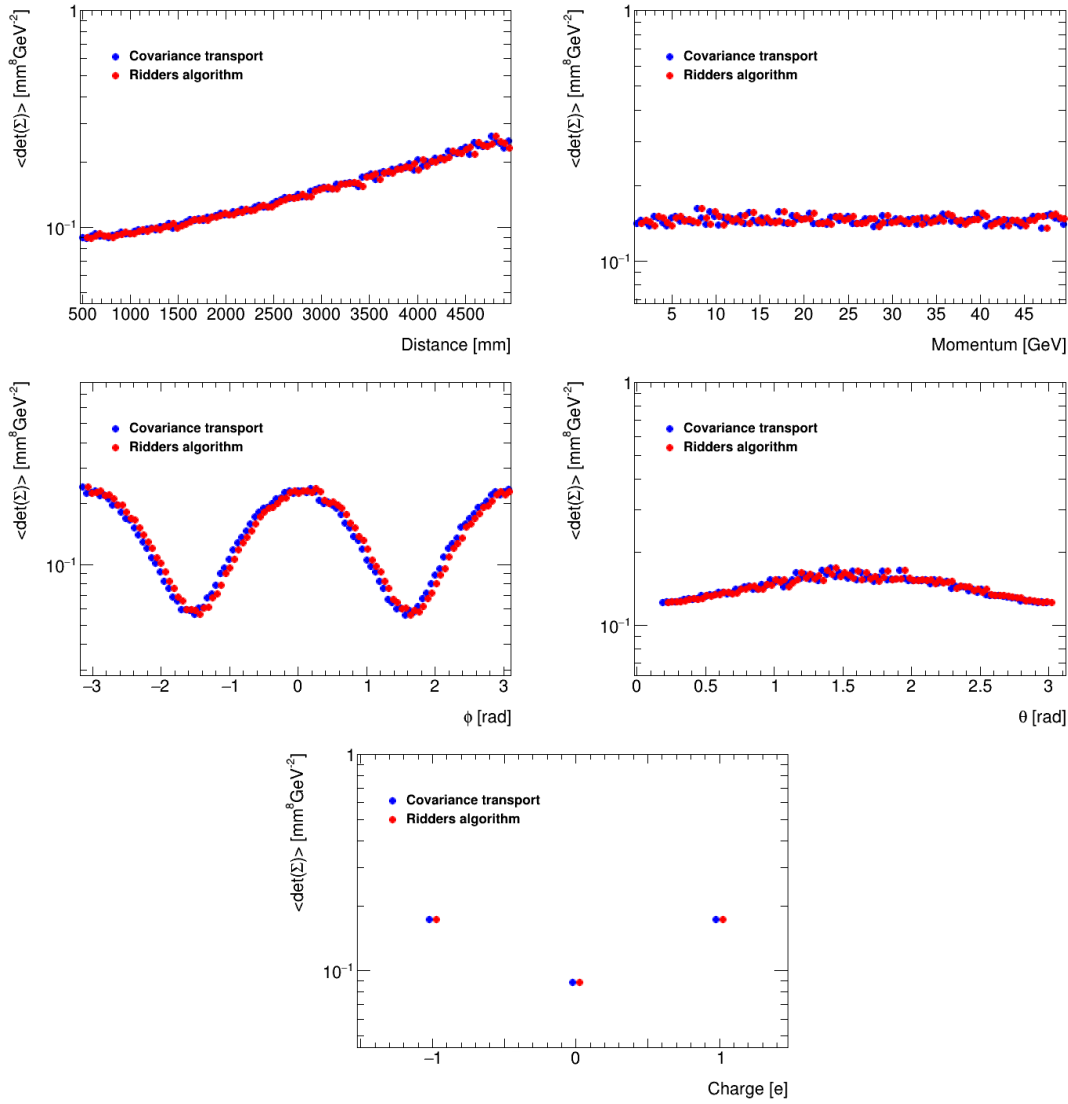
Figure 8.5: Determinant of the covariance matrix obtained from covariance transport and the Ridders algorithms in an extrapolation from free to free parameters versus the extrapolation distance (top left), initial momentum (top right), azimuthal angle (middle left), polar angle (middle right) and particle charge (bottom). The bin centres are shifted for visibility.

bound measurements, the location of the measurement has to trigger the extrapolation while the trajectory is inside the volume. The Kalman filter updates the parameters at a certain point along the trajectory. Hence, the measurement does not just trigger the extrapolation in this case but also has to dictate the update position. As a first step the update position will be treated. The update formalism will be derived afterwards.
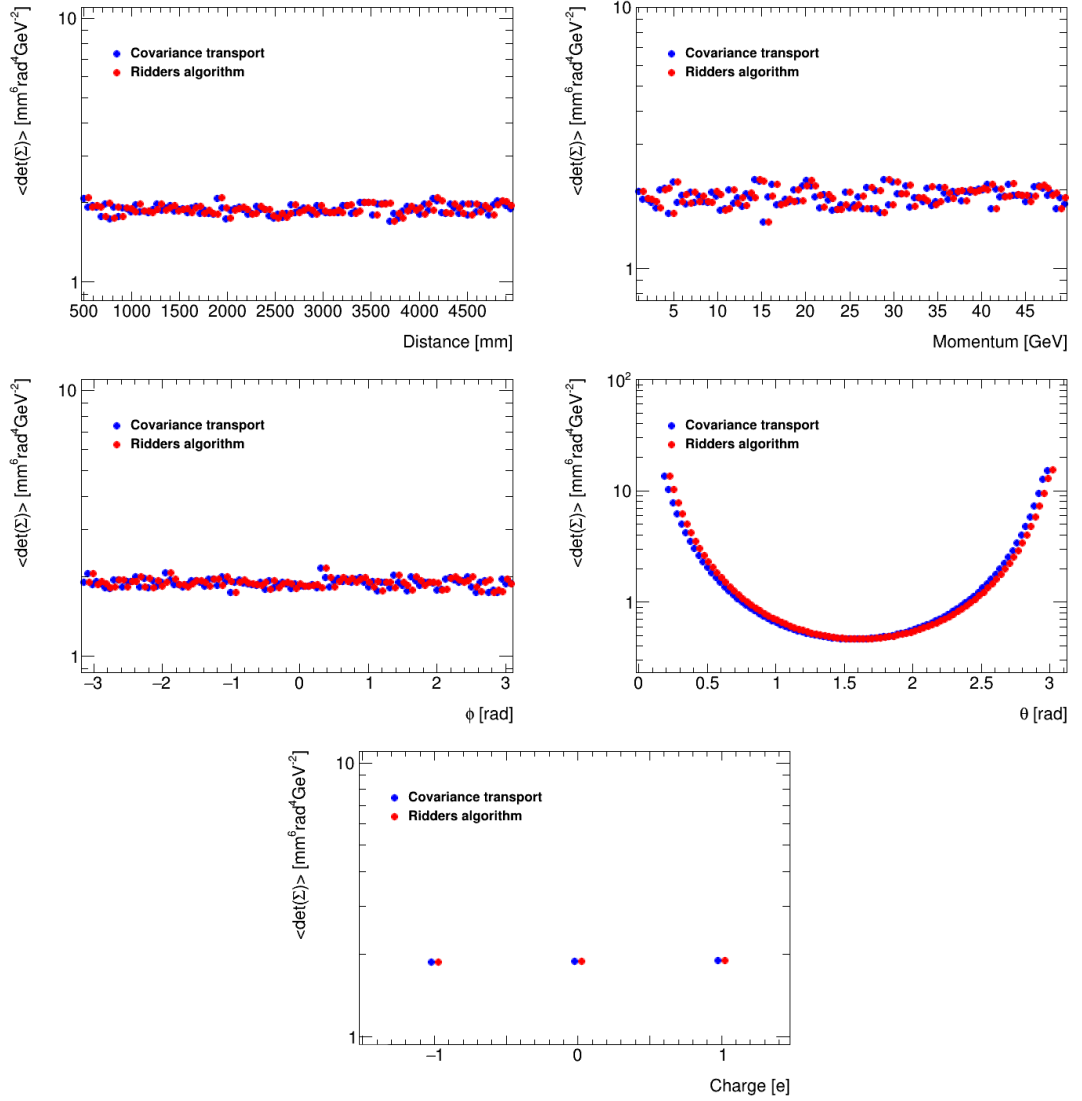
Figure 8.6: Determinant of the covariance matrix obtained from covariance transport and the Ridders algorithms in an extrapolation from free to curvilinear parameters versus the extrapolation distance (top left), initial momentum (top right), azimuthal angle (middle left), polar angle (middle right) and particle charge (bottom). The bin centres are shifted for visibility.

The predicted parameters (before the parameter update) at the point of the Kalman filter update is given by an extrapolation of the filtered parameters (after the parameter update) from a previous measurement. If no previous measurement was utilised the prior is used instead. In order to investigate the position for an unbiased parameter update, the predicted parameters for the kth measurement will be treated as a free parameter

depending on the filtered parameters of the $(k-1)$th measurement such that

$$
\begin{aligned}
\mu_k^{\text{predicted}}(s) &= f\left(s, \mu_{k-1}^{\text{filtered}}\right) \\
&= E\left[S\left(s|\lambda, \mu_{k-1}^{\text{filtered}}, \Sigma_{k-1}^{\text{filtered}}\right) P\left(\lambda|\mu_{k-1}^{\text{filtered}}, \Sigma_{k-1}^{\text{filtered}}\right)\right]
\end{aligned}
$$

is a function of s. According to the extrapolation likelihood in Eq. (4.38) this can be expressed as the expectation value of posterior pdf obtained from the extrapolation. This mean can be considered as a sum of the true parameters λ_k^{true} and some deviation $\tilde{\lambda}_k^{\text{predicted}}(s)$ [101]. An analogous statement can be built for the filtered mean μ_k^{filtered} and the mean of the measurement m_k. One obtains therewith the relations

$$
\begin{aligned}
\mu_k^{\text{predicted}}(s) &= \lambda_k^{\text{true}} + \tilde{\lambda}_k^{\text{predicted}}(s) \\
\mu_k^{\text{filtered}}(s) &= \lambda_k^{\text{true}} + \tilde{\lambda}_k^{\text{filtered}}(s) \\
m_k &= H_k \lambda_k^{\text{true}} + v_k
\end{aligned}
\tag{8.4}
$$

of each component to the underlying truth. $\tilde{\lambda}_k^{\text{filtered}}(s)$ and v_k denote thereby the deviation term of the filtered parameters and the measurement respectively. As the kth measurement can be a subset of the particles state, the matrix H_k denotes the projection into the measured subset. The parameter s for the filtered mean and its deviation denote that the filtered parameters are a consequence of used predicted position.

The parameters of the filtered state in the Kalman filter can be considered as a linear combination of the prediction and the measurement

$$
\mu_k^{\text{filtered}}(s) = K_k' \mu_k^{\text{predicted}}(s) + K_k m_k
\tag{8.5}
$$

with the linear maps K_k' and K_k. For the surface bound measurements it can be found that K_k is the gain matrix used in Eqs. (4.35) and (4.36). K_k' is thereby given by $K_k' = 1 - K_k H_k$. Under the assumption that the deviation terms in Eq. (8.4) are in the case of volume bound measurements normal distributed as in the case of surface bound measurements, the linear combination will also lead to the optimal filter [100]. The validity of the normal distribution is assumed in the following.

By inserting Eq. (8.4) into Eq. (8.5) one obtains

$$
\tilde{\lambda}_k^{\text{filtered}}(s) = \left(K_k' + K_k H_k - 1\right) \lambda_k^{\text{true}} + K_k' \tilde{\lambda}_k^{\text{predicted}}(s) + K_k v_k.
\tag{8.6}
$$

The expectation value of this expression is then given by

$$
\begin{aligned}
E\left[\tilde{\lambda}_k^{\text{filtered}}(s)\right] &= E\left[\left(K_k' + K_k H_k - 1\right) \lambda_k^{\text{true}}\right] + E\left[K_k' \tilde{\lambda}_k^{\text{predicted}}(s)\right] + E\left[K_k v_k\right] \\
0 &= \left(K_k' + K_k H_k - 1\right) \lambda_k^{\text{true}} + E\left[K_k' \tilde{\lambda}_k^{\text{predicted}}(s)\right] \\
&\overset{!}{=} \left(K_k' + K_k H_k - 1\right) \lambda_k^{\text{true}}.
\end{aligned}
\tag{8.7}
$$

The expectation value $E\left[\tilde{\lambda}_k^{\text{filtered}}(s)\right]$ has to become zero in order to provide an unbiased filtered state. As the deviation term of the measurement $E\left[v_k\right]$ is assumed to be normal

distributed, the expectation value is by assumption zero. The addend related to the true particle parameters does not vanish in general. Using the same argument as for the filtered state, the predicted deviation term has to have a zero mean. Since this expression can be written as

$$E\left[K_k' \tilde{\lambda}_k^{\text{predicted}}(s)\right] = K_k' E\left[\mu_k^{\text{predicted}}(s) - \lambda_k^{\text{true}}\right]$$
$$= K_k'\left(E\left[\mu_k^{\text{predicted}}(s)\right] - \lambda_k^{\text{true}}\right)$$

by using Eq. (8.4), the extrapolation parameter s is given such that the expectation value of the extrapolated mean is the truth itself. Given that this is fulfilled, Eq. (8.7) leads to $K' = K_k H_k - 1$ and therewith to the formalism of surface bound measurements as well as to an unbiased formalism of the Kalman filter.

While for the surface bound measurement case the position of the true parameters is known to be at the same surface as where the update occurs the volume bound measurement case has this additional degree of freedom in s. The former scenario would be obtained here in case of extrapolations to the true position over a distance s_k^{true}. However, since this just needs to be fulfilled for the mean of s, the actual distance can be $s_k^{\text{true}} + \tilde{s}_k$ with $E\left[\tilde{s}_k\right] = 0$.

The most general scenario for a measurement in a gas detector is given by assuming that the true position is unknown but only the position of the measurement is available. In this case, the only special position along the extrapolation is given by the position of the measurement. Thus, using the position closest to the measurement as the parameter update position, the update is biased by construction due to an additional extrapolation distance $\tilde{s}_k$ from the true position. This distance is related to the fluctuation of the measurement position v_k and therewith itself a statistical quantity as required. While the fluctuations of the other terms are given by the underlying parametrisation as discussed in Sec. 4.2, the distribution of $\tilde{s}_k$ needs further modelling.

In order to derive a distribution one can use four different major models with increasing complexity but a more accurate description. These are described in the following:

1. Straight line and spherical uncertainty approximation
   This scenario represents the simplest case. Assuming a high-momentum particle or a sufficiently weak magnetic field leads to an approximately straight line of the particles trajectory in short distances around a certain position. In addition, the uncertainty vector v_k can be used to approximate the uncertainty region for the true measurement by a sphere with radius $|v_k|$ as shown in Fig. 8.7. As the position closest to the true position as well as to the measurement is defined by a line between the mean of the extrapolation and one of the other two, with the requirement that the particle direction is orthogonal to this line, the extrapolation distance deviation is given by $\tilde{s}_k = |v_k|$ and consequently, the position of the trajectory is biased by

$$\tilde{\lambda}_k^{\text{bias}} = f(s_k^{\text{true}} + \tilde{s}_k | \lambda_{k-1}) - f(s_k^{\text{true}} | \lambda_{k-1}) = |v_k| T_{k-1}^{\text{filtered}} \tag{8.8}$$

   with the direction vector $T_{k-1}^{\text{filtered}}$ after the extrapolation and the spatial extrapolation expression for straight lines.
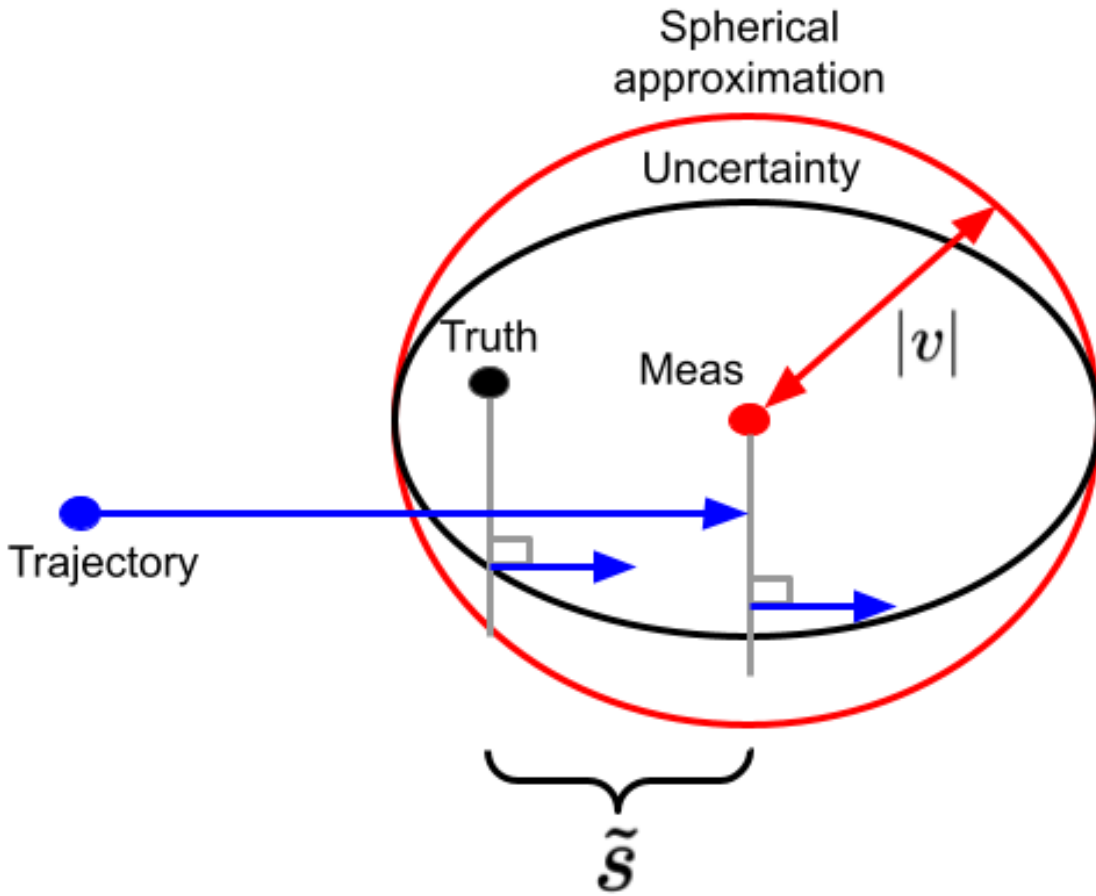
Figure 8.7: Illustration of the extrapolation distance bias using a straight line trajectory and a spherical uncertainty around the measurement. The particles trajectory is shown as blue arrows. Its direction defines the closest points to the truth and the measurement (meas) due to orthogonality. The spherical approximation shows an region dependent overestimation of the uncertainty.

2. Straight line approximation and ellipsoidal uncertainty
   While the spherical approximation simplifies the calculation but potentially overestimates its contribution, a more precise treatment is given by handling the actual uncertainty ellipsoid as shown as black ellipse in Fig. 8.7. As for the spherical case, the bias contribution is defined by a point on the surface of the body. For an ellipsoid centred at the origin of the coordinate system this is given by the equation

$$\frac{x_s^2}{v_x^2} + \frac{y_s^2}{v_y^2} + \frac{z_s^2}{v_z^2} = 1$$

   with the spatial parameters x_s, y_s, z_s on the surface of the ellipsoid. For the reason of simplicity it is assumed here that the components of the measurement uncer-

tainty align with the global coordinate system. In this case a point on the surface is given by

$$x_s = v_k^x \sin(\theta)\cos(\phi)$$
$$y_s = v_k^y \sin(\theta)\sin(\phi)$$
$$z_s = v_k^z \cos(\theta).$$

Since the direction vector T is related to the angles θ and ϕ via Eq. (5.3) and these define the bias direction, the bias contribution becomes with $\tilde{s}_k = |(x_s, y_s, z_s)^T|$

$$\tilde{\lambda}_k^{\text{bias}} = f(s_k^{\text{true}} + \tilde{s}_k | \lambda_{k-1}) - f(s_k^{\text{true}} | \lambda_{k-1})$$
$$= \sqrt{\left(v_k^x T_{x,k-1}^{\text{filtered}}\right)^2 + \left(v_k^y T_{y,k-1}^{\text{filtered}}\right)^2 + \left(v_k^z T_{z,k-1}^{\text{filtered}}\right)^2} T_{k-1}^{\text{filtered}}.$$

Although this expression is more accurate, the bias term would need to be calculated for each measurement independently whereas the spherical approximation allows for re-usage of results while the uncertainty remains unchanged or even to perform the calculations before the track reconstruction.

3. Helical trajectory and ellipsoidal uncertainty
   The two previous concepts used the approximation of a straight line trajectory. While this holds in the high-momentum or low magnetic field case, a more general description is given by considering the trajectory as actual helix. The uncertainty ellipsoid is treated thereby as in the previous case[1]. The main difference that is encountered in this scenario is that due to the helical trajectory of the lines connecting the extrapolated mean at s_k^{true} with the truth and at $s_k^{\text{true}} + \tilde{s}_k$ with the measurement are not parallel anymore to each other.

   In order to find the point of the parameter update, the particle trajectory need to be parametrised. For a helix in z-direction the point closest to the truth will be denoted as

   $$\mu_k^{\text{predicted,true}} = \begin{pmatrix} r\cos(2\pi t_k^0) \\ r\sin(2\pi t_k^0) \\ ht_k^0 + c \end{pmatrix} \tag{8.9}$$

   with the radius of the helix r, an iteration step-length h and offset c. The parameter t_k^0 is defined by the minimal distance $|\mu^{\text{true}} - \mu_k^{\text{predicted}}(s)|$. With a measurement located at $m_k = H_k \lambda_k^{\text{true}} + v_k$, the point of the parameter update

   $$\mu_k^{\text{predicted}} = \mu_k^{\text{predicted,true}} + \begin{pmatrix} r\cos(2\pi t_k) \\ r\sin(2\pi t_k) \\ ht_k \end{pmatrix} \tag{8.10}$$

---

[1] For completeness, a considerable step in between would be a helical trajectory with a spherical uncertainty approximation.

is defined via

$$\frac{\partial |\mu_k^{\text{predicted}} - m_k|}{\partial t_k} = 0$$

$$\Leftrightarrow 4\pi r(m_k^x \sin(2\pi t_k) - m_k^y \cos(2\pi t_k) + 4\pi r^2(\sin(2\pi t_k^0)\cos(2\pi t_k)$$
$$- \cos(2\pi t_k^0)\sin(2\pi t_k)) + 2h^2 t_k - 2m_k^z h + 2h^2 t_k^0 + 2hc = 0.$$

Assuming that the deviation due to v_k leads to a path length that is way smaller that than a turnaround, the trigonometric functions can be approximated such that $\sin(2\pi t_k) \approx 2\pi t_k$ and $\cos(2\pi t_k) \approx 1 - 2\pi^2 t_k^2$. Therewith, one obtains

$$t_k^2 + \frac{8\pi^2 r(m_k^x - r\cos(2\pi t_k^0)) + 2h^2}{8\pi^3 r(m_k^y - r\sin(2\pi t_k^0))} t_k + \frac{-2m_k^z h + 2h^2 t_k^0 + 2hc}{8\pi^3 r(m_k^y - r\sin(2\pi t_k^0))} = 0$$

$$\Leftrightarrow t_k^2 + \frac{4\pi^2 r v_k^x + h^2}{4\pi^3 r v_k^y} t_k - \frac{v_k^z h}{4\pi^3 r v_k^y} = 0$$

which is a quadratic equation solvable for t_k. From the difference of Eq. (8.10) and Eq. (8.9) one obtains the bias term

$$\tilde{\lambda}_k^{\text{bias}} = \begin{pmatrix} r\cos(2\pi t_k) \\ r\sin(2\pi t_k) \\ ht_k \end{pmatrix}$$

with the found solution for t_k. The corresponding arc length of the helix is then given by

$$\tilde{s}_k(t_k) = 2\pi r \sqrt{1 + \left(\frac{h}{2\pi r}\right)^2} t_k.$$

4. General case

   The most general case considerable is given as soon as the helical approximation does not hold anymore. This is given in case of non-uniform magnetic fields or the consideration of interactions with the gas inside the detector such as scattering, ionisation or space-charge distortion. Also, if the electric field contribution cannot be neglected and its non-uniform strength gets taken into account, the situation gets more complicated. If this is the case then no analytical solution can be found anymore. Hence, the bias term needs to be estimated using the extrapolation from Sec. 7.4, potentially with the additional consideration of the electric field as given in Eq. (8.1). Therewith the difference between the update position and the intersection of the trajectory with the ellipsoid and thus the bias can be estimated.

The parameters mean along the particles trajectory is given by

$$\mu_k^{\text{predicted/filtered}} = \lambda_k^{\text{true}} + \tilde{\lambda}_k^{\text{predicted/filtered}} + \tilde{\lambda}_k^{\text{bias}} \tag{8.11}$$

before and after the kth measurement is used for updating the parameter estimation[2]. Using the result for K' found in Eq. (8.7) together with Eq. (8.6) and (8.4) leads to

$$\mu_k^{\text{filtered}} = (1 - K_k H_k)\mu_k^{\text{predicted}} + K_k m_k$$

$$\Leftrightarrow \lambda_k^{\text{true}} + \tilde{\lambda}_k^{\text{filtered}} + \tilde{\lambda}_k^{\text{bias}} = (1 - K_k H_k)\left(\lambda_k^{\text{true}} + \tilde{\lambda}_k^{\text{predicted}} + \tilde{\lambda}_k^{\text{bias}}\right) + K_k\left(H_k\lambda_k^{\text{true}} + v_k\right)$$

$$\Leftrightarrow \tilde{\lambda}_k^{\text{filtered}} + \tilde{\lambda}_k^{\text{bias}} = (1 - K_k H_k)\left(\tilde{\lambda}_k^{\text{predicted}} + \tilde{\lambda}_k^{\text{bias}}\right) + K_k v_k.$$

From the definition of the covariance matrix one obtains therewith

$$\Sigma_k^{\text{filtered,biased}} = E\left[\left(\mu_k^{\text{filtered}} - \lambda_k^{\text{true}}\right)\left(\mu_k^{\text{filtered}} - \lambda_k^{\text{true}}\right)^T\right] \tag{8.12}$$

$$= E\left[\left(\tilde{\lambda}_k^{\text{filtered}} + \tilde{\lambda}_k^{\text{bias}}\right)\left(\tilde{\lambda}_k^{\text{filtered}} + \tilde{\lambda}_k^{\text{bias}}\right)^T\right] \tag{8.13}$$

$$= E\left[\left((1 - K_k H_k)\left(\tilde{\lambda}_k^{\text{predicted}} + \tilde{\lambda}_k^{\text{bias}}\right) + K_k v_k\right)\right.$$
$$\left.\left(\left(\tilde{\lambda}_k^{\text{predicted}} + \tilde{\lambda}_k^{\text{bias}}\right)^T (1 - K_k H_k)^T + v_k^T K_k^T\right)\right]$$

$$= E\left[(1 - K_k H_k)\left(\tilde{\lambda}_k^{\text{predicted}} + \tilde{\lambda}_k^{\text{bias}}\right)\left(\tilde{\lambda}_k^{\text{predicted}} + \tilde{\lambda}_k^{\text{bias}}\right)^T (1 - K_k H_k)^T\right]$$

$$+ E\left[(1 - K_k H_k)\left(\tilde{\lambda}_k^{\text{predicted}} + \tilde{\lambda}_k^{\text{bias}}\right)v_k^T K_k^T\right]$$

$$+ E\left[K_k v_k \left(\tilde{\lambda}_k^{\text{predicted}} + \tilde{\lambda}_k^{\text{bias}}\right)^T (1 - K_k H_k)^T\right]$$

$$+ E\left[K_k v_k v_k^T K_k^T\right].$$

Since K_k and H_k are considered as constants with respect to the expectation value operator $E[\cdot]$, these factors do not require further treatment. Utilising further that $\tilde{\lambda}_k^{\text{predicted}}$ is independent from $\tilde{\lambda}_k^{\text{bias}}$ and v_k one obtains

$$\Sigma_k^{\text{filtered,biased}} = (1 - K_k H_k)\left(\Sigma_k^{\text{predicted}} + \Sigma_k^{\text{bias}}\right)(1 - K_k H_k)^T$$

$$+ (1 - K_k H_k)Q_k K_k^T + K_k Q_k^T (1 - K_k H_k)^T + K_k \Sigma_k^{\text{det}} K_k^T \tag{8.14}$$

with the definition of Σ_k^{det} as given in Eq. (4.13), $\Sigma^{\text{predicted}} = E\left[\tilde{\lambda}_k^{\text{predicted}}\tilde{\lambda}_k^{\text{predicted},T}\right]$, $\Sigma_k^{\text{bias}} = E\left[\tilde{\lambda}_k^{\text{bias}}\tilde{\lambda}_k^{\text{bias},T}\right]$ and $Q = E\left[\tilde{\lambda}_k^{\text{bias}}v_k^T\right]$.

This matrix Q has thereby a special behaviour. Although it is associated to the position of the mean of the trajectory it is linked via the used bias model to the uncertainty

---

[2]Depending on the used model for the description of the bias term and the measured parameters, $\tilde{\lambda}_k^{\text{bias}}$ might be different for the predicted and the filtered state. An example would be a different momentum changing the curvature of the trajectory. In this case the bias terms need to be distinguished. For the reason of simplicity it is assumed in the following that both are identical.

of the measurement. Calculating this matrix explicitly for the straight line and spherical uncertainty approximation from Eq. (8.8) leads to

$$
\begin{aligned}
E\left[\tilde{\lambda}_k^{\text{bias}} v_k^T\right] &= E\left[|v_k| T_k v_k^T\right] = \mu_{T,k} E\left[|v_k|^2 \hat{v}_k^T\right] \\[2mm]
&= \mu_{T,k} \int_V |v_k|^2 \hat{v}_k^T \mathcal{G}\left(v_k | 0, \Sigma_{\text{det},k}\right) dV \\[2mm]
&= \mu_{T,k} \int_V \frac{|v_k|^2 \hat{v}_k^T}{\sqrt{(2\pi)^{\dim(v_k)} det(\Sigma_{\text{det},k})}} e^{-\frac{1}{2} v_k^T \Sigma_{\text{det},k}^{-1} v_k} dV \\[2mm]
&= \frac{\mu_{T,k}}{\sqrt{(2\pi)^{\dim(v_k)} det(\Sigma_{\text{det},k})}} \int \frac{\sqrt{\pi}\hat{v}_k^T}{2\left(\frac{1}{2}\hat{v}_k^T \Sigma_{\text{det},k}^{-1} \hat{v}_k\right)^{\frac{3}{2}}} d\xi
\end{aligned}
\tag{8.15}
$$

with the mean direction vector $\mu_{T,k}$, the normalised measurement uncertainty vector $\hat{v}_k$ and the integral with $dV = d|v_k| d\xi$ using the n-sphere coordinates representation of the uncertainty vector. ξ is thereby used as short notation for the angular components. The underlying normal distribution has thereby a zero mean by definition.

Assuming a three dimensional measurement with the diagonal matrix Σ^{det} leads to

$$
\hat{v}_k^T \Sigma_{\text{det},k}^{-1} \hat{v}_k = \sin^2(\theta)\cos^2(\phi)\Sigma_{\text{det},k,(1,1)}^{-1} + \sin^2(\theta)\sin^2(\phi)\Sigma_{\text{det},k,(2,2)}^{-1} + \cos^2(\theta)\Sigma_{\text{det},k,(3,3)}^{-1}
$$

with the entry $\Sigma_{\text{det},k,(i,j)}^{-1}$ in the ith row and jth column of the precision matrix. In the case of $\Sigma_{\text{det},k,(1,1)}^{-1} = \Sigma_{\text{det},k,(2,2j)}^{-1}$ this expression leads due to Eq. (8.15) to $Q = 0$. However, as this result was obtained using several assumptions, a general statement can not be formed for Q. Since in the following the measurements inside the TPC are assumed to just contain three dimensional spatial information with no favoured uncertainty direction, i.e. the measurement uncertainty in x- and y-direction is identical, Q will be considered as zero matrix.

Based on the definition of the filtered covariance matrix in Eq. (8.12) the maximal knowledge from a measurement is obtained if the diagonal elements become as small as possible. Since the only free parameter is thereby given by the gain matrix K_k, the optimal choice [101] of this matrix is given for

$$
\left(\frac{\partial \text{tr}\left(\Sigma_k^{\text{filtered,biased}}\right)}{\partial K_k(i,j)}\right)_{i,j} = \frac{\partial \text{tr}\left(\Sigma_k^{\text{filtered,biased}}\right)}{\partial K_k} = 0
$$

with the trace operator $\text{tr}(\cdot)$ and the matrix element $K_k(i,j)$. By applying the properties $\partial \text{tr}(ABA^T)/\partial A = 2AB$ [101] for the matrices A, B with B being symmetric and

$\partial \text{tr}(AB)/\partial A = B^T$ [136] one obtains using Eq. (8.14) in the case of $Q = 0$ for K_k:

$$\frac{\partial \text{tr}\left(\Sigma_k^{\text{filtered,biased}}\right)}{\partial K_k} = 0$$

$$\Leftrightarrow -2(1 - K_k H_k)\left(\Sigma_k^{\text{predicted}} + \Sigma_k^{\text{bias}}\right) H_k^T + 2K_k \Sigma_k^{\text{det}} = 0$$

$$\Leftrightarrow K_k = \left(\Sigma_k^{\text{predicted}} + \Sigma_k^{\text{bias}}\right) H_k^T \left(H_k \left(\Sigma_k^{\text{predicted}} + \Sigma_k^{\text{bias}}\right) H_k^T + \Sigma_k^{\text{det}}\right)^{-1} \quad (8.16)$$

The form of the gain matrix K_k shows that due to the bias term, the learning rate is suppressed compared to the surface bound measurement case as it can be interpret as additional contribution to the measurement uncertainty.

With this matrix the filtered mean from Eq. (8.5) with K_k' can be calculated. For the corresponding covariance matrix however, additional steps can be taken. The covariance matrix $\Sigma_k^{\text{filtered,biased}}$ as defined in Eq. (8.13) can be written as

$$\Sigma_k^{\text{filtered,biased}} = E\left[\tilde{\lambda}_k^{\text{filtered}} \tilde{\lambda}_k^{\text{filtered},T}\right] + E\left[\tilde{\lambda}_k^{\text{bias}} \tilde{\lambda}_k^{\text{bias},T}\right]$$

$$+ E\left[\tilde{\lambda}_k^{\text{filtered}} \tilde{\lambda}_k^{\text{bias},T}\right] + E\left[\tilde{\lambda}_k^{\text{bias}} \tilde{\lambda}_k^{\text{filtered},T}\right] \quad (8.17)$$

exploiting the fact that $\tilde{\lambda}_k^{\text{filtered}}$ and $\tilde{\lambda}_k^{\text{bias}}$ are independent. While Eq. (8.14) denotes a general update of the covariance matrix, this equation can be understood as learning about the covariance matrix of the track parameters but also about the bias term itself. Since only the former one is of interest, Eqs. (8.11), (8.14), (8.16) and (8.17) are used to formulate a pure track parameter update:

$$E\left[\tilde{\lambda}_k^{\text{filtered}} \tilde{\lambda}_k^{\text{filtered},T}\right] + E\left[\tilde{\lambda}_k^{\text{bias}} \tilde{\lambda}_k^{\text{bias},T}\right] + E\left[\tilde{\lambda}_k^{\text{filtered}} \tilde{\lambda}_k^{\text{bias},T}\right] + E\left[\tilde{\lambda}_k^{\text{bias}} \tilde{\lambda}_k^{\text{filtered},T}\right]$$

$$= \Sigma_k^{\text{filtered}} + \Sigma_k^{\text{bias}} - K_k H_k \Sigma_k^{\text{bias}} - \Sigma_k^{\text{bias}} H_k^T K_k^T$$

$$= (1 - K_k H_k)\left(\Sigma_k^{\text{predicted}} + \Sigma_k^{\text{bias}}\right)(1 - K_k H_k)^T + K_k \Sigma_k^{\text{det}} K_k^T$$

$$\Leftrightarrow \Sigma_k^{\text{filtered}} = (1 - K_k H_k)\Sigma_k^{\text{predicted}}(1 - K_k H_k)^T + K_k \Sigma_k^{\text{det}} K_k^T + K_k H_k \Sigma_k^{\text{bias}} H_k^T K_k^T$$

$$= (1 - K_k H_k)\Sigma_k^{\text{predicted}} + \Sigma_k^{\text{bias}} H_k^T K_k^T$$

In comparison to Eq. (4.36) the filtered covariance has the additional addend $\Sigma_k^{\text{bias}} H_k^T K_k^T$ and a modified gain matrix. As both are related to the bias term, in case of its absence, the Kalman filter formalism for surface bound measurements from literature is obtained. Hence, this can be thought of as a generalisation of the Kalman filter, applicable in a broader range of problems.

Beside the formulation of Kalman filter for the volume bound measurements, further conceptional differences can be considered in comparison to the application for surface bound measurements. In the latter case, it can be assumed that if the particle trajectory intersects with a surface, the particle produced up to one measurement on the surface. In a TPC the situation is a bit different as a particle can produce multiple measurements

while traversing the gas volume. Hence, as soon as the volume is entered, all measurements associated to the volume can be considered as candidates in the first place. By parameter space selection and distance ordering the next measurement candidate can be chosen. However, this requires a step-wise re-evaluation of possible candidates, providing a more complicated scenario than in the surface scenario that requires the measurement lookup just in case the mean of the particle trajectory is at the surface itself.

Another difference is given by the combinatorial complexity given in the described scenario. A set of surfaces provide a set of discrete points along the trajectory that require a decision whether a measurement belongs to a track or not. In the most general case of arbitrary points with measurements inside a volume, already two nearby measurements lead to four possible, different assignments to a track. Hence, a proper track isolation needs to be present in order to avoid an excessive combinatorial problem. Since this is an experiment specific issue, it is just mentioned here for completeness.

A further aspect obtained from this formalism is that while surface bound measurements, e.g. in a tracking detector occur at discrete points, being capable of updating the track parameters in the global frame while having the measurements distributed anywhere inside a volume leads to the natural limit of infinite measurements along the trajectory. By identifying Eq. (7.10) as linear mapping of the track parameters as well as the measurements, dependent on the continuous parameter h and considering the case of the continuous Kalman filter as discussed in [101], the formalism found in this chapter can be transformed accordingly.

8.5 Application of the Free Kalman Filter

In order to investigate the found formalism for the Kalman filter for gas detectors a simulation setup is required. As the underlying detector geometry a simplified version of the sPhenix experiment [137] is used in a preliminary version. A schematic overview of the detector layout is shown in Fig. 8.8. From the geometry only the tracking detector and the TPC was used as the focus of this chapter is the latter. While this detector consists of pixel and strip detectors, it was chosen to have five layer of pixel detectors instead with a resolution 25 μm in local x- and 100 μm in local y-direction. Within the simulation the uncertainty for all measurements is identical. The surrounding TPC utilises 48 rows of read-out pads in radial direction aligned concentric around the beam pipe. It is simplified that each pad produces a single measurement when the particle traverses the corresponding region in the volume. The thereby created volume bound measurements are assigned with an uncertainty of 175 μm in the global x- and y-direction and with 750 μm in the global z-direction. Again, each measurement is assigned with the same uncertainty. In the case of the TPC the reconstruction of the registered measurements at the pads is not performed but taken into account by the uncertainties. Inside the entire setup a constant magnetic field of 1.4 T in z-direction is applied. The entire detector material is disabled. As the material add additional smearing to the reconstruction parameters, observable effects and differences caused by the reconstruction formalism may vanish in the presence of material.
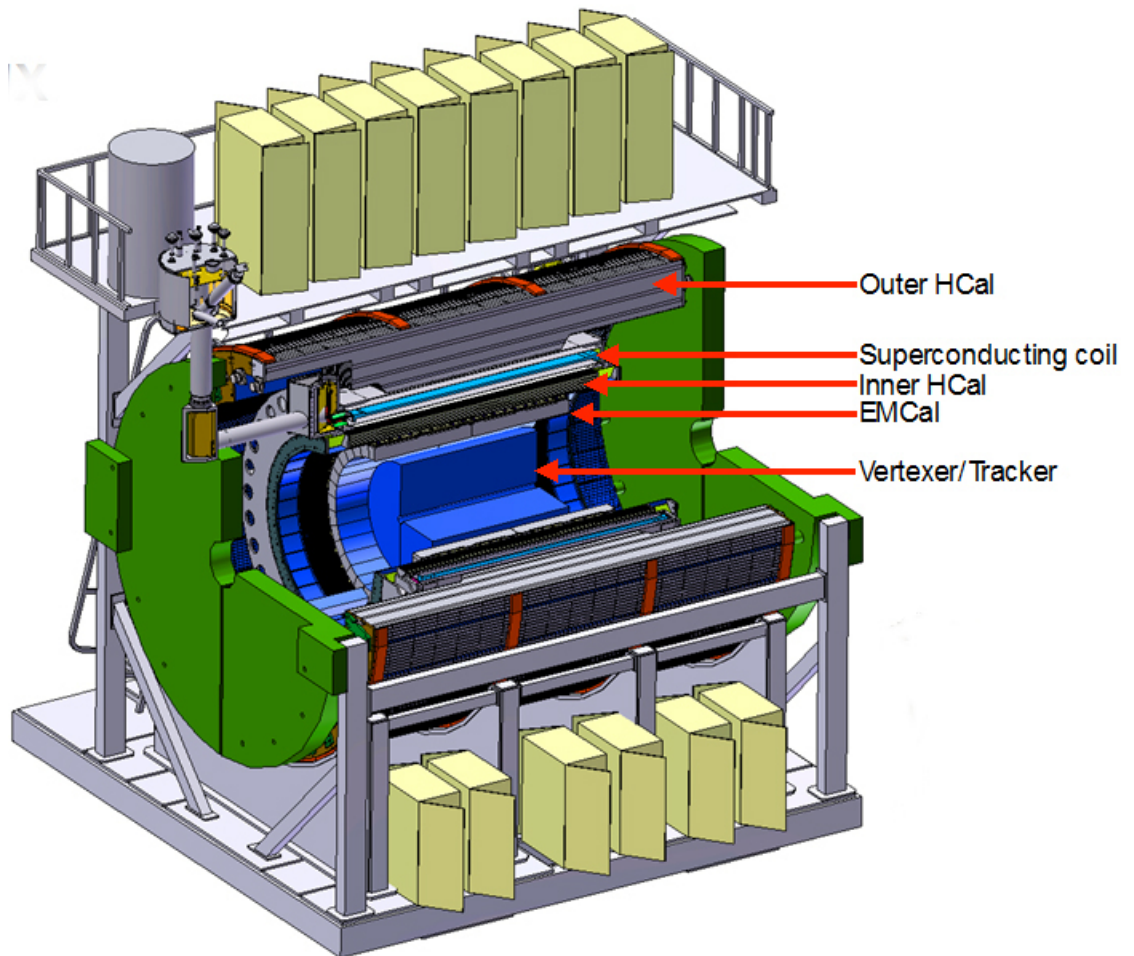
Figure 8.8: Schematic overview of the sPhenix detector. The interaction point lies in the centre of the detector. The figure is taken from Reference [138].

This detector setup is used for simulation and track reconstruction. The former is described in Sec. 8.5.1, the latter in Sec. 8.5.2. The results are then compared in Sec. 8.5.3.

8.5.1 Simulation Setup

As the combinatorial problem of the track reconstruction is too specific and the formalism of the track fitting is the major component of investigation, a particle gun for a single muon event is utilised for the simulation rather than a Monte Carlo event generator. The vertex position of the gun is fixed at the origin of the coordinate system defined at the centre of the detector. The gun direction is picked randomly per event over the full azimuthal range and within $\eta \in [-1, 1]$. The initial transverse momentum of the particle was used with fixed values of 1,5,10 and 100 GeV per run. The uneven spacing

between the intervals is motivated by the increasing curvature of the particles track for low momenta and the therewith increasing complexity of extrapolation.

The event simulation as well as the track reconstruction are performed with ACTS. Thus, as both utilise the same extrapolation algorithms the underlying equation of motion can be controlled altogether. Since the electric field in the TPC has a minor impact on the particle trajectories in case of a sufficiently high momentum, it is neglected for both cases. Additionally, the absence of material causes in this scenario no additional energy loss due to interactions with the gas. Finally, since simulation and reconstruction undergo the lack of its influence, the absence is unimportant for the intended investigation. A consequence of the neglected electric field and the absence of material is that according to Eq. (8.1) the variation of the particles initial momentum is equivalent to a variation of the magnetic field.

The measurements are created in the tracker on the surfaces intersected by the extrapolated particle trajectory from the particle gun. Using the mean of the extrapolation as the truth position, the mean of the measurements is obtained from smearing this position using a normal distributed sample with the widths defined by the uncertainty of the measurement. The uncertainty is then assigned to the measurement. Due to the normal distribution the symmetry $P(\lambda^{\text{truth}}|m, \Sigma) = P(m|\lambda^{\text{truth}}, \Sigma)$ is guaranteed. While the truth information is stored for comparison, the track fitting utilises only the smeared measurement parameters. For the TPC the situation is more complex. For each radial pad row a cylindrical surface is added to the geometry with the radius of the surface defined by the centre of the pad. The length of the cylinder is defined by the length of the TPC. These surfaces are only used for the event generation and do not modify the trajectory. Therewith, it is possible to assure that each pad has at most a single measurement. Whenever the trajectory is at the surface a measurement is created by smearing the global parameters as described before. The utilisation of the produced measurements is discussed in Sec. 8.5.2.

8.5.2 Reconstruction Models

For the reconstruction four different models are considered. One utilises the volume bound measurements whereas the three others are intended to allow for a comparison to the found expressions. Each of the models utilises the same propagation algorithm with smeared initial parameters around the nominal particle gun position. As for the measurement creation, the smearing also defines the initial uncertainties upon the parameters. Thus, the result of a seeding is emulated. In curvilinear parameters, the

smearing is defined as

$$\sigma_x = \left(20 + 30e^{-0.3p_T\,\mathrm{GeV}^{-1}}\right)\mu\mathrm{m}$$

$$\sigma_y = \left(20 + 30e^{-0.3p_T\,\mathrm{GeV}^{-1}}\sin(\theta)\right)\mu\mathrm{m}$$

$$\sigma_\phi = 1°$$

$$\sigma_\theta = 1°$$

$$\sigma_{q/p} = \frac{0.2}{p}.$$

The difference between these models is how the data is handled. An overview of the used models is described in the following.

The first model utilises only data obtained from the tracking detector. This model is labelled as *Baseline*. Therewith the effect of the measurements obtained from the TPC can be estimated. Furthermore, it provides a threshold for the considerable resolution and uncertainty of the track parameters.

The remaining models utilise data from the tracking detector and the TPC. The first one described here is the Kalman filter (KF) utilising volume bound measurements as well as tracking detector data. Since it utilises measurements free from the surface constrained it is labelled as *Free KF*. In the absence of material and an electric field as well as a constant magnetic field, the straight line and spherical approximation is used for the bias term. As the uncertainties of the TPC measurements are chosen to be constant and identical in x- and y-direction, the symmetry of the measurement with respect to the chosen bias model is granted. Hence, the $Q = 0$ is obtained. In order to obtain a comparable amount of measurements, the surfaces drawn through the TPC are used as the points where the measurement is created. From the nominal position obtained from the particle gun at the surface, the smearing by the corresponding uncertainty in global parameters is performed as shown in Fig. 8.9 (left). Therewith, measurements are created in similar distance but smeared in the volume.

In comparison to the Free KF, the remaining two models utilise a concept with surface bound measurements. The first one is labelled as *Projected KF*. As shown in Fig. 8.9 (middle), for this model the measurements are produced in an interval corresponding to the radial length of the pad around the central surface. The obtained measurement is then mapped onto the central surface. As the measurement is produced in a certain interval, the possible particle states are not fixed. Due to the projection, this results in a larger range of possible locations of the mean around the particle trajectory at the surface. The corresponding uncertainty assigned to the measurement is kept at the values stated above except for the marginalised dimension.

As last model, a mixture of the two former is used. This model is labelled as *Curvilinear KF*. Within this model the measurements are created and stored as for the Free KF. As shown in Fig. 8.9, once the point of closest approach is reached, the measurement is projected onto a curvilinear surface defined by the position and direction of the particles mean.
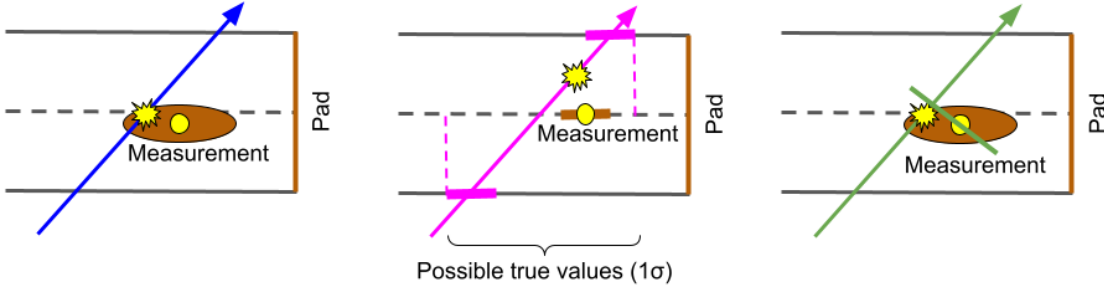
Figure 8.9: Schematic illustration as r-z-projection for the reconstruction utilising TPC data. The Free KF (left) produces at the centre of a pad a measurement smeared around this position in the volume. The Projected KF (middle) produces in a certain interval a measurement. The produced measurement is, independent of its actual position, projected onto the surface at the centre of the pad. The Curvilinear KF (right) measurement production is identical to the Free KF. Hereby, the measurement is mapped on a curvilinear surface at the point of closest approach.

Other than the backwards extrapolation in Eq. (4.47), for the smoothing an equivalent expression exist [139]. Although the alternative expression tends to perform better in terms of computational speed and is therefore widely used, the backwards extrapolation will be used. This has two different reasons: On the one hand, this relies on the Jacobian stored during the forward filtering. Since the Free and Curvilinear KF are not fixed to a surface, the Jacobian may be wrong. On the other hand, the covariance matrix is projected on the surfaces in the tracker to update the track parameters. As the transport of the covariance happens due to multiplication of Jacobians, the rang of the covariance matrix remains six. Although due to material effects and volume bound measurements in the TPC, the rang can be increased eventually up to seven, at most a mixture of smoothing formalisms can be applied. As a consequence, only the backwards extrapolation is used in the following for all models.

Another aspect for the Kalman filter is that due to the applied simplifications of the detector geometry and the measurement creation, the track parameters along the filtering but mostly for the smoothing are found to be very precisely. While Eq. (4.47) allows for a combination of the entire forward and backward state, the precision of the state together with the high amount of the measurements in the TPC led to parameter uncertainties in the order of the floating point precision and thus eventually to ill-defined covariance matrices. In order to avoid these issues, the utilised information in the smoothing is restricted to the spatial information in the entire detector setup.

The last issue related to the smoothing is the position of the smoothing itself. Due to Eq. (4.39), the smoothing position along the trajectory between two measurements is in principle arbitrary. For the Free and Curvilinear KF, the position closest to the filtered track state is chosen in the TPC. In the tracking detector the surface that created the filtered state is used. For the Curvilinear KF the smoothing formalism is intended to remain purely oriented around surface bound measurements. In the smoothing phase however, two entire states need to be combined. It was chosen to define the surface

based on the filtered position and direction. While the Free KF requires the bias term in order to take the displacement of the update into account, during the smoothing this term is not required since the true position is irrelevant. Since all measurements of the Projected KF are bound to surfaces, those are used for the smoothing.

8.5.3 Results

Within this section the different models are compared with each other in the context of the simulation and reconstruction workflow. As the working point the 10 GeV initial momentum simulation is used. The other initial momenta are picked to monitor the behaviour for different conditions. For completeness, the distributions for different momenta or the remaining plots of a certain set that are not shown in this section can be found in Sec. D.2.

In order to compare the four models with each other, the fitting can be split into different steps. Starting at the origin with the initial parameters, the extrapolated track will traverse the tracking detector first. The key term is thereby the unbiased extrapolation and parameter update along the trajectory. A parameter capable of judging this term is given by the pull distribution [140]. These distributions consider in the one dimensional case that if a random variable x is drawn from a normal distribution with mean μ and standard deviation σ then the distribution of the parameter

$$g = \frac{x - \mu}{\sigma}$$

is a random variable from the distribution $\mathcal{G}(g|0,1)$. Considering x as a true parameter leads to the inverse statement that μ and σ need to be chosen such that the distribution of g remains unchanged. While during the track extrapolation and filtering the true parameters are fixed, the estimation of the mean and covariance matrix of the particle trajectory, since it is modelled according to Sec. 4.2, need to fulfil this property.

The situation here is more complicated than mentioned above due to two reasons: The presence of a measurement and the dimensionality of the parameters. The former can be considered as an additional constraint to the track parameters and vice versa. By construction the true parameter follows the distribution $\mathcal{G}(\lambda_k^{\text{true}}|m_k, \Sigma_k^{\text{det}})$. In addition, the predicted state at that point can be considered as the constraint provided from knowledge about the truth gathered at earlier filter steps. Consequently, the true parameters have to follow

$$\mathcal{G}(\lambda_k^{\text{true}}|H_k^T m_k, H_k^T \Sigma^{\text{det}} H_k)\mathcal{G}(\lambda_k^{\text{true}}|\lambda_k, \Sigma_k^{\text{predicted}} + \Sigma_k^{\text{bias}}) = \mathcal{G}(\lambda_k^{\text{true}}|\mu'_{\lambda,k}, \Sigma'_{\lambda,k}) \quad (8.18)$$

$$= \mathcal{G}(\lambda_k^{\text{true}}|\mu_k^{\text{filtered,biased}}, \Sigma_k^{\text{filtered,biased}}) \quad (8.19)$$

with the $\mu'_{\lambda,k}$ and $\Sigma'_{\lambda,k}$ as defined in Eq. (4.32) using $\Sigma_k^{\text{predicted}} + \Sigma_k^{\text{bias}}$ as covariance matrix of the track parametrisation. H_k denotes the projection matrix between free parameters and the measurement frame. The last equality is hereby a direct consequence of Eqs. (4.35) and (4.36).

The other object that needs to be discussed is based on the dimensionality of the parameters. While the pull distribution is designed to express the exponent of the

normal distribution proportional to g^2, the underlying multivariate normal distributions do not allow this method for a general covariance matrix. However, for a diagonal covariance matrix the exponent of the distribution becomes

$$- \frac{1}{2} \left(\lambda_k - \mu_k^{\text{filtered,biased}} \right)^T \Sigma_k^{\text{filtered,biased},-1} \left(\lambda_k - \mu_k^{\text{filtered,biased}} \right)$$

$$= -\frac{1}{2} \sum_i \frac{\left(\lambda_{k,i} - \mu_{k,i}^{\text{filtered,biased}} \right)^2}{\Sigma_k^{\text{filtered,biased}}(i,i)}$$

and thus a dimension-wise product of one dimensional normal distributions. In order to utilise the pull distributions as defined, the covariance matrix needs to diagonalised. Hence, the distribution from Eqs. (8.18) and (8.19) is transformed in the eigenspace defined by the covariance matrix.

For the data in the tracking detector with $\lambda_k^{\text{bias}} = 0$ by construction, the application of this concept leads to the distribution shown in Fig. 8.10. While the prediction refers to the expression in Eq. (8.18), the filtered state refers to Eq. (8.19). With respect to the statistics, the spatial coordinates show the expected behaviour. For the angles slightly enhanced oscillations are observable. This is even more visible for the q/p distribution. The reason lies in the provided data itself. While the data of the tracking detector provides only spatial information, the learning rate is dominant in those parameters. Due to $dr/ds = T$ and Eq. (5.3), any angular information is provided indirectly. A similar argument can be built for q/p as the knowledge of this parameter gets improved due to Eq. (7.6). Considering additionally the rather small distances between the start of the extrapolation and the surfaces as well as the amount of surfaces then fluctuations become reasonable.

As the distributions show the expected behaviour, it can be deduced that the prediction and filtering are performed unbiased. More explicitly, the distributions of the predictions show that the extrapolation is performed without producing a bias between the surfaces. The distributions of the filtered states that due to applying the Kalman filter formalism no bias is introduced into the parametrisation.

After the last tracking detector layer, the TPC is reached. Here, only the Projected, Curvilinear and Free KF utilise any data and are therefore the only considerable models. Starting with the Projected KF, the corresponding pull distributions are shown in Fig. 8.11. For these distributions the underlying truth of the measurement was also projected on the surface. While the left column and the q/p pull distribution look as expected, the right column shows too broad distributions. In those distributions the effect of the projection becomes visible. While the obtained measurement is projected onto the surface at the centre of the pad, the actual area of one standard deviation defined by the all trajectory states in the range of the pad are not considered. This effect becomes stronger for slower particles and becomes also visible in other parameters as shown in Fig. 8.12. Beside too broad pull distributions one can see a small difference between the predicted and filtered state around $\phi = 0$ due to the transformation in the eigenspace.

Furthermore, the projection itself marginalises the radial uncertainty of the measurement. Consequently, the KF handles a measurement with an underlying perfect
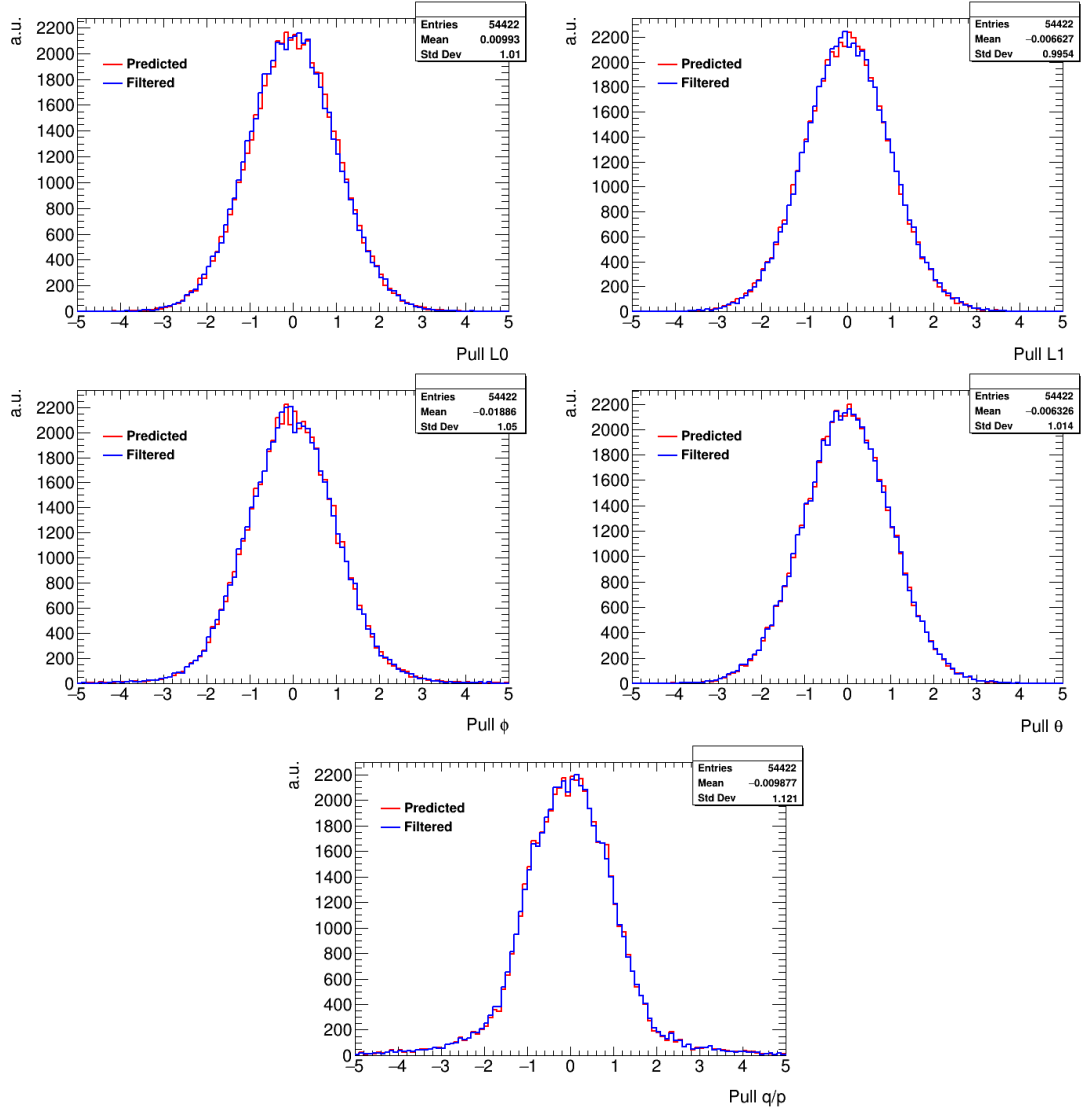
Figure 8.10: Pull distributions of predicted and filtered parameters at the corresponding measurement surfaces in the tracking detector with 10 GeV initial momentum. The statistics refer to the filtered distributions.

knowledge of the radial position of the measurement, leading to underestimated filtered uncertainties.

While this is obviously also the case for the Curvilinear KF, this model does not rely on the projection. Hence, the width of the measurement does not require any adjustments. However, another aspect is thereby important: λ_k^{bias}. Compared to the Projected KF, this model has the additional degrees of freedom due to the placement of the curvilinear surface leading on the other hand to a KF formalism that is identical to the one from the tracking detector. The model has therewith the same flexibility as the Free KF of

187
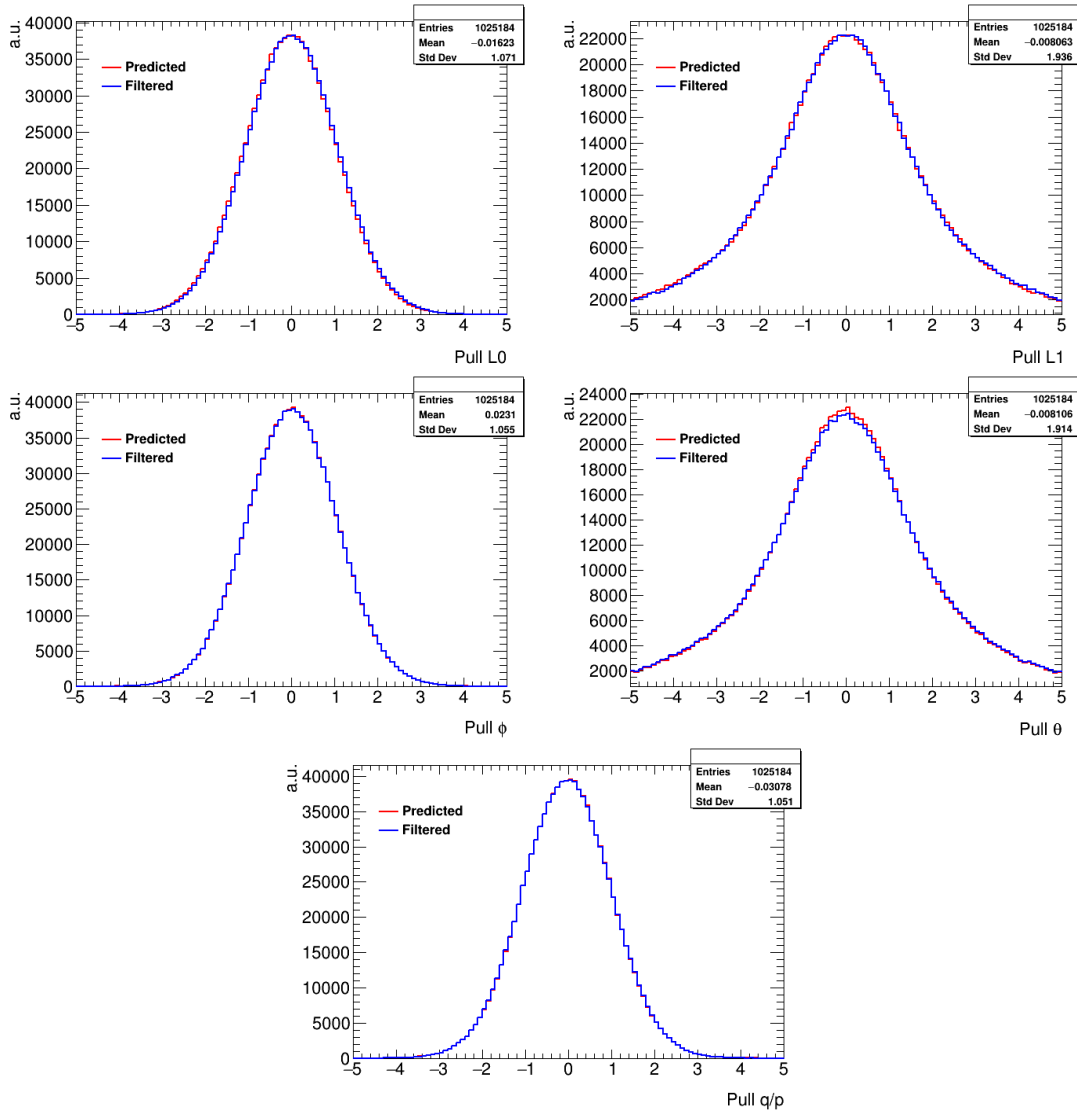
Figure 8.11: Pull distributions of predicted and filtered parameters obtained for the Projected KF at the point of filtering in the TPC with 10 GeV initial momentum. The statistics refer to the filtered distributions.

parameter updates that occur before or after the true measurement. An overview of the obtained distances in relation to the true position is shown in Fig. 8.13. Although the curvature varies a lot between the 1 GeV and 100 GeV initial momentum and therewith the state density in the one standard deviation of the measurement, no strong deviation of the ratio was found across neither in the collection of all tracks nor in the mean of a single event. The latter one has due to the limited amount of measurements some small deviations per event but show in total that the effect due to the bias is less important. In addition, a slight broadening of the variance can be observed for both
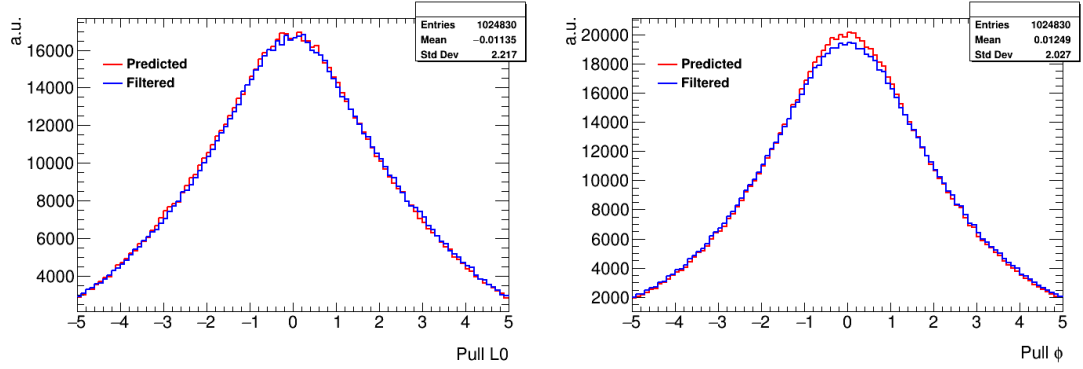
Figure 8.12: Pull distributions of predicted and filtered parameters obtained for the Projected KF at the point of filtering in the TPC with 1 GeV initial momentum. The statistics refer to the filtered distributions.

cases as a function of the distance. This can be explained with the deflection from the magnetic field leading to different entry and exit points of the uncertainty ellipsoid of the measurement compared to the inner measurements.

While the 100 GeV particle can be considered as trajectory with a rather low curvature, the situation is different for the 1 GeV particle. Since nevertheless the distributions in the top row of Fig. 8.13 are symmetric in both cases, the obtained bias can be treated in a simplified way. As it was chosen to use the simplest model for the bias term evaluation, the observation strengthens the confidence that it is sufficient for describing the bias. With this model, the resulting pull distributions of the Free KF are shown in Fig. 8.14.
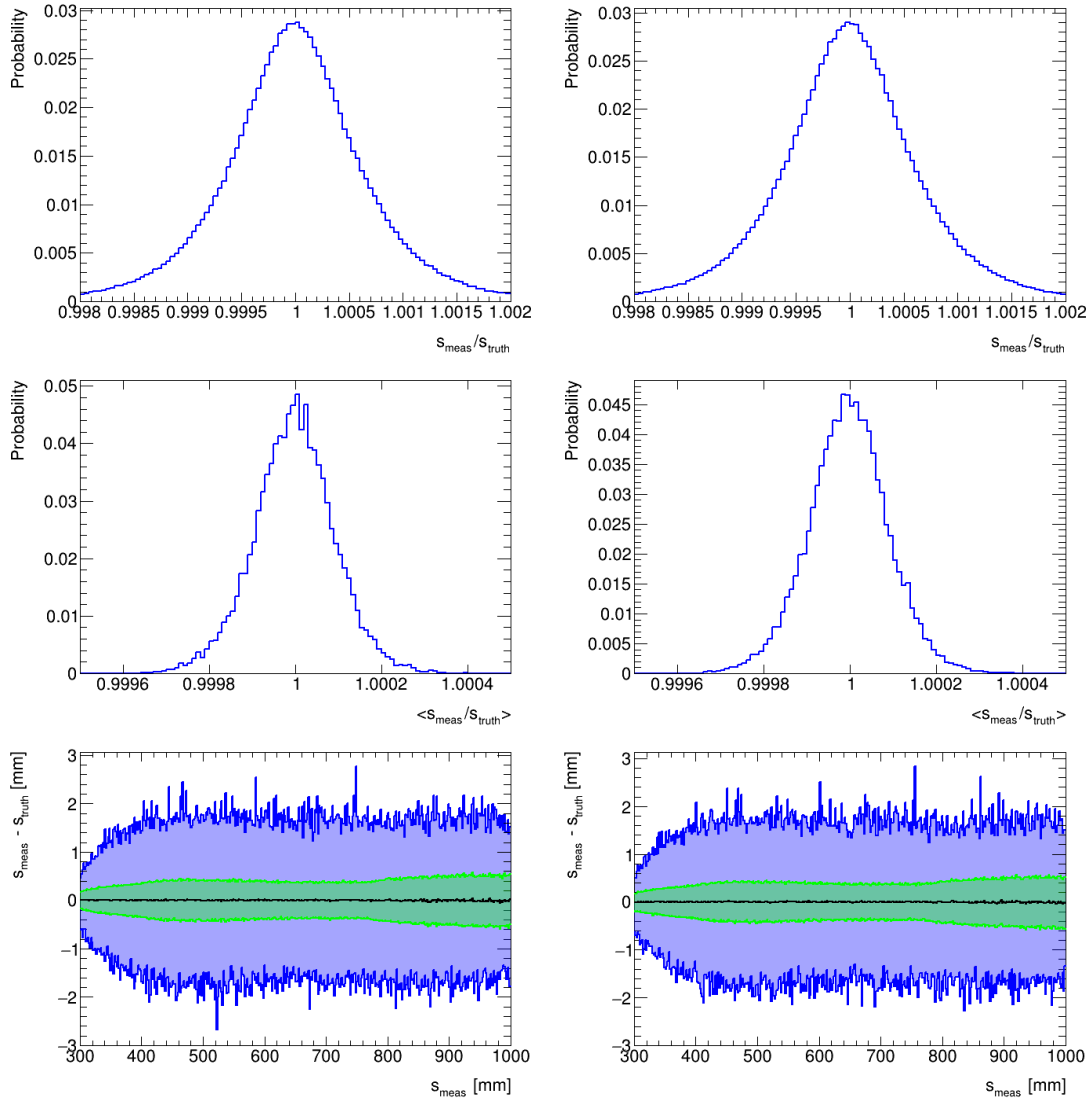
Figure 8.13: Step length distributions for 100 GeV (left) and 1 GeV (right) muons. The top row shows the probability distribution of the ratio between $s_{\mathrm{meas}} = s_k^{\mathrm{true}} + \tilde{s}_k$ and s_k^{true} for all tracks and measurements. The middle row shows the mean of this ratio per track. The bottom row shows the interval of a standard deviation (green) and the interval of the maximal deviations (blue) versus the extrapolation distance.
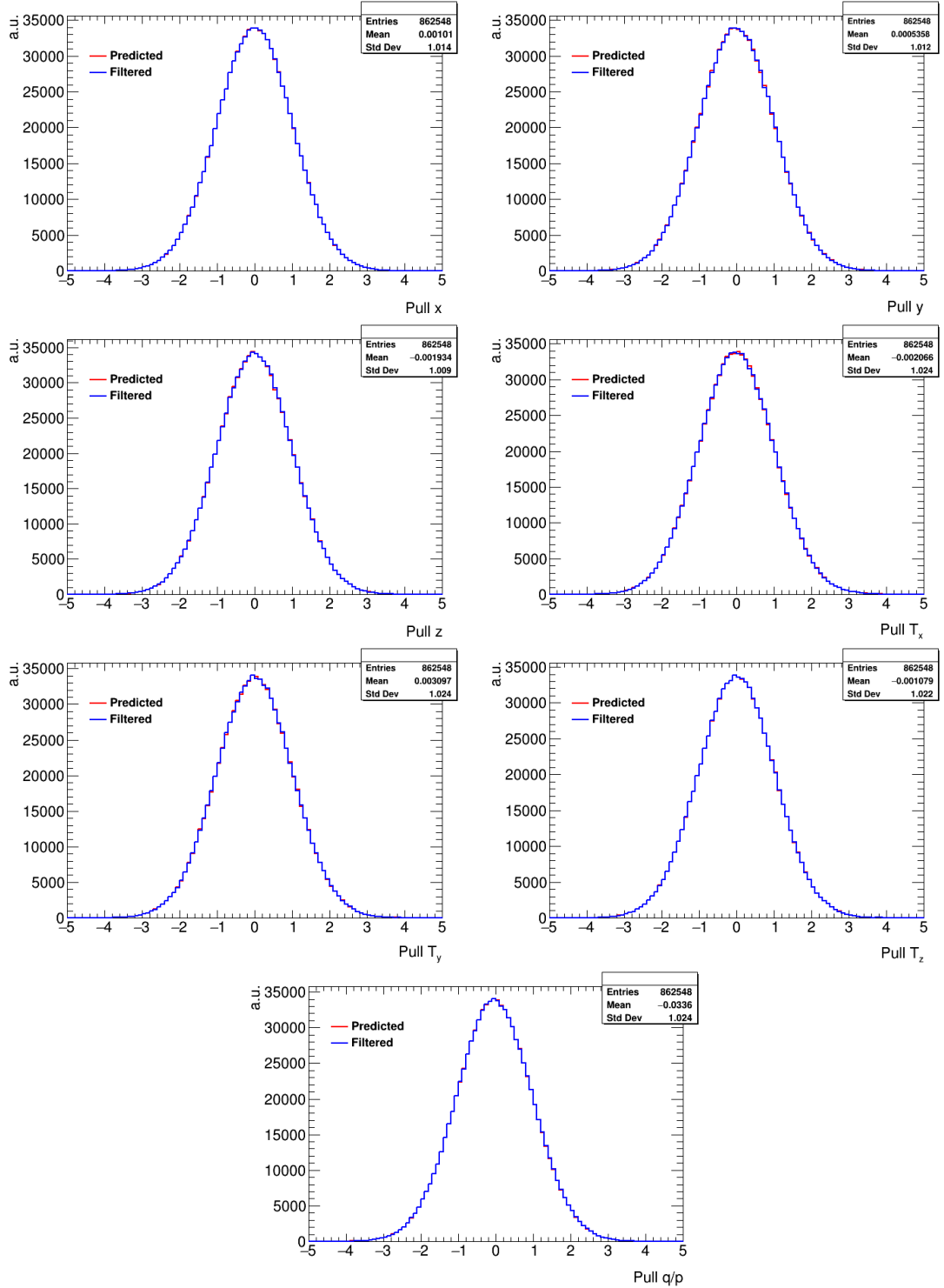
Figure 8.14: Pull distributions of predicted and filtered parameters obtained for the Free KF at the point of filtering in the TPC with 10 GeV initial momentum. The statistics refer to the filtered distributions.

For those distributions non-zero contribution of the bias in the KF formalism is present. The prediction covariance matrix is then given by $\Sigma_k^{\text{predicted}} + \Sigma_k^{\text{bias}}$ and the filtered covariance matrix is given by $\Sigma_k^{\text{filtered,biased}}$. As the pull distributions for all free parameters are within the statistics centred around zero with a standard deviation of about one, the extrapolation to free parameters as well as the KF formalism derived in Sec. 8.4 provide the desired behaviour. In addition, these plots show that the bias contributions to the covariance matrix before and after filtering remain unchanged. The limitation for the range of validity for the applied bias term approximation becomes visible in Fig. 8.15. Although the parameters are measured indirectly, on sees slightly
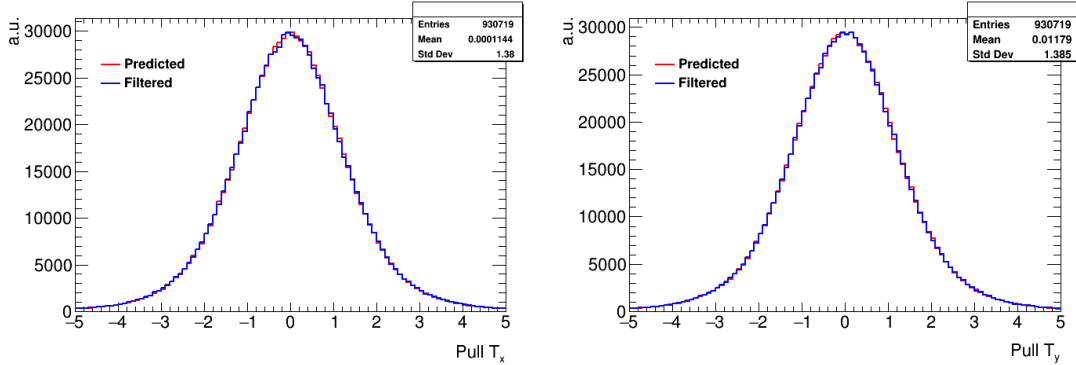
Figure 8.15: Pull distributions of predicted and filtered parameters obtained for the Free KF at the point of filtering in the TPC with 1 GeV initial momentum. The statistics refer to the filtered distributions.

too broad pull distributions. These are a consequence of a more complicated trajectory than a straight line.

Beside the filtering, the smoothing needs to be considered. Thereby the innermost layer in the tracking detector is a special point of interest as this point is the last location in backward direction that carries data. Further extrapolation would consequently just lead to broader variances. The obtained resolutions are shown in Fig. 8.16. The almost identical results obtained for the $L0$ resolution present the dominance of the tracking detector with the resolution of 25 μm upon the spatial coordinates in that direction. This accuracy also leads to a very comparable result in the ϕ resolution. Hence, no significant gain in resolution can be observed in these parameters compared to the TPC data utilising models, given the prior described setup. For the $L1$ resolution a similar impact of the tracking detector is visible with the exception of the Curvilinear KF. The reason for the deviation from the other three models is due to the smoothing procedure. This concept provides additional degrees of freedom by the surface placement for the parameter filtering and smoothing. While for the filtering the surface properties are predefined by the particles trajectory, for the smoothing two trajectories need to be combined. Thereby, the same surface is used and two different trajectories get combined in the spatial parameters. The surface itself defines then the degree of freedom for possible smoothed or shifted spatial parameters. Considering on top that the backwards
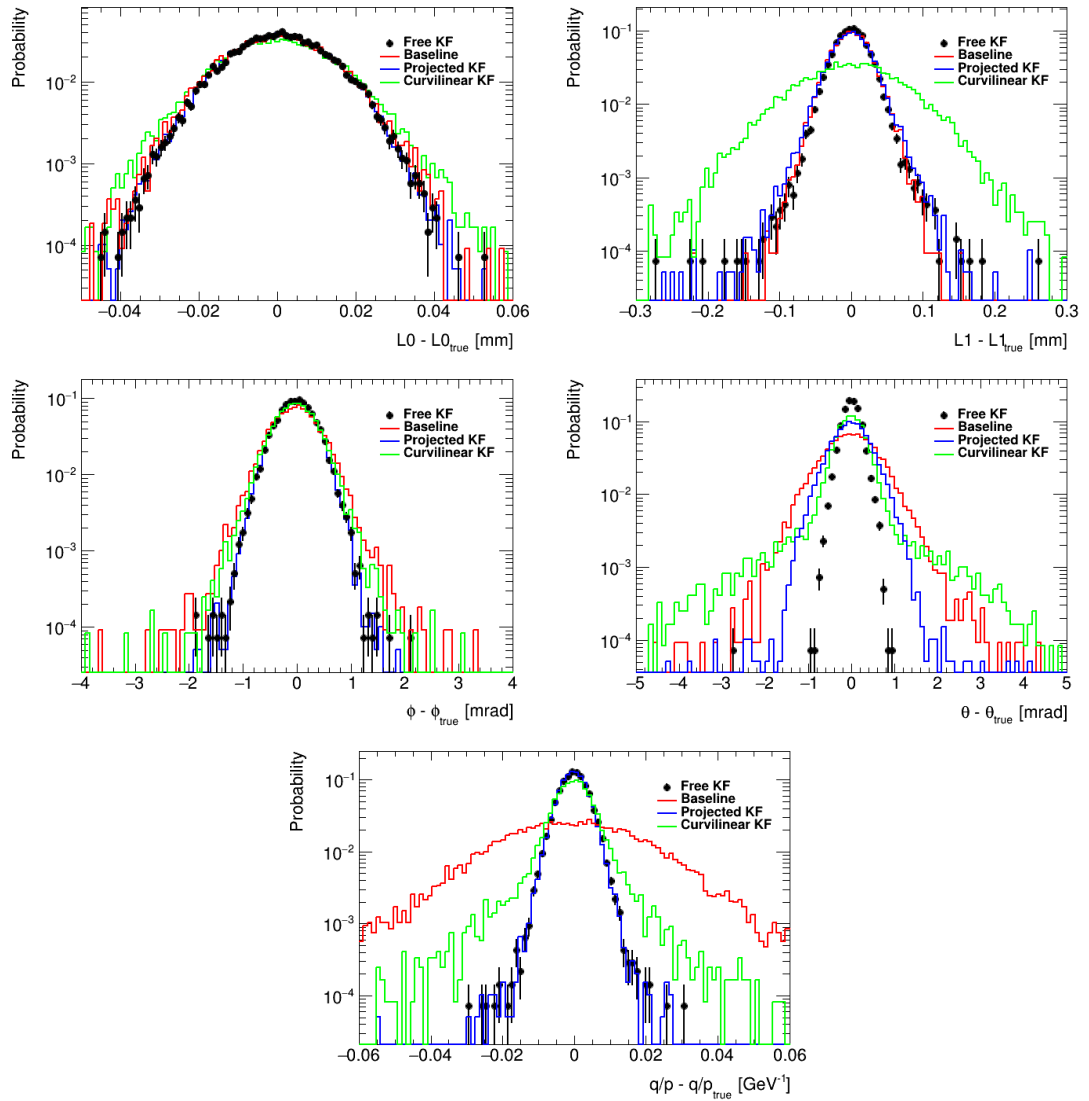
**Figure 8.16:** Smoothed resolution at the innermost surface of the tracking detector for 10 GeV initial momentum particles.

extrapolated trajectory is more precise w.r.t. the forward extrapolation then leads to large deviations per surface. Using the backwards extrapolated trajectory instead leads to a smoothing that is unregulated by the truth position. While the filtered state is placed normal distributed around the truth, the trajectory of the backwards extrapolation treats only the closest distance to the filtered state. Hence, a surface built from the former trajectory will consequently ignore any spatial regulation. For the same reason no other dynamically built orientation of the surface that is based on both trajectories provides a more reliable stability.

As the surfaces from the filtered state itself have per treated measurement a different orientation then leads to larger oscillations around the true parameters. Since thereby the $L1$ resolution was chosen to be worse in comparison to $L0$, the effect becomes visible. The long lever of many data points considered in this model alongside correlations between the parameters allow on the other hand to partially improve the resolutions for θ and q/p.

For the θ resolution the combination of pure indirect learning about the direction and the projections performed in the Projected KF becomes visible. Although this model underestimates the uncertainties, the $L1$ residuals are very similar to the Free KF. While this model also utilises surfaces, the orientation is fixed in comparison to the Curvilinear KF. Due to this stabilisation for the entire fitting procedure, the impact of the approximations gets suppressed, for $L1$ even almost negligible.

In the θ and q/p residuals, the effect of the TPC upon the smoothed residual becomes visible. For both parameters Baseline provides worse results than the Free and Projected KF, for the latter even than the Curvilinear KF.

Effects for the Curvilinear KF from different initial momenta upon the resolution are shown in Fig. 8.17. For a lower momentum, the curvature gets larger, hence the forward
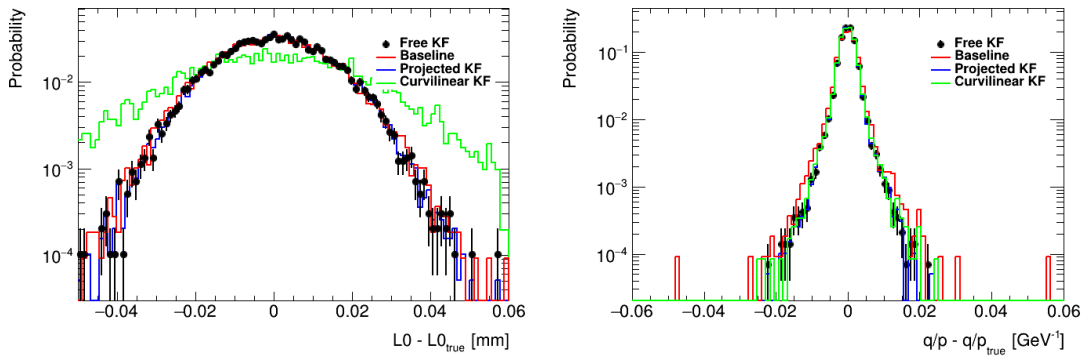
Figure 8.17: Smoothed resolution at the innermost surface of the tracking detector for 5 GeV (left) and 100 GeV (right) initial momentum particles.

and backward extrapolations tend to have larger variations when the smoothing is evaluated. This leads to deviations in $L0$ and also in ϕ compared to the other models. At that point it cannot be compensated by the detector resolution for $L0$ in the tracking detector. For high momentum the extrapolations have less curvature. While the combination is still from different states and the effects upon the $L1$ and θ distributions are still worse compared to the other models, as Fig. 8.17 shows the Curvilinear KF is in good agreement with the other models.

In addition to the resolution, the uncertainties of the smoothed parameters on the innermost tracking detector surface are of interest. The results are shown in Fig. 8.18. For all parameters, the utilisation of TPC show an improvement of the uncertainties. Especially for the spatial parameters, the TPC data utilising models show a shift of the Baseline distribution towards smaller values. The different absolute shift in σ_{L0}
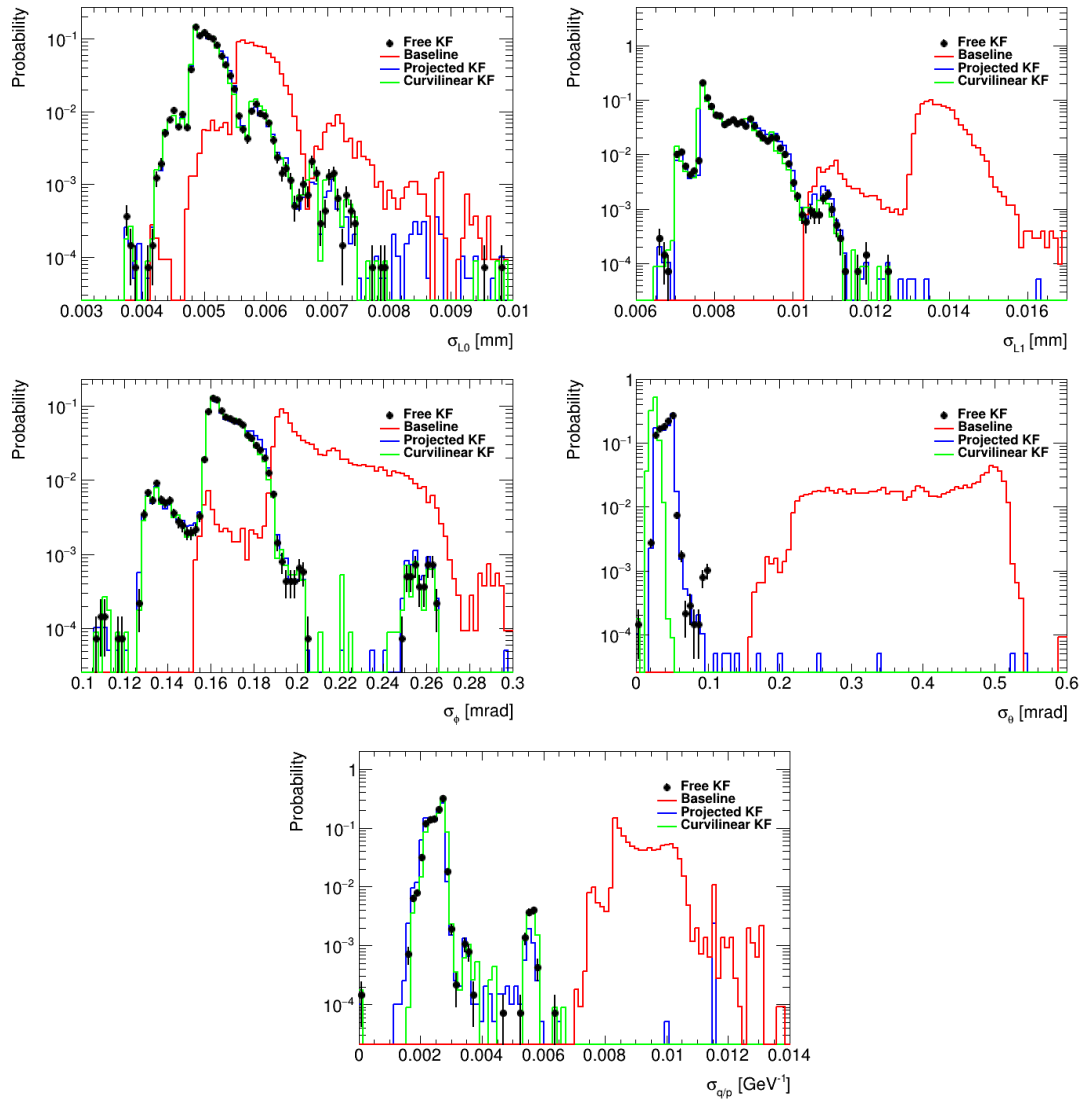
Figure 8.18: Smoothed uncertainty at the innermost surface of the tracking detector for 10 GeV initial momentum particles.

and σ_{L1} are again a direct consequence of the tracking detector resolution. Since the azimuthal angle uncertainty is linked to σ_{L0}, a similar effect is visible here. For θ and q/p the scenario is a bit different. While those parameters are measured indirectly, the lever represented by the extrapolation distance to the measurements have a significant impact upon the parameter uncertainties.

Furthermore the Free, Projected and Curvilinear KF have almost identical uncertainties for each parameter and initial momentum. The last one has even slightly better σ_θ values. In comparison to the Projected KF and considering the chosen TPC measurement uncertainties, the Curvilinear KF uses different projections of Σ^{det} compared to

the projection. This leads to smaller ellipses during the filtering. The better uncertainty and simultaneously worse resolution of the Curvilinear KF for the polar angle can be explained due to the non-interference of parameters update from Eq. (4.35) on the covariance matrix in Eq. (4.36). Since the Free KF bias term is given by the spherical approximation, the shown uncertainties are the lower bound.

Noteworthy is a combined consideration of the resolutions and uncertainties for the Projected KF with respect to the chosen measurement uncertainties. While the systematical underestimation leads to comparable uncertainties of the Free and Curvilinear KF, the resolution of the Projected KF is similar or worse compared to the Free KF. If the uncertainty attached to the measurement would be adjusted, the resolution would be improved at the cost of the uncertainties since the information in each measurement is drastically reduced.

Considering the detector, simulation and reconstruction setup, the obtained smoothed parameters are ideal values that tend to worse values in a more realistic setup. This includes material interaction in the tracking detector and the TPC or inhomogeneities in the magnetic field. At this stage smaller differences get covered by those effects leading to more similarities between the TPC data utilising models. Furthermore, the found results within the used setup show that the Free KF concept serves as a reliable alternative to the KF concepts utilising surface bound measurements.

9 Fast Track Simulation

In high-energy particle physics the simulation of particles and their trajectories and interactions with the detector play a major role in the understanding of the underlying physics and the behaviour of the detector itself. Primary interactions are covered by Monte Carlo generators and occur close to the interaction point itself. For the purpose of the extrapolation and material interaction the Geant4 toolkit provides a high precision simulation (full simulation) of interactions of particles and material. The CPU consumption of full simulations is usually too high to allow for processing all Monte Carlo data sets. Fast simulation techniques are often used instead in order to augment the full simulation setup. Evidently, there is a trade-off in play: a fast simulation usually approximates the underlying geometry and physics processes even further than the full simulation already does and hence, the simulation response is in general worse. A common approach is to reduce the simulated interactions to a limited set that cover the most relevant interactions for the final state particles used for physics analyses. The general idea of selection of the interaction processes and their modelling is driven by the requirement of producing events that look similar[1] to the full simulated ones but are calculated more quickly.

The fast track simulation for tracking detectors of the ATLAS experiment is called *Fatras* (Fast Atlas TRAck Simulation) [141]. Due to historical reasons, the name is also used in ACTS. Since ACTS provides the possibility to extrapolate a particle parameterisation along its trajectory, the formalism found in Chapter 7 can be re-interpreted and used for the simulation. Within a simulation context, the extrapolation of the covariance matrix is ignored and the mean is considered as the truth parameters. While the initial parameters for the track reconstruction have to be estimated, the simulation is initialised with the truth parameters. In the ACTS model of a tracking detector, all material is attached to surfaces, restricting the material interactions to the ActionList and simplifying the extrapolation formalism.

Within the context of this thesis, various contributions to the structure of the ACTS Fatras were implemented and a list of major physical effects was implemented. The formulation of a subset of physical effects is the main content of this chapter. The implementation of most effects is either based on code from Geant4 and Athena or on textbook formulas. While those kinds of effects are part of the first part of this chapter, the second half describes the formulation of the nuclear interaction in the context of the fast simulation. This parametrisation method was developed and implemented as part of this thesis. A detailed study of the ACTS Fatras performance will be executed by the ATLAS collaboration in the future.

---

[1]The similarity between full and fast simulation depends on the choice of observables and of the applied metric. The term is kept purposely general.

9.1 Physical Effects

Unlike a full simulation, the set of considered physics effects is restricted in a fast simulation. Those are given by major electromagnetic interactions, (in-)elastic or multiple scattering and particle decays. Exclusively for hadrons, the nuclear interaction called inelastic process can occur additionally. Since all effects occur on surfaces, a single actor class is used in ACTS to handle all effects, the so-called *Interactor*.

However, not all effects are applicable to all particles. As suggested in Chapter 7 a simplified extrapolation formalism can be utilised for neutral particles. This splits the per-particle extrapolation into two distinct Propagators, depending on the particles charge. Also a different list of physical effects is in use for neutral than for charged particles. The lists themselves are extendable in order to allow for dedicated simulation including more detailed effects which are not covered by the set of effects implemented in ACTS. The top-level simulation workflow extrapolates one particle after another until the particle dies or exits the detector. The particles produced during the extrapolation are stored and extrapolated afterwards.

The actor is called before and after each step within the extrapolation. While the charge of the particle allows to distinguish the general set of effects, not all effects are applicable for charged or neutral particles. This requires a per-effect selection of the input particle based on e.g. the particle type or its momentum. An additional selection is applicable to the eventually produced particles in an effect. In addition to the selection criteria, the Interactor handles per-effect properties. The applied selections and properties are presented in the following alongside the corresponding effect.

Continuous Effects

The first set of effects are those that influence charged particles whenever material is present but do not kill the particle. Since those effects are applied on each surface with material, the effects are grouped by the term *continuous effects*. The concept of applying those effects by utilising an actor is also performed in the context of the track reconstruction. Compared to the former scenario, the considered truth parameters extrapolated within ACTS Fatras are modified randomly by sampling from the underlying distributions. The continuous effects implemented in ACTS Fatras are scattering, atom excitation and ionisation and bremsstrahlung.

- Scattering
  Scattering is a process that symmetrically manipulates the parameters centred around the direction before the interaction occurred. The Highland formula from Eq. (7.40) and the Rossi-Greisen formula from Eq. (7.39) describe the width in θ. Together with a zero mean, a normal distribution can be formed and the scattering angle can be sampled. θ can be understood as the opening angle between the direction before and after the scattering. Hence, the width is scaled by an additional factor of $\sqrt{2}$ [17]. While the opening angle follows these distributions, the corresponding azimuthal angle is expected to be uniform over its domain. As these

models utilise normal distributions, large opening angles are suppressed by the distribution. That disfavours back-scattering of particles at the material stronger than observed. By modifying the underlying distribution to improve the large angle description, so-called *Gaussian mixtures* are formed. Since the implemented set in ACTS Fatras is intended to provide the minimal set of common effects, no mixture distribution is utilised. The scattering is independent of any kinematic constraints. The only selection is whether an $e^\pm$ is simulated or not in order to pick the corresponding distribution.

- Atom excitation and ionisation
  Charged particles traversing a material excites and ionises the atom. While the track reconstruction utilises the mean, given by the Bethe-Bloch formula in Eq. (7.33), the simulation utilises the most probable value. An approximation to obtain the mode of the energy loss from the mean is given by reducing the latter parameter by 10% [119]. The energy loss in ACTS Fatras is obtained from sampling from a normal distribution with the mode of the energy loss as mean and the standard deviation as given in Eq. (7.37). This effect upon charged particles is restricted to a minimum velocity of $\beta\gamma \approx 0.1$ as shown in Fig. 4.2.

- Bremsstrahlung
  Bremsstrahlung affects all charged particles. In the context of a fast simulation, the effect is restricted to $e^\pm$ as this effect mainly affects their trajectories. The energy loss fraction of the total energy $z \in (0, 1)$ due to bremsstrahlung is given by [142]

$$z = e^{-\Gamma(t/ln(2))}$$

with the thickness t expressed in radiation lengths. While a sample from the Gamma distribution leads to the energy of the photon, the corresponding angular distributions of the $e^\pm$ and the photon are extracted from the Geant4 parameterisation following the parameterisation from L. Urban. This parameterisation samples the polar angle of the produced photon around the central value $\theta_0 = m_e/E$ [125] with the electron mass m_e and the energy of the $e^\pm$ before the radiation E. The approximation provides the polar angle with respect to the $e^\pm$ direction as

$$\theta = \begin{cases} -\theta_0 \frac{8\ln(u_1 u_2)}{15}, & u_3 \geq 0.25 \\ -\theta_0 \frac{8\ln(u_1 u_2)}{5}, & u_3 < 0.25 \end{cases}$$

with the three random numbers u_1, u_2, u_3 sampled from a uniform distribution in $[0, 1]$. The azimuthal angle is sampled uniformly in $[0, 2\pi)$. The obtained photon energy and direction allow to modify the initial $e^\pm$ direction from momentum conservation[2]. After the direction is set, the energy loss to the lepton is applied. This order follows the steps occurring during bremsstrahlung as introduced by [125].

---

[2]The application of momentum conservation implies that any recoil with the material is neglected.

Those effects can be applied whenever a surface with material is intersected by the trajectory and the selection criteria are met. Furthermore, none of these effects kill the extrapolated particle.

Point-like Effects

In addition to the continuous effects, interaction may occur (randomly) at a certain point along the trajectory. The point of interaction is characterised by certain parameters steering the point of interaction. Within the ACTS Fatras, the point of interaction per parameter is sampled at the beginning of the extrapolation. The effect is applied as soon as the condition associated to the parameter is fulfilled. In ACTS Fatras, these so-called *point-like effects* cover the photon conversion, the particle decay and the nuclear interaction.

- Photon Conversion
  The photon conversion $\gamma \to e^+ e^-$ has been ported from the Athena and Geant4 implementations into ACTS. In order to adapt the workflow for ACTS Fatras, modifications were performed. Starting with the interaction point, the photon conversion is driven by the radiation length X_0. Based on [143], the distance in X_0 at which the photon conversion occurs can be sampled from

  $$X_0 = -\frac{9}{7}\frac{\ln(1-u)}{1-\xi}$$

  with the uniform distribution random number $u \in [0,1]$. The parameter ξ denotes the momentum dependent photon conversion cross section. This parameter is obtained from a fit in Athena. The fit relies on the aluminium data from [143] and is given by

  $$\xi = -7.01612 \cdot 10^{-3} + 7.69040 \cdot 10^{-2} p^{-0.607682} GeV^{-1}$$

  with the photon momentum p. Since material effects are only considered between the steps, the Interactor has to accumulate and monitor the passed material in X_0. As soon as enough material was passed, the conversion is triggered. The conversion itself utilises the Geant4 implementation. Although the Geant4 module is not applicable as standalone, the kinematic parameterisation was extracted and implemented in ACTS. As the underlying calculations are lengthy and mostly transcribed, their mentioning is skipped here in favour of the general workflow. The idea is to sample the momentum fraction of a single lepton depending on the photon momentum. Analogue to the bremsstrahlung, the angular distribution is obtained for the first lepton with respect to the photon. The kinematic properties of the second lepton are obtained from four momentum conservation. The lepton charges are assigned randomly. The photon is killed after the process. The produced particles put a constraint on the input selection of $E \geq 2m_e$ for the energy of the photon E and the electron mass m_e.

- Particle Decay

  The particle decay depends in ACTS Fatras directly on Geant4. Compared to the photon conversion, no parameterisation of the lifetime and the decay products exists. However, the Geant4 decay modules are rather independently applicable. This allows to utilise the Geant4 tables in order to sample the particle lifetime. The table provides the decay constant τ, the sampled lifetime is then given by

  $$t = -\tau \ln(u)$$

  with the uniformly distributed random number $u \in [0, 1]$. t is the proper lifetime of the particle and has to be monitored by the Interactor. Compared to the photon conversion, the decay does not rely on material interactions. Hence, without any restrictions, the sampled proper lifetime may be passed within an extrapolation step. In order to regulate the decay point, a step size limitation is applied. Since the particle never gains additional momentum within a step, the maximal proper time that can elapse can be estimated from the last known momentum. By constraining the step size, the next evaluation of the elapsed proper time is shorter or equal to the set limit. In order to overcome floating point comparisons for the decay triggering and to avoid additional, tiny steps, a relative acceptance region of 10^{-3} around t is set. Once the decay is triggered, the particle properties are passed to the corresponding Geant4 module that builds the decay products and its properties. The initial particle is killed after this process. The application of this effect is not constrained by kinematic parameters but is driven by the lifetime provided by Geant4.

While the photon conversion and the particle decay either utilise Geant4 or are transcribed from Geant4, their presentation for the implementation in ACTS was kept short. The last point-like effect, the nuclear interaction on the other hand requires more explanation. Its parameterisation will be the content of the next section.

9.2 Parameterisation of Nuclear Interaction

While the previously mentioned effects in ACTS Fatras rely on Geant4 or are expressed in textbook formulas, for the nuclear interaction the situation is different and a parameterisation has to be built. There exists a previously built parameterisation in Athena [141] which serves as starting point for the following considerations. Within this section the derivation of the parameterisation is presented, starting with data generation, event selection and categorisation. Afterwards the properties of the parameterisation are discussed.

9.2.1 Event Simulation and Selection

The parameterisation of the earlier nuclear interaction in Athena Fatras is based on the simulation of charged pions with energies between 15 and 50 GeV, sampled from a flat

distribution in η and ϕ. The interpolation region is very small in the context of centre-of-mass energies $\sqrt{s}$ in the pp system of 13 or 14 TeV at the LHC. The extrapolation is further limited to a 1 GeV lower threshold for a nuclear interaction[3].

The parameterisation method which will be presented also uses Geant4 to generate reference data for its derivation. In order to provide a broad range of applications the momentum range has to be extendable. Within this study various particle momenta are used and the simulation is performed in certain steps using fixed initial momenta. As the initial direction is not relevant for the interaction but only for the slightly different amount of penetrated material by the particle, no special treatment of η or ϕ regions is considered.

The simulations are performed using the OpenData Detector (ODD) [144], a realistic but non-existing tracking detector which is described in DD4hep [106]. The description language allows a translation of the geometry into a Geant4 based full simulation as well as a fast simulation using the ACTS algorithms.

Geant4 is used to simulate single particles and the interaction of the particles with detector material has been recorded. The produced collection of outgoing particles are registered for further analysis. For the event record, the library HEPMC3 [145] was used. In order to use this event recording library together with ACTS and Geant4 (inside ACTS), an interface was created that allows the translation between the individual objects. Additionally, the library allows to attach additional information to the record that eases the parameterisation afterwards. Since the content in the event record is under full control within ACTS, it can be selected which events are written to file, depending on certain criteria.

The events fulfilling the following criteria have been used for the parameterisation of the the nuclear interaction: The first criterion is a selection whether a nuclear interaction occurred in the event. The interaction vertex in the HepMC3 record is tagged accordingly. As the events without nuclear interaction are not considered any further, these are not stored but are used to model the nuclear interaction probability. The events with a nuclear interaction are categorised and the participating particles selected. A first selection criterion is a lower momentum threshold of 50 MeV for outgoing particles. This is performed since the curvature of charged particles below the threshold are computationally complex and the interaction models are less accurate.

Geant4 does not perform nuclear interaction simulations exclusively. This requires a filtering of the final state particles collection. As second step, only final state hadrons are considered in order to suppress minor contributions from leptons, nuclei from the detector material or particles that occur too rarely. The considered hadrons are p, n, K^+, K^0_S, π^+, K^0_L, π^-, K^-, $\bar{n}$, $\bar{p}$. Finally, it is mandatory that the initial particle performs the interaction.

The received final state particles are split into two different types of events: The first considers a soft interaction that preserves the initial hadron ($X \rightarrow X + Y$) and a second, hard interaction due to which the initial hadron gets destroyed ($X \rightarrow Y$). The distin-

---

[3]In many analyses a minimum momentum cut of 1 GeV is considered for particles, and hence the focus has been put on particles with higher momenta than this threshold.

guishing is done due to a major change in the final state kinematics. A soft interacting initial particle preserves almost all its initial momentum after the interaction while the momentum distribution in hard interactions are spread wider among the final state particles. Since Geant4 describes both types using the same process name, this selection is performed afterwards using the recorded data. For that purpose all inelastic events are tested for the conditions that a final state particle is of the same particle type as the initial one and that this final state particle (leading particle) has a higher momentum than all other final state particles. These events are tagged as soft interactions. However, this allows to include several hard interactions which fulfil these conditions. An event could actually look like an event from the other kind and as the parameterisation is required to describe the phenomena rather than the underlying physics processes it is associated to the type of which the criteria are fulfilled.

In order to remove hard interactions with low momentum leading particles from the collection of soft labelled events the transverse momentum of the sum of final state particles is considered. It seems convenient to just label soft events as soft in the case that this value is at least as big as the initial particles transverse momentum. The impact of the additional classification is shown in Fig. 9.1. The two particles final state using an
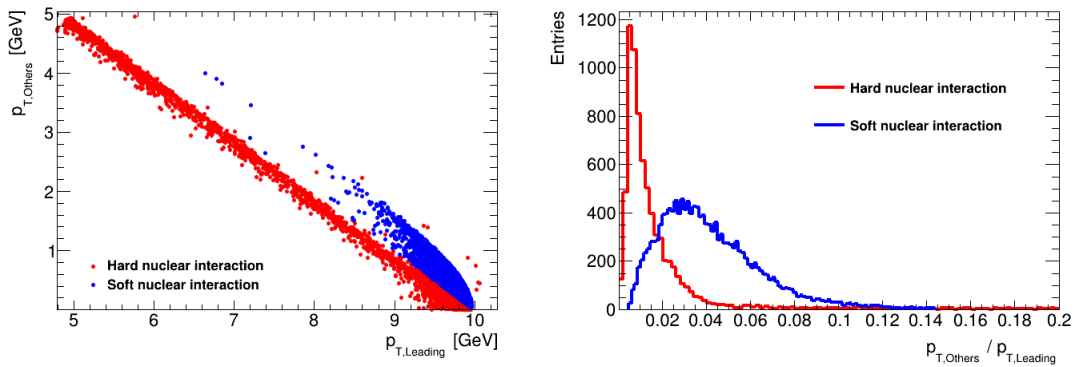
Figure 9.1: Comparison between the p_T of the leading particle and the non-leading particle within a soft (blue) and hard (red) two particle final state event with 10 GeV initial momentum π^+. The left plot shows a 2D representation of the p_T values. The right plot shows the fraction of the non-leading particles p_T and the leading p_T.

initial π^+ with a momentum of 10 GeV shows in the two dimensional representation of the particles (left) a clear overlay of two different shapes. Using this third criterion on top allows a sharp distinction between the two interaction types. Another argument for the usage of this criterion instead of demanding a certain momentum of the leading particle compared to the others is given by the Fig. 9.1 (right). Any applied threshold for the leading particles momentum would not allow to separate the two partially overlapping distributions but mostly assign events to a certain type by a fixed value border in this plot. However, higher multiplicity final states show that the strict boarder between soft and hard interactions show a final state multiplicity dependent mixing as shown in
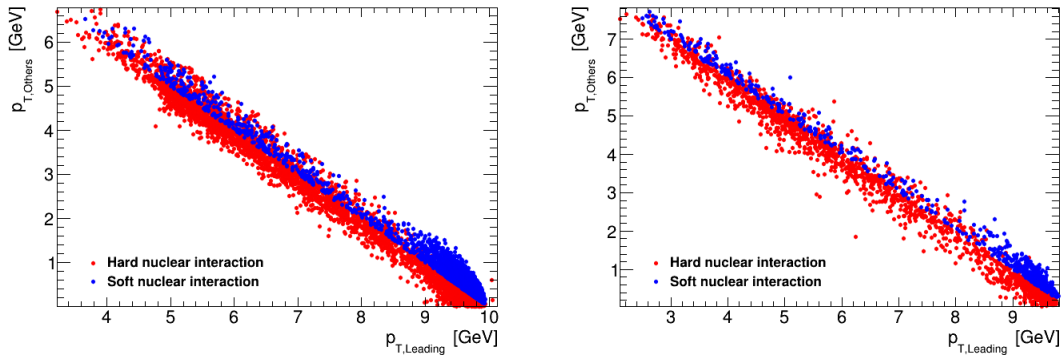
Figure 9.2: Representation of the final state p_T of 10 GeV initial momentum π^+ with the corresponding label as soft (blue) and hard (red). The transverse momentum of the leading particle and the sum of transverse momenta of all other final state particles is shown for a final state multiplicity of three (left) and six (right).

Fig. 9.2. Since this is a comparison of a single particle with all other final state particles instead of particle-to-particle comparison, this observation is reasonable and expected.

After adding this third criterion to the classification procedure, denoting the types soft or hard may not refer to the actual selection process anymore. Though, this terminology will be kept in the following to distinguish two different event shapes. This observed distinction between the event types was not considered in the former parameterisation but a superposition was described. The recorded, selected and tagged data set serves as input for the parameterisation.

9.2.2 Parameterisation of Fixed Initial Momenta

A parameterisation should describe the final state given a certain initial state with respect to the recorded reference data. The term *state* requires further specification as it describes the target properties of interest and the required input parameters. In the former parameterisation the process was split into several steps which can be processed in sequential order:

1. Evaluation whether a nuclear interaction occurs

2. Evaluation of the final state multiplicity

3. Evaluation of the final state particle composition

4. Evaluation of the particle momenta and directions

The required properties which have to be evaluated define the term *state*. Furthermore, the order of evaluation will be kept and the components are described in this section.

As a first attempt, these steps and the corresponding fit functions from [141] are used. The function serves as a first prototype for the parameterisation. However, the reproduction of the accuracy of the former fitting functions was not possible. Small variations

to the used models were introduced and further corrections were applied to produce a simulated result similar to the recorded data. The resulting fitting model became very complex while it was very unstable and sensitive to changing initial conditions. As a consequence, the ansatz of fitting the distributions has been rejected and a refinement of the parameterisation has been performed. The focus moved to considering the distributions of each initial momentum value (working point) directly and for each working point independently. Finally, an interpolation is developed that utilises the parameterisations obtained per working point. As central working point, π^+ particles with 10 GeV initial momentum are used for constructing and testing. The obtained concepts are then applied to higher and lower initial momenta to investigate conceptional stability.

9.2.2.1 Nuclear Interaction Probability

The probability for a nuclear interaction to occur depends on the penetrated material. This is summarised by the nuclear interaction length λ. While this parameter steers the nuclear interaction distance pdf as

$$P(d|\lambda) = \frac{1}{\lambda}\exp(-d/\lambda). \tag{9.1}$$

with the traversed distance d, the ACTS Fatras concept would sample d instead of a repetitive sampling from this pdf. Beside this dependency, for a fixed initial momentum, pseudorapidity and azimuthal angle, Fig. 9.3 shows the interaction probability within the ODD as a function of the initial momentum. This implies the requirement of a
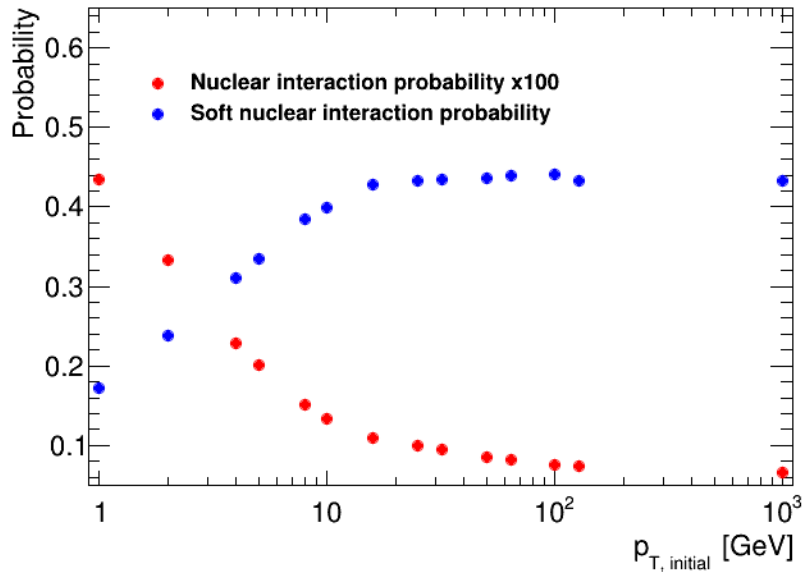
Figure 9.3: Dependency of the nuclear interaction probability on the initial momentum of the particle (red) and the dependency of the probability of a soft nuclear interaction in the case of a nuclear interaction on the initial momentum.

scaling of the nuclear interaction probability to treat the exponentially shaped decrease of the probability.

The ODD is a tracking detector with the material concentrated on detector modules which are placed in discrete steps along the trajectory with air (which is treated as vacuum) in between. The traversed length through the material is therefore given by the modules thickness scaled by the angle of incidence of the particle. In order to consider that the particle will traverse multiple material layers the total length is accumulated. A reasonable choice for the travelled distance is the accumulation of d_i/λ_i in the ith layer.

Since the initial momenta are treated independently during the parameterisation of the working points, the momentum dependency is negligible. In order to sample the interaction distance, the recorded distances are stored in a histogram. The histogram is normalised by the total number of generated events. The sampling has to follow the distribution. In order to fulfil this condition, inverse transform sampling is applied using the cumulative probability distribution of the interaction distances. By sampling random numbers in $[0, 1]$ a bin look-up in the cumulative distribution is performed rather than relying on fitting the distribution. Since the binning introduces a level of granularity, the number of bins has to be set such that (optimally) at most a single entry is in each bin. The for the inverse transform method provided granularity serves to avoid binning artefacts such as sampling multiple times the same value. However artefacts are unavoidable due to the limited statistics. In order to smooth the cumulative probability distribution neighbouring bins are interpolated linearly to provide intermediate values and to partially compensate the lack of available statistics.

In the case of a nuclear interaction the type of the interaction needs to be evaluated. The probability for a soft event $P(\text{soft}|\text{nuclear interaction})$ is shown in Fig. 9.3 as function of the momentum. The current momentum is in this case the only dependency. A hard event is given by the probability 1-$P(\text{soft}|\text{nuclear interaction})$. Thus, the soft interaction probability is a single number. While the interaction distance is sampled prior to the extrapolation, the interaction type is decided when the interaction occurs.

9.2.2.2 Multiplicity

In case of a nuclear interaction the multiplicity is the next quantity that needs to be evaluated. The multiplicity distributions of the final state can be extracted immediately from the record as shown in Fig. 9.4. The multiplicity distributions differ visibly between soft and hard interactions and need to be treated as such. The shown distributions are based on the filtered and tagged reference data set. A consequence of the filter is the dominant amount of one particle final states in hard nuclear interactions. Considering furthermore that only in a small amount of the events a nuclear interaction occurred, the available statistics for higher multiplicities is rather low. Hence only up to ten final state particles are considered.

Analogue to the nuclear interaction distance sampling, an inverse sampling is performed with the multiplicity distributions after the interaction type is sampled. Compared to the former situation, the multiplicity is an integer and thus, no interpolation between bins is necessary.
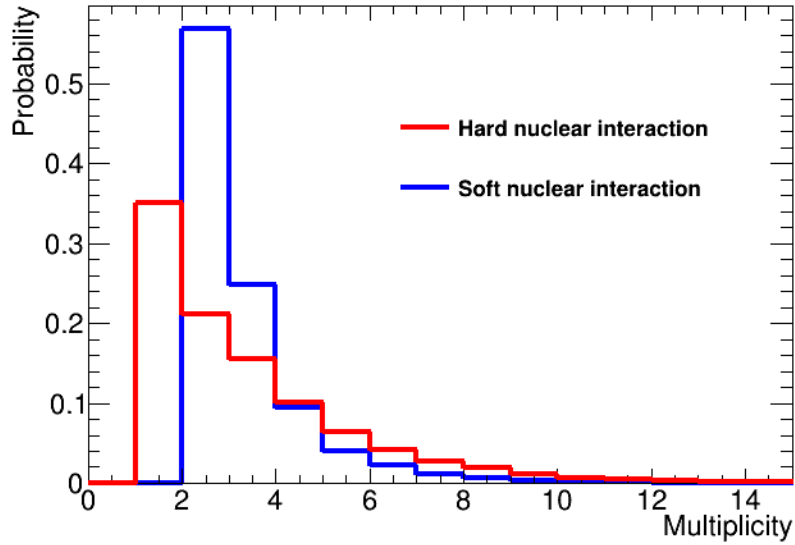
Figure 9.4: Soft and hard final state multiplicity distribution for 10 GeV initial momentum π^+. Only common hadrons with sufficient momentum were considered in the distributions.

9.2.2.3 Particle Kinematics

For each outgoing particle, the particle kinematics has to be sampled. As a first starting point the absolute momentum is treated. The corresponding momentum distribution needs to be split up between the interaction types in order to provide sufficiently accurate simulation results. Especially for soft interactions the leading particle obtains most of the initial momentum while all non-leading particles have rather low momenta. Consequently, each category is split up further into further sub-categories, which all have dedicated parameterisations. In order to derive a reasonable pattern for the splitting, the multiplicity provides a further separation possibility as the phase space of the final state momenta changes dramatically dependent on the multiplicity. In order to allow a structured sampling per multiplicity bin, the outgoing particles are ordered by their momenta. Depending on their position in that order (production generation), the particle properties from the event record are assigned to different histograms.

Using the set of distributions of a given initial momentum, interaction type and corresponding multiplicity to perform a sampling without constraints would lead to an arbitrary momentum composition of the final state. The required constraint will be considered by adding to each set of distributions the distribution of $p_{\text{sum}} = \sum_i p_i/p_{\text{initial}}$ of all per event created particle momenta p_i and the initial momentum p_{initial}. In order to provide all other distributions of a set in a similar value range along the abscissa, the values are re-scaled to p_i/p_{initial}. That way, all distributions are in a similar range.

The final momenta are then evaluated by re-scaling each individual momentum by the fraction $p_{\text{sum}}/\sum_i p_i$ with the individual samples p_i.

The histograms are intended to be utilised analogously to the nuclear interaction distance sampling using an inverse sampling method with additional interpolation. However, if the sampling is performed independently from each distribution the correlation between the generations is not considered. As a consequence the simulation would produce a correct sum of momenta but the individual values per event look very different compared to Geant4. This is compensated by correlating the sampling.

In the context of the inverse transform method all samples are uniform distributed values $U(0,1)$ which are then associated to quantities by the corresponding cumulative probability distribution. As the cumulative distribution is invertible the used input data can be projected uniformly in the interval $[0,1]$ by calculating for each generation i of type t and multiplicity j with the given momentum p_i and the corresponding probability density function $P_{ijt}(p)$

$$U_{ijt}(p_i) \equiv \int_0^{p_i} P_{ijt}(p)dp \sim U(0,1).$$

The obtained uniform distribution is transformed into a normal distribution $\mathcal{G}(0,1)$ with mean 0 and standard deviation 1 by using the inverse error function

$$\mathcal{G}_{ijt}(p_i) \equiv \text{erf}^{-1}(2U_{ijt}(p_i) - 1) \overset{!}{\sim} \mathcal{G}(0,1) \tag{9.2}$$

with the mapping of $U_{ijt}(p_i)$ onto the domain of erf^{-1}. As a result of transforming each event, the combination $p_{jt,\mathcal{G}} \equiv \{\mathcal{G}_{1jt}(p_1), \mathcal{G}_{2jt}(p_2), \ldots, \mathcal{G}_{(j+1)jt}(p_{j+1})\}$ is distributed according to the multivariate normal distribution

$$\mathcal{G}(p_{jt,\mathcal{G}}|\mu_{jt}, \Sigma_{jt}) = \frac{1}{\sqrt{(2\pi)^{\dim(p_{jt,\mathcal{G}})}\det(\Sigma_{jt})}}\exp\left(-\frac{1}{2}(p_{jt,\mathcal{G}} - \mu_{jt})^T\Sigma_{jt}^{-1}(p_{jt,\mathcal{G}} - \mu_{jt})\right)$$

with $\dim(p_{jt,\mathcal{G}}) = j+1$. In the case that the covariance matrix Σ_{jt} is sufficient to describe the correlation between the elements of $p_{jt,\mathcal{G}}$ the mean μ_{jt} becomes a zero vector and $\forall k : 1 \leq k \leq j+1, \Sigma_{jt,kk} = 1$. This is the behaviour expected by Eq. (9.2). As examples of the results two different two-dimensional projections are shown in Fig. 9.5. Considering the correlation pairwise between certain parameters in different sets of distributions, some become a two-dimensional normal distributions as expected. In the case of the right plot, it becomes visible that the distribution is clinched on one side and not normal distributed. This can indicate that in such cases a more complicated and non-linear correlation or boundary is present. This phenomenon is especially strong pronounced in low final state multiplicity cases. With increasing multiplicity more final states become possible which brings the pairwise comparison closer to a normal distributed shape. As these non-normal distributed cases would require a more complicated evaluation it is not further treated at this point.

Beside the possible insight into the systems behaviour the evaluation of all $p_{jt,\mathcal{G}}$ for a fixed j and t from the reference data allows the estimation of μ_{jt} and Σ_{jt}. The idea
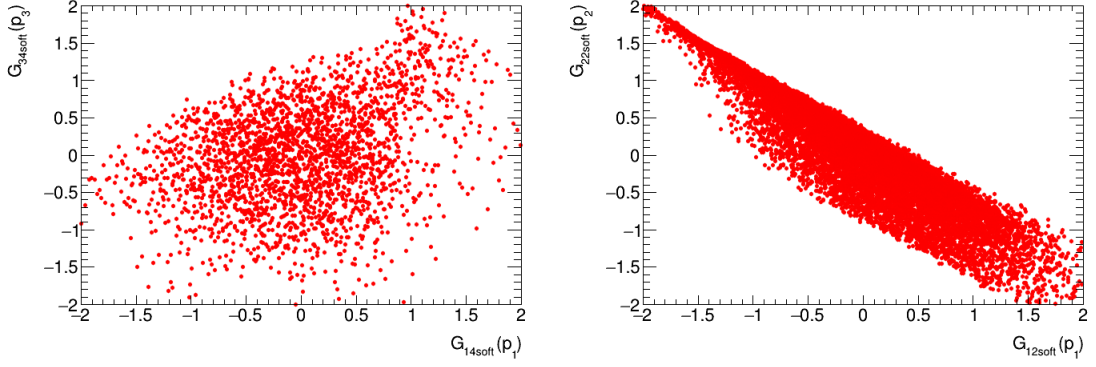
Figure 9.5: Left: First versus third generation from a soft four particle final state of 10 GeV initial momentum π^+ in the normal distributed representation. Right: First versus second generation from a soft two particle final state of 10 GeV initial momentum π^+ in the normal distributed representation.

is to diagonalise the covariance matrix to sample independent random numbers. This requires a change of basis into the eigenspace of Σ_{jt}. The obtained matrix $\Sigma_{jt,\text{ES}}$ is assumed to be diagonal containing the eigenvalues λ_k. The representation of μ_{jt} in this space will be denoted as $\mu_{jt,\text{ES}}$.

As the covariance matrix might not describe the correlation between the generations perfectly, a similar result is obtained for the representation in the eigenspace. As a consequence, an independent sampling from normal distributions in this space is not guaranteed to provide reasonable results but as the individual momenta get re-scaled afterwards a normal distributed sampling from a clinched or correlated distribution in the eigenspace gets partially compensated.

In the process of sampling for the simulation the required calculations are performed in inverse order:

1. Sample of independent normal distributed values $E_{ijt}(p_i) \sim \mathcal{G}(\mu_{jt,ES,i}|\sqrt{\lambda_i})$ to obtain the vector $p_{jt,\text{ES}} = \{E_{0jt}(p_0), E_{1jt}(p_1), \ldots, E_{(j+1)jt}(p_{j+1})\}$ in the eigenspace.

2. Transform $p_{jt,\text{ES}}$ to the normal space to obtain $p_{jt,\mathcal{G}}$.

3. Transform $p_{jt,G}$ to the dimension-wise flat distribution using $U_{ijt}(p_i) = (\text{erf}(\mathcal{G}_{ijt}(p_i)+1)/2$.

4. Extract the corresponding cumulative probability distribution as the abscissa value that belongs to the ordinate value $U_{ijt}(p_i)$.

As this is processed per event the resulting vector obtained is

$$p_{\text{sample}} = \left\{ \frac{p_1}{p_{\text{initial}}}, \frac{p_2}{p_{\text{initial}}}, \ldots, \frac{p_n}{p_{\text{initial}}}, \frac{p_{\text{sum}}}{p_{\text{initial}}} \right\} \tag{9.3}$$

for the final state multiplicity n. In order to constrain the individual momenta $p_1, p_2, \ldots, p_n$ to reasonable values each value is re-scaled by the factor $p_{\text{sum}}/\sum_{i=1}^{n} p_i$. However, this

process is only required for multiple final state particles. The special case of a single final state particle requires no further constraints and can be sampled directly from the corresponding cumulative probability distribution using a uniform distributed value and evaluating the momentum.

The obtained absolute value of the momenta will be used in the following the provide directions for the particles. The directions are defined by two angles in spherical coordinates, the polar angle θ and the azimuthal angle ϕ. The evaluation of these angles is designed to follow the same approach as done for the absolute momenta. Since the angles are a result of the underlying kinematics, a direct sampling from the angular distributions as performed for the momenta would lead to artefacts like back-to-back emitted particles with large momenta. This will be avoided by considering the pairwise invariant masses

$$M_{0i} = \sqrt{(E_0 + E_i)^2 - (p_0 + p_i)^2} = \sqrt{2p_0 p_i(1 - \cos(\theta_{0i}))} \tag{9.4}$$

with the particle energy E and its momentum vector p, using the approximation that all particles are mass-less in this context. A pair consists thereby of the ith final state and the initial particle (indicated with index 0). This parameter allows the calculation of the opening angle θ_{0i} dependent on the absolute momentum of the produced particle.

For the sampling, the distributions are again split into their type, multiplicity and generation. The generation is defined by the index received from the momentum ordering of the data. Though, a distribution for normalisation as used for the momenta is not added. The workflow to obtain the sampled invariant masses is identical to the procedure for the momenta. The angle θ_{0i} is obtained from Eq. (9.4) as

$$\theta_{0i} = \cos^{-1}\left(1 - \frac{M_{0i}^2}{2p_0 p_i}\right). \tag{9.5}$$

Since the set of momenta is sampled independently from the set of invariant masses it can lead to the point that $M_{0i}^2/(p_0 p_i) > 4$ and to no possible solution for θ_{0i}. This occurs preferably for low momentum final state particles. Hence, the total impact on observables is small. However, in order to handle this scenario the sample must be modified. This affects either the momentum p_i or the invariant mass M_{0i}. No value for any of both values is forbidden by the sampling method but for some value regions the density of possible combinations is low. This is especially the case for higher invariant masses. It was decided to produce a new momentum sample in these cases. That way an under-population of the invariant mass distributions is prevented. On the other hand, the questionable p_i cannot be sampled independently but this requires a full re-evaluation of p_{sample} to avoid inconsistencies within the set due to their correlation. A new sample implies a re-evaluation of all θ_{0i} and also that either all these angles can be evaluated or a new momentum sample is required. Depending on the final state multiplicity and the type of the interaction approximately 10-25% of events can be affected by this case. An alternative approach would be a combined sample of the momenta and invariant masses. Since this requires much more computational operations without receiving a guaranteed fitting set of parameters it is not performed here.

The polar angle θ_{0i} obtained with this method is given relative to the initial particles angle and defines the opening angle of a cone. The corresponding relative azimuthal angle ϕ_{0i} is sampled from a uniform distribution in $[0,2\pi)$. By rotating accordingly the angles in the global coordinate system are obtained.

9.2.2.4 Particle Decomposition

The last property to be parametrised is the particle type. Since the outgoing particles are ordered according to their momenta, the order of the produced particles is shuffled, too. In order to structure the particle creation it is assumed that the initial particle produces in the nuclear interaction just a single particle, the leading particle. This particle then creates again a single particle and so on. The sequence ends when the target multiplicity is reached. Consequently, the created particle type only depends on the particle type of the previous one. Since the order of the particle production is interchanged, the particles that may be produced from a given one needs to be derived explicitly for each particle type by counting. Thus, the resulting branching is not related to real physics processes. As a consequence, the particles are produced plainly on certain probabilities based on the observation.

The production lists are only produced for the reduced set of hadrons which are treated in the parameterisation. From all recorded nuclear interactions per initial momentum a single production table was created. Since the production of the leading final state particle in soft interactions is already covered by the corresponding probability, these were not taken into account in order to avoid double counting and a biased result. Additionally, the data record showed that some particles do not have any particles they produce. In such cases a flat distribution among all considered hadrons is assigned. Heavier hadrons like protons are not produced from low momentum particles. For higher initial momenta the branching possibilities get broader. In total, a single table for all momenta is not possible but must be treated individually depending on the initial momentum.

Another aspect that is related to the way of massless particle type association is the simplification that was used in Eq. (9.4). It was shown that the sampling of two independent sets of absolute values of momenta could lead to unsolvable equations for the opening angle θ_{0i}. Based on Eq. (9.4) the angle is given as a function $\theta_{0i}(M_{0i}, m_i, p_i | m_0, p_0)$ with the fixed initial particles mass m_0 and the corresponding momentum p_0. An additional dependency upon the opening angle by the mass would aggravate the evaluation. Since it was seen that the individual generations of each final state multiplicity leads to different distributions for the momenta and the invariant masses, this would split further up into different pairs of particles. Besides the struggle that the individual statistics for each distribution would be very low, the tracking detector treats it indifferently. The only important property for the particles trajectory is the charge of the particle as shown in Eq. (7.6) and it is reproduced by this procedure.

9.2.3 Parameterisation Performance

In the following the performance of the parameterisation is investigated. The first step will be the investigation of 10 GeV initial momentum π^+. Afterwards other initial momenta will be considered.

Only inelastic nuclear interactions are considered within this section. The selection of soft and hard nuclear interactions is thereby used as shown for 10 GeV π^+ in Fig. 9.3. Since the inverse sampling method allows a reproduction of a given distribution using a sufficient amount of uniform distributed values the multiplicity distributions can be reproduced by this method and do not require any further testing. The same accounts for a single particle final state as this does not depend on any correlations but only on one input histogram. Therefore it is not considered in the following but only higher multiplicities. The focus relies hereby on the elements that are necessary for the trajectory: momentum, direction and charge. Since the categorisations used to split up each distribution is a custom labelling, the combination of all distributions will be used. For that purpose, for each multiplicity and interaction type 10000 events were generated. The distributions of each type are then combined using the probability of the corresponding multiplicity as shown in Fig. 9.4. Finally, the hard and soft interactions are combined with the respective probability as shown in Fig. 9.3. Hence an effective distribution can be considered.

The first distribution of interest is the sum of final state absolute values of momenta. The result for π^+ with initial momentum of 10 GeV is shown in Fig. 9.6. This serves as
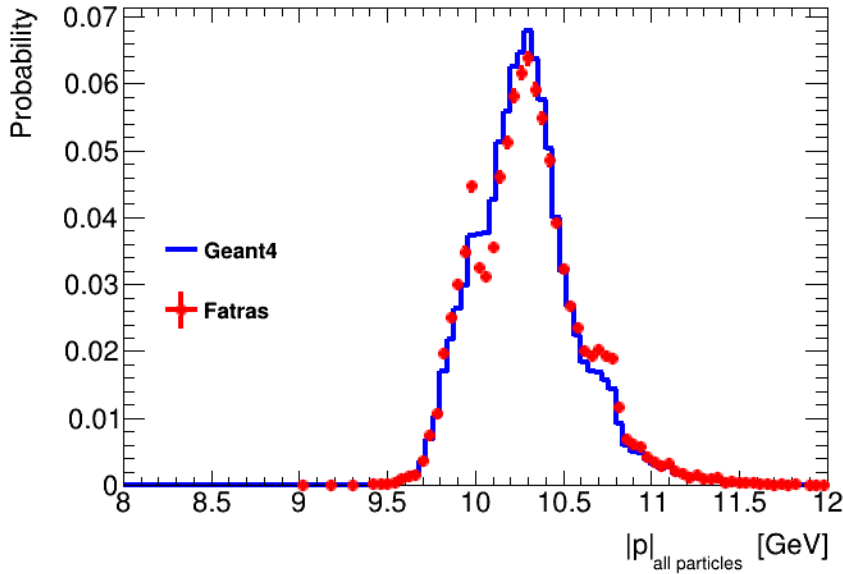
Figure 9.6: Sum of absolute values of final state particles momenta originated from 10 GeV π^+.

a control plot of the correlated sampling method. As was shown Fig. 9.5 the expected multivariate normal distribution is not fulfilled for all scenarios. Also the re-sampling

in the case of non-fitting combinations of invariant masses and momenta could enhance artefacts. That way it is possible to see whether the collective sample leads to reasonable results. For the working point of 10 GeV initial momentum the simulation mostly reproduces the target distribution. The only visible differences are at the shoulders around 10 and 10.7 GeV. In total the approach using the correlated sampling leads to reasonable results in the parameter.

The second distributions of interest is the invariant mass of the sum of the final state particles which is shown in Fig. 9.7. In this case any deviation originated from the
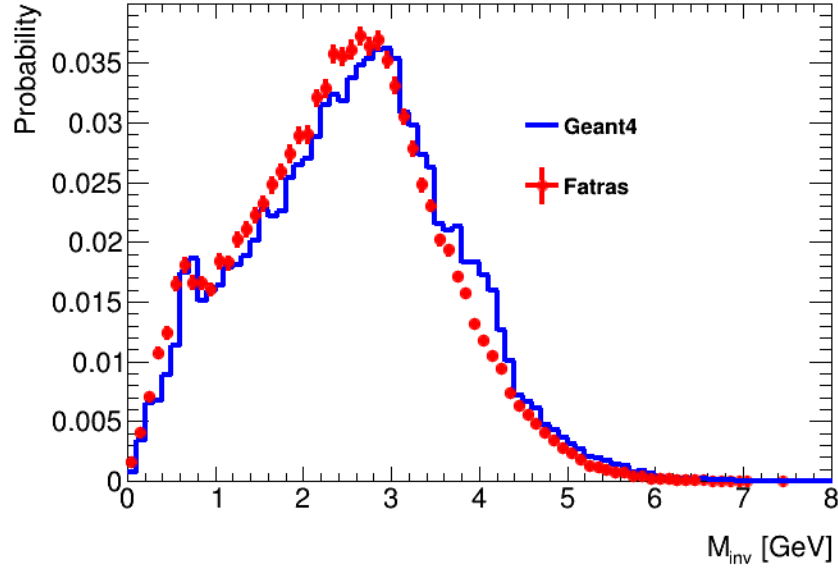
Figure 9.7: Invariant mass of the sum of final state particles originated from 10 GeV π^+.

sampling of momenta will partially propagate to the evaluation of the opening angles. The plot shows that while for some points the fast and the full simulation fit very well, there is a slight tendency towards smaller values in the fast simulation compared to Geant4. However the general shape is in good agreement with the full simulation. This justifies that the applied re-sampling approach leads to reasonable results.

The third distribution of interest is the transverse momentum of the final state particles. This observable allows an insight into the event shape as it is the result of a composition of absolute values of momenta and angles in a global frame. It therefore propagates sampling errors over multiple levels. The result is shown in Fig. 9.8. The shapes of the samples have a similar structure compared to the Geant4 simulation. However is visible that the ACTS Fatras distribution is too broad. This is a result of the slightly too low invariant masses from Fig. 9.7 leading to too high transverse momenta.

Finally the particle type assignment for 10 GeV π^+ is investigated. The comparison between the fast and the full simulation is shown in Fig. 9.9. For the main final state particle types p, n, π^+ and π^- some deviations are visible. For the rare appearing kaons, $\bar{p}$ and $\bar{n}$ the probability fits very well. The decreased production rate of π^+ could
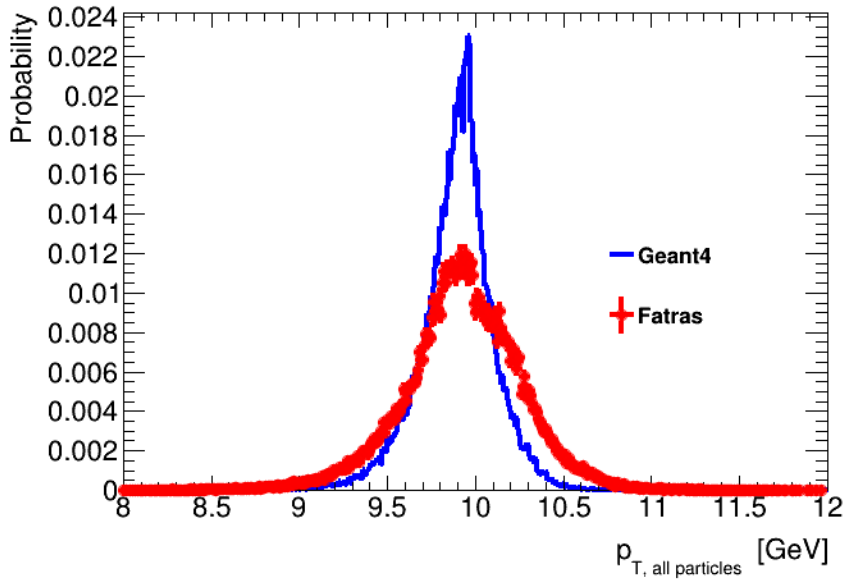
Figure 9.8: Transverse momentum of the sum of final state particles originated from 10 GeV π^+.

hereby be a result of a non-ideal separation between soft and hard processes. However the general tendency of the individual particles compared to the Geant4 data is very similar. As the table of the branching probabilities are derived from the recorded data and a limited data set is used a strong bias due to the approach is not visible.

The comparison performed for the π^+ with 10 GeV initial momentum will be repeated in the following with different momenta. Since the sampling of the sum of absolute values of momenta works conceptually as shown for 10 GeV, it will not be treated in the following. The first one will be towards higher momenta. As a simulation point 100 GeV initial momentum is chosen. The resulting observables are shown in Fig. 9.10. Again the invariant masses of the sum produce slightly too low values but in total the result is closer to the Geant4 result than in the 10 GeV case. This improvement can be observed in the transverse momentum plot on the right. In summary the approach produces more precise results for simulations with higher initial momentum.

Looking towards lower momenta the same simulation procedure was repeated for 1 GeV initial momentum. The results are shown in Fig. 9.11. Both distributions show the effects which were already described in Fig. 9.7 and 9.8 but with a higher impact. As this selection procedure performed in Sec. 9.2.1 filters events with nuclear interactions but does not purifies the selected and categorised events from other effects but only suppresses them to a certain amount, effects like multiple scattering play a more and more dominant role as the initial momentum decreases. Therefore without an explicit treatment within the parameterisation these effects became a part of the parameterisation enhancing deviations between fast and full simulation.
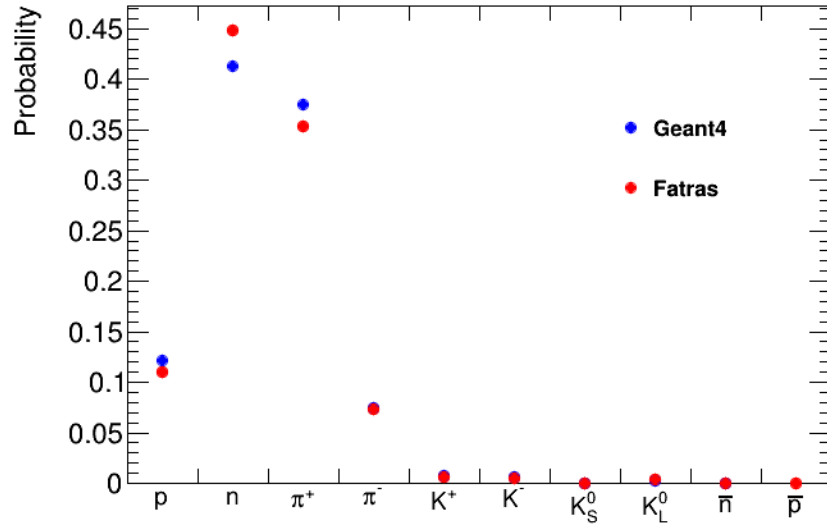
Figure 9.9: Final state particle types originated from 10 GeV π^+.

However since Fatras chains up multiple effects in a list and evaluates one after the other the deviations will become smeared out as a combination of nuclear interaction, multiple scattering etc. are applied on the particles. Additionally, in these momentum regimes the kinematics derived from the nuclear interaction become sub-dominant compared to other effects.

The last parameter that is treated for different initial momenta is the particle type association. The obtained distributions are shown in Fig. 9.12. Both distributions show a similar effect as seen in Fig. 9.9. The overall shape of both is very similar compared to the Geant4 simulation. Therewith the distributions of the most important hadrons
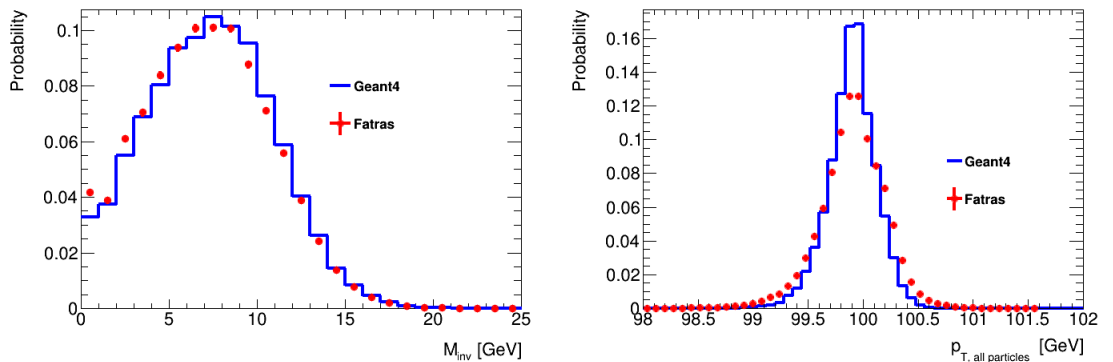
Figure 9.10: Invariant mass (left) and transverse momentum (right) of the sum of final state particles originated from 100 GeV pi^+.
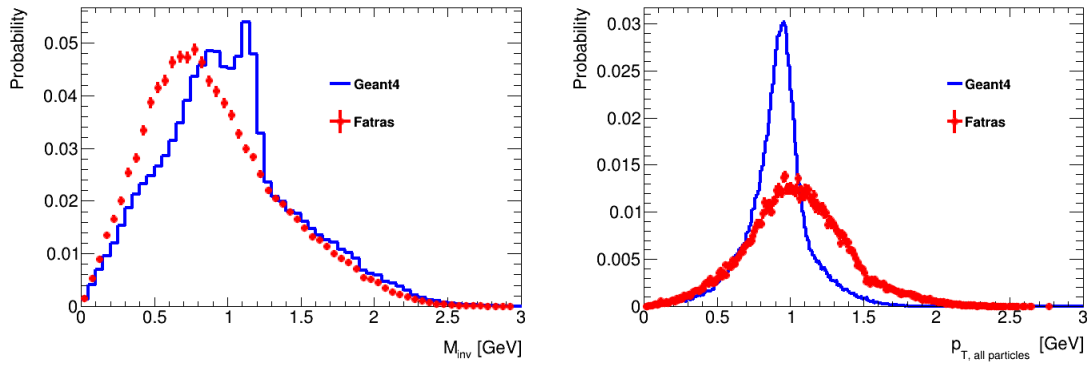
Figure 9.11: Invariant mass (left) and transverse momentum (right) of the sum of final state particles originated from 1 GeV pi^+.
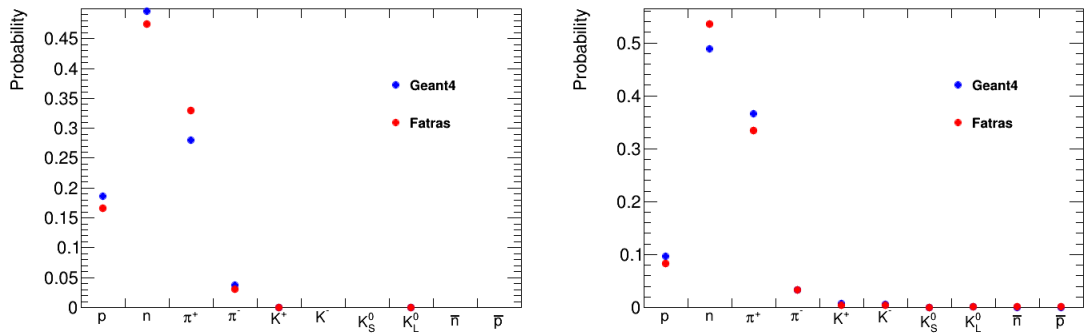
Figure 9.12: Final state particle types originated from 1 GeV (left) and 100 GeV (right) π^+.

can be reproduced. However an excess of π^+ is also visible for the 1 GeV case which affects the multiplicity of other hadron types. For the 100 GeV case too few π^+ were found causing the same effect. Both deviations can be an effect of the association to soft and hard nuclear interactions. Furthermore the method is able to allow only final state particles that were recorded and so the 1 GeV case shows that $\bar{p}$ and $\bar{n}$ are not present as required. For the more rare kaons the excess of the π^+ do not affect their multiplicity much and the result is very similar.

9.2.4 Interpolation

Beside the reproduction of distributions from a Geant4 simulation using the parameterisation at the working points, the key element is the interpolation using the different parametrised points in order to cover the range of possible states in the event simulation. The interpolation demands to fulfil the same four points described in the beginning of Sec. 9.2.2. To achieve this the obtained data and the thereby derived parameterisations are used to estimate the corresponding distributions at a certain point. The strategy is to perform the same procedure as before but use a suitable combination of multiple

parametrised points. In the following only the two neighbours in terms of initial momentum will be considered. This means that the closest parameterisations with less momentum and with more momentum than the target momentum are picked. In order to construct an interpolation from these two it is assumed that the distribution shapes are (beside a scaling factor) similar to each other. Hence the target momentum distributions in between should be similar to both. The second assumption is that these shapes change slower with increasing momentum. The similarity assumption will be the origin of two different interpolation approaches presented in the following. In this section two different interpolation ansatzes based on the similarity of the parameterisations are presented. Since these originated from each other, they will be presented in the corresponding order. The second assumptions allows to justify the spacings between the parameterisations as will be discussed alongside.

9.2.4.1 First Interpolation Ansatz

For reasons of guidance through the interpolation concept the final state kinematics are considered firstly, starting with the absolute values of momenta. As described in Sec. 9.2.2.3 the actual sampling happens in the eigenspace of the mapped pdfs. The independently sampled normal values are then transformed into the normal space which produces a correlated, normal distributed sample. Afterwards, it is mapped onto a uniform distribution and finally using the cumulative distribution function back into the momentum representation. This workflow provides several challenges as many different parameters and distributions would need to be combined although the combination does not have to reproduce the observed distribution. In order to avoid this difficult and error-prone situation a sample will be processed through both chains of the used neighbours and combined afterwards.

As sampled sets of momenta of multiple events might look very differently a constraint is required that allows to derive a similar set of momenta from both neighbours. The in Sec. 9.2.2.3 introduced normalisation of the momenta, allows to receive values that are in a similar range for different momenta. In order to sample a similar set of values it is convenient to produce a single set of values, considered in the eigenspace and process it further in both neighbours independently. In order to produce such a set of values the key assumption is that the spectrum of eigenvalues between the neighbouring covariance matrices is approximately similar. The same accounts for the mean of the normal distributions but since these are rather small the issue will not be further investigated but applied.

A weighted combination of the individual eigenvalues is calculated and used for sampling. For the weighting scheme different simple models were tested, based on the development of distribution shapes for various target momenta. It was observed that the shape of the momentum distribution looks rapidly similar to the higher momentum neighbour as the target momentum is increased. Additionally, as the simulation is required to produce final state particles within a small time frame and the sampled momenta and invariant masses have to match such that the opening angle θ_{0i} is calculable by Eq. (9.5), a sufficient small re-sampling rate is required. This is partially steered

by the weighting scheme. In order to involve these observations into the weighting each combined eigenvalue e_{target} is calculated by

$$e_{\text{target}} = \frac{1}{\sqrt{p_{0,\text{target}} - p_{0,\text{lower}}}} e_{\text{lower}} + \left(1 - \frac{1}{\sqrt{p_{0,\text{target}} - p_{0,\text{lower}}}}\right) e_{\text{upper}} = w e_{\text{lower}} + (1-w) e_{\text{upper}}$$

with the eigenvalue of the lower neighbour e_{lower} and the upper one e_{upper}. The neighbouring eigenvalues are both sorted by their value. The same approach is applied for the mean of the normal distributions and for all following required combinations except the invariant masses. In order to conserve a normalisation of the weights, it is assumed that a sample looks similar to the neighbour such that it only requires a scaling to the target momentum.

As the received sample is used independently in both neighbouring chains in order to receive the values in the momentum representation, these need to be combined as well. It was found that the scaling factor for the momenta from Eq. (9.3) is the most sensitive parameter upon the weighting scheme. In order to weaken its effect on the combined sample, the scaling is applied individually for both neighbours prior to the combination. Furthermore, at that stage all values are scaled to the target momentum. The combination is performed after the scaling to the target momentum.

Since the invariant masses do not rely on a normalisation, the individual values of such a sample can be combined immediately after the projection. The critical part of the procedure is the evaluation of the opening angle. As neither the sample of momenta nor the invariant masses are directly sampled from a simulated distribution, the efficiency of fitting associations can drop very much depending on the phase-space density of this artificial parameterisation. Taking the observation into account that these parameter change slower as the momentum is increased, the linear weighting model

$$M_{\text{inv,target}} = \frac{p_{0,\text{upper}} - p_{0,\text{target}}}{p_{0,\text{upper}} - p_{0,\text{lower}}} M_{\text{inv,lower}} + \frac{p_{0,\text{target}} - p_{0,\text{lower}}}{p_{0,\text{upper}} - p_{0,\text{lower}}} M_{\text{inv,upper}} \tag{9.6}$$

is applied. Using this weighting scheme a fitting rate within the first iteration was observed to be comparable to sampling from simulated histograms. However, for some values many iterations of momentum sampling are required. As a consequence, after a certain number of iterations both samples, the momenta and the invariant masses, are re-sampled.

The remaining components are the nuclear interaction distance, type multiplicity and the particle decomposition. As these attributes can be sampled independent from the kinematics the method for combining does not need to be the same as for the kinematics. Additionally, all those parts do not rely on the correlated sampling method but on the inverse transform method. Furthermore, as the number of nuclear interactions of any kind as well as the total amount of produced particles vary between the neighbouring samples, the total numbers recorded from the simulations are used. After the combination the normalisation is applied. For the weighting no tight constraining pattern exists as in the kinematics part. Using the observation how events evolve as the target momentum is increased, it is a reasonable assumption that the previously introduced weighting scheme for eigenvalues applies to these parameters component-wise, too.

9.2.4.2 Interpolation Performance of the First Ansatz

In order to test the performance of the interpolation a dedicated value for the initial momentum is chosen and simulated using the same setup as before to provide a sufficient sample size. Since the momentum is thereby known prior, no dynamic neighbour selection is needed. While Geant4 is used to simulate the final state particles, the ACTS Fatras distributions are obtained from a direct function call to produce final state particles of a certain interaction type. The individual distributions are combined afterwards, weighted by their probability.

The first points for evaluating the interpolation are chosen between 10 and 100 GeV initial momentum. For the first target momentum 50 GeV was chosen to visualise the interpolation over a long distance between the neighbouring points. A second point will be 25 GeV. The reason for the second point is the in Sec. 9.2.4 described behaviour of the development of kinematic shapes: a point closer to the lower momentum neighbour was chosen.

The first property to investigate is the multiplicity, shown in Fig. 9.13. The multi-
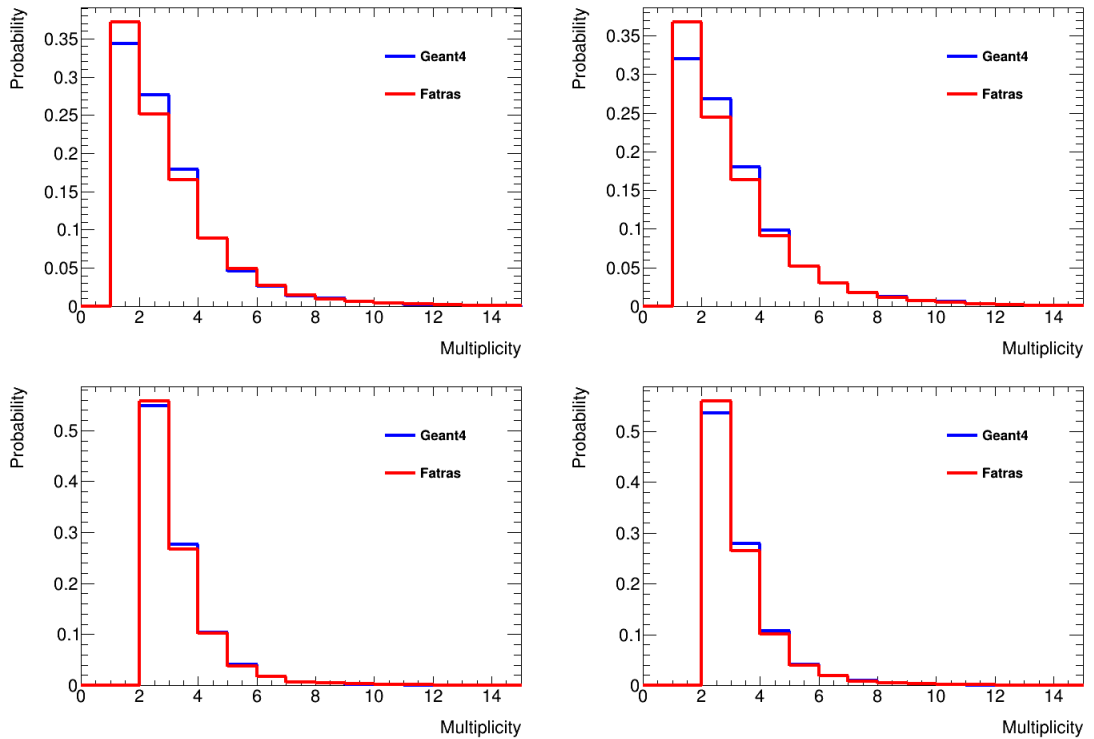
Figure 9.13: Multiplicity distribution for 50 GeV (left) and 25 GeV (right) initial momentum π^+ obtained from simulation and interpolation. The upper row shows the multiplicity distributions for hard interactions, the lower row for soft interactions.

plicity distributions show a stable behaviour along the different target momenta. The hard interactions show slight deviations in regions of lower multiplicity while it describes

higher multiplicities more accurate. The differences between the interpolation and simulation for soft interactions are smaller compared to the hard interactions. In total the multiplicity distributions are similarly shaped as the Geant4 simulation.

The combined kinematic distributions are shown in Fig. 9.14. Considering the sum
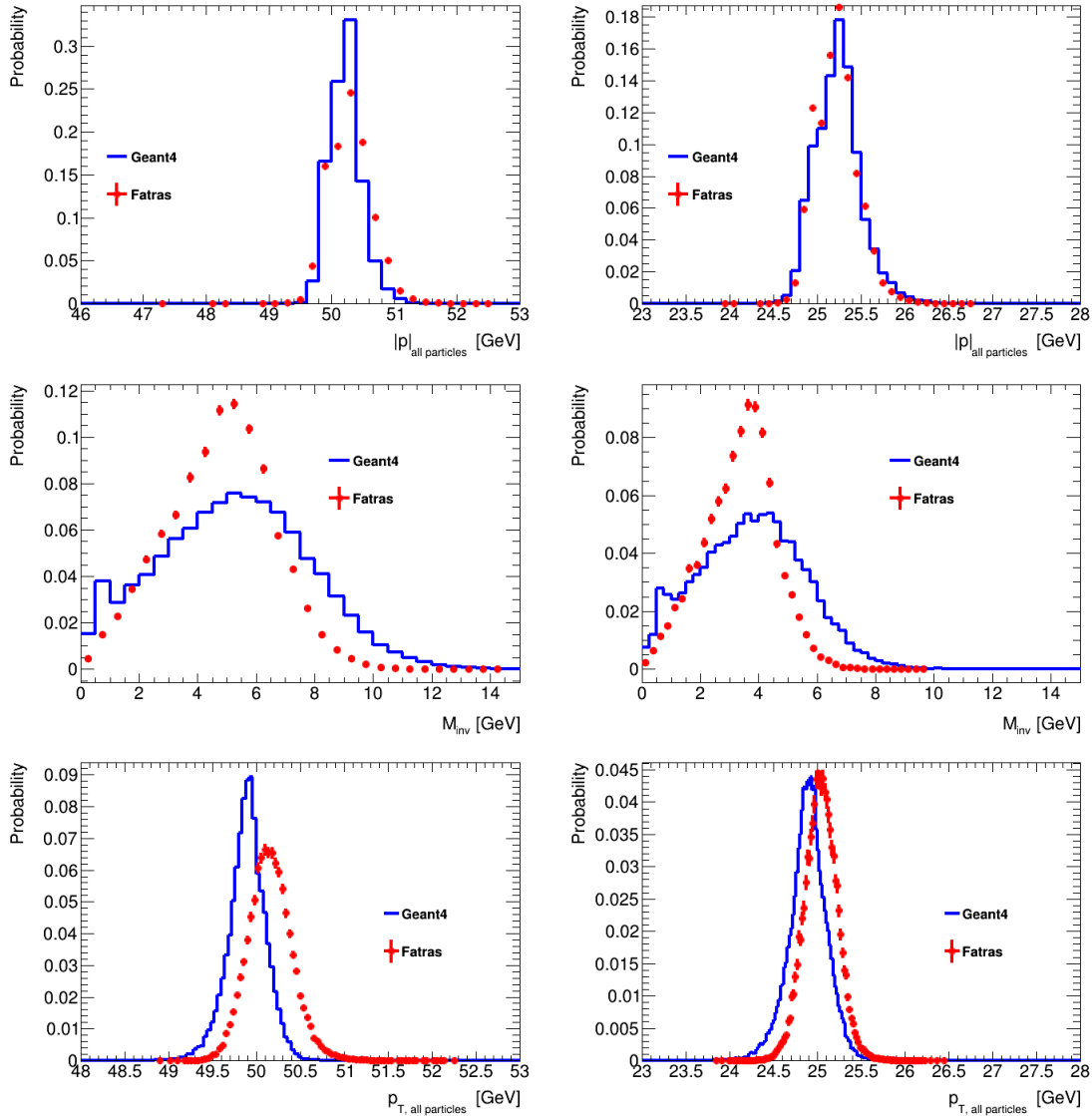
Figure 9.14: Kinematic distributions for 50 GeV (left) and 25 GeV (right) initial momentum π^+ obtained from simulation and interpolation. The top row shows the sum of absolute values of final state momenta, the middle row the invariant mass of the final state, the bottom row the transverse momentum of the final state.

of the absolute values of final state momenta the result of the interpolation is almost as precise as the initial sampling shown in Fig. 9.6. This shows that for both cases, 25

and 50 GeV initial momentum, the weighting scheme introduced in Sec. 9.2.4 provides a reliable method to combine the samples obtained from the neighbours. Furthermore, the spectrum of eigenvalues changes sufficient slow to allow a combined sample without the introduction of major artefacts.

The final states invariant mass on the other hand shows obvious deviations between the interpolation and the simulation. The general shape is similar to the simulation but for both target momenta too narrow. This leads on the other side to a too high peak near 5 GeV (left) and 4 GeV (right). This observable is the most sensitive upon the applied weighting scheme. Since the fitting of the sampled momenta and the invariant masses needs to fulfil Eq. (9.5), the achieved rate of finding matches was found to be comparable to the direct sampling from histograms at a working point. Remarkable is the stability of the sum of momenta considering the mentioned constraint by the invariant mass, though this affects the invariant mass distribution on the other hand.

While the invariant masses are too narrow and produce smaller peak values, the transverse momenta tend to become too large. The width of the transverse momenta is very similar to the simulated distribution for both target momenta. Although these distributions encapsulate an error propagation from the invariant mass, this observable hides the prior deviations mostly.

The last distribution of interest is the distribution of particle types. The final state particle types are shown in Fig. 9.15. Both distributions show a similar structure as in
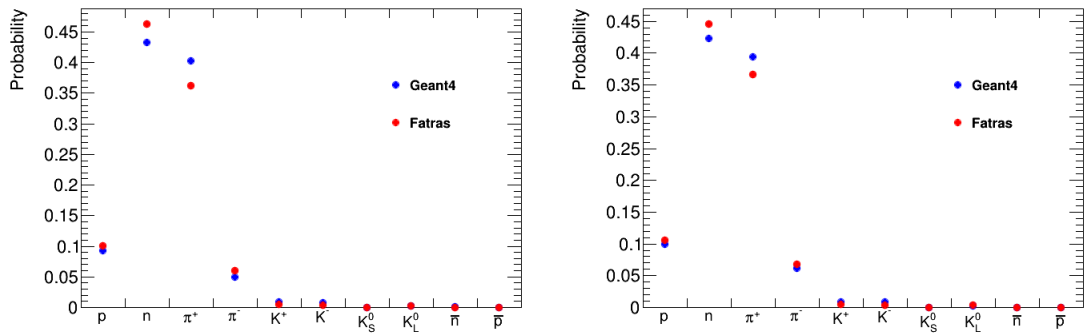
Figure 9.15: Particle type distribution for 50 GeV (left) and 25 GeV (right) initial momentum π^+ obtained from simulation and interpolation.

Fig. 9.9 and 9.12. Most of the different particle types are reproduced very well except for the π^+ and n probability. Though, this effect is already observed for the individual distributions and rather enhanced due to the combination. However, the combination method does not introduce new artefacts.

9.2.4.3 Second Interpolation Ansatz

The previously presented method led to a second ansatz to perform the interpolation based on the observed issues. It seems reasonable that the interpolation is possible by

just applying a fitting weighting scheme in order to obtain a combination. However, it is also visible that the result strongly depends on the scheme itself. Another issue was the low rate of finding fitting momenta and invariant masses such that multiple re-samplings were required. This results in the creation of deviations as shown in Fig. 9.14 and an increased run-time. Since the acceptance rate was significantly higher in the parameterisation step in Sec. 9.2.2, it is reasonable to use the full workflow of random sampling and transformation from a single neighbour instead of combining the results of both. The obtained result is then scaled to the target momentum afterwards. This allows the removal of constructing distributions that may look like the ones from the target momentum. Keeping the neighbour selection as before, a selection of the neighbour used for the sample is required. This is performed randomly, using the weighting scheme from Eq. (9.6) as neighbour selector.

This ansatz simplifies the considerations from Sec. 9.2.4 but needs additional treatment, too. In the first ansatz it was shown that different distributions require different weighting schemes to provide sufficient high quality results. Moreover, the target distributions are very sensitive upon the chosen scheme. Within this second ansatz it will be reduced to a single weighting scheme that requires to cover all aspects. In order to cover this up the similarity aspect from Sec. 9.2.4 can be taken into account. As it was initially assumed that the parametrised neighbours should look similar, this needs further investigation using the presented simplifications. Within this context the performance will be investigated in the following for different spacings between the parameterisations.

9.2.4.4 Interpolation Performance of the Second Ansatz

The first interpolation ansatz encountered several issues with the simulation of kinematic properties. Therefore, this section is focused on investigating the effect of the second ansatz on these observables. Firstly, the kinematic interpolation will be considered. The momenta and invariant mass distributions using the same neighbours as in the first ansatz are shown in Fig. 9.16. Both distributions show a superposition of two different
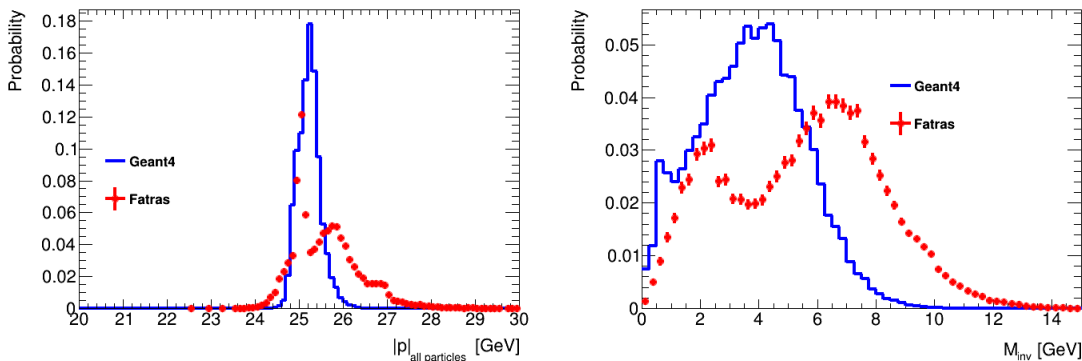

Figure 9.16: Sum of the absolute final state momenta (left) and the invariant mass of the final state (right) for a 25 GeV pi^+. These distributions are based on the interpolation using the parameterisations at 10 and 100 GeV.

distributions, leading to two peaks. The origin lies in the used neighbours. Additionally, a shift is visible. In summary this ansatz does not reproduce the target distributions at all but need further investigation.

It is assumed that both neighbouring distributions look shape-wise similar to each other. Within this ansatz the target distributions are obtained only by scaling the sampled values. Comparing Fig. 9.6 and 9.7 with Fig. 9.10 shows that this is roughly the case. An additional scaling of the parameters by a significant factor, in case of 25 GeV it is 2.5 and 0.25 respectively, any deviation between the parameterisation and the Geant4 simulation gets enhanced. In order to improve the reproduction of the target momentum, the spacing between the neighbouring distributions needs to be adapted to fulfil the similarity condition. Additionally, if the distributions become more similar then the impact of the applied weighting scheme upon the target distributions gets reduced. In Fig. 9.17 the effect of the spacing upon the target distribution is shown. The distance between the neighbours as well as their distance to the target momentum gets reduced from the top to bottom row while the weighting scheme is applied as before. For both, the sum of momenta and the final state invariant mass distributions, become closer to the target distribution. The double peak merges to a single one and the shifts are more and more suppressed. Therewith, the assumption of the similarity is supported and the interpolation accuracy can be further enhanced by reducing the spacing. As this construction allows to invoke additional parameterisations afterwards without the need of re-parametrizing earlier samples, it can be adapted to different target momenta (ranges) in order to achieve a sufficient accuracy.

Using this interpolation for a target momentum of 25 GeV with the parameterisations at 16 and 32 GeV, the corresponding multiplicity distributions and particle compositions of the final states are shown in Fig. 9.18. Compared to the Geant4 results, the multiplicity distributions from the interpolation are in very good agreement. Concerning the produced final state particle types the deviations from the parameterisations are still present without any new artefacts.

In total, the second ansatz provides a higher rate of finding fitting momenta and invariant masses. As a single weighting scheme is applied, the level of necessary fine-tuning is reduced compared to the first ansatz. With this simplification and the possibility and to extend an existing parameterisation afterwards using additional working points and parameters, the concept provides the required flexibility to be applicable in HEP simulations in general.

9.2.5 Conclusion

A new method was introduced for the parameterisation of nuclear interactions. This method is based on sampling random numbers from common normal distributions specified by the covariance matrix of transformed histograms. Using this method allows the evaluation of properties based on the input histograms without the requirement of fitting these distributions. Thus, the final state of a nuclear interaction can be computed in a stable way, allowing the exchange and addition of histograms without modifying an existing parameterisation. Since the evaluation of final state properties is performed
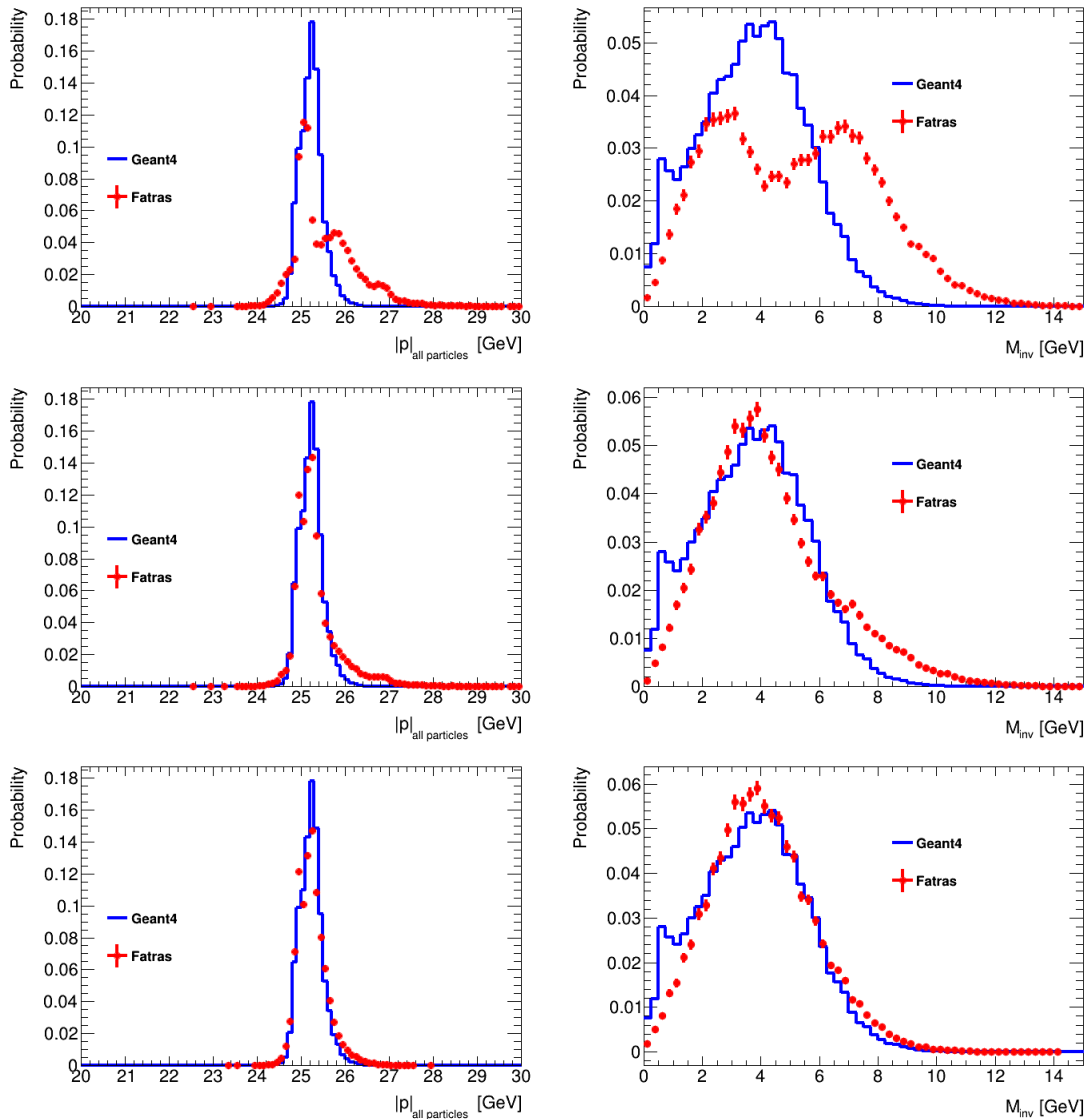
Figure 9.17: Sum of the absolute final state momenta (left) and the invariant mass of the final state (right) for a 25 GeV pi^+. These distributions are based on the interpolation using the parameterisations at 10 and 64 GeV (top row), 10 and 32 GeV (middle row) and 16 and 32 GeV (bottom row).

directly on the histograms, a high level of insight is granted which allows improving and extending the method and the obtained results. Especially for low momentum particles and final state particle type compositions, further investigations could improve the parameterisation process. Additionally, a larger sample quantity would allow to include higher multiplicities which rarely occur and therefore were neglected within this study.
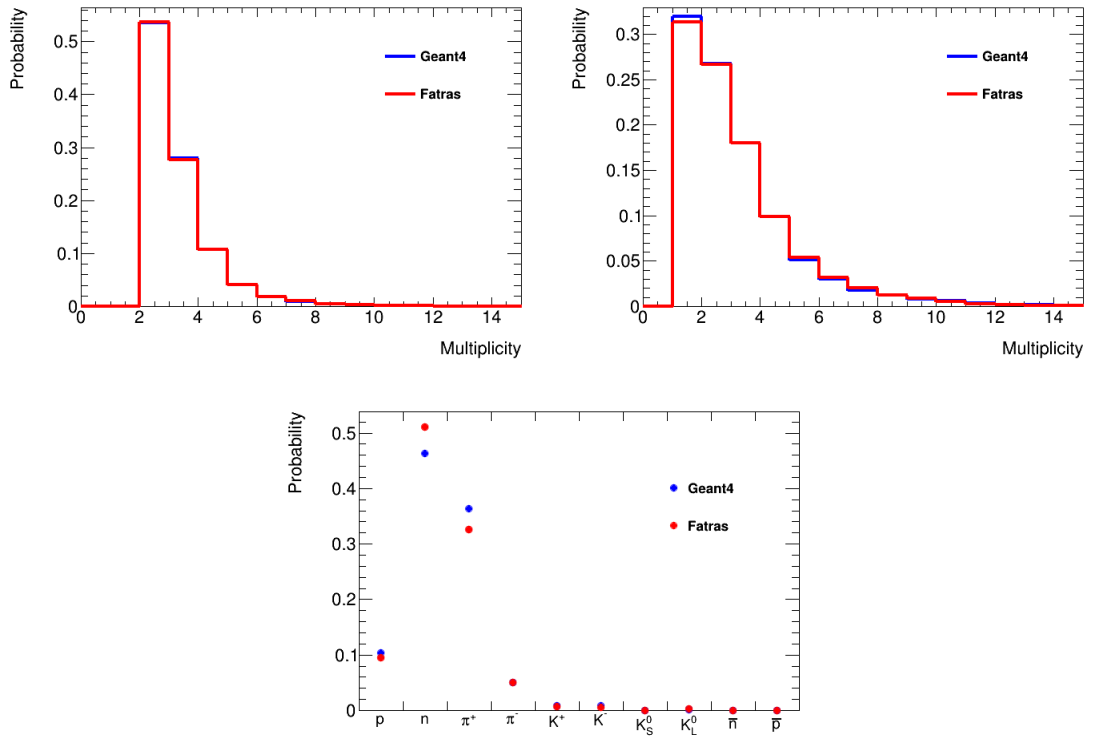
Figure 9.18: Multiplicity distributions (top row) for soft (left) and hard (right) nuclear interactions using the interpolation method from Sec. 9.2.4.3 with the parameterisations at 16 and 32 GeV π^+ for 25 GeV target momentum of π^+. The bottom plot shows the corresponding final state particles.

The presented interpolation methods are based on a weighted combination of neighbouring parameterisations. It was observed that the spacing between the parameterisations and the weighting are the only dependencies that steer the interpolation quality. Furthermore the importance of the weighting gets suppressed by smaller spacings between the parameterisations. As a consequence of this observation, the amount of parameterisations and the therewith related memory consumption is in direct trade-off with the impact on the applied weights. For the interpolation, two different ansatzes were shown based on the weighted combination of distributions. While the first ansatz allowed for a larger set of weightings and therefore a higher granularity, the second ansatz requires a single scheme. Within this study the weights were chosen heuristically and are meant as a starting point for further investigations. The same accounts for choosing only two neighbouring parameterisations. The design of an appropriate weighting scheme might be an application scenario for a neural network.

Since the number of parameterisations can be increased while, compared to a fit based approach, the former produced ones can remain untouched. This allows to improve or adapt the accuracy for the required performance. In summary, the method provides a

reliable and controllable formulation for parametrizing the nuclear interaction in particle detectors. The parameterisation and interpolation method itself can be applied due to its generality on other problems with similar structure and complexity.

10 Conclusion

The detectors utilised in HEP measure the properties of (quasi-)stable particles. A reliable reconstruction of their trajectories is crucial for certain observables and the understanding of the underlying event structure. As a reconstruction algorithm has a combinatorial complexity, an increasing centre-of-mass energy, bunch crossing rate and pile-up will require more and more computing power. Using the example of the ATLAS detector, a prediction of the expected, required CPU performance and disc space consumption during the HL-LHC era were shown (see Sec. 3.3.4). In order to estimate the seriousness of the extrapolation into the future, the fast track reconstruction was introduced within this thesis (see Chapter 6). This modification of the existing ATLAS track reconstruction workflow and the proper adaption of cuts led to a speed-up of approximately a factor six to eight for the expected HL-LHC pile-up while only a minor loss in the physics performance was observed. The aggressive manipulation showed that the CPU requirements for tracking are less constraining than initially predicted. However, this study also implies that further R&D is required to match the expected computing performance without losses in the physics performance.

R&D can be performed in different ways, e.g. by exploiting a certain hardware architecture or by optimising the code performance. Those fields are a part of the ACTS project. This project is intended to become a detector-independent collection of tools for track reconstruction and simulation. As this project is flexible R&D platform, the work presented within this thesis is performed in this context.

In order to optimise software for a certain problem, it has to be understood. It was shown that the entire tracking workflow can be derived from Bayes' theorem with a few assumptions and approximations (see Chapter 4). The consequences as well as the limitations of the assumptions were shown. Compared to the common approach of treating the individual components of track reconstruction independently, this theoretical consideration of the underlying problem shows the interconnection between all the parts. The statistical treatment of tracking points out the degrees of freedom for modelling and performance gains.

While the modelling of measurements and the prior lead to the (combinatorial) Kalman filter formalism, the parametrisation of the particle and the extrapolation of the parameters are neither unique nor fixed. It was shown that two types of parametrisations, one bound to surfaces and an unbound, are necessary to describe the particle during the extrapolation (see Chapter 7). The parametrisation was extended by treating the time as additional parameter. Furthermore, it was shown that the extrapolation can be split into continuous and discrete effects affecting the trajectory. With methods, the ActionList and the RKN4, that are independent of the underlying problem, both parts can be decoupled. The design of the Auctioneer was introduced within this the-

sis as an environment-dependent selector of continuous effects that are solved by the RKN4. While the RKN4 is commonly used for these kinds of problems, the theoretical consideration shows that it is not mandatory. By comparing the accuracy of the extrapolation under the applied approximations with a detailed simulation using Geant4, the limitations of the model were pointed out.

Since ACTS is intended to be applicable for any detector layout, a detector layout from the sPhenix experiment was considered (see Chapter 8). Within this context a generalised expression for the extrapolation was found that allows to switch between the parametrisations. By considering a special arrangement of measurements in the detector, a generalisation of the Kalman filter formalism was found. This formalism does not rely on the relation between measurements and surfaces but treats this classical case as a special case. By comparing the found formalism with two different classical tracking designs, it was found that the extended Kalman filter formalism behaves less aggressive but may provide more accurate results than the classical approaches. Beside the consideration of the problem, this solution shows that further R&D can be performed close to the already found formalism.

As the fast track reconstruction would allow to reduce the CPU demands of tracking drastically, the fraction spent in simulation becomes larger. While some analyses require detailed, computational expensive simulations, it is sufficient for others to utilise approximated results that can be calculated in a fraction of the time needed for full simulation. Denoted by the term fast simulation, it was shown how the ACTS track reconstruction formalism can be modified to perform such an approximated simulation by covering a minimal but expandable set of physical effects (see Chapter 9). While most of the effects can be transcribed from other sources, the derivation of a flexible parametrisation describing the nuclear interaction was presented in detail. Since the fast simulation relies on algorithms from track reconstruction, any performance gain in these algorithms is beneficial for the reconstruction and the simulation.

In summary, the upcoming challenges for track reconstruction and simulation can be encountered in many different ways. While code optimisation and hardware exploitation are common performance gains, this thesis introduces a theoretical approach to the field by generalising the underlying problems and deriving their interplay as future chances for optimisations beyond the current formalism.

Appendices

A Theory of Model Based Track Reconstruction

$$\Sigma_\lambda' \left(\Sigma_\lambda^{-1}\mu_\lambda + (H_A^T\Sigma_{\text{det}}^{-1}H_A)H_A^Tm\right) \overset{!}{=} \mu_\lambda + \Sigma_\lambda H_A^T \left(H_A\Sigma_\lambda H_A^T + \Sigma_{\text{det}}\right)^{-1}(m - H_A\mu_\lambda) \quad \text{(A.1)}$$

Proof:

$$\Sigma_\lambda' \left(\Sigma_\lambda^{-1}\mu_\lambda + (H_A^T\Sigma_{\text{det}}^{-1}H_A)H_A^Tm\right) \overset{!}{=} \mu_\lambda + \Sigma_\lambda H_A^T \left(H_A\Sigma_\lambda H_A^T + \Sigma_{\text{det}}\right)^{-1}(m - H_A\mu_\lambda)$$

$$\Leftrightarrow \Sigma_\lambda^{-1}\mu_\lambda + H_A^T\Sigma_{\text{det}}^{-1}m = \Sigma_\lambda^{-1}\mu_\lambda + H_A^T\Sigma_{\text{det}}^{-1}H_A\mu_\lambda + H_A^T\left(H_A\Sigma_\lambda H_A^T + \Sigma_{\text{det}}\right)^{-1}(m - H_A\mu_\lambda)$$

$$+ H_A^T\Sigma_{\text{det}}^{-1}H_A\Sigma_\lambda H_A^T\left(H_A\Sigma_\lambda H_A^T + \Sigma_{\text{det}}\right)^{-1}(m - H_A\mu_\lambda)$$

$$\Leftrightarrow H_A^T\Sigma_{\text{det}}^{-1}(m - H_A\mu_\lambda) = H_A^T\left(\left(H_A\Sigma_\lambda H_A^T + \Sigma_{\text{det}}\right)^{-1}(m - H_A\mu_\lambda)\right.$$

$$+ \left.\Sigma_{\text{det}}^{-1}H_A\Sigma_\lambda H_A^T\left(H_A\Sigma_\lambda H_A^T + \Sigma_{\text{det}}\right)^{-1}(m - H_A\mu_\lambda)\right)$$

$$\Leftrightarrow m - H_A\mu_\lambda = H_A\Sigma_\lambda H_A^T\left(H_A\Sigma_\lambda H_A^T + \Sigma_{\text{det}}\right)^{-1}(m - H_A\mu_\lambda)$$

$$+ \Sigma_{\text{det}}\left(H_A\Sigma_\lambda H_A^T + \Sigma_{\text{det}}\right)^{-1}(m - H_A\mu_\lambda)$$

$$\Leftrightarrow m - H_A\mu_\lambda = (H_A\Sigma_\lambda H_A^T + \Sigma_{\text{det}})\left(H_A\Sigma_\lambda H_A^T + \Sigma_{\text{det}}\right)^{-1}(m - H_A\mu_\lambda))$$

In the second line the definition of Σ_λ' from Eq. (4.32) was applied. In the third line, the terms are rearranged and H_A^T is dropped from the equation. By multiplying the equation with Σ_{det}^{-1}, the fourth line is obtained. Another rearranging shows in the fifth line the equality.

$$(\Sigma_\lambda^{-1} + H_A^T\Sigma_{\text{det}}^{-1}H_A)^{-1} \overset{!}{=} (1 - \Sigma_\lambda H_A^T(H_A\Sigma_\lambda H_A^T + \Sigma_{\text{det}})^{-1}H_A)\Sigma_\lambda \quad \text{(A.2)}$$

Proof:

$$(\Sigma_\lambda^{-1} + H_A^T\Sigma_{\text{det}}^{-1}H_A)^{-1} \overset{!}{=} (1 - \Sigma_\lambda H_A^T(H_A\Sigma_\lambda H_A^T + \Sigma_{\text{det}})^{-1}H_A)\Sigma_\lambda$$

$$\Leftrightarrow 1 = (1 - \Sigma_\lambda H_A^T(H_A\Sigma_\lambda H_A^T + \Sigma_{\text{det}})^{-1}H_A) \cdot (1 + \Sigma_\lambda H_A^T\Sigma_{\text{det}}^{-1}H_A)$$

$$\Leftrightarrow \Sigma_\lambda H_A^T(H_A\Sigma_\lambda H_A^T + \Sigma_{\text{det}})^{-1}H_A(1 + \Sigma_\lambda H_A^T\Sigma_{\text{det}}^{-1}H_A) = \Sigma_\lambda H_A^T\Sigma_{\text{det}}^{-1}H_A$$

$$\Leftrightarrow (H_A\Sigma_\lambda H_A^T + \Sigma_{\text{det}})^{-1}H_A(1 + \Sigma_\lambda H_A^T\Sigma_{\text{det}}^{-1}H_A) = \Sigma_{\text{det}}^{-1}H_A$$

$$\Leftrightarrow H_A(1 + \Sigma_\lambda H_A^T\Sigma_{\text{det}}^{-1}H_A) = H_A\Sigma_\lambda H_A^T\Sigma_{\text{det}}^{-1}H_A + H_A$$

The second line is obtained by multiplying the equation with $(\Sigma_\lambda^{-1} + H_A^T \Sigma_{\text{det}}^{-1} H_A)$. The third line is obtained by rearranging the terms and the fourth line by dropping Σ_{T_A}. Finally, by multiplying the fourth line with $(H_A \Sigma_\lambda H_A^T + \Sigma_{\text{det}})$ shows the equality in the fifth line.

B A Common Tracking Software

B.1 Space Point Formation

A space point (SP) is a point in global coordinates with three spatial coordinates $(x\ y\ z)$ and if applicable, the time t. SPs are built from the pixel and strip clusters. While the former contain local $x - y$-information, the strip detector measures just one dimensional spatial clusters. For pixel clusters, r is obtained from the inverse transformation from the surface to global coordinates (see Sec. 5.2.2). The time does not require an additional transformation. The situation is different for a strip detector.

A single strip measures precisely in one dimension but due to its length the other direction does not allow to provide a reasonable global position. For that purpose, strip detectors with the intention to form SPs are built in two layers with a certain angle between the layers. This angle allows to obtain data in a different direction and defines together with the distance between the layers the resolution. The general problem of SP formation from strip measurements is a geometrical problem. As the distribution of the data over two layers require additional computation, the complexity depends on the distance and the angle.

Before the SP formation is expressed, the cluster needs a few more explanation. A strip cluster consists of neighbouring strips that produced a signal. Due to the dimensions of a strip, it can be assumed that for a cluster the relation between the cluster width w and its height h is

$$w \ll h$$

with the convention that additional strips contributing to the cluster size expand the width. The centre in the width direction can be obtained from a weighted mean of all strips that are part of the cluster. Since the SP formation is intended to give a first hint of a potential track, the statistical correctness can be approximated and uncertainties neglected. In case of a shared cluster, i.e. a cluster that was produced by multiple particles, additional processing steps are required in order to refine the cluster description.

By considering two strip layers, denoted as 1 and 2 with one cluster on each layer, the first question that has to be resolved is whether both clusters can be produced by a single track. Under the assumption that the particle comes from the beam line, the distance of the cluster centre vectors c_1 and c_2 have to be sufficiently close together. Additionally, the azimuthal angles ϕ_1 and ϕ_2 and the polar angles θ_1 and θ_2 are calculated from the line connecting the position of the origin $(0\ 0\ 0)^T$ with the centres. This constraint allows to filter combinations based on the angular deviation between the centres. With additional time measurements, the constraint can become tighter.

The result of these tests is a set of cluster pair candidates. In a second step, the SP formation for each pair is performed with three different setups. For each setup, the vectors r and q for the first and second cluster respectively are required. These vectors are defined along each cluster height and point from the bottom β to the top τ:

$$r = \tau_1 - \beta_1 \qquad q = \tau_2 - \beta_2.$$

As first setup the general combination is considered. The final result is a point on the inner strip layer. With $|c_1| < |c_2|$ this point x is located along r. The location of x can be parametrised as

$$2x = (1 + m)\tau_1 + (1 - m)\beta_1 \qquad \text{(B.1)}$$

with $m \in [-1, 1]$. The limits of m imply that x in on the strip module. As the particle also produced a cluster on the second strip and the assumption that both strip modules are close to each other, a straight line from the origin can be constructed and thus, the point y with

$$y = k \cdot x$$

with $k \in \mathbb{R}$ can be constructed on the second layer. Again, y has be located on the line q, analogue to x and r. The assumption that y is a point on q can be expressed as

$$y \cdot (\tau_2 \times \beta_2) = kx \cdot (\tau_2 \times \beta_2) = 0.$$

The right hand side is the result of the zero volume of the parallelepiped formed by three vectors on a line. By replacing x with Eq. (B.1), an expression for m can be found that only depends on the end points of the strips. Finally, the SP x can be obtained. An equivalent formalism can be found for a parametrised point y.

Since the consideration was built on a geometrical combination of two clusters, a neglected statistical uncertainty, a straight line trajectory between both clusters and a vertex position at the origin of the coordinate system, it is possible that a SP formation fails under the above constraints. For that purpose, tolerances may be used to recover from this scenario. The tolerances allow to stretch r and q or to obtain $|m| > 1$. Also different vertex positions can used. The explicit tolerance depend on the tolerances depend on the expected particles and the detector architecture and hence, remain as configurable parameters in ACTS.

The last setup considers vertices that do not originate from particle accelerator. This configurations use case allows to form SPs from cosmic particles. Hence, the line construction from a given vertex position is not applicable in this scenario. In order to obtain a SP, the parametrisation is modified as

$$x = \tau_1 + \lambda_1 r \quad y = \tau_2 + \lambda_2 q$$

with $\lambda_{1/2} \in \mathbb{R}$ The SP is then obtained from solving for the shortest distance $|x - y|$ between the two skew lines.

C Track parameter propagation

Variable	Meaning
m	Incident particles mass
v	Incident particles velocity
r_e	Classical electron radius
N_A	Avogadro's number
K	$4\pi N_A r_e^2 m_e c^2$
Z	Atomic number of absorber
A	Atomic mass of absorber
ρ	Density
m_e	Electron mass
β	v/c
γ	$1/\sqrt{1-\beta^2}$
T_{max}	$\frac{2m_e\beta^2\gamma^2}{1+2\gamma m_e/m+(m_e/m)^2}$
I	Mean excitation energy
δ	Density effect correction to ionisation energy loss

Table C.1: Overview of parameters required by the Bethe-Bloch equation, introduced in Eq. (7.33). The explanation is extracted from Reference [17]

C.1 Comparison between Covariance Transport Formalism and Ridders Algorithm
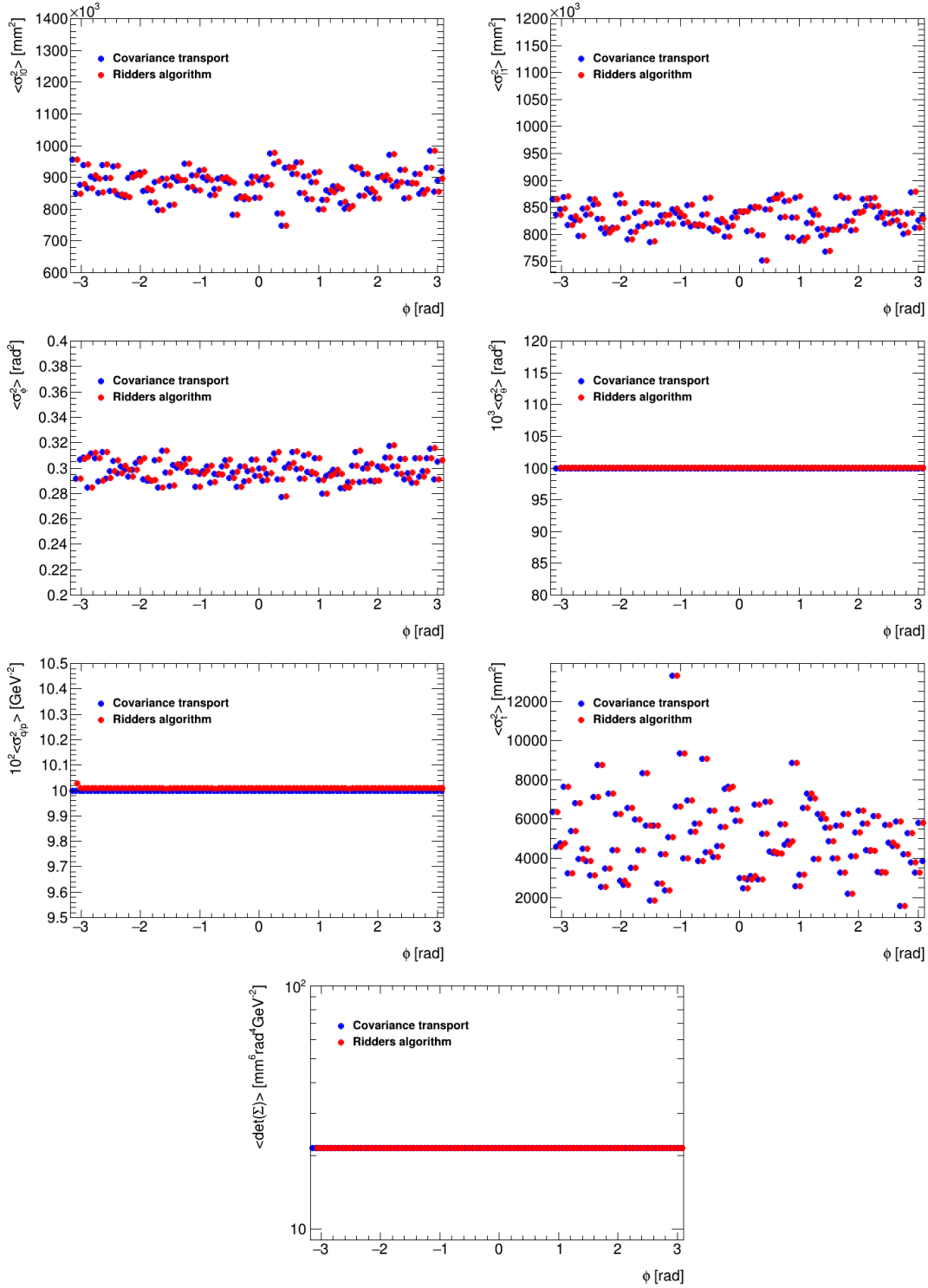
Figure C.1: Comparison of the diagonal terms of the covariance matrix and the determinant for an extrapolation from curvilinear to curvilinear parameters in vacuum between the Ridders algorithm and the covariance transport as function of the initial azimuthal angle. The bin centres are shifted for visibility.
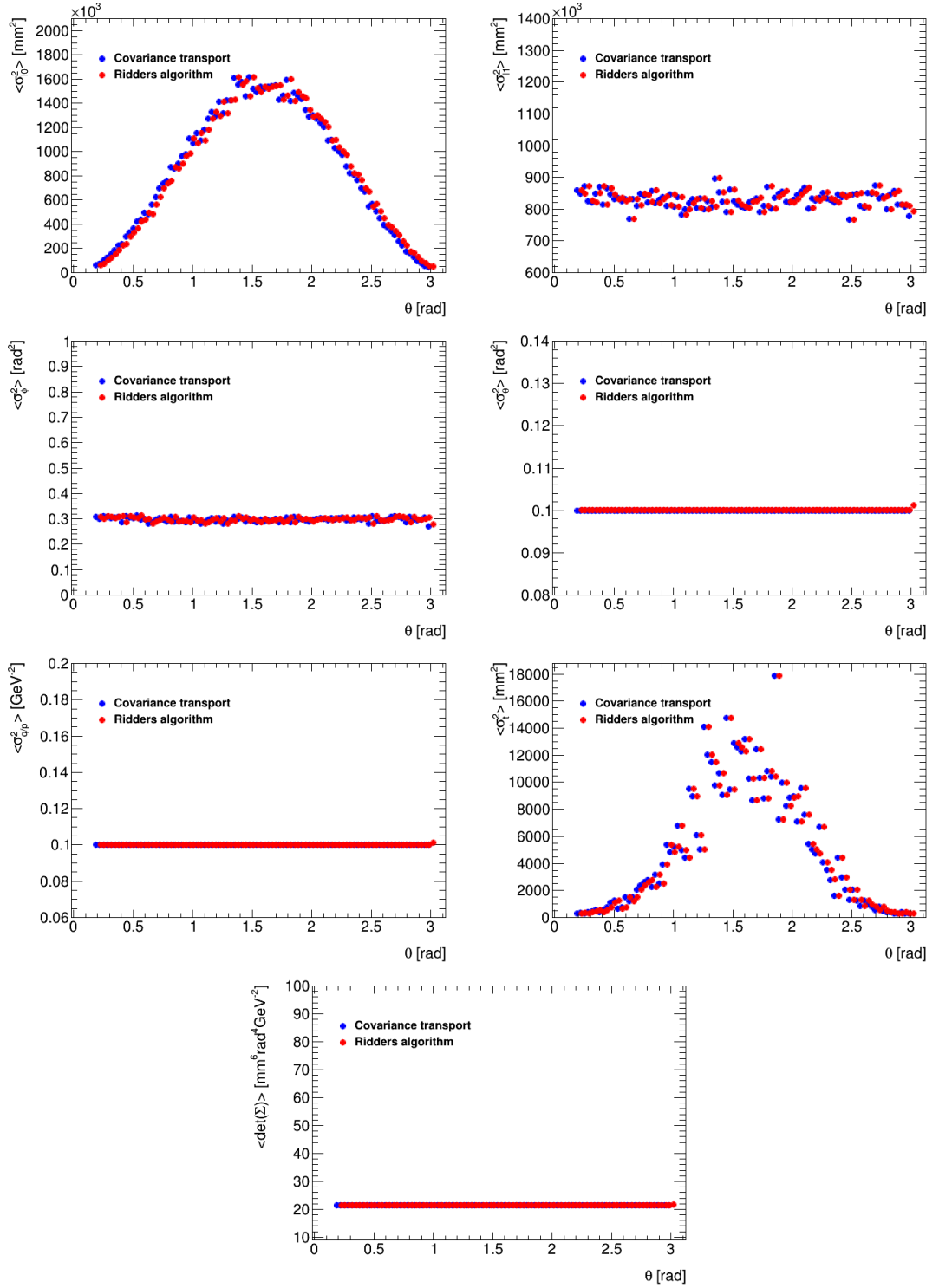
Figure C.2: Comparison of the diagonal terms of the covariance matrix and the determinant for an extrapolation from curvilinear to curvilinear parameters in vacuum between the Ridders algorithm and the covariance transport as function of the initial polar angle. The bin centres are shifted for visibility.
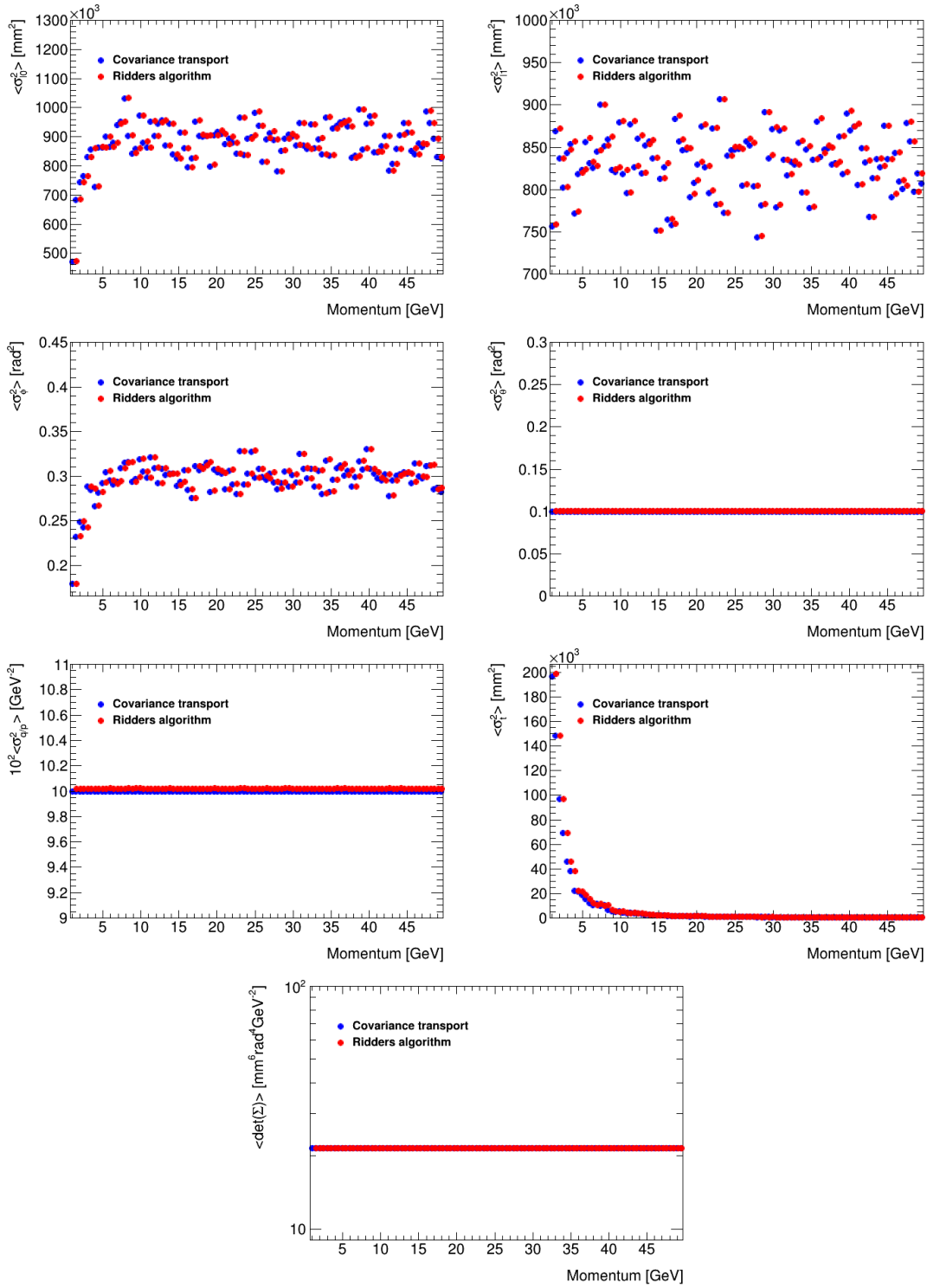
Figure C.3: Comparison of the diagonal terms of the covariance matrix and the determinant for an extrapolation from curvilinear to curvilinear parameters in vacuum between the Ridders algorithm and the covariance transport as function of the initial momentum. The bin centres are shifted for visibility.
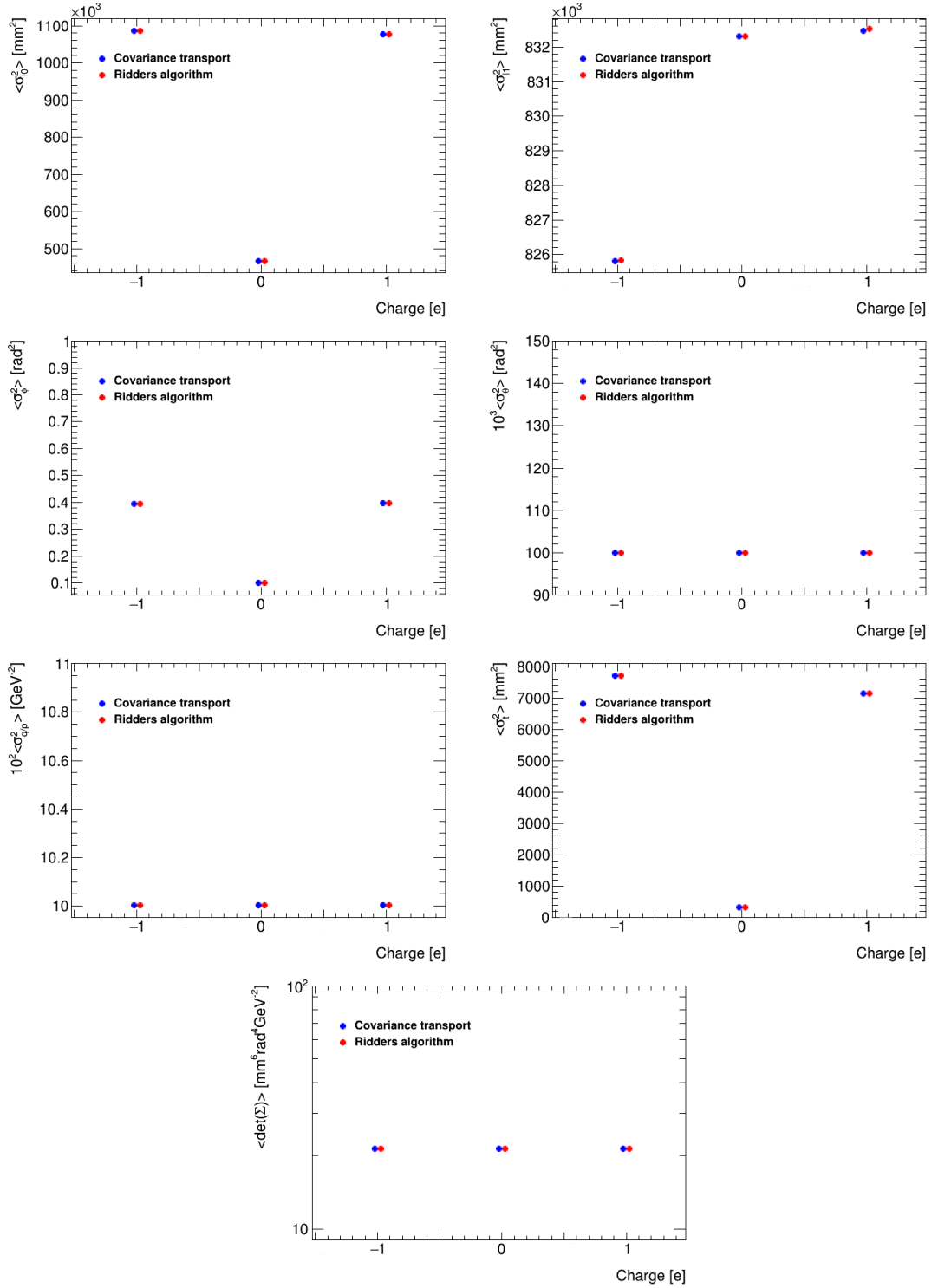
**Figure C.4:** Comparison of the diagonal terms of the covariance matrix and the determinant for an extrapolation from curvilinear to curvilinear parameters in vacuum between the Ridders algorithm and the covariance transport as function of the charge. The bin centres are shifted for visibility.
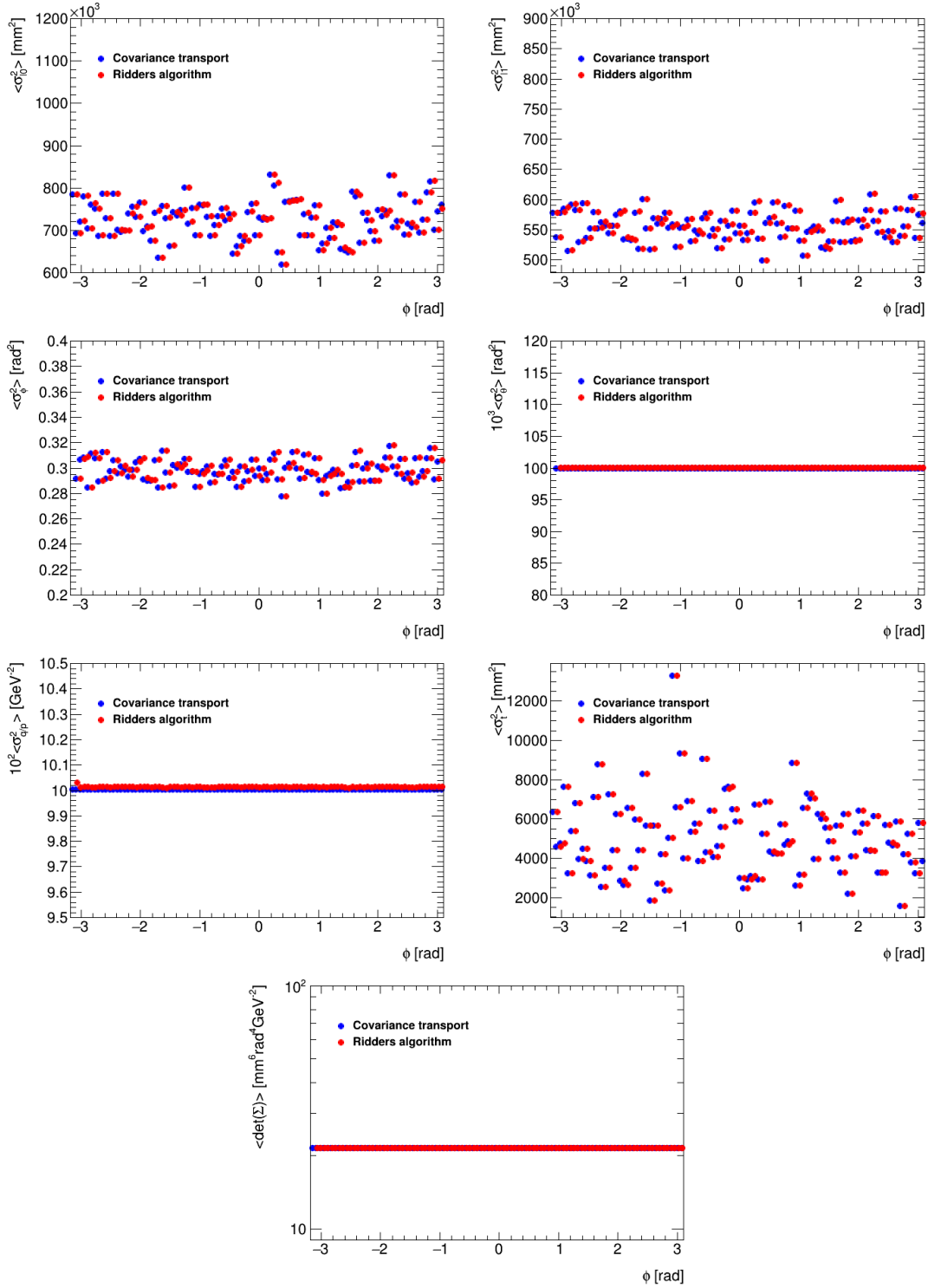
Figure C.5: Comparison of the diagonal terms of the covariance matrix and the determinant for an extrapolation from curvilinear to curvilinear parameters in matter between the Ridders algorithm and the covariance transport as function of the initial azimuthal angle. The bin centres are shifted for visibility.
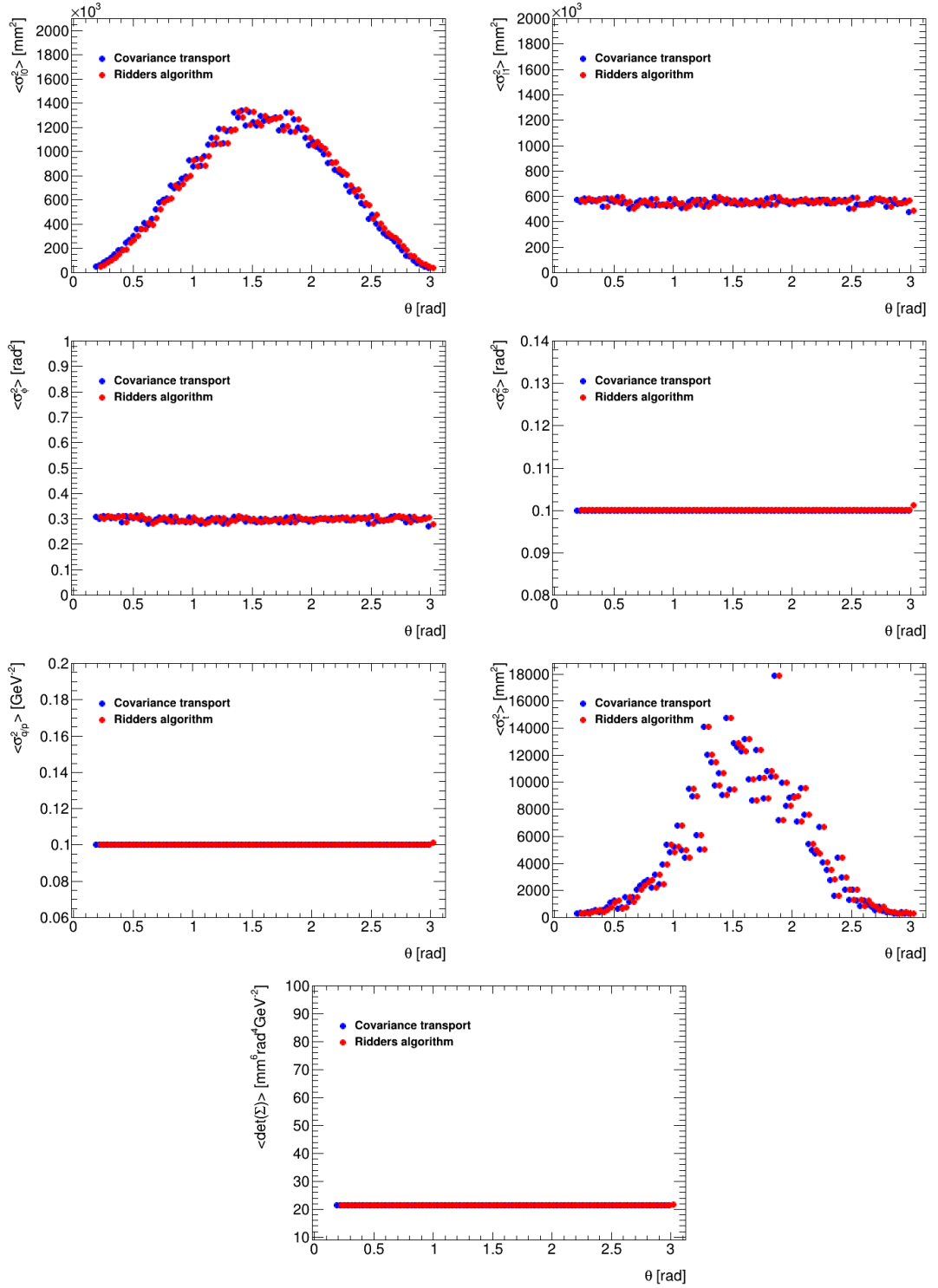
Figure C.6: Comparison of the diagonal terms of the covariance matrix and the determinant for an extrapolation from curvilinear to curvilinear parameters in matter between the Ridders algorithm and the covariance transport as function of the initial polar angle. The bin centres are shifted for visibility.

Figure C.7: Comparison of the diagonal terms of the covariance matrix and the determinant for an extrapolation from curvilinear to curvilinear parameters in matter between the Ridders algorithm and the covariance transport as function of the initial momentum. The bin centres are shifted for visibility.
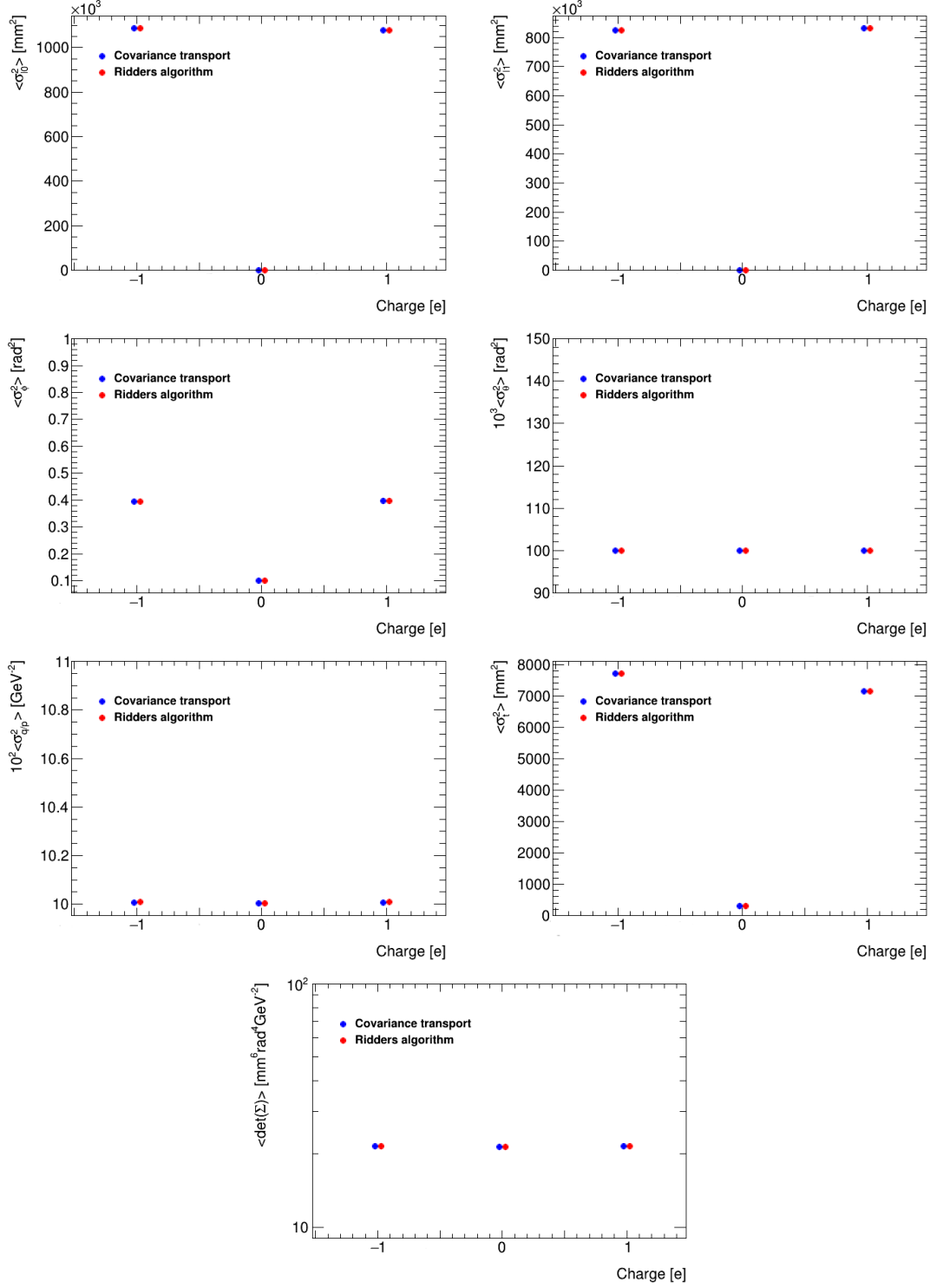
Figure C.8: Comparison of the diagonal terms of the covariance matrix and the determinant for an extrapolation from curvilinear to curvilinear parameters in matter between the Ridders algorithm and the covariance transport as function of the charge. The bin centres are shifted for visibility.

D Track reconstruction with displaced measurements

D.1 Covariance Transport
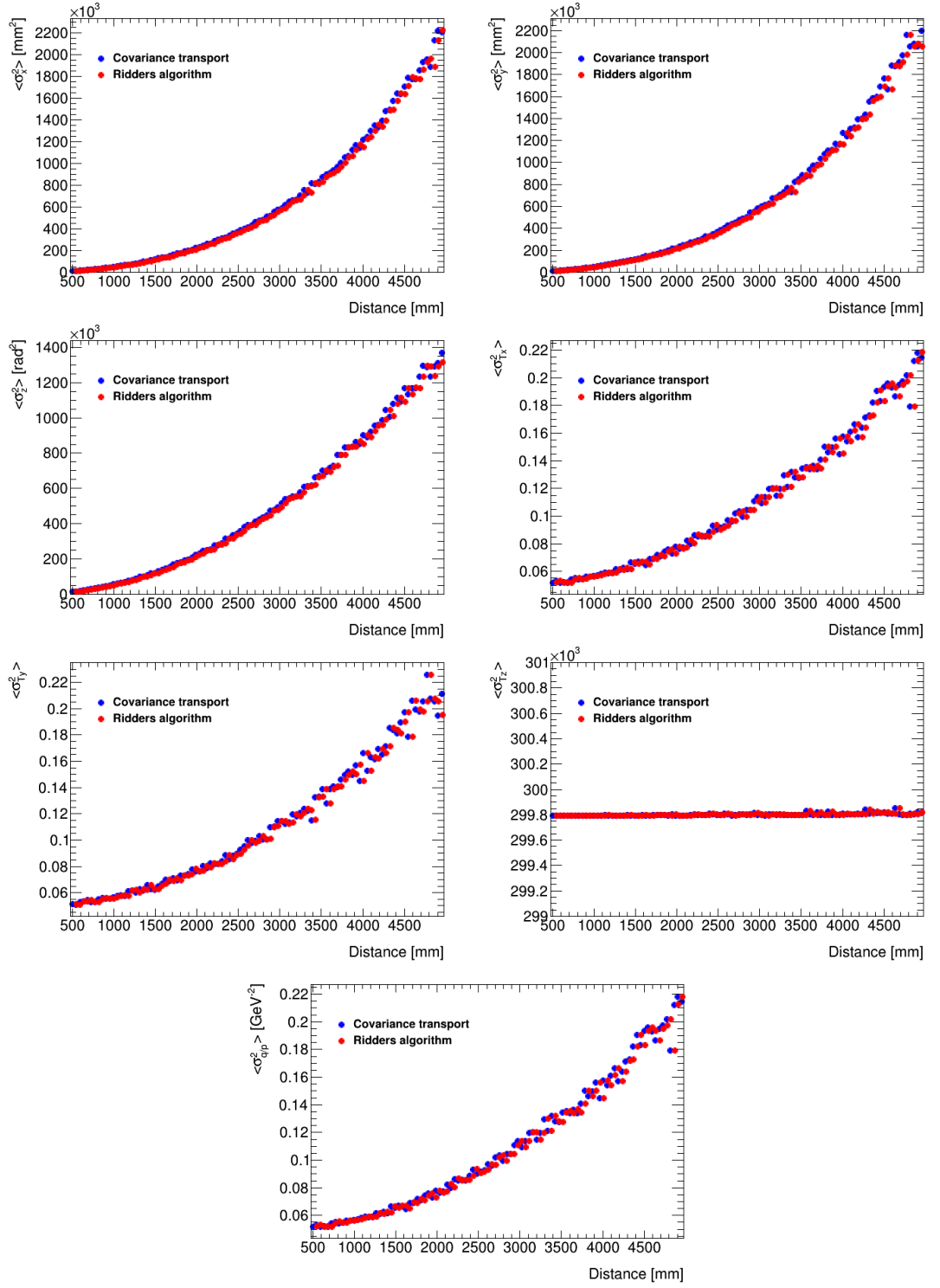
Figure D.1: Comparison of the diagonal terms of the covariance matrix from curvilinear to free parameters between the Ridders algorithm and the covariance transport as function of the distance. The bin centres are shifted for visibility.
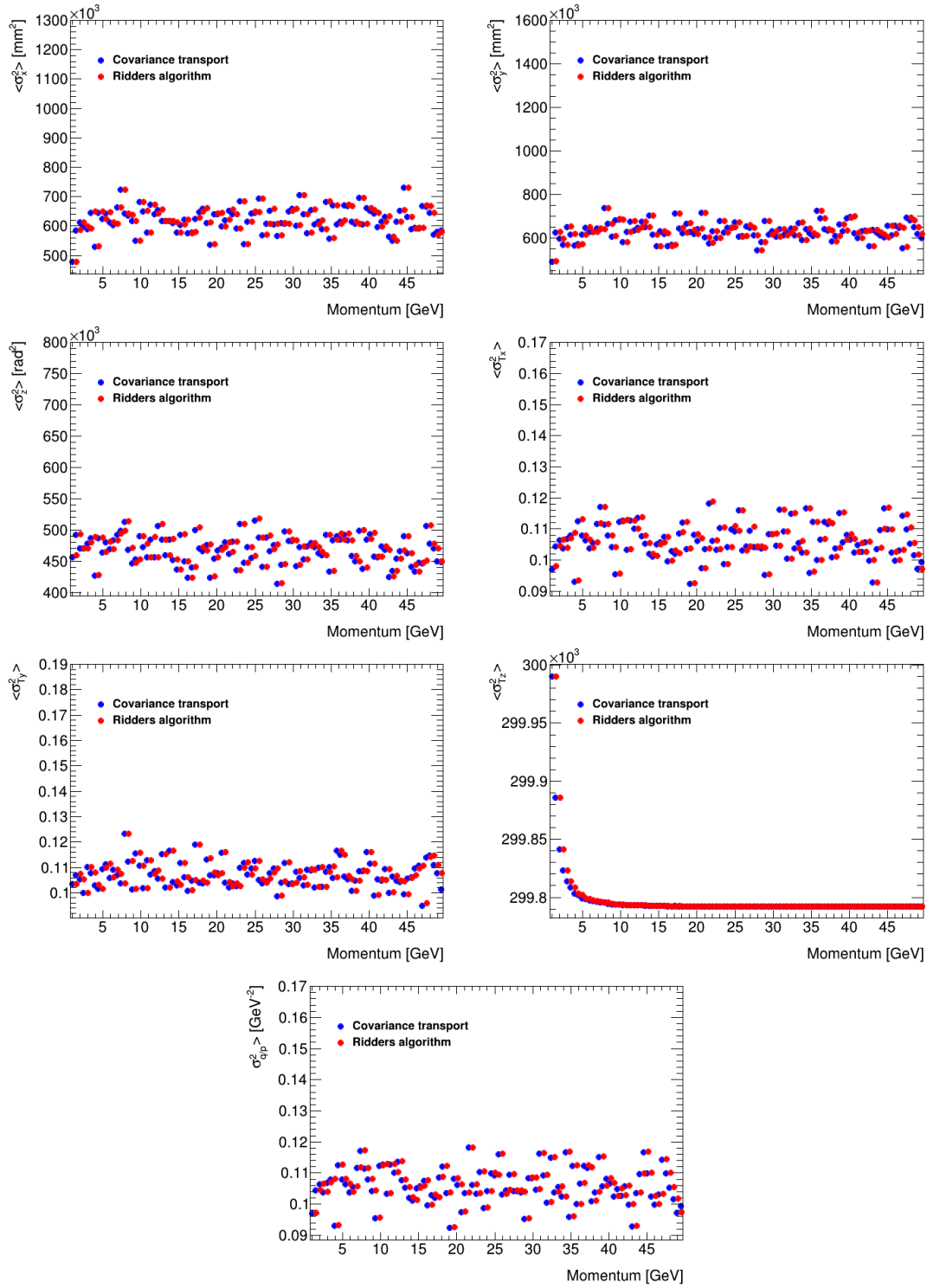
Figure D.2: Comparison of the diagonal terms of the covariance matrix from curvilinear to free parameters between the Ridders algorithm and the covariance transport as function of the initial momentum. The bin centres are shifted for visibility.
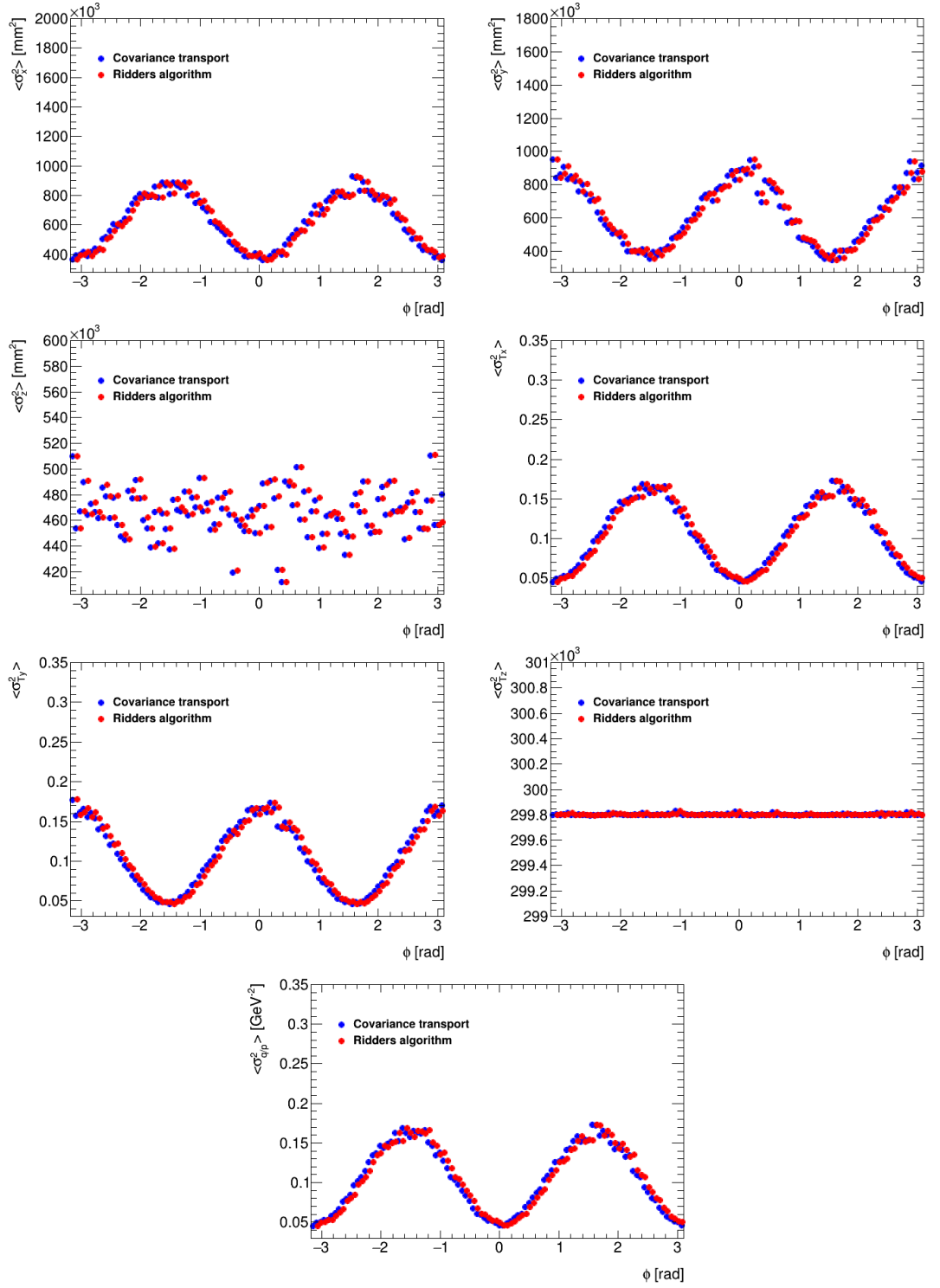
Figure D.3: Comparison of the diagonal terms of the covariance matrix from curvilinear to free parameters between the Ridders algorithm and the covariance transport as function of the initial azimuthal angle. The bin centres are shifted for visibility.

Figure D.4: Comparison of the diagonal terms of the covariance matrix from curvilinear to free parameters between the Ridders algorithm and the covariance transport as function of the initial polar. The bin centres are shifted for visibility.
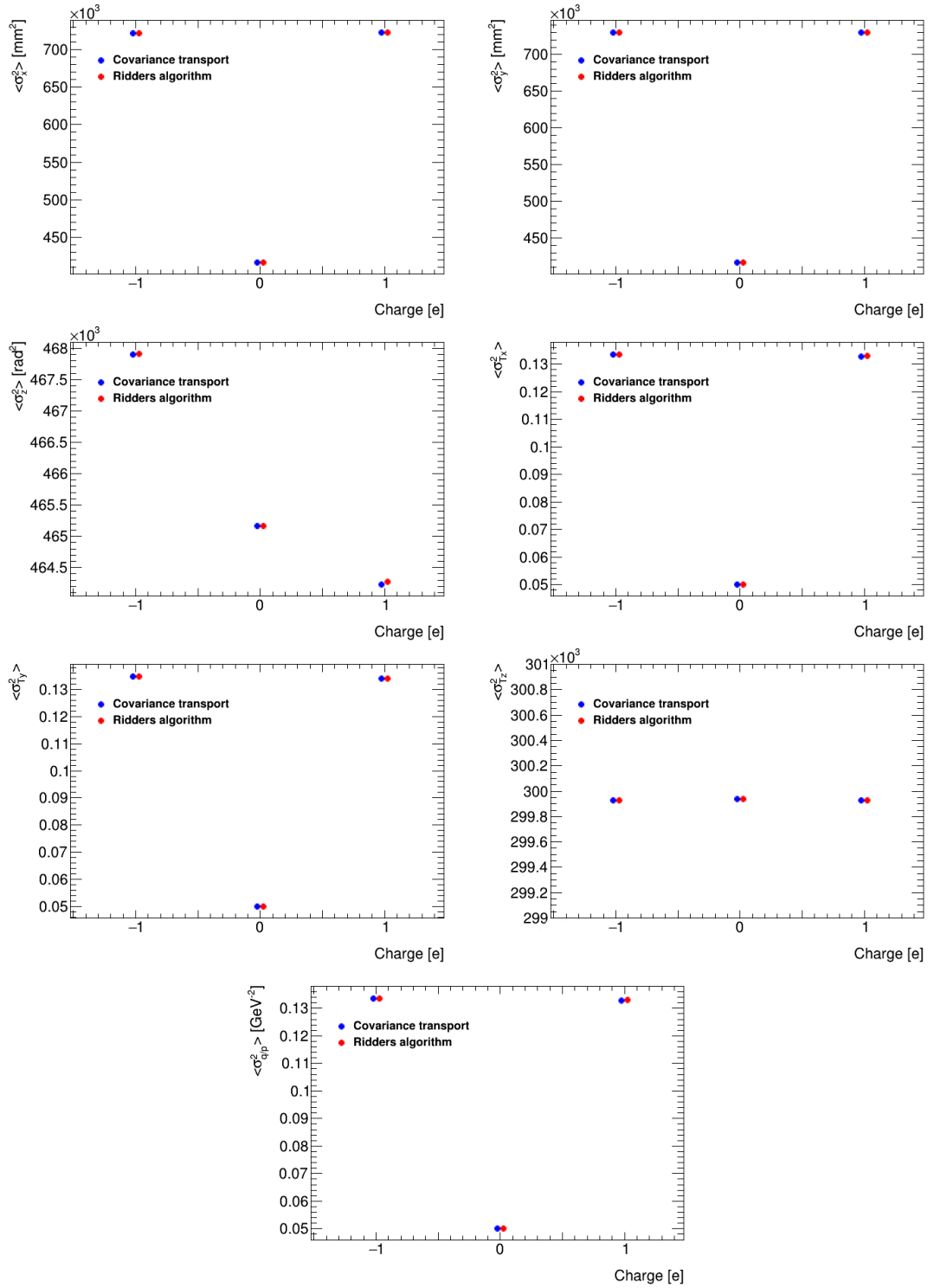
Figure D.5: Comparison of the diagonal terms of the covariance matrix from curvilinear to free parameters between the Ridders algorithm and the covariance transport as function of the particles charge. The bin centres are shifted for visibility.

Figure D.6: Comparison of the diagonal terms of the covariance matrix from free to free parameters between the Ridders algorithm and the covariance transport as function of the distance. The bin centres are shifted for visibility.

Figure D.7: Comparison of the diagonal terms of the covariance matrix from free to free parameters between the Ridders algorithm and the covariance transport as function of the initial momentum. The bin centres are shifted for visibility.

Figure D.8: Comparison of the diagonal terms of the covariance matrix from free to free parameters between the Ridders algorithm and the covariance transport as function of the initial azimuthal angle. The bin centres are shifted for visibility.

Figure D.9: Comparison of the diagonal terms of the covariance matrix from free to free parameters between the Ridders algorithm and the covariance transport as function of the initial polar angle. The bin centres are shifted for visibility.

Figure D.10: Comparison of the diagonal terms of the covariance matrix from free to free parameters between the Ridders algorithm and the covariance transport as function of the particles charge. The bin centres are shifted for visibility.

Figure D.11: Comparison of the diagonal terms of the covariance matrix from free to curvilinear parameters between the Ridders algorithm and the covariance transport as function of the distance. The bin centres are shifted for visibility.

Figure D.12: Comparison of the diagonal terms of the covariance matrix from free to curvilinear parameters between the Ridders algorithm and the covariance transport as function of the initial momentum. The bin centres are shifted for visibility.

Figure D.13: Comparison of the diagonal terms of the covariance matrix from free to curvilinear parameters between the Ridders algorithm and the covariance transport as function of the initial azimuthal angle. The bin centres are shifted for visibility.

Figure D.14: Comparison of the diagonal terms of the covariance matrix from free to curvilinear parameters between the Ridders algorithm and the covariance transport as function of the initial polar angle. The bin centres are shifted for visibility.

Figure D.15: Comparison of the diagonal terms of the covariance matrix from free to curvilinear parameters between the Ridders algorithm and the covariance transport as function of the particles charge. The bin centres are shifted for visibility.

D.2 Simulation Results
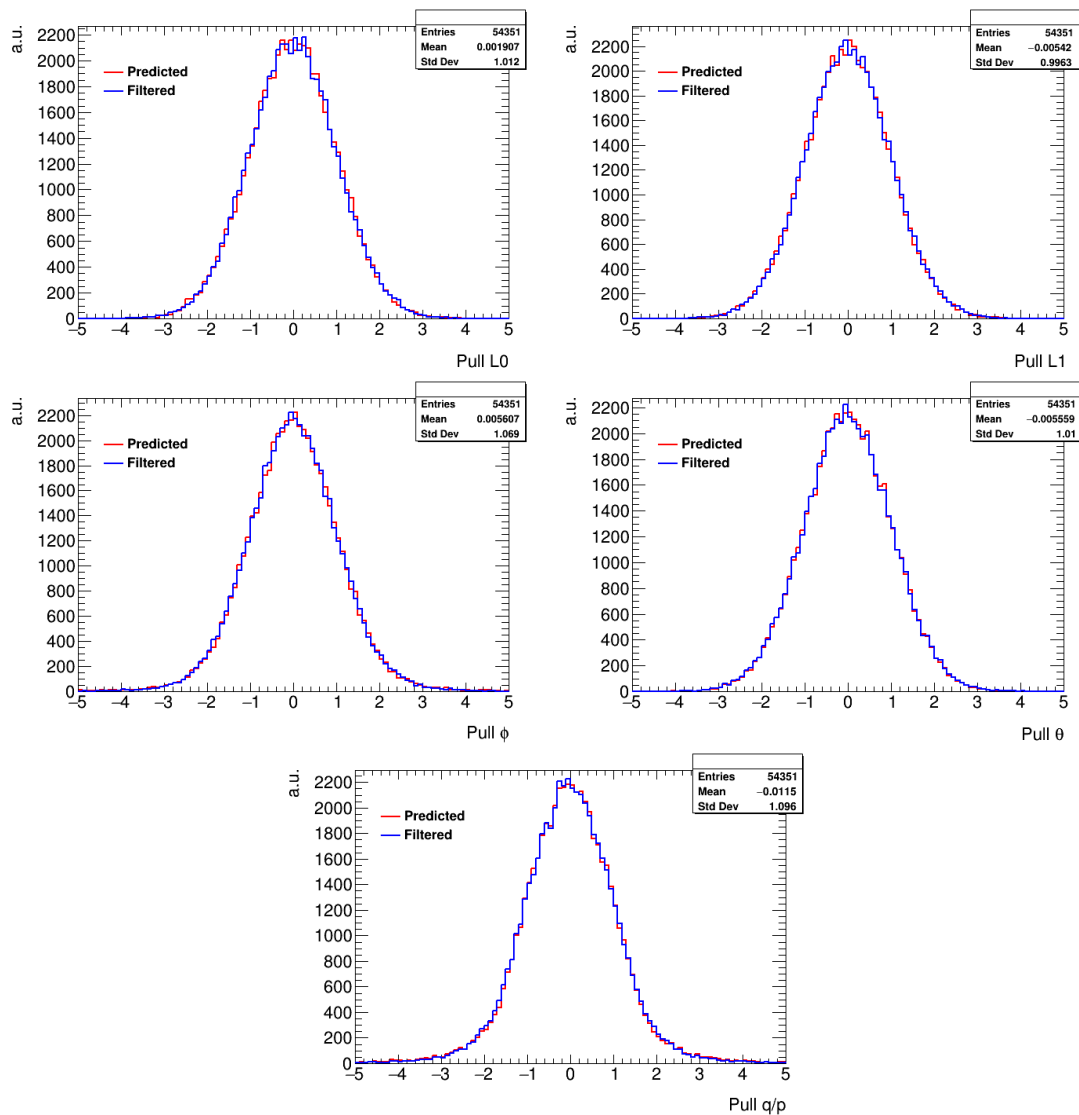
Figure D.16: Pull distributions of predicted and filtered parameters at the corresponding measurement surfaces in the tracking detector with 1 GeV initial momentum. The statistics refer to the filtered distributions.
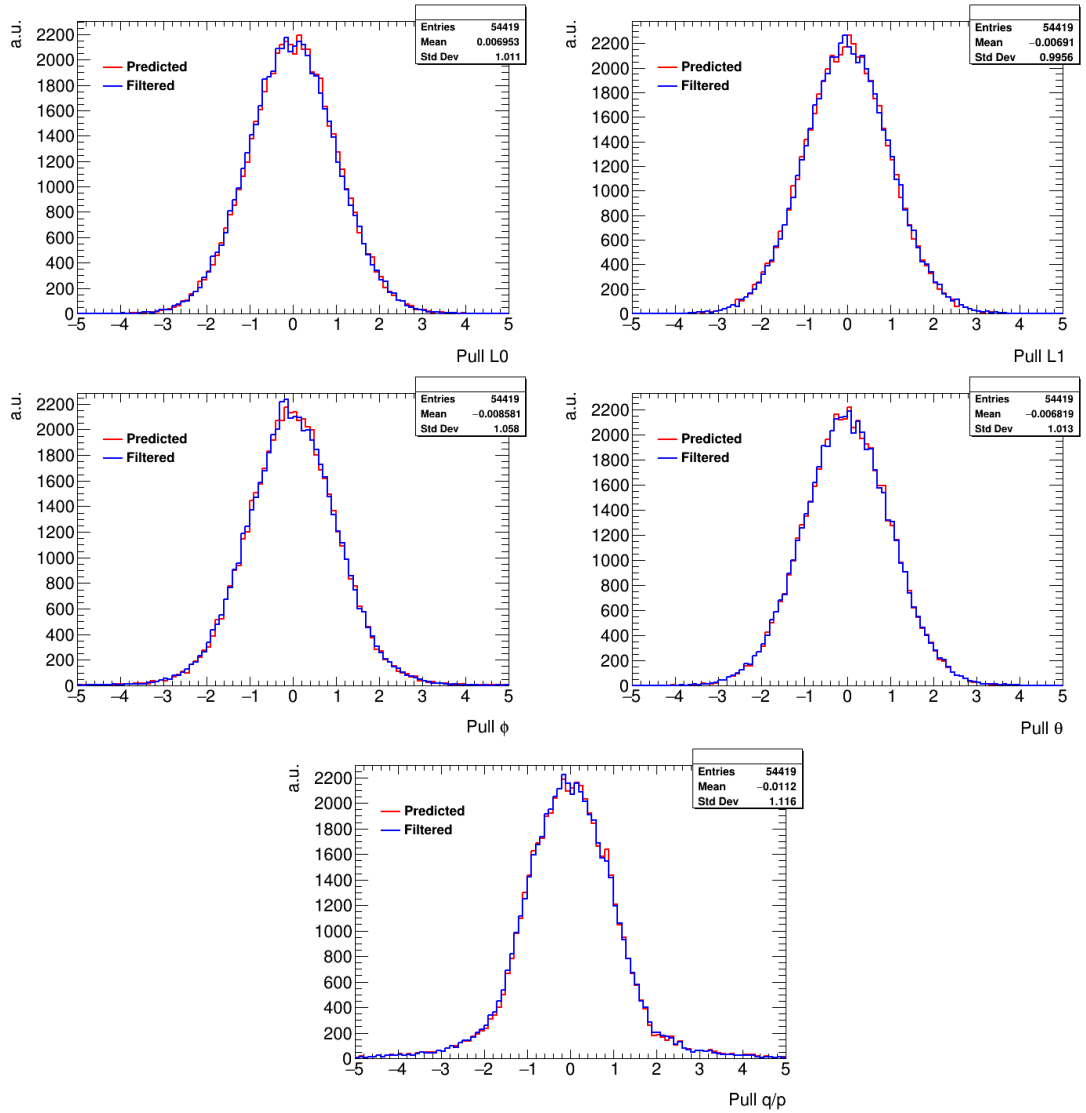
Figure D.17: Pull distributions of predicted and filtered parameters at the corresponding measurement surfaces in the tracking detector with 5 GeV initial momentum. The statistics refer to the filtered distributions.
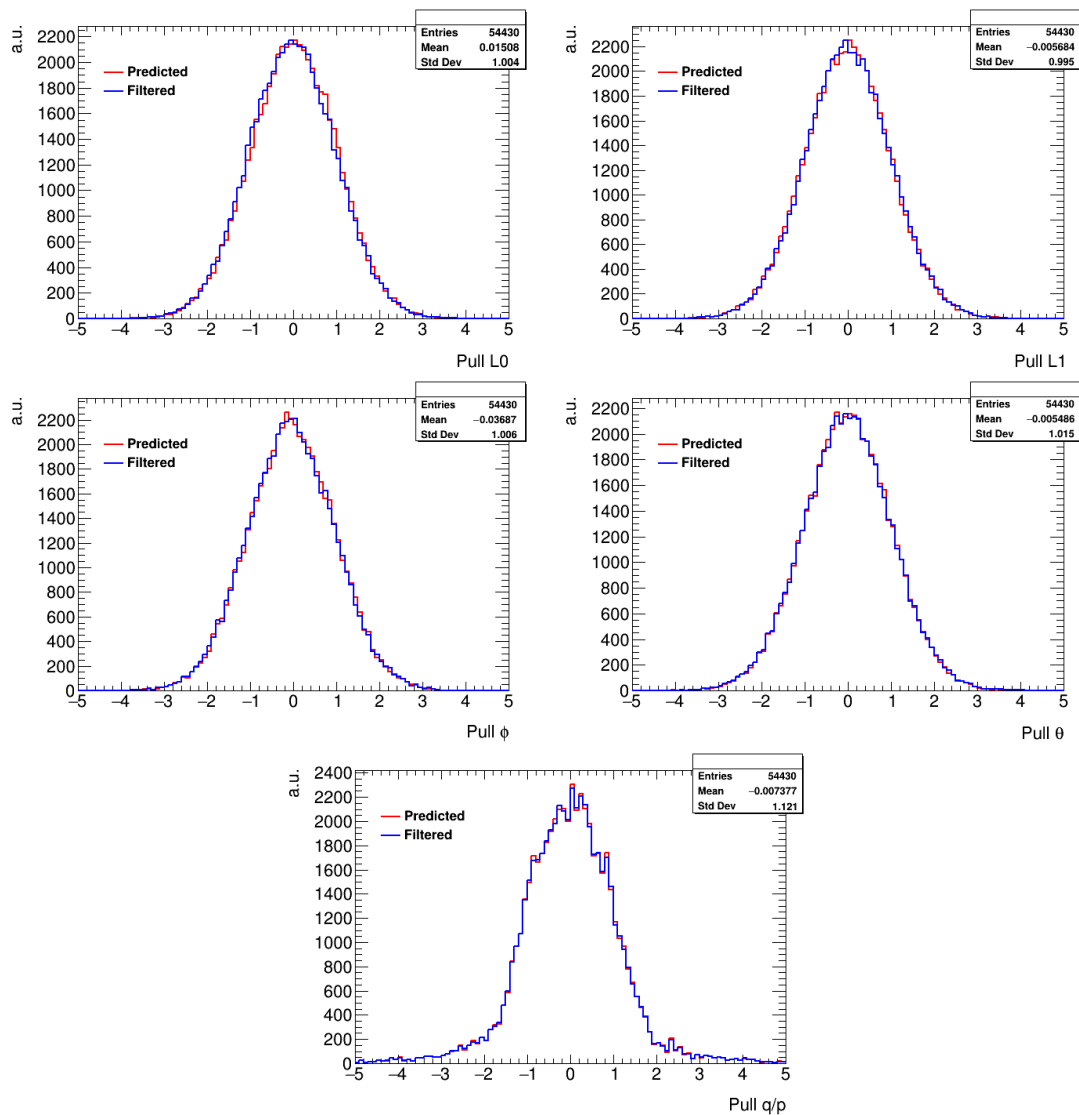
Figure D.18: Pull distributions of predicted and filtered parameters at the corresponding measurement surfaces in the tracking detector with 100 GeV initial momentum. The statistics refer to the filtered distributions.
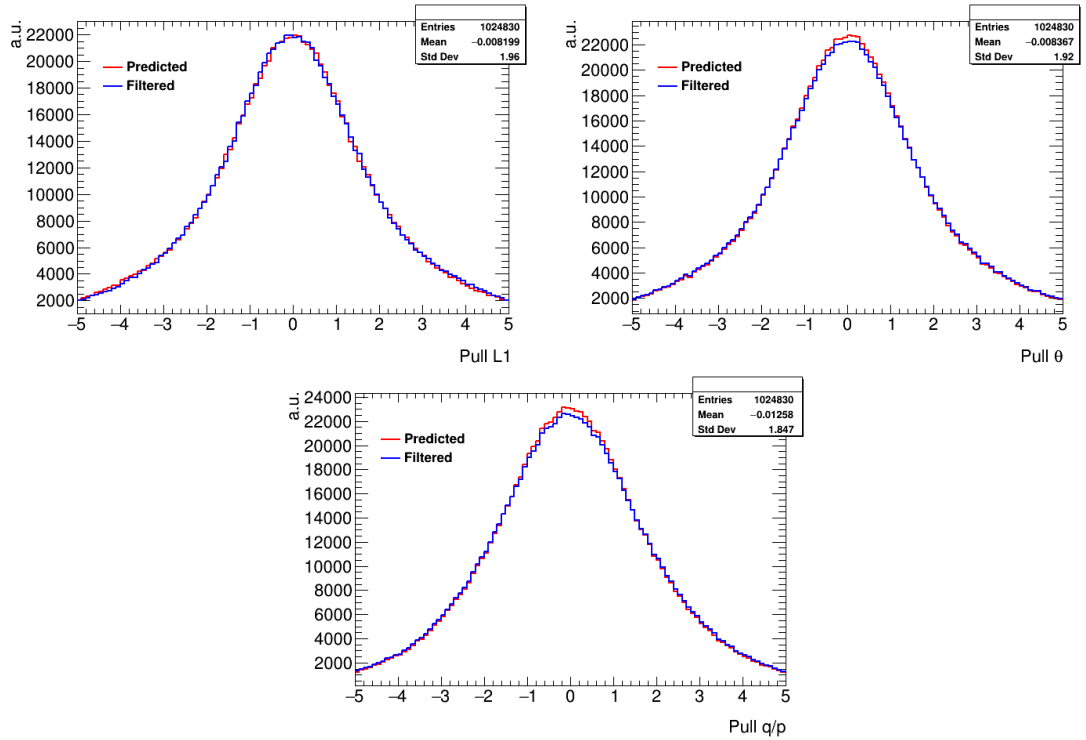
Figure D.19: Pull distributions of predicted and filtered parameters obtained for the Projected KF at the point of filtering in the TPC with 1 GeV initial momentum. The statistics refer to the filtered distributions.
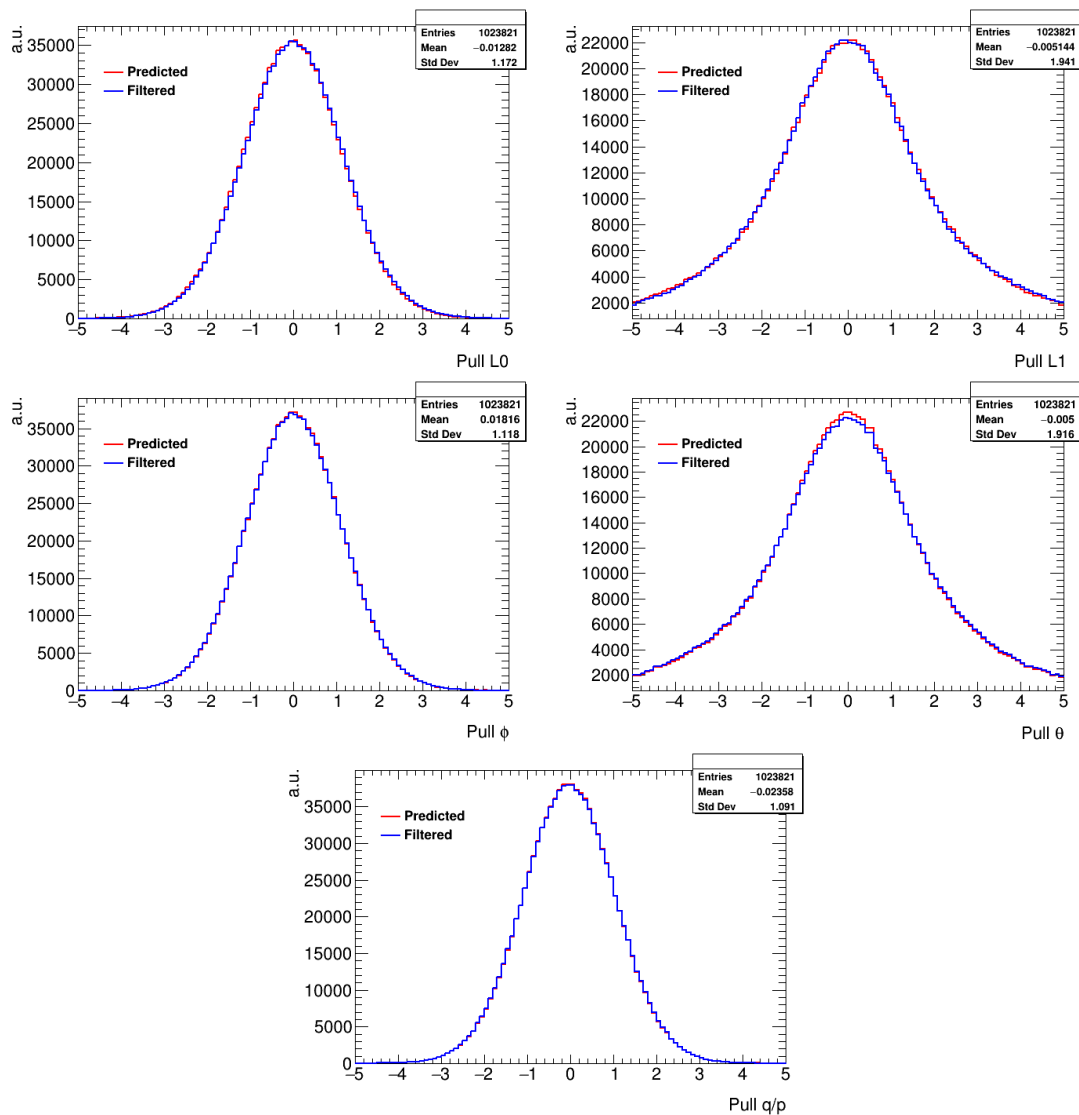
Figure D.20: Pull distributions of predicted and filtered parameters obtained for the Projected KF at the point of filtering in the TPC with 5 GeV initial momentum. The statistics refer to the filtered distributions.
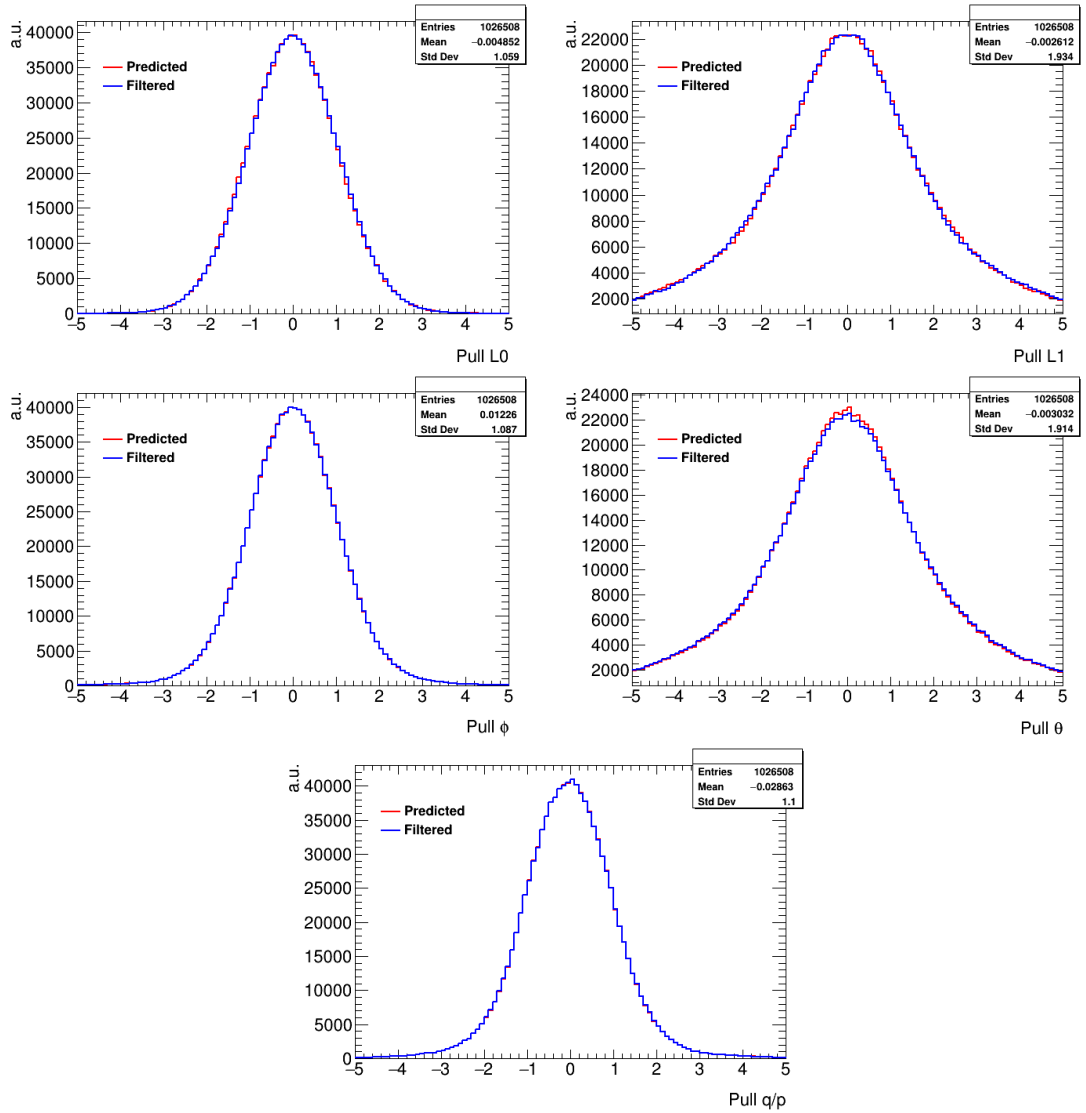
Figure D.21: Pull distributions of predicted and filtered parameters obtained for the Projected KF at the point of filtering in the TPC with 100 GeV initial momentum. The statistics refer to the filtered distributions.
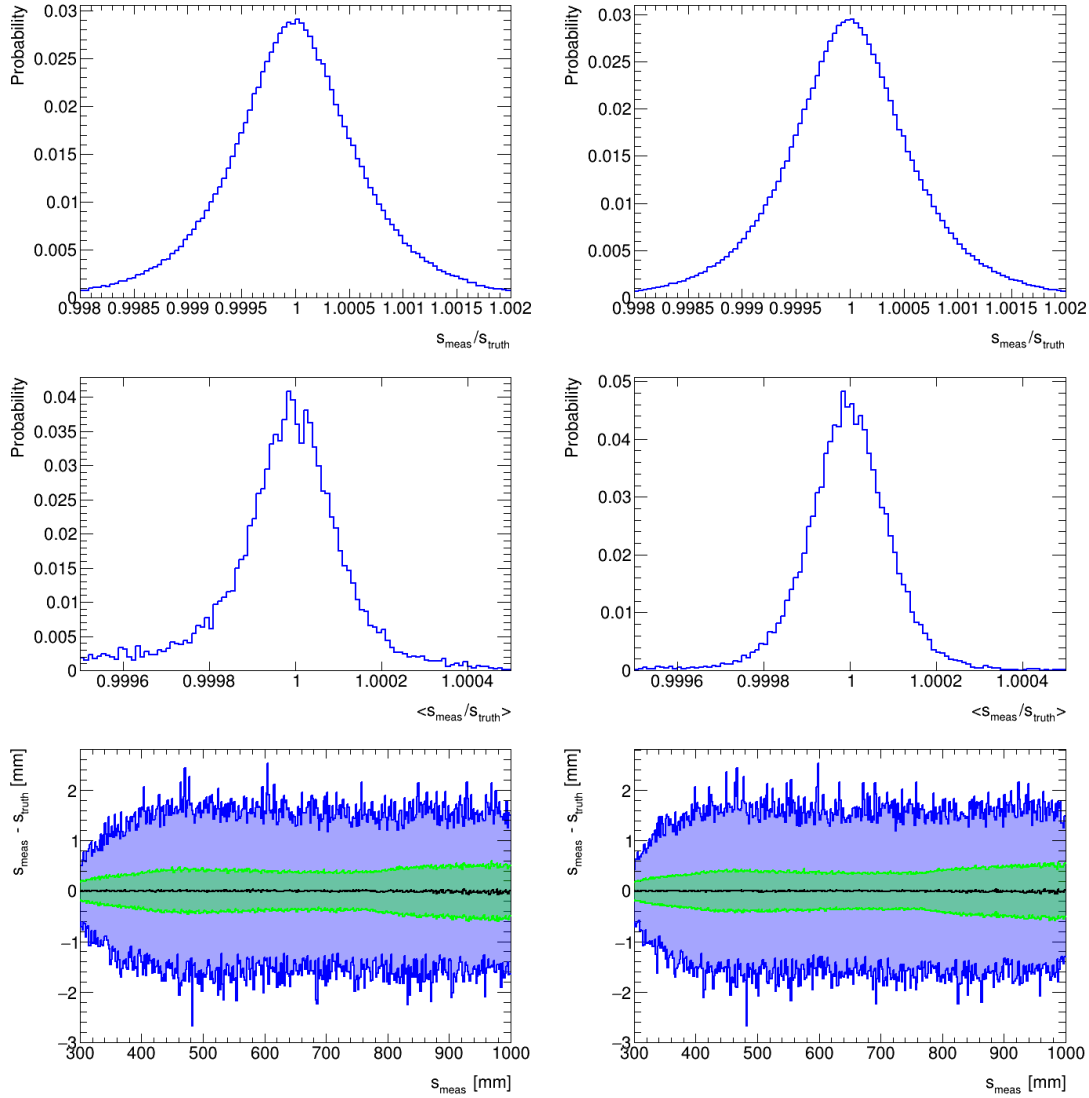
Figure D.22: Step length distributions for 5 GeV (left) and 10 GeV (right) muons. The top row shows the probability distribution of the ratio between $s_k^{true} + \tilde{s}_k$ and s_k^{true} for all tracks and measurements. The middle row shows the mean of this ratio per track. The bottom row shows the interval of a standard deviation (green) and the interval of the maximal deviations (blue) versus the extrapolation distance.
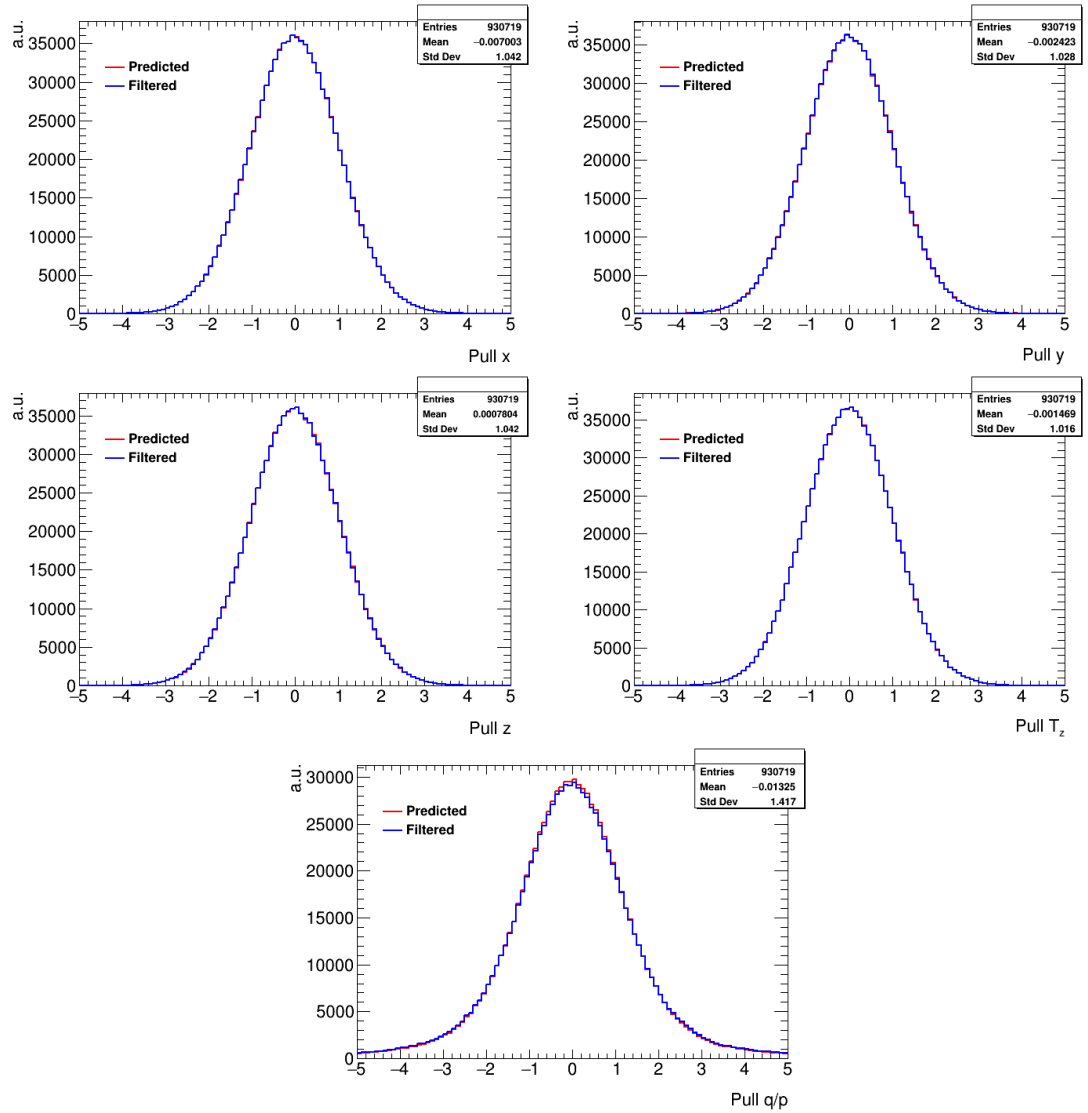
Figure D.23: Pull distributions of predicted and filtered parameters obtained for the Free KF at the point of filtering in the TPC with 1 GeV initial momentum. The statistics refer to the filtered distributions.
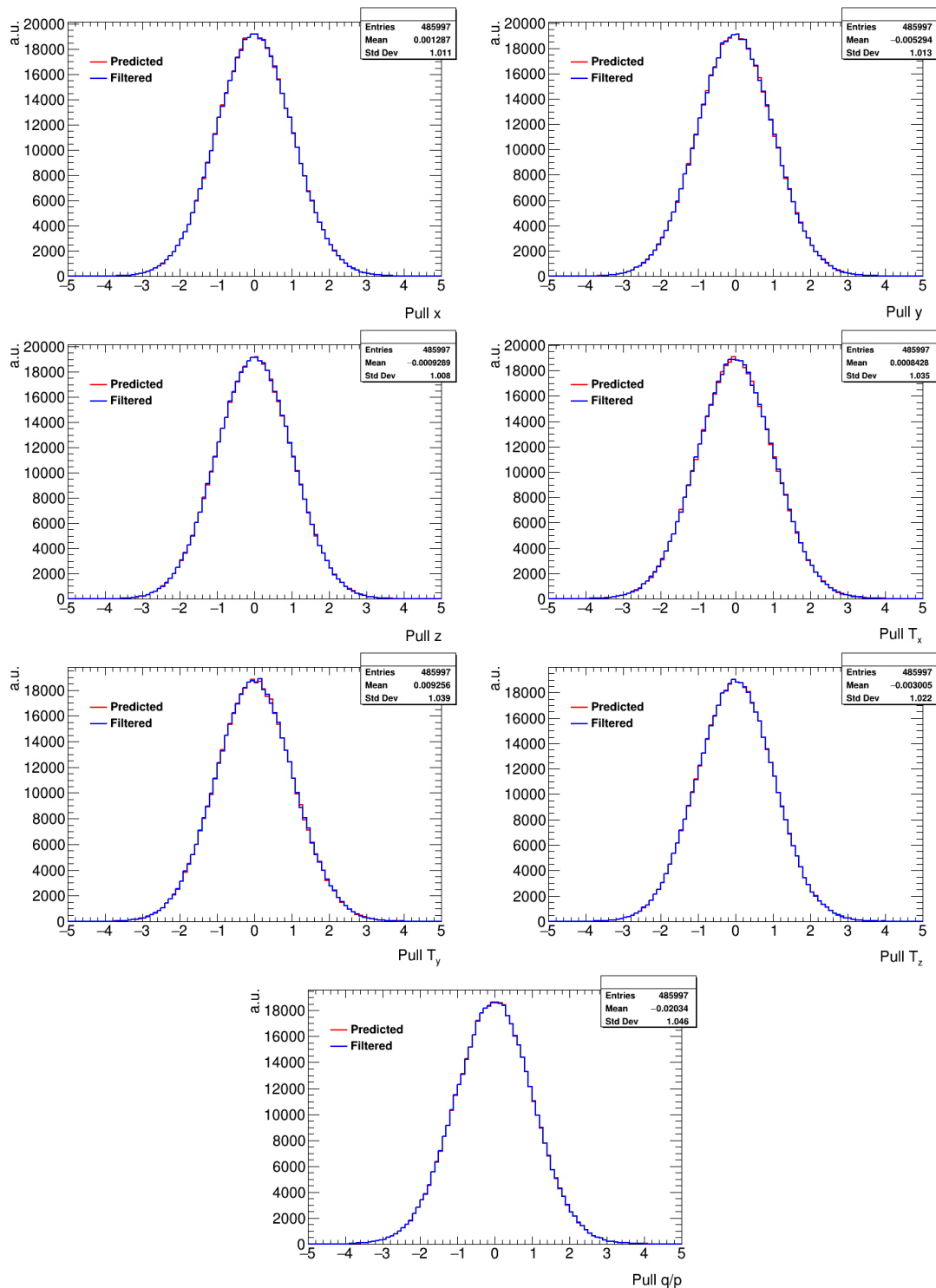
Figure D.24: Pull distributions of predicted and filtered parameters obtained for the Free KF at the point of filtering in the TPC with 5 GeV initial momentum. The statistics refer to the filtered distributions.

Figure D.25: Pull distributions of predicted and filtered parameters obtained for the Free KF at the point of filtering in the TPC with 100 GeV initial momentum. The statistics refer to the filtered distributions.
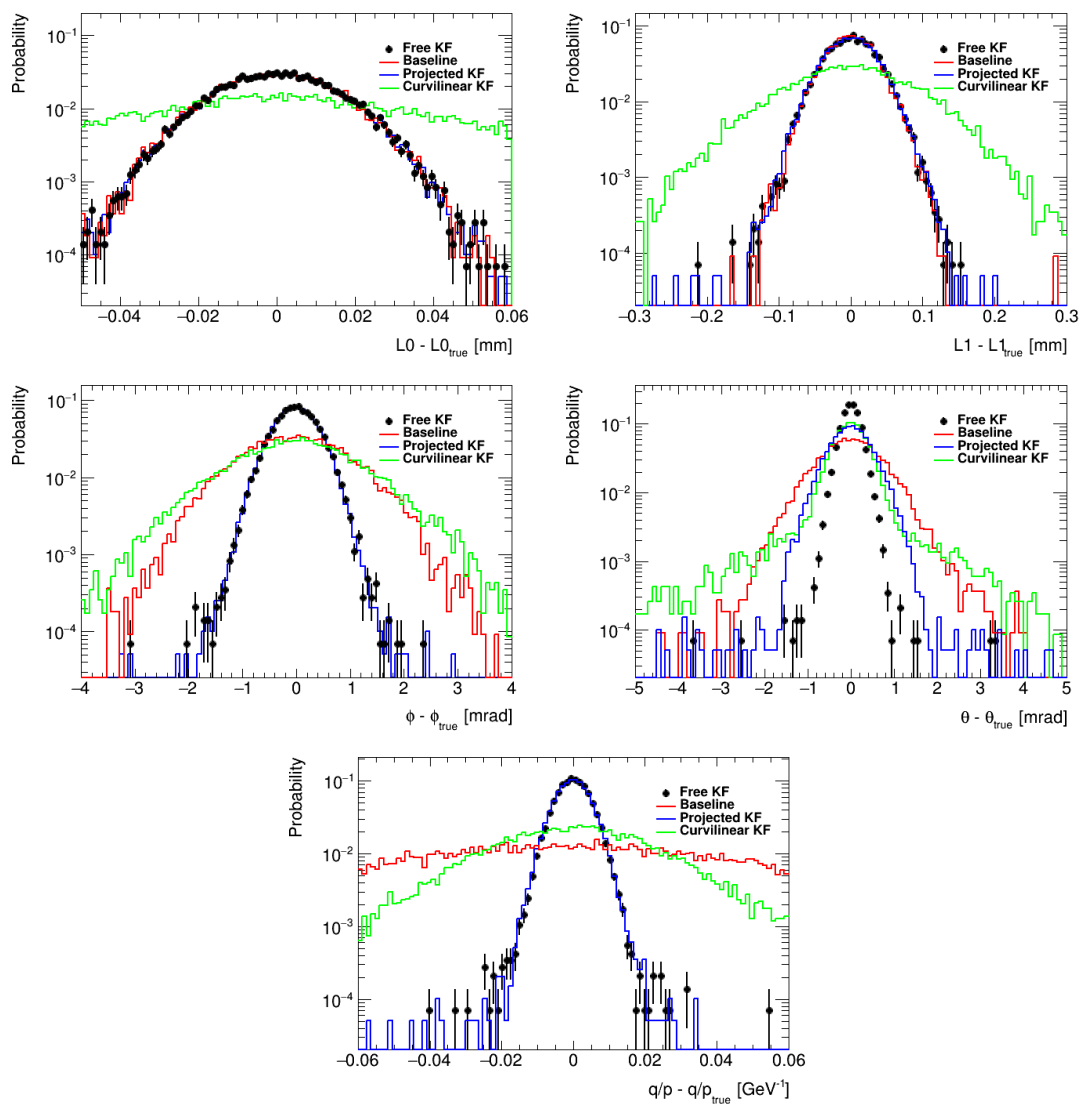
Figure D.26: Smoothed resolution of the models in Sec. 8.5.2 at the innermost surface of the tracking detector for 1 GeV initial momentum particles.
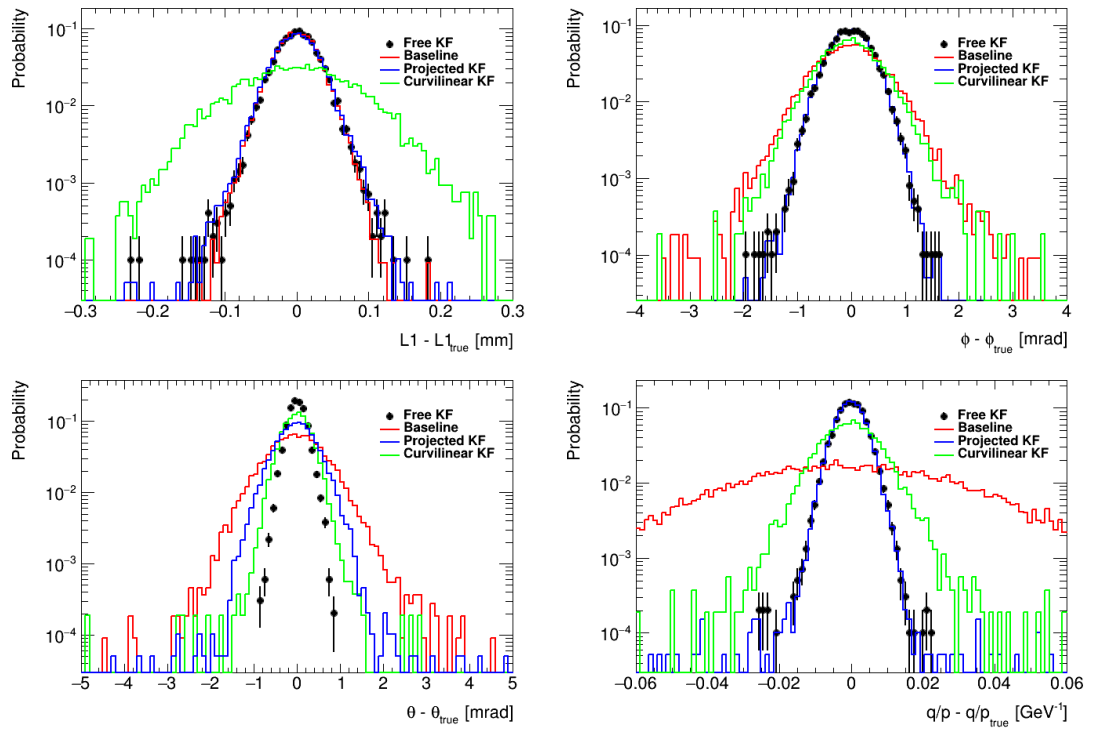
Figure D.27: Smoothed resolution of the models in Sec. 8.5.2 at the innermost surface of the tracking detector for 5 GeV initial momentum particles.
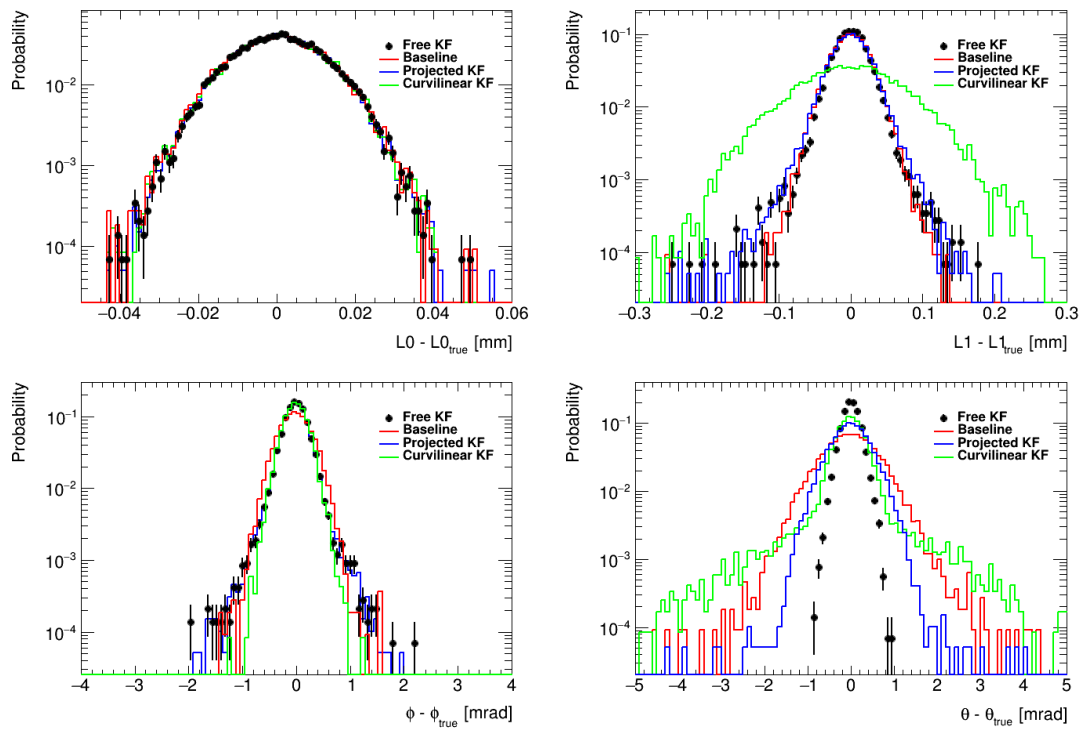
Figure D.28: Smoothed resolution of the models in Sec. 8.5.2 at the innermost surface of the tracking detector for 100 GeV initial momentum particles.
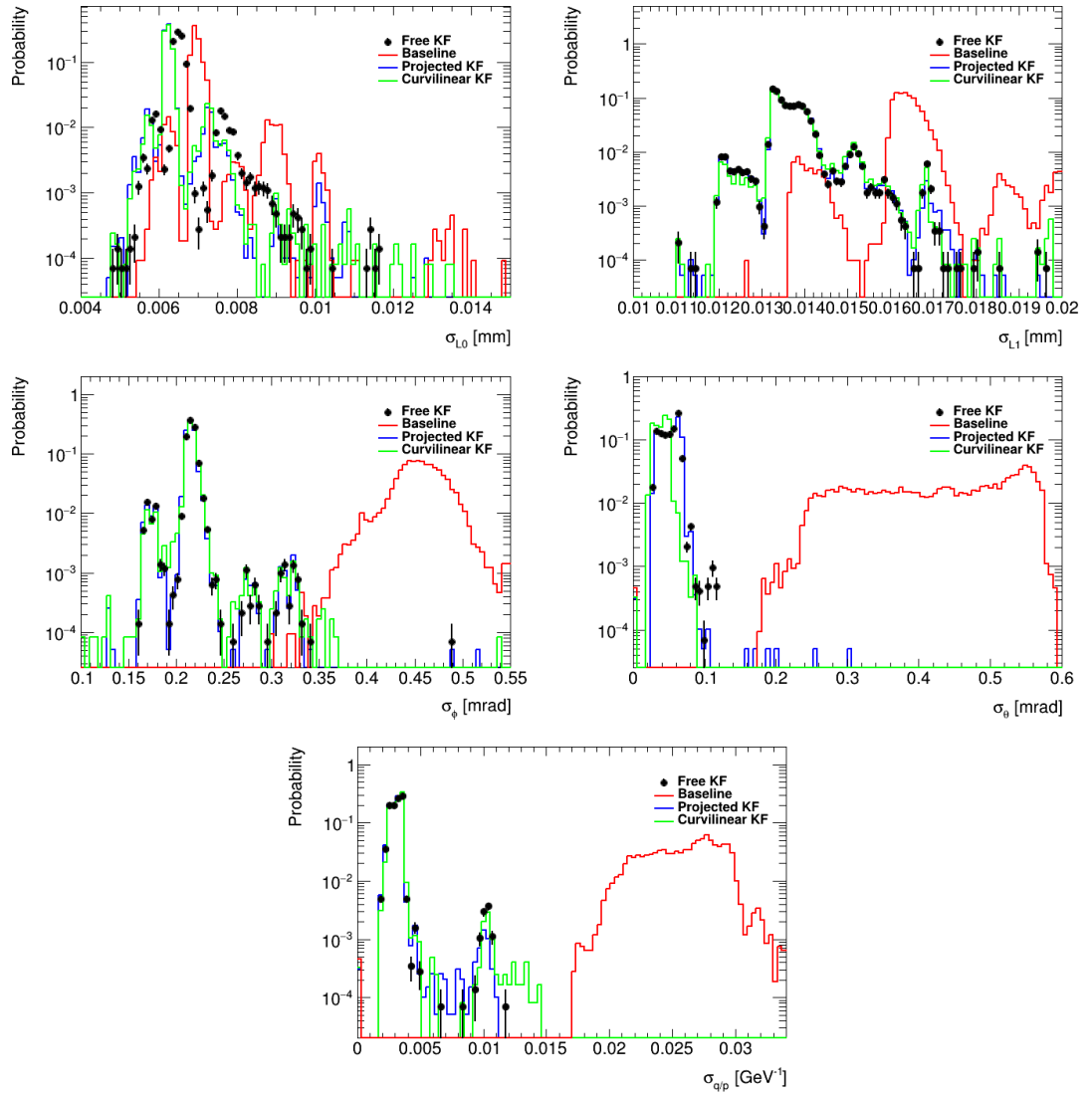
Figure D.29: Smoothed uncertainty of the models in Sec. 8.5.2 at the innermost surface of the tracking detector for 1 GeV initial momentum particles.
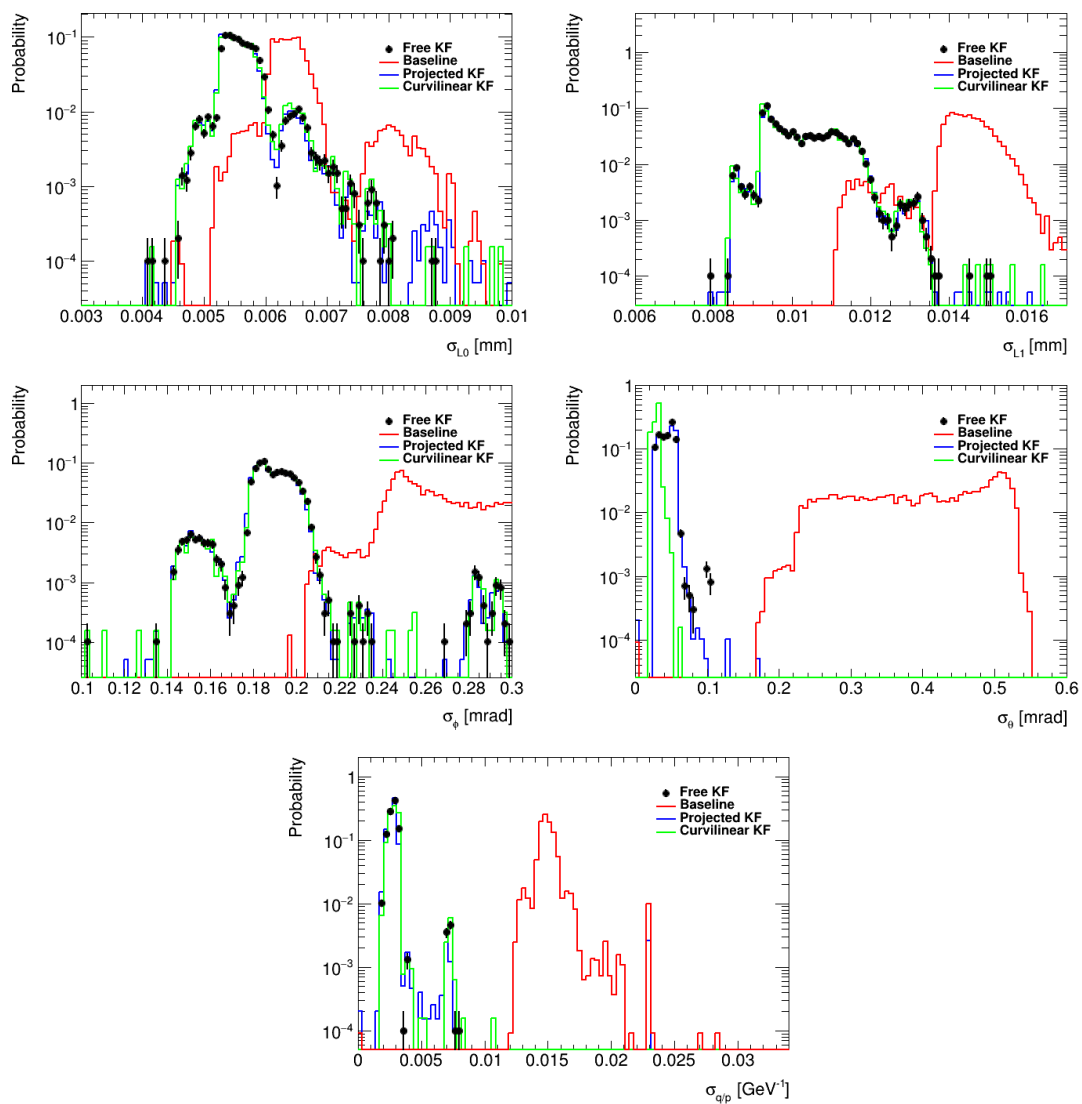
Figure D.30: Smoothed uncertainty of the models in Sec. 8.5.2 at the innermost surface of the tracking detector for 5 GeV initial momentum particles.
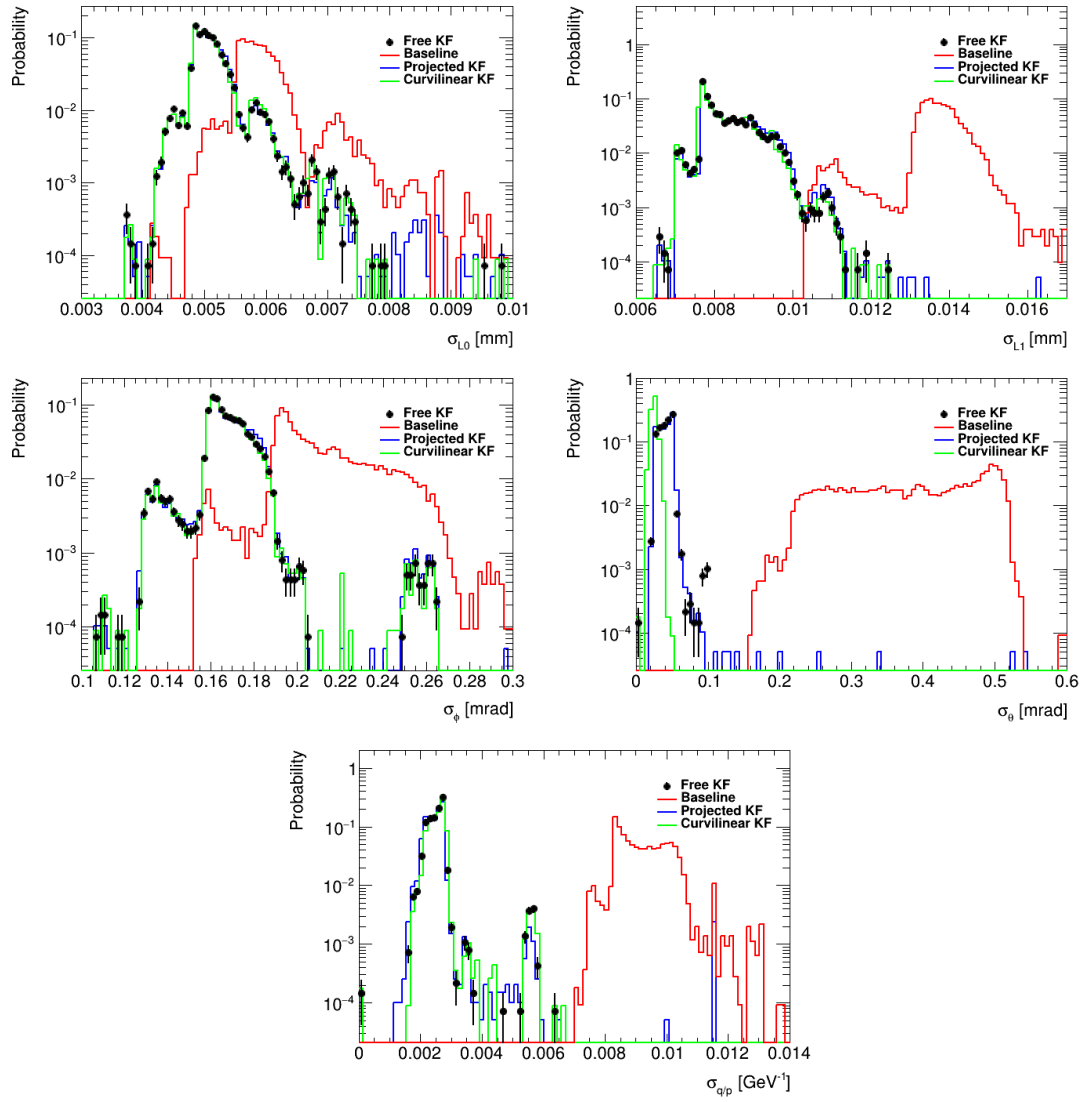
Figure D.31: Smoothed uncertainty of the models in Sec. 8.5.2 at the innermost surface of the tracking detector for 100 GeV initial momentum particles.

Bibliography

[1] S. Berryman, "Ancient atomism."
https://plato.stanford.edu/archives/fall2008/entries/atomism-ancient, 2005.

[2] J. Dalton, *A New System of Chemical Philosophy*, 1817.

[3] J.J. Thomson, *Cathode rays, Phil. Mag. Ser. 5* **44** (1897) 293–316.

[4] O. Masson, *XXIV. the constitution of atoms*, Feb. 1921, Zenodo.
https://doi.org/10.1080/14786442108636219, 10.1080/14786442108636219.

[5] J. Chadwick, *The Existence of a Neutron, Proc. Roy. Soc. Lond. A* **136** (1932)
692–708.

[6] J.A. Angelo, *Nuclear Technology*. Greenwood, 2004.

[7] A. Pais and S.B. Treiman, *How Many Charm Quantum Numbers Are There?*,
Phys. Rev. Lett. **35** (1975) 1556.

[8] J.M. Sánchez Ron, *The World after the Revolution: Physics in the Second Half
of the Twentieth Century*. BBVA, Madrid, 2008.

[9] H. Rechenberg, *Weltreise und Weltruhm*, 755–815. Springer Berlin Heidelberg,
Berlin, Heidelberg, 2009. 10.1007/978-3-540-69222-5_12.

[10] A. Einstein, *Ist die Trägheit eines Körpers von seinem Energieinhalt abhängig?*,
Annalen der Physik **323** 639–641.

[11] S. Weinberg, *The Making of the standard model, Eur. Phys. J. C* **34** (2004) 5–13
[arXiv:`hep-ph/0401010`].

[12] M. Brice and L. Egli, "Higgs announcement seminar on 4 July 2012." Jul 2012.

[13] M. Gell-Mann, *A Schematic Model of Baryons and Mesons, Phys. Lett.* **8** (1964)
214–215.

[14] G. Zweig, *An SU(3) model for strong interaction symmetry and its breaking;
Version 1*, Tech. Rep. CERN-TH-401, CERN, Geneva, Jan 1964.

[15] J.D. Bjorken, *Asymptotic sum rules at infinite momentum, Phys. Rev.* **179**
(1969) 1547–1553.

[16] T.M. Yan and S.D. Drell, *The parton model and its applications, International
Journal of Modern Physics A* **29** (2014) 1430071.

Bibliography

[17] PARTICLE DATA GROUP collaboration, M. Tanabashi, K. Hagiwara, K. Hikasa et al., *Review of particle physics*, *Phys. Rev. D* **98** (2018) 030001.

[18] M. Mulders, ed., *2013 European School of High-Energy Physics: Paradfurdo, Hungary 5 - 18 Jun 2013. Proceedings, 2013 European School of High-Energy Physics (ESHEP 2013)*, (Geneva), CERN, Sep 2016. 10.5170/CERN-2015-004.

[19] B. Pontecorvo, *Inverse beta processes and nonconservation of lepton charge*, *Zh. Eksp. Teor. Fiz.* **34** (1957) 247.

[20] J. Schechter and J.W. Valle, *Neutrino masses in SU(2)×U(1) theories*, *Phys. Rev., D; (United States)* .

[21] F. Scheck, *Theoretische Physik 1*. Springer-Verlag Berlin Heidelberg, 2007.

[22] P. Higgs, *Broken symmetries, massless particles and gauge fields*, *Physics Letters* **12** (1964) 132 – 133.

[23] T. Kibble, *Englert-Brout-Higgs-Guralnik-Hagen-Kibble mechanism (history)*, *Scholarpedia* **4** (2009) 8741.

[24] F.J. Yndurain, *The Theory of Quark and Gluon Interactions*, Theoretical and Mathematical Physics. Springer, Berlin, Germany, 2006, 10.1007/3-540-33210-3.

[25] PARTICLE DATA GROUP collaboration, P. Zyla et al., *Review of Particle Physics*, *PTEP* **2020** (2020) 083C01.

[26] R. Alkofer and J. Greensite, *Quark confinement: the hard problem of hadron physics*, *Journal of Physics G: Nuclear and Particle Physics* **34** (2007) S3–S21.

[27] D.J. Gross, *The discovery of asymptotic freedom and the emergence of QCD*, .

[28] LHCB collaboration, R. Aaij, C.A. Beteta, T. Ackernley, B. Adeva et al., *Test of lepton universality in beauty-quark decays*, 2021.

[29] E. Fermi, *Nuclear Physics*. University of Chicago Press, 1949.

[30] MUON $g-2$ collaboration, B. Abi, T. Albahri, S. Al-Kilani et al., *Measurement of the Positive Muon Anomalous Magnetic Moment to 0.46 ppm*, *Phys. Rev. Lett.* **126** (2021) 141801.

[31] T. Aoyama, N. Asmussen, M. Benayoun et al., *The anomalous magnetic moment of the muon in the Standard Model*, *Physics Reports* **887** (2020) 1–166.

[32] MUON $g-2$ collaboration, G.W. Bennett, B. Bousquet, H.N. Brown et al., *Final report of the E821 muon anomalous magnetic moment measurement at BNL*, *Phys. Rev. D* **73** (2006) 072003.

[33] S.P. Martin, *A supersymmetry primer*, *Advanced Series on Directions in High Energy Physics* (1998) 1–98.

[34] O.S. Brüning, P. Collier, P. Lebrun et al., *LHC Design Report*, CERN Yellow Reports: Monographs. CERN, Geneva, 2004, 10.5170/CERN-2004-003-V-1.

[35] E. Mobs, *The cern accelerator complex - 2019. complexe des accélérateurs du cern - 2019*, Jul 2019. https://cds.cern.ch/record/2684277.

[36] L. Arnaudon, P. Baudrenghien, M. Baylac et al., *Linac4 Technical Design Report*, Tech. Rep. CERN-AB-2006-084. CARE-Note-2006-022-HIPPI, CERN, Geneva, Dec 2006.

[37] K. Hanke, *Past and present operation of the CERN PS Booster*, *Int. J. Mod. Phys. A* **28** (2013) 1330019. 25 p.

[38] E. Regenstreif, *The CERN Proton Synchrotron*, CERN Yellow Reports: Monographs. CERN, Geneva, 1962, 10.5170/CERN-1962-003.

[39] R. Vanden Broeck, "CCC – Proton Synchrotron (PS). Synchrotron à Proton." Sep 2019.

[40] R. Steerenberg, "Accelerator physics." `https://indico.fnal.gov/event/43762/contributions/192686/attachments/132948/163699/rs20200813_HCPSS-2020_Lecture-1.pdf`, 2020.

[41] R. Steerenberg, *Batch Compression Merging and Splitting (BCMS)*, Apr 2017. https://cds.cern.ch/record/2259071.

[42] R. Vanden Broeck, "CCC – Super Proton Synchrotron (SPS). Le Supersynchrotron à Proton." Sep 2019.

[43] Press release. NobelPrize.org. Nobel Media AB 2021, `https://www.nobelprize.org/prizes/physics/1984/press-release/`, October 1984.

[44] N. Tahir, R. Schmidt, M. Brugger et al., *The CERN Super Proton Synchrotron as a tool to study high energy density physics*, *New J. Phys.* **10** (2008) 073028.

[45] *LEP design report.* CERN, Geneva, 1984.

[46] G. Giacomelli and R. Giacomelli, *The LEP Legacy*, *Non-Accelerator Astroparticle Physics* (2005) .

[47] D. Abbaneo et al., *A Combination of preliminary electroweak measurements and constraints on the standard model*, [arXiv:`hep-ex/0112021`].

[48] A. Martin, J. Outhwaite and M. Ryskin, *A new determination of the QED coupling $\alpha(M_Z^2)$ lets the Higgs off the hook*, *Physics Letters B* **492** (2000) 69–73.

[49] ALEPH, DELPHI, L3, OPAL, LEP ELECTROWEAK collaboration, S. Schael et al., *Electroweak Measurements in Electron-Positron Collisions at W-Boson-Pair Energies at LEP*, Phys. Rept. **532** (2013) 119–244 [arXiv:1302.3415].

[50] K. Wille, "Synchrotron radiation." `https://indico.cern.ch/event/218284/contributions/1520454/attachments/352184/490697/JUAS2013_Synchrotron_Radiation_1.pdf`, 2013.

[51] W. Herr and B. Muratori, *Concept of luminosity*, 2006. http://cds.cern.ch/record/941318, 10.5170/CERN-2006-002.361.

[52] D. Brandt, H. Burkhardt, M. Lamont et al., *Accelerator Physics at LEP*, Rep. Prog. Phys. **63** (2000) 939–1000. 56 p.

[53] "Recorded luminosity by the ATLAS detector." `https://atlas.web.cern.ch/Atlas/GROUPS/DATAPREPARATION/PublicPlots/2018/DataSummary/figs/intlumivsyear.png`.

[54] "Recorded pile-up by the ATLAS detector." `https://atlas.web.cern.ch/Atlas/GROUPS/DATAPREPARATION/PublicPlots/2018/DataSummary/figs/mu_2015_2018.pdf`.

[55] "HL-LHC project schedule." `https://project-hl-lhc-industry.web.cern.ch/content/project-schedule`.

[56] G. Apollinari, I. Béjar Alonso, O. Brüning et al., *High-Luminosity Large Hadron Collider (HL-LHC): Preliminary Design Report*, CERN Yellow Reports: Monographs. CERN, Geneva, 2015, 10.5170/CERN-2015-005.

[57] V. Shiltsev and F. Zimmermann, *Modern and future colliders*, 2020.

[58] R. Calaga, *Crab Cavities for the High-luminosity LHC*, in *18th International Conference on RF Superconductivity*, THXA03, 2018, DOI.

[59] ATLAS collaboration, G. Aad, E. Abat, J. Abdallah et al., *The ATLAS experiment at the CERN large hadron collider*, Journal of Instrumentation **3** (2008) S08003–S08003.

[60] M. Aleksa, *Status of the ATLAS Experiment*, Journal of Physics: Conference Series **452** (2013) 012041.

[61] C. Kourkoumelis and S. Vourakis, *HYPATIA – an online tool for ATLAS event visualization*, Physics Education **49** (2014) 21.

[62] ATLAS collaboration, *ATLAS inner detector: Technical Design Report, 1*, Technical Design Report ATLAS. CERN, Geneva, 1997.

[63] ATLAS collaboration, *The upgraded Pixel detector and the commissioning of the Inner Detector tracking of the ATLAS experiment for Run-2 at the Large Hadron Collider*, Tech. Rep. ATL-PHYS-PROC-2016-104, CERN, Geneva, Aug 2016.

[64] B. Mindur, T. Akesson, F. Anghinolfi et al., *Gas gain stabilisation in the ATLAS TRT detector*, *Journal of Instrumentation* **11** (2016) P04027–P04027.

[65] ATLAS collaboration, *ATLAS Insertable B-Layer Technical Design Report*, Tech. Rep. CERN-LHCC-2010-013. ATLAS-TDR-19, Sep 2010.

[66] G. Aad, M. Ackers, F.A. Alberti et al., *ATLAS pixel detector electronics and sensors*, *Journal of Instrumentation* **3** (2008) P07007–P07007.

[67] J. Jentzsch, *Pixel detector modules performance for ATLAS IBL and future pixel detectors*, Ph.D. thesis, Tech. U., Dortmund (main), 3 2015. 10.17877/DE290R-16400.

[68] W. de Boer, K.H. Hoffmann, A. Sabellek et al., *Lorentz shift measurements in heavily irradiated silicon detectors in high magnetic fields*, *Proceedings of Science* (2010) .

[69] A. Abdesselam and T. Akimoto, *The Barrel Modules of the ATLAS SemiConductor Tracker*, Tech. Rep. ATL-INDET-PUB-2006-005. ATL-COM-INDET-2006-009. CERN-ATL-COM-INDET-2006-009, CERN, Geneva, Jul 2006. 10.1016/j.nima.2006.08.036.

[70] A. Abdesselam, *ATLAS SCT Endcap Module Production*, Tech. Rep. ATL-INDET-PUB-2006-007. ATL-COM-INDET-2006-008, CERN, Geneva, Jul 2006.

[71] X. Artru, G.B. Yodh and G. Mennessier, *Practical theory of the multilayered transition radiation detector*, *Phys. Rev. D* **12** (1975) 1289–1306. 49 p.

[72] M. Aaboud, G. Aad, B. Abbott et al., *Performance of the ATLAS Transition Radiation Tracker in Run 1 of the LHC: tracker properties*, *Journal of Instrumentation* **12** (2017) P05002–P05002.

[73] ATLAS TRT collaboration, E. Abat, T.N. Addy, T.P.A. Åkesson et al., *The ATLAS TRT barrel detector*, *Journal of Instrumentation* **3** (2008) P02014–P02014.

[74] ATLAS TRT collaboration, E. Abat, T.N. Addy, T.P.A. Åkesson et al., *The ATLAS TRT end-cap detectors*, *Journal of Instrumentation* **3** (2008) P10003–P10003.

[75] D. Cockerill, "Introduction to calorimetry." `https://indico.cern.ch/event/518474/contributions/1198681/attachments/1267581/1877122/Calorimetry-lecture-to-Southampton-students-4May2016-Cockerill-compressed.pdf`, May 2016.

Bibliography

[76] J. Pequenao, *Computer Generated image of the ATLAS calorimeter*, Mar 2008. https://cds.cern.ch/record/1095927.

[77] V. Rossetti, *Performance of the ATLAS Calorimeters and Commissioning for LHC Run-2*, Jul 2015. https://cds.cern.ch/record/2037117.

[78] J. Pequenao, *Computer generated image of the ATLAS Muons subsystem*, Mar 2008. https://cds.cern.ch/record/1095929.

[79] H.H.J. Ten Kate, *ATLAS Superconducting Toroids — The Largest Ever Built*, International Journal of Modern Physics A **25** (2010) 2933–2954.

[80] ATLAS collaboration, *ATLAS Computing: technical design report*, Technical design report. ATLAS. CERN, Geneva, 2005.

[81] M. Aaboud, G. Aad, B. Abbott et al., *Modelling radiation damage to pixel sensors in the ATLAS detector*, Journal of Instrumentation **14** (2019) P06012–P06012.

[82] ATLAS collaboration, *Technical Design Report for the ATLAS Inner Tracker Pixel Detector*, Tech. Rep. CERN-LHCC-2017-021. ATLAS-TDR-030, CERN, Geneva, Sep 2017.

[83] ATLAS collaboration, *Technical Design Report for the ATLAS Inner Tracker Strip Detector*, Tech. Rep. CERN-LHCC-2017-005. ATLAS-TDR-025, CERN, Geneva, Apr 2017.

[84] "ITk Pixel Layout Updates." https://atlas.web.cern.ch/Atlas/GROUPS/PHYSICS/PLOTS/ITK-2020-002/, April 2020.

[85] RD53 collaboration, *RD53B Manual*, Tech. Rep. CERN-RD53-PUB-19-002, CERN, Geneva, Mar 2019.

[86] ATLAS collaboration, *Expected Tracking Performance of the ATLAS Inner Tracker at the HL-LHC*, Tech. Rep. ATL-PHYS-PUB-2019-014, CERN, Geneva, Mar 2019.

[87] ATLAS collaboration, *Technical Design Report: A High-Granularity Timing Detector for the ATLAS Phase-II Upgrade*, Tech. Rep. CERN-LHCC-2020-007. ATLAS-TDR-031, CERN, Geneva, Jun 2020.

[88] "Latest Performance Studies of the ATLAS Inner Tracker (ITk) in the HL-LHC." https://atlas.web.cern.ch/Atlas/GROUPS/PHYSICS/PLOTS/IDTR-2019-009/, February 2020.

[89] ATLAS collaboration, *Technical Design Report for the Phase-II Upgrade of the ATLAS TDAQ System*, Tech. Rep. CERN-LHCC-2017-020. ATLAS-TDR-029, CERN, Geneva, Sep 2017.

[90] P. Calafiura, J. Catmore, D. Costanzo et al., *ATLAS HL-LHC Computing Conceptual Design Report*, Tech. Rep. CERN-LHCC-2020-015. LHCC-G-178, CERN, Geneva, Sep 2020.

[91] B.W. Group, "Hepix." https://w3.hepix.org/benchmarking.html, 2017.

[92] S. Agostinelli et al., *Geant4—a simulation toolkit*, *Nucl Instrum Meth A* **506** (2003) 250–303.

[93] J. Allison et al., *Geant4 developments and applications*, *IEEE T Nucl Sci* **53** (2006) 270–278.

[94] *The decay of a lambda particle in the 32 cm hydrogen bubble chamber*, 1960. https://cds.cern.ch/record/39474.

[95] T. Bayes, Rev., *An essay toward solving a problem in the doctrine of chances*, *Phil. Trans. Roy. Soc. Lond.* **53** (1764) 370–418.

[96] A. Caldwell, "Model-based data analysis, parameter interference and model testing." Notes of the lecture *Data Analysis* held during winter semester 2015/2016 at Technical University Munich.

[97] A.N. Kolmogorov, *Grundbegriffe der Wahrscheinlichkeitsrechnung*. Springer, 1933.

[98] G. Cowan, *Statistical Data Analysis*, Oxford science publications. Clarendon Press, 1998.

[99] K. Petersen and M. Pedersen, *The Matrix Cookbook*. 2008.

[100] R.E. Kalman, *A new approach to linear filtering and prediction problems*, *Transactions of the ASME–Journal of Basic Engineering* **82** (1960) 35–45.

[101] A. Gelb, *Applied optimal estimation*. MIT Press, 1974.

[102] D. Fraser and J. Potter, *The optimum linear smoother as a combination of two optimum linear filters*, *IEEE Transactions on Automatic Control* **14** (1969) 387–390.

[103] X. Ai, C. Allaire, N. Calace et al., *A common tracking software project*, [arXiv:2106.13593].

[104] X. Ai, C. Allaire, N. Calace, P. Gessinger et al., *Acts project: v3.0.0*, Nov. 2020, Zenodo. https://doi.org/10.5281/zenodo.3937454, 10.5281/zenodo.3937454.

[105] ISO/IEC, *Programming Languages — C++*, Draft International Standard N4660, March 2017.

[106] M. Frank, F. Gaede, C. Grefe et al., *DD4hep: A Detector Description Toolkit for High Energy Physics Experiments*, *J. Phys. Conf. Ser.* **513** (2014) 022010.

Bibliography

[107] R. Brun and F. Rademakers, *Root — an object oriented data analysis framework*, *Nuclear Instruments and Methods in Physics Research Section A: Accelerators, Spectrometers, Detectors and Associated Equipment* **389** (1997) 81 – 86.

[108] "Acts Common Tracking Software." https://acts.readthedocs.io.

[109] R. Frühwirth, W. Waltenberger and P. Vanlaer, *Adaptive vertex fitting*, *J. Phys. G* **34** (2007) N343.

[110] R. Frühwirth and W. Waltenberger, *Adaptive Multi-vertex fitting*, tech. rep., CERN, Geneva, Sep 2004. 10.5170/CERN-2005-002.280.

[111] "ATLAS computing model projections for Phase-II." https://twiki.cern.ch/twiki/bin/view/AtlasPublic/ComputingandSoftwarePublicResults.

[112] ATLAS collaboration, M. Elsing, I. Gavrilenko and F. Klimpel, *Fast Track Reconstruction for HL-LHC*, Oct 2019. https://cds.cern.ch/record/2693670.

[113] ATLAS collaboration, F. Klimpel, *Fast tracking for the HL-LHC ATLAS detector*, Jun 2020. https://cds.cern.ch/record/2721751.

[114] *Early Inner Detector Tracking Performance in the 2015 data at $\sqrt{s} = 13$ TeV*, Tech. Rep. ATL-PHYS-PUB-2015-051, CERN, Geneva, Dec 2015.

[115] "TrackML Particle Tracking Challenge." https://sites.google.com/site/trackmlparticle/.

[116] ATLAS collaboration, *Improved electron reconstruction in ATLAS using the Gaussian Sum Filter-based model for bremsstrahlung*, tech. rep., CERN, Geneva, May 2012.

[117] E. Lund, L. Bugge, I. Gavrilenko et al., *Track parameter propagation through the application of a new adaptive Runge-Kutta-Nyström method in the ATLAS experiment*, *JINST* **4** (2008) P04001. 13 p.

[118] E. Lund, L. Bugge, I. Gavrilenko et al., *Transport of covariance matrices in the inhomogeneous magnetic field of the ATLAS experiment by the application of a semi-analytical method*, *JINST* **4** (2008) P04016. 14 p.

[119] E. Lund, L. Bugge, E.W. Hughes et al., *Treatment of energy loss and multiple scattering in the context of track parameter and covariance matrix propagation in continuous material in the ATLAS experiment*, Tech. Rep. ATL-SOFT-PUB-2008-003. ATL-COM-SOFT-2008-008, CERN, Geneva, July 2008.

[120] A. Strandlie and W. Wittek, *Propagation of Covariance Matrices of Track Parameters in Homogeneous Magnetic Fields in CMS*, Tech. Rep. CMS-NOTE-2006-001, CERN, Geneva, Jan 2006.

[121] E.J. Nyström, *Über die numerische Integration von Differentialgleichungen*, *Acta Soc. Sci. Fenn.* **50** (1925) 1–55.

[122] E. Fehlberg, *Classical Fifth-, Sixth-, Seventh-, and Eighth-Order Runge-Kutta Formulas with Stepsize Control*, .

[123] J. Butcher, *Coefficients for the study of runge-kutta integration processes*, *Journal of the Australian Mathematical Society* **3** (1963) 185 – 201.

[124] C. Ridders, *Accurate computation of $F'(x)$ and $F'(x)F''(x)$*, *Advances in Engineering Software (1978)* **4** (1982) 75–76.

[125] H. Bethe and W. Heitler, *On the Stopping of fast particles and on the creation of positive electrons*, *Proc. Roy. Soc. Lond. A* **146** (1934) 83–112.

[126] ATLAS collaboration, *Technical Design Report for the ATLAS Inner Tracker Pixel Detector*, Tech. Rep. CERN-LHCC-2017-021. ATLAS-TDR-030, CERN, Geneva, Sep 2017.

[127] B. Rossi and K. Greisen, *Cosmic-ray theory*, *Rev. Mod. Phys.* **13** (1941) 240–309.

[128] V.L. Highland, *Some Practical Remarks on Multiple Scattering*, *Nucl. Instrum. Meth.* **129** (1975) 497.

[129] F. Klimpel, *Track propagation for different detector and magnetic field setups in Acts*, *Journal of Physics: Conference Series* **1525** (2020) 012080.

[130] J.N. Marx and D.R. Nygren, *The Time Projection Chamber*, *Phys. Today* **31N10** (1978) 46–53.

[131] O. Schäfer, "Working Principle of a TPC." https://www.lctpc.org/e8/e57671.

[132] F. Sauli, *Drift and diffusion of charges in gases*, 76–128. Cambridge Monographs on Particle Physics, Nuclear Physics and Cosmology. Cambridge University Press, 2014. 10.1017/CBO9781107337701.006.

[133] F. Sauli, *Collisional excitations and charge multiplication in uniform fields*, 129–159. Cambridge Monographs on Particle Physics, Nuclear Physics and Cosmology. Cambridge University Press, 2014. 10.1017/CBO9781107337701.007.

[134] L. Ounalli, *Micromegas time projection chamber development for rare event detection*, Ph.D. thesis, Neuchatel U., 2006.

[135] F.M. Penning, *Über Ionisation durch metastabile Atome*, *Naturwissenschaften* **15** (1927) 1432–1904.

[136] J. Duchi, "Properties of the trace and matrix derivatives." https://web.stanford.edu/~jduchi/projects/matrix_prop.pdf.

Bibliography

[137] A. Adare, S. Afanasiev, C. Aidala et al., *An Upgrade Proposal from the PHENIX Collaboration*, [arXiv:1501.06197].

[138] "A new collaboration takes aim at understanding how the ultra-hot, ultra-dense plasma that formed our early universe gets its intriguing properties.." https://npl.illinois.edu/news/story.asp?id=17812, June 2016.

[139] R. Frühwirth, *Application of Kalman filtering to track and vertex fitting*, Nucl. Instrum. Meth. A **262** (1987) 444–450.

[140] L. Demortier and L. Lyons, "Everything you always wanted to know about pulls." https://lucdemortier.github.io/assets/papers/cdf5776_pulls.pdf, 2008.

[141] K. Edmonds, S. Fleischmann, T. Lenz et al., *The Fast ATLAS Track Simulation (FATRAS)*, tech. rep., CERN, Geneva, Mar 2008.

[142] R. Frühwirth, *A Gaussian-mixture approximation of the Bethe–Heitler model of electron energy loss by bremsstrahlung*, Computer Physics Communications **154** (2003) 131–142.

[143] Y.S. Tsai, *Pair production and bremsstrahlung of charged leptons*, Rev. Mod. Phys. **46** (1974) 815–851.

[144] C. Allaire, P. Gessinger, J. Hrdinka, M. Kiehn et al., *OpenDataDetector*, Apr. 2021, Zenodo. https://doi.org/10.5281/zenodo.4674402, 10.5281/zenodo.4674402.

[145] A. Buckley, P. Ilten, D. Konstantinov et al., *The HepMC3 event record library for Monte Carlo event generators*, Computer Physics Communications **260** (2021) 107310.

Acknowledgments

Throughout the last couple of years I had the chance to work together and exchange ideas with many people and I am very thankful for everyone that helped me on this journey. As the list of names would be pretty long, I will just mention a few colleagues.

First of all, I would like to thank my colleagues at CERN for the great time and the possibility to learn from you. In this context, I would like to thank Martin for the great fun I had in the last couple of years. Also, I would like to express my thanks to Corentin for helping me on short notice and to Xiaocong for the fascinating discussions. Last but not least, I would like to thank Andi and Markus for their supervising and their guidance down the rabbit hole of tracking.

Mein weiterer Dank richtet sich an das Max-Planck-Institut für Physik. Hier insbesondere an meine Gruppe, die mich durch die letzten Jahre begleitet hat und mich mit regelmäßigem Feedback meine Arbeit reflektieren ließ. Besonders für das letzte Jahr danke ich Stefan, Daniel, Andrii und Ludovic für ihr Feedback zu dieser Thesis. Eure Sichtweise hat mir beim Schreiben dieser Thesis sehr geholfen.

Des weiteren möchte ich mich bei meinem Mitbewohner Martin für die wunderbare Zeit in Crozet bedanken, in der ich von dir lernen und mit dir diskutieren konnte. Auch sei hier Holger erwähnt, der mich seit mehr als zwei Jahrzehnten auf meinen Reisen begleitet. Ich bin überaus dankbar, dich als steten Wegbegleiter zu haben und freue mich auf viele weitere Jahre in denen wir uns austauschen können. Außerdem möchte ich meinen Eltern danken, die meine Reise noch länger miterlebt haben und mich bei meinem Weg unterstützt haben. Vielen Dank für all die Hilfe, die es mir nun ermöglichte diese Thesis zu schreiben.